

Oceanologia

Official Journal of the Polish Academy of Sciences



EDITOR-IN-CHIEF

Jacek Piskozub
Institute of Oceanology, Polish Academy of Sciences, Sopot, Poland

MANAGING EDITOR

Agata Bielecka – abielecka@iopan.pl

Editorial Office Address

Institute of Oceanology, Polish Academy of Sciences (IO PAN)
Powstańców Warszawy 55
81–712 Sopot, Poland
e-mail address: editor@iopan.pl

THEMATIC EDITORS

Katarzyna Błachowiak-Samołyk – Institute of Oceanology, Polish Academy of Sciences, Sopot, Poland

Artur Burzyński – Institute of Oceanology, Polish Academy of Sciences, Sopot, Poland

Piotr Kowalczyk – Institute of Oceanology, Polish Academy of Sciences, Sopot, Poland

Krzysztof Opaliński – Institute of Ecology and Bioethics, Warsaw, Poland

Żaneta Polkowska – Gdańsk University of Technology, Gdańsk, Poland

Krzysztof Rychert – Pomeranian University in Stupsk, Poland

Marek Zajączkowski – Institute of Oceanology, Polish Academy of Sciences, Sopot, Poland

ADVISORY BOARD

Xosé Antón Álvarez Salgado
Marine Research Institute, Spanish Research Council (CSIC), Vigo, Spain

Mirosław Darecki
Institute of Oceanology, Polish Academy of Sciences, Sopot, Poland

Jerzy Dera
Institute of Oceanology, Polish Academy of Sciences, Sopot, Poland

Jan Harff
University of Szczecin, Poland; Leibniz-Institute for Baltic Sea Research, Warnemünde, Germany

Agnieszka Herman
Institute of Oceanography, University of Gdańsk, Gdynia, Poland

Alicja Kosakowska
Institute of Oceanology, Polish Academy of Sciences, Sopot, Poland

Matti Leppäranta
Institute of Atmospheric and Earth Sciences, University of Helsinki, Finland

Ewa Lupikasza
Faculty of Earth Sciences, University of Silesia, Sosnowiec, Poland

Hanna Mazur-Marzec
Institute of Oceanography, University of Gdańsk, Gdynia, Poland

David McKee
University of Strathclyde, Glasgow, Scotland, United Kingdom

Dag Myrhaug
Norwegian University of Science and Technology (NTNU), Trondheim, Norway

Tarmo Soomere
Tallinn University of Technology, Estonia

Hans von Storch
Institute of Coastal Research, Helmholtz Center Geesthacht, Germany

Piotr Szefer
Department of Food Sciences, Medical University of Gdańsk, Poland

Muhammet Türkoğlu
Çanakkale Onsekiz Mart University, Turkey

Jan Marcin Węśławski
Institute of Oceanology, Polish Academy of Sciences, Sopot, Poland

This journal is supported by the Ministry of Science and Higher Education, Warsaw, Poland

Indexed in: ISI Journal Master List, Science Citation Index Expanded, Scopus, Current Contents, Zoological Record, Thomson Scientific SSCI, Aquatic Sciences and Fisheries Abstracts, DOAJ

IMPACT FACTOR ANNOUNCED FOR 2021 IN THE 'JOURNAL CITATION REPORTS' IS 2.526; 5-year IF is 2.778. CITESCORE ANNOUNCED FOR 2021 IS 4.7

Publisher
Elsevier B.V.
Radarweg 29
1043 NX Amsterdam
The Netherlands

Senior Publisher
Tobias Wesselius
+31 6 5370 3539

ISSN 0078-3234

Available online at www.sciencedirect.com

ScienceDirect

journal homepage: www.journals.elsevier.com/oceanologia

ORIGINAL RESEARCH ARTICLE

Coastal cliff erosion as a source of toxic, essential and nonessential metals in the marine environment

Magdalena Bełdowska^a, Jacek Bełdowski^b, Urszula Kwasigroch^a,
Marta Szubska^b, Agnieszka Jędruch^{b,*}

^aInstitute of Oceanography, University of Gdańsk, Gdynia, Poland

^bInstitute of Oceanology, Polish Academy of Sciences, Sopot, Poland

Received 27 December 2021; accepted 15 April 2022

Available online 4 May 2022

KEYWORDS

Metals;
Coastal erosion;
Cliffs;
Sediments;
Baltic Sea

Abstract Due to the rising environmental awareness, emissions and releases of pollutants, including metals, have been considerably reduced in the last decades. Therefore, the remobilization of natural and anthropogenic contaminants is gaining importance in their biogeochemical cycle. In the marine coastal zone, this process occurs during the erosion of a shore, especially the most vulnerable cliffs. The research was conducted in the Gulf of Gdańsk (southern Baltic Sea) from 2016 to 2017. The sediment cores were collected from four cliffs; additionally, marine surface sediments were also taken. The concentrations of essential (Cr, Mn, Fr, Cu, Zn) and nonessential (Rb, Sr, Y, Zr, Ba) metals were analyzed using the XRF technique. The levels of the analyzed metals were relatively low, typical of nonpolluted areas. However, considering the mass of eroded sediments, the annual load of metals introduced into the sea in this way is significant. In the case of Cu, Zn, and Y the load can amount to a few kilograms, for Cr and Rb – over ten kilograms, for Mn, Sr, and Zr – several tens of kilograms, for toxic Ba – over 100 kg, and in the case of Fe – 4.8 tonnes. During strong winds and storms, when the upper part of a cliff is eroded, especially the load of Zn and Cr entering the sea may increase. The content of Cr, Zr, and Ba in the cliffs was higher compared to marine sediments from the deep accumulation bottom, which indicates that coastal erosion may be an important source of these metals.

© 2022 Institute of Oceanology of the Polish Academy of Sciences. Production and hosting by Elsevier B.V. This is an open access article under the CC BY-NC-ND license (<http://creativecommons.org/licenses/by-nc-nd/4.0/>).

* Corresponding author at: Institute of Oceanology, Polish Academy of Sciences, Powstańców Warszawy 55, 81-712 Sopot, Poland.
E-mail address: ajedruch@iopan.pl (A. Jędruch).

Peer review under the responsibility of the Institute of Oceanology of the Polish Academy of Sciences.



<https://doi.org/10.1016/j.oceano.2022.04.001>

0078-3234/© 2022 Institute of Oceanology of the Polish Academy of Sciences. Production and hosting by Elsevier B.V. This is an open access article under the CC BY-NC-ND license (<http://creativecommons.org/licenses/by-nc-nd/4.0/>).

1. Introduction

The main sources of metals in the marine environment are atmospheric deposition and terrestrial runoff. The latter is of particular importance in the coastal zone, especially near the outlets of large rivers. These account for up to 80–90% of the metal load introduced into the Baltic Sea (HELCOM, 2021; Uściłowicz et al., 2011). Direct point sources make the smallest contribution to the total input of metals (about 2%, except Zn, for which they constitute almost 5%). However, as indicated by HELCOM (2021), the role of point sources can be underestimated. One of the potentially important sources, which has been overlooked so far, is the erosion of the shore (Bełdowska et al., 2016). Given the significant volume of sediments introduced into the sea by landslides and other mass movements (Regard et al., 2022), coastal erosion may play a role in the metal budget in the marine environment (Wells et al., 2003), which was demonstrated in the example of the Hg inflow into the Gulf of Gdańsk (Bełdowska et al., 2016; Kwasigroch et al., 2018).

The emission of metals, especially toxic ones, to the environment has been reduced in recent decades. In European and North American countries, high public awareness has led to a series of restrictions and programs aimed at reducing the levels of toxic substances in the environment, e.g., the Clean Water Act (US EPA), the Baltic Marine Environment Protection Commission, more usually known as the Helsinki Convention (Helsinki Commission), the Convention for the Protection of the Marine of the North-East Atlantic, also known as the OSPAR Convention (Oslo and Paris Commissions), the Convention on Long-range Transboundary Air Pollution, often abbreviated as the Air Convention (UNECE), the Stockholm Convention on Persistent Organic Pollutants (UNEP), or the Minamata Convention for Mercury (UNEP). Despite the decrease in emissions in Europe, both from the industry sector (mainly from the energy supply, manufacturing, and extractive industries) and individual households (EEA, 2021), the concentration of many metals in the environment is not decreasing proportionally to the introduced restrictions (HELCOM, 2021; Jędruch et al., 2021). One reason for this situation is the reemission and remobilization of pollutants that have been deposited for decades in soils, land, and sea sediments. These so-called ‘legacies’ have the potential to continue to impact the environment long after they were first introduced (Clarke et al., 2015; Zaborska et al., 2019). The release and mobility of metals from terrestrial and marine deposits may be intensified under climate change-induced alterations of meteorological or hydrological conditions: increased precipitation, thaws, downpours, floods, storms, higher temperatures, and changes in acidic conditions (Bełdowska et al., 2016; Biswas et al., 2018; Saniewska et al., 2014a; Xu et al., 2015). As people are unable to control these processes, it is essential to recognize their scale and significance.

An example of remobilization is the erosion of the shore, which is of particular importance in marine coastal areas. Given recent observations and predictions of climatic evolution in the Baltic Sea basin, the risk of erosion of the Polish coast will increase. The consequences include a higher frequency of extreme weather phenomena, but also a rise in sea level, milder winters, and a decrease in ice cover, which will also increase the exposure of the coast to hy-

drodynamic forces (Bełdowska, 2015; Meier et al., 2022; Różyński and Lin, 2021). The combination of these factors will promote the release of chemical elements accumulated over the years in coastal deposits into the marine environment. In the near past, the average rate of shore retreat in the study area was 0.5 m per year (Zawadzka-Kahlau, 2012). In recent years, an increase in erosion has been observed along most of the length of the Polish coast. Further intensification of this process is also inevitable in the next decades, and the most threatened areas include the vicinity of the Tricity agglomeration (Dubrawski and Zawadzka-Kahlau, 2006; Pruszek and Zawadzka, 2008).

It is continuously discussed which elements should be classified as toxic, beneficial, or essential for living organisms. Nowadays, around 20 of the known elements are defined as essential for humans. It applies to basic organic elements (H, C, N, O), seven macroelements (Na, Mg, P, S, Cl, K, Ca) and several trace elements (Cr, Mn, Fe, Co, Cu, Zn, Se, Mo) (Kabata-Pendias and Mukherjee, 2007; Zoroddu et al., 2019). As for Cr, despite its effect on metabolism, it is sometimes excluded from the list of essential elements (Di Bona et al., 2011; Vincent, 2017). In addition to their beneficial functions, essential elements can be toxic if the dose is high enough, pointing to the principle ‘the dose makes the poison’. Excess of essential trace metals may lead to neurological and metabolic disorders, DNA damage, and promote carcinogenesis (Emsley, 2011) (Table 1). The level of metals listed as priority environmental pollutants (e.g., Hg, Pb, Cd, As, Cr, Cu, Zn) is monitored according to the guidelines of the EU Water Framework Directive and the regulations of the Environment Ministry in Poland (HELCOM, 2021; Zaborska et al., 2019). On the contrary, little is known about the level of trace metals that do not have a known biological role in humans, and their toxicity is moderate. Certain elements have attracted much attention in recent years due to their increased industrial and economic importance. These include elements extensively used in modern technology: advanced electronics, lighting, power generation, medicine, space, and aeronautic industries. These ‘tech metals’ are relatively rare in the environment; however, in recent years, their use has gradually increased and due to future demand, growth will continue to increase in the coming decades (Goodenough et al., 2017; Mikulski et al., 2016). Consequently, the inflow of these metals into the natural environment will increase simultaneously and the environmental consequences of it are difficult to predict given the low number of studies. Therefore, it is important to recognize and estimate the sources of these elements in the sea.

This study aims to determine the inflow of selected essential (Cr, Mn, Fe, Cu, Zn) and nonessential (Rb, Sr, Y, Zr, Ba) trace metals (Table 1) to the marine environment along with the eroded shore, based on the example of the Gulf of Gdańsk (southern Baltic Sea) (Figure 1). Cliffs are one of the clearest examples of coastal erosion. They are also a significant component of world coastal zones (Zelaya Wziątek et al., 2019). Despite that, cliffs have not received as much attention as other possible sources of elements in the marine ecosystem, and their role in the biogeochemical cycle of metals is still poorly recognized. However, as shown in previous works concerning Hg, erosion introduces a significant load of this metal into the marine en-

Table 1 Biological properties and use of the studied metals (Emsley, 2011; Kabata-Pendias and Mukherjee, 2007; Rumble, 2021).

	Beneficial role	Harmful role	Uses
Ba	No known biological role	Toxic: neurological disorders	Geotechnics, metallurgy, electronics, paint and glassmaking, medicine
Cr	Essential: role in insulin metabolism, DNA synthesis	Toxic in excess: damage to the DNA, increased cancer risk, gastrointestinal disorders	Metallurgy, aerospace, military, automotive, manufacture of many everyday items
Cu	Essential: important components of many enzymes, energy transfer in cells	Toxic in excess: brain, cardiac and gastrointestinal disorders	Electronics, civil engineering, industrial machinery, agriculture
Fe	Essential: blood production, oxygen and electron transport, DNA synthesis	Toxic in excess: cardiac and gastrointestinal disorders, increased cancer risk	Metallurgy, civil engineering, oil and petroleum industry, aerospace, automotive, medicine
Mn	Essential: a cofactor for many enzymes	Toxic in excess: anaemia, depression, neurological disorders, impotence	Metallurgy, electronics, paints, medicine
Rb	No known biological role	Toxic in higher concentrations: growth and reproduction disorders	Various electronic and chemical applications, medicine
Sr	No known biological role	Toxic in higher concentrations: calcium metabolism disorders leading to e.g. bone diseases	Various electronic applications, medicine
Y	No known biological role	Toxic: lung diseases, increased cancer risk	Various electronic and chemical applications, medicine applications
Zn	Essential: involved in numerous aspects of cellular metabolism	Toxic in excess: increased cancer risk, immune system suppression	Metallurgy, civil engineering, electronics, manufacture of many everyday items, medicine
Zr	No known biological role	Toxic in higher concentrations: lung diseases	Nuclear power stations, superconducting magnets, aerospace, many biomedical applications

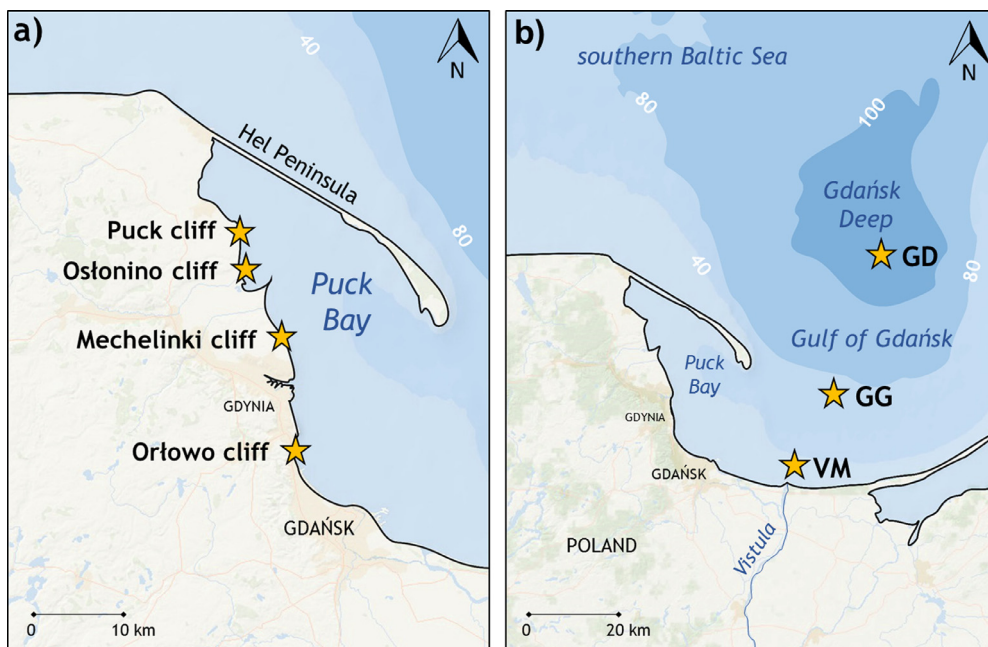


Figure 1 Location of sampling stations in the Gulf of Gdańsk (southern Baltic Sea) and the type of collected material: a) cliff sediments, b) marine sediments (VM – Vistula mouth, GG – Gulf of Gdańsk, GD – Gdańsk Deep).

vironment, acts as its nonpoint source, and should not be neglected (Beldowska et al., 2016; Jędruch et al., 2017; Kwasigroch et al., 2018). As evidenced by Andriolo and Gonçalves (2022), coastal erosion can also be accounted as a diffuse source of marine littering pollution. Given that the eroded sediments are mostly fine-grained, they can easily be transported to distant regions and deposited in the deeper areas of the bottom. Therefore, our objective was also to estimate the distribution of metals in marine sediments under specific depositional conditions.

2. Material and methods

2.1. Study area

The Polish shore is a nontidal area with short-term sea level variations. Its coastal forms are mainly composed of loose sand, till, and peat, which results in low durability and vulnerability to degradation processes. Cliffs occupy about 20% (about 101 km in total) of the length of the Polish coast (without internal lagoons) (Łabuz, 2014; Uścińowicz et al., 2004). The genesis of the cliffs goes back to the Littorina transgression, during which they were formed in postglacial formations composed of Quaternary deposits, Pleistocene tills, clays and sands on moraine uplands, and Holocene muds and sands on lowlands. On the western coast of the Gulf of Gdańsk, Tertiary (Miocene) sandy and sandy-clayey deposits are also cropped out in the cliffs (Mojski, 2000; Uścińowicz et al., 2004). The rate of coastal cliff retreat depends on its geological structure, as well as factors controlling coastal hydrodynamics (e.g., wave climate, sea-level fluctuations, coastal orientation, and antecedent or nearshore morphology).

Waves are mainly responsible for the destruction of the cliffs of the Gulf of Gdańsk, triggering landslides and subsidence processes. Storm surges and extreme meteorological events are the most important factors in the development of cliff slopes (Zaleszkiewicz and Koszka-Maróń, 2005). These phenomena are episodic, and their frequency varies throughout the year. However, over the past decades, the number and intensity of storms in the study area has been increasing (Różyński and Lin, 2021; Stanisławczyk, 2012). The coastline is also shaped by weathering, erosion, and mass movements, the extent of which depends on the type of rock, the geometry of the cliff slope, and the vegetation. Flushing of slopes caused by rainwater and snowmelt also plays an important role in the studied area. Unlike extreme phenomena, these processes have a continuous character (Zaleszkiewicz and Koszka-Maróń, 2005). The magnitude and occurrence of coastal erosion are also affected by and anthropogenic activities, which generally accelerate the process (Janušaitė et al., 2021; Różyński and Lin, 2021).

The catchment of the Gulf of Gdańsk has an agricultural and forestry character. Agriculture constitutes about half, while 30–40% is forested. Artificial surfaces account for about 5–6% of the region's area, with their share gradually increasing, particularly transportation networks, commercial, industrial, and housing areas (Bielecka et al., 2020). Gdańsk (Figure 1), the largest city in the studied region, forms together with Sopot and Gdynia the Tricity agglom-

eration. In 2021, Tricity was inhabited by 750,000 people, while its metropolitan area had a population of between 1 and 1.5 million people, depending on the definition of its boundaries. Tricity is a large industrial center related mainly to the maritime economy. The chemical, machinery, metal, and electronics industries have also developed in agglomeration. Tricity is also an important transport hub (air, sea, rail and road). In the rest of the region, the economy is based mainly on agriculture, fishing, and the food and wood processing industries. Combined heat and power plants, a refinery and shipyards contribute the most to air pollution by metals (<http://emgsp.pgi.gov.pl>).

The research was conducted in the area of four cliffs located on the western coast of the Gulf of Gdańsk: Orłowo (650 m in length, 1544 m high), Mechelinki (250 m in length, 25–30 m high), Ostonino (400 m in length, 15 m high) and Puck (500 m in length, 10 m high) (Figure 1a). The most active part of the Gulf of Gdańsk shore is the Orłowo cliff. The other three cliffs are characterized by a much less retreat rate due to the protective nature of the Hel Peninsula (Łabuz, 2013; Zawadzka-Kahlau, 2012) (Figure 1a). The cliff sediments in Orłowo and Ostonino are mostly built of clay mixed with fluvioglacial sands and laminated silts and sandy silts, while in Mechelinki and Puck are dominated by boulder clays with sand and gravel layers (Kaulbarsz, 2005; Łęczyński and Kubowicz-Grajewska, 2013).

2.2. Sample collection

Samples of cliff sediments were collected during three sampling campaigns in June 2016 and March 2017. On each cliff (Figure 1a), three stations were set at intervals of about 50 m. During the study period, the location of the sampling sites remained the same and was determined each time using a high-sensitivity GPS receiver (eTrexH, GARMIN, USA). In the case of cliffs in Mechelinki, Ostonino, and Puck, six sediment cores (0–65 cm) were collected from each cliff using a soil core probe (AMS, USA): three vertical cores, taken from the top of the cliff, and three horizontal cores, taken from the cliff colluvium (Figure 2). The Orłowo cliff is located within a nature reserve (Kępa Redłowska), which made it impossible to collect sediment cores. In this case, the sediments from the colluvium and the top of the cliff were collected manually (approx. 20 cm of the sediment surface layer). In addition, during the r/v *Oceania* cruise in May 2016, with use of the van Veen grab sampler, three samples of surface sediments (approx. top 20 cm) were taken at each of three stations that differed in terms of environmental conditions and sediment characteristics: near the mouth of the Vistula River (VM, depth of 16 m, distance from the shore approx. 5 km, transportation bottom), in the central part of the Gulf of Gdańsk (GG, depth of 70 m, distance from the shore approx. 20 km, area of temporary sediment deposition), and from the Gdańsk Deep (depth of 105 m, distance from the shore approx. 50 km, accumulation bottom) (Burska and Szymczak, 2019; Damrat et al., 2013; Jędruch et al., 2015) (Figure 1b). The total number of sediment samples collected was 129, including 120 cliff sediment samples and 9 samples of marine sediments.

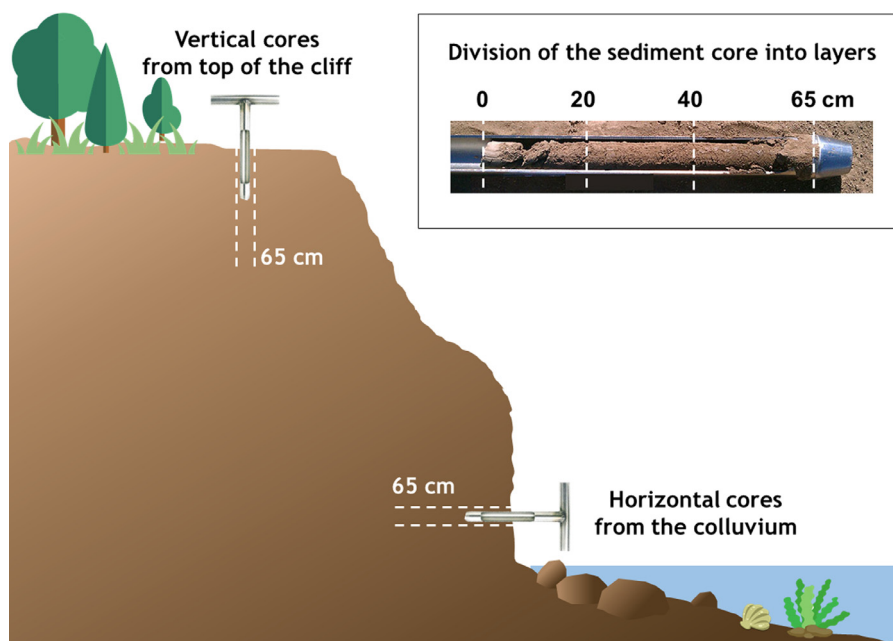


Figure 2 Scheme of the sediment cores collection (reproduced from a study by Kwasiroch et al. (2018) under the terms of the Creative Commons Attribution 4.0 International License <http://creativecommons.org/licenses/by/4.0/>).

2.3. Laboratory analysis

The sediment cores were divided into layers: 0–20 cm, 20–40 cm, and 40–65 cm (Figure 2). Samples for metal analysis were stored in polythene zip-lock bags at -20°C , freeze-dried (Alpha 1–4 LDplus, Martin Christ, Germany) and homogenized in a ball mill (8000D Mixer/Mill, SPEX Sample Prep, USA) with a tungsten vessel immediately before analysis.

The analysis of selected metals (Cr, Mn, Fe, Cu, Zn, Rb, Sr, Y, Zr, and Ba) was performed using X-ray fluorescence spectroscopy (XRF). In this method, atoms of the analyzed material are externally excited by X-rays, making electrons move, which results in the release of energy emitted as photons. Each element emits characteristic energy, the intensity of which increases with the concentration of the element. The XRF technique is characterized by good selectivity and a low detectability limit of ppm-ppb; moreover, it is also fast, cost-effective, and environmentally friendly (Dijair et al., 2020). It also belongs to the nondestructive analytical methods that do not damage the sample under study (Szyzewski et al., 2009). About seven grams of each sample were used to determine the element concentrations, as in the studies by Gashi et al. (2009) and Allafta and Opp (2020). The samples were placed in open-ended XRF cups with a diameter of 40 mm and sealed with a $4.0\ \mu\text{m}$ -thick X-ray film. To perform analysis, a portable XRF (pXRF) analyzer S1 Titan (Bruker, Germany), using the Geochem calibration package designed for trace element analysis in geochemical matrices adjusted for coastal and bottom sediments. XRF readings were performed in triplicate for 60 s in dual soil mode. The final results were obtained by averaging three scanning results. The accuracy of the method was verified using certified reference material JMS-1 – marine sediment (GCJ, Japan) ($78\ \text{mg kg}^{-1}$ of Cr, $22.6\ \text{g kg}^{-1}$ of Mn, $109.6\ \text{g kg}^{-1}$ of Fe, $447\ \text{mg kg}^{-1}$ of Cu, $166\ \text{mg kg}^{-1}$ of Zn,

$65\ \text{mg kg}^{-1}$ of Rb, $454\ \text{mg kg}^{-1}$ of Sr, $254\ \text{mg kg}^{-1}$ of Y, $220\ \text{mg kg}^{-1}$ of Zr and $1.8\ \text{g kg}^{-1}$ of Ba), which was analyzed five times, at the beginning of each measurement series. The recovery values of the method were, respectively: 96.0% for Cr, 102.3% for Mn, 100.4% for Fe, 95.7% for Cu, 95.5% for Zn, 94.2% for Rb, 98.1% for Sr, 96.9% for Y, 92.6% for Zr, and 97.1% for Ba. The precision of the analysis, given as a relative standard deviation, is equal to 1.3% for Cr, 1.9% for Mn, 0.8% for Fe, 0.5% for Cu, 1.2% for Zn, 1.5% for Rb, 0.9% for Sr, 1.6% for Y, 1.4% for Zr, and 0.8% for Ba.

The physical parameters of the collected sediments were also analyzed. The content of water (W) was determined by drying the sample at 60°C for 24 h, while the content of organic matter (OM) in sediments was determined using a loss of ignition (LOI) at 550°C for 6 h. The granulometric composition of sediments was investigated by sieve analysis using a mechanical shaker for 10 min, through the following mesh sizes: 2.0, 1.0, 0.5, 0.25, 0.125, and 0.063 mm. Sediments with a diameter below 0.063 mm were defined as a fine particle sediment fraction (FSF).

2.4. Cliff erosion analysis

A load of individual metals introduced to the Gulf of Gdańsk with coastal erosion was estimated based on its concentration in cliff sediments and the mass of deposits crumbling to the sea during the year. A sedimentary material was calculated by analyzing the temporal changes in the active layer of deposits of the investigated cliffs with the use of an airborne laser scanning (ALS) technique using a light detection and ranging (LiDAR) sensor. The LiDAR surveys were conducted in 2009 and 2013 by the ZUI Apeks geodetic company, providing a 4-year period to analyze changes in cliff profiles. Scanned sections included cliffs in Ortowo, Mechelinki, and Ostonino (Figure 1a) with a total length of about 1.3 km. Based on LiDAR data (density: $7.32\ \text{points m}^{-2}$),

high-resolution elevation models of the investigated cliffs were created (vertical resolution: ± 0.15 m, lateral resolution: ± 0.20 m) using SURFER 12 software (Golden Software). A detailed description of spatial data processing was provided in the previous work by Beldowska et al. (2016). Comparative analysis of models from two different periods enables to determine the volumetric changes in cliff profiles (Earlie et al., 2015; Zelaya Wziątek et al., 2019). The mass of the crumbling deposits was calculated with constant sediment density of 2.65 g cm^{-3} – typical values for clays, sandy clays and clay sands (Myślińska, 1992). Based on the results obtained for surveyed cliffs, an average annual sediment loss per km of the cliff shore was calculated (29,460 tonnes). A total load of deposits introduced to the Gulf of Gdańsk was calculated assuming that the combined length of the cliffs along its coast is 3.05 km (Dubrawski and Zawadzka-Kahlau, 2006). To estimate the present load of metals, concentrations in the surface layer (0–20 cm) of colluvium were used (Figure 2). To calculate the load introduced to the sea during extreme events, concentrations measured in sediments collected from the top (0–60 cm) of the cliff were used. Estimation of the future load was based on metal concentrations in deeper layers of colluvial sediments (0–40 cm).

2.5. Processing of results

Statistical analysis was carried out using STATISTICA 12 software (StatSoft). To assess the distribution of the data, the Shapiro-Wilk normality test was used ($\alpha=0.05$). Except for Rb ($p=0.09$), data on the concentrations of most investigated elements were not normally distributed ($p<0.05$). Therefore, to determine the strength and direction of association between the analyzed variables the nonparametric Spearman rank-order correlation coefficient (ρ) was used ($\alpha=0.05$). All calculations for sediment grain size statistical parameters were performed using the GRADISTAT 9.1 software package (Blot and Pye, 2001) running in Microsoft Excel 365. The grain size of the sediments was determined on the Wentworth (1922) classification. To describe the relationship between the size fractions, the Folk's (1974) scheme was used. The map of the study area with the distribution of sampling stations was created using ArcGIS 10.4.1 software (ESRI).

3. Results and discussion

3.1. Lithologic features of sediments

Samples of sediments collected from cliffs had grains of varying sizes (from silt-sized particles with diameters below 0.063 mm to gravel with grains over 2 mm) and were mostly poorly sorted, which is characteristic for glacial sediments, deposited by the slow plowing action of an ice sheet (Easterbrook, 1982). Based on texture, the cliff sediments were mostly classified as silty sands (Table 2), which is consistent with the results of previous studies (Beldowska et al., 2016; Woźniak and Czubała, 2014). The contribution of FSF ranged from 3.9 to 27.8%, however, the vertical cores of sediments collected from the top of the

cliff contained more than two times more FSF and OM (17.8% and 5.0% on average, respectively) compared to horizontal cores from the colluvium (7.9% and 1.9% on average, respectively), which was influenced by eluviation of these constituents from the top soil. The physical sediment properties of the studied cliffs were similar, although in the Puck cliff the proportion of FSF and OM was the lowest, while the content of coarse sediments (sand and gravel) was the highest. Given the lithological and morphogenetic criteria, all investigated cliffs were classified as sandy-clay and fall-landslide types, respectively (Kostrzewski et al., 2020).

The distribution of surface sediments in the Gulf of Gdańsk followed the general scheme of grain sorting in the water bodies distribution of sediments in the Gulf of Gdańsk and was associated with water depth and energy of the environment (Łukawska-Matuszewska and Bolątek, 2008). The samples collected in the shallow water area of the Vistula mouth (VM) were poorly sorted and dominated by fine-grained sands (Table 2). It is typical of a dynamic estuarine environment, in which the movement of sea water is generated by a number of factors, including the inflow of Vistula waters, waves, as well as surface and near-bottom currents. An interplay of these factors prevents the sedimentation of fine particles near the mouth and determines their remobilization, transport, and redeposition (Damrat et al., 2013; Szymczak and Burska, 2019). Consequently, sediments from the VM station contained significantly less FSF and OM (20.6% and 5.8%, respectively) than sediments deposited in the deeper areas of the Gulf of Gdańsk. The sediment properties of the samples collected in the central part of the Gulf of Gdańsk (GG) and Gdańsk Deep (GD), known as the depositional bottom (Burska and Szymczak, 2019; Kwasigroch et al., 2021), were similar to each other: they both mainly consisted of sandy silts and contained 34.1–35.2% of FSF and 12.4–14.3% of OM.

3.2. Concentration of metals in cliff sediments

The concentration of the investigated essential (Cr, Mn, Fe, Cu, Zn) and non-essential (Rb, Sr, Y, Zr, Ba) metals in the horizontal cores of sediments collected at the base of the cliff colluvium and the vertical cores taken from the top of the cliff in Orłowo, Mechelinki, Ostonino and Puck was characteristic of sediments from uncontaminated areas (Kabata-Pendias and Mukherjee, 2007). Taking into account the median, the concentrations of metals increased as follows: Cu (9.3 mg kg^{-1}) < Y (14.0 mg kg^{-1}) < Zn (20 mg kg^{-1}) < Rb (50.7 mg kg^{-1}) < Cr (60.3 mg kg^{-1}) < Sr (62.2 mg kg^{-1}) < Zr (164.0 mg kg^{-1}) < Mn (200.0 mg kg^{-1}) < Ba (273.7 mg kg^{-1}) < Fe (13 g kg^{-1}) (Figure 3). The lowest concentration variability was found for Cu, Zn, Cr, and Rb, and the highest range was found for Fe values (Table 3). The strongest positive correlations were found between Fe, Zn, and Rb ($\rho=0.77$ and higher, $p<0.05$), which indicate the similar geochemical behavior or common origin (Algül and Beyhan, 2020). The concentrations of Fe, Cu, Rb and Sr correlated with the content of fine sediment fraction ($\rho=0.43$, $\rho=0.40$, $\rho=0.46$, $\rho=0.48$, respectively, $p<0.05$) (Table 4). This is related to the fact that fine sediment particles have a higher ability to adsorb metals due to the increase of specific surface area, the presence of clay minerals, as well as Fe and Mn oxides (Jędruch et al., 2015; Pempkowiak, 1997;

Table 2 Physical characteristics of the cliff and marine sediments (values are medians and ranges).

Sediment type	Station	layer	N	Textural group	FSF (%)	OM (%)	W (%)
Cliff	Orłowo	H	6	Silty sand	10.1 (9.8–10.3)	2.9 (2.8–3.1)	6.6 (6.2–7.1)
		V	6	Silty sand	24.9 (22.3–27.8)	8.4 (8.1–9.0)	8.5 (8.1–8.8)
	Mechelinki	H	18	Sand	7.9 (6.8–10.2)	2.4 (1.4–3.0)	6.4 (5.8–7.5)
		V	18	Silty sand	17.5 (12.2–22.9)	5.7 (4.6–6.5)	7.6 (5.8–9.6)
	Ostonino	H	18	Silty sand	10.1 (8.8–11.8)	1.6 (1.3–2.3)	6.7 (4.9–8.6)
		V	18	Silty sand	19.0 (14.2–24.2)	5.0 (3.2–8.1)	6.4 (4.9–7.9)
	Puck	H	18	Fine sand	4.5 (3.9–5.1)	1.4 (1.0–2.2)	6.4 (6.1–7.0)
		V	18	Silty sand	14.4 (6.9–22.8)	3.2 (1.5–5.5)	8.0 (4.3–14.5)
Marine	VM	T	3	Fine sand	20.6 (19.9–21.0)	5.8 (5.7–6.0)	48.4 (47.4–49.8)
	GG	T	3	Sandy silt	35.2 (34.8–35.7)	14.3 (14.2–14.4)	66.1 (65.2–66.7)
	GD	T	3	Sandy silt	34.1 (33.8–34.3)	12.4 (12.1–12.6)	71.1 (70.5–71.6)

VM – Vistula mouth, GG – Gulf of Gdańsk, GD – Gdańsk Deep

H – horizontal core, V – vertical core, T – top

N – number of samples, FSF – fine sediment fraction, OM – organic matter, W – water content

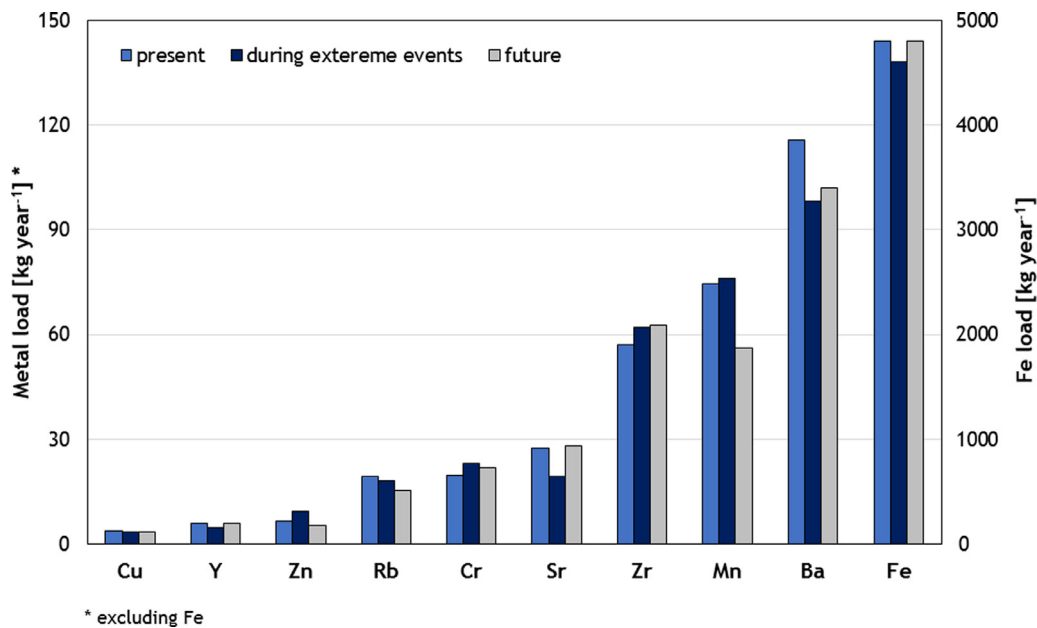


Figure 3 Load of metals entering the Gulf of Gdańsk along with the coastal erosion: at present with eroded colluvium, during extreme events with eroded top of the cliff, and in the future with deeper layers of sediments.

Yao et al., 2015). The formation of metal complexes with Fe and Mn oxides was manifested in the dependence of Cu, Zn, Rb, and Zr concentrations on the content of Fe ($\rho=0.57$, $\rho=0.87$, $\rho=0.81$, $\rho=0.66$, respectively, $p<0.05$) and Mn ($\rho=0.47$; $\rho=0.57$, $\rho=0.48$, $\rho=0.44$, respectively, $p<0.05$) (Table 4). However, the lack of correlation between Fe and Mn ($\rho=0.01$, $p>0.05$) in cliff sediments may indicate an anthropogenic origin of one of these elements (Skorbitowicz et al., 2020). The anthropogenic impact may also be evidenced by the absence of relationships between metal concentrations and both FSF and OM contributions (Algül and Beyhan, 2020; Jędruch et al., 2015), found for Zn ($\rho=0.24$ and $\rho=-0.20$ respectively, $p>0.05$) and Y ($\rho=0.14$ and $\rho=-0.11$ respectively, $p>0.05$).

The anthropogenic origin of metals in cliff sediments of the Gulf of Gdańsk is primarily related to the proximity to a large urban center. Average metal concentrations in the

Tricity agglomeration area were higher compared to values in soils of undeveloped areas located by the Gulf of Gdańsk, especially in the case of Cu, Zn and Cr (Bielicka et al., 2009; Falandysz et al., 2011; <http://emgsp.pgi.gov.pl>). Therefore, this indicates the deposition of metals close to point emission sources. In contrast to areas far from potential pollution sources, higher metal concentrations were also found in plants (sea buckthorn *Hippophaë rhamnoides*) and fungi (king bolete *Boletus edulis*, fly agaric *Amanita muscaria*), considered indicator species, collected in the Tricity area (Falandysz et al., 2011, 2018; Prądyński et al., 2010), as well as the algae *Enteromorpha* spp. collected in the urbanized coastal zone (Haroon et al., 1995). Elevated concentrations of metals, especially Cr, were also found in the sediments of streams and reservoirs in the Tricity area (Wojciechowska et al., 2019). However, apart from a few exceptions, the measured values were well below the ac-

Table 3 Statistical characteristic of metal concentrations [mg kg^{-1}] in cliff sediments (SD – standard deviation, SE – standard error).

	Mean	Median	Minimum	Maximum	SD	SE
Cr	60.1	60.3	27.7	86.3	13.9	2.0
Mn	216.7	200.0	102.3	386.7	82.4	12.0
Fe	13 819.3	12 924.5	4 839.7	32 935.0	6 018.6	877.9
Cu	10.5	9.3	6.0	21.3	3.3	0.5
Zn	22.1	20.0	8.0	46.0	10.1	1.5
Rb	50.8	50.7	29.5	85.0	14.5	2.1
Sr	69.2	62.2	40.0	130.2	22.7	3.4
Y	16.4	14.0	8.0	82.0	13.5	2.0
Zr	159.3	164.0	24.3	262.0	58.9	8.6
Ba	260.2	273.7	102.0	559.0	108.9	15.9
FSF	13.2	12.5	2.9	26.5	6.3	0.9
OM	3.3	2.6	0.7	8.2	2.2	0.3

FSF – fine sediment fraction, OM – organic matter.

Table 4 Spearman's rank-order correlation matrix of metal concentrations and physical characteristics of cliff sediments (values marked with a star symbol are statistically significant, $p < 0.05$).

	Cr	Mn	Fe	Cu	Zn	Rb	Sr	Y	Zr	Ba	FSF	OM
Cr		0.44*	-0.39*	-0.11	-0.06	-0.28*	-0.16	0.41*	-0.42*	1.00	-0.23*	-0.08
Mn	0.44*		0.01	0.47*	0.58*	0.48*	0.08	0.65*	0.44*	0.44*	-0.12	-0.34*
Fe	-0.39*	0.01		0.58*	0.87*	0.81*	0.47*	-0.00	0.65*	-0.39*	0.43*	0.32*
Cu	-0.11	0.47*	0.58*		0.60*	0.54*	0.48*	0.18	0.30*	-0.11	0.40*	-0.14
Zn	-0.06	0.58*	0.87*	0.60*		0.77*	0.13	0.46*	0.46*	-0.06	0.27	0.20
Rb	-0.28*	0.48*	0.81*	0.54*	0.77*		0.45*	0.36*	0.77*	-0.28*	0.47*	0.29*
Sr	-0.16	0.08	0.47*	0.48*	0.13	0.45*		0.23*	0.35*	-0.16	0.49*	0.33*
Y	0.41*	0.65*	-0.00	0.18	0.46*	0.36*	0.23*		0.59*	0.41*	0.14	-0.11
Zr	-0.42*	0.44*	0.65*	0.30*	0.46*	0.77*	0.35*	0.59*		-0.42*	0.31*	0.03
Ba	0.08	0.23	0.08	0.17	0.09	0.19	-0.04	0.14	0.02		0.07	-0.23
FSF	-0.23*	-0.12	0.43*	0.40*	0.27	0.47*	0.49*	0.14	0.31*	0.07		0.62*
OM	-0.08	-0.34*	0.32*	-0.14	0.20	0.29*	0.33*	-0.11	0.03	-0.23	0.62*	

FSF – fine sediment fraction, OM – organic matter.

ceptable metal concentrations. As shown in the study by Falandysz et al. (2011), the concentrations of metals, including Mn, Fe, Cu, Zn, Sr, and Ba, in soils in the study area were similar to or lower than in soils in the Polish territory, especially those located in its heavily industrialized southern part of the country. Relatively low level of metals in the soils of the investigated area may be related with the outflow of metals to the Gulf Gdańsk. Given that watercourses are mostly regulated and their catchments are strongly modified by humans, the retention of chemicals in soils is low (Saniewska et al., 2014b; Wojciechowska et al., 2019). Therefore, the gradual growth of artificial surfaces and urbanized lands in the last decades, especially in the Tricity agglomeration, may contribute to the increased runoff of metals to the Gulf of Gdańsk (Bielecka et al., 2020). This indicates that the decrease in metal concentrations in the topsoil of the Tricity observed since the 1990s (Jędruch et al., 2021) may be attributed not only to the reduction of anthropogenic emission but also to the more intensive outflow of metals to the marine environment.

Cliffs of the Gulf of Gdańsk contained significantly less Cr, Fe, Cu, Zn, and Zr compared to cliffs of the Kerala coast

(southwestern India) (Renjith et al., 2021). The level of elements in deposits of Kerala cliffs was from three (for Zn) to almost 30 times (for Fe) higher than in cliffs investigated in this study. The concentrations of Rb, Sr and Ba in both regions were similar, whereas in the case of Mn and Y higher values were measured in deposits from the Gulf of Gdańsk coast. However, given the differences in geology, it is difficult to compare the results of these regions with each other. Beaches of Kerala are world-famous for their heavy mineral concentration, especially Fe minerals, e.g., jarosite and ilmenite. In addition to the geology of the hinterland, the Kerala cliffs are also influenced by subtropical to tropical climates. A consequence is the varied structure of the cliffs, which consist of arkosic sand, kaolinitic sandy clay carbonaceous clay, and peat with plant remains (Singh et al., 2016).

The concentrations of metals in cliffs of the Gulf of Gdańsk were similar to values measured in sediments collected from bluffs along the Chincoteague Bay coast (Maryland, USA) (Wells et al., 2003). Maryland coastal bays generally have low levels of metals (US EPA, 2002); therefore, given the same sandy-clay type of deposits at both locations, it can be concluded that metal burdens in sediments

are comparable. However, the contribution of FSF in sediments eroded from the Chincoteague Bay coast (54.7% on average) (Wells et al., 2003) was a few times higher than in cliffs investigated in this study (Table 2). On the other hand, the bluff sediments contained significantly less OM (approx. 0.1% on average) compared to the cliff sediments of the Gulf of Gdańsk. As confirmed by higher ρ values (Table 4), the FSF content was the strongest factor determining the concentration of elements than OM in the case of both studies. Taking into account the differences in textural composition, the FSF-normalized metal concentrations in the Polish cliffs were, therefore, higher than in Chincoteague Bay.

In the case of the Baltic Sea, metal levels, other than Hg (Bełdowska et al., 2016; Kwasigroch et al., 2018), in cliff sediments have not been investigated so far. However, there are some studies on metal concentrations in deposits of southern Baltic beaches (Antonowicz et al., 2017; Karlonienė et al., 2021; Kupczyk et al., 2021). The concentrations measured in beach sands were lower than in cliff sediments: a few times for Zn, a few to about a dozen times for Cu and Mn, and several dozen times for Cr and Fe. The lower level of metals in beach deposits reflects the overall lower content of silt fractions in comparison to clays from cliffs. These differences may also indicate that Cr and Fe are adsorbed mainly on fine-grained particles, which are usually washed away from sandy sediments. Silty sediments of the southern Baltic Sea are mostly composed of micas and clay minerals (e.g., illite, glauconite, montmorillonite) which serve as a sink for Fe and Cr. On the other hand, metals such as Zn, Cu, and Mn co-occur with coarser quartz particles and are associated with heavy minerals (e.g., ilmenite, garnet, amphibole) or terrigenous carbonates (Karlonienė et al., 2021; Mikulski et al., 2016; Uścińowicz, 2011; Uścińowicz and Sokółowski, 2011; Wajda, 1970).

3.3. Load of metals released to the sea

Coastal erosion has been identified as an important source of sediments to the marine environment (Janušaitė et al., 2021; Łabuz, 2014; Uścińowicz et al., 2011; Wells et al., 2003). Along with sediments, chemicals sorbed onto particles are also released into the water, turning cliffs into a possible nonpoint source, which affects the quality of the coastal zone (Jędruch et al., 2017; Karlonienė et al., 2021; Wells et al., 2003). The impact of eroded coast on the input of chemical elements, including metals, to the sea, is rarely considered by researchers or monitoring institutions. Therefore, attempts to quantify that contribution and compare it to other sources are seldom (Jarsjö et al., 2017; Karlonienė et al., 2021). However, as shown in previous studies by Bełdowska et al. (2016), coastal erosion is the third most significant source of Hg introduced to the Gulf of Gdańsk, after rivers and wet atmospheric deposition. It should be noted that nearly all the riverine input of Hg to the Gulf of Gdańsk is introduced by the Vistula, the second largest river that disembogues into the Baltic Sea (Figure 1b). In comparison to the smaller, local rivers (e.g., Reda, Kacza, and Gizdepka), the importance of coastal erosion is more meaningful. It was shown that coastal erosion introduces to the sea over 13 times more Hg than these rivers combined (Bełdowska et al., 2014, 2016). If the contribution of the

Vistula River is not included in the Hg budget in the Gulf of Gdańsk, the significance of coastal erosion increased to more than 30% of the Hg load reaching the basin. It means that the abrasion process may be a particularly significant source of Hg in areas far from the mouths of large rivers or in bays without major river outlets.

The erosion of the foot slope of the cliff is the main factor responsible for the formation of landslides and other mass movements (Kostrzewski et al., 2020; Uścińowicz et al., 2004). On the Polish coast, erosion is mainly caused by meteorologically forced storm surges. Storms are mostly recorded in the fall-winter months, from November to February. Storm surges are not a regular annual event. Their number differs from year to year, from a few to a dozen or so (Łabuz, 2014; Stanisławczyk, 2012). During storm surges of a relatively small scale, mainly the surface layer of a cliff face, located at the foot of the colluvium, is destroyed. A load of sediments released into the Gulf of Gdańsk with eroded cliffs was estimated at 89,854 tonnes annually (Bełdowska et al., 2016). Taking into account median concentrations of the investigated metals in sediments collected from the surface layer of the colluvium (first 20 cm of horizontal core), coastal erosion is responsible for introducing to the Gulf of Gdańsk following loads: several kilograms of Cu, Y and Zn, over ten kilograms of Rb and Cr, up to a few tens of kilograms of Sr, Zr, and Mn, over 100 kg of Ba, and as much as 4.8 tonnes of Fe (Figure 4).

Shore destruction is more significant when two or more storm surges occur in succession during a single season. However, the most dangerous are the most severe extreme storms. Along the coast of the southern Baltic, the number of such events is more than a dozen per decade (Łabuz, 2014). In the future, the frequency and strength of storms are expected to increase (Różycki and Lin, 2021). During the most severe storms, when the cliff wall is largely destroyed, also the upper part of the cliff may crumble. Given that the top of the cliff is often overgrown with trees and shrubs, the soil and underlying layers of sediments have different chemical compositions and sorption properties. Along with large landslides disturbing the upper parts of the cliff wall, the input of metals introduced into the sea changes. Compared to the load released into the Gulf of Gdańsk with eroded colluvium, the input of metals during extreme events may increase. As evidenced by the analysis of vertical cores of sediments taken from the top of the investigated cliffs, the load can increase by 41% for Zn, 18% for Cr, 9% for Zr, and 2% for Mn. On the other hand, for some of the elements, the load can be reduced by: 29% for Sr, 20% for Y, 15% for Ba, 8% for Cu, 6% for Rb, and 4% for Fe (Figure 4). These differences may be related to the natural occurrence of metals in cliff deposits, mainly associated with their mineralogical composition and the content of the fine fraction or organic matter. However, surface soil and underlying sediments may be affected by human activity. This substantial enrichment of cliff-top sediments in Zn is probably an effect of atmospheric deposition of metal and its infiltration with rainfall, especially as Zn in precipitation in the coastal zone of the Gulf of Gdańsk is of anthropogenic origin (Szefer, 1990).

Currently, erosion affects the surface layer of the cliff face and the colluvium (0–20 cm). Estimation of changes in a metal load along with cliff erosion in the future was car-

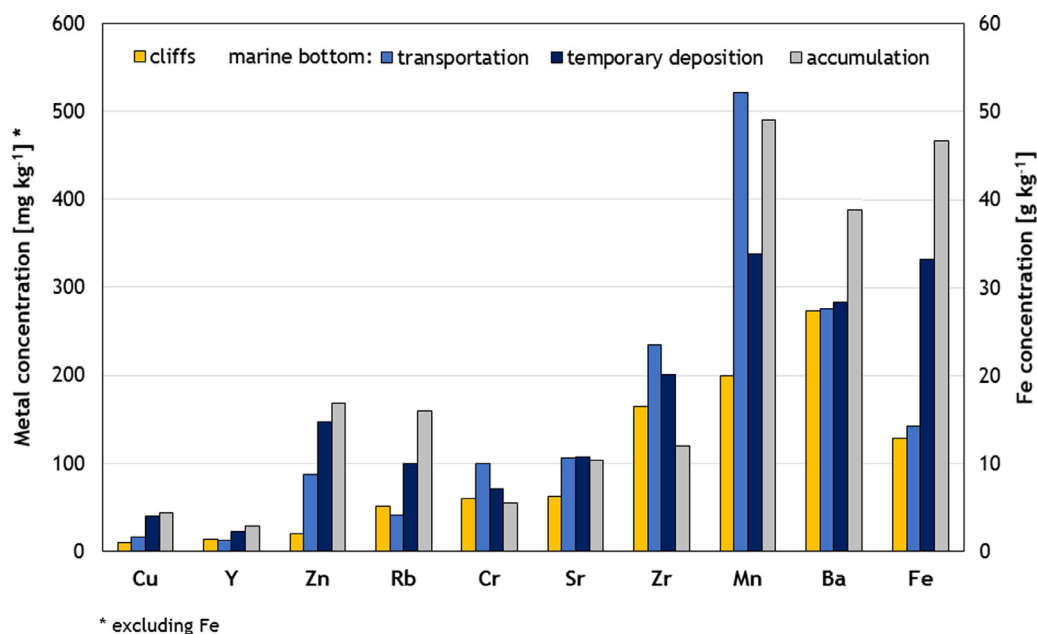


Figure 4 Concentrations of metals in sediments of a cliff and different types of marine bottom: transportation bottom (VM – Vistula mouth), area of temporary deposition of sediments (GG – Gulf of Gdańsk), and accumulation bottom (GD – Gdańsk Deep).

ried out based on the concentrations of metals in deeper layers of sediments (20–40 cm and 40–65 cm sections of the horizontal cores) deposited at the foot of cliffs. The obtained results indicated that a load of some metals introduced into the sea with coastal erosion in the future is expected to increase slightly: 11% for Cr, 10% for Zr, and 3% for Sr (Figure 4). On the other hand, the inflow of some metals will be lower: 25% for Mn, 21% for Rb, 20% for Zn, 12% for Ba, 8% for Cu, and 2% for Y, while the load of Fe will remain the same.

3.4. Distribution of metals in marine sediments

Landslides that are dominant mass movements on cliffs with a complex structure, such as those along the Gulf of Gdańsk shore, are most hazardous because they sometimes affect a zone of hundreds of meters away from the cliff edge (Uścińowicz et al., 2004). Consequently, both the metals accumulated in cliff deposits and remobilized from resuspended marine sediments recovered are released into the water. The influence of coastal erosion on metal concentration in the marine environment was previously evidenced in the example of Hg and the Orłowo cliff (Beldowska et al., 2016; Jędruch et al., 2017). After the introduction of a considerable load of eroded sedimentary material into the coastal zone, the concentration of Hg in suspended particulate matter increased almost three times, while, in phytoplankton, a ten-fold increase was observed. This confirms the potential impact of coastal erosion on metal inflow into the marine trophic chain. It should also be noted that these changes occurred as a consequence of a single, one-day event that was engineering work conducted for safety reasons.

Although the concentrations of metals in the cliff deposits were mostly relatively low (Table 3, Figure 4) the in-

fluence of coastal erosion on their input to the sea cannot be ignored. The importance of this source is not related to the high concentration of metals in cliff sediments, but to the large mass of sediments introduced into the marine environment annually. Fine-grained sediments eroded from the cliff are quickly washed out of the coastal zone and transported to deeper parts of the bottom. The area considered to be the site of final sediment deposition in the Gulf of Gdańsk is the Gdańsk Deep (Burska and Szymczak, 2019). Nevertheless, fine-grained sediments also temporarily accumulate in shallower places, e.g., Puck Bay or the Vistula River prodelta (Damrat et al., 2013; Sokółowski et al., 2021) (Figure 1). Given the complex pattern of surface and bottom currents, the fate of sediments delivered to the Gulf of Gdańsk is difficult to determine (Zachowicz et al., 2002). Identification of the origin of deposited particles is difficult due to the variety of sources of terrigenous matter, e.g., eroded cliffs, rivers, soils, snowmelt water (Jędruch et al., 2017; Sokółowski, 2009).

Cu, Y, and Zn in the cliff sediments were similar to those measured in the sands of the southern Baltic Sea, in which their concentrations were, respectively: below 20 mg kg⁻¹, between 6 and 69 mg kg⁻¹, and between 5 and 50 mg kg⁻¹ (Mikulski et al., 2016; Uścińowicz et al., 2011). The same applies to Mn and Fe, belonging to the main constituents of the Baltic Sea sediments. In the cliff sediments, the levels of these elements were low, close to the typical values for sand sediments, in which they represented 10 to 9,500 mg kg⁻¹, and not more than 19 g kg⁻¹, respectively (Uścińowicz and Sokółowski, 2011). In the case of Rb, Cr and Sr, their concentrations in cliff deposits were higher relative to sand, but comparable to fine-grained silty clay sediments of the southern Baltic Sea, in which they were around 60 mg kg⁻¹ for Rb and from 40 to 70 mg kg⁻¹ for both Cr and Sr (Kumblad and Bradshaw, 2008; Uścińowicz et al., 2011). The level of Zr in southern Baltic sediments is not well recog-

nized, as previous studies have focused on possible Zr concentrates, including Fe-Mn nodules. However, the level of Zr in cliff sediments was high enough to be comparable to values measured in metal-rich nodules in a range of 110 to 185 mg kg⁻¹ (Szamalek et al., 2018). The amount of Ba in the cliff sediments was also elevated, higher than in the silt-clay deposits, which contained 100 to 200 mg kg⁻¹. Concentrations of Ba similar to the values measured in cliffs occurred only locally in the soft bottom of the southern Baltic, in the Eastern Gotland and the Gulf Basin (Uścińowicz et al., 2011). The results obtained indicate that the investigated cliffs are not a significant source of Cu, Y, Zn, Mn, and Fe in the sediments of the southern Baltic Sea. Instead, they may, to some extent, be a source of Rb, Cr, and Sr, whereas, in the case of Zr and Ba, the influence of cliffs seems undeniable. For Ba, the level measured in cliff deposits was also a few times higher than found in river sediments in Poland (below 52 mg kg⁻¹), as well as alluvial deposits in Germany, Denmark, Lithuania and Latvia (up to 128 mg kg⁻¹) (Bojakowska, 2011). The high content of Ba in the cliff deposits is probably due to the presence of feldspar and plagioclases, as well as terrigenous Ba sulfate (Szamalek et al., 2018).

In coastal areas, especially in estuaries, rivers are generally the most important source of metals in marine sediments (Betdowska et al., 2021; HELCOM, 2021). Rivers transport metals washed out from the catchment area and those originating from treated and untreated sewage. Therefore, the concentrations of metals in the bottom sediments increase in the areas where riverine material is transported and deposited. It is confirmed by the higher concentrations of Zn, Cr, Sr, Zr, and Mn in sediments collected from the station located near the mouth of the Vistula River (VM), compared to the concentration of these metals in the cliffs (Figure 4). Due to the dynamics of the sedimentary environment, only a small part of the material carried by the Vistula is deposited near its mouth. It is estimated that more than two thirds of the sediment mass can be remobilized and then redeposited in deeper parts of the Gdańsk Basin (Damrat et al., 2013). The distance from the mouth of the river significantly influences sediment accumulation rates and the fate of sediments in the Gulf of Gdańsk. As it increases, the terrigenous material is dispersed in seawater, and the metal load reaching the sediments is diluted.

The decrease in concentrations, resulting from the mixing of river material with marine sediments with lower concentration, was recorded for Cr and Zr (Figure 4). Because Cr contents show exponential dependence on the grain size of the sediments and are usually highest in fine-grained sediments (Uścińowicz et al., 2011), elevated Cr concentrations found in sands of the Vistula mouth are most likely an indicator of anthropopressure. This is confirmed by the fact that Cr concentrations measured in sediments collected near the river outlet were approximately 10 times higher than the average Cr content in sands of the southern Baltic Sea (about 10 mg kg⁻¹) (Uścińowicz et al., 2011). They were also a few times higher compared to the Cr level in the sediments of most rivers that flow into the southern Baltic Sea (below 13 mg kg⁻¹) (Bojakowska, 2011). In the case of Zr, its content in coastal sediments was probably related to limited mobility in the marine environment resulting from its high gravity and specific grain shape, as well as chemical resis-

tance (Kabata-Pendias and Mukherjee, 2007; Wajda, 1970). In the second half of the twentieth century, the possibility of obtaining Zr from beaches and marine sands in the southern Baltic region was even taken into consideration (Pilch et al., 1990). However, the amounts of Zr in the sediments of the Gulf of Gdańsk were sub-economic. An increase in concentration with distance from the Vistula mouth was recorded for Cu, Y, Zn, Rb, Sr, Ba, and Fe, which may indicate additional sources of metals. In the case of Cu, Zn, Sr, and Fe, due to their low concentration in cliff sediments, the role of coastal erosion is rather small. For Y, Rb, and Ba concentrations in cliff sediments were similar or higher compared to Vistula mouth sediments, therefore it can be concluded that the role of cliffs in a load of this metal introduced to the Gulf of Gdańsk may be important.

4. Conclusions

In the coming years, as a result of the combination of declining ice phenomena and increased hydrodynamic forces, the abrasion of the southern Baltic coast will accelerate. Consequently, the retreat rate of the most erosion-prone cliffs will most likely increase. Moreover, many parts of the coast that were inactive or persisted in an equilibrium state will be eroded. Although a considerable part of the cliff section of the Polish coast is under protection (or is planned to be in the near future), the management strategy for the Gulf of Gdańsk is unlikely to change. The most important form of maintaining the coast and preventing the loss of beaches in the studied area is nourishment. The cliff in Orłowo is additionally protected by three submerged breakwaters, two stone groins, and a concrete seawall. However, conducted research has shown that the influence of underwater thresholds on shoreline transformation is minor (Łęczyński and Kubowicz-Grajewska, 2013). The probability of introducing more effective methods to protect the Orłowo cliff from erosion is low. Due to its unique natural character, interference with the cliff landscape raises objections from both scientists and the public. The projected changes are expected to result in a substantial increase in the mass of terrestrial deposits entering the marine environment. Numerous studies and models indicate that as a result of the reduction in anthropogenic emissions and releases, reemission from land will be the major source of metals in the coastal seas. As shown in this study, coastal erosion is an important source of elements in the marine environment and should be considered along with rivers, atmospheric deposition or point sources. The erosion of soft cliffs composed of fine-grained sediments affects not only the coastal zone, but also the features of the distal bottom, as confirmed by the results of isotopic analyzes of suspended matter described in earlier work by the authors (Jędruch et al., 2017). As shown in the example of metals, the cliff sediments contained more Y, Rb and Ba than sediments collected near the mouth of Vistula, the main source of pollutants to the Gulf of Gdańsk, as well as one of their most important sources in the Baltic Sea. The concentrations of Cr, Zr and Ba in cliff sediments were also higher than in the fine-grained sediments from the accumulation bottom of the southern Baltic Sea. Cliff sediments can be carriers not only of metals, but also of contaminants that have accumulated in them over

decades. Therefore, we recommend that cliff sediments be included in studies of marine pollution and sampled for purposes of environmental monitoring purposes.

Declaration of competing interest

The authors declare that they have no known competing financial interests or personal relationships that could have appeared to influence the work reported in this paper.

Funding

This work was supported by the National Science Centre grant No. 2014/13/B/ST10/02807.

Acknowledgements

The authors express their gratitude to Jakub Beldowski and Dorota Pałubicka for help with sample collection. We also thank the Editor and two anonymous Reviewers for their suggestions to improve and clarify the manuscript.

References

- Algül, F., Beyhan, M., 2020. Concentrations and sources of heavy metals in shallow sediments in Lake Bafa, Turkey. *Sci. Rep.* 10, 11782. <https://doi.org/10.1038/s41598-020-68833-2>
- Allafta, H., Opp, C., 2020. Spatio-temporal variability and pollution sources identification of the surface sediments of Shatt Al-Arab River, Southern Iraq. *Sci. Rep.* 10, 6979. <https://doi.org/10.1038/s41598-020-63893-w>
- Andriolo, U., Gonçalves, G., 2022. Is coastal erosion a source of marine litter pollution? Evidence of coastal dunes being a reservoir of plastics. *Mar. Pollut. Bull.* 174, 113307. <https://doi.org/10.1016/j.marpolbul.2021.113307>
- Antonowicz, J.P., Grobela, M., Opalińska, M., Motąła, R., 2017. Heavy metals in beach deposits, bottom sediments of a Baltic fishing port and surface water. *Balt. Coast. Zone* 21, 211–224.
- Beldowska, M., 2015. The influence of weather anomalies on mercury cycling in the marine coastal zone of the Southern Baltic – future perspective. *Water Air Soil Pollut.* 226, 2248. <https://doi.org/10.1007/s11270-014-2248-7>
- Beldowska, M., Saniewska, D., Falkowska, L., 2014. Factors influencing variability of mercury input to the southern Baltic Sea. *Mar. Pollut. Bull.* 86, 283–290. <https://doi.org/10.1016/j.marpolbul.2014.07.004>
- Beldowska, M., Jędruch, A., Łęczyński, L., Saniewska, D., Kwasigroch, U., 2016. Coastal erosion as a source of mercury into the marine environment along the Polish Baltic shore. *Environ. Sci. Pollut. Res.* 23, 16372–16382. <https://doi.org/10.1007/s11356-016-6753-7>
- Beldowska, M., Jędruch, A., Sieńska, D., Chwiałkowski, W., Magnuszewski, A., Kornijów, R., 2021. The impact of sediment, fresh and marine water on the concentration of chemical elements in water of the ice-covered Lagoon. *Environ. Sci. Pollut. Res.* 28, 61189–61200. <https://doi.org/10.1007/s11356-021-14936-w>
- Bielecka, E., Jenerowicz, A., Pokonieczny, K., Borkowska, S., 2020. Land Cover Changes and Flows in the Polish Baltic Coastal Zone: A Qualitative and Quantitative Approach. *Remote Sens.* 12, 2088. <http://dx.doi.org/10.3390/rs12132088>
- Bielicka, A., Ryłko, E., Bojanowska, I., 2009. Zawartość pierwiastków metalicznych w glebach i warzywach z ogrodów działkowych Gdańska i okolic. *Ochr. Środ. Zas. Nat.* 40, 209–216 (in Polish).
- Biswas, B., Qi, F., Biswas, J.K., Wijayawardena, A., Khan, M.A.I., Naidu, R., 2018. The Fate of Chemical Pollutants with Soil Properties and Processes in the Climate Change Paradigm – A Review. *Soil Syst.* 2, 51. <https://doi.org/10.3390/soilsystems2030051>
- Blott, S.J., Pye, K., 2001. GRADISTAT: a grain size distribution and statistics package for the analysis of unconsolidated sediments. *Earth Surf. Process. Landf.* 26, 1237–1248. <https://doi.org/10.1002/esp.261>
- Bojakowska, I., 2011. Geochemical Characteristics of River Sediments in the Baltic Sea Catchment Area. In: Uścińowicz, S. (Ed.), *Geochemistry of Baltic Sea surface sediments*. Polish Geological Institute, Warsaw, 36–46.
- Burska, D., Szymczak, E., 2019. The conditions of sedimentation of Gdańsk Bay sediments (Baltic Sea, Poland) in the light of lithological features and carbon content. *IOP Conf. Ser.: Earth Environ. Sci.* 362, 012098. <https://doi.org/10.1088/1755-1315/362/1/012098>
- Clarke, L.W., Janerette, G.D., Bain, D.J., 2015. Urban legacies and soil management affect the concentration and speciation of trace metals in Los Angeles community garden soils. *Environ. Pollut.* 197, 1–12. <https://doi.org/10.1016/j.envpol.2014.11.015>
- Damrat, M., Zaborska, A., Zajączkowski, M., 2013. Sedimentation from suspension and sediment accumulation rate in the River Vistula prodelta, Gulf of Gdańsk (Baltic Sea). *Oceanologia* 55 (4), 937–950. <https://doi.org/10.5697/oc.55-4.937>
- Di Bona, K.R., Love, S., Rhodes, N.R., McAdory, D., Sinha, S.H., Kern, N., Kent, J., Strickland, J., Wilson, A., Beaird, J., Ramage, J., Rasco, J.F., Vincent, J.B., 2011. Chromium is not an essential trace element for mammals: effects of a “low-chromium” diet. *J. Biol. Inorg. Chem.* 16, 381–390. <https://doi.org/10.1007/s00775-010-0734-y>
- Dijair, T.S.B., Silva, F.M., Teixeira, A.F.S., Silva, S.E.G., Guilherme, L.R.G., Curi, N., 2020. Correcting field determination of elemental contents in soils via portable X-ray fluorescence spectrometry. *Cienc. Agrotecnologia* 44, e002420. <https://doi.org/10.1590/1413-7054202044002420>
- Dubrawski, R., Zawadzka-Kahlau, E., 2006. *Przyszłość ochrony polskich brzegów morskich*. Maritime Institute in Gdańsk, Gdańsk, 302 pp. (in Polish).
- Earlie, C.S., Masselink, G., Russell, P.A., Shail, R.K., 2015. Application of airborne LiDAR to investigate rates of recession in rocky coast environments. *J. Coast. Conserv.* 19, 831–845. <https://doi.org/10.1007/s11852-014-0340-1>
- Easterbrook, D.J., 1982. Characteristic Features of Glacial Sediments. In: Scholle, P.A., Spearing, D. (Eds.), *Sandstone Depositional Environments*. American Association of Petroleum Geologists, Tulsa, 1–10. <https://doi.org/10.1306/M31424C2>
- EEA, 2021. European Union emission inventory report 1990-2019, under the UNECE Convention on Long-range Transboundary Air Pollution (LRTAP), EEA Report, 5/2021. European Environment Agency, 161 pp.
- Emsley, J., 2011. *Nature's Building Blocks: An A-Z Guide to the Elements*. Oxford Univ. Press, New York, 710 pp.
- Falandysz, J., Frankowska, A., Jarzyńska, G., Dryżałowska, A., Kojta, A.K., Zhang, D., 2011. Survey on composition and bioconcentration potential of 12 metallic elements in King Bolete (*Boletus edulis*) mushroom that emerged at 11 spatially distant sites. *J. Environ. Sci. Health B* 46, 231–246. <https://doi.org/10.1080/03601234.2011.540528>
- Falandysz, J., Mędyk, M., Treu, R., 2018. Bio-concentration potential and associations of heavy metals in *Amanita muscaria* (L.) Lam. from northern regions of Poland. *Environ.*

- Sci. Pollut. Res. 1730, 25190–25206. <https://doi.org/10.1007/s11356-018-2603-0>
- Folk, R.L., 1974. The petrology of sedimentary rocks. Hemphill Publ. Co., Austin, 182 pp.
- Gashi, F., Frančišković-Bilinski, S., Bilinski, H., 2009. Analysis of sediments of the four main rivers (Drini i Bardhë, Morava e Binçës, Lepenc and Sitnica) in Kosovo. *Fresenius Environ. Bull.* 18, 1462–1471.
- Goodenough, K.M., Wall, F., Merriman, D., 2017. The rare earth elements: demand, global resources, and challenges for resourcing future generations. *Nat. Resour. Res.* 27, 201–216. <https://doi.org/10.1007/s11053-017-9336-5>
- Haroon, A.M., Szaniawska, A., Surosz, W., 1995. Changes in heavy metal accumulation in *Enteromorpha* spp. from the Gulf of Gdańsk. *Oceanologia* 37 (1), 99–110.
- HELCOM, 2021. Inputs of hazardous substances to the Baltic Sea. *Balt. Sea Environ. Proc.* 179, 48 pp.
- Janušaitė, R., Jarmalavičius, D., Pupienis, D., Žilinskas, G., Jukna, L., 2021. Nearshore sandbar switching episodes and their relationship with coastal erosion at the Curonian Spit, Baltic Sea. *Oceanologia*, (in press). <https://doi.org/10.1016/j.oceano.2021.11.004>
- Jarsjö, J., Chalov, S.R., Pietron, J., Alekseenko, A.V., Thorslund, J., 2017. Patterns of soil contamination, erosion and river loading of metals in a gold mining region of northern Mongolia. *Reg. Environ. Change* 17, 1991–2005. <https://doi.org/10.1007/s10113-017-1169-6>
- Jędruch, A., Beldowski, J., Beldowska, M., 2015. Long-term changes and distribution of mercury concentrations in surface sediments of the Gdansk Basin (Southern Baltic Sea). *J. Soil Sed.* 15, 2487–2497. <https://doi.org/10.1007/s11368-015-1148-9>
- Jędruch, A., Kwasigroch, U., Beldowska, M., Kuliński, K., 2017. Mercury in suspended matter of the Gulf of Gdańsk: Origin, distribution and transport at the land–sea interface. *Mar. Pollut. Bull.* 118, 354–367. <https://doi.org/10.1016/j.marpolbul.2017.03.019>
- Jędruch, A., Falkowska, L., Saniewska, D., Durkalec, M., Nawrocka, A., Kalisińska, E., Kowalski, A., Pacyna, J.M., 2021. Status and trends of mercury pollution of the atmosphere and terrestrial ecosystems in Poland. *Ambio* 50, 1698–1717. <https://doi.org/10.1007/s13280-021-01505-1>
- Kabata-Pendias, A., Mukherjee, A., 2007. Trace elements from soil to human. Springer, Berlin Heidelberg, 550 pp. <https://doi.org/10.1007/978-3-540-32714-1>
- Karlonienė, D., Pupienis, D., Jarmalavičius, D., Dubikaltinienė, A., Žilinskas, G., 2021. The impact of coastal geodynamic processes on the distribution of trace metal content in sandy beach sediments, south-eastern Baltic Sea coast (Lithuania). *Appl. Sci.* 11, 1106. <https://doi.org/10.3390/app11031106>
- Kaulbarsz, D., 2005. Geology and glaciotectonics of the Ortowo Cliff in Gdynia, northern Poland. *Prz. Geol.* 53, 572–581.
- Kostrzewski, A., Winowski, M., Zwoliński, Z., 2020. Morphodynamic types of postglacial cliffs of the Southern Baltic. EGU General Assembly, 20486. <https://doi.org/10.5194/egusphere-egu2020-20486>
- Kumblad, L., Bradshaw, C., 2008. Element composition of biota, water and sediment in the Forsmark area, Baltic Sea, Technical Report TR-08-09. Swedish Nuclear Fuel and Waste Management, 109 pp.
- Kupczyk, A., Kotecka, K., Gajewska, M., Siedlewicz, G., Szubska, M., Grzegorzczak, K., Walecka, D., Kotwicki, L., Beldowski, J., Beldowska, M., Graca, B., Staniszevska, M., Chubarenko, B., Schubert, H., Woelfel, J. (Eds.), 2021. Nutrient and pollutant flux to coastal zone originating from decaying algae and plants on beaches. Case studies for innovative solutions of beach wrack use, 63–73.
- Kwasigroch, U., Beldowska, M., Jędruch, A., Saniewska, D., 2018. Coastal erosion – a „new” land-based source of labile mercury to the marine environment. *Environ. Sci. Pollut. Res.* 25, 28682–28694. <https://doi.org/10.1007/s11356-018-2856-7>
- Kwasigroch, U., Beldowska, M., Jędruch, A., Łukawska-Matuszewska, K., 2021. Distribution and bioavailability of mercury in the surface sediments of the Baltic Sea. *Environ. Sci. Pollut. Res.* 28, 35690–35708. <https://doi.org/10.1007/s11356-021-13023-4>
- Łabuz, T., 2013. Sposoby ochrony brzegów morskich i ich wpływ na środowisko przyrodnicze polskiego wybrzeża Bałtyku: Raport. WWF Poland, Warszawa, 187 pp. (in Polish).
- Łabuz, T., 2014. Erosion and its rate on an accumulative Polish dune coast: the effects of the January 2012 storm surge. *Oceanologia* 56 (2), 307–326. <https://doi.org/10.5697/oc.56-2.307>
- Łęczyński, L., Kubowicz-Grajewska, A., 2013. Studium przypadku: Klif Ortowski. In: Łabuz, T. (Ed.), Sposoby ochrony brzegów morskich i ich wpływ na środowisko przyrodnicze polskiego wybrzeża Bałtyku: Raport. WWF Poland, Warszawa, 152–161 (in Polish).
- Łukawska-Matuszewska, K., Bolatek, J., 2008. Spatial distribution of phosphorus forms in sediments in the Gulf of Gdańsk (southern Baltic Sea). *Cont. Shelf Res.* 28, 977–990. <https://doi.org/10.1016/j.csr.2008.01.009>
- Meier, M., Dieterich, C., Gröger, M., Dutheil, C., Börgel, F., Safonova, K., Christensen, O.B., Kjellström, E., 2022. Oceanographic regional climate projections for the Baltic Sea until 2100. *Earth Syst. Dynam.* 13, 159–199. <https://doi.org/10.5194/esd-13-159-2022>
- Mikulski, S.Z., Kramarska, R., Zieliński, G., 2016. Rare earth elements pilot studies of the Baltic marine sands enriched in heavy minerals. *Miner. Resour. Manage.* 32, 5–28. <https://doi.org/10.1515/gospo-2016-0036>
- Mojski, J.E., 2000. The evolution of the southern Baltic coastal zone. *Oceanologia* 42 (3), 285–303.
- Myślińska, E., 1992. Laboratoryjne badania gruntów. PWN, Warszawa 244 pp. (in Polish).
- Pempkowiak, J., 1997. Zarys Geochemii Morskiej. University of Gdańsk Press, Gdańsk, 170 pp. (in Polish).
- Pilch, W., Stachurski, J., Sztaba, K., 1990. Badania i możliwości wykorzystania minerałów ciężkich z bałtyckich piasków plażowych. *Physicochem. Probl. Miner. Process.* 23, 71–79 (in Polish).
- Prądzyński, W., Zborowska, M., Waliszewska, B., Szulc, A., 2010. Chemical composition and content of selected heavy metals in the wood of common sea buckthorn (*Hippophaë rhamnoides* L.) growing in the coastal regions of the Baltic Sea. *Acta Sci. Pol. Silv. Colendar. Rat. Ind. Lignar.* 9, 45–51.
- Pruszek, Z., Zawadzka, E., 2008. Potential Implications of Sea-Level Rise for Poland. *J. Coast Res.* 24, 410–422. <http://www.jstor.org/stable/30137846>
- Regard, V., Prémaillon, M., Dawez, T.J.B., Carretier, S., Jandel, C., Godderis, Y., Bonnet, S., Schott, J., Padoja, K., Martinod, J., Viers, J., Fabre, S., 2022. Rock coast erosion: An overlooked source of sediments to the ocean. Europe as an example, *Earth Planet. Sci. Lett.* 578, 117356. <https://doi.org/10.1016/j.epsl.2021.117356>
- Renjith, R.A., Rejith, R.G., Sundararajan, M., 2021. Evaluation of coastal sediments: an appraisal of geochemistry using ED-XRF and GIS techniques. In: Rani, M., Seenipandi, K., Rehman, S., Kumar, P., Sajjad, H. (Eds.), Remote Sensing of Ocean and Coastal Environments. Elsevier, Amsterdam, 99–116. <https://doi.org/10.1016/B978-0-12-819604-5.00007-X>
- Różyński, G., Lin, J.G., 2021. Can climate change and geological past produce enhanced erosion? A case study of the Hel Peninsula, Baltic Sea, Poland. *Appl. Ocean Res.* 115, 102852. <https://doi.org/10.1016/j.apor.2021.102852>
- Rumble, J.R., 2021. CRC Handbook of Chemistry and Physics. CRC Press, Boca Raton, 1624 pp.

- Saniewska, D., Beldowska, M., Beldowski, J., Jędruch, A., Saniewski, M., Falkowska, L., 2014a. Mercury loads into the sea associated with extreme flood. *Environ. Pollut.* 191, 93–100. <https://doi.org/10.1016/j.envpol.2014.04.003>
- Saniewska, D., Beldowska, M., Beldowski, J., Saniewski, M., Szubska, M., Romanowski, A., Falkowska, L., 2014b. The impact of land use and season on the riverine transport of mercury into the marine coastal zone. *Environ. Monit. Assess.* 186, 7793–7604. <https://doi.org/10.1007/s10661-014-3950-z>
- Singh, M., Rajesh, V.J., Sajinkumar, K.S., Sajeev, K., Kumar, S.N., 2016. Spectral and chemical characterization of jarosite in a palaeolacustrine depositional environment in Warkalli formation in Kerala, South India and its implications. *Spectrochim. Acta Mol. Biomol. Spectrosc.* 168, 86–97. <https://doi.org/10.1016/j.saa.2016.05.035>
- Skorbiłowicz, M., Skorbiłowicz, E., Łapiński, W., 2020. Assessment of Metallic Content, Pollution, and Sources of Road Dust in the City of Białystok (Poland). *Aerosol Air Qual. Res.* 20, 2507–2518. <https://doi.org/10.4209/aaqr.2019.10.0518>
- Sokołowski, A., 2009. Tracing the Flow of Organic Matter Based upon Dual Stable Isotope Technique, and Trophic Transfer to Trace Metals in Benthic Food Web of the Gulf of Gdansk (Southern Baltic Sea). *Univ. Gdańsk Press, Sopot*, 213 pp.
- Sokołowski, A., Jankowska, E., Bałazy, P., Jędruch, A., 2021. Distribution and extent of benthic habitats in Puck Bay (Gulf of Gdansk, southern Baltic Sea). *Oceanologia* 63 (3), 301–320. <https://doi.org/10.1016/j.oceano.2021.03.001>
- Stanisławczyk, I., 2012. Storm-surges Indicator for the Polish Baltic Coast. *Int. J. Mar. Navig. Saf. Sea Transp.* 6, 123–129.
- Szamalek, K., Uścińowicz, K., Zglinicki, K., 2018. Rare earth elements in Fe-Mn nodules from the southern Baltic sea – a preliminary study. *Biul. Państw. Inst. Geol.* 472, 199–212. <https://doi.org/10.5604/01.3001.0012.7118>
- Szefer, P., 1990. Mass-balance of metals and identification of their sources in both river and fallout fluxes near Gdańsk Bay, Baltic Sea. *Sci. Total Environ.* 95, 131–139. [https://doi.org/10.1016/0048-9697\(90\)90058-3](https://doi.org/10.1016/0048-9697(90)90058-3)
- Szyczewski, P., Siewak, J., Niedzielski, P., Sobczyński, T., 2009. Research on Heavy Metals in Poland. *Polish J. Environ. Stud.* 18, 755–768.
- Szymczak, E., Burska, D., 2019. Distribution of Suspended Sediment in the Gulf of Gdansk off the Vistula River mouth (Baltic Sea, Poland). *IOP Conf. Ser.: Earth Environ. Sci.* 221, 012053. <https://doi.org/10.1088/1755-1315/221/1/012053>
- US EPA, 2002. Mid-Atlantic Integrated Assessment (MAIA) Estuaries 1997-98, Summary Report. US Environmental Protection Agency, 115 pp.
- Uścińowicz, S., Uścińowicz, S. (Ed.), 2011. Surface Sediments and Sedimentation Processes. *Geochemistry of Baltic Sea surface sediments*, 76–80.
- Uścińowicz, S., Sokołowski, K., Uścińowicz, S. (Ed.), 2011. Main constituents of the Baltic Sea sediments. *Geochemistry of Baltic Sea surface sediments*, 164–171.
- Uścińowicz, S., Szefer, P., Sokołowski, K., Uścińowicz, S. (Ed.), 2011. Trace elements in the Baltic Sea sediments. *Geochemistry of Baltic Sea surface sediments*, 214–274.
- Uścińowicz, S., Zachowicz, J., Graniczny, M., Dobracki, R., 2004. Geological structure of the southern Baltic coast and related hazards. *Pol. Geol. Inst. Spec. Pap.* 15, 61–68.
- Vincent, J.B., 2017. New evidence against chromium as an essential trace element. *J. Nutr.* 147, 2212–2219. <https://doi.org/10.3945/jn.117.255901>
- Wajda, W., 1970. Heavy minerals of the bottom sands (Polish Baltic Coast). *Ann. Soc. Geol. Pol.* XL, 131–149.
- Wells, D.V., Hennessee, E.L., Hill, J.M., 2003. Shoreline Erosion as a Source of Sediments and Nutrients Middle Coastal Bays, Maryland. Maryland Geological Survey, Coastal and Estuarine Geology File Report No. 03-07, 163 pp.
- Wentworth, C.K., 1922. A scale of grade and class terms for clastic sediments. *J. Geol.* 30, 377–392. <https://doi.org/10.1086/622910>
- Wojciechowska, E., Nawrot, N., Walkusz-Miotk, J., Matej-Łukowicz, K., Pazdro, K., 2019. Heavy Metals in Sediments of Urban Streams: Contamination and Health Risk Assessment of Influencing Factors. *Sustainability* 11, 563. <http://dx.doi.org/10.3390/su11030563>
- Woźniak, P.P., Czubała, P., 2014. Nowe spojrzenie na gliny lodowcowe w Gdyni Orłowie. In: Sokołowski, R. (Ed.), *Ewolucja środowisk sedymentacyjnych regionu Pobrzeża Kaszubskiego*. Univ. Gdańsk Press, Gdańsk, 115–122 (in Polish).
- Xu, W., Li, X., Wai, O.W.H., Huang, W., Yan, W., 2015. Remobilization of trace metals from contaminated marine sediment in a simulated dynamic environment. *Environ. Sci. Pollut. Res.* 22, 19905–19911. <https://doi.org/10.1007/s11356-015-5228-6>
- Yao, Q., Wang, X., Jian, H., Chen, H., Yu, Z., 2015. Characterization of the particle size fraction associated with heavy metals in suspended sediments of the Yellow River. *Int. J. Environ. Res. Public Health* 12, 6725–6744. <https://doi.org/10.3390/ijerph120606725>
- Zaborska, A., Siedlewicz, G., Szymczycha, B., Dzierzbicka-Głowacka, L., 2019. Legacy and emerging pollutants in the Gulf of Gdańsk (southern Baltic Sea) – loads and distribution revisited. *Mar. Pollut. Bull.* 139, 238–255. <https://doi.org/10.1016/j.marpolbul.2018.11.060>
- Zachowicz, J., Laban, C., Uścińowicz, S., Ebbing, J., Emelyanov, E.M., 2002. Recent sedimentation in the Gulf of Gdansk and its geochemical expression. In: Emelyanov, E.M. (Ed.), *Geology of the Gdansk Basin, Baltic Sea*. Russian Academy of Sciences, Yantarny Skaz, 380–387.
- Zaleszkiewicz, L., Koszka-Maróń, D., 2005. Activation processes of degradation of cliff coast of Puck Lagoon. *Prz. Geol.* 53, 55–62.
- Zawadzka-Kahlau, E., 2012. *Morfodynamika brzegów wydmywanych południowego Baltyku*. Univ. Gdańsk Press, Gdańsk, 352 pp. (in Polish).
- Zelaya Wziątek, D., Terefenko, P., Kurulczyk, A., 2019. Multi-Temporal Cliff Erosion Analysis Using Airborne Laser Scanning Surveys. *Remote Sens.* 11, 2666. <https://doi.org/10.3390/rs11222666>
- Zoroddu, M.A., Aaseth, J., Crisponi, G., Medici, S., Peana, M., Nurchi, V.M., 2019. The essential metals for humans: A brief overview. *J. Inorg. Biochem.* 195, 120–129. <https://doi.org/10.1016/j.jinorgbio.2019.03.013>



ORIGINAL RESEARCH ARTICLE

Are fatty acids in fish the evidence of trophic links? A case study from the southern Baltic Vistula Lagoon

Agnieszka Góra*, Joanna Szlinder-Richert, Ryszard Kornijów

National Marine Fisheries Research Institute, Gdynia, Poland

Received 19 January 2022; accepted 15 April 2022

Available online 4 May 2022

KEYWORDS

Trophic marker;
Feeding ecology;
Ontogenetic shift;
PUFA biosynthesis

Abstract Most knowledge on the feeding ecology of fish has been based on the analyses of food remains from the alimentary tracks. This traditional method, however, only provides information about recently consumed food, and is burdened with a risk of incorrect assessment of the role of individual diet components due to the different rates of digestion. A method free from such limitations is the analysis of fatty acids. The objective of our study was to recognise the potential of fatty acid signatures in providing information on the diet and feeding habits of six fish species from the shallow brackish Vistula Lagoon, southern Baltic Sea (*Anguilla anguilla*, *Abramis brama*, *Rutilus rutilus*, *Pelecus cultratus*, *Perca fluviatilis*, *Sander lucioperca*). Multivariate statistical analyses of fatty acid signatures permitted relevant grouping of the fish according to species and their diet, as well as evidenced substantial ontogenetic changes in perch, roach, and bream. They might be caused by dietary changes but can also result from internal regulatory processes. The obtained results confirmed that fatty acids provide useful, time-integrated dietary information, contributing to expanding knowledge regarding the feeding ecology of fish in shallow coastal water ecosystems. They also pointed to the necessity of assessment of the invertebrates and fish's ability to perform endogenous synthesis of polyunsaturated fatty acids, particularly in research on benthic communities. To our best knowledge, this is the first attempt to investigate the feeding habits of fish and food-web relationships in the coastal waters of the Baltic Sea using fatty acids.

© 2022 Institute of Oceanology of the Polish Academy of Sciences. Production and hosting by Elsevier B.V. This is an open access article under the CC BY-NC-ND license (<http://creativecommons.org/licenses/by-nc-nd/4.0/>).

1. Introduction

Most knowledge on the feeding ecology of fish has been achieved through dietary studies based on morphological identification of undigested food remains from the alimentary tracks (Amundsen and Sanchez-Hernandez, 2019; Hyslop, 1980). This traditional method provides essential information to understand the biology of fish species and their ecological role in the aquatic system, important in planning and implementing appropriate measures to protect biota

* Corresponding author at: National Marine Fisheries Research Institute, Kornijów 1, 81–332 Gdynia, Poland.

E-mail address: agora@mir.gdynia.pl (A. Góra).

Peer review under the responsibility of the Institute of Oceanology of the Polish Academy of Sciences.



Production and hosting by Elsevier

and ecosystems. Although stomach content analysis prevails as the basic source of information on the diet and feeding habits of fish, it has some considerable limitations. Firstly, such an approach provides information only about recently consumed food items, and single estimates may not give an accurate picture of the diet from a longer perspective. Secondly, stomachs may be empty at the time of capture or via regurgitation (Arrington et al., 2002; Sutton et al., 2004). Moreover, due to differential rates of digestion of different types of prey, it tends to overestimate prey with long-retained hard parts, and underestimate easily digestible food (Baker et al., 2014; Buckland et al., 2017; dos Santos and Jobling, 1991).

In aquatic food webs, trophic relationships are increasingly frequently investigated through the analysis of fatty acid signatures of organisms (Czesny et al., 2011; Legeżyńska et al., 2014; Thiemann et al., 2008), because it provides a time-integrated depiction of a consumer's diet (Elsdon, 2010; Kirsch et al., 1998). It should be emphasised that in ecological studies, other biochemical techniques have also continued to develop to complement stomach content analysis (Nielsen et al., 2018). Considerable progress in feeding ecology also occurred owing to the integration of research concerning fatty acids and stable isotopes (Futia et al., 2021; Kelly and Scheibling, 2012). Fatty acids are compounds of lipids that occur in every body cell. Most of them, particularly polyunsaturated fatty acids (PUFA), have important physiological roles in the proper functioning of the organism, affecting its growth, reproduction, and survival (Parrish, 2009; Tocher, 2003). Most animals are not able to synthesize PUFA *de novo* at all, apart from elongating and desaturating them, but the rate of such conversion is very variable, and generally cannot meet the physiological requirements (Bell and Tocher, 2009; Tocher, 2003, 2010). Animals must therefore obtain PUFA primarily through diet.

The application of fatty acids trophic markers (FATM) in research on food-web relations is based on the assumption that particular species of prey have unique and identifiable fatty acid signatures that become incorporated into the consumer adipose tissue with little modification and in a predictable way (Budge et al., 2006; Dalsgaard et al., 2003). Such conclusions were primarily drawn based on research on the marine environment. Nevertheless, fatty acid analyses also proved useful in investigating the feeding habits of organisms in the freshwater environment, delineating spatial and temporal differences in diets both within and between species, and elucidating food web structure (Czesny et al., 2011; Käkälä et al., 2005; Thiemann et al., 2008). Moreover, this method is particularly promising due to the possibility of estimating the relative contributions of prey species in the diets of individual predators based on quantitative fatty acid signature analysis (QFASA). It has been applied in the investigation of the diet of seabirds and marine mammals (Iverson et al., 2004, 2007), and recently also fish (Happel et al., 2016a). It should be emphasised that although fatty acid compositions in consumers are undeniably influenced by diet, they can also be affected by other factors. According to the latest research, more species than previously believed are capable of modifying their dietary fatty acids

or even synthesising new fatty acids that had been considered to belong to essential fatty acids (Kabeya et al., 2018; Monroig and Kabeya, 2018). Furthermore, it has been proven that in addition to biosynthetic capacities, differences in the fatty acid composition may also vary with other intrinsic factors such as phylogeny and developmental and reproductive stages (Gladyshev et al., 2018; Maazouzi et al., 2011; Scharnweber et al., 2021; Szlinder-Richert et al., 2010). According to Chaguaceda et al. (2020), internal regulatory processes, associated with changes in physiological demands for PUFA over ontogeny, have similarly important effects on the fatty acid composition of fish as the diet. Research has also documented the effect of environmental conditions on the fatty acid composition in aquatic ecosystems (Galloway and Winder, 2015; Janer et al., 2007; Merad et al., 2018). Therefore, even though the importance of FATM has been demonstrated in numerous studies involving consumers from all trophic levels, including invertebrates, fish, birds, and mammals (Käkälä et al., 2005; Legeżyńska et al., 2014; Stowasser et al., 2009; Thiemann et al., 2008), the issue in the context of recent knowledge appears to be more complicated than was previously assumed.

The Baltic Sea, the largest brackish water body in the world, is becoming increasingly affected by climate change and anthropogenic pressures and all these stressors can lead to changes in the structure and functions of the ecosystem. The Baltic food web, from plankton communities via fish stocks to top predator populations, has undergone large changes during the few last decades (Casini et al., 2009; Möllmann et al., 2008, 2009; Wasmund and Uhlig, 2003). The increased pressure of many factors adversely affecting the quality of the environment and basic ecological processes particularly accumulates in estuarine and coastal environments (Airoldi and Beck, 2007; Collie et al., 2008). Like all over the world, also in the Baltic Sea, coastal waters play a crucial role in maintaining biodiversity in marine systems (Kraufvelin et al., 2018). However, the understanding of the structure and functioning of food webs in coastal waters such as estuaries and lagoons is a challenge because they are very productive and dynamic ecosystems (McLusky and Elliott, 2004).

The Vistula Lagoon is a coastal water body typical of the southern non-tidal Baltic Sea, where the structure of biocoenoses and ecological processes, including top-down regulations, are primarily determined by salinity (Kornijów, 2018). It provides a habitat for fish across various life stages, including spawning, juvenile development, feeding, and migration (Psuty and Wilkońska, 2009). It is one of the largest coastal lagoons in Europe which has been included in the NATURA 2000 protection program under the EU Habitats Directive and placed on the list of Baltic Sea Protection Areas. This study investigates the usefulness of fatty acid analysis in providing information on the diet and feeding habits of ichthyofauna in the Vistula Lagoon. Six fish species were selected due to their high abundance and importance in local fisheries, as well as their different feeding habits (omnivory, zooplanktivory, benthivory and piscivory). Special emphasis was placed on detailed fatty acid composition analysis to elucidate inter- and intraspecies differ-

ences, and reveal food sources and feeding behaviour discussed in the context of current knowledge of feeding ecology.

2. Material and methods

2.1. Study area

The study was carried out in the Vistula Lagoon, a large semi-enclosed shallow water body (area 838 km², mean depth 2.5 m, max. depth 5.2 m). The lagoon is separated from the Baltic Sea by the Vistula Spit. The inflow of sea-water is possible only through the Baltiysk Strait, contributing to uneven salinity along the basin (0.5–7.0 PSU). The area is influenced by both maritime and continental climates. The lagoon is very productive, with advanced eutrophic processes. The concentrations of total nitrogen and phosphorus in the water are high, reaching 1.1–4.4 mg dm⁻³ and 0.06–0.19 mg dm⁻³, respectively. The low water transparency usually oscillates around 40 cm (Kownacka et al. 2020; Nawrocka and Kobos, 2011). Despite highly advanced eutrophication and the accumulation of organic matter in the sediments, water oxygenation is high, even in winter under long-lasting ice cover (Glazunova and Polunina, 2013; Kornijów et al., 2020).

The near-shore littoral zone is primarily occupied by an intermittent belt of reed *Phragmites australis* (Cav.). In deeper waters, down to approximately 2 m, scattered patches of perfoliate pondweed *Potamogeton perfoliatus* L. and sago pondweed *Stuckenia pectinata* (L.) Börner occur (Kornijów, 2018; Pawlikowski and Kornijów, 2019). The phytoplankton of the lagoon is dominated by cyanobacteria, slightly more abundant in the middle than in the western basin. In the latter, a higher contribution is reached by diatoms and green algae (Kownacka et al., 2020). The zooplankton is dominated by Cladocera in the western, and Copepoda in the middle basin. Cladocera include numerous filtrators, as well as predatory *Leptodora kindtii*. Rotifera are relatively more abundant in the western basin (Paturej and Gutkowska, 2015; Paturej et al., 2017). Due to the brackish water conditions, the zoobenthos lacks many freshwater taxa, e.g. insects (Odonata, Ephemeroptera, Trichoptera) and gastropods. In terms of density, macroinvertebrates are dominated by detritivorous Tubificinae and larvae of Chironomidae. In the biomass, two alien species prevail, namely a bivalve clam *Rangia cuneata* and a polychaete *Marenzelleria* sp. (Kornijów, 2018). The ichthyofauna is mostly composed of freshwater species (Kornijów, 2018; Psuty and Wilkońska 2009). Marine fish such as flounder (*Platichthys flesus*), turbot (*Scophthalmus maximus*), and Atlantic herring (*Clupea harengus*) occur in the lagoon only periodically. Non-piscivores (except for periodically occurring herring) are dominated by ruffe (*Gymnocephalus cernua*), roach (*Rutilus rutilus*), bleak (*Alburnus alburnus*), European smelt (*Osmerus operlanus*), and silver bream (*Blicca bjoerkna*). Piscivores are dominated by pikeperch and perch.

2.2. Sampling and laboratory analyses

Specimens of several most frequently fished fish species, such as sichel (*Pelecus cultratus*), pikeperch (*Sander lucioperca*), European perch (*Perca fluviatilis*), European eel (*Anguilla anguilla*), bream (*Abramis brama*), and roach (*Rutilus rutilus*), were collected from May to June 2016 from the Polish part of the Vistula Lagoon. The fish were measured (wet mass and total length) and frozen immediately after collection. Before analysis, they were filleted and skinned. Then, the muscle tissue from each individual was homogenised and freeze-dried.

Fatty acids were analysed in the total lipid fraction. Lipids were extracted with a mixture of dichloromethane:methanol (2:1 v/v), according to the procedure by Folch et al. (1957). The dichloromethane phase containing total lipids was collected and reduced to dryness under a stream of nitrogen. Fatty acid methyl esters (FAME) were prepared following the methods by Usydus et al. (2011). Briefly, 0.1 g of the extracted lipid was dissolved in 1.6 ml of 2 M methanolic potassium hydroxide solution, and shaken vigorously. The solution was heated, and after its cooling, 3.2 ml of 4% methanolic solution of hydrochloric acid was added. The samples were reheated. After their cooling, 1.6 ml of isoctane was added. Then the solution was vortexed and adjusted to a volume of 10 ml with a saturated solution of sodium chloride. Anhydrous sodium sulphate was added to dry the extracts. The resultant solution of FAME on the top layer was diluted with methanol in a proportion of 1:4 v/v, and was subject to final determination. FAME were determined using gas chromatography equipped with a flame ionisation detector (GC-FID). The column used was a Restek Rt-2560 (100 m x 0.25 mm x 0.2 µm film thickness). The chromatography conditions were as follows: split injection; split ratio – 100:1; injection volume – 2 µm; carrier gas flowing at 1.1 ml min⁻¹ – helium; injector port temperature – 250°C; FID temperature – 260°C; oven temperature – initial oven temperature 140°C held for 2 min, then increased to 225°C at a rate of 2°C min⁻¹ and held for 10 min, followed by an increase to 240°C at a rate of 40°C min⁻¹ and held for 10 min. The instrumental analytical precision was determined by 5 replicate injections of the standard, which gave coefficients of variation in the response value in the range of 0.2–2.1%. The identity of several FAME was confirmed by gas chromatography-mass spectrometry (GC-MS). The same column and temperature programme as described above were used. The interface to the mass analyzer was maintained at 240°C, and the mass analyzer used a 70-eV ionization potential, and scanned over a mass range of 50–500 m/z. The individual FAME were identified by comparison of retention times with PUFA1, PUFA3, and a 37-component FAME mixture supplied by Supelco, and confirmed by comparing our mass spectrum with that from the American Oil Chemists' Society Lipid Library (<http://lipidhome.co.uk/ms/masspec.html>). Results for each FAME were presented in relative units, as percentages of total fatty acids, throughout the paper. The fatty acids were grouped into saturated fatty acids (SFA), monounsaturated fatty acids (MUFA), and polyunsaturated fatty acids

(PUFA). The latter were further divided into sums of n-3 PUFA and n-6 PUFA.

2.3. Statistical analysis

We detected a total of 37 fatty acids in fish tissue, but fatty acids that did not exceed 0.5% of total fatty acid in at least one fish sample were excluded from all statistical analyses. The remaining ones were re-calculated to 100%. To explore overall patterns in fatty acid data, we performed multivariate analyses. Multidimensional scaling (MDS) analysis seeks to capture compositional similarities in the fewest dimensional space. We used MDS to illustrate the relations between particular specimens of the studied species. Principal Component Analysis (PCA) was performed to identify fatty acids that contributed the most to the observed inter- and intraspecific differences. Principal components (PC) were extracted based on eigenvalues greater than 1. Variables with a loading factor of >0.6 were considered significant. The relationships between fish length and fatty acids were examined by means of the Spearman rank correlation test. Statistical analyses were performed using the Statistica software version 10.0 (StatSoft, 2011).

3. Results

The analysis involved twenty-one fatty acids quantified in all species with a percentage in the sum of all identified fatty acids greater than 0.5%. The selected fatty acids constituted 97.9% to 99.5% (average 98.8%) of the total of all detected fatty acids. The summary information for the tested samples and fatty acids is presented in Table 1. For most of the studied species, a higher proportion of PUFA than that of MUFA and SFA was generally observed, except for bream and European eel in which MUFA predominated (Table 1). The percentages of PUFA in the tested species varied from 19.5% in eel to more than 50% in perch and pikeperch, while the percentage of MUFA ranged from 13.9% in perch to 52.8% in eel. SFA contents were comparable in all the studied species, and were within a fairly narrow range from 22.8% to 29.2%. Another common feature shown for all the studied species was a significant predominance of fatty acids from the n-3 PUFA family (15.0–51.3% of total fatty acids) over fatty acids from the n-6 PUFA family (4.5–10.1% of total fatty acids). The average value of the n-3/n-6 PUFA ratio differed between the species, and reached from 2.2 in bream to 5.4 in perch. The value was broadly variable within fish. It ranged 3.0–9.0, 1.0–6.2, 0.4–4.3, 2.5–5.9, and 3.1–4.8 in pikeperch and perch, roach, bream, eel and sichel, respectively.

3.1. Interspecies variation in fatty acid compositions

The studied species differed in terms of the highest abundance of particular fatty acids. In perch and pikeperch, docosahexaenoic acid (22:6n-3, DHA) reached the highest percentage. In contrast, the fatty acid signatures in eel, bream, and sichel were dominated by 18:1n-9, while in

the lipid of roach, 16:0 predominated. The analysis of the data from Table 1 evidently shows that the most apparent differences found between the studied species were the mean percentages of the following six out of 21 quantified fatty acids: 16:0 (15.6–20.4%), 16:1 (3.8–9.8%), 18:1n-9 (6.0–37.2%), arachidonic acid (20:4n-6, ARA) (1.5–7.3%), eicosapentaenoic acid (20:5n-3, EPA) (2.9–9.3%) and DHA (4.2–35.0%).

MDS analysis permitted illustrating the relationship between the studied fish based on their fatty acid signatures (Figure 1). The samples were grouped by species in the diagram. Samples representing perch and pikeperch, eel, and sichel evidently formed compact clusters, relatively distant from each other, while samples representing roach and bream formed a common group, quite extended in the diagram, suggesting greater intraspecific variability for these two latter species. The position of the groups corresponding to each species in the diagram can be to some extent explained by the type of their diet. Samples representing two piscivorous species, namely perch and pikeperch, were located on the left side of the diagram in close proximity to each other, and could be distinguished from other species by negative values on the MDS1 axis, while most samples of the other species showed positive values on the MDS1 axis. Roach and bream, whose dietary composition is very diverse and includes both benthic and pelagic prey, commonly formed a large cluster stretching from the middle to the right part of the diagram. Samples that formed that cluster exhibited values on the MDS2 axis ranging from -0.9 to +2.5. Samples of zooplanktivorous/facultative piscivorous sichel were located close to roach and bream, while samples of opportunistic carnivorous species – eel were relatively distant from the other studied species, and characterised by the lowest values on the MDS2 axis. It is also worth emphasising that although in Figure 1 pikeperch and perch form a single cluster evidently separated from the remaining species, the MDS2 axis to a certain extent separates specimens of both species in terms of their length. Pikeperch with a body length from 31 cm to 50 cm reached higher values on the MDS2 axis (from 0.3 to 0.9) than 2 specimens of pikeperch with a body length of 53 cm and 56 cm (from -0.5 to -0.1). In the case of perch, all specimens with a body length below 27 cm were characterised by low values on the MDS2 axis (from -0.5 to 0.4), whereas the largest specimens of perch (>27 cm) showed positive and negative values on the MDS2 axis.

The principal component analysis (PCA) was used to identify fatty acids that contributed the most to the observed differences between the studied fish species (Figure 2). Overall, this PCA explained 85.6% of total variability using 5 principal components. The first principal component (PC1) explained 44.4% of the total variance. This PC was strongly negatively correlated with ARA, EPA, and DHA, and strongly positively correlated with 14:0, 16:1, 18:1n-9. On the one hand, this factor distinguished pikeperch and perch among the studied species due to the high percentage of ARA, EPA, and DHA in their tissues. On the other hand, a high percentage of 14:0 and monounsaturated fatty acids were a characteristic feature of eel. The second principal component (PC2) accounted for 16.7% of the total variance, and was negatively associated with the majority of SFA, particularly 16:0, 18:0, and 20:0. Samples representing bream, roach

Table 1 Morphological characteristics (mean, min-max) and fatty acid composition (mean±SD) in fish from the Vistula Lagoon.

	sichel <i>Pelecus cultratus</i>	pikeperch <i>Sander lucioperca</i>	perch <i>Perca fluviatilis</i>	bream <i>Abramis brama</i>	roach <i>Rutilus rutilus</i>	eel <i>Anguilla anguilla</i>
n	31	16	38	53	34	12
length [cm]	35.4	40.9	22.6	30.2	22.7	58.0
mass [g]	30.5–42.0	31.0–56.0	16.5–31.0	13.0–49.5	15.0–31.0	56.0–60.0
	263.6	606.3	154.0	444.5	156.5	342.6
	163.3–440.5	250.0–1433.5	51.5–329.4	25.9–1521.4	36.7–431.3	284.9–398.5
fatty acid [%]						
14:0	1.78±0.28	1.14±0.14	1.09±0.24	2.17±0.48	1.90±0.50	3.91±0.29
15:0	0.33±0.04	0.43±0.05	0.37±0.06	0.46±0.09	0.54±0.14	0.36±0.06
16:0	15.55±0.68	20.01±1.47	18.44±2.27	20.43±3.98	19.83±2.30	18.45±0.69
17:0	0.67±0.07	0.81±0.14	0.64±0.13	0.82±0.15	0.90±0.20	0.58±0.11
18:0	4.42±0.48	6.15±0.97	4.34±0.58	5.33±1.27	4.71±0.60	4.22±0.29
20:0	0.19±0.02	0.24±0.08	0.19±0.05	0.27±0.08	0.20±0.04	0.14±0.02
SFA	22.76±0.93	28.54±1.84	24.89±2.82	29.22±5.18	27.87±3.10	27.52 ±0.86
16:1	8.58±1.48	4.58±0.77	3.80±1.35	9.81±2.24	9.40±2.76	9.26±0.61
18:1n-9	21.01±2.58	7.39±0.84	6.03±1.50	23.50±4.74	16.92±4.36	37.17±1.41
18:1n-7	5.50±0.41	4.01±0.50	3.28±0.61	5.17±0.72	4.95±0.96	4.37±0.22
20:1n-11	0.27±0.11	0.14±0.05	0.09±0.05	1.12±0.72	1.06±0.64	0.65±0.37
20:1n-9	1.57±0.15	0.40±0.05	0.40±0.10	0.93±0.31	1.12±0.27	1.27±0.27
24:1	0.14±0.02	0.40±0.07	0.29±0.11	0.13±0.11	0.11±0.04	0.07±0.02
MUFA	37.06±3.89	16.93±1.46	13.89±3.40	40.66±7.06	33.57±7.71	52.80±1.34
18:2n-6 (LA)	2.83±0.54	2.02±0.31	2.04±0.68	4.03±1.29	3.23±1.72	2.25±0.72
18:3n-3 (ALA)	1.62±0.21	1.17±0.14	0.98±0.22	2.38±0.66	2.70±0.84	1.83±0.20
20:2n-6	0.85±0.15	0.50±0.10	0.39±0.07	1.08±0.26	0.95±0.16	0.60±0.19
20:3n-6	0.26±0.04	0.24±0.07	0.20±0.04	0.43±0.13	0.41±0.09	0.22±0.02
20:3n-3	0.55±0.07	0.35±0.07	0.27±0.04	0.60±0.19	0.54±0.13	0.43±0.07
20:4n-6 (ARA)	3.99±0.64	7.34±1.54	7.16±1.00	3.77±1.67	4.45±1.17	1.45±0.26
20:5n-3 (EPA)	6.97±0.65	8.35±0.61	9.32±0.99	5.03±2.14	5.72±1.43	2.86±0.62
22:5n-3	4.12±0.41	6.37±1.08	5.72±1.48	3.79±1.65	5.10±1.13	5.68±0.99
22:6n-3 (DHA)	18.78±2.62	27.94±3.27	34.96±6.12	8.74±5.07	15.27±8.28	4.23±1.12
PUFA	39.99±3.49	54.29±2.35	61.03±6.05	29.85±9.73	38.36±9.88	19.54±1.60
n-3 PUFA	32.05±3.04	44.18±3.10	51.25±6.84	20.54±8.44	29.32±9.56	15.02±1.63
n-6 PUFA	7.94±0.88	10.11±1.74	9.78±1.48	9.31±2.07	9.04±1.58	4.52±0.73

SFA – Saturated fatty acids; MUFA – Monounsaturated fatty acids; PUFA – Polyunsaturated fatty acids; LA – Linoleic acid; ALA – α -linolenic acid; ARA – Arachidonic acid; EPA – Eicosapentaenoic acid; DHA – Docosahexaenoic acid.

and perch adopted wide ranges of scores. The next principal component (PC3) (13.4% of total variance) had high positive factor loadings for 15:0 and 17:0 among SFA, 20:1 n-11 among MUFA, and α -linolenic acid (18:3n-3, ALA), 20:2n-6 and 20:3n-6 among PUFA. Roach and bream were grouped together in this ordination. The fourth principal component (PC4) accounted for 6.3% of the total variance, and linoleic acid (18:2n-6, LA) had the largest effect on that PC. The last principal component (PC5), explaining 4.8% of the total variance, was marked by high loading on 20:1n-9. The last two principal components distinguished mainly bream and sichel, respectively.

Very wide ranges of scores obtained for some principal components suggest high intra-species variability of the

fatty acid composition in certain cases (Figure 2). Due to this, separate PCA analyses were performed for each species to investigate the intraspecific variability in more detail.

3.2. Intra-species variation in fatty acid compositions

The PCA conducted for each species separately indicated differences in fatty acid signatures between different size classes of perch, bream, and roach (Figure 3). For perch, the first two components explained 56.0% of the total variance, whereas the first component explained 41.6% of the total

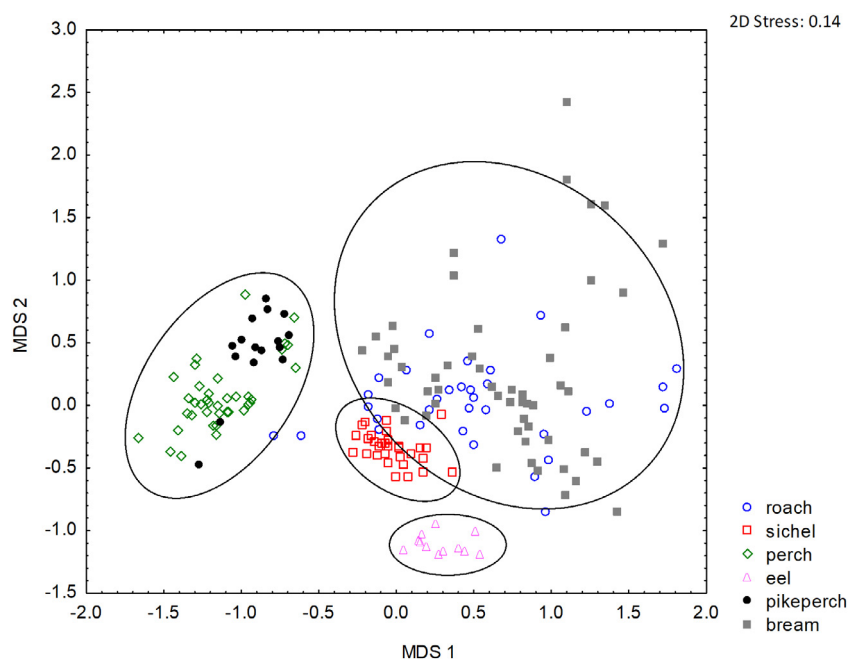


Figure 1 Multidimensional scaling (MDS) plot for all studied fish species. The analysis was based on 21 fatty acids with a percentage higher than 0.5%. The data were standardised to equal 100% prior to analysis. Each point represents an individual fish.

variance. PCA analysis (Figure 3A) confirmed the conclusions previously drawn in the interpretation of the MDS analysis. The samples, represented by smallest size class perch (16.5–19 cm), reached high positive values on the PC2 axis, whereas the samples representing perch in the medium size class (21–26 cm) largely showed negative values on the PC2 axis. The PC2 axis was positively correlated with 20:0, and negatively correlated with 20:1n-11. All these samples (small- and medium-size classes) also showed negative values on the PC1 axis which was strongly negatively correlated with DHA, and strongly positively correlated particularly with 16:0, 18:1n-9, and 18:1n-7. Furthermore, PC 1 separated the largest specimens (>27 cm) into two groups. The analysis of individual fatty acids for their relationship with perch length indicated a statistically significant relationship between these variables ($p < 0.05$, $0.46 < R_s < 0.71$). With an increase in body length, the percentage of EPA and DHA in the muscle tissue decreased, and the percentage of 16:0, 16:1, 18:1n-9, 18:1n-7, 20:1n-9, and 18:2n-6 increased.

According to PCA analyses, the largest size classes of bream and roach were closely grouped, while the variation was high for specimens measuring less than 24 cm (Figure 3B,C). For bream, the first (PC1) and second principal components (PC2) explained 37.7 and 26.3% of the total variance, respectively (Figure 3B). The samples represented by bream with a body length of more than 24 cm largely showed negative values on the PC1 axis which had high negative factor loadings primarily for EPA and 22:5n-3, and high positive factor loadings for 16:0, 18:0, 20:0, and 24:1. Specimens smaller than 24 cm formed two groups that showed both positive and negative values on the PC1 and PC2 axis. PC2 was strongly positively correlated with ARA, and strongly negatively correlated with 14:0, 15:0, and 16:1. For bream, the statistically significant correlation between individual fatty acids and fish length was indi-

cated ($p < 0.05$, $0.44 < R_s < 0.82$). With an increase in length in bream, the percentage of 15:0, 20:1n-11, 18:3n-3, 20:2n-6, 20:3n-3 and EPA increased, and the percentage of 16:0, 18:0, 20:0, and 24:1 decreased.

For roach, the PC1 axis accounted for 34.3% of the total variance, and showed a strong negative correlation with PUFA, mainly DHA and EPA, while SFA and MUFA were positively correlated with PC1. PC2 (22.3% of total variance) was strongly positively correlated with 20:1n-11 and 22:5n-3, and negatively correlated with 18:2n-6. Moreover, 15:0, 17:0, 18:1n-7, 20:1n-11, and 18:3n-3 were positively correlated with both PC1 and PC2. Roach from different size classes were separated as presented in Figure 3C. Furthermore, in roach, like in bream, a positive length-related trend with 15:0, 20:1n-11, and 18:3n-3 was observed ($p < 0.05$, $0.35 < R_s < 0.69$). In roach, a similar positive relationship was also found for 18:1n-7 and 20:1n-9, while for 18:2n-6, a negative length-related trend was found ($p < 0.05$, $0.49 < R_s < 0.65$).

4. Discussion

Our study demonstrated that the majority of the investigated fish species could be distinguished by their fatty acid signatures. The applied multivariate analyses permitted grouping of the studied fish samples according to their fatty acid signatures into four clusters (Figure 1). Based on the current knowledge of the ecology of the studied species, the obtained pattern can be largely explained by the diet characteristic of particular species. A deeper analysis of the data additionally allows for the identification of factors other than the diet that may affect fatty acids composition in fish. As shown in Figure 1, cluster 1 collected samples representing two predatory species of the Percidae

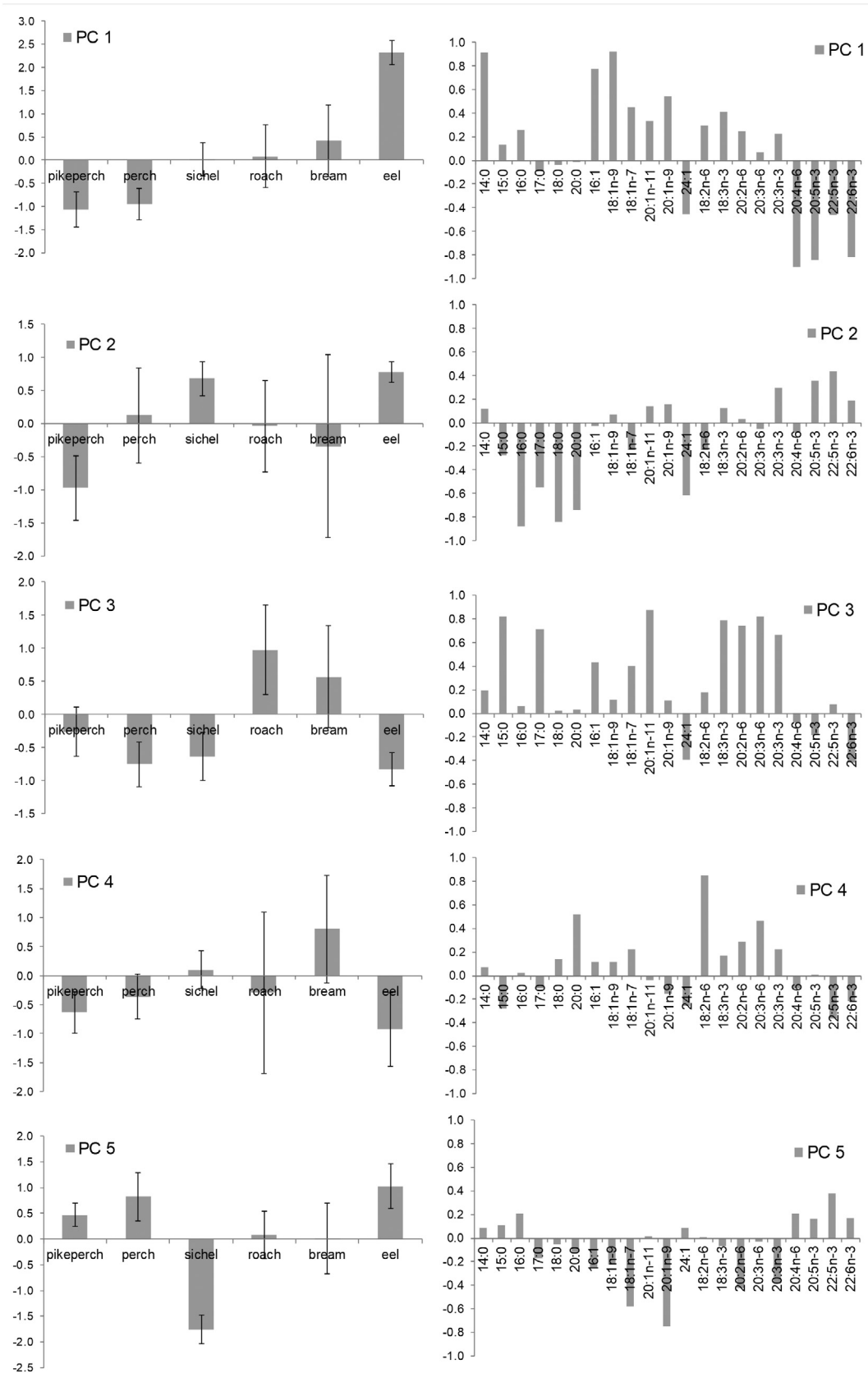


Figure 2 Principal component analysis (PCA) of fatty acids in the muscle tissue for all studied fish species. Diagrams of mean scores (to the left) and factor loadings (to the right) for the defined principal components. The PCA employed normalised Varimax rotation.

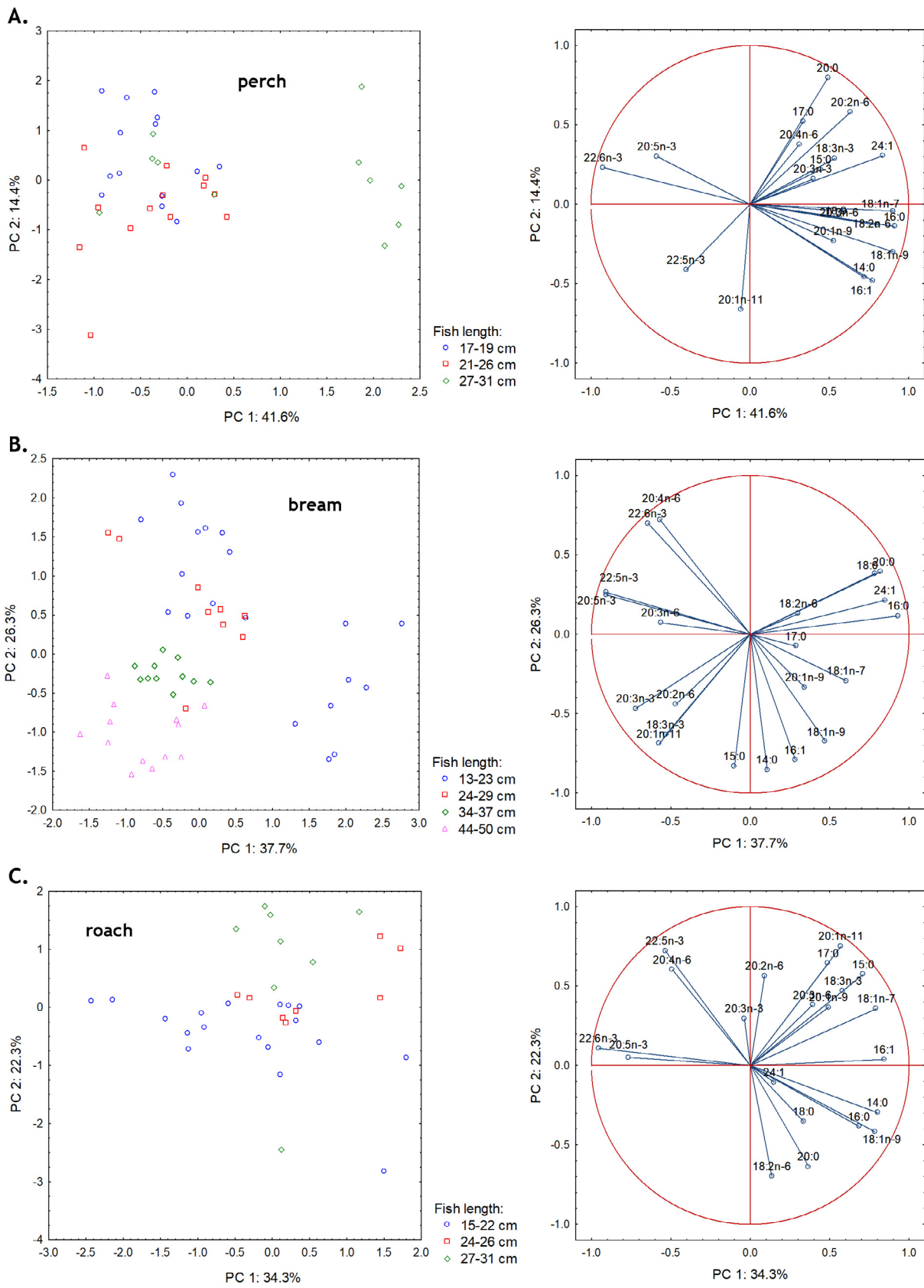


Figure 3 Scores (to the left) and the factor loadings (to the right) of the first two principal components in a PCA model built based on fatty acid compositions in the muscle of perch (A), bream (B) and roach (C).

family: perch and pikeperch. Samples representing species from the Cyprinidae family formed two closely located clusters, cluster 2 (bream and roach) and cluster 3 (sichel), while cluster 4 covered samples representing individuals of European eel. The differences in fatty acid signatures between the studied species are largely attributable to differences in DHA, EPA, ARA, and 18:1n-9. Samples forming cluster 1 were characterised by high proportions of DHA, EPA, and ARA. Samples involved in clusters 2 and 3 were in turn characterised by a much lower content of those fatty acids, but also by a distinctly higher proportion of 18:1n-9 in comparison to predatory species. Samples from cluster 4 had the lowest proportion of DHA, EPA, and ARA among all analysed samples, and the highest proportion of 18:1n-9 and 14:0.

The feeding ecology of pikeperch and perch assigned to cluster 1 in the current study are well known (Demchuk et al., 2021; Hansson et al., 1997; Hjelm et al., 2000; Lehtonen et al., 1996; Mustamaki et al., 2014). Pikeperch can be classified as an obligatory piscivorous, while perch is considered as an omnivorous predator. Pikeperch usually becomes piscivorous during the first year of life, while perch undergoes ontogenetic diet shifts from feeding on zooplankton, through benthic invertebrates, to the piscivory phase. DHA, EPA, and ARA occurring in the lipid of their muscle tissue in a significant proportion belong to highly unsaturated fatty acids (HUFA) with high nutritional value and high potential to affect consumer fitness through their impact on many vital processes (Tocher, 2003). Dietary deficiencies of these fatty acids can have serious consequences, including inhibited growth, limited ability to reproduce, and increased incidences of disease and metabolic disorders. Probably due to the physiological importance of these compounds, they are retained in aquatic food webs and are effectively transferred to higher trophic levels (Gladyshev et al., 2011; Koussoroplis et al., 2011; Lau et al., 2012; Strandberg et al., 2015). According to the current knowledge, DHA is selectively and highly accumulated over other PUFA in fish. Investigating the retention of PUFA in different fish taxa from streams, Guo et al. (2017) indicated that Perciformes had higher proportions of DHA, EPA, and ARA than fish from the Cyprinidae family, but significant differences were only found in DHA. A similar result was obtained for fish from the Vistula Lagoon in the current study. Sushchik et al. (2017) also confirmed a higher proportion of DHA in piscivorous fish, including perch and pike, in comparison to Cyprinidae (roach and bream). The cited study also evidenced, however, that the percentage of EPA in Cyprinidae can be higher than in Percidae, as was the case for fish from the Krasnoyarsk Reservoir (Siberia, Russia).

The differences in fatty acid signatures between perch below and above 27 cm length indicated in the current study are intriguing. This result suggests that in the Vistula Lagoon, perch start feeding on similar prey (fish) as pikeperch only after reaching 27 cm body length. Our results also suggest that even after reaching a certain size threshold that predisposes perch to piscivory, it may still feed on invertebrates. This is suggested by the dispersal of perch samples larger than 27 cm observed in the MDS and PCA analyses (Figures 1, 3A). A similar conclusion was drawn by Mustamaki et al. (2014). According to the authors, irrespec-

tive of its size, perch feeds both on fish and invertebrates in the northern Baltic Proper. The PCA analysis also revealed high variability of fatty acid signatures in perch from different size classes (Figure 3A). Perch individuals included in the current study showed a significant variation in body length (16.5–31.0 cm). Individuals of small and medium size classes generally showed a higher percentage of n-3 PUFA, particularly DHA, and a lower percentage of SFA (i.e. 16:0) and MUFA (i.e. 16:1, 18:1-9, 18:1n-7) than the largest size class. Medium-sized perch had higher proportions of 20:1n-11 and 22:5n-3 than the remaining individuals. Although the determination of perch's detailed diet based on the analysis of fatty acid signatures is difficult due to the lack of fatty acid signatures of putative prey species, certain conclusions can be drawn. The results suggest that perch become piscivorous after reaching a body size of 27 cm, and below that size feeds on various invertebrates. According to Chaguaceda et al. (2020), piscivorous perch in comparison to planktivorous and benthivorous ones is characterised by higher proportions of 16:1 and 18:1n-9, and a lower proportion of EPA. In our study, the piscivory of perch was additionally confirmed by the MSD analysis in which perch with high proportions of 16:1 and 18:1n-9, and a low proportion of EPA was identified together with pikeperch (Figure 1). The literature (Czesny et al., 2011; Happel et al., 2015; Kornijów et al., 2016; Lau et al. 2012; Makhutova et al., 2011) and our results suggest that the small-size class of perch relies more on pelagic crustaceans, while the medium-size class, first of all, depends on benthic invertebrates. The difference between perch of small- and medium-size classes was primarily driven by differences in proportions of 20:1n-11, DHA and EPA (Figure 3A). EPA and DHA are commonly found to be prevalent in pelagic sources, while 20:1n-11 is frequently detected only in oligochaetes and bivalves, typical benthic invertebrates (Kornijów et al., 2021; Lau et al. 2012; Makhutova et al., 2011). Medium-sized perch also showed a higher proportion of 16:1, and lower proportions of n-3 PUFA in comparison to the smallest perch, which additionally supports the thesis on the influence of benthic feeding (Czesny et al., 2011; Happel et al., 2015).

On the other hand, according to Chaguaceda et al. (2020), in perch, the diet explains only a limited part of fatty acid variability. Equally important are internal regulatory processes. A decrease in the proportion of EPA and DHA, and an increase in MUFA in the muscle tissue during fish growth were also reported for other fish species, and are probably related to changes in the energy requirements throughout the life cycle (Maazouzi et al., 2011; Makhutova and Stoyanov, 2021; Tocher, 2010). Another factor that may be responsible for changes in fatty acid profiles is the ability of some species to biosynthesise HUFA through bioconversion. In fish, like in all vertebrates, C18 PUFA such as ALA and LA cannot be synthesised *de novo* and must come from the diet. However, some fish species can convert dietary ALA and LA to their biologically active long-chain derivatives, including n-3 EPA and DHA, and n-6 ARA. The ability of fish to elongate and desaturate C18 precursors varies greatly between species, and has been assumed to be habitat- and trophic level dependent (Tocher, 2003; Trushenski and Rombenso, 2020). It is generally accepted that most marine fishes and many carnivorous fishes are not

capable of such biochemical conversion at a physiologically significant rate. In contrast, freshwater fish, mainly herbivorous and omnivorous, are capable of meeting the physiological demand for HUFA through such biosynthetic capacity. Nevertheless, knowledge of the bioconversion capabilities in fish is still limited, particularly for wild fish, and therefore further research is required. The latest study on perch from the natural environment showed that EPA levels in the muscle tissue corresponded with those in consumed resources, but a mismatch was recorded between ARA and DHA proportions in the consumer muscle tissue compared to their resources in the diet (Scharnweber et al., 2021). Sawyer et al. (2016) showed, based on the mass-balance model, that in the case of yellow perch (*Perca flavescens*), the main source of EPA and ARA was diet, while DHA came primarily from bioconversion. Henrotte et al. (2011) demonstrated that Eurasian perch was able to elongate and desaturate ALA into DHA but showed a rather limited capacity for the elongation of LA to ARA. Moreover, they indicated the dependency of bioconversion efficiency on ontogeny. To sum up, the current study does not unequivocally point to specific factors responsible for the observed change in fatty acid profiles in perch. However, they suggest that in certain species, EPA is a better indicator of diet than DHA.

As previously mentioned, fish from the Cyprinidae family, namely sichel, bream, and roach were characterised by significantly lower proportions of DHA, EPA, and ARA, and a higher proportion of 18:1n-9 than predatory species. Additionally, sichel had the highest percentage of 20:1n-9 among the studied fish species, and a lower percentage of 16:0 and 20:1n-11 compared to bream and roach. Higher content of 20:1n-9 in Cyprinidae indicates zooplankton in their diet, since monounsaturated fatty acids with 20 and 22 carbon atoms are particularly abundant specifically in Calanoid copepods, and have been recommended as zooplankton markers (Dalsgaard et al., 2003; Kelly and Scheibling, 2012). Specifically herbivorous copepods are able to synthesise *de novo* considerable amounts of 20:1n-9 and 22:1n-11 fatty acids, which typically accumulate in wax esters as a long-term energy reserve (Lee et al., 2006). In the case of the tested species, the content of 22:1 did not exceed 0.2% of total fatty acids, while 20:1n-9 showed relatively high content in sichel (1.1–1.8%). This result is in agreement with some studies from the Baltic Sea region (Keinanen et al., 2017; Lind et al., 2018), where a higher ratio of 20:1 to 22:1 was detected in other zooplanktivorous species such as herring *Clupea harengus membras* and sprat *Sprattus sprattus* which predominantly consumed small-sized copepods such as *Temora longicornis*, *Eurytemora affinis*, and *Acartia* spp. (Ojaveer et al., 2018). Our results are also consistent with a previous study based on stomach content analysis which classified sichel as a zooplanktivore/facultative piscivore (Specziár and Rezsú, 2009; Stolarski, 1995). Total lengths of sichel studied in the Vistula Lagoon ranged from 30.5 cm to 42 cm. According to the literature, in the Vistula Lagoon sichel larger than 20 cm starts to feed on fish and becomes a facultative predator (Stolarski, 1995). Its prey is primarily small pelagic fish such as smelt, as well as all juvenile fish, which in turn rely on zooplankton. It is important to emphasise that zooplankton plays a key role in linking food webs, serving as the main energy pathway from primary producers to higher trophic level organisms. Copepods are the main

component of zooplankton by biomass in the Vistula Lagoon, with a distinct spring peak largely accounted for by *Eurytemora affinis* (Dmitrieva and Semenova, 2012). This is of particular importance for larval survival and subsequent recruitment of fish because copepods have a high DHA content compared to other crustacean zooplankton (Persson and Vrede, 2006). Especially, larvae and juveniles require a large amount of DHA for proper development and ultimately survival (Bell et al., 1995; Ishizaki et al., 2001; Mourente et al., 1991).

Samples representing bream and roach formed one scattered cluster (Fig. 1). This confirms the general opinion that the diet of both species, feeding mainly on zooplankton and macroinvertebrates is diverse and partly overlaps (Lammens and Hoogenboezem, 1991; Nagelkerke and Sibbing, 1996; Specziár et al., 1997). Roach is considered one of the most successful generalists, feeding on zooplankton and macroinvertebrates, including molluscs and live or dead plant material (Demchuk et al., 2021; Kornijów et al., 2005; Specziár and Rezsú, 2009). Compared with roach, bream is more dependent on the food of animal origin, with a preference for soft-bodied macroinvertebrates buried in sediments (Lammens et al., 1985; Nagelkerke and Sibbing, 1996). It is also worth emphasising that in the case of both fish species from the Vistula Lagoon, the highest variability of fatty acid signatures particularly concerned specimens of small size classes (roach: 15–22 cm; bream: 13–23 cm; Figure 3B, C). The variation observed between individuals of different size classes was primarily related to the percentage of HUFA and 20:1n-11, 18:3n-3. The proportion of 20:1n-11 and 18:3n-3 increased with an increase in body length in both species. While for roach, the proportion of 15:0, 17:0 and 18:1n-7, used as tracers for the contribution of bacteria (Kelly and Scheibling, 2012), also increased. This suggests that the diet of bream and roach was rich in bivalves and/or oligochaetes, as previously 20:1n-11 has been detected only in these invertebrates (Makhutova et al., 2011). According to the literature, molluscs are the most important constituent of the roach diet (Specziár and Rezsú, 2009; Specziár et al., 1997). It is related to the structure and functioning of their feeding system. Molluscs have also been found in the digestive tracts of bream, although it is believed that roach can switch to feed on molluscs faster than bream (Nagelkerke and Sibbing, 1996; Prejs et al., 1990). The reason is that bream is able to penetrate the sediment to a greater depth than roach (Lammens et al., 1985; Persson and Brönmark, 2002), and is, therefore, more efficient at feeding on benthic organisms associated with the sediments.

Although the analysis of fatty acid signatures in roach and bream allows for tracing some shifts in their diet composition in relation to their size, it would be very difficult to precisely conclude the detailed composition of their diet. As previously indicated, the use of FATM to study benthic food web interactions is very complicated (Kelly and Scheibling, 2012). Moreover, contrary to what has been believed for decades, recent studies provide evidence that not only primary producers but also a wide range of invertebrates possess genes involved in the biosynthetic pathways of PUFA, including *de novo* biosynthesis of C18 PUFA (Kabeya et al., 2018; Monroig and Kabeya, 2018). It has been recently confirmed that various aquatic inver-

tebrates such as annelids as well as molluscs and arthropods which dominate benthic habitats can produce PUFA endogenously, which presents challenges when reconstructing dietary links. The bottom fauna of the Vistula Lagoon is not abundant in terms of a number of species. The major components of zoobenthos are larvae of Chironomidae and Oligochaeta (Ezhova et al., 2005; Kornijów et al., 2021). Over the last few decades, *Marenzelleria* sp., belonging to the group of Polychaetes, has also been found in large numbers in the Vistula Lagoon (Żmudziński, 1996). Nonetheless, probably due to the ability of these invertebrates to burrow deep in the bottom sediments, they do not constitute food available for benthivorous fish (Golubkov et al., 2021; Żmudziński, 1996). The most numerous taxa among molluscs are bivalves, dominated by two alien species – *Dreissena polymorpha* and *Rangia cuneata* (Kornijów, 2018). Fatty acid data of Oligochaeta are scarce, whereas data regarding Chironomidae and *Dreissena polymorpha* are more abundant. According to the literature, the main difference between bivalves and Chironomidae and Oligochaeta is the fact that the latter are almost devoid of DHA, whereas in bivalves it occurs in considerably higher proportion (Budge et al., 2001; Czesny et al., 2011; Makhutova et al., 2011). The presence of 20:1n-11 is a characteristic feature of Oligochaeta and bivalves while it is not recorded in Chironomidae. Moreover, in comparison to Chironomidae, Oligochaeta show a lower percentage of 16:1, LA, ALA and EPA (Goedkoop et al., 2000; Makhutova et al., 2011; Sushchik et al., 2006). It is worth emphasising that, based on stomach content analysis, the importance of oligochaetes in fish diets is often underestimated due to their high rate of digestion and therefore frequently impossible identification of their remains in the digestive contents (Bouguenec and Giani, 1989; Wiśniewski, 1978). Bivalves can be in turn overestimated due to the resistance of their shell to the digestive processes. This research, however, does not permit detailed determination of the prey of roach and bream, because probably the key importance lies in the ability to modify fatty acids by these fish species (Galloway and Budge, 2020). According to the literature, larvae and pupae of Chironomidae are an important component of the diet of benthivorous and omnivorous fish (Filuk and Żmudziński, 1965; Kakareko, 2002; Kornijów et al., 2005; Kornijów et al., 2016). It is however difficult to find an unequivocal confirmation of this fact in the fatty acid signatures of these fishes. It is due to the fact that these insects are a scarce source of DHA, but rich in C18 PUFA, whereas LA can serve as a precursor for ARA, while ALA can serve as a precursor for EPA and DHA (Bell and Tocher, 2009; Castro et al., 2016; Monroig et al., 2018). Therefore, consistent with previous controlled dietary studies in species that have the enzymatic capacity to synthesize HUFA from their precursors, which is highly likely in fish of the Cyprinidae family, their fatty acid composition may not directly reflect the diet (Garrido et al., 2020; Happel et al., 2016b; Janaranjani and Shu-Chien, 2020; Prigge et al., 2012). The absence of DHA in Chironomidae, like in Oligochaeta, might have induced a high conversion of dietary ALA to ensure sufficient DHA supply in roach and bream. It therefore cannot be excluded that the process of endogenous synthesis of HUFA in the organisms of individual studied fish species affects their fatty acid

composition, especially when experiencing food resources that are relatively poor in HUFA.

Samples representing eel from the Vistula Lagoon formed a relatively compact group pointing to low variability within the group of tested individuals (Figure 1). It is worth emphasising, however, that individuals covered by the study were characterised by a relatively narrow range of body length. Fatty acid signatures in eels strongly differed from fatty acid signatures determined for the remaining species. The major difference was the low proportion of EPA, DHA and ARA (less than 5% for each fatty acid) and the extremely high proportion of 18:1n-9 in European eel in comparison with other species. Another important feature was higher than in other species content of 14:0. Fatty acid signatures observed for eel from the Vistula Lagoon were the same as in the study by Tverin et al. (2019). The study of grey seal foraging habits included 11 fish species representing pelagic, demersal and coastal habitats of the Baltic Sea (Tverin et al., 2019). Like in our study, European eel was characterised by high content of 14:0 and MUFA, especially 16:1 and 18:1n-9, and low content of DHA. Stomach content and stable isotope analyses suggest that the European eel is an opportunistic carnivore, and adapts its diet to food availability (Bouchereau et al., 2009; Dörner et al., 2009). Based on the measured fatty acid signatures, it is difficult to conclude the type of prey consumed by eels from the Vistula Lagoon. The difficulty in correlating the fatty acid composition of European eel muscle tissue with suitable food resources was previously reported by Prigge et al. (2012). According to experimental studies, the authors found that fatty acid composition in eel muscle tissue seemed to be rather insensitive to fatty acids supplied in the diet. This phenomenon may be related to the biology of this species. The European eel, a catadromous species, lives in rivers, lakes, and estuaries, where it feeds and grows as a “yellow” eel, and after reaching the threshold size and physiological condition, including sufficient lipid reserves, it migrates back to its spawning site as a “silver” eel, and at this stage stops feeding. During the spawning migration, the energy required to travel thousands of kilometres and successfully reproduce is taken from the lipids accumulated in its body (Clevestam et al., 2011). This may explain the high content of MUFA in eels, as these fatty acids are heavily catabolised for energy in fish (Tocher, 2003). Moreover, it has been evidenced that during the maturation process, EPA and DHA are selectively moved from the muscle, and incorporated into gonads (Baeza et al., 2015; Nowosad et al., 2015). The composition of fatty acids in eels from the Vistula Lagoon may therefore indicate that these fish are already undergoing certain physiological and biochemical changes connected with the preparation of their organisms for reproductive migration. Note, it has been established that anguillid eels possess enzymatic capacities which allow modifying PUFA content in their tissues. Kissil et al. (1987) showed that European glass eel had the ability to convert LA into ARA. The complete enzymatic repertoire required for the biosynthesis of HUFA from C18 PUFA has been in turn confirmed for Japanese eel (*Anguilla japonica*) (Wang et al., 2014; Xu et al., 2020). This makes interpretations more difficult, because it may complicate any relationship between the contents of these fatty acids in the prey and tissues of consumers.

5. Conclusions

This study is the first step toward the application of fatty acids to highlight the role fish played in the food webs of the shallow coastal waters of the Baltic Sea. The presented results not only allowed for differentiating the studied fish species based on fatty acid signatures but also pointed to intraspecific changes in their diet. They expanded knowledge obtained based on stomach content analysis. However, our study revealed that further research, also experimental, is needed, in the case of many fish species, to take full advantage of the possibilities offered by fatty acids. The study conducted emphasised the importance of understanding the roles of different fatty acids in the organism's physiology and lipid metabolism before attempting to infer diet from fatty acid data. Particularly, the explanation of endogenous PUFA synthesis ability in different species of invertebrates and fish can considerably improve the usefulness of fatty acids in research on food webs in shallow coastal waters.

Declaration of competing interest

The authors declare that they have no known competing financial interests or personal relationships that could have appeared to influence the work reported in this paper.

Acknowledgments

The article is a result of the implementation of research project No. 2012/05/N/NZ8/00906 financed by the National Science Centre, Poland. Three referees provided exceptionally insightful suggestions which substantially helped us to improve the manuscript.

References

- Airoidi, L., Beck, M.W., 2007. Loss, status and trends for coastal marine habitats of Europe. *Oceanogr. Mar. Biol.* 45, 345–405. <https://doi.org/10.1201/9781420050943.ch7>
- Amundsen, P.A., Sanchez-Hernandez, J., 2019. Feeding studies take guts - critical review and recommendations of methods for stomach contents analysis in fish. *J. Fish Biol.* 95, 1364–1373. <https://doi.org/10.1111/jfb.14151>
- Arrington, D.A., Winemiller, K.O., Loftus, W.F., Akin, S., 2002. How often do fishes "run on empty"? *Ecology* 83, 2145–2151. <https://doi.org/10.2307/3072046>
- Baeza, R., Mazzeo, I., Vilchez, M.C., Gallego, V., Penaranda, D.S., Perez, L., Asturiano, J.F., 2015. Relationship between sperm quality parameters and the fatty acid composition of the muscle, liver and testis of European eel. *Comp. Biochem. Phys. A* 181, 79–86. <https://doi.org/10.1016/j.cbpa.2014.11.022>
- Baker, R., Buckland, A., Sheaves, M., 2014. Fish gut content analysis: robust measures of diet composition. *Fish Fish.* 15, 170–177. <https://doi.org/10.1111/faf.12026>
- Bell, M.V., Batty, R.S., Dick, J.R., Fretwell, K., Navarro, J.C., Sargent, J.R., 1995. Dietary deficiency of docosahexaenoic acid impairs vision at low light intensities in juvenile herring (*Clupea harengus* L.). *Lipids* 30, 443–449. <https://doi.org/10.1007/bf02536303>
- Bell, M.V., Tocher, D.R., 2009. Biosynthesis of polyunsaturated fatty acids in aquatic ecosystems: general pathways and new directions. In: Kainz, M., Brett, M., Arts, M. (Eds.), *Lipids in Aquatic Ecosystems*. Springer, New York, 211–236. https://doi.org/10.1007/978-0-387-89366-2_9
- Bouchereau, J.L., Marques, C., Pereira, P., Guelorget, O., Vergne, Y., 2009. Food of the European eel *Anguilla anguilla* in the Mauguio lagoon (Mediterranean, France). *Acta Adriat.* 50, 159–170.
- Bouguenec, V., Giani, N., 1989. Aquatic oligochaetes as prey of invertebrates and vertebrates: a review. *Acta Oecol. Oecol. Appl.* 10, 177–196.
- Budge, S.M., Iverson, S.J., Koopman, H.N., 2006. Studying trophic ecology in marine ecosystems using fatty acids: A primer on analysis and interpretation. *Mar. Mammal Sci.* 22, 759–801. <https://doi.org/10.1111/j.1748-7692.2006.00079.x>
- Budge, S.M., Parrish, C.C., McKenzie, C.H., 2001. Fatty acid composition of phytoplankton, settling particulate matter and sediments at a sheltered bivalve aquaculture site. *Mar. Chem.* 76, 285–303. [https://doi.org/10.1016/s0304-4203\(01\)00068-8](https://doi.org/10.1016/s0304-4203(01)00068-8)
- Buckland, A., Baker, R., Loneragan, N., Sheaves, M., 2017. Standardising fish stomach content analysis: the importance of prey condition. *Fish. Res.* 196, 126–140. <https://doi.org/10.1016/j.fishres.2017.08.003>
- Casini, M., Hjelm, J., Molinero, J.C., Lovgren, J., Cardinale, M., Bartolino, V., Belgrano, A., Kornilovs, G., 2009. Trophic cascades promote threshold-like shifts in pelagic marine ecosystems. *Proc. Natl. Acad. Sci. U. S. A.* 106, 197–202. <https://doi.org/10.1073/pnas.0806649105>
- Castro, L.F.C., Tocher, D.R., Monroig, O., 2016. Long-chain polyunsaturated fatty acid biosynthesis in chordates: Insights into the evolution of Fads and Elovl gene repertoire. *Prog. Lipid Res.* 62, 25–40. <https://doi.org/10.1016/j.plipres.2016.01.001>
- Chaguaceda, F., Eklov, P., Scharnweber, K., 2020. Regulation of fatty acid composition related to ontogenetic changes and niche differentiation of a common aquatic consumer. *Oecologia* 193, 325–336. <https://doi.org/10.1007/s00442-020-04668-y>
- Clevestam, P.D., Ogonowski, M., Sjoberg, N.B., Wickstrom, H., 2011. Too short to spawn? Implications of small body size and swimming distance on successful migration and maturation of the European eel *Anguilla anguilla*. *J. Fish Biol.* 78, 1073–1089. <https://doi.org/10.1111/j.1095-8649.2011.02920.x>
- Collie, J.S., Wood, A.D., Jeffries, H.P., 2008. Long-term shifts in the species composition of a coastal fish community. *Can. J. Fish. Aquat. Sci.* 65, 1352–1365. <https://doi.org/10.1139/f08-048>
- Czesny, S.J., Rinchar, J., Hanson, S.D., Dettmers, J.M., Dabrowski, K., 2011. Fatty acid signatures of Lake Michigan prey fish and invertebrates: among-species differences and spatiotemporal variability. *Can. J. Fish. Aquat. Sci.* 68, 1211–1230. <https://doi.org/10.1139/f2011-048>
- Dalsgaard, J., St John, M., Kattner, G., Muller-Navarra, D., Hagen, W., 2003. Fatty acid trophic markers in the pelagic marine environment. *Adv. Mar. Biol.* 46, 225–340. [https://doi.org/10.1016/S0065-2881\(03\)46005-7](https://doi.org/10.1016/S0065-2881(03)46005-7)
- Demchuk, A.S., Uspenskiy, A.A., Golubkov, S.M., 2021. Abundance and feeding of fish in the coastal zone of the Neva Estuary, eastern Gulf of Finland. *Boreal Environ. Res.* 26, 1–16.
- Dmitrieva, O.A., Semenova, A.S., 2012. Seasonal dynamics and trophic interactions of phytoplankton and zooplankton in the Vistula Lagoon of the Baltic Sea. *Oceanology* 52, 785–789. <https://doi.org/10.1134/S0001437012060033>
- Dörner, H., Skov, C., Berg, S., Schulze, T., Beare, D.J., Van der Velde, G., 2009. Piscivory and trophic position of *Anguilla anguilla* in two lakes: importance of macrozoobenthos density. *J. Fish Biol.* 74, 2115–2131. <https://doi.org/10.1111/j.1095-8649.2009.02289.x>
- dos Santos, J., Jobling, M., 1991. Gastric emptying in cod, *Gadus morhua* L.: emptying and retention of indigestible solids. *J. Fish Biol.* 38, 187–197. <https://doi.org/10.1111/j.1095-8649.1991.tb03105.x>

- Eldson, T.S., 2010. Unraveling diet and feeding histories of fish using fatty acids as natural tracers. *J. Exp. Mar. Biol. Ecol.* 386, 61–68. <https://doi.org/10.1016/j.jembe.2010.02.004>
- Ezhova, E., Żmudziński, L., Maciejewska, K., 2005. Long-term trends in the macrozoobenthos of the Vistula Lagoon, southeastern Baltic Sea. Species composition and biomass distribution. *Bull. Sea Fish. Inst.* 1, 55–73.
- Filuk, J., Żmudziński, L., 1965. Feeding of the Vistula Lagoon ichthyofauna. *Rep. Sea Fish. Inst.* 13 A, 43–55 (in Polish).
- Folch, J., Lees, M., Stanley, G.H.S., 1957. A simple method for the isolation and purification of total lipides from animal tissues. *J. Biol. Chem.* 226, 497–509. [https://doi.org/10.1016/S0021-9258\(18\)64849-5](https://doi.org/10.1016/S0021-9258(18)64849-5)
- Futia, M.H., Colborne, S.F., Fisk, A.T., Gorsky, D., Johnson, T.B., Lantry, B.F., Lantry, J.R., Rinchar, J., 2021. Comparisons among three diet analyses demonstrate multiple patterns in the estimated adult diet of a freshwater piscivore, *Salvelinus namaycush*. *Ecol. Indic.* 127. <https://doi.org/10.1016/j.ecolind.2021.107728>
- Galloway, A.W.E., Budge, S.M., 2020. The critical importance of experimentation in biomarker-based trophic ecology. *Philos. Trans. R. Soc. B: Biol. Sci.* 375, 20190638. <https://doi.org/10.1098/rstb.2019.0638>
- Galloway, A.W.E., Winder, M., 2015. Partitioning the relative importance of phylogeny and environmental conditions on phytoplankton fatty acids. *Plos One* 10. <https://doi.org/10.1371/journal.pone.0130053>
- Garrido, D., Monroig, O., Galindo, A., Betancor, M.B., Perez, J.A., Kabeya, N., Marrero, M., Rodríguez, C., 2020. Lipid metabolism in *Tinca tinca* and its n-3 LC-PUFA biosynthesis capacity. *Aquaculture* 523, 735147. <https://doi.org/10.1016/j.aquaculture.2020.735147>
- Gladyshev, M.I., Sushchik, N.N., Anishchenko, O.V., Makhutova, O.N., Kolmakov, V.I., Kalachova, G.S., Kolmakova, A.A., Dubovskaya, O.P., 2011. Efficiency of transfer of essential polyunsaturated fatty acids versus organic carbon from producers to consumers in a eutrophic reservoir. *Oecologia* 165, 521–531. <https://doi.org/10.1007/s00442-010-1843-6>
- Gladyshev, M.I., Sushchik, N.N., Tolomeev, A.P., Dgebuadze, Y.Y., 2018. Meta-analysis of factors associated with omega-3 fatty acid contents of wild fish. *Rev. Fish Biol. Fish.* 28, 277–299. <https://doi.org/10.1007/s11160-017-9511-0>
- Glazunova, A.A., Polunina, J.J., 2013. Peculiarities of under-ice zooplankton in the Curonian and Vistula Lagoons of the Baltic Sea. *Inland Water Biol.* 6, 301–304. <https://doi.org/10.1134/S1995082913040081>
- Goedkoop, W., Sonesten, L., Ahlgren, G., Boberg, M., 2000. Fatty acids in profundal benthic invertebrates and their major food resources in Lake Erken, Sweden: seasonal variation and trophic indications. *Can. J. Fish. Aquat. Sci.* 57, 2267–2279. <https://doi.org/10.1139/f00-201>
- Golubkov, S., Tiunov, A., Golubkov, M., 2021. Food-web modification in the eastern Gulf of Finland after invasion of *Marenzelleria arctica* (Spionidae, Polychaeta). *Neobiota* 66, 75–94. <https://doi.org/10.3897/neobiota.66.63847>
- Guo, F., Bunn, S.E., Brett, M.T., Kainz, M.J., 2017. Polyunsaturated fatty acids in stream food webs - high dissimilarity among producers and consumers. *Freshw. Biol.* 62, 1325–1334. <https://doi.org/10.1111/fwb.12956>
- Hansson, S., Arrhenius, F., Nellbring, S., 1997. Diet and growth of pikeperch (*Stizostedion lucioperca* L.) in a Baltic Sea area. *Fish. Res.* 31, 163–167. [https://doi.org/10.1016/S0165-7836\(97\)00022-2](https://doi.org/10.1016/S0165-7836(97)00022-2)
- Happel, A., Creque, S., Rinchar, J., Hooeek, T., Bootsma, H., Janssen, J., Jude, D., Czesny, S., 2015. Exploring yellow perch diets in Lake Michigan through stomach content, fatty acids, and stable isotope ratios. *J. Great Lakes Res.* 41, 172–178. <https://doi.org/10.1016/j.jglr.2015.03.025>
- Happel, A., Stratton, L., Kolb, C., Hays, C., Rinchar, J., Czesny, S., 2016a. Evaluating quantitative fatty acid signature analysis (QFASA) in fish using controlled feeding experiments. *Can. J. Fish. Aquat. Sci.* 73, 1222–1229. <https://doi.org/10.1139/cjfas-2015-0328>
- Happel, A., Stratton, L., Patridge, R., Rinchar, J., Czesny, S., 2016b. Fatty-acid profiles of juvenile lake trout reflect experimental diets consisting of natural prey. *Freshw. Biol.* 61, 1466–1476. <https://doi.org/10.1111/fwb.12786>
- Henrotte, E., Kpogue, D., Mandiki, S.N.M., Wang, N., Douxfils, J., Dick, J., Tocher, D., Kestemond, P., 2011. n-3 and n-6 fatty acid bioconversion abilities in Eurasian perch (*Perca fluviatilis*) at two developmental stages. *Aquacult. Nutr.* 17, 216–225. <https://doi.org/10.1111/j.1365-2095.2010.00754.x>
- Hjelm, J., Persson, L., Christensen, B., 2000. Growth, morphological variation and ontogenetic niche shifts in perch (*Perca fluviatilis*) in relation to resource availability. *Oecologia* 122, 190–199. <https://doi.org/10.1007/pl00008846>
- Hyslop, E.J., 1980. Stomach contents analysis – a review of methods and their application. *J. Fish Biol.* 17, 411–429. <https://doi.org/10.1111/j.1095-8649.1980.tb02775.x>
- Ishizaki, Y., Masuda, R., Uematsu, K., Shimizu, K., Arimoto, M., Takeuchi, T., 2001. The effect of dietary docosahexaenoic acid on schooling behaviour and brain development in larval yellowtail. *J. Fish Biol.* 58, 1691–1703. <https://doi.org/10.1006/jfbi.2001.1579>
- Iverson, S.J., Field, C., Bowen, W.D., Blanchard, W., 2004. Quantitative fatty acid signature analysis: a new method of estimating predator diets. *Ecol. Monogr.* 74, 211–235. <https://doi.org/10.1890/02-4105>
- Iverson, S.J., Springer, A.M., Kitaysky, A.S., 2007. Seabirds as indicators of food web structure and ecosystem variability: qualitative and quantitative diet analyses using fatty acids. *Mar. Ecol. Prog. Ser.* 352, 235–244. <https://doi.org/10.3354/meps07073>
- Janaranjani, M., Shu-Chien, A.C., 2020. Complete repertoire of long-chain polyunsaturated fatty acids biosynthesis enzymes in a cyprinid, silver barb (*Barbonymus gonionotus*): cloning, functional characterization and dietary regulation of Elovl2 and Elovl4. *Aquacult. Nutr.* 26, 1835–1853. <https://doi.org/10.1111/anu.13133>
- Janer, G., Navarro, J.C., Porte, C., 2007. Exposure to TBT increases accumulation of lipids and alters fatty acid homeostasis in the ramshorn snail *Marisa cornuarietis*. *Comp. Biochem. Phys. C* 146, 368–374. <https://doi.org/10.1016/j.cbpc.2007.04.009>
- Kabeya, N., Fonseca, M.M., Ferrier, D.E.K., Navarro, J.C., Bay, L.K., Francis, D.S., Tocher, D., Castro, L.F.C., Monroig, O., 2018. Genes for de novo biosynthesis of omega-3 polyunsaturated fatty acids are widespread in animals. *Sci. Adv.* 4, eaar6849. <https://doi.org/10.1126/sciadv.aar6849>
- Kakareko, T., 2002. The importance of benthic fauna in the diet of small common bream *Abramis brama* [L.], roach *Rutilus rutilus* [L.], pikeperch *Sander lucioperca* [L.] and ruffe *Gymnocephalus cernuus* [L.] in the Włocławek Reservoir. *Arch. Pol. Fish.* 10, 221–231.
- Käkelä, R., Käkelä, A., Kahle, S., Becker, P.H., Kelly, A., Furness, R.W., 2005. Fatty acid signatures in plasma of captive herring gulls as indicators of demersal or pelagic fish diet. *Mar. Ecol. Prog. Ser.* 293, 191–200. <https://doi.org/10.3354/meps293191>
- Keinanen, M., Kakela, R., Ritvanen, T., Myllylä, T., Ponni, J., Vuorinen, P.J., 2017. Fatty acid composition of sprat (*Sprattus sprattus*) and herring (*Clupea harengus*) in the Baltic Sea as potential prey for salmon (*Salmo salar*). *Helgol. Mar. Res.* 71, 4. <https://doi.org/10.1186/s10152-017-0484-0>
- Kelly, J.R., Scheibling, R.E., 2012. Fatty acids as dietary tracers in benthic food webs. *Mar. Ecol. Prog. Ser.* 446, 1–22. <https://doi.org/10.3354/meps09559>
- Kirsch, P.E., Iverson, S.J., Bowen, W.D., Kerr, S.R., Ackman, R.G., 1998. Dietary effects on the fatty acid signature of whole At-

- lantic cod (*Gadus morhua*). Can. J. Fish. Aquat. Sci. 55, 1378–1386. <https://doi.org/10.1139/cjfas-55-6-1378>
- Kissil, G.W., Youngson, A., Cowey, C.B., 1987. Capacity of the European eel (*Anguilla anguilla*) to elongate and desaturate dietary linoleic acid. J. Nutr. 117, 1379–1384. <https://doi.org/10.1093/jn/117.8.1379>
- Kornijów, R., 2018. Ecosystem of the Polish part of the Vistula Lagoon from the perspective of alternative stable states concept, with implications for management issues. Oceanologia 60 (3), 390–404. <https://doi.org/10.1016/j.oceano.2018.02.004>
- Kornijów, R., Karpowicz, M., Ejsmont-Karabin, J., Nawrocka, L., de Eyto, E., Grzonkowski, K., Magnuszewski, A., Jakubowska, A., Wodzinowski, T., Woźniczka, A., 2020. Patchy distribution of phyto- and zooplankton in large and shallow lagoon under ice cover and resulting trophic interactions. Mar. Freshw. Res. 71, 1327–1341. <https://doi.org/10.1071/Mf19259>
- Kornijów, R., Measey, G.J., Moss, B., 2016. The structure of the littoral: effects of waterlily density and perch predation on sediment and plant-associated macroinvertebrate communities. Freshw. Biol. 61, 32–50. <https://doi.org/10.1111/fwb.12674>
- Kornijów, R., Pawlikowski, K., Błędzki, L.A., Drgas, A., Piwosz, K., Ameryk, A., Calkiewicz, J., 2021. Co-occurrence and potential resource partitioning between oligochaetes and chironomid larvae in a sediment depth gradient. Aquat. Sci. 83, 51. <https://doi.org/10.1007/s00027-021-00800-z>
- Kornijów, R., Vakkilainen, K., Horppila, J., Luokkanen, E., Kairesalo, T., 2005. Impacts of a submerged plant (*Elodea canadensis*) on interactions between roach (*Rutilus rutilus*) and its invertebrate prey communities in a lake littoral zone. Freshw. Biol. 50, 262–276. <https://doi.org/10.1111/j.1365-2427.2004.01318.x>
- Koussoroplis, A.-M., Bec, A., Perga, M.-E., Koutrakis, E., Bourdier, G., Desvillettes, C., 2011. Fatty acid transfer in the food web of a coastal Mediterranean lagoon: Evidence for high arachidonic acid retention in fish. Estuar. Coast. Shelf S. 91, 450–461. <https://doi.org/10.1016/j.ecss.2010.11.010>
- Kownacka, J., Calkiewicz, J., Kornijów, R., 2020. A turning point in the development of phytoplankton in the Vistula Lagoon (southern Baltic Sea) at the beginning of the 21st century. Oceanologia 62 (4), 538–555. <https://doi.org/10.1016/j.oceano.2020.08.004>
- Kraufvelin, P., Pekcan-Hekim, Z., Bergstrom, U., Florin, A.-B., Lehikoinen, A., Mattila, J., et al., 2018. Essential coastal habitats for fish in the Baltic Sea. Estuar. Coast. Shelf S. 204, 14–30. <https://doi.org/10.1016/j.ecss.2018.02.014>
- Lammens, E.H.R.R., Geursen, J., McGillivray, P.J., 1985. Diet shifts, feeding efficiency and coexistence of bream *Abramis brama*, roach *Rutilus rutilus* and white bream *Blicca bjoerkna* in hypertrophic lakes. In: Kullander, S.O., Fernholm, B. (Eds.), Proceedings of the Fifth Congress of European Ichthyologists. Department of Vertebrate Zoology, Swedish Museum of Natural History, Stockholm, 153–162.
- Lammens, E.H.R.R., Hoogenboezem, W., 1991. Diets and feeding behaviour. In: Winfield, I.J., Nelson, J.S. (Eds.), Cyprinid fishes: systematics, biology and exploitation. Chapman and Hall, London, 353–376. https://doi.org/10.1007/978-94-011-3092-9_12
- Lau, D.C.P., Vrede, T., Pickova, J., Goedkoop, W., 2012. Fatty acid composition of consumers in boreal lakes - variation across species, space and time. Freshw. Biol. 57, 24–38. <https://doi.org/10.1111/j.1365-2427.2011.02690.x>
- Lee, R.F., Hagen, W., Kattner, G., 2006. Lipid storage in marine zooplankton. Mar. Ecol. Prog. Ser. 307, 273–306. <https://doi.org/10.3354/meps307273>
- Legeżyńska, J., Kędra, M., Walkusz, W., 2014. Identifying trophic relationships within the high Arctic benthic community: how much can fatty acids tell? Mar. Biol. 161, 821–836. <https://doi.org/10.1007/s00227-013-2380-8>
- Lehtonen, H., Hansson, S., Winkler, H., 1996. Biology and exploitation of pikeperch, *Stizostedion lucioperca* (L), in the Baltic Sea area. Ann. Zool. Fenn. 33, 525–535.
- Lind, Y., Huovila, T., Kakela, R., 2018. A retrospective study of fatty acid composition in Baltic herring (*Clupea harengus membras*) caught at three locations in the Baltic Sea (1973-2009). ICES J. Mar. Sci. 75, 330–339. <https://doi.org/10.1093/icesjms/fsx127>
- Maazouzi, C., Medoc, V., Pihan, J.-C., Masson, G., 2011. Size-related dietary changes observed in young-of-the-year pumpkinseed (*Lepomis gibbosus*): stomach contents and fatty acid analyses. Aquat. Ecol. 45, 23–33. <https://doi.org/10.1007/s10452-010-9320-1>
- Makhotova, O.N., Stoyanov, K.N., 2021. Fatty acid content and composition in tissues of Baikal grayling (*Thymallus baicalensis*), with a special focus on DHA synthesis. Aquac. Int. 29, 2415–2433. <https://doi.org/10.1007/s10499-021-00755-w>
- Makhotova, O.N., Sushchik, N.N., Gladyshev, M.I., Ageev, A.V., Pryanichnikova, E.G., Kalachova, G.S., 2011. Is the fatty acid composition of freshwater zoobenthic invertebrates controlled by phylogenetic or trophic factors? Lipids 46, 709–721. <https://doi.org/10.1007/s11745-011-3566-9>
- McLusky, D.S., Elliott, M., 2004. The Estuarine Ecosystem; Ecology, Threats and Management. Oxford University Press, Oxford, 214 pp.
- Merad, I., Bellenger, S., Hichami, A., Khan, N.A., Soltani, N., 2018. Effect of cadmium exposure on essential omega-3 fatty acids in the edible bivalve *Donax trunculus*. Environ. Sci. Pollut. R. 25, 18242–18250. <https://doi.org/10.1007/s11356-017-9031-4>
- Möllmann, C., Diekmann, R., Müller-Karulis, B., Kornilovs, G., Plikshs, M., Axe, P., 2009. Reorganization of a large marine ecosystem due to atmospheric and anthropogenic pressure: a discontinuous regime shift in the Central Baltic Sea. Glob. Change Biol. 15, 1377–1393. <https://doi.org/10.1111/j.1365-2486.2008.01814.x>
- Möllmann, C., Müller-Karulis, B., Kornilovs, G., St John, M.A., 2008. Effects of climate and overfishing on zooplankton dynamics and ecosystem structure: regime shifts, trophic cascade, and feedback loops in a simple ecosystem. ICES J. Mar. Sci. 65, 302–310. <https://doi.org/10.1093/icesjms/fsm197>
- Monroig, O., Kabeya, N., 2018. Desaturases and elongases involved in polyunsaturated fatty acid biosynthesis in aquatic invertebrates: a comprehensive review. Fish. Sci. 84, 911–928. <https://doi.org/10.1007/s12562-018-1254-x>
- Monroig, O., Tocher, D.R., Castro, L.F.C., 2018. Polyunsaturated fatty acid biosynthesis and metabolism in fish. In: Burdge, G.C. (Ed.), Polyunsaturated fatty acid metabolism. AOCs Press, London, 31–60. <https://doi.org/10.1016/B978-0-12-811230-4.00003-X>
- Mourente, G., Tocher, D.R., Sargent, J.R., 1991. Specific accumulation of docosahexaenoic acid (22:6n-3) in brain lipids during development of juvenile turbot *Scophthalmus maximus* L. Lipids 26, 871–877. <https://doi.org/10.1007/bf02535970>
- Mustamaki, N., Cederberg, T., Mattila, J., 2014. Diet, stable isotopes and morphology of Eurasian perch (*Perca fluviatilis*) in littoral and pelagic habitats in the northern Baltic Proper. Environ. Biol. Fish. 97, 675–689. <https://doi.org/10.1007/s10641-013-0169-8>
- Nagelkerke, L.A.J., Sibbing, F.A., 1996. Efficiency of feeding on zebra mussel (*Dreissena polymorpha*) by common bream (*Abramis brama*), white bream (*Blicca bjoerkna*), and roach (*Rutilus rutilus*): The effects of morphology and behavior. Can. J. Fish. Aquat. Sci. 53, 2847–2861. <https://doi.org/10.1139/cjfas-53-12-2847>
- Nawrocka, L., Kobos, J., 2011. The trophic state of the Vistula Lagoon: an assessment based on selected biotic and abiotic parameters according to the Water Framework Directive. Oceanologia

- 53 (3), 881–894. <https://doi.org/10.5697/oc.53-3.881>
- Nielsen, J.M., Clare, E.L., Hayden, B., Brett, M.T., Kratina, P., 2018. Diet tracing in ecology: Method comparison and selection. *Methods Ecol. Evol.* 9, 278–291. <https://doi.org/10.1111/2041-210x.12869>
- Nowosad, J., Kucharczyk, D., Łuczyńska, J., Targońska, K., Czarkowski, T.K., Biłas, M., Krejszef, S., Horváth, L., Müller, T., 2015. Changes in European eel ovary development and body and ovary chemistry during stimulated maturation under controlled conditions: preliminary data. *Aquacult. Int.* 23, 13–27. <https://doi.org/10.1007/s10499-014-9794-2>
- Ojaveer, H., Lankov, A., Raid, T., Pllumae, A., Klais, R., 2018. Selecting for three copepods-feeding of sprat and herring in the Baltic Sea. *ICES J. Mar. Sci.* 75, 2439–2449. <https://doi.org/10.1093/icesjms/fsx249>
- Parrish, C.C., 2009. Essential fatty acids in aquatic food webs. In: Arts, M.T., Brett, M.T., Kainz, M.J. (Eds.), *Lipids in Aquatic Ecosystems*. Springer, New York, 309–326. https://doi.org/10.1007/978-0-387-89366-2_13
- Paturej, E., Gutkowska, A., 2015. The effect of salinity levels on the structure of zooplankton communities. *Arch. Biol. Sci.* 67, 483–492. <https://doi.org/10.2298/abs140910012p>
- Paturej, E., Gutkowska, A., Koszalka, J., Bowszys, M., 2017. Effect of physicochemical parameters on zooplankton in the brackish, coastal Vistula Lagoon. *Oceanologia* 59 (1), 49–56. <https://doi.org/10.1016/j.oceano.2016.08.001>
- Pawlikowski, K., Kornijów, R., 2019. Role of macrophytes in structuring littoral habitats in the Vistula Lagoon (southern Baltic Sea). *Oceanologia* 61 (1), 26–37. <https://doi.org/10.1016/j.oceano.2018.05.003>
- Persson, A., Brönmark, C., 2002. Foraging capacities and effects of competitive release on ontogenetic diet shift in bream, *Abramis brama*. *Oikos* 97, 271–281. <https://doi.org/10.1034/j.1600-0706.2002.970213.x>
- Persson, J., Vrede, T., 2006. Polyunsaturated fatty acids in zooplankton: variation due to taxonomy and trophic position. *Freshw. Biol.* 51, 887–900. <https://doi.org/10.1111/j.1365-2427.2006.01540.x>
- Prejs, A., Lewandowski, K., Stańczykowska-Piotrowska, A., 1990. Size-selective predation by roach (*Rutilus rutilus*) on zebra mussel (*Dreissena polymorpha*): field studies. *Oecologia* 83, 378–384. <https://doi.org/10.1007/bf00317563>
- Prigge, E., Malzahn, A.M., Zumholz, K., Hanel, R., 2012. Dietary effects on fatty acid composition in muscle tissue of juvenile European eel, *Anguilla anguilla* (L.). *Helgol. Mar. Res.* 66, 51–61. <https://doi.org/10.1007/s10152-011-0246-3>
- Psuty, I., Wilkońska, H., 2009. The stability of fish assemblages under unstable conditions: a ten-year series from the Polish part of the Vistula Lagoon. *Arch. Pol. Fish.* 17, 65–76. <https://doi.org/10.2478/v10086-009-0004-1>
- Sawyer, J.M., Arts, M.T., Arhonditsis, G., Diamond, M.L., 2016. A general model of polyunsaturated fatty acid (PUFA) uptake, loss and transformation in freshwater fish. *Ecol. Model.* 323, 96–105. <https://doi.org/10.1016/j.ecolmodel.2015.12.004>
- Scharnweber, K., Chaguaceda, F., Eklov, P., 2021. Fatty acid accumulation in feeding types of a natural freshwater fish population. *Oecologia* 196, 53–63. <https://doi.org/10.1007/s00442-021-04913-y>
- Specziár, A., Rezsű, E.T., 2009. Feeding guilds and food resource partitioning in a lake fish assemblage: an ontogenetic approach. *J. Fish Biol.* 75, 247–267. <https://doi.org/10.1111/j.1095-8649.2009.02283.x>
- Specziár, A., Tölg, L., Biró, P., 1997. Feeding strategy and growth of cyprinids in the littoral zone of Lake Balaton. *J. Fish Biol.* 51, 1109–1124. <https://doi.org/10.1111/j.1095-8649.1997.tb01130.x>
- StatSoft, 2011. *Electronic statistics textbook* StatSoft. Tulsa, OK, USA.
- Stolarski, J., 1995. Sichel (*Pelecus cultratus*, L.) from the Vistula Lagoon. *Bull. Sea Fish. Inst.* 2, 11–21.
- Stowasser, G., Pond, D.W., Collins, M.A., 2009. Using fatty acid analysis to elucidate the feeding habits of Southern Ocean mesopelagic fish. *Mar. Biol.* 156, 2289–2302. <https://doi.org/10.1007/s00227-009-1256-4>
- Strandberg, U., Hiltunen, M., Jelkänen, E., Taipale, S.J., Kainz, M.J., Brett, M.T., Kankaala, P., 2015. Selective transfer of polyunsaturated fatty acids from phytoplankton to planktivorous fish in large boreal lakes. *Sci. Tot. Environ.* 536, 858–865. <https://doi.org/10.1016/j.scitotenv.2015.07.010>
- Sushchik, N.N., Gladyshev, M.I., Kalachova, G.S., Makhutova, O.N., Ageev, A.V., 2006. Comparison of seasonal dynamics of the essential PUFA contents in benthic invertebrates and grayling *Thymallus arcticus* in the Yenisei river. *Comp. Biochem. Phys. B* 145, 278–287. <https://doi.org/10.1016/j.cbpb.2006.05.014>
- Sushchik, N.N., Rudchenko, A.E., Gladyshev, M.I., 2017. Effect of season and trophic level on fatty acid composition and content of four commercial fish species from Krasnoyarsk Reservoir (Siberia, Russia). *Fish. Res.* 187, 178–187. <https://doi.org/10.1016/j.fishres.2016.11.016>
- Sutton, T.M., Cyterski, M.J., Ney, J.J., Duval, M.C., 2004. Determination of factors influencing stomach content retention by striped bass captured using gillnets. *J. Fish Biol.* 64, 903–910. <https://doi.org/10.1111/j.1095-8649.2004.0358.x>
- Szlinder-Richert, J., Usydus, Z., Wyszynski, M., Adamczyk, M., 2010. Variation in fat content and fatty-acid composition of the Baltic herring *Clupea harengus membras*. *J. Fish Biol.* 77, 585–599. <https://doi.org/10.1111/j.1095-8649.2010.02696.x>
- Thiemann, G.W., Iverson, S.J., Stirling, I., 2008. Polar bear diets and Arctic marine food webs: insights from fatty acid analysis. *Ecol. Monogr.* 78, 591–613. <https://doi.org/10.1890/07-1050.1>
- Tocher, D.R., 2003. Metabolism and functions of lipids and fatty acids in teleost fish. *Rev. Fish. Sci.* 11, 107–184. <https://doi.org/10.1080/713610925>
- Tocher, D.R., 2010. Fatty acid requirements in ontogeny of marine and freshwater fish. *Aquac. Res.* 41, 717–732. <https://doi.org/10.1111/j.1365-2109.2008.02150.x>
- Trushenski, J.T., Rombenso, A.N., 2020. Trophic levels predict the nutritional essentiality of polyunsaturated fatty acids in fish-introduction to a special section and a brief synthesis. *N. Am. J. Aquacult.* 82, 241–250. <https://doi.org/10.1002/naaq.10137>
- Tverin, M., Esparza-Salas, R., Strömberg, A., Tang, P., Kokkonen, I., Herrero, A., Kauhala, K., Karlsson, O., Tiilikainen, R., Vetemaa, M., Sinisalo, T., Käkälä, R., Lundström, K., 2019. Complementary methods assessing short and long-term prey of a marine top predator - Application to the grey seal-fishery conflict in the Baltic Sea. *Plos One* 14, e0208694. <https://doi.org/10.1371/journal.pone.0208694>
- Usydus, Z., Szlinder-Richert, J., Adamczyk, M., Szatkowska, U., 2011. Marine and farmed fish in the Polish market: Comparison of the nutritional value. *Food Chem.* 126, 78–84. <https://doi.org/10.1016/j.foodchem.2010.10.080>
- Wang, S.Q., Monroig, O., Tang, G.X., Zhang, L., You, C.H., Tocher, D.R., Li, Y., 2014. Investigating long-chain polyunsaturated fatty acid biosynthesis in teleost fish: functional characterization of fatty acyl desaturase (Fads2) and Elovl5 elongase in the catadromous species, Japanese eel *Anguilla japonica*. *Aquaculture* 434, 57–65. <https://doi.org/10.1016/j.aquaculture.2014.07.016>
- Wasmund, N., Uhlig, S., 2003. Phytoplankton trends in the Baltic Sea. *ICES J. Mar. Sci.* 60, 177–186. [https://doi.org/10.1016/S1054-3139\(02\)00280-1](https://doi.org/10.1016/S1054-3139(02)00280-1)

- Wiśniewski, R.J., 1978. Effect of predators on Tubificidae groupings and their production in lakes. *Pol. J. Ecol.* 26, 493–512.
- Xu, W.J., Wang, S.Q., You, C.H., Zhang, Y.L., Monroig, O., Tocher, D.R., Li, Y, 2020. The catadromous teleost *Anguilla japonica* has a complete enzymatic repertoire for the biosynthesis of docosahexaenoic acid from alpha-linolenic acid: cloning and functional characterization of an Elovl2 elongase. *Comp. Biochem. Phys. B* 240, 110373. <https://doi.org/10.1016/j.cbpb.2019.110373>
- Żmudziński, L., 1996. The effect of the introduction of the American species *Marenzelleria viridis* (Polychaeta: Spionidae) on the benthic ecosystem of Vistula lagoon. *Mar. Ecol.* 17, 221–226. <https://doi.org/10.1111/j.1439-0485.1996.tb00503.x>

Available online at www.sciencedirect.com

ScienceDirect

journal homepage: www.journals.elsevier.com/oceanologia

ORIGINAL RESEARCH ARTICLE

Dynamics of absorption properties of CDOM and its composition in Likas estuary, North Borneo, Malaysia

Saiyidah Munirah Mohd-Shazali^a, Jafar-Sidik Madihah^{a,*}, Nurzaliah Ali^a,
Chen Cheng-Ann^a, Robert J.W. Brewin^b, Md. Suffian Idris^c, P. Purba Noir^d

^aBorneo Marine Research Institute, University of Malaysia of Sabah, Sabah, Malaysia

^bCentre for Geography and Environmental Science, College of Life and Environmental Sciences, University of Exeter, Penryn, Cornwall, United Kingdom

^cFaculty of Science and Marine Environment, University of Malaysia Terengganu, Terengganu, Malaysia

^dMarine Research Laboratory (MEAL), Faculty of Fishery and Marine Science, Padjadjaran University, Jatinangor, Indonesia

Received 18 May 2021; accepted 15 April 2022

Available online 17 May 2022

KEYWORDS

Coloured dissolved organic matter (CDOM);
The absorption coefficient of CDOM (a_{CDOM});
Molecular weight and degradation of CDOM;
High molecular weight (HMW) CDOM;
Low molecular weight (LMW) CDOM

Abstract Chromophoric Dissolved Organic Matter (CDOM) is a vital water constituent in aquatic ecosystems that contributes to water colour, affects light penetration, and impacts primary production. This study aims to determine the spatial and monsoonal variability of CDOM absorption properties in the Likas estuary, characterise the source of CDOM, and investigate the correlations between CDOM absorption properties and salinity. Likas estuary is a small estuary located in Kota Kinabalu city on the west coast of Sabah, facing the South China Sea. A mangrove ecosystem surrounds it with manufactured structures such as residential areas and public facilities. Surface water samples were collected at 19 stations: upstream of rivers to the river mouth and coastal area during spring tides every month, from June 2018 to July 2019, for 14-months. The distribution of $a_{CDOM}(440)$ in the study area is predictable as a signature in a coastal area with a decreasing gradient from the upstream towards coastal water ($0.29 \pm 0.19 \text{ m}^{-1}$ to $1.05 \pm 0.39 \text{ m}^{-1}$). There are increasing spatial patterns of spectral slopes $S_{275-295}$ and S_R . However, $S_{350-400}$ and $S_{300-600}$ declined spatial gradients from the upstream to coastal water. Thus, $S_{300-600}$ indicates a linear relationship between $a_{CDOM}(440)$, which unconventional results

* Corresponding author at: Borneo Marine Research Institute, Universiti Malaysia Sabah, Jalan UMS 88400, Kota Kinabalu, Sabah, Malaysia.
E-mail address: madihah@ums.edu.my (J.-S. Madihah).

Peer review under the responsibility of the Institute of Oceanology of the Polish Academy of Sciences.



<https://doi.org/10.1016/j.oceano.2022.04.005>

0078-3234/© 2022 Institute of Oceanology of the Polish Academy of Sciences. Production and hosting by Elsevier B.V. This is an open access article under the CC BY-NC-ND license (<http://creativecommons.org/licenses/by-nc-nd/4.0/>).

in coastal water. We suspect this is due to a small coverage of the study site with a distance of 0.5 m intervals of each station. This could be why the $S_{300-600}$ had constant values throughout the study area (with no statistical difference between stations). In addition, $S_{300-600}$ was merely varied in the stations located at the river mouth and coastal water. Based on the spectral slope ratio (S_R), most of the stations located in the Darau, Inanam, and Bangka-Bangka rivers had S_R values less than 1. Hence, CDOM in these stations is a terrestrial-dominated source. Therefore, from our observations during the study period, monsoonal variation could alter the source of CDOM in the study area.

© 2022 Institute of Oceanology of the Polish Academy of Sciences. Production and hosting by Elsevier B.V. This is an open access article under the CC BY-NC-ND license (<http://creativecommons.org/licenses/by-nc-nd/4.0/>).

1. Introduction

Chromophoric Dissolved Organic Matter (CDOM) is a fragment of Dissolved Organic Matter (DOM) with chromophores molecules that absorb visible and ultra-violet (UV) light. CDOM contributes to the colour of natural water, with water with high CDOM concentration appearing brown as it absorbs UV preferentially, then blue and green regions of the light spectrum (Coble and Nelson, 2009; Kirk, 1994). The sources of CDOM vary from being allochthonous to autochthonous. The allochthonous sources are mainly from the decomposition of terrestrial vegetation and soil by rivers and wetlands that carry decomposed terrestrial plants, sewage, and sediments or known as a terrestrial-dominated source of CDOM. Whereas autochthonous results from in-situ biological activity such as the production of aquatic primary producers, namely phytoplankton and zooplankton (Bowen et al., 2017; Brandão et al., 2018; Minu et al., 2020), which is associated with a marine-dominated source of CDOM. CDOM has also been used as a natural tracer to study the dispersion, transport, and mixing of water masses (Nelson et al., 2007; Stedmon et al., 2010).

CDOM can act as a protective barrier in shielding biota and coral reefs from damaging UV radiation in shallow coastal areas due to its strong absorption of UV light. However, the increasing supply of CDOM concentration by rivers can affect underwater light availability, reducing the photic depth and causing light limitation for phytoplankton, impacting primary production and surface ocean heating by altering the energy and heat budget of coastal waters (Granskog et al., 2007; Guèguen et al., 2005; Nelson et al., 1998). The optical properties of CDOM that can provide information on DOM and DOC are useful for quantifying carbon transport and continuous monitoring of wastewater discharge (Ferrari, 2000; Shanmugam et al., 2016).

The spectral shape of CDOM can also be used to help separate the absorption of phytoplankton, detritus, and minerals and provide insights into CDOM composition (Grunert et al., 2018). CDOM plays an essential role in assessing water quality and biogeochemical cycling (Andrew et al., 2013; Hickman et al., 2010; Kim et al., 2016). The spectral characteristics of CDOM absorption provide valuable insights into the composition and origins of CDOM and allow retrievals of CDOM in coastal and estuarine waters from ocean colour remote sensing (Grunert et al., 2018; Menon et al., 2011). The spectral slope parameter (S) of CDOM describes the spectral dependence of the CDOM absorption coefficient with wave-

length and can provide information on the source of CDOM and its susceptibility to biological and photochemical processes (Blough and Del Vecchio, 2002; Osburn and Stedmon, 2011; Stedmon and Markager, 2001). The S value has also been related to the molecular weight and aromaticity of DOM (Blough and Green, 1995; Helms et al., 2008). For instance, the spectral slope between 275–295 nm ($S_{275-295}$) is a good indicator of the different CDOM pools, marine and terrestrial (Grunert et al., 2018; Helms et al., 2008; Nima et al., 2019; Stedmon and Markager, 2001). The slope ratio (SR) of $S_{275-295}$ and $S_{350-500}$ (subscript reflects the wavelength range in nm) have also been shown to be useful for characterising CDOM in natural waters, with lower relative values indicative of DOM of higher molecular weight, greater aromaticity and increasing vascular plant inputs (Helms et al., 2008; Osburn et al., 2012; Spencer et al., 2010a).

The Darau River is a part of the Likas estuary. It is bounded by a large stretch of mangrove forest distributed from upstream towards the river mouth, with a few residential areas. The coastal and river mouth receives terrestrial input from three rivers: the Darau River, Bangka-Bangka River, and Inanam River. In addition, there is a wide range in salinity in the study area, resulting from the mixing of inflowing coastal water with outflowing freshwater. Due to these particular conditions, it is hypothesised that the CDOM pool may have different origins and compositions in the study area. The aims of this study are to 1) determine, for the first time, the spatial variability of CDOM absorption and spectral composition to help characterise its source; and 2) investigate correlations between CDOM absorption properties, spectral slopes, and salinity in the study region. Results will provide better insights into the dynamics of CDOM in the region and for the future development of regional remote-sensing algorithms of water colour.

2. Methodology

2.1. Study area and plan of sampling

The study was conducted in the Likas estuary, Kota Kinabalu, which is located on the west coast of Sabah and faces the South China Sea. The Likas Estuary is a small estuary surrounded by urban development influenced by mixed-tidal action. It receives water input from several connected rivers, such as the Darau River, Inanam River, and Bangka-Bangka River. The study area stretched about 2 km to 5 km

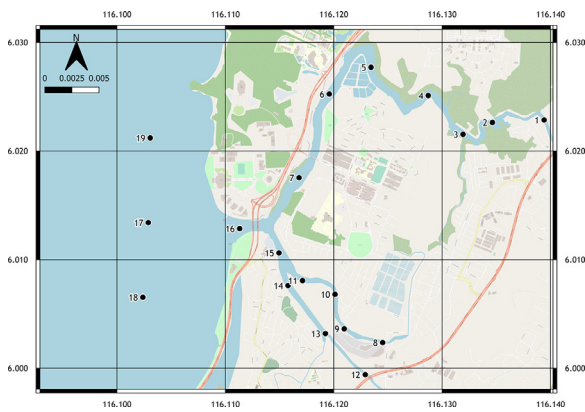


Figure 1 The map of Darau river with 19 sampling points (black dots) that distributed from upstream of Darau river towards the coastal area of Likas estuary, Kota Kinabalu, Sabah.

in length, which measured from the river mouth towards the upstream Darau River, Bangka-Bangka River, and Inanam River. The study area is bounded by natural features such as a single large stretch of mangrove forest and manufactured structures, such as fisherman villages and developments. Another aspect is the variability in surface salinity exhibited in this region (from 0.13 ppt to 31.83 ppt) due to substantial freshwater input.

The climate in Kota Kinabalu is hot and humid, having an equatorial climate with consistent temperatures throughout the year, influenced by monsoon circulation. The Northeast monsoon (NEM) is driven by northeasterly winds and brings cool temperatures and less rainfall between November and March. The Southwest monsoon (SWM) is driven by southwesterly winds and brings warm temperatures but more rainfall between May and September. These two distinct monsoon seasons are separated by shorter two inter-monsoon periods that take place from April to May (summer inter-monsoon) and from September to October (fall inter-monsoon) (Teong et al., 2017). The tropical climate influences changes in the physicochemical conditions in tropical estuaries, such as rainfall, humidity, solar radiation, air temperature, and wind direction (Teong et al., 2017).

The sampling was carried out on a monthly basis starting from June 2018 until July 2019. There were 19 sampling points that were located from the upper stream of rivers towards the river mouth and coastal area of Likas estuary. The sampling was carried out in the daytime during spring tide. The surface water samples were collected for further laboratory analyses (Figure 1).

2.2. Determination of CDOM absorption coefficient and spectral slopes

For precautions, the collected surface water for CDOM analysis was stored in amber bottles and kept refrigerated before analysis in the laboratory. Before absorption analysis, water samples were filtered through a 0.2 µm cellulose nitrate membrane filter. Pure water was used as a blank to determine the CDOM absorbance of samples for wavelengths between 220 nm to 750 nm at 1 nm intervals using a UV-Vis DR 500 Hach spectrophotometer with a 10 cm quartz cu-

vette. CDOM absorbance was assumed to be zero for wavelengths above 700 nm. Therefore, the average CDOM absorbance for the interval between 700 nm to 750 nm was subtracted from the spectrum to correct for offsets due to instrument baseline drift, temperature and scattering effects (Green and Blough, 1994). The absorbance values were transformed into the absorption coefficient according to Helms et al. (2008), where the CDOM absorption coefficient, $a_{CDOM}(\lambda)$ in m^{-1} , was calculated according to

$$a_{CDOM}(\lambda) = 2.303 * O_{CDOM}(\lambda) / l, \tag{1}$$

where l is the path length of the optical cell in meters, $a_{CDOM}(\lambda)$ is the absorption coefficient of CDOM at a given wavelength, and $O_{CDOM}(\lambda)$ is the absorbance at a given wavelength, from 300 nm to 600 nm. In this study, the CDOM absorption coefficient at a single wavelength of 440 nm ($a_{CDOM}(440)$) is used to describe the changes in CDOM quantity and to examine the spatial variability of CDOM within the studies area. The magnitudes of CDOM were measured by the absorption coefficient of CDOM, $a_{CDOM}(440)$. The absorption coefficient at 440 nm is chosen because it is the midpoint of the blue waveband peak that is related to the photosynthetic action spectrum of most classes of algae. It is also a wavelength measured by many ocean-colour satellites.

The CDOM spectral slope was determined by fitting the absorption coefficients to a single-exponential non-linear curve, to the wavelengths from 300 nm to 600 nm, using the equation of Bricaud et al. (1981), such that

$$a_{CDOM}(\lambda) = a_{CDOM}(\lambda_r) \exp(-S_{CDOM} [\lambda - \lambda_r]), \tag{2}$$

where S_{CDOM} is the spectral slope of a_{CDOM} and λ_r is the reference wavelength at 440 nm. CDOM spectral characteristics and its spectral slope are typically indicative of the chemical composition of CDOM (Helms et al., 2008; Stedmon and Markager, 2001). The spectral slopes for intervals of 275–295 nm ($S_{275-295}$) and 350–500 nm ($S_{350-500}$) were calculated by fitting the log-transformed CDOM absorption coefficient to linear regression. Higher slopes indicate a more rapid decrease in CDOM absorption with increasing wavelength. The slope ratio (S_R) between $S_{275-295}$ and $S_{350-500}$ was also calculated. These wavelengths were chosen to help determine the composition and source of CDOM in the study area.

2.3. Statistical analysis

The statistical analysis was carried out using IBM SPSS Statistics 25 software. The normality of the dataset was checked by using the Shapiro-Wilk (SW) test to determine if the response variable of each group of data had a normal distribution. Based on the distribution pattern of each variable, one-way ANOVA (for a normal distribution) or the Kruskal-Wallis test (for non-normal distributions) were used to test for significant differences among study areas and between monsoons. The correlation coefficient (r) was determined from the regression analysis to study the relationship between CDOM, optical properties, and salinity.

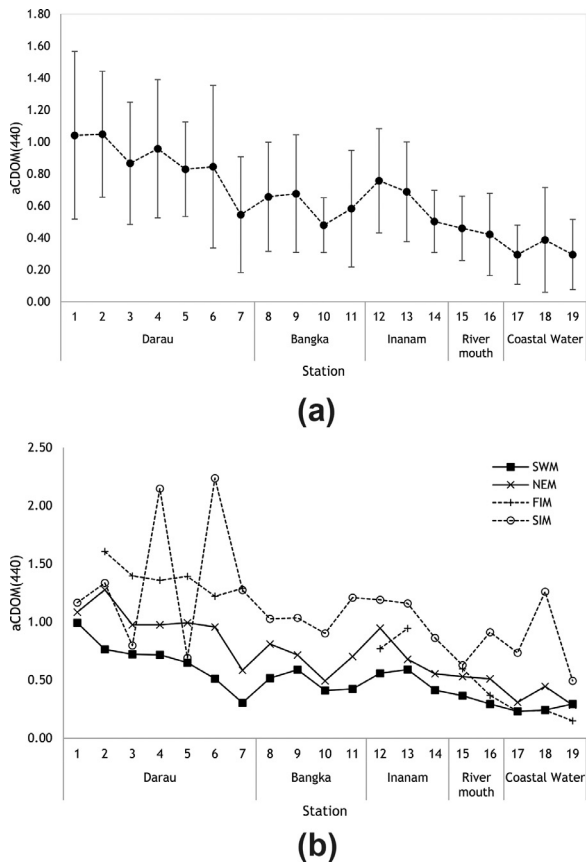


Figure 2 The temporal and monsoonal mean of $a_{CDOM}(440)$ at each station during 14-month observation in the study area. Error bars in Figure 2a indicated standard deviation of the 14-month observation means.

3. Results

3.1. Spatio-temporal variations of $a_{CDOM}(440)$

The temporal mean $a_{CDOM}(440)$ varied between $0.29 \pm 0.19 \text{ m}^{-1}$ (station 17) at coastal water and $1.05 \pm 0.39 \text{ m}^{-1}$ (Station 2) upstream of Darau, as plotted in Figure 2a. There was an apparent spatial gradient of $a_{CDOM}(440)$ in the study area that was relatively higher upstream (Station 1, 2, 8, and 12) compared to the station in the coastal area (Station 17, 18, and 19). The spatial distribution of $a_{CDOM}(440)$ showed statistically significant differences between sampling points ($p < 0.05$), where the $a_{CDOM}(440)$ decreased from the river to the coastal area ($p < 0.05$).

The monsoonal mean of $a_{CDOM}(440)$ was relatively low and had a decreasing pattern from the upstream to the coastal water during SWM with the range of 0.23 m^{-1} (Station 17) and 0.99 m^{-1} (Station 1) (Figure 2b). SIM, on the other hand, had a greater $a_{CDOM}(440)$, which fluctuated between 0.49 m^{-1} (Station 19 – coastal area) and 2.24 m^{-1} (Station 6 – Darau), with the value of $a_{CDOM}(440)$ nearly twice in SWM (Figure 2b). The monsoonal distribution of $a_{CDOM}(440)$ showed statistically significant differences between monsoons ($p < 0.05$).

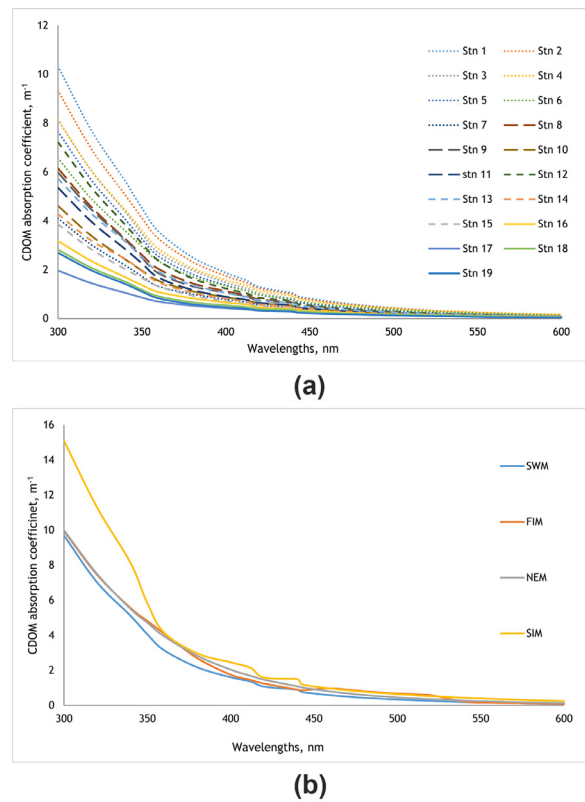


Figure 3 Mean CDOM absorption spectra obtained by averaging over absorption coefficient from 300–600 nm and fitted to non-linear exponential decay function for a) Spatial distribution at 19 sampling stations and b) the monsoonal distribution during Southwest monsoon (SWM), FIM (Fall-Intermonsoon), North-east Monsoon (NEM) and Summer Intermonsoon (SIM) during the study period.

3.2. CDOM absorption spectra

The CDOM absorption coefficient showed a decreasing trend in response to spatial and monsoonal variations (Figure 3). Figure 3 illustrates the mean absorption spectra of CDOM at all stations (Figure 3a) and the slope of monsoonal variations in the study area (Figure 3b). The spatial-spectral slope was higher at Station 1, located upstream of the Darau River ($S = 0.015 \text{ nm}^{-1}$), whereas the lowest spectral slope was found at station 17 in the coastal water ($S = 0.011 \text{ nm}^{-1}$), as plotted in Figure 3a.

For monsoonal trend, SIM monsoon attributed lower spectral slope with $14 \mu\text{m}^{-1}$, primarily bigger CDOM absorption coefficient at 300 to 350 nm than other observed monsoons (Figure 3b). In contrast, an identical slope with small difference was observed during SWM ($S = 0.016 \text{ nm}^{-1}$), FIM ($S = 0.015 \text{ nm}^{-1}$) and NEM ($S = 0.015 \text{ nm}^{-1}$) monsoons (Figure 3b).

3.3. Spectral slope $S_{275-295}$, $S_{350-500}$, and S_R of absorption properties

The spatial means of CDOM spectral slope from 275 to 295 nm ($S_{275-295}$) had smaller differences between stations, ranging from $0.015 \pm 0.002 \text{ nm}^{-1}$ (Station 1, upstream Darau

River) to $0.019 \pm 0.010 \text{ nm}^{-1}$ (Station 17, coastal water), as illustrated in Figure 4a. However, when compared to other stations, Station 7 (Darau) and Station 13 (Inanam) showed a substantial standard deviation of $0.019 \pm 0.010 \text{ nm}^{-1}$ and $0.017 \pm 0.005 \text{ nm}^{-1}$ (Figure 4a) compared to other stations. Nevertheless, the spatial distribution of $S_{275-295}$ showed significant differences where $S_{275-295}$ increased from the river to the coastal area ($p < 0.05$). The monsoonal means of $S_{275-295}$ peaked at Station 7 (Darau) during SWM (0.023 nm^{-1}) and Station 11 (Bangka) during SIM (0.024 nm^{-1}), as shown in Figure 4b. The monsoonal range of $S_{275-295}$ indicated relatively higher were coastal area with the ranges of 0.014 nm^{-1} to 0.023 nm^{-1} (SWM), 0.015 nm^{-1} to 0.018 nm^{-1} (NEM), 0.015 nm^{-1} to 0.020 nm^{-1} (FIM) and 0.015 nm^{-1} to 0.024 nm^{-1} (SIM) (Figure 4b). No significant differences were observed in the distribution of $S_{275-295}$ between monsoons ($p > 0.05$).

As shown in Figure 4c, the spectral slope from 350 to 400 nm ($S_{350-400}$) displayed a fluctuating pattern with a range of $0.015 \pm 0.003 \text{ nm}^{-1}$ (coastal water station) to $0.019 \pm 0.002 \text{ nm}^{-1}$ (upstream) as shown in Figure 4c. $S_{350-400}$ of Darau, and Inanam rivers showed a declining pattern, ranging from $0.017 \pm 0.002 \text{ nm}^{-1}$ to $0.016 \pm 0.002 \text{ nm}^{-1}$ and $0.019 \pm 0.002 \text{ nm}^{-1}$ to $0.017 \pm 0.002 \text{ nm}^{-1}$, respectively (Figure 4c). Bangka stations reported a fluctuation in the value of $S_{350-400}$, ranging from $0.016 \pm 0.003 \text{ nm}^{-1}$ to $0.018 \pm 0.002 \text{ nm}^{-1}$. $S_{350-400}$ values between $0.015 \pm 0.005 \text{ nm}^{-1}$ and $0.017 \pm 0.003 \text{ nm}^{-1}$ reveal a declining pattern in river mouth and coastal water (Figure 4c). The spatial distribution of $S_{350-400}$ showed statistically opposite pattern from $S_{275-295}$ where the $S_{350-400}$ decreased from rivers to the coastal area ($p < 0.05$).

During the SIM, the monsoonal means of $S_{350-400}$ fluctuated, especially from Station 1 to Station 7 (Darau), as shown in Figure 4d. During FIM, a sharp drop in the $S_{350-500}$ value (0.006 nm^{-1}) was seen at Station 17, which is located near the coast (Figure 4d). The $S_{350-400}$ of monsoonal variations during the study period were 0.016 nm^{-1} to 0.019 nm^{-1} (SWM), 0.015 nm^{-1} to 0.018 nm^{-1} (NEM), 0.006 nm^{-1} to 0.019 nm^{-1} (FIM), and 0.010 nm^{-1} to 0.020 nm^{-1} (SIM) (Figure 4d). In general, the monsoonal distribution of $S_{350-400}$ showed statistically significant differences between monsoons ($p < 0.05$).

Figure 4e displays the spatial mean of $S_{300-600}$ at the Darau, Inanam, and Bangka stations, which showed a consistent trend ranging from $0.014 \pm 0.002 \text{ nm}^{-1}$ to $0.016 \pm 0.004 \text{ nm}^{-1}$. $S_{300-600}$ value drops from the river mouth (Station 15 and 16) to coastal area stations (Station 17, 18, and 19), with a range of $0.012 \pm 0.003 \text{ nm}^{-1}$ to $0.013 \pm 0.004 \text{ nm}^{-1}$ (Figure 4e). However, the $S_{300-600}$ did not show any significant pattern between sampling points during the 14-months of the study period ($p > 0.05$). As shown in Figure 4f, the monsoonal pattern of $S_{300-600}$ revealed an up and down trend in SIM at Darau stations with the value of 0.007 nm^{-1} (Station 4) and 0.017 nm^{-1} (Station 3). There were very slight monsoonal changes in $S_{300-600}$, ranging from 0.012 to 0.015 (SWM), 0.012 to 0.018 (NEM), and 0.009 to 0.015 (FIM) (Figure 4f). Statistically, the monsoonal distribution of $S_{300-600}$ showed significant differences between monsoons throughout the study period ($p < 0.05$).

The spatial means and their standard deviations of spectral ratio (S_R) peaked at Station 7 (Darau) and Station 17

(coastal water) with values of 1.22 ± 0.61 and 1.40 ± 0.68 , respectively, as plotted in Figure 4g. Furthermore, an increased pattern of S_R values at the Darau stations (0.86 ± 0.13 to 1.22 ± 0.61) and Inanam River (0.81 ± 0.16 to 1.01 ± 0.45) was recorded during the study period (Figure 4g). In contrast, Station 17, 18, and 19 located at the coastal water indicated a declining slope with 1.60 ± 0.48 to 1.13 ± 0.31 (Figure 4g). The spatial distribution of S_R showed statistically significant differences between sampling points during the study period ($p < 0.05$).

Overall, the monsoonal distribution of SR showed statistically significant differences between monsoons ($p < 0.05$). In FIM, the most significant monsoonal mean of S_R was observed at Station 17, located near the coast, with a value of 3.46, as shown in Figure 4h. S_R readings ranged from 0.81 to 1.51 in Darau stations during SIM and from 0.70 to 1.29 in Bangka stations (Figure 4h). The monsoonal mean of S_R during NEM and SWM at the study area, on the other hand, had a constant trend, ranging from 0.79 (Station 1) to 1.44 (Station 7) at Darau Station and 0.81 (Station 12 at Inanam River) to 1.34 (Station 19 at the coastal water) respectively (Figure 4h).

3.4. Relationship between salinity with $a_{CDOM}(440)$, $S_{275-295}$, $S_{350-400}$, and S_R

The regression analysis between $a_{CDOM}(440)$ and salinity during 14-month observation in the study period showed a weak negative relationship with R-value of -0.322 ($p = 0.000$, $n = 254$) as illustrated in Figure 5a. Therefore, the inter-seasonal monsoon attributed the highest correlation between $a_{CDOM}(440)$ and salinity with R-value of -0.73 ($p = 0.000$, $n = 31$) during FIM, -0.59 ($p = 0.000$, $n = 37$) in SIM monsoon (Figure 5a). A moderate correlation between $S_{275-295}$ and salinity with R-value of 0.55 ($p = 0.00$, $n = 252$) as plotted in Figure 5b. The monsoonal trends of $S_{275-295}$ and salinity correlation showed more or less the same in observed monsoons with R-value of 0.60 ($p = 0.00$, $n = 30$) (FIM), 0.51 ($p = 0.00$, $n = 71$) (NEM), and 0.44 ($p = 0.006$, $n = 37$) (SIM). However, $S_{275-295}$ and salinity correlation during SWM was relatively higher compared to another observed monsoon with R-value of 0.66 ($p = 0.00$, $n = 111$) (Figure 5b).

There is a low inverse correlation between $S_{350-400}$ and salinity with R-value of 0.33 ($p = 0.00$, $n = 254$) during 14-month observation in the study period as shown in Figure 5c. The lowest correlation between $S_{350-400}$ and salinity was in NEM monsoon (R-value = -0.11 , $p = 0.36$, $n = 71$), while R-value of $S_{350-400}$ and salinity is relatively larger ($r = -0.48$, $p = 0.005$, $n = 31$) in FIM monsoon (Figure 5c). The relationship between the ratio of spectra slope (SR) and salinity indicate a lenient correlation at the study area with R-value of 0.53 ($p = 0.00$, $n = 253$) based on the 14-month observation (Figure 5d). Moreover, SWM depicts a relatively good correlation with R-value of 0.67 ($p = 0.000$, $n = 111$) (Figure 5d). On the other hand, r-value of 0.39 ($p = 0.001$, $n = 71$) was recorded in NEM monsoon, which the lowest magnitude compared to other observed monsoons (Figure 5d). As for the $S_{300-600}$, no significant correlations were observed throughout the 14-month observation and during each monsoon.

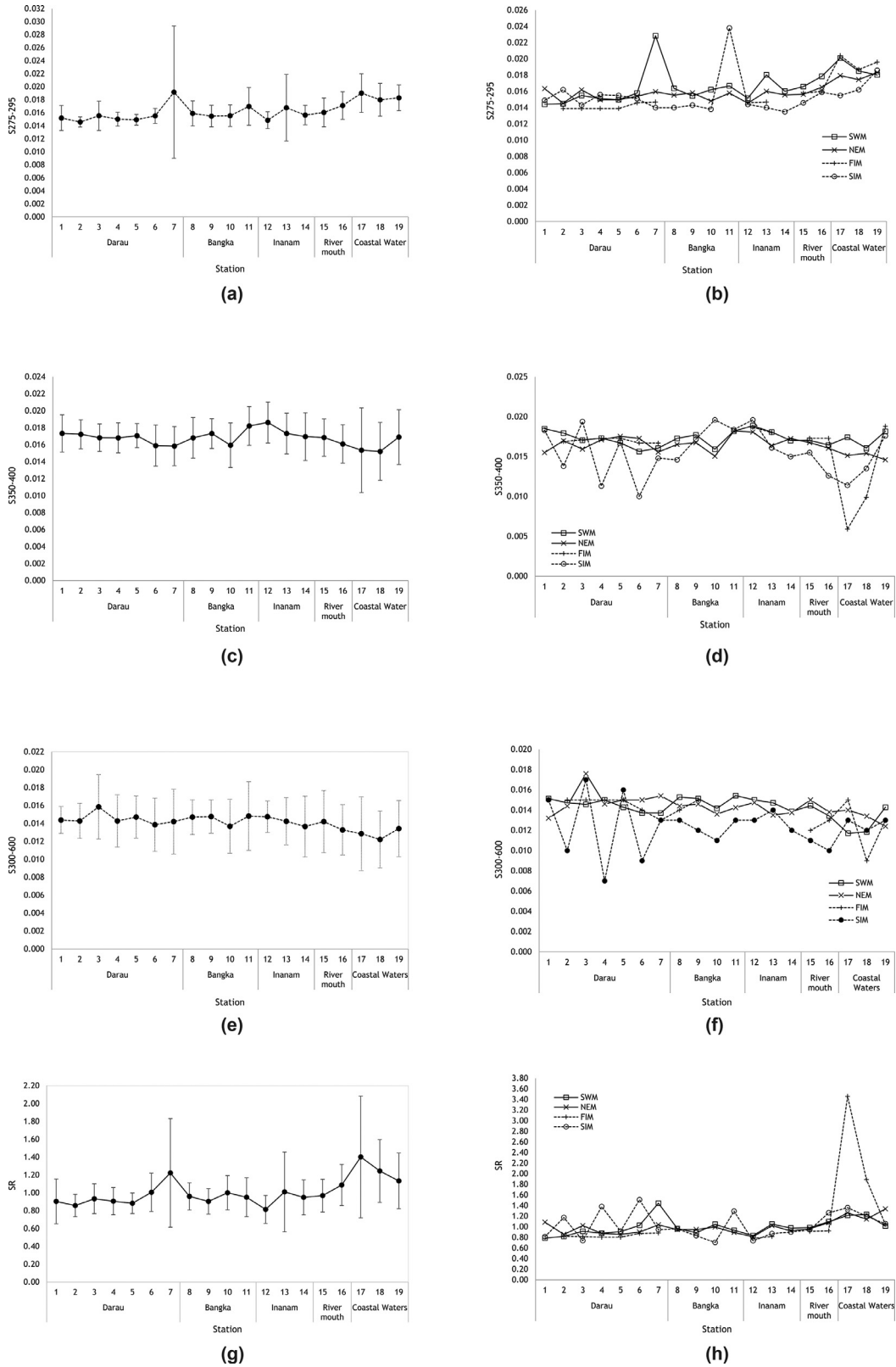


Figure 4 The temporal and monsoonal mean of spectral slopes: $S_{275-295}$, $S_{350-440}$, and S_R at each station during 14-month observation in the study area.

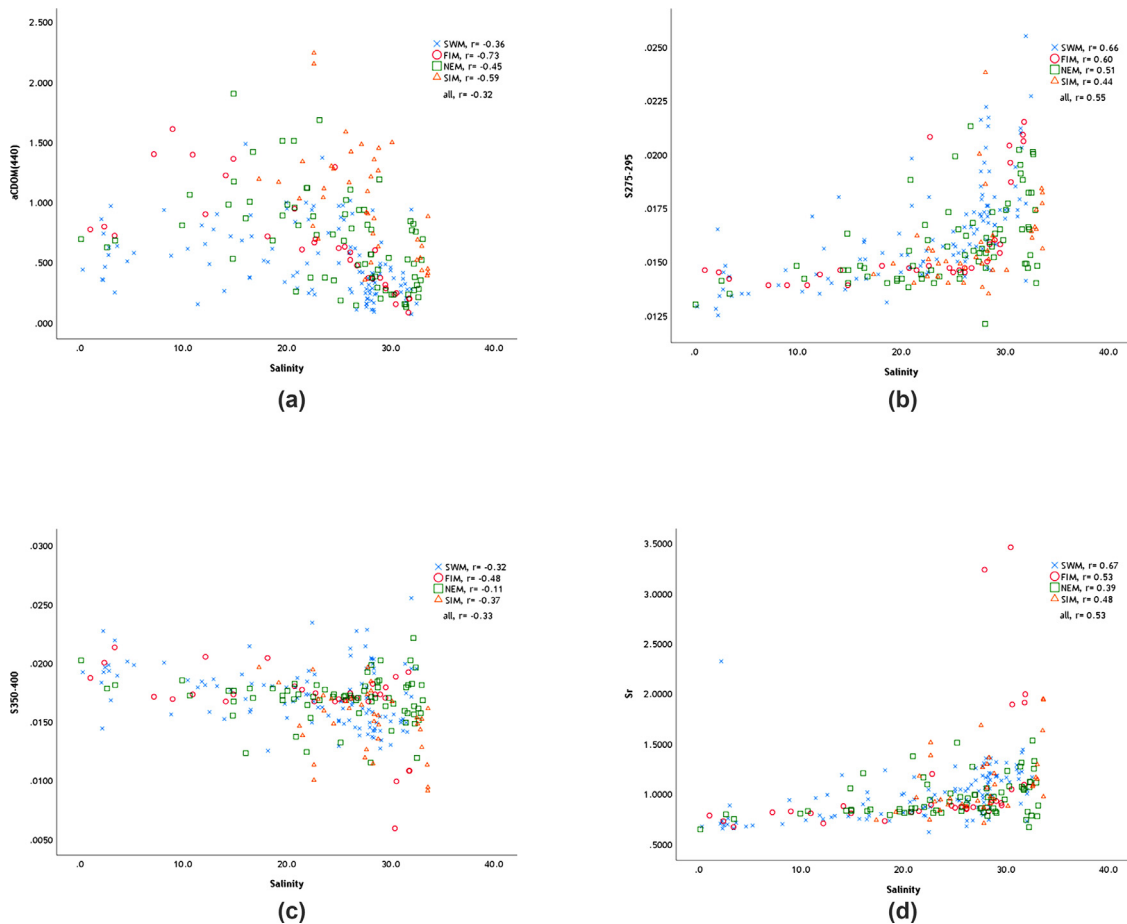


Figure 5 Scatter plots of regression correlation (r) between salinity and a) CDOM absorption coefficient at 440 [$a_{CDOM}(440)$], b) $S_{275-295}$, c) $S_{350-440}$ and d) the ratio of spectral slope (S_R) for the 14-month observation at the study area. The r -value stated in the legend of the plot.

3.5. Relationship between $S_{275-295}$, $S_{350-440}$, and S_R with $a_{CDOM}(440)$

A moderate correlation between $S_{275-295}$ and $a_{CDOM}(440)$ was observed in the study area based on the 14-month observation with R -value of -0.57 ($p=0.000$, $n=252$) as illustrated in Figure 6a. For the monsoonal pattern of relationship of $S_{275-295}$ and $a_{CDOM}(440)$, SWM, FIM and NEM depict a relatively strong correlation with R -values of -0.65 ($p=0.000$, $n=111$), -0.67 ($p=0.000$, $n=30$) and -0.70 ($p=0.000$, $n=71$) respectively (Figure 6a). A lenient $S_{275-295}$ and $a_{CDOM}(440)$ correlations were recorded during SIM with R -values of 0.37 ($p=0.023$, $n=37$) (Figure 6a). There is a very weak relationship between $S_{350-400}$ and $a_{CDOM}(440)$ in this study as indicated by the small R -value of 0.05 ($p=0.456$, $n=254$), which is plotted in Figure 6b. Of all observed monsoons were reported smaller R -values; SWM (0.11 , $p=0.244$, $n=112$), NEM (0.19 , $p=0.113$, $n=71$), and SIM (0.11 , $p=0.532$, $n=37$), FIM monsoon attributed a relatively larger R -value (0.33 , $p=0.068$, $n=31$) compared to other monsoons (Figure 6b). The R -value of regression correlation between S_R and $a_{CDOM}(440)$ in the study area is -0.30 ($p=0.000$, $n=253$) as shown in Figure 6c. There are two monsoonal patterns of S_R and $a_{CDOM}(440)$ during the study period, where NEM (-0.56 , $p=0.000$, $n=71$) and FIM

(-0.50 , $p=0.004$, $n=31$) monsoon a moderate correlation (Figure 6c). Meanwhile, SWM and SIM monsoon attributed a weak relationship between S_R and $a_{CDOM}(440)$ with R -value of (-0.35 , $p=0.000$, $n=112$) and (-0.27 , $p=0.103$, $n=37$) respectively (Figure 6c).

4. Discussion

4.1. Dynamics of $a_{CDOM}(440)$

The spatial mean $a_{CDOM}(440)$ in the study area, ranging from $0.29 \pm 0.19 \text{ m}^{-1}$ to $1.05 \pm 0.39 \text{ m}^{-1}$, indicated a decreasing pattern towards the coastal water. The spatial declining trends of $a_{CDOM}(440)$ in the study area are predictable as a signature of CDOM distribution in coastal waters. Several studies recorded a spatial gradient of $a_{CDOM}(440)$ in coastal waters with a range of 2.5 to 7.6 m^{-1} in the mangrove area in the Indian Suburbans (Sanyal et al., 2020). The $a_{CDOM}(440)$ of 0.063 to 0.35 m^{-1} was recorded worldwide in the natural water bodies (Nima et al., 2019). In addition, $a_{CDOM}(440)$ of 0.35 m^{-1} to $>50 \text{ m}^{-1}$ at peatland-draining rivers and coastal waters of Sarawak, Borneo (Martin et al., 2018). The $a_{CDOM}(440)$ at the continental shelf of the northern Bay of Bengal ranged from 0.1002 m^{-1} and 0.6631 m^{-1}

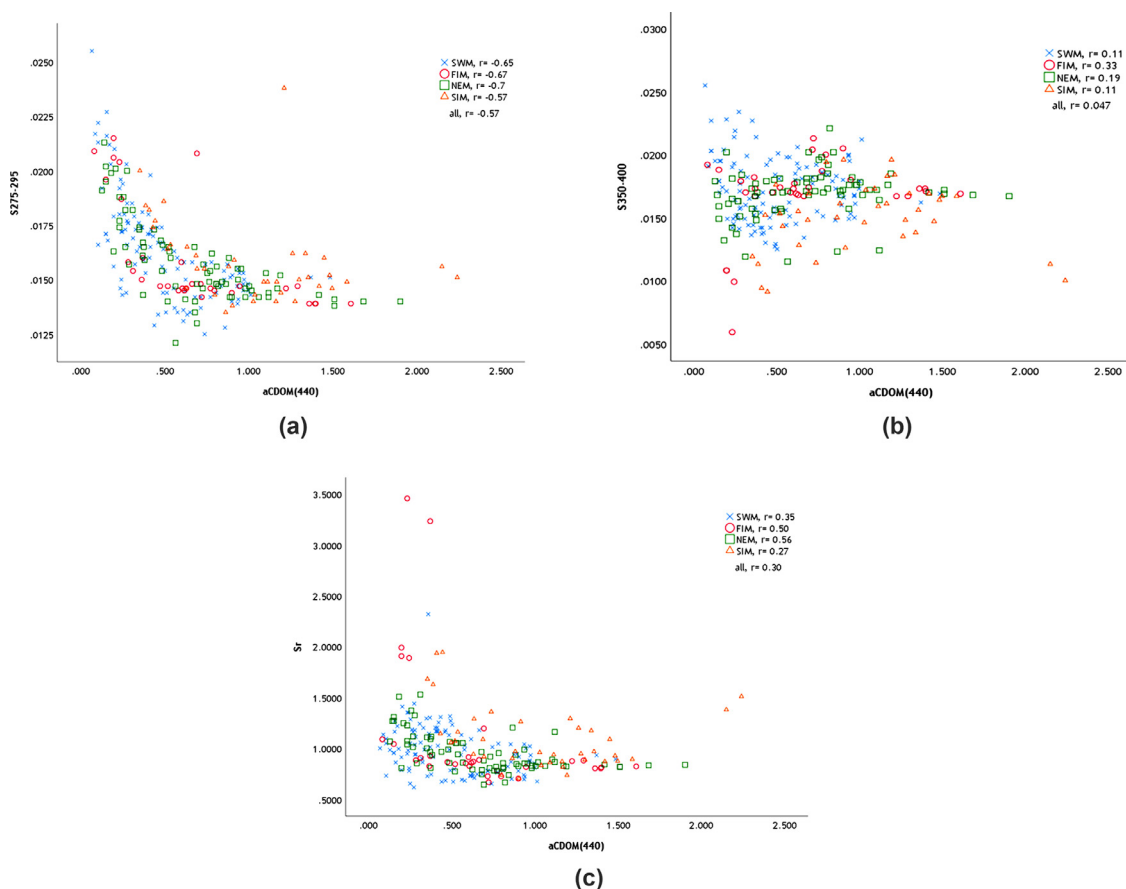


Figure 6 Scatter plots of regression correlation (r) between CDOM absorption coefficient at 440 [$a_{CDOM}(440)$] and a) $S_{275-295}$, b) $S_{350-440}$ and c) the ratio of spectral slope (SR) for the 14-month observation at the study area. The r -value stated in the legend of the plot.

(Das et al., 2017); and 0.66 to 3.82 m^{-1} at microtidal estuary in south-western Australia (Kostoglidis et al., 2005).

Higher $a_{CDOM}(440)$ upstream in the study area might be associated with a strong influence of terrestrial organic matter and humic substances carried by freshwater input (aligned with the lowest salinity). Many studies have shown that terrigenous DOM is the primary source of natural CDOM in coastal and nearshore areas, where freshwater runoff mixes with seawater (Coble, 2007; Granskog et al., 2007; Li et al., 2014; Stedmon et al., 2011). In addition, as a mangrove area fringes the study area, the possible source of higher CDOM concentration upstream was likely mangrove influenced water flushing organic matter from the decomposition of mangrove forests. Several studies have revealed that mangrove leaf litter can produce CDOM more rapidly than other local indigenous CDOM sources (Das et al., 2017; Sanyal et al., 2020; Shank and Evans, 2011). The decreasing pattern of $a_{CDOM}(440)$ from the upstream to coastal areas in the study area could be attributed to several possible factors, such as (i) the mixing of CDOM-rich riverine water with CDOM-poor coastal water (del Vecchio and Blough, 2004; Gonsior et al., 2008), (ii) enhancing the photodegradation of chromophores present in riverine CDOM after they reach the coastal regions (Blough and del Vecchio, 2002; del Vecchio and Blough, 2004; Osburn et al., 2009), (iii) microbial degradation of the autochthonous fraction that is the cen-

tral part of CDOM in marine waters (Boyd and Osburn, 2004; Broman et al., 2019; Winter et al., 2007), as well as (iv) flocculation and precipitation of riverine CDOM due to increased salinity (Blough et al., 1993; Guo et al., 2007; Sholkovitz, 1976).

The monsoonal variations of $a_{CDOM}(440)$ were relatively higher during the SIM (April 2019) and FIM (October 2018) monsoons with varied from 0.49 to 2.24 m^{-1} and 0.15 to 1.61 m^{-1} , respectively. However, the former indicated a fluctuated pattern in Darau the stations. Higher $a_{CDOM}(440)$ during the inter-seasonal monsoons (SIM and FIM) may be attributable to the fact that east coast Malaysian water is well-mixed, with water temperature distributed evenly throughout the water body (Mohd-Akhir et al., 2014). On the other hand, the current circulation may impact it by allowing stratification or stimulating mixing during inter-seasonal monsoon (Mohd-Akhir et al., 2014). In the continental shelf of the northern Bay of Bengal, seasonal mean $a_{CDOM}(440)$ showed a significant difference in magnitudes during the three seasons, with lower values of 0.1200 to 0.0327 m^{-1} during the pre-monsoon (February to May), increasing to 0.3064 0.1595 m^{-1} during the monsoon season (June to September), and 0.1621 to 0.0790 m^{-1} during the post-monsoon (October to January) (Das et al., 2017). Li et al. (2017) also found a seasonal variability of $a_{CDOM}(400)$, higher in Yinma River, China. The temporal variability is due

to strong riverine influence during specific monsoon or season (Das et al., 2016, Li et al., 2017).

4.2. Spatio-temporal trends of spectral slopes

There was a slight spatial variation of spectral slope of $S_{275-295}$ between stations during the study period ranging from 0.015 to 0.019 nm^{-1} in the study area. $S_{275-295}$ showed an increment of 0.004 nm^{-1} from the upstream of Darau River, located 5.1 km from the river mouth (station 16). The monsoon patterns of $S_{275-295}$ indicated relatively higher spatial variability during SWM (June to September 2018, June to July 2019) and SIM (April 2019) monsoon with an increment of 0.009 nm^{-1} . In contrast, NEM (November 2018 to March 2019) indicated a smaller spatial gradient of $S_{275-295}$ with an increment of 0.003 nm^{-1} . In other studies, in peatland draining rivers and coastal waters of Sarawak, Borneo, $S_{275-295}$ values ranged from 0.0102 to 0.0144 nm^{-1} (Martin et al., 2018), which was a little lower compared to the study area. However, there was no clear seasonality of $S_{275-295}$ in peatland draining rivers and coastal waters of Sarawak, Borneo. The distance of observed rivers ranged between 15 to 550 km (Martin et al., 2018), in contrast with the monsoonal variability in the study area. In a river and mangrove-dominated estuaries in Indian Sundarbans, a slight spatial difference of $S_{275-295}$ was recorded with 0.002 to 0.007 nm^{-1} (Sanyal et al., 2020), which is lower compared to this study. The spatial difference of $S_{275-295}$ in this study compared to Sanyal et al. (2020) is due to the morphology of the estuary in Indian Sundarbans, which have a wider inlet than the study area. While the $S_{275-295}$ varies with 0.0130 nm^{-1} to 0.0361 nm^{-1} were recorded from the Elizabeth River towards Chesapeake Bay estuary with increasing spatial gradient, as it receives substantial input of CDOM-rich water from the Great Dismal Swamp canal system (Helms et al., 2008).

The small range of spatial distribution of $S_{350-400}$ in the study area was 0.015 nm^{-1} to 0.019 nm^{-1} , with higher at the upstream and lower at the coastal water of the study area. The monsoonal pattern indicated that inter-seasonal monsoon had more considerable spatial differences with 0.010 nm^{-1} and 0.013 nm^{-1} during FIM and SIM. These values were about three and four times the increment of $S_{350-400}$ during SWM and NEM monsoon, which had 0.003 of $S_{350-400}$ declining pattern from the upstream to coastal water. In another study, a small variability of $S_{350-400}$ was found in the Elizabeth River towards Chesapeake Bay estuary with 0.0104 to 0.0187 (Helms et al., 2008), which is also within the range of this study area. The shallower slope of $S_{350-400}$ is probably due to a decrease in molecular weight, which diminishes the potential for intramolecular charge transfer interaction (Helms et al., 2008).

A decreased pattern spatial variation of $S_{300-600}$ with a range of 0.012 to 0.016 nm^{-1} was observed apparently at the river mouth towards coastal water in the study area. The other stations were mainly recorded with a consistent mean $S_{300-600}$ with 0.014 nm^{-1} . Similar to the monsoonal trend of $S_{350-400}$ in the study area, $S_{300-600}$ had a relatively more significant spatial variation during the inter-seasonal monsoons: SIM (0.007 to 0.017 nm^{-1}), and FIM (0.009 to 0.015 nm^{-1}) with 0.010 nm^{-1} and 0.09 nm^{-1} spatial differences, respectively. Whilst, the spatial variations of $S_{300-600}$

were lower during SWM, with a gap of 0.003 and 0.006 in the NEM monsoon. In the Arctic Ocean, $S_{300-600}$ varies between 0.008 nm^{-1} and 0.047 nm^{-1} . Still, in the Eurasian part of the Arctic Ocean and the Greenland Sea, the values are lower, 0.015–0.021 nm^{-1} (Stedmon et al., 2011) and 0.016–0.020 nm^{-1} (Stedmon and Markager, 2001), respectively. Moreover, the $S_{300-600}$ in the Eurasian part of the Arctic Ocean and the Greenland Sea is within the range with corresponding values for our study area. Past studies have shown strong relationships between a_{CDOM} and SCDOM along transects from lower salinity coastal waters to higher salinity offshore waters, where the range in $a_{\text{CDOM}}(\lambda)$ typically varies by orders of magnitude (Kowalczyk et al., 2006; Pavlov et al., 2016; Stedmon and Markager, 2005), which was a contrast with the values in our study area. However, the value of $S_{300-600}$ (SCDOM) in our study area was in agreement with a study in the Arctic Ocean that found that CDOM absorption and SCDOM do not relate well between marine and terrestrially derived CDOM pools (Granskog, 2012). In addition, a study by Astoreca et al. (2009) found S increases with increasing salinity and decreasing a_{CDOM} as a result of the alteration of terrestrial CDOM (Blough and Del Vecchio, 2002 and references therein, S : 0.018–0.030 nm^{-1} for salinities 30–35).

The spatial patterns of S_{R} and $S_{275-295}$ in the study area had an identical trend, higher in the coastal water and lowered numbers upstream. The spatial range of $S_{300-600}$ was 0.81 to 1.40. The SIM and FIM, which are inter-seasonal monsoons, showed higher values of S_{R} with monsoonal differences of 2.68 and 0.81, respectively, compared to $S_{300-600}$ in SWM (0.65) and NEM (0.53) monsoons. The S_{R} values observed upstream of the river mouth were typical of terrestrially dominated samples (0.81), while the S_{R} values observed in coastal areas were specific to marine-dominated samples (1.40). We observed an increasing trend in S_{R} from upstream (terrestrial-dominated) to coastal areas (marine-dominated) sources. Despite most of the stations that are located in the Darau, Inanam, and Bangka-Bangka rivers had S_{R} values that were less than 1. Hence, CDOM in these stations is a terrestrial-dominated source. On the other hand, as the value of S_{R} is more than one at the river mouth to coastal waters, it indicates that the CDOM is a marine-dominated source. The increasing importance of S_{R} from upstream toward the coastal area may indicate a compositional change in the DOM pool and a shift from high molecular weight to low molecular weight (Helms et al., 2008; Nima et al., 2019; Xie et al., 2012).

4.3. Relationship of $a_{\text{CDOM}}(440)$, spectral slopes $S_{275-295}$, $S_{350-440}$, and S_{R} and salinity

In the study area, a higher value of $a_{\text{CDOM}}(440)$ corresponded with lower values of salinity at upstream stations of the river, which could be related to revealing that the higher CDOM concentration of terrigenous origin contained chromophores of larger molecular size and weight, linked to lignin derivatives which can be explained by the abundance of mangrove forests distributed along the river. The $a_{\text{CDOM}}(440)$ variability showed a strong inverse correlation with salinity, which indicated the conservative behaviour of CDOM in the study area as observed in other estuarine

systems (Blough and Del Vecchio, 2002; Bowers and Brett, 2008; Chen et al., 2007; Das et al., 2017; Del Vecchio and Blough, 2004; Nima et al., 2019; Twardowski and Donaghay, 2001). A strong correlation between $a_{\text{CDOM}}(440)$ and salinity during inter-seasonal monsoons probably can be due to the strong riverine influence (Das et al., 2017; Li et al., 2017; Nima et al., 2019) which could be associated with transition monsoon in the study area.

There was a moderate correlation between spectral slopes of $S_{275-295}$ and salinity, greater for the NEM monsoon (R -value = 0.5, p = 0.00, n = 71) in the study area. The trend of $S_{275-295}$ was inversely proportional to $S_{350-400}$ in the study area, in which the former had an increasing pattern from the upstream towards coastal water and vice versa for the latter. Nevertheless, the correlation between $S_{350-400}$ and salinity was relatively greater during the FIM monsoon (r -value = 0.48, p = 0.005, n = 31). As $S_{350-400}$ was greater than $S_{275-295}$ upstream of the river mouth, terrestrially dominated CDOM prevails (Helms et al., 2008). In contrast, as $S_{275-295}$ was greater than $S_{350-500}$ in coastal stations, marine-dominated CDOM prevails in coastal waters, composed of a smaller molecular size and weight.

$S_{300-600}$ was relatively constant over the same salinity range and $a_{\text{CDOM}}(440)$ in our study area. In addition, there was no statistical difference in $S_{300-600}$ test during the study period due to the small coverage of the study area. As a result, the relationship between $S_{300-600}$ versus salinity and $a_{\text{CDOM}}(440)$ was not executed. Upstream to the river mouth, $S_{300-600}$ values were constant ($\sim 0.014 \text{ nm}^{-1}$), indicating a continuous influence of terrestrial inputs to the region throughout the sampling period (Figure 4e). However, $S_{300-600}$ values were more variable near the river mouth areas and coastal areas in the study area, presumably due to different CDOM pools entering the system in these areas and could be related to renewed high freshwater inflow after rain (Stedmon et al., 2015).

The spatial distribution of $S_{275-295}$ and S_{R} are linear correlated in the study area. As a result, the relationship between S_{R} and salinity in response to monsoonal variability is identical correlated to the greater degree during SWM (r -value = 0.66, p = 0.000) for the former, and (r -value = 0.67, p = 0.000) for the latter. Generally, S_{R} increases with salinity and may be linked to photobleaching processes that usually occur in coastal areas or on open seas (Granskog, 2012; Helms et al., 2008; Lei et al., 2019; Nima et al., 2019). In high salinity regions, higher S_{R} values and low $a_{\text{CDOM}}(440)$ values are indicative of photobleaching of decomposed humic substances, which produced more low-molecular-weight fractions as exposed to solar irradiance in coastal areas (Helms et al., 2008; Nima et al., 2019). Photodegradation of CDOM can shift the absorption spectrum by breaking up large humic complexes and thus decreasing the number and size of the low-energy chromophores associated with large humic complexes (Helms et al., 2008; Nima et al., 2019).

The correlation between $S_{275-295}$ and $a_{\text{CDOM}}(440)$ in the study area during the study period indicated a good relationship with an R -value of 0.51, which is stronger correlated compared to other spectral wavelengths. This condition agrees with Grunert et al. (2018), which also found that $S_{275-295}$ is better correlated with $a_{\text{CDOM}}(440)$ than other spectral wavelengths because of lignin or lignin derivatives.

According to Helms et al. (2008), both $S_{275-295}$ and S_{R} were inversely correlated to the molecular weight of CDOM. Both $S_{275-295}$, $S_{350-400}$, and S_{R} showed a significant inverse relationship with $a_{\text{CDOM}}(440)$ and salinity in the study, which agrees with Nima et al. (2019) and Li et al. (2017).

5. Conclusions

Monsoonal variation of $a_{\text{CDOM}}(440)$ in the study area with higher concentration was associated with a steeper slope at 300 to 350 nm during inter-seasonal monsoon. $S_{300-600}$ indicates a linear relationship between $a_{\text{CDOM}}(440)$, these unconventional results in coastal water might be due to the limited coverage of the study site.

The upstream of the Likas estuary indicated terrestrial-dominated sources of CDOM. However, the CDOM at the river mouth to coastal water showed a marine-dominated source. Therefore, our observations during the study period indicate that the monsoonal variation could alter the source of CDOM in the study area.

Acknowledgements

This study was funded by Universiti Malaysia Sabah: (SLB0158-2017 and UMSGreat 2018/2019 grants) and by the Ministry of Higher Education of Malaysia FRGS Grant: (FRGS/1/2019/STG03/UMS/02/2). The staff from Borneo Marine Research Institute (BMRI) UMS, especially boathouse crews and laboratory assistants, are thanked for their assistance during field and laboratory assistance.

References

- Andrew, A., Del Vecchio, R., Subramaniam, A., Blough, N., 2013. Chromophoric dissolved organic matter (CDOM) in the Equatorial Atlantic Ocean: Optical properties related to CDOM structure and source. *Mar. Chem.* 148, 33–43. <https://doi.org/10.1016/j.marchem.2012.11.001>
- Astoreca, R., Rousseau, V., Lancelot, C., 2009. Coloured dissolved organic matter (CDOM) in Southern North Sea waters: Optical characterisation and possible origin. *Estuar. Coast. Shelf Sci.* 85 (4), 633–640. <https://doi.org/10.1016/j.ecss.2009.10.010>
- Blough, N., Zafiriou, O., Bonilla, J., 1993. Optical absorption spectra of waters from the Orinoco River outflow: terrestrial input of colored organic matter to the Caribbean. *J. Geophys. Res.* 98 (C2), 2271–2278. <https://doi.org/10.1029/92JC02763>
- Blough, N.V., Green, S.A., 1995. Spectroscopic characterisation and remote sensing of non-living organic matter. In: Zepp, R.G., Sonntag, C. (Eds.), *The Role of Non-living Organic Matter in the Earth's Carbon Cycle*. John Wiley & Sons, 23–45.
- Blough, N.V., Del Vecchio, R., 2002. Chromophoric DOM in the Coastal Environment. In: Hansell, D.A., Carlson, C.A. (Eds.), *Biogeochemistry of Marine Dissolved Organic Matter*. Academic Press, California, 509–546.
- Bowers, D.G., Brett, H.L., 2008. The relationship between CDOM and salinity in estuaries: an analytical and graphical solution. *J. Mar. Syst.* 73 (1–2), 1–7. <https://doi.org/10.1016/j.jmarsys.2007.07.001>
- Bowen, J.C., Clark, C.D., Keller, J.K., De Bruyn, W.J., 2017. Optical properties of chromophoric dissolved organic matter (CDOM) in surface and pore waters adjacent to an oil well in a south-

- ern California salt marsh. *Mar. Pollut. Bull.* 114 (1), 157–168. <https://doi.org/10.1016/j.marpolbul.2016.08.071>
- Brandão, L.P.M., Brighenti, L.S., Staehr, P.A., Asmala, E., Massicotte, P., Tonetta, D., Barbosa, F.A.R., Pujoni, D., Bezerra-Neto, J.F., 2018. Distinctive effects of allochthonous and autochthonous organic matter on CDOM spectra in a tropical lake. *Biogeosciences* 15 (9), 2931–2943. <https://doi.org/10.5194/bg-15-2931-2018>
- Bricaud, A., Morel, A., Prieur, L., 1981. Absorption by dissolved organic matter of the sea (yellow substance) in the UV and visible domains. *Limnol. Oceanogr.* 26 (1), 45–53. <https://doi.org/10.4319/lo.1981.26.1.0043>
- Broman, E., Asmala, E., Carstensen, J., Pinhassi, J., Dopson, M., 2019. Distinct coastal microbiome populations are associated with autochthonous- and allochthonous-like Dissolved Organic Matter. *Front. Microbiol.* 10, 2579. <https://doi.org/10.3389/fmicb.2019.02579>
- Boyd, T.J., Osburn, C.L., 2004. Changes in CDOM fluorescence from allochthonous and autochthonous sources during tidal mixing and bacterial degradation in two coastal estuaries. *Mar. Chem.* 89 (1–4), 189–210. <https://doi.org/10.1016/j.marchem.2004.02.012>
- Chen, Z., Hu, C., Conmy, R.N., Muller-Karger, F., Swarzenski, P., 2007. Colored dissolved organic matter in Tampa Bay, Florida. *Mar. Chem.* 104 (1–2), 98–109. <https://doi.org/10.1016/j.marchem.2006.12.007>
- Coble, P.G., 2007. Marine Optical Biogeochemistry: The Chemistry of Ocean Color. *Chem. Rev.* 107 (2), 402–418. <https://doi.org/10.1021/cr050350>
- Coble, P.G., Nelson, N., 2009. *Optical Analysis of Chromophoric Dissolved Organic Matter*. In: Wurl, O. (Ed.), *Practical guidelines for the Analysis of Seawater*. CRC Press, Boca Raton, 18–27.
- Das, S., Hazra, S., Lotlikar, A.A., Das, I., Giri, S., Chanda, A., Akhand, A., Maity, S., Kumar, T.S., 2016. Delineating the relationship between chromophoric dissolved organic matter (CDOM) variability and biogeochemical parameters in a shallow continental shelf. *Egypt. J. Aquat. Res.* 42 (3), 241–248. <https://doi.org/10.1016/j.ejar.2016.08.001>
- Das, S., Das, I., Giri, S., Chanda, A., Maity, S., Lotlikar, A.A., Kumar, T.S., Akhand, A., Hazra, S., 2017. Chromophoric dissolved organic matter (CDOM) variability over the continental shelf of the northern Bay of Bengal. *Oceanologia* 59 (3), 271–282. <https://doi.org/10.1016/j.oceano.2017.03.002>
- Del Vecchio, R., Blough, N.V., 2004. On the Origin of the Optical Properties of Humic Substances. *Environ. Sci. Technol.* 38 (14), 3885–3891. <https://doi.org/10.1021/es049912h>
- Ferrari, G.M., 2000. The relationship between chromophoric dissolved organic matter and dissolved organic carbon in the European Atlantic coastal area and in the West Mediterranean Sea (Gulf of Lions). *Mar. Chem.* 70 (4), 339–357. [https://doi.org/10.1016/S0304-4203\(00\)00036-0](https://doi.org/10.1016/S0304-4203(00)00036-0)
- Gonsior, M., Peake, B., Jaffe, R., Heather, Y., Dickens, A., Kowalczyk, P., 2008. Spectral characterisation of chromophoric dissolved organic matter (CDOM) in a fjord (Doubtful Sound, New Zealand). *Aquat. Sci.* 70, 397–409. <https://doi.org/10.1007/s00027-008-8067-4>
- Granskog, M.A., Macdonald, R.W., Mundy, C.J., Barber, D.G., 2007. Distribution, characteristics and potential impacts of Chromophoric dissolved organic matter (CDOM) in Hudson Strait and Hudson Bay, Canada. *Cont. Shelf Res.* 27 (15), 2032–2050. <https://doi.org/10.1016/j.csr.2007.05.00>
- Granskog, M.A., 2012. Changes in spectral slopes of colored dissolved organic matter absorption with mixing and removal in a terrestrially dominated marine system (Hudson Bay, Canada). *Mar. Chem.* 134–135, 10–17. <https://doi.org/10.1016/j.marchem.2012.02.008>
- Green, Sarah A., Blough, N.V., 1994. Optical absorption and fluorescence properties of chromophoric dissolved organic matter in natural waters. *Limnol. Oceanogr.* 39 (8), 1903–1916. <https://doi.org/10.4319/lo.1994.39.8.1903>
- Grunert, B.K., Mouw, C.B., Ciochetto, A.B., 2018. Characterising CDOM Spectral Variability across Diverse Regions and Spectral Ranges. *Global Biogeochem. Cy.* 32 (1), 57–77. <https://doi.org/10.1002/2017GB005756>
- Guèguen, C., Guo, L., Tanaka, N., 2005. Distributions and characteristics of colored dissolved organic matter in the Western Arctic Ocean. *Cont. Shelf Res.* 25, 1195–1207. <https://doi.org/10.1016/j.csr.2005.01.005>
- Guo, W., Stedmon, C.A., Han, Y., Wu, F., Yu, X., Hu, M., 2007. The conservative and non-conservative behavior of chromophoric dissolved organic matter in Chinese estuarine waters. *Mar. Chem.* 107 (3), 357–366. <https://doi.org/10.1016/j.marchem.2007.03.006>
- Helms, J.R., Stubbins, A., Ritchie, J.D., Minor, E.C., Kieber, D.J., Mopper, K., 2008. Absorption spectral slopes and spectral ratios as indicators of molecular weight, source and photobleaching of chromophoric dissolved organic matter. *Limnol. Oceanogr.* 53 (3), 955–969. <https://doi.org/10.4319/lo.2008.53.3.0955>
- Hickman, A.E., Dutkiewicz, S., Williams, R.G., Follows, M.J., 2010. Modelling the effects of chromatic adaptation on phytoplankton community structure in the oligotrophic ocean. *Mar. Ecol. Prog. Ser.* 406, 1–17. <https://doi.org/10.3354/MEPS08588>
- Kim, G.E., Gnanadesikan, A., Pradal, M.A., 2016. Increased Surface Ocean Heating by Colored Detrital Matter (CDM) Linked to Greater Northern Hemisphere Ice Formation in the GFDL CM2Mc ESM. *J. Clim.* 29 (24), 9063–9076. <https://doi.org/10.1175/JCLI-D-16-0053>
- Kirk, J.T.O., 1994. Characteristics of the light field in highly turbid waters: a Monte Carlo study. *Limnol. Oceanogr.* 39 (3), 702–706. <https://doi.org/10.4319/lo.1994.39.3.0702>
- Kostoglidis, A., Pattiaratchi, C.B., Hamilton, D.P., 2005. CDOM and its contribution to the underwater light climate of a shallow, microtidal estuary in south-western Australia. *Estuar. Coast. Shelf Sci.* 63 (4), 469–477. <https://doi.org/10.1016/j.eccs.2004.11.016>
- Kowalczyk, P., Stedmon, C.A., Markager, S., 2006. Modeling absorption by CDOM in the Baltic Sea from season, salinity and chlorophyll. *Mar. Chem.* 101, 1–11.
- Lei, X., Pan, J., Devlin, A.T., 2019. Characteristics of Absorption Spectra of Chromophoric Dissolved Organic Matter in the Pearl River Estuary in Spring. *Remote Sens.* 11 (13), 1533. <https://doi.org/10.3390/rs11131533>
- Li, G., Liu, J., Ma, Y., Zhao, R., Hu, S., Li, Y., Wei, H., Xie, H., 2014. Distribution and spectral characteristics of chromophoric dissolved organic matter in a coastal bay in northern China. *J. Environ. Sci. (China)* 26 (8), 1585–1595. <https://doi.org/10.1016/j.jes.2014.05.025>
- Li, S., Zhang, J., Guo, E., Zhang, F., Ma, Q., Mu, G., 2017. Dynamics and ecological risk assessment of chromophoric dissolved organic matter in the Yinma River Watershed: Rivers, reservoirs, and urban waters. *Environ. Res.* 158, 245–254. <https://doi.org/10.1016/j.envres.2017.06.020>
- Martin, P., Cherukuru, N., Tan, A.S.Y., Sanwlan, N., Mujahid, A., Müller, M., 2018. Distribution and cycling of terrigenous dissolved organic carbon in peatland-draining rivers and coastal waters of Sarawak, Borneo. *Biogeosciences* 15, 6847–6865. <https://doi.org/10.5194/bg-15-6847-2018>
- Menon, H.B., Sangekar, N.P., Lotlikar, A.A., Vethamony, P., 2011. Dynamics of chromophoric dissolved organic matter in Mandovi and Zuari estuaries – A study through in situ and satellite data. *ISPRS J. Photogramm. Remote Sens.* 66 (4), 545–552. <https://doi.org/10.1016/j.isprsjprs.2011.02.011>
- Minu, P., Souda, V.P., Baliarsingh, S.K., Dwivedi, R.M., Ali, Y., Ashraf, P.M., 2020. Assessing temporal variation of coloured dissolved organic matter in the coastal waters of South East-

- ern Arabian Sea. *Acta Oceanologica Sinica* 39 (1), 102–109. <https://doi.org/10.1007/s13131-020-1534-z>
- Mohd Akhir, M.F., Zakaria, N.Z., Tangang, F., 2014. Intermonsoon variation of physical characteristics and current circulation along the east coast of Peninsular Malaysia. *Int. J. Oceanogr.* 1–9. <https://doi.org/10.1155/2014/527587>
- Nelson, N.B., Siegel, D.A., Michaels, A.F., 1998. Seasonal dynamics of colored dissolved material in the Sargasso Sea. *Deep Sea Res. Pt. I* 45 (6), 931–957. [https://doi.org/10.1016/S0967-0637\(97\)00106-4](https://doi.org/10.1016/S0967-0637(97)00106-4)
- Nelson, N.B., Siegel, D.A., Carlson, C.A., Swan, C., Smethie, W.M., Khatiwala, S., 2007. Hydrography of chromophoric dissolved organic matter in the North Atlantic. *Deep Sea Res. Pt. I* 54 (5), 710–731. <https://doi.org/10.1016/j.dsr.2007.02.006>
- Nima, C., Frette, Ø., Hamre, B., Stamnes, J.J., Chen, Y.C., Sørensen, K., Norli, M., Xing, Q., Muyimbwa, Y.C., Ssenyonga, T., Stamnes, K.H., Erga, S.R., 2019. CDOM absorption properties of natural water bodies along extreme environmental gradients. *Water* 11 (10), 1–19. <https://doi.org/10.3390/w11101988>
- Osburn, C.L., O'Sullivan, D.W., Boyd, T.J., 2009. Increases in the longwave photobleaching of chromophoric dissolved organic matter in coastal waters. *Limnol. Oceanogr.* 54 (1). <https://doi.org/10.4319/lo.2009.54.1.0145>
- Osburn, C.L., Stedmon, C., 2011. Linking the chemical and optical properties of dissolved organic matter in the Baltic-North Sea transition zone to differentiate three allochthonous inputs. *Mar. Chem.* 126, 281–294. <https://doi.org/10.1016/j.marchem.2011.06.007>
- Osburn, C.L., Handsel, L.T., Mikan, M.P., Paerl, Montgomery, M.T., 2012. Fluorescence tracking of dissolved and particulate organic matter quality in a river-dominated estuary. *Environ. Sci. Technol.* 46 (16), 8628–8636. <https://doi.org/10.1021/es3007723>
- Pavlov, A.K., Stedmon, C.A., Semushin, A.V., Martma, T., Ivanov, B.V., Kowalczyk, P., Granskog, M.A., 2016. Linkages between the circulation and distribution of dissolved organic matter in the White Sea. *Arctic Ocean. Cont. Shelf Res.* 119, 1–13. <https://doi.org/10.1016/j.csr.2016.03.004>
- Sanyal, P., Ray, R., Paul, M., Gupta, V.K., Acharya, A., Bakshi, S., Jana, T.K., Mukhopadhyay, S.K., 2020. Assessing the Dynamics of Dissolved Organic Matter (DOM) in the Coastal Environments Dominated by Mangroves. *Indian Sundarbans. Front. Earth Sci.* 8, 1–21. <https://doi.org/10.3389/feart.2020.00218>
- Shank, G.C., Evans, A., 2011. Distribution and photoreactivity of chromophoric dissolved organic matter in northern Gulf of Mexico shelf waters. *Cont. Shelf Res.* 31, 1128–1139. <https://doi.org/10.1016/j.csr.2011.04.009>
- Shanmugam, P., Varunan, T., Jaiganesh, S.N.N., Sahay, A., Chauhan, P., 2016. Optical assessment of colored dissolved organic matter and its related parameters in dynamic coastal water systems. *Estuar. Coast. Shelf Sci.* 175, 126–145. <https://doi.org/10.1016/j.ecss.2016.03.020>
- Sholkovitz, E.R., 1976. Flocculation of dissolved organic and inorganic matter during the mixing of river water and seawater. *Geochim. Cosmochim. Acta* 40 (7), 831–845. [https://doi.org/10.1016/0016-7037\(76\)90035-1](https://doi.org/10.1016/0016-7037(76)90035-1)
- Spencer, R.G.M., Hernes, P.J., Ruf, R., Baker, A., Dyda, R.Y., Stubbins, A., Six, J., 2010a. Temporal controls on dissolved organic matter and lignin biogeochemistry in a pristine tropical river, Democratic Republic of Congo. *J. Geophys. Res.* 115 (G03013), 1–12. <https://doi.org/10.1029/2009JG001180>
- Stedmon, C.A., Markager, S., 2001. The optics of chromophoric dissolved organic matter (CDOM) in the Greenland Sea: An algorithm for differentiation between marine and terrestrially derived organic matter. *Limnol. Oceanogr.* 46 (8), 2087–2093. <https://doi.org/10.4319/lo.2001.46.8.2087>
- Stedmon, C.A., Markager, S., 2005. Resolving the variability in dissolved organic matter fluorescence in a temperate estuary and its catchment using PARAFAC analysis. *Limnol. Oceanogr.* 50 (2), 686–697. <https://doi.org/10.4319/lo.2005.50.2.0686>
- Stedmon, C.A., Osburn, C.L., Kragh, T., 2010. Tracing water mass mixing in the Baltic – North Sea transition zone using the optical properties of coloured dissolved organic matter. *Estuar. Coast. Shelf Sci.* 87 (1), 156–162. <https://doi.org/10.1016/j.ecss.2009.12.022>
- Stedmon, C.A., Amon, R.M.W., Rinehart, A.J., Walker, S.A., 2011. The supply and characteristics of colored dissolved organic matter (CDOM) in the Arctic Ocean: Pan Arctic trends and differences. *Mar. Chem.* 124 (1–4), 108–118. <https://doi.org/10.1016/j.marchem.2010.12.007>
- Stedmon, C.A., Granskog, M.A., Dodd, P.A., 2015. An approach to estimate the freshwater contribution from glacial melt and precipitation in East Greenland shelf waters using colored dissolved organic matter (CDOM). *J. Geophys. Res.* 120 (2), 1107–1117. <https://doi.org/10.1002/2014JC010501>
- Teong, K.V., Sukarno, K., Chang, J.H.W., Chee, F.P., Ho, C.M., Dayou, J., 2017. The monsoon effect on rainfall and solar radiation in Kota Kinabalu. *Trans. Sci. Technol.* 4 (4), 460–465.
- Twardowski, M.S., Donaghay, P.L., 2001. Separating in situ and terrigenous sources of absorption by dissolved materials in coastal waters. *J. Geophys. Res.* 106, 2545–2560. <https://doi.org/10.1029/1999JC000039>
- Winter, A.R., Fish, T.A.E., Playle, R.C., Smith, D.S., Curtis, P.J., 2007. Photodegradation of natural organic matter from diverse freshwater sources. *Aquat. Toxicol.* 84, 215–222. <https://doi.org/10.1016/j.aquatox.2007.04.014>
- Xie, H., Aubry, C., Bélanger, S., Song, G., 2012. The dynamics of absorption coefficients of CDOM and particles in the St. Lawrence estuarine system: Biogeochemical and physical implications. *Mar. Chem.* 128–129, 44–56. <https://doi.org/10.1016/j.marchem.2011.10.001>

Available online at www.sciencedirect.com

ScienceDirect

journal homepage: www.journals.elsevier.com/oceanologia

ORIGINAL RESEARCH ARTICLE

Inconsistent response of biophysical characteristics in the western Bay of Bengal associated with positive Indian Ocean dipole

Vivek Seelanki^a, Tanuja Nigam^{a,b}, Vimlesh Pant^{a,*}

^aCentre for Atmospheric Sciences, Indian Institute of Technology Delhi, New Delhi, India

^bNational Institute of Oceanography, Goa, India

Received 30 August 2021; accepted 20 April 2022

Available online 4 May 2022

KEYWORDS

Chlorophyll-a;
Ekman transport;
Bay of Bengal;
Primary productivity;
Indian Ocean Dipole;
Biophysical model

Abstract The Bay of Bengal (BoB) is known to have high primary productivity at its western margin during the Indian summer monsoon season (June–September). This higher coastal productivity is mainly caused due to the near-surface nutrient availability maintained by the local coastal upwelling process. The surface winds in the Indian Ocean significantly vary during El-Niño/La-Niña and Indian Ocean dipole (IOD). The current study examines the sea surface temperature (SST) and Chlorophyll-a (Chl-a) anomalies in the western BoB for the period of 18 years (2000 to 2017), using a coupled regional ocean biophysical model. All considered positive IOD (pIOD) years show discrete behavior of biophysical features in the western BoB. The co-occurrence years of pIOD and El-Niño modes are associated with contrast biophysical anomalies. In the analyzed pIOD events, the years 2006 and 2012 show an enhancement in the Chl-a anomalies whereas, the other two years (2015 and 2017) experience Chl-a decrement. The western BoB was anomalously warmer during the 2015 and 2017 pIOD years compared to the other two pIOD years (2006, 2012). This inconsistent response of biophysical features associated with pIOD years is investigated in terms of local surface flux (momentum, heat, and freshwater) changes over the western BoB. The combined impact of local surface flux changes during the individual years remains the major contributing factor affecting the upper-ocean stratification.

* Corresponding author at: Centre for Atmospheric Sciences, Indian Institute of Technology Delhi, New Delhi-110016, India.

E-mail address: vimlesh@cas.iitd.ac.in (V. Pant).

Peer review under the responsibility of the Institute of Oceanology of the Polish Academy of Sciences.



<https://doi.org/10.1016/j.oceano.2022.04.003>

0078-3234/© 2022 Institute of Oceanology of the Polish Academy of Sciences. Production and hosting by Elsevier B.V. This is an open access article under the CC BY-NC-ND license (<http://creativecommons.org/licenses/by-nc-nd/4.0/>).

Ultimately, the stratification changes are responsible for the observed inconsistent response of biophysical features by significantly altering the upper-ocean mixing, upwelling, and nutrient availability in the western BoB.

© 2022 Institute of Oceanology of the Polish Academy of Sciences. Production and hosting by Elsevier B.V. This is an open access article under the CC BY-NC-ND license (<http://creativecommons.org/licenses/by-nc-nd/4.0/>).

1. Introduction

The Northern Indian Ocean (NIO) possesses two semi-enclosed basins, namely the Bay of Bengal (BoB) and Arabian Sea (AS) which are similar in geographical latitudinal position but differ in their physical characteristics and dynamical processes. These basins experience reversing monsoonal wind conditions from southwesterly to northeasterly during summer to winter (Madhupratap et al., 2003; McCreary et al., 1996a, 2009; Schott and McCreary, 2001; Shenoi, 2002; Wyrski, 1973). During the southwest monsoon season, strong southwesterly winds blowing along the western boundary of the BoB make conditions favorable for coastal upwelling (McCreary et al., 1996a; Shankar et al., 2002; Shetye et al., 1991; Thushara and Vinayachandran, 2016; Vinayachandran et al., 1996). On the other hand, the winds are northeasterly during the northeast monsoon season, which causes coastal downwelling (Shetye et al., 1996). The BoB is also known for high SST (average temperature $>28^{\circ}\text{C}$) (Shenoi, 2002; Vinayachandran and Shetye, 1991) and this warm SST is favorable for the cyclogenesis (Gadgil et al., 2004; Sikka, 1980) over the BoB.

The wind-generated mixing and coastal upwelling are lower in the BoB with respect to AS (Murty and Varadachari, 1968). The major river systems over the Indian subcontinent converge to the BoB. Hence, the BoB receives a copious amount of freshwater flux (Martin et al., 1981; Qasim et al., 1988; Sen Gupta et al., 1978; Shetye et al., 1993). This freshwater distribution in the upper ocean changes the temperature and salinity distribution over the BoB, especially during monsoon (June to September) to post-monsoon (October–November) season (Akhil et al., 2016; Miranda et al., 2019; Sandeep et al., 2018; Seo et al., 2009). The altered temperature and salinity conditions govern peculiar thermodynamic phenomena such as temperature inversion and the presence of a strong barrier layer that can be characterized by less saline (fresher) and warmer seawater and, hence, highly stratified sea surface over the BoB (Dandapat et al., 2020; Jian et al., 2012; Mahadevan et al., 2016; Thadathil et al., 2016; Vinayachandran et al., 2002). These underlined distinct physical and thermodynamical characteristics easily distinguish the BoB from the AS. The coastal upwelling and downwelling along the east coast of India are governed by the favourable wind stress and alongshore current with the associated local stratification conditions (Babu et al., 2008; Sil and Chakraborty, 2011; Thushara and Vinayachandran, 2016; Vinayachandran et al., 1996). The wind stress is the primary forcing that generates the upwelling process, but the source depth of upwelled water is highly sensitive to the stratification conditions and wind strength

(Gomes et al., 2000; Shetye et al., 1991). Therefore, changing the strength of the wind (wind stress) and stratification jointly decide the upwelling intensity by significantly altering the total amount of offshore volume transport.

The BoB is an important constituent of NIO that exhibits dynamic water quality attributed to the seasonal reversal of monsoon, high amount of river discharge, effluent discharge from coastal industrial setups, and effect of extreme events such as tropical cyclones. Physical oceanographic processes, the freshwater influx from major rivers, and cyclones proved to be controlling factors in the distribution of Chl-a in the BoB. Variations in Chl-a were influenced significantly by oscillations in surface salinity due to the ingress of fresh water in coastal regions of the western BoB (Gomes et al., 2000; Vinayachandran, 2009). Moreover, several pockets of coastal waters of the western BoB are experiencing recurring algal blooms (Baliarsingh et al., 2016; D'Silva et al., 2012). Regular screening of physicochemical-biological parameters is, therefore, crucial for the ecological evaluation of coastal waters of the BoB.

The western coastal BoB receives a huge freshwater discharge of $1.6 \times 10^{12} \text{ m}^3 \text{ yr}^{-1}$ from various rivers, such as the Ganges, Mahanadi, Godavari, Krishna and Cauvery (UNESCO, 1979), and sediment load of $1.1 \times 10^9 \text{ t}$ (Milliman and Meade, 1983; Milliman and Syvitski, 1992) during southwest monsoon (June–September) when the Indian subcontinent receives maximum rainfall. During the same period, winds blow from the southwest over the coastal western BoB and favour coastal upwelling (Shetye et al., 1996). But, the intensity of upwelling is weak and confined close to the coast due to strong stratification driven by freshwater discharge (Gopalakrishna and Sastry, 1985; Murty and Varadachari, 1968; Shetye et al., 1991). A strong stratification in the region affects the upper-ocean mixing and controls the primary productivity of the region (Prasanna Kumar et al., 2002).

The BoB differs from the AS not only in terms of the intensity of coastal upwelling but also in terms of primary productivity (Prasanna Kumar et al., 2002, 2007, 2010). Several modelling and observational studies have been conducted over the AS (Banse and English, 2000; Banse and McClain, 1986; Banzon et al., 2004; McCreary et al., 1996b) and the west coast of India (Lierheimer and Banse, 2002), revealing the role of monsoonal wind mixing and transport of nutrients in supporting biological productivity. Whereas most of these studies mainly focused on the AS, not enough attention was given to performing extensive studies on its counterpart the BoB, where the observed Chl-a blooms are relatively weaker. This happens since plenty of nutrients brought by high river discharge are mainly limited to the disphotic and aphotic zones in the presence of strongly

stratified and less mixed water column near the coast (Gauns et al., 2005; Gomes et al., 2000; Madhupratap et al., 2003; Prasanna Kumar et al. 2010). However, the western margin of BoB remains one of the highly productive zones for the basin during summer (Naidu et al., 1999; Shetye et al., 1993). The current study aims at understanding the inter-annual variability of the primary productivity in the western margin of BoB by analyzing the Chl-a anomalies during the monsoon season.

The first evidence of coastal upwelling along the western BoB was seen between 1952 and 1965, during the International Indian Ocean Expedition (IIOE). Using hydrographic data, the first report published for the western BoB, although albeit lacking evidence of coastal upwelling or downwelling for a season, was by La Fond (1954, 1957, 1958, 1959). Evidence of coastal upwelling during the summer monsoon along the western BoB was reported by Varadachari (1961). During both summer and spring, stronger upwelling at Visakhapatnam compared to Chennai founded by Murty and Varadachari (1968). The studies, based on hydrographic measurements (Babu et al., 2003; Sanilkumar et al., 1997; Shetye et al., 1991, 1993, 1996), and satellite-observed sea levels (Durand et al., 2009; Shankar et al., 2002), described upwelling along the western BoB. The coastal upwelling can extend vertically up to a depth of ~70 m (Shetye et al., 1991). During the summer monsoon season, both moored and hydrography observed current show evidence of downwelling below upwelling along the east coast of India (Francis et al., 2020; Mukherjee et al., 2014; Shetye et al., 1991).

The upwelling favorable southwesterly winds drive the alongshore current northward but, due to the presence of freshwater towards the northwestern bay, its upwelling strength reduces (Thushara and Vinayachandran, 2016). The East India Coastal Current (EICC) is a semi-permanent current due to its interaction with the local eddies in the vicinity (Jagadeesan et al., 2019; Jyothibabu et al., 2008, 2015; Patnaik et al., 2014). The presence of cyclonic and anti-cyclonic eddies throughout the year over BoB is mentioned by several studies (Gomes et al., 2000; Jyothibabu et al., 2008; Prasanna Kumar et al., 2004). The mesoscale eddies, present in the vicinity of EICC, have also a remarkable effect on the coastal upwelling and its associated primary productivity in the region (Sarma et al., 2016). The cold-core eddies (warm-core eddies) support the enrichment (decrement) of nutrients to the surface hence, enhancing (reducing) the overall primary productivity associated with coastal upwelling (Jagadeesan et al., 2019; Prasanna Kumar et al., 2004). The local mesoscale variability (like eddies) in the western BoB is not only produced by Kelvin and Rossby waves. In the center and eastern BoB, the eddy generation is mainly attributed to these waves (Cheng et al., 2013, 2018). While in the western BoB, it is attributed to the baroclinic instability of EICC (Chen et al., 2012, 2018; Cheng et al., 2013; Kurien et al., 2010). The impact of these waves that travel along the BoB coastal rim as coastal Kelvin wave is also discernable to assess the strength of alongshore current and its consequences upwelling mechanism at the east coast of India (McCreary et al., 1993; Shankar et al., 2002; Vinayachandran and Yamagata, 1998). These coastal waves exhibit the inter-annual variability controlled by the vari-

ability of winds over the equatorial ocean (Huang et al., 2021; Rao et al., 2010; Trott and Subrahmanyam, 2019).

It is well established by previous studies (Aparna et al., 2012; Cherchi and Navarra, 2012; Currie et al., 2013; Shaji and Ruma, 2019) that the variability in winds over the Indian Ocean is dominantly driven by two inter-annual modes El-Niño Southern Oscillations (ENSO) and IOD. Sarma et al. (2015), compared the impact of two different climatic events of pIOD and negative IOD (nIOD) and revealed that the upwelling intensity increases during pIOD whereas it decreases during nIOD along the east coast of India. However, this study was limited to single events of both IOD modes. Currie et al. (2013) used a coupled biophysical ocean model to show that the primary productivity is positively affected by El-Niño and pIOD, unlike the negative effect of the La-Niña and nIOD over the southern BoB. The current study uses a coupled biophysical model and observations to analyze the influence of these interannual modes on biophysical characteristics over the western BoB coastal upwelling region which is not yet investigated adequately.

Several studies analyzed the biophysical features influenced by cyclones (Maneesha et al., 2011; Vinayachandran and Mathew, 2003) and eddies (Prasanna Kumar et al., 2007, 2010) over the BoB. Madhu et al. (2006) studied the lack of phytoplankton seasonality over the western BoB. The biophysical features studied by Chen et al. (2013) showed the dominant role of eddies in episodic bloom events over the southwestern and southeastern BoB. Xu et al. (2021) has studied the inter-annual variability of Chl-a over the eastern BoB. Pramanik et al. (2020) studied the interannual variability of Chl-a near the Sri Lankan dome. The present study consists of the main upwelling driven regions over the east coast of India during the southwest monsoon season. This part of the BoB is not well studied for its biophysical features and variability.

The variability of coastal upwelling induced primary productivity along the east coast of India is examined in detail in the current study. Numerical simulations from a coupled ocean-biophysical model are performed for 18 years (2000 to 2017). Since this period covers four strong pIOD (2006, 2012, 2015, 2017) events, it provides comprehensive data for a detailed assessment of the response of these events on the associated changes of Chl-a anomalies along the east coast of India during the summer season. Further, the model simulated Chl-a anomalies are analyzed to understand the changes in primary productivity along the western margin of the BoB under the influence of the positive mode of IOD.

2. Methods

2.1. Physical ocean model

The Regional Ocean Modelling System (ROMS) is used to study the impact of the interannual positive mode of IOD on BoB primary productivity during summer (June to September) in the current study. The ROMS model is also utilized to study the circulation pattern over regional scales and for analyzing the different temporal and spatial scale phenomenon/processes such as ENSO, IOD, cyclones, eddies,

upwelling, etc., their interactions and responses to the upper ocean (Chakraborty et al., 2018; Jacox et al., 2015; Nigam et al., 2018; Pramanik et al., 2019; Sandeep and Pant, 2018; Seelanki et al., 2021; Seelanki and Pant, 2021; Song et al. 2012). In this study, a coupled biophysical model comprising ROMS together with Bio-Fennel (the biogeochemical (BGC) model component as described by Fennel et al., 2006, 2008) was used to simulate the physical and biogeochemical processes in the Indian Ocean. The configuration details for the Bio-Fennel are provided in section 2.2.

The ROMS model is a free-surface, three-dimensional primitive equations (i.e., Reynolds averaged Navier-Stokes's equations) model which follows the hydrostatic, and Boussinesq approximations to solve these equations over the curvilinear grid with the terrain-following vertical s -coordinate system (Haidvogel et al., 2000, 2008; Shchepetkin and McWilliams, 2005). Several studies utilized this coupled model for biogeochemical studies over different basins such as the middle Atlantic Bight (Fennel et al., 2006), California current system (Fiechter et al., 2018; Powell et al., 2006), North Pacific (Kishi et al., 2007), and tropical Indian Ocean (Chakraborty et al., 2018; Seelanki et al. 2021; Seelanki and Pant, 2021) and proven the capability of this model in simulating biogeochemical processes.

The model is configured over the Indian Ocean domain (30°N–30°S, 30°E–120°E). The model has a quarter-degree spatial resolution and 40 vertical sigma levels. The 30 sigma levels are prescribed in the upper 200 m in which the topmost 5 sigma levels are located within 0.2 to 2 meters from the sea surface and around 20 sigma levels are lying in deep oceanic regions. The K-Profile Parameterization (KPP) scheme (Large et al., 1994) deals with the vertical mixing in the model. The model is initialized with monthly temperature and salinity profiles derived from World Ocean Atlas 2013 (WOA-13), the lateral boundary conditions in the East and South of the domain are also provided by WOA-2013 data and the model is forced using daily climatological data for the period 2000–2008. The physical model ROMS is started from a state of rest and spun up for ten years with barotropic (fast) and baroclinic (slow) time steps as 54 and 900 seconds, respectively. After stabilization of the physical model, the ecosystem model (Bio-fennel) is coupled with the physical model and the coupled model run is executed for further 10 years with the same daily climatological forcing. The tenth-year output of the coupled biophysical simulation is used as the initial condition for the interannual simulations. Further details of this model configuration are described in Seelanki et al. (2021). The inter-annual simulations are forced with daily surface forcing of net longwave and shortwave radiation, air temperature, specific humidity, and surface pressure provided from the National Center for Environmental Prediction (NCEP) reanalysis-1 data (<https://psl.noaa.gov/data/gridded/data.ncep.reanalysis.html>). The daily surface wind data to provide momentum surface forcing is taken from QuikScat data (2000 to 2009) and ASCAT (Advanced Scatterometer) data (2009 to 2018). The QuikScat operates in Ku-band, whereas ASCAT uses C-band. Both QuikScat and ASCAT data are accessed from <ftp://ftp.remss.com/wind/>. To prescribe the freshwater flux at the surface the pre-

cipitation from Tropical Rainfall Measuring Mission (TRMM) (<http://daac.gsfc.nasa.gov/precipitation>) is used. With this configuration, the model is simulated for a period of 18 years (from 2000 to 2017) and these interannual simulations have been used to study the impact of pIOD modes on western BoB, the upwelling zone during summer monsoon and its associated biogeochemical responses over the model domain (Fig. 1b).

2.2. Biogeochemical model

We used the BGC model, Bio-Fennel (Fennel et al., 2006, 2008) which was developed initially in the Atlantic Bight for nitrogen cycling. Fennel et al. (2006) stated that the nitrogen available in inorganic nutrients is initially consumed by phytoplankton biomass for its growth. Further, zooplankton biomass uptake the needed nitrogen via grazing of phytoplankton and the remaining is utilized into the small and large detrital pools through mortality. Zooplankton mortality additionally contributes to the detrital pool. Zooplankton losses because of inefficient grazing and detritus are transferred via a decay price into the ammonium group, which is converted into nitrate via nitrification processes. Large and small detritus, as well as phytoplankton, have a related vertical sinking rate (Fennel et al., 2006). All state variables such as phytoplankton, zooplankton, large and small detritus, ammonia and chlorophyll are initialized with a seeding population of $0.1 \text{ mmole N m}^{-3}$. The WOA13 climatological data of Nitrate (NO_3) and Oxygen are used to provide the initial and boundary conditions to the BGC model

2.3. Observational datasets

Remotely sensed sea surface temperature (SST) is obtained from Advanced Very High-Resolution Radiometer (AVHRR) blended SST with a spatial resolution of 0.25 degree (<http://www.ncdc.noaa.gov>) and utilized for the validation of model SST simulations. Remotely sensed surface chlorophyll estimates are obtained from the European Space Agency Ocean Color-Climate Change Initiative (ESA OC-CCI) programme. This product was generated for improving the inter-sensor biases by merging three different sensors data as SeaWiFS (Sea-viewing Wide Field-of-view Sensor), MODIS (Moderate Resolution Imaging Spectroradiometer)-Aqua and MERIS (Medium Imaging Spectrometer). This product has a 4 km spatial and daily temporal resolution (<https://www.oceancolour.org>), its version 5.0. data set is used to validate the surface Chl-a simulated by the model. Further, model-simulated subsurface temperature over the BoB is validated against a Gridded Argo dataset accessed from <https://las.incois.gov.in/las>. Validation of model-simulated subsurface chlorophyll and nitrate is performed with respect to the Bio-Argo float's profile observations along its trajectory (available from <http://www.coriolis.eu.org/>). The data from two Argo floats (WMO ID: 2902193, 2902195) and one nitrate float (WMO ID: 5903712) is considered for validation of simulated chlorophyll and nitrate profiles. These Bio-Argo floats collect the data using a fluorescence-based sensor and represent the bio-optical process in the water column within 5 m to 2000 m depth in 5-day intervals. The

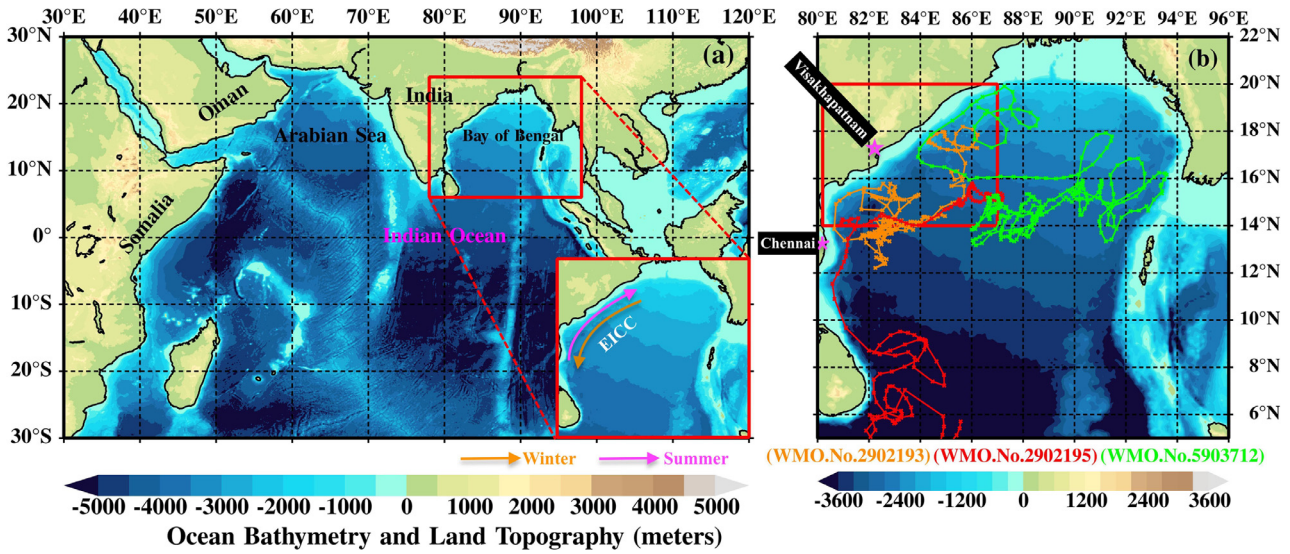


Figure 1 (a) The model domain over the Indian Ocean with bathymetry (m) and topography (m). Shades and the arrows in zoomed inset show the direction of the East Indian Coastal Current (EICC) which flows northward during summer and southward during winter; (b) The analysis area [80.2°E–87°E, 14°N–20°N, red box] in the western Bay of Bengal. The tracks of Bio-Argo floats are shown in orange (WMO ID: 2902193), red (WMO ID: 2902195), and green (WMO ID: 5903712). The purple color stars show the locations of Visakhapatnam and Chennai.

technical specifications of floats are described in detail at <http://www.ifremer.fr/co-argoFloats/>.

The mixed layer depth (MLD) is defined as the depth at which the σ_t (sigma-t) increases by an amount corresponding to a 1°C change in temperature (Girishkumar et al., 2019; Kara et al., 2000; Thangaprakash et al., 2016). The isothermal layer depth (ILD) is defined as the depth where the temperature is 1°C lower than SST. The barrier layer thickness (BLT) is defined as the layer between the base of the MLD and the top of the thermocline (Girishkumar et al., 2019; Rao and Sivakumar, 2003; Thangaprakash et al., 2016; Vinayachandran et al., 2002). The zonal (u) and meridional components (v) of surface winds were used to derive the zonal and meridional wind stress calculated using the following equations.

$$\tau_x = \rho_a C_D U_{10} u \tag{1}$$

$$\tau_y = \rho_a C_D U_{10} v \tag{2}$$

$$\text{curl}(\tau) = \left(\frac{\partial \tau_y}{\partial x} - \frac{\partial \tau_x}{\partial y} \right) \tag{3}$$

where ρ_a is the density of air taken as 1.22 kg m⁻³, C_D is the dimensionless drag coefficient and U_{10} is the wind speed at 10 m above the sea surface. The value of drag coefficient that varies with wind speed as per Large and Pond (1981) were used. Further, the Ekman pumping velocity (Price, 1981) and Ekman mass transport (Koračín et al., 2004) were computed using the following equations.

$$\text{Ekman pumping velocity (EPV)} = \frac{\text{curl}(\tau)}{\rho_o f} \tag{4}$$

$$\text{Ekman mass transport (EMT)} = \frac{\tau}{f} \tag{5}$$

where τ_x and τ_y are the zonal and meridional wind stress components, ρ_o is the density of seawater, f is the Coriolis parameter, and EMT in kgm⁻¹s⁻¹.

The Brunt Väisälä frequency (N^2 in s⁻²) represents stratification and is calculated using the formula:

$$N^2 = - \frac{g}{\rho_o} \frac{\partial \rho_o}{\partial z} \tag{6}$$

where g is acceleration due to gravity (9.8 m s⁻²).

3. Results and discussion

3.1. Model validation

The model domain with overlaid bathymetry and land topography (meter) is shown in Figure 1a. The model simulations for 18 years (2000 to 2017) period is analyzed over the BoB (5°N–22°N, 80°E–6°E) as shown in Figure 1b. The figure also indicates Bio-Argo float trajectories used for validation of model-simulated temperature (°C), Chl-a concentration (mg m⁻³) and nitrate estimates (μmol kg⁻¹). The Bio-Argo float trajectories are shown (Figure 1b) in red (WMO ID: 2902193) and orange (WMO ID: 2902195) colors. These two floats used in this study do not provide nitrate measurements. Whereas, the float with green trajectory (WMO ID: 5903712) in Figure 1b measures nitrate and is used for validation of model-simulated nitrate concentration. The highlighted zoomed region in Figure 1a represents the BoB domain. The rectangular red box in Figure 1b represents the region of the western margin of BoB (80.2°E to 87°E and 14°N to 20°N) which is the main analysis area where the biogeochemical processes and their associated impacts are analyzed to assess the role of pIOD interannual modes during 2000 to 2017. In the western BoB, a prominent bloom development is observed during the summer monsoon

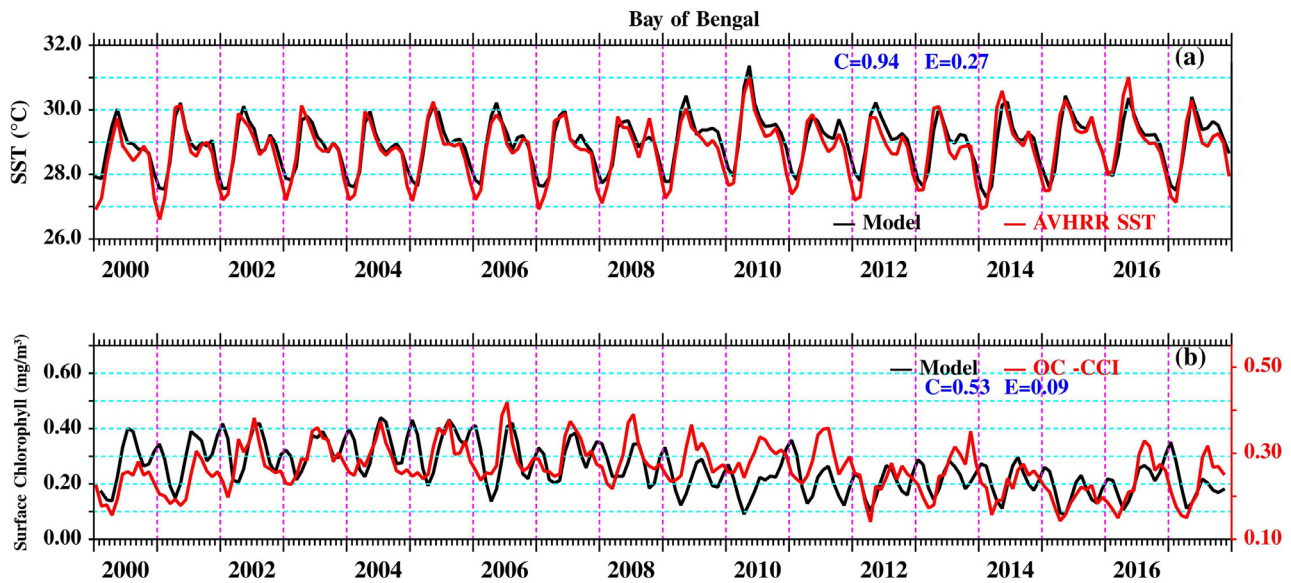


Figure 2 a) Sea surface temperature ($^{\circ}\text{C}$) and b) surface Chlorophyll-a concentration (mg m^{-3}) from model simulation (black) and satellite observed (red) averaged over the BoB region from 2000–2017.

(Thushara and Vinayachandran, 2016). This region along the east coast of India has major fishing zones including Visakhapatnam and Kakinada. To establish the model capabilities in simulating the biogeochemical features over the BoB region, the model simulated SST and Chl-a concentration for 18 years (2000–2017) are compared with satellite in-situ observations.

The BoB domain averaged, time series of model-simulated SST is compared with AVHRR SST during the study period (2000 to 2017) and shown in Figure 2a. It is observed that model simulated SST well captures the seasonal and interannual variability with a high correlation coefficient of 0.94 and low root mean square error (RMSE) 0.27 $^{\circ}\text{C}$ and it ensures that model SST can represent the interannual variations to a large extent over the BoB region. The simulated surface Chl-a concentration are compared with a merged satellite product (OC-CCI), and it is seen that model simulation is able to reproduce the Chl-a variability with respect to observations during the analysis period (Figure 2b). A positive correlation coefficient of 0.53 with 0.09 mg m^{-3} less RMSE between model simulation and observation of Chl-a over BoB region is observed, indicating that the model reasonably captures the pattern, but some marginal bias in the magnitude of Chl-a.

The current study focuses on understanding the biogeochemical variability in the summer season from the year 2000 to 2017 over the coastal region of western BoB (marked in Figure 1b). Therefore, a validation for the model-simulated SST and Chl-a concentration averaged over the red box region (80.2°E – 87°E , 14°N – 20°N) in western BoB is shown in Figure 3a–b. The ribbon plot in Figure 3a–b clearly displays an inverse relationship between the SST and Chl-a concentration. It is seen that the model well-depicted this inverse relationship between SST and Chl-a concentration (Figure 3). The statistical analysis shows a positive correlation coefficient of 0.94 and with a low RMSE value of 0.32 $^{\circ}\text{C}$ between simulated and observed SST. Similarly, a

positive correlation coefficient of 0.53 and RMSE of 0.21 mg m^{-3} was observed between the simulated and observed Chl-a concentration over the western margin of BoB.

Ocean subsurface information plays a curial role in a better understanding and prediction of oceanic characteristics. Tourre and White (1995) reported that the interannual variability of the subsurface temperature of the IO is significantly affected by ENSO modes. They found that the first two modes of empirical orthogonal function analysis are influenced by El-Nino explaining 31%, 18% of variability for the major peaks in SST during the 1981–1982, 1983, and 1987 summer–fall seasons over the Indian Ocean. Zhang et al. (2021) showed that the BoB subsurface variability is highly correlated to the IOD on the interannual time scale. They highlighted the role of coastal Kelvin waves in carrying signals of positive (negative) salinity anomalies from the eastern equatorial Indian Ocean up to the coastal BoB during positive (negative) IOD events. The subsurface features of model simulations are also validated and shown in Figures 4–6. The model simulated monthly temperature up to a depth of 200 m is averaged over the BoB domain and validated for a period from 2002 to 2017 with respect to the gridded Argo data since this data is available from 2002, July onwards (Figure 4a,b). The subsurface temperature simulations are able to represent the seasonal surface cooling and warming with its associated shoaling and deepening of the thermocline and display a good agreement with the gridded Argo product. The model has captured well the pattern and magnitude of temperature variability with comparatively more accuracy up to a depth of 95 m and below this depth to 200-m, the model has maintained to capture the pattern with a bit higher warming with respect to the gridded Argo observations. The two Bio-Argo, *in-situ* observations are also utilized to assess the subsurface simulations and shown in Figure 5 (a–d: WMO ID: 2902193, e–h: WMO ID: 2902195). The choice of the considered Bio-Argo is made on the basis of their comparatively larger tempo-

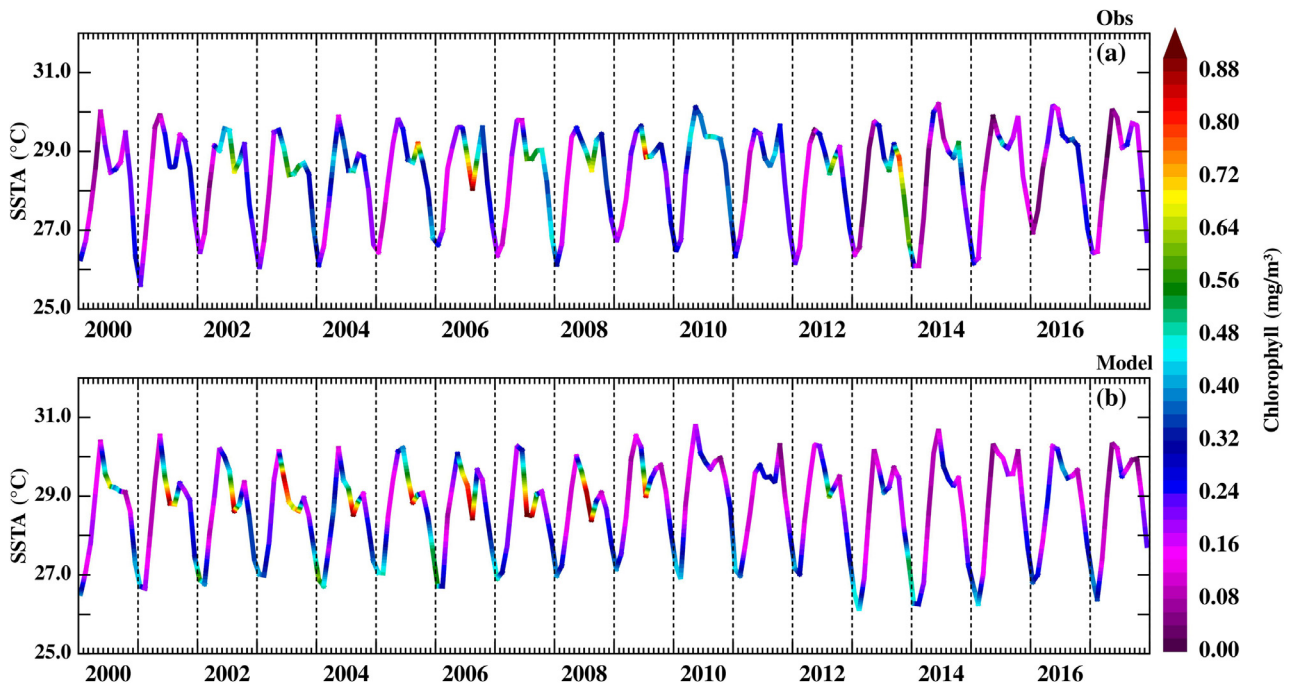


Figure 3 The observation (a) and model-simulated (b) sea surface temperature ($^{\circ}\text{C}$) and surface Chlorophyll-a (mg m^{-3}) averaged over the coastal analysis region in the western BoB (marked in Figure 1b) from 2000 to 2017. The curve shows SST and the shading of the curve shows surface Chl-a.

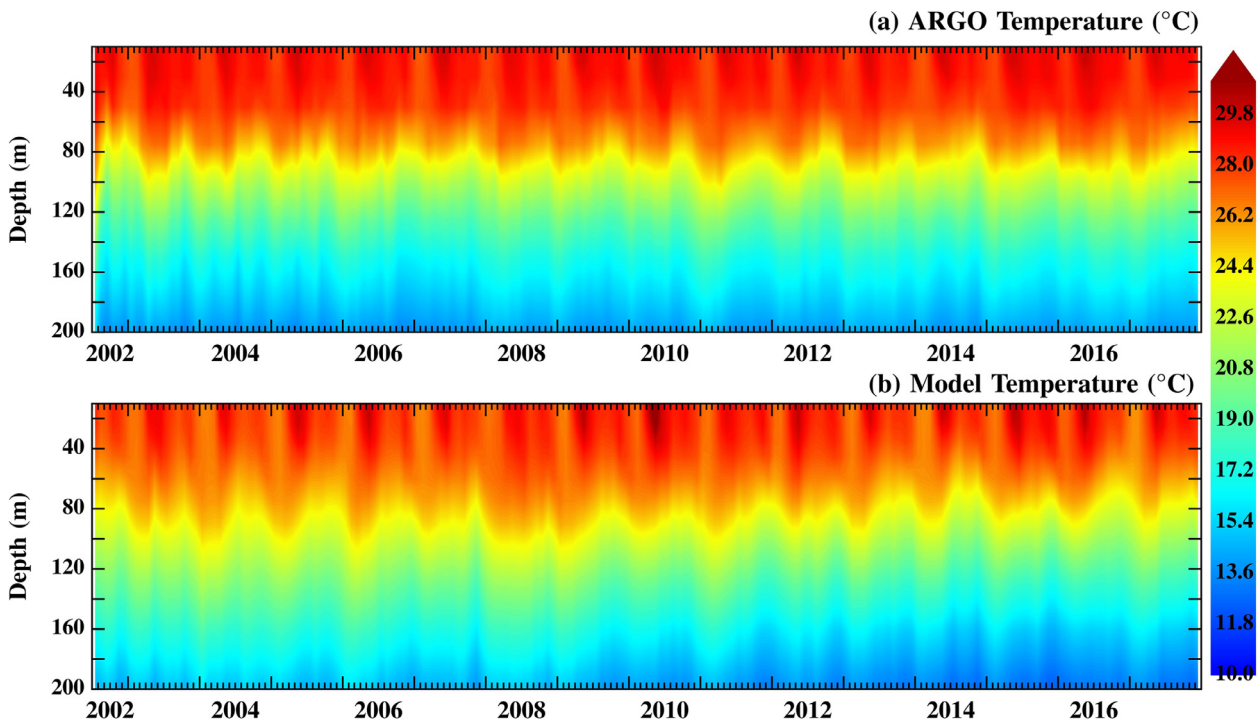


Figure 4 Gridded Argo *in-situ* observations (a) and model simulations (b) for temperature ($^{\circ}\text{C}$) averaged over the BoB region from 2002 to 2017.

ral coverage since they were deployed for a longer period over the BoB. The temperature and subsurface Chl-a simulations are plotted along the selected Bio-Argo trajectories (shown in red and orange in Figure 1b) those are deployed in western BoB and considered for the period of January

2016 to December 2017 (Figure 5). It is observed that the model has well simulated the warm water patch extended to the deeper depths during summer and subsequent winter cooling in the water column along both Bio-Argo trajectories from 2016 to 2017 (Figure 5c–d, g–h). Further, the model

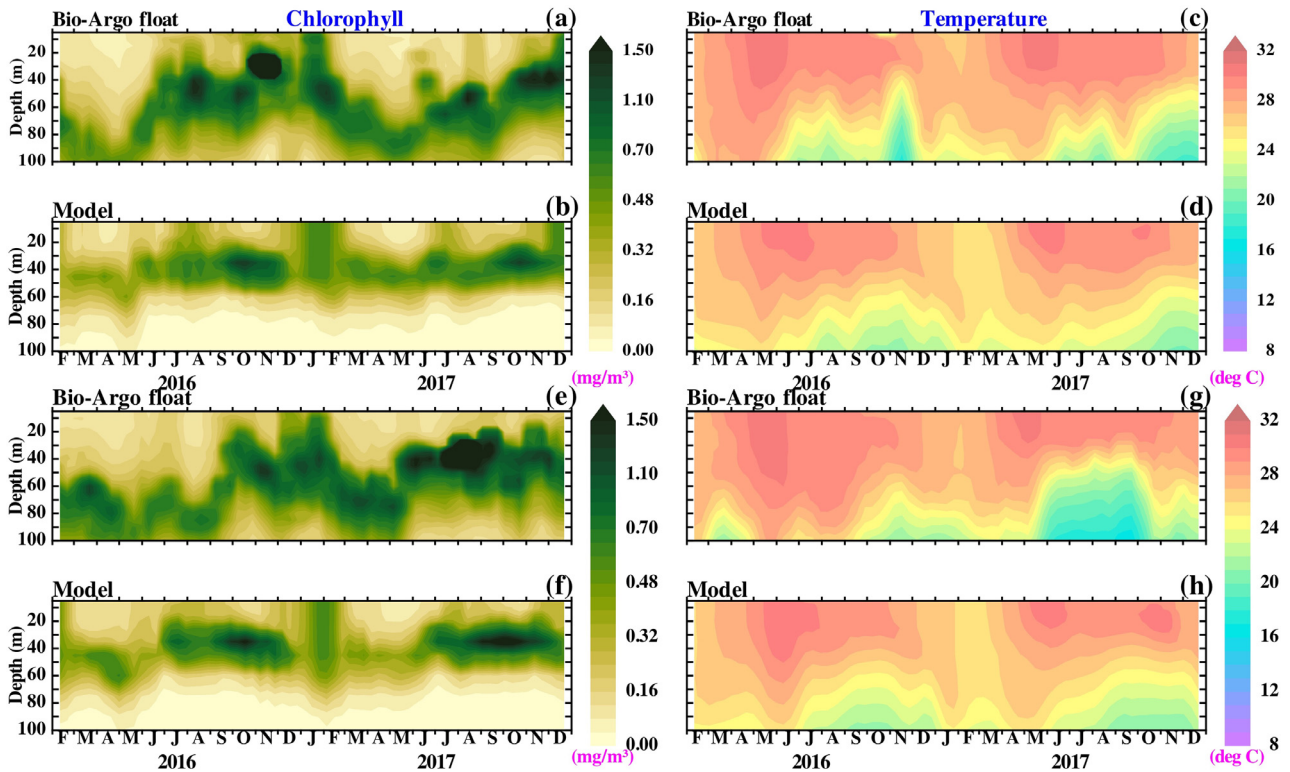


Figure 5 Time-depth section of chlorophyll-a (mg m^{-3}) from observation (a, e), model simulations (b, f) and temperature ($^{\circ}\text{C}$) from observation (c, g), model simulations (d, h) along the trajectories of two Bio-Argo floats WMO ID: 2902193 (a–d) and WMO ID: 2902195 (e–h).

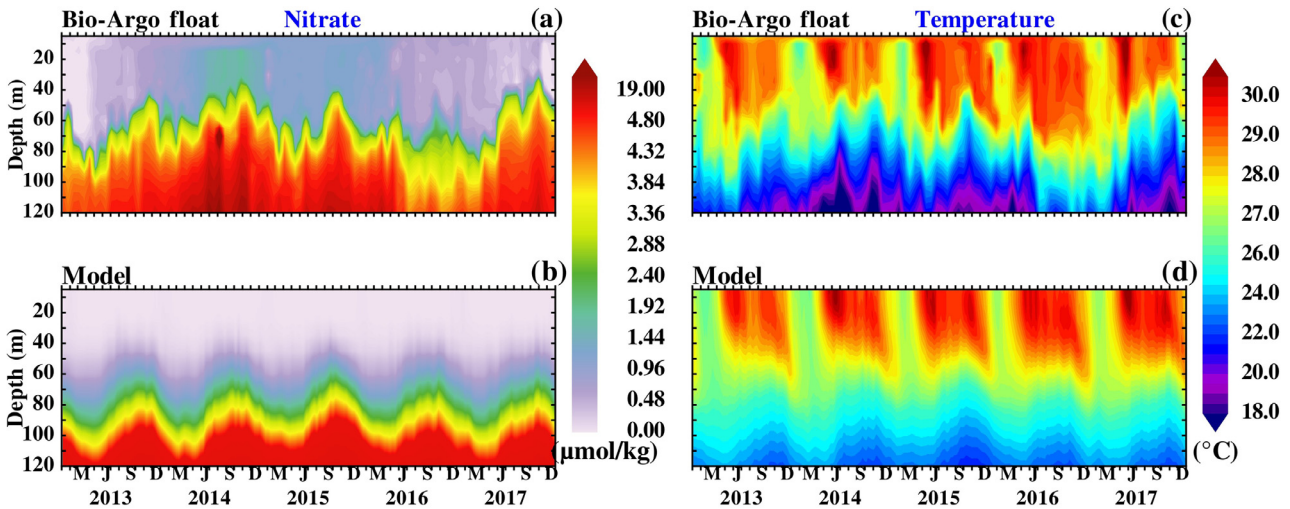


Figure 6 Time-depth section of nitrate ($\mu\text{mol kg}^{-1}$) from observation (a), model simulations (b) and temperature ($^{\circ}\text{C}$) from observation (c), model simulations (d) along the trajectory of Bio-Argo floats WMO ID: 5903712 (a–d).

has also attempted to capture the subsurface colder water upwelling during 2017, monsoon season as shown along the Bio-Argo trajectory (WMO ID: 2902195, in Figure 5g–h). The agreement between Chl-a simulations along these Bio-Argo trajectories is also satisfactory. It is clearly depicted that model has shown its efficiency to represent the existence of subsurface chlorophyll maxima layer almost similar to the considered in-situ observation. As shown by observation and reasonably well reproduced by the model simulations, the

cooling displayed in the winter season (Figure 5c–d, g–h) was associated with subsurface Chl-a upwelling (Figure 5a–b, e–f) from December 2016 to February 2017. In general, the model is found to be well simulating the Chl-a concentration features from 2016 to 2017 along the selected in-situ observed trajectories of Bio-Argo with some disparities in capturing the Chl-a variability due to the limitation of the model resolution and mixing parameterization schemes that limit its ability to simulate the small-scale processes.

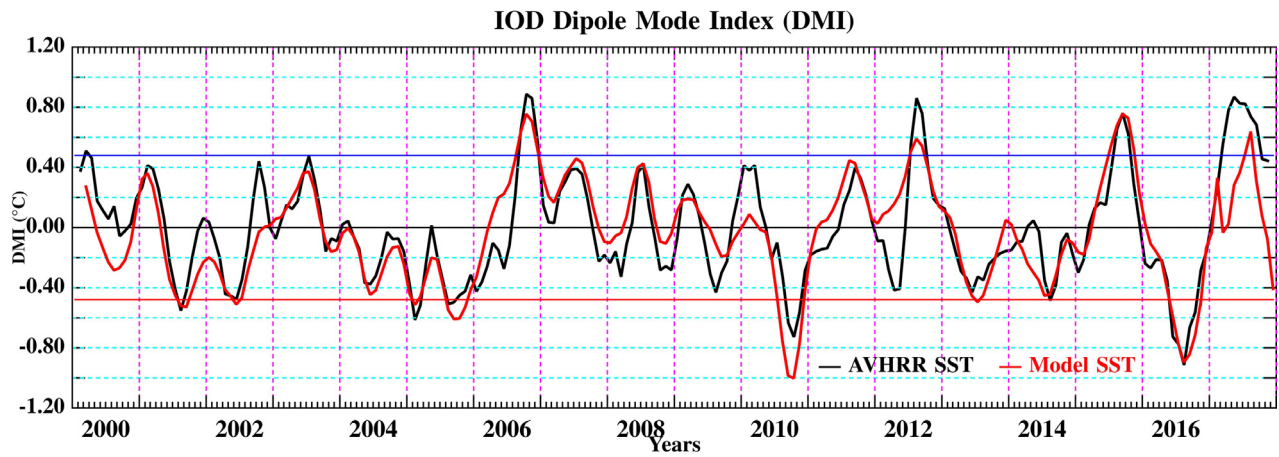


Figure 7 Dipole Mode Index (DMI) calculated from the AVHRR (black line), and model simulated (red line) sea surface temperature anomalies (°C) data during the study period 2000–2017. Horizontal lines (blue, red) are drawn at $\pm 0.48^\circ\text{C}$ as the threshold value for the classification of positive and negative IOD years.

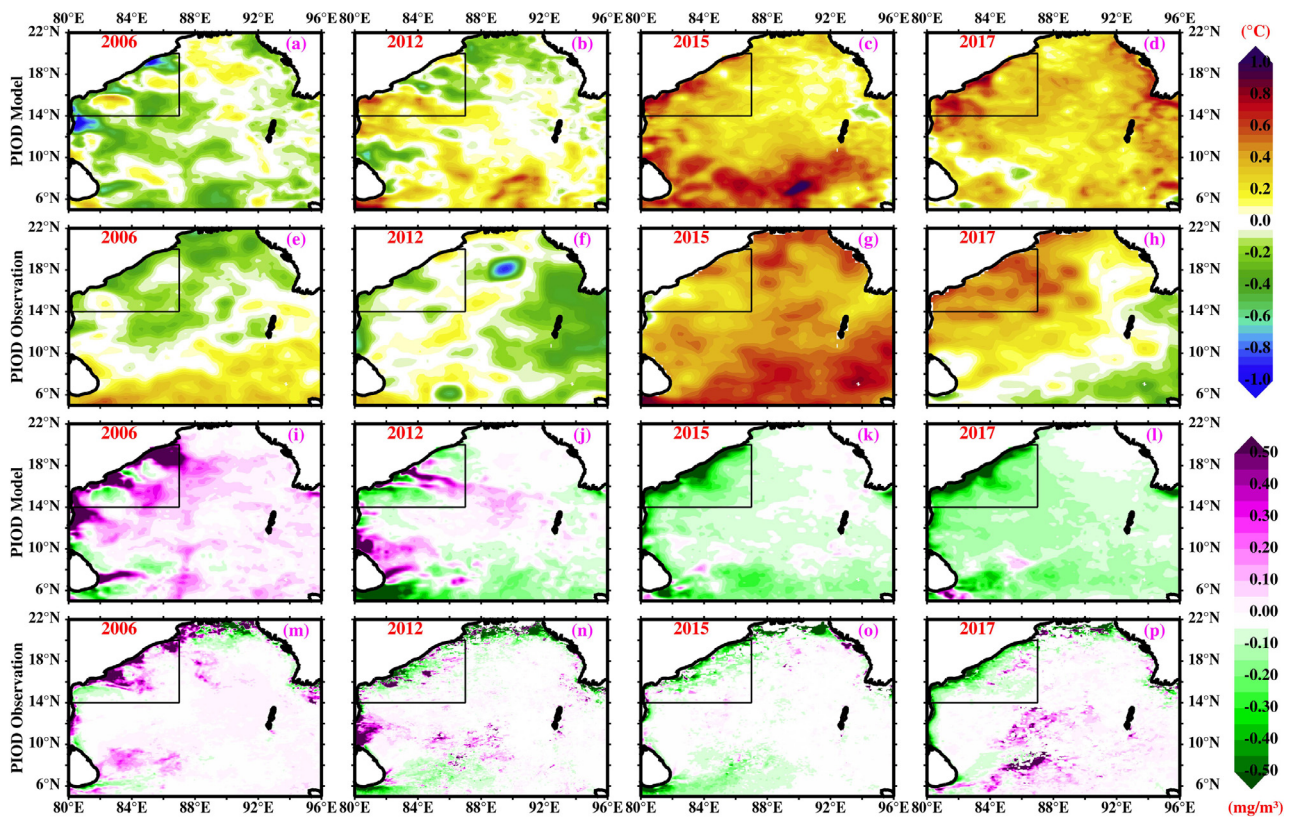


Figure 8 The SST anomalies from the model (a–d), observation (e–h) and Chl-a anomalies from the model (i–l), observation (m–p) for the summer monsoon season (June to September) of all selected pIOD years during 2000–2017 over BoB.

Further, to validate the model simulated nitrate and its associated temperature, the only Bio-Argo with nitrate profiler (shown by green color in Figure 1b) over the BoB is used and shown in Figure 6a–d for the period of 5 years (2013 to 2017). The model simulated temperature along this Bio-Argo trajectory has shown its efficiency to simulate the seasonal warming and cooling episodes and respective upward and downward movement of nitracline that is present almost at a depth of 60 to 65 meters in both observations and model. This seasonal availability of nutrients to the photic depth

has the potential to enhance the surface bloom. The magnitude of surface nitrate and temperature deeper to 100 m are underpredicted by the model. In the current section, the validation of model simulations for subsurface temperature, Chl-a concentration and nitrate, interannual SST and surface Chl-a with respect to satellites and in-situ observations has confirmed these model simulations to be considered for further analysis of the impact of IOD modes on the biogeochemical features of the upper ocean over the western margin coastal box region of BoB during 2000 to 2017.

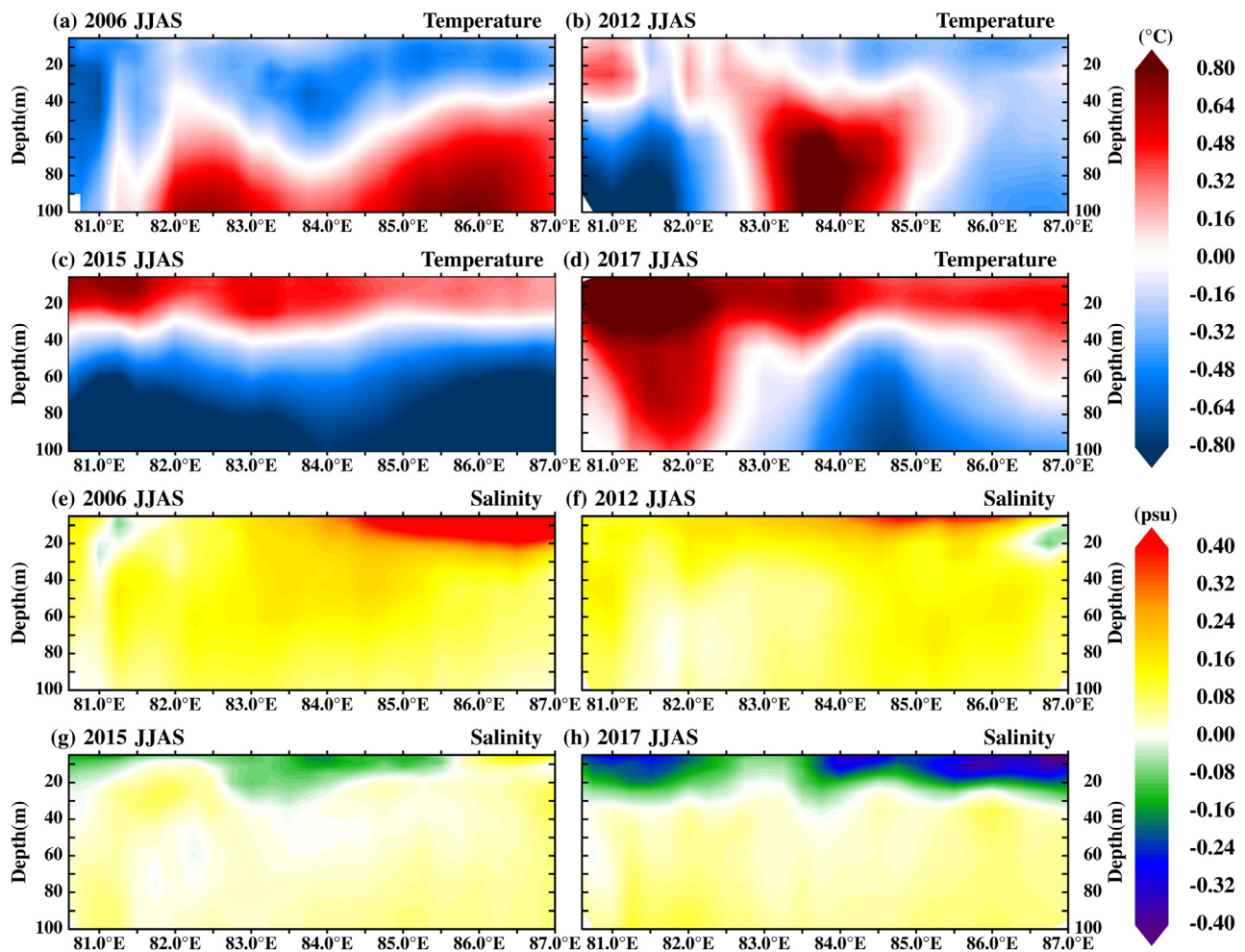


Figure 9 Vertical cross-section of model-simulated latitudinally averaged (14°N – 20°N) temperature (a–d) and salinity (e–h) anomalies over the western BoB for the summer monsoon season (June to September) of considered pIOD years.

In the next section, the model simulated fields are analyzed to first check the behavior of the biophysical parameters under the influence of both pIOD over the coastal box region shown in Figure 1b and over the BoB domain.

3.2. Impact of pIOD events on the biophysical processes in the BoB

In the Indian Ocean, one of the predominant modes of interannual variability is IOD events (Saji et al., 1999; Webster et al., 1999). The Dipole Mode Index (DMI) (Saji et al., 1999), an index highlighting the strength of IOD, is calculated by using model-simulated and AVHRR SST anomalies averaged over the western (50°E – 70°E , 10°S – 10°N) and eastern (90°E – 110°E , 10°S – 0°) IO region for the analysis period of 18 years (2000 to 2017). The DMI index is used to identify positive and negative modes of IOD during the analysis period (Figure 7). To define the events, the DMI threshold value of $\pm 0.48^{\circ}\text{C}$ is considered. It is clear from Figure 7 that the DMI calculated from the model and observed data are in very good agreement. There are four strong pIOD events (2006, 2012, 2015, 2017) and three nIOD (2005, 2010, 2016) events that occurred during the study pe-

riod (2000 to 2017). In further analysis, we considered these four strong pIOD years to study their anomalous biophysical response.

The model simulated SST anomalies averaged for the summer monsoon season along with the AVHRR SST anomalies data over BoB are plotted for these selected four pIOD years in Figure 8a–h. The response of pIOD years on the SST over this region is not consistent for all four years (Figure 8a–h). It is observed that the model and observations both depicted that the pIOD years of 2015, and 2017 are causing warming (represented by positive SST anomalies). However, the pIOD years 2006 and 2012 are found to be associated with cooling (represented by negative SST anomalies) over BoB. Figure 8i–p shows model simulated Chl-a anomalies along with OC-CCI Chl-a anomalies averaged for the summer monsoon season over the BoB. The changes in Chl-a concentration over this region for the four pIOD years are not consistent. The model and observations both depicted that 2006, 2012 pIOD years have positive Chl-a anomalies (and negative SST anomalies). Whereas in 2015, 2017 pIOD years, negative Chl-a anomalies (and positive SST anomalies) are observed in model and observations. It is evident that all four considered pIOD years in our study period (2000 to 2017) show a clear demarcation in terms of their

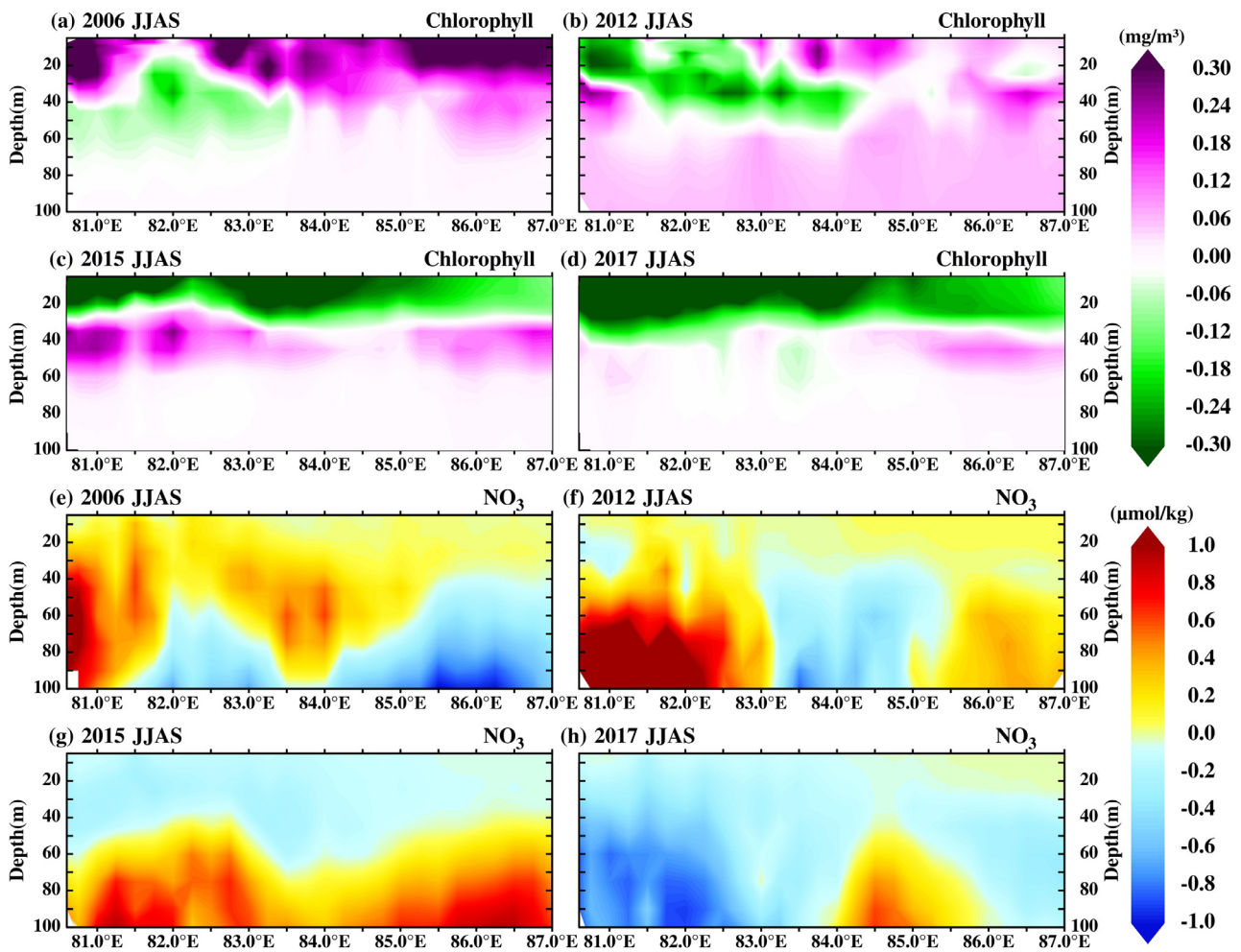


Figure 10 Vertical cross-section of model-simulated latitudinally averaged (14°N – 20°N) Chl-a (a–d) and Nitrate (NO_3 , e–h) anomalies over the western BoB for the summer monsoon season (June to September) of considered pIOD years.

anomalous SST and Chl-a over the BoB, particularly over the coastal upwelling region of western BoB. The impact of pIOD years on the biophysical features of BoB is not yet studied in detail. Our analysis clearly shows an inconsistent behavior of SST and Chl-a anomalies of the same pIOD mode for different years. Figure 8 not only highlights the difference in the SST and Chl-a anomalies response during pIOD years but also establishes the model’s efficiency in capturing these anomalous impacts of pIOD along with the response disparity between 2006, 2012 and 2015, 2017 pIOD years with respect to satellite observations.

In order to understand the varying impacts of these pIOD years, here onwards we are representing 2006, 2012 as cold class (CC) pIOD years and 2015, 2017 as the warm class (WC) pIOD years. These years showed a comparable response for their associated period of summer monsoon season (June–September) with anomalous SST and Chl-a variability over the western BoB. It is seen from Figure 8 that the model and observations both are in good agreement to represent the remarkable difference as cooling is associated with an increase in Chl-a concentration for CC pIOD years and warming associated with a decrease in Chl-a concentration for WC pIOD years in the summer monsoon season over the western BoB. However, the model simulations along the coast show

comparatively higher values than the satellite observations. The satellite observations and model simulations both have their limitations and associated errors. However, the model and satellite observations show similar variations of SST and Chl-a and their spatial distribution in the study region during the summer monsoon season.

Aparna et al. (2012) found that pIOD events are characterized by negative sea surface height anomalies (SSHA) over the coastal western BoB. In summer monsoon (June–September), the circulation along western BoB does not follow any consistent pattern in contrast to other seasons and appears to be disorganized (McCreary et al., 1993) in the presence of several cyclonic and anticyclonic eddies. A hydrographic study shows that eddies associated with discontinuity are generated at the interface of two opposing flows along the western boundary, where the northward flow is wind-driven while the southward flow is forced by freshwater influx and wind stress (Babu et al., 1991). The sea level variability along the western BoB largely depends on the upwelling produced by monsoonal winds (Han and Webster, 2001). Further, the eddies (both cyclonic and anticyclonic) in the western BoB are largely influenced by the winds (Dandapat and Chakraborty, 2016) and play a crucial role in seasonal sea-level variation in their path-

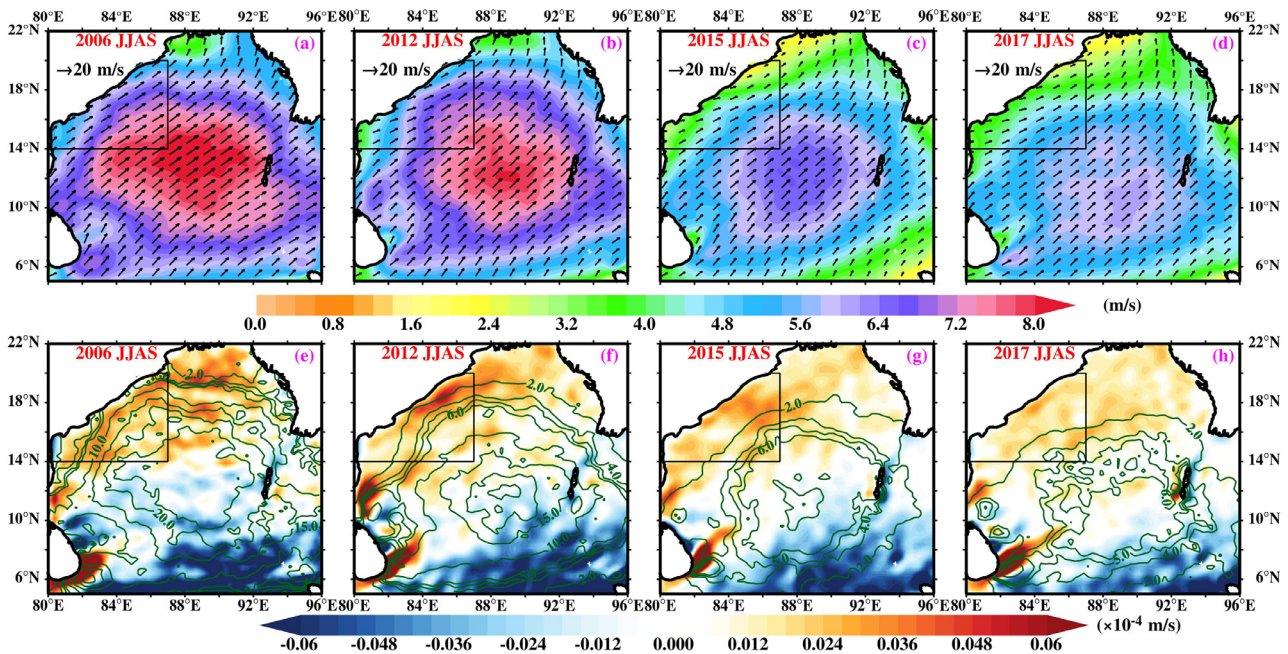


Figure 11 Wind speed anomalies (m s^{-1} , shaded) overlay with anomaly wind vectors (a–d) and anomalies of Ekman pumping velocity (m s^{-1} , shaded) overlaid with Ekman mass transport anomalies ($\text{kg m}^{-1} \text{s}^{-1}$, contours, e–h) for the summer monsoon season (June to September) of all selected pIOD years during 2000–2017 over BoB.

ways (Cheng et al., 2013). However, separating the individual contribution of mesoscale eddies, upwelling, stratification, and mixing, etc. is beyond the scope of the present study. The pIOD generally increases the strength of monsoon winds and associated rainfall and, hence, is found to support upwelling favorable wind stress in the western BoB. A large part of it is associated with cyclonic circulation (negative/lowering SSHA) (Fig. S1) favorable for upwelling due to the strong wind-driven northward flow. The southward flow is forced with less freshwater influx in CC pIOD years (2006, 2012). In WC pIOD years (2015, 2017) years, the large part is associated with anticyclonic circulation (positive/high SSHA) which inhibits the upwelling. The northward flow is weak wind-driven and the southward flow is forced by a high freshwater influx in WC pIOD years during the summer monsoon.

As noted before, the box area selected in the western coastal BoB is the main analysis region due to its importance in supplying the subsurface nutrients to the photic layers through upwelling. The sustained supply of nutrients leads to a comparatively higher bloom (primary productivity) in this region than in the rest of the bay during the summer monsoon season. To estimate the extent of the inconsistent behaviour of SST and Chl-a anomalies of all four pIOD years in the subsurface, the model-simulated vertical cross-section of temperature, salinity and Chl-a, nitrate concentration along the longitudes of the box region (80.2°E – 87°E) are plotted and shown in Figures 9, 10 for all four pIOD years considered in the present study. Figure 9(a–d) shows the vertical cross-section of model-simulated latitudinally averaged (14°N – 20°N) temperature anomalies ($^{\circ}\text{C}$) during the four pIOD years over the western BoB region. It can be observed from Figure 9a–d that the anomalously warm water of almost 0.8°C to 0.4°C to a depth of 40–60 m is present in WC (2015, 2017) pIOD years whereas, in 2006, anomalously

colder water of -0.8°C to -0.35°C is present to a depth of 100 m near the coast and 60 to 35 m away from the coast. In the year 2012, anomalous colder water around -0.5°C to -0.2°C was present to a depth of 100 m (in coastal and off-shore regions where mixing occurs). Overall, in the CC pIOD years colder water was found in western BoB whereas, it was the opposite feature in the WC pIOD years (Figure 9a–d). The contrast in the magnitude and vertical extent of this anomalous temperature for both the CC and WC pIOD years is found higher adjacent to the coast and shows a decrement on moving away from the coast. Figure 9e–h shows a vertical cross-section of model-simulated latitudinally averaged (14°N – 20°N) salinity anomalies (psu) over the western BoB region during the summer monsoon season of the four pIOD years. It shows a clear demarcation between the CC and WC pIOD years in the anomaly distribution over the study region. In WC pIOD years, a surface freshening of -0.3 psu is seen in 2017 and -0.2 psu in 2015 which extend vertically up to 40 m in 2017 and up to 25 m in 2015. On the other hand, higher surface salinity (0.2 to 0.5 psu) was present in the CC (2006, 2012) pIOD years. To ensure the salinity differences associated with these CC and WC years, the vertical distribution of model-simulated salinity is analyzed and found to be retaining their respective saltiness for CC years and freshening for WC years up to 100 m depth in the study region. These contrast features of salinity distribution with higher magnitude are concentrated within the upper 30 m oceanic layer. This is also evident from Figure 9e–h that all four pIOD years are not similar in their salinity features due to the disparity found in precipitation, heat fluxes (both shown in Figures 11–12) which offered different stratification and mixing states (shown in Figures 13–14).

Since there exists an inverse relationship between temperature and Chl-a, the Figure 10a–d shows the verti-

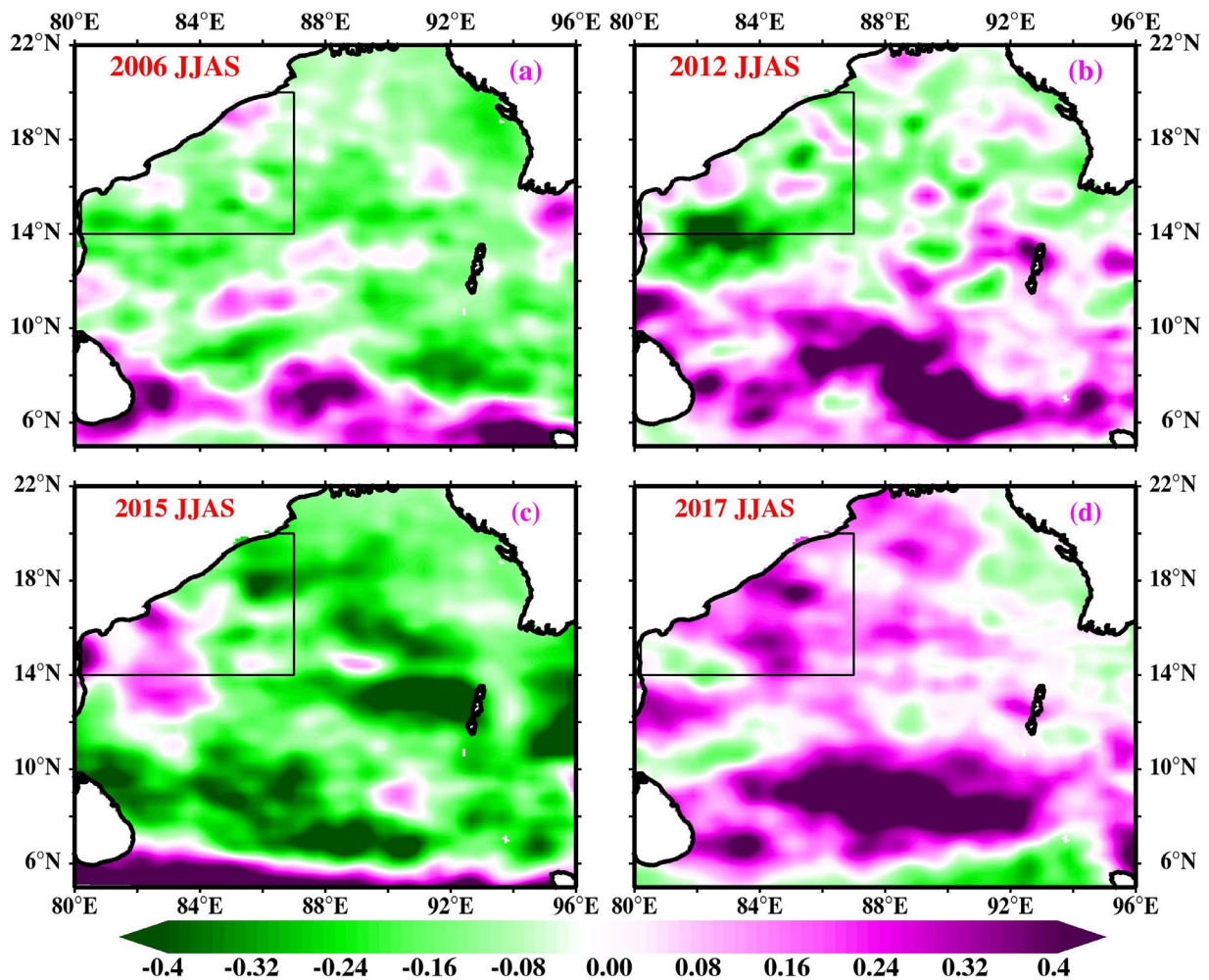


Figure 12 Precipitation anomalies (cm day^{-1}) for the summer monsoon season (June to September) of all selected pIOD years during 2000–2017 over BOB.

cal cross-section of model-simulated latitudinally averaged (14°N – 20°N) Chl-a anomalies over the western BoB for the summer monsoon season of the four pIOD years reveals that the availability of negative ($\approx -0.3 \text{ mg m}^{-3}$, lesser primary productivity) and positive (≈ 0.12 to 0.3 mg m^{-3} , higher primary productivity) Chl-a anomalies maintenance to a depth of 30 to 35 m for both WC and CC pIOD years, respectively (see Figure 10a–d). Further, the vertical cross-section of model-simulated latitudinally averaged (14°N – 20°N) nitrate concentration anomalies are illustrated in Figure 10e–h over the study region for summer for all four considered pIOD years to support the noticed anomalous low and high bloom over the coastal BoB region. The lower (-0.1 to $-0.3 \mu\text{mol kg}^{-1}$) and higher ($+0.1$ to $0.32 \mu\text{mol kg}^{-1}$) values of nitrate anomalies are present in the WC and CC pIOD years, respectively (Figure 10e–h) that can efficiently explain the subsurface chlorophyll distribution displayed in Figure 10a–d for their respective years of pIOD during summer monsoon season over the coastal analysis region (western BoB). These subsurface features also justify the significant differences in response to pIOD events associated with these CC and WC years. In this section, the evidence from Figures 7–10 consisting of the model simulations and observations have confirmed that there is a significant difference in the

bio-physical response on the surface as well as subsurface for all four considered pIOD years (both CC and WC) over BoB and coastal box region (marked in Figure 1b). In the next section, the causative mechanisms behind this inconsistent bio-physical response of the selected pIOD years are investigated.

3.3. Investigation of the inconsistent bio-physical response during pIOD events

The wind reversal from northeast to southwest direction from winter to summer used to bring the high monsoon rainfall, which covers a large part of the IO and Indian subcontinent (Schott and McCreary, 2001). The monsoon winds over the AS and BoB are used to establish favorable upwelling conditions along the different coasts of the Arabian Sea (Somalia, Oman, southeastern AS) and at the western margin of the BoB (Rao et al., 2010). The strength of upwelling and its resultant responses such as subsurface nutrient-enriched colder water updraft towards the surface and related offshore Ekman transport are significantly impacted by the combination of surface wind and ocean stratification conditions. These atmospheric and oceanic components are es-

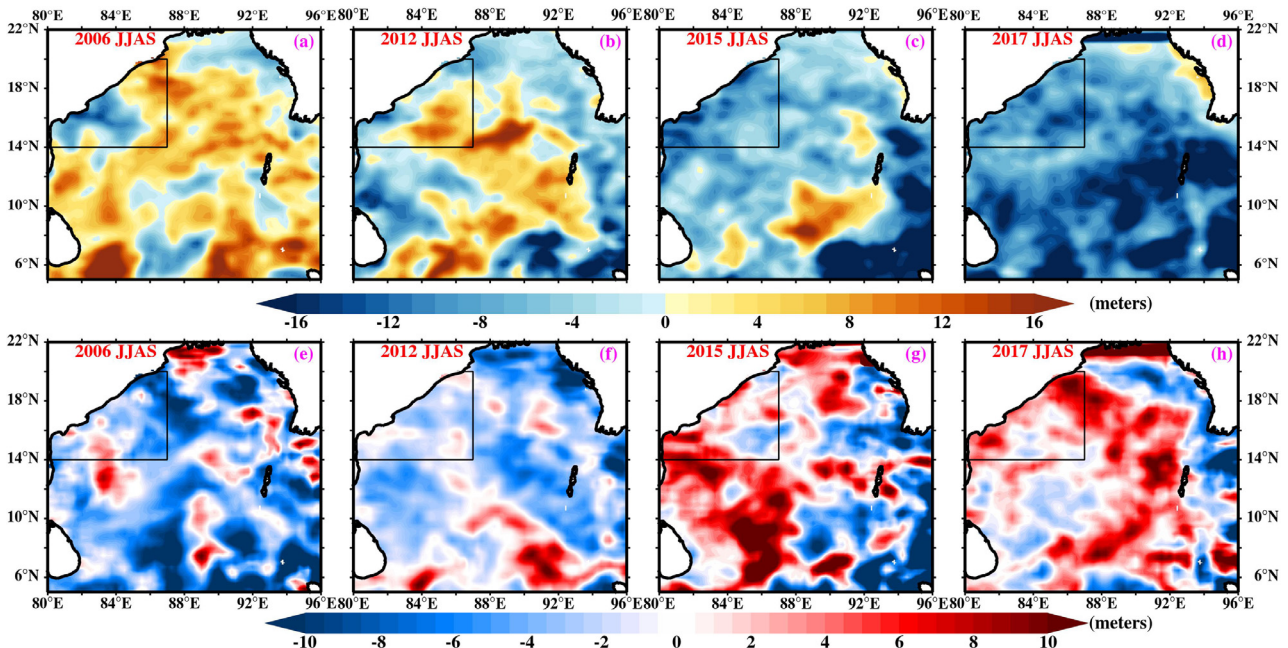


Figure 13 Model simulated mixed layer depth (in meters) anomalies (a–d) and barrier layer depth (in meters) anomalies (e–h) for the summer monsoon season (June to September) of all selected pIOD years from 2000 to 2017 over BOB.

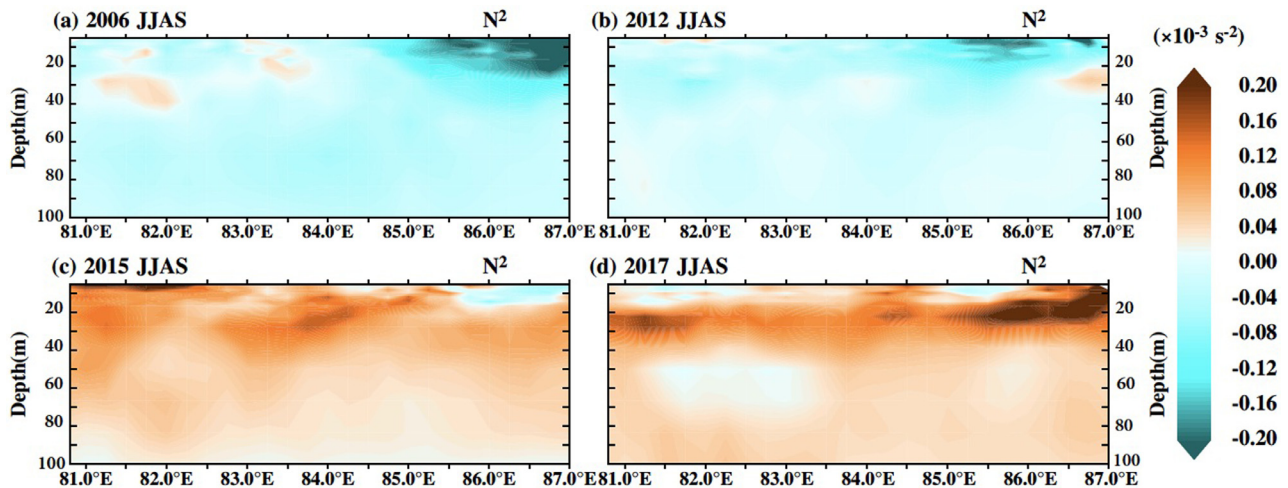


Figure 14 Vertical cross-section of model-simulated latitudinally averaged (14°N–20°N) Brunt Väisälä frequency (N^2 in s^{-2}) anomalies over the western BoB for the summer monsoon season (June to September) of considered pIOD years.

essential to be investigated in order to understand the possible causes for the inconsistent biophysical response associated with the different pIOD events. The summer monsoon season averaged wind speed ($m s^{-1}$) and wind vector anomalies (Figure 11a–d) along with the resultant Ekman pumping velocity ($m s^{-1}$) and overlay with Ekman mass transport ($kg m^{-1} s^{-1}$) contour anomalies are calculated and plotted in Figure 11e–h for all the four considered pIOD years (both CC and WC) over the BoB. It is noted that all the four pIOD years are associated with positive wind anomalies over the region during the summer monsoon. But CC (2006, 2012) years observe stronger (by 4 to $7.5 m s^{-1}$) positive wind anomalies than 2.3 to $5 m s^{-1}$ in the WC (2015, 2017) of pIOD years over the BoB and including the selected coastal upwelling region

in western BoB (Figure 11a–d). Further, the wind stress curl anomalies are calculated during the summer monsoon season for all four individual years (2006, 2012, 2015, 2017) of pIOD. During the initial period of the season, the years 2006 and 2012 (CC) have higher positive wind stress curl (more than $4 \times 10^{-7} N m^{-3}$) favorable for coastal upwelling in comparison to years 2015, 2017 (WC) which can be observed with the comparatively weaker magnitude of wind stress curl (up to $2 \times 10^{-7} N m^{-3}$) (Figure S2). The estimates of wind stress curl support the inferences made as the upwelling process becomes weaker in the WC pIOD years from June to September compared to the CC pIOD years. This reduction in upwelling strength affected the temperature and nutrient supply in the region leading to an inconsistent

bio-physical response to the CC and WC pIOD years in the western BoB.

Wang et al. (2011) stated that the positive wind stress curl signifies the upward (+ve) pumping velocity and supports the upwelling process whereas, a weaker wind stress curl represents a lowering in upward pumping velocity and weakening of the upwelling process. The current study utilized wind anomalies and their associated Ekman pumping anomalies to investigate the biophysical response. These higher positive wind anomalies generated higher offshore Ekman mass transport leading to a greater pumping velocity ($6 \times 10^6 \text{ m s}^{-1}$) in the CC with respect to WC pIOD years (Figure 11e–h). It is seen that during the 2015 and 2017 of WC pIOD years, there is a drop in the magnitude (both Ekman pumping velocity and Ekman mass transport) of positive (upward) Ekman pumping with the presence of negative Ekman pumping anomalies too in the study region with respect to the other two pIOD years (2006, 2012) belonging to CC. The changes of the upward to downward Ekman pumping are directly affecting the total subsurface nutrient-rich and colder water entrainment to the euphotic water layer. Subsequently, the weaker mixing due to the stronger stratification (Figure 14) limits the nutrient availability in the euphotic zone leading to a decrease in the primary productivity and lowering of Chl-a during WC compared to CC pIOD years.

The anomalous features shown in Figure 11 explain the negative and positive SST anomalies over the BoB during summer for CC and WC pIOD years, respectively shown in Figure 8a–h. This difference in anomalous wind results in larger upwelling-induced surface cooling in the CC years of pIOD than in the case of WC years. The nutrient supply from the subsurface to the illuminated upper-ocean layers of water can be quantified with an estimation of stratification. It is well known that the BoB stratification is primarily controlled by salinity changes which are maintained by the monsoonal rainfall and freshwater discharge from the major river system of the Indian subcontinent. Therefore, the precipitation anomalies (shown in Figure 12) are analyzed for the four pIOD years (both CC and WC). The precipitation anomalies during June to September in Figure 12a–b of CC pIOD years (2006, 2012) show comparatively less precipitation in the coastal upwelling region (highlighted by box) in the western BoB than the WC pIOD years (2015, 2017). Even though the stronger monsoonal winds are present in CC pIOD years, the precipitation anomalies are higher in the WC years over the whole BoB and coastal analysis box region. These higher positive precipitation anomalies associated with WC augment a more stratified near-surface water column for WC with respect to CC pIOD years. Precipitation adds to surface freshwater flux and promotes higher freshwater discharge from the contributing rivers in the region. The freshwater affects the mixed layer depth, salinity and temperature of the water column. The low salinity and warm temperature of near-surface water enhance density gradient in the vertical and reduce vertical mixing. The enhanced stratification in the upper ocean can be noticed in the Brunt Väisälä frequency (Figure 14) in the water column.

Further, to confirm the upper-ocean stratification strength associated with these CC and WC pIOD years, the mixed layer depth (MLD) and barrier layer thickness (BLT)

anomalies are calculated and plotted in Figure 13 for all four pIOD years. The MLD estimation revealed positive MLD (up to 10 m) and negative MLD (–8 m to –16 m) anomalies for CC (Figure 13a, b) and WC (Figure 13c, d) pIOD years over western BoB during the analysis period. From Figure 13a–d, it is clear that due to a combination of stronger monsoonal winds and lower precipitation (availability of freshwater flux), the mixing was more intense during the CC pIOD years concerning weaker mixing during the WC pIOD years. The WC years experienced comparatively weaker monsoon wind and higher precipitation surface flux leading to a stronger haline stratification than in the case of CC years. The intensified mixing of the water column for the CC years further reduces the stratification in the water column. The CC pIOD years show a comparatively higher mixing resulting in a colder and nutrient-rich euphotic zone than that of the other two pIOD years associated with WC. Further, the mixing process is supported/caused by the existence of a lower BLT implying lower stratification during summer in CC pIOD with respect to the higher BLT that implies higher stratification during WC pIOD.

The barrier layer, a freshwater layer lying between the thermocline and mixed layer is also calculated and presented in Figure 13e–h. The BLT anomalies confirm the presence of weaker (stronger) stratification during the CC (WC) years of pIOD. The figure shows a large region with negative BLT (–6 m to –2 m) over the western BoB during the summer season in CC years. Whereas in WC years, anomalous positive BLT (2 m to 8 m) was present. In this section, the analysis of different air-sea fluxes and oceanic parameters has indicated that colder SST (-0.4°C) and stronger Chl-a positive (0.45 mg m^{-3}) anomalies during CC years can be explained by the combination of anomalously higher wind (4 to 7.5 m s^{-1} higher) and associated stronger offshore Ekman transport (15 to $25 \text{ kg m}^{-1} \text{ s}^{-1}$) than WC pIOD years. Further, the strong upwelling leads to colder and nutrient-enriched water near-surface (see Figures 9, 10) which spreads horizontally on the surface over a large area by virtue of greater mixing (represented by 5 to 10 m positive MLD anomalies) resulting from the weaker stratification (as BLT is showing negative anomalies –6 m). This weaker stratification in CC years is caused by a reduction in surface precipitation ($-0.32 \text{ cm day}^{-1}$) with respect to WC years. Similarly, in the WC years, the biophysical response of warmer SST (0.45°C) anomalies along with negative Chl-a anomalies (-0.35 mg m^{-3}) are caused due by a simultaneous presence of anomalously weaker (2.3 to 5 ms^{-1}) wind leading to weaker offshore Ekman mass transport (only 3 to $4 \text{ kg m}^{-1} \text{ s}^{-1}$) with weak Ekman pumping velocity ($2.5 \times 10^{-6} \text{ m s}^{-1}$) which results in a reduction in upwelling and surface cooling. Consequently, in the case of WC years, there is a reduction in nutrient supply to the near-surface photic zone and due to its comparatively weaker vertical entrainment extent (shown by Figure 10e–h) than CC pIOD years.

Maes and O'kane (2014) analyzed a reanalysis data of temperature and salinity to show that the seasonal variation of Brunt Väisälä (N^2) frequency in upper 300 m depth can define the degree of stratification (where positive values depict a more stable water column due to haline part) in the tropical oceans. Figure 14 shows a vertical cross-section of model-simulated latitudinally averaged (14°N – 21°N) of Brunt Väisälä frequency (N^2 in s^{-2}) anomalies over the west-

ern BoB for the summer season of all the four pIOD years. From surface to 70-meter depth, positive anomalies indicating the strong stratification ($0.2 \times 10^{-3} \text{ s}^{-2}$ to $0.12 \times 10^{-3} \text{ s}^{-2}$) generally inhibited the nutrients from subsurface to the euphotic zone for WC pIOD years (2015 and 2017) as compared to CC pIOD years negative anomalies of -0.2×10^{-3} to $-0.04 \times 10^{-3} \text{ s}^{-2}$ indicating weak stratification caused the mixing, resulting in the colder and nutrient rich euphotic zone. The higher precipitation leads to thicker BLT in WC pIOD years as compared to CC pIOD years. Therefore, the anomalous higher precipitation, thicker BLT, and negative MLD anomalies cause the observed inconsistent biophysical response in the WC pIOD years with respect to CC pIOD years over the western BoB.

4. Discussion and conclusions

The IOD and ENSO are the two dominant modes of interannual variability over the Indian Ocean (Murtugudde and Busalacchi, 1999). The Chl-a variability associated with these modes has been studied over the IO by Currie et al. (2013) by utilizing four decades of hindcast data from a coupled biophysical ocean general circulation model. They stated that the ENSO and pIOD both impact the variability of Chl-a anomalies over the IO, but the southern BoB region is mainly affected by the IOD modes. However, the previous studies have not focused on addressing the Chl-a variability over the western margin of BoB. Therefore, the current study has attempted to understand the impact on the Chl-a anomalies due to the IOD modes with an emphasis on pIOD mode over the western margin of BoB using a coupled biophysical (ROMS + Bio-Fennel) model. The coupled model simulations were performed for 18 years (2000 to 2017). The model simulations of SST and Chl-a are validated with respect to satellite and in-situ Bio-Argo observations over the BoB domain including the western margin of BoB (main analysis region marked in Figure 1b). A thorough validation of model simulation shows the model's capability in simulating the temperature, Chl-a and nutrient concentration reasonably well on the surface and subsurface with respect to the observations over the BoB. The study period covers the four strong pIOD (2006, 2012, 2015, 2017) events. The four strong pIOD years considered in our study period (2000 to 2017) exhibit inconsistency in the SST and Chl-a anomalies over the BoB. The CC pIOD years (2006, 2012) observe negative SST with positive (high) Chl-a concentration anomalies, whereas WC pIOD years (2015, 2017) have positive SST with negative (low) Chl-a concentration anomalies. The study reports an inconsistent response of biophysical features (i.e., temperature, Chl-a, and nutrient concentration) associated with CC and WC years of pIOD over the BoB with an emphasis on the western coastal BoB region. These inconsistent anomalous biophysical characteristics of the CC and WC pIOD years are noticed in model simulations and verified through satellite observations.

The CC pIOD years show anomalously colder water column with positive chlorophyll anomaly in response to a greater vertical entrainment extent of colder water in the western margin of the BoB. It results in a higher supply of nutrients from subsurface to near-surface layers during

the summer monsoon season (June to September). In contrast to the CC years, the WC pIOD years has been found to have an anomalously warmer water column with a negative Chl-a anomaly in response to lower vertical entrainment of colder water (due to reduced upwelling) at the western margin of BoB. Therefore, the nutrient availability in the near-surface layers reduces in the WC years during the summer monsoon season. A comparison of wind speed and wind stress curl for these four pIOD years showed that the CC and WC experience positive anomalies (with respect to climatology) of southwesterly winds during summer monsoon with higher strength associated with class CC than WC pIOD years. Whereas, precipitation anomalies are negative in CC and positive in WC pIOD years. The difference in wind speed and precipitation between CC and WC leads to differences in upper-ocean stratification, mixing, Ekman transport, upwelling, SST, nutrient and Chl-a concentrations. In the CC pIOD years, the stronger winds and higher offshore Ekman mass transport with strong Ekman pumping velocity leads to more vigorous upwelling and mixing which helps to enhance nutrient concentration in the near-surface photic zone and, thereby, enhances primary productivity and Chl-a concentration. On the other hand, the weaker winds and lesser offshore Ekman mass transport with weak Ekman pumping velocity reduce the upwelling strength in the WC pIOD years which inhibits the nutrient concentration in the near-surface photic zone and, thereby, reduces primary productivity and Chl-a concentration. Therefore, it can be concluded that the disparity in the surface fluxes (wind speed and precipitation) influences the oceanic stratification, upwelling and mixing processes which are found to be responsible for different biophysical characteristics observed during different pIOD years in the BoB.

Declaration of competing interest

Conflict of interest/competing interests: The authors have no known conflict of interest to declare.

Acknowledgments

The high-performance computing (HPC) facility provided by IIT Delhi and the Department of Science and Technology (DST-FIST, 2014 at CAS, IIT Delhi), Government of India are thankfully acknowledged. We acknowledge the funding support provided by the Ministry of Earth Sciences, Govt. of India. Graphics were generated in this paper using PyFerret, Python, Ferret and NCL.

Availability of data and material

The NCEP reanalysis data is available at <https://psl.noaa.gov/data/gridded/data.ncep.reanalysis.html>. The daily surface wind data from QuikScat and ASCAT are acquired from <ftp://ftp.remss.com/wind/>. TRMM precipitation data obtained from <http://daac.gsfc.nasa.gov/precipitation>. The gridded data of Argo is available at <https://las.incois.gov.in/las>. Our model output data is available on request from the corresponding author.

Authors' contributions: VS performed model simulations and prepared draft figures. VS and TN carried out the analysis in consultation with VP. VS and TN wrote the manuscript draft and VP improved the manuscript with numerous corrections. All the authors contributed to the scientific interpretation of results and revision of the manuscript.

Supplementary materials

Supplementary material associated with this article can be found, in the online version, at <https://doi.org/10.1016/j.oceano.2022.04.003>.

References

- Akhil, V.P., Lengaigne, M., Vialard, J., Durand, F., Keerthi, M.G., Chaitanya, A.V.S., Papa, F., Gopalakrishna, V.V., de Boyer Montégut, C., 2016. A modeling study of processes controlling the Bay of Bengal sea surface salinity interannual variability. *J. Geophys. Res. Oceans* 121 (12), 8471–8495. <https://doi.org/10.1002/2016jc011662>
- Aparna, S.G., McCreary, J.P., Shankar, D., Vinayachandran, P.N., 2012. Signatures of Indian Ocean Dipole and El Niño-Southern Oscillation events in sea level variations in the Bay of Bengal. *J. Geophys. Res. Oceans* 117 (C10). <https://doi.org/10.1029/2012jc008055>
- Babu, M.T., Kumar, P.S., Rao, D.P., 1991. A subsurface cyclonic eddy in the Bay of Bengal. *J. Mar. Res.* 49 (3), 403–410. <https://doi.org/10.1357/002224091784995846>
- Babu, M.T., Sarma, Y.V.B., Murty, V.S.N., Vethamony, P., 2003. On the circulation in the Bay of Bengal during Northern spring intermonsoon (March–April 1987). *Deep Sea Res. Part II* 50 (5), 855–865. [https://doi.org/10.1016/s0967-0645\(02\)00609-4](https://doi.org/10.1016/s0967-0645(02)00609-4)
- Babu, S.V., Rao, A.D., Mahapatra, D.K., 2008. Pre-monsoon variability of ocean processes along the East Coast of India. *J. Coast. Res.* 243, 628–639. <https://doi.org/10.2112/06-0744.1>
- Baliarsingh, S.K., Lotliker, A.A., Trainer, V.L., Wells, M.L., Parida, C., Sahu, B.K., Kumar, T.S., 2016. Environmental dynamics of red Noctiluca scintillans bloom in tropical coastal waters. *Mar. Pollut. Bull.* 111 (1–2), 277–286. <https://doi.org/10.1016/j.marpolbul.2016.06.103>
- Banase, K., English, D., 2000. Geographical differences in seasonality of CZCS-derived phytoplankton pigment in the Arabian Sea for 1978–1986. *Deep Sea Res. Part II* 47 (7–8), 1623–1677. [https://doi.org/10.1016/s0967-0645\(99\)00157-5](https://doi.org/10.1016/s0967-0645(99)00157-5)
- Banase, K., McClain, C., 1986. Winter blooms of phytoplankton in the Arabian Sea as observed by the Coastal Zone Color Scanner. *Mar. Ecol. Prog. Ser.* 34, 201–211. <https://doi.org/10.3354/meps034201>
- Banzon, V.F., Evans, R.E., Gordon, H.R., Chomko, R.M., 2004. SeaWiFS observations of the Arabian Sea southwest monsoon bloom for the year 2000. *Deep Sea Res. Part II* 51 (1–3), 189–208. <https://doi.org/10.1016/j.dsr2.2003.10.004>
- Chakraborty, K., Valsala, V., Gupta, G.V.M., Sarma, V.V.S.S., 2018. Dominant biological control over upwelling on pCO₂ in sea east of Sri Lanka. *J. Geophys. Res. Biogeosci.* 123 (10), 3250–3261. <https://doi.org/10.1029/2018jg004446>
- Chen, G., Li, Y., Xie, Q., Wang, D., 2018. Origins of eddy kinetic energy in the Bay of Bengal. *J. Geophys. Res. Oceans* 123 (3), 2097–2115. <https://doi.org/10.1002/2017jc013455>
- Chen, G., Wang, D., Hou, Y., 2012. The features and interannual variability mechanism of mesoscale eddies in the Bay of Bengal. *Cont. Shelf Res.* 47, 178–185. <https://doi.org/10.1016/j.csr.2012.07.011>
- Chen, X., Pan, D., Bai, Y., He, X., Chen, C.-T.A., Hao, Z., 2013. Episodic phytoplankton bloom events in the Bay of Bengal triggered by multiple forcings. *Deep Sea Res. Part I* 73, 17–30. <https://doi.org/10.1016/j.dsr.2012.11.011>
- Cheng, X., McCreary, J.P., Qiu, B., Qi, Y., Du, Y., Chen, X., 2018. Dynamics of Eddy Generation in the Central Bay of Bengal. *J. Geophys. Res. Oceans* 123 (9), 6861–6875. <https://doi.org/10.1029/2018JC014100>
- Cheng, X., Xie, S.-P., McCreary, J.P., Qi, Y., Du, Y., 2013. Intraseasonal variability of sea surface height in the Bay of Bengal. *J. Geophys. Res. Oceans* 118 (2), 816–830. <https://doi.org/10.1002/jgrc.20075>
- Cherchi, A., Navarra, A., 2012. Influence of ENSO and of the Indian Ocean Dipole on the Indian summer monsoon variability. *Clim. Dyn.* 41 (1), 81–103. <https://doi.org/10.1007/s00382-012-1602-y>
- Currie, J.C., Lengaigne, M., Vialard, J., Kaplan, D.M., Aumont, O., Naqvi, S.W.A., Maury, O., 2013. Indian Ocean Dipole and El Niño/Southern Oscillation impacts on regional chlorophyll anomalies in the Indian Ocean. *Biogeosciences* 10 (10), 6677–6698. <https://doi.org/10.5194/bg-10-6677-2013>
- D'Silva, M.S., Anil, A.C., Naik, R.K., D'Costa, P.M., 2012. Algal blooms: a perspective from the coasts of India. *Nat. Hazard.* 63 (2), 1225–1253. <https://doi.org/10.1007/s11069-012-0190-9>
- Dandapat, S., Chakraborty, A., 2016. Mesoscale eddies in the Western Bay of Bengal as Observed from satellite altimetry in 1993–2014: statistical characteristics, variability and three-dimensional properties. *IEEE J. Sel. Top. Appl. Earth Obs. Remote Sens.* 9 (11), 5044–5054. <https://doi.org/10.1109/jstars.2016.2585179>
- Dandapat, S., Gnanaseelan, C., Parekh, A., 2020. Impact of excess and deficit river runoff on Bay of Bengal upper ocean characteristics using an ocean general circulation model. *Deep-Sea Res. Part II* 172, 104714. <https://doi.org/10.1016/j.dsr2.2019.104714>
- Durand, F., Shankar, D., Birol, F., Shenoi, S.S.C., 2009. Spatiotemporal structure of the East India Coastal Current from satellite altimetry. *J. Geophys. Res.* 114. <https://doi.org/10.1029/2008jc004807>
- Fennel, K., Wilkin, J., Levin, J., Moisan, J., O'Reilly, J., Haidvogel, D., 2006. Nitrogen cycling in the Middle Atlantic Bight: Results from a three-dimensional model and implications for the North Atlantic nitrogen budget. *Glob. Biogeochem. Cy.* 20 (3). <https://doi.org/10.1029/2005gb002456>
- Fennel, K., Wilkin, J., Previdi, M., Najjar, R., 2008. Denitrification effects on air-sea CO₂ flux in the coastal ocean: Simulations for the northwest North Atlantic. *Geophys. Res. Lett.* 35 (24). <https://doi.org/10.1029/2008gl036147>
- Fiechter, J., Edwards, C.A., Moore, A.M., 2018. Wind, circulation, and topographic effects on alongshore phytoplankton variability in the California current. *Geophys. Res. Lett.* 45 (7), 3238–3245. <https://doi.org/10.1002/2017gl076839>
- Francis, P.A., Jithin, A.K., Chatterjee, A., Mukherjee, A., Shankar, D., Vinayachandran, P.N., Ramakrishna, S.S.V.S., 2020. Structure and dynamics of undercurrents in the western boundary current of the Bay of Bengal. *Ocean Dyn.* 70 (3), 387–404. <https://doi.org/10.1007/s10236-019-01340-9>
- Gadgil, S., Vinayachandran, P.N., Francis, P.A., Gadgil, S., 2004. Extremes of the Indian summer monsoon rainfall, ENSO and equatorial Indian Ocean oscillation. *Geophys. Res. Lett.* 31 (12). <https://doi.org/10.1029/2004gl019733>
- Gauns, M., Madhupratap, M., Ramaiah, N., Jyothibabu, R., Fernandes, V., Paul, J.T., Prasanna Kumar, S., 2005. Comparative accounts of biological productivity characteristics and estimates of carbon fluxes in the Arabian Sea and the Bay of Bengal. *Deep Sea Res. Part II* 52 (14–15), 2003–2017. <https://doi.org/10.1016/j.dsr2.2005.05.009>
- Grishkumar, M.S., Thangaprakash, V.P., Udaya Bhaskar, T.V.S., Suprit, K., Sureshkumar, N., Baliarsingh, S.K., Jofia, J., Pant, V.,

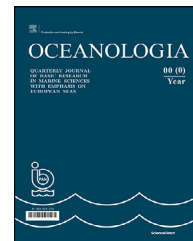
- Vishnu, S., George, G., Abhilash, K.R., Shivaprasad, S., 2019. Quantifying tropical cyclone's effect on the biogeochemical processes using profiling float observations in the Bay of Bengal. *J. Geophys. Res. Oceans* 124 (3), 1945–1963. <https://doi.org/10.1029/2017jc013629>
- Gomes, H.R., Goes, J.I., Saino, T., 2000. Influence of physical processes and freshwater discharge on the seasonality of phytoplankton regime in the Bay of Bengal. *Cont. Shelf Res.* 20 (3), 313–330. [https://doi.org/10.1016/s0278-4343\(99\)00072-2](https://doi.org/10.1016/s0278-4343(99)00072-2)
- Gopalakrishna, V.V., Sastry, J.S., 1985. Surface circulation over the shelf off the east coast of India during southwest monsoon. *Indian J. Mar. Sci.* 14, 62–65.
- Haidvogel, D.B., Arango, H.G., Hedstrom, K., Beckmann, A., Malanotte-Rizzoli, P., Shchepetkin, A.F., 2000. Model evaluation experiments in the North Atlantic Basin: simulations in nonlinear terrain-following coordinates. *Dyn. Atmos. Oceans* 32 (3–4), 239–281. [https://doi.org/10.1016/s0377-0265\(00\)00049-x](https://doi.org/10.1016/s0377-0265(00)00049-x)
- Haidvogel, D.B., Arango, H., Budgell, W.P., Cornuelle, B.D., Curchitser, E., Di Lorenzo, E., Fennel, K., Geyer, W.R., Hermann, A.J., Lanerolle, L., Levin, J., McWilliams, J.C., Miller, A.J., Moore, A.M., Powell, T.M., Shchepetkin, A.F., Sherwood, C.R., Signell, R.P., Warner, J.C., Wilkin, J., 2008. Ocean forecasting in terrain-following coordinates: Formulation and skill assessment of the Regional Ocean Modeling System. *J. Comput. Phys.* 227 (7), 3595–3624. <https://doi.org/10.1016/j.jcp.2007.06.016>
- Han, W., Webster, P.J., 2001. Forcing mechanisms of sea level inter-annual variability in the Bay of Bengal. *J. Phys. Oceanogr.* 32 (1), 216–239. [https://doi.org/10.1175/1520-0485\(2002\)032%3C0216:FMOSLI%3E2.0.CO;2](https://doi.org/10.1175/1520-0485(2002)032%3C0216:FMOSLI%3E2.0.CO;2)
- Huang, H., Wang, D., Yang, L., Huang, K., 2021. Enhanced intraseasonal variability of the upper layers in the Southern Bay of Bengal during the summer 2016. *J. Geophys. Res. Oceans* 126 (7). <https://doi.org/10.1029/2021jc017459>
- Jacox, M.G., Bograd, S.J., Hazen, E.L., Fiechter, J., 2015. Sensitivity of the California Current nutrient supply to wind, heat, and remote ocean forcing. *Geophys. Res. Lett.* 42 (14), 5950–5957. <https://doi.org/10.1002/2015gl065147>
- Jagadeesan, L., Kumar, G.S., Rao, D.N., babu, N.S., Srinivas, T.N.R., 2019. Role of eddies in structuring the mesozooplankton composition in coastal waters of the western Bay of Bengal. *Ecol. Indic.* 105, 137–155. <https://doi.org/10.1016/j.ecolind.2019.05.068>
- Jian, L., Lei, Y., Ye-Qiang, S., Dong-Xiao, W., 2012. Temperature Inversion in the Bay of Bengal Prior to the Summer Monsoon Onsets in 2010 and 2011. *Atmos. Oceanic Sci. Lett.* 5 (4), 290–294. <https://doi.org/10.1080/16742834.2012.11447004>
- Jyothibabu, R., Madhu, N.V., Maheswaran, P.A., Jayalakshmy, K.V., Nair, K.K.C., Achuthankutty, C.T., 2008. Seasonal variation of microzooplankton (20–200 μ m) and its possible implications on the vertical carbon flux in the western Bay of Bengal. *Cont. Shelf Res.* 28 (6), 737–755. <https://doi.org/10.1016/j.csr.2007.12.011>
- Jyothibabu, R., Vinayachandran, P.N., Madhu, N.V., Robin, R.S., Karnan, C., Jagadeesan, L., Anjusha, A., 2015. Phytoplankton size structure in the southern Bay of Bengal modified by the Summer Monsoon Current and associated eddies: implications on the vertical biogenic flux. *J. Mar. Syst.* 143, 98–119. <https://doi.org/10.1016/j.jmarsys.2014.10.018>
- Kara, A.B., Rochford, P.A., Hurlburt, H.E., 2000. Mixed layer depth variability and barrier layer formation over the North Pacific Ocean. *J. Geophys. Res.* 105 (C7), 16783–16801. <https://doi.org/10.1029/2000jc900071>
- Kishi, M.J., Kashiwai, M., Ware, D.M., Megrey, B.A., Eslinger, D.L., Werner, F.E., Noguchi-Aita, M., Azumaya, T., Fujii, M., Hashimoto, S., Huang, D., Iizumi, H., Ishida, Y., Kang, S., Kantakov, G.A., Kim, H., Komatsu, K., Navrotsky, V.V., Smith, S.L., Zvalinsky, V.I., 2007. NEMURO—a lower trophic level model for the North Pacific marine ecosystem. *Ecol. Model.* 202 (1–2), 12–25. <https://doi.org/10.1016/j.ecolmodel.2006.08.021>
- Koračin, D., Dorman, C.E., Dever, E.P., 2004. Coastal perturbations of marine-layer winds, wind stress, and wind stress curl along California and Baja California in June 1999. *J. Phys. Oceanogr.* 34 (5), 1152–1173. [https://doi.org/10.1175/1520-0485\(2004\)034<1152:cpomww>2.0.co;2](https://doi.org/10.1175/1520-0485(2004)034<1152:cpomww>2.0.co;2)
- Kurien, P., Ikeda, M., Valsala, V.K., 2010. Mesoscale variability along the east coast of India in spring as revealed from satellite data and OGCM simulations. *J. Oceanogr.* 66 (2), 273–289. <https://doi.org/10.1007/s10872-010-0024-x>
- La Fond, E.C., 1954. On upwelling and sinking off the east coast of India. *Andhra Univ. Mem. Oceanogr.* 1, 117–121.
- La Fond, E.C., 1957. Oceanographic studies in the Bay of Bengal. *Proc. Indian Acad. Sci.* 46, 1–46. <https://doi.org/10.1007/BF03052445>
- La Fond, E.C., 1958. On the circulation of the surface layers on the east coast of India. *Andhra Univ. Mem. Oceanogr.* 2, 1–11.
- La Fond, E.C., 1959. Sea surface features and internal waves in the sea. *Indian J. Meteorol. Geophys.* 10, 415–419.
- Large, W.G., McWilliams, J.C., Doney, S.C., 1994. Oceanic vertical mixing: A review and a model with a nonlocal boundary layer parameterization. *Rev. Geophys.* 32 (4), 363. <https://doi.org/10.1029/94rg01872>
- Large, W.G., Pond, S., 1981. Open ocean momentum flux measurements in moderate to strong winds. *J. Phys. Oceanogr.* 11 (3), 324–336. [https://doi.org/10.1175/1520-0485\(1981\)011\(0324:oofmji\)2.0.co;2](https://doi.org/10.1175/1520-0485(1981)011(0324:oofmji)2.0.co;2)
- Lierheimer, L.J., Banse, K., 2002. Seasonal and interannual variability of phytoplankton pigment in the Laccadive (Lakshadweep) Sea as observed by the Coastal Zone Color scanner. *J. Earth Syst. Sci.* 111 (2), 163–185. <https://doi.org/10.1007/bf02981144>
- Madhu, N.V., Jyothibabu, R., Maheswaran, P.A., John Gerson, V., Gopalakrishnan, T.C., Nair, K.K.C., 2006. Lack of seasonality in phytoplankton standing stock (chlorophyll a) and production in the western Bay of Bengal. *Cont. Shelf Res.* 26 (16), 1868–1883. <https://doi.org/10.1016/j.csr.2006.06.004>
- Madhupratap, M., Gauns, M., Ramaiah, N., Prasanna Kumar, S., Muraleedharan, P.M., de Sousa, S.N., Sardesai, S., Muraleedharan, U., 2003. Biogeochemistry of the Bay of Bengal: physical, chemical and primary productivity characteristics of the central and western Bay of Bengal during summer monsoon 2001. *Deep Sea Res. Part II* 50 (5), 881–896. [https://doi.org/10.1016/s0967-0645\(02\)00611-2](https://doi.org/10.1016/s0967-0645(02)00611-2)
- Maes, C., O’Kane, T.J., 2014. Seasonal variations of the upper ocean salinity stratification in the Tropics. *J. Geophys. Res.: Oceans* 119 (3), 1706–1722. <https://doi.org/10.1002/2013jc009366>
- Mahadevan, A., Spiro Jaeger, G., Freilich, M., Omand, M., Shroyer, E., Sengupta, D., 2016. Freshwater in the Bay of Bengal: its fate and role in air-sea heat exchange. *Oceanogr.* 29 (2), 72–81. <https://doi.org/10.5670/oceanog.2016.40>
- Maneesha, K., Sarma, V.V.S.S., Reddy, N.P.C., Sadhuram, Y., Murty, T.V.R., Sarma, V.V., Kumar, M.D., 2011. Meso-scale atmospheric events promote phytoplankton blooms in the coastal Bay of Bengal. *J. Earth Syst. Sci.* 120 (4), 773–782. <https://doi.org/10.1007/s12040-011-0089-y>
- Martin, J.M., Burton, J.D., Eisma, D., 1981. *River Inputs to Ocean Systems*. U.N. Univ. Press, Tokyo, 384 pp.
- McCreary, J.P., Han, W., Shankar, D., Shetye, S.R., 1996a. Dynamics of the East India Coastal Current: 2. Numerical solutions. *J. Geophys. Res.: Oceans* 101 (C6), 13993–14010. <https://doi.org/10.1029/96jc00560>
- McCreary Jr, J.P., Kohler, K.E., Hood, R.R., Olson, D.B., 1996b. A four-component ecosystem model of biological activity in the Arabian Sea. *Prog. Oceanogr.* 37 (3–4), 193–240. [https://doi.org/10.1016/s0079-6611\(96\)00005-5](https://doi.org/10.1016/s0079-6611(96)00005-5)
- McCreary Jr, J.P., Kundu, P.K., Molinari, R.L., 1993. A numerical investigation of dynamics, thermodynamics and mixed-layer pro-

- cesses in the Indian Ocean. *Prog. Oceanogr.* 31 (3), 181–244. [https://doi.org/10.1016/0079-6611\(93\)90002-u](https://doi.org/10.1016/0079-6611(93)90002-u)
- McCreary, J.P., Murtugudde, R., Vialard, J., Vinayachandran, P.N., Wiggert, J.D., Hood, R.R., Shetye, S., 2009. Biophysical processes in the Indian Ocean. *Geophys. Monogr. Ser.* 9–32. <https://doi.org/10.1029/2008gm000768>
- Milliman, J.D., Meade, R.H., 1983. World-wide delivery of river sediment to the oceans. *J. Geol.* 91 (1), 1–21. <https://doi.org/10.1086/628741>
- Milliman, J.D., Syvitski, J.P.M., 1992. Geomorphic/tectonic control of sediment discharge to the ocean: the importance of small mountainous rivers. *J. Geol.* 100 (5), 525–544. <https://doi.org/10.1086/629606>
- Miranda, J., Baliarsingh, S.K., Lotliker, A.A., Sahoo, S., Sahu, K.C., Kumar, T.S., 2019. Long-term trend and environmental determinants of phytoplankton biomass in coastal waters of northwestern Bay of Bengal. *Environ. Monit. Assess.* 192 (1). <https://doi.org/10.1007/s10661-019-8033-8>
- Mukherjee, A., Shankar, D., Fernando, V., Amol, P., Aparna, S.G., Fernandes, R., Vernekar, S., 2014. Observed seasonal and intraseasonal variability of the East India Coastal Current on the continental slope. *J. Earth Syst. Sci.* 123 (6), 1197–1232. <https://doi.org/10.1007/s12040-014-0471-7>
- Murtugudde, R., Busalacchi, A.J., 1999. Interannual variability of the dynamics and thermodynamics of the tropical Indian ocean. *J. Clim.* 12 (8), 2300–2326. [https://doi.org/10.1175/1520-0442\(1999\)012<2300:ivotda>2.0.co;2](https://doi.org/10.1175/1520-0442(1999)012<2300:ivotda>2.0.co;2)
- Murty, C. S., Varadachari, V. V. R., 1968. Upwelling along the east coast of India. *Bulletin of the National Institute of Sciences of India*, 38, pp. 80–86.
- Naidu, P.D., Ramesh Kumar, M.R., Ramesh Babu, V., 1999. Time and space variations of monsoonal upwelling along the west and east coasts of India. *Cont. Shelf Res.* 19 (4), 559–572. [https://doi.org/10.1016/S0278-4343\(98\)00104-6](https://doi.org/10.1016/S0278-4343(98)00104-6)
- Nigam, T., Pant, V., Prakash, K.R., 2018. Impact of Indian ocean dipole on the coastal upwelling features off the southwest coast of India. *Ocean Dyn.* 68 (6), 663–676. <https://doi.org/10.1007/s10236-018-1152-x>
- Patnaik, K.V.K.R.K., Maneesha, K., Sadhuram, Y., Prasad, K.V.S.R., Ramana Murty, T.V., Brahmananda Rao, V., 2014. East India Coastal Current induced eddies and their interaction with tropical storms over Bay of Bengal. *J. Oper. Oceanogr.* 7 (1), 58–68. <https://doi.org/10.1080/1755876x.2014.11020153>
- Powell, T.M., Lewis, C.V.W., Curchitser, E.N., Haidvogel, D.B., Hermann, A.J., Dobbins, E.L., 2006. Results from a three-dimensional, nested biological-physical model of the California Current System and comparisons with statistics from satellite imagery. *J. Geophys. Res.* 111 (C7). <https://doi.org/10.1029/2004jc002506>
- Pramanik, S., Sil, S., Gangopadhyay, A., Singh, M.K., Behera, N., 2020. Interannual variability of the Chlorophyll-a concentration over Sri Lankan Dome in the Bay of Bengal. *Int. J. Remote Sens.* 41 (15), 5974–5991. <https://doi.org/10.1080/01431161.2020.1727057>
- Pramanik, S., Sil, S., Mandal, S., Dey, D., Shee, A., 2019. Role of interannual equatorial forcing on the subsurface temperature dipole in the Bay of Bengal during IOD and ENSO events. *Ocean Dyn.* 69 (11–12), 1253–1271. <https://doi.org/10.1007/s10236-019-01303-0>
- Prasanna Kumar, S., Narvekar, J., Nuncio, M., Kumar, A., Ramaiah, N., Sardesai, S., Gauns, M., Fernandes, V., Paul, J., 2010. Is the biological productivity in the Bay of Bengal light limited? *Curr. Sci.* 98, 1331–1339.
- Prasanna Kumar, S., Muraleedharan, P.M., Prasad, T.G., Gauns, M., Ramaiah, N., de Souza, S.N., Sardesai, S., Madhupratap, M., 2002. Why is the Bay of Bengal less productive during summer monsoon compared to the Arabian Sea? *Geophys. Res. Lett.* 29 (24). <https://doi.org/10.1029/2002gl016013>, 88-1-88–4
- Prasanna Kumar, S., Nuncio, M., Narvekar, J., Kumar, A., Sardesai, S., de Souza, S.N., Gauns, M., Ramaiah, N., Madhupratap, M., 2004. Are eddies nature's trigger to enhance biological productivity in the Bay of Bengal? *Geophys. Res. Lett.* 31 (7). <https://doi.org/10.1029/2003gl019274>
- Prasanna Kumar, S., Nuncio, M., Ramaiah, N., Sardesai, S., Narvekar, J., Fernandes, V., Paul, J.T., 2007. Eddy-mediated biological productivity in the Bay of Bengal during fall and spring intermonsoons. *Deep Sea Res. Part I* 54 (9), 1619–1640. <https://doi.org/10.1016/j.dsr.2007.06.002>
- Price, J.F., 1981. Upper ocean response to a hurricane. *J. Phys. Oceanogr.* 11 (2), 153–175. [https://doi.org/10.1175/1520-0485\(1981\)011<0153:uortah>2.0.co;2](https://doi.org/10.1175/1520-0485(1981)011<0153:uortah>2.0.co;2)
- Qasim, S.Z., Gupta, R.S., Kureishy, T.W., 1988. Pollution of the seas around India. *Proc. Anim. Sci.* 97 (2), 117–131. <https://doi.org/10.1007/bf03179939>
- Rao, R.R., Girish Kumar, M.S., Ravichandran, M., Rao, A.R., Gopalakrishna, V.V., Thadathil, P., 2010. Interannual variability of Kelvin wave propagation in the wave guides of the equatorial Indian Ocean, the coastal Bay of Bengal and the southeastern Arabian Sea during 1993–2006. *Deep Sea Res. Part I* 57 (1), 1–13. <https://doi.org/10.1016/j.dsr.2009.10.008>
- Rao, R.R., Sivakumar, R., 2003. Seasonal variability of sea surface salinity and salt budget of the mixed layer of the North Indian Ocean. *J. Geophys. Res.* 108 (C1), C02013. <https://doi.org/10.1029/2001JC000907>
- Saji, N.H., Goswami, B.N., Vinayachandran, P.N., Yamagata, T., 1999. A dipole mode in the tropical Indian Ocean. *Nature* 401 (6751), 360–363. <https://doi.org/10.1038/43854>
- Sandeep, K.K., Pant, V., 2018. Evaluation of interannual simulations and Indian ocean dipole events during 2000–2014 from a basin scale general circulation model. *Pure Appl. Geophys.* 175, 4579–4603. <https://doi.org/10.1007/s00024-018-1915-9>
- Sandeep, K.K., Pant, V., Girishkumar, M.S., Rao, A.D., 2018. Impact of riverine freshwater forcing on the sea surface salinity simulations in the Indian Ocean. *J. Mar. Syst.* 185, 40–58. <https://doi.org/10.1016/j.jmarsys.2018.05.002>
- Sanilkumar, K.V., Kuruville, T.V., Jogendranath, D., Rao, R.R., 1997. Observations of the Western Boundary Current of the Bay of Bengal from a hydrographic survey during March 1993. *Deep Sea Res. Part I* 44 (1), 135–145. [https://doi.org/10.1016/S0967-0637\(96\)00036-2](https://doi.org/10.1016/S0967-0637(96)00036-2)
- Sarma, V.V.S.S., Paul, Y.S., Vani, D.G., Murty, V.S.N., 2015. Impact of river discharge on the coastal water pH and pCO₂ levels during the Indian Ocean Dipole (IOD) years in the western Bay of Bengal. *Cont. Shelf Res.* 107, 132–140. <https://doi.org/10.1016/j.csr.2015.07.015>
- Sarma, V.V.S.S., Rao, G.D., Viswanadham, R., Sherin, C.K., Salisbury, J., Omand, M., Mahedevan, A., Murty, V.S.N., Shroyer, E., Baumgartner, M., Stafford, K., 2016. Effects of freshwater stratification on nutrients, dissolved oxygen, and phytoplankton in the Bay of Bengal. *Oceanogr.* 29 (2), 222–231. <https://doi.org/10.5670/oceanog.2016.54>
- Schott, F.A., McCreary Jr., J.P., 2001. The monsoon circulation of the Indian Ocean. *Prog. Oceanogr.* 51 (1), 1–123. [https://doi.org/10.1016/S0079-6611\(01\)00083-0](https://doi.org/10.1016/S0079-6611(01)00083-0)
- Seelanki, V., Nigam, T., Pant, V., 2021. Upper-ocean physical and biological features associated with Hudhud cyclone: a bio-physical modelling study. *J. Mar. Syst.* 215, 103499. <https://doi.org/10.1016/j.jmarsys.2020.103499>
- Seelanki, V., Pant, V., 2021. An evaluation of the impact of pandemic driven lockdown on the phytoplankton biomass over the North Indian ocean using observations and model. *Front. Mar. Sci.* 8. <https://doi.org/10.3389/fmars.2021.722401>
- Sen Gupta, R., Naik, S., Singbal, S.Y.S., 1978. A study of fluoride, calcium and magnesium in the Northern Indian Ocean. *Mar. Chem.* 6 (2), 125–141. [https://doi.org/10.1016/0304-4203\(78\)90023-3](https://doi.org/10.1016/0304-4203(78)90023-3)

- Seo, H., Xie, S.-P., Murtugudde, R., Jochum, M., Miller, A.J., 2009. Seasonal effects of Indian Ocean freshwater forcing in a regional coupled model*. *J. Clim.* 22 (24), 6577–6596. <https://doi.org/10.1175/2009jcli2990.1>
- Shaji, C., Ruma, S., 2019. On the seasonal and inter-annual variability of the equatorial Indian Ocean surface winds. *Meteorol. Atmos. Phys.* 132 (3), 353–376. <https://doi.org/10.1007/s00703-019-00690-9>
- Shankar, D., Vinayachandran, P.N., Unnikrishnan, A.S., 2002. The monsoon currents in the north Indian Ocean. *Prog. Oceanogr.* 52 (1), 63–120. [https://doi.org/10.1016/s0079-6611\(02\)00024-1](https://doi.org/10.1016/s0079-6611(02)00024-1)
- Shchepetkin, A.F., McWilliams, J.C., 2005. The regional oceanic modeling system (ROMS): a split-explicit, free-surface, topography-following-coordinate oceanic model. *Ocean Model.* 9 (4), 347–404. <https://doi.org/10.1016/j.ocemod.2004.08.002>
- Shenoi, S.S.C., 2002. Differences in heat budgets of the near-surface Arabian Sea and Bay of Bengal: Implications for the summer monsoon. *J. Geophys. Res.* 107 (C6). <https://doi.org/10.1029/2000jc000679>
- Shetye, S.R., Gouveia, A.D., Shankar, D., Shenoi, S.S.C., Vinayachandran, P.N., Sundar, D., Nampoothiri, G., 1996. Hydrography and circulation in the western Bay of Bengal during the northeast monsoon. *J. Geophys. Res. Oceans* 101 (C6), 14011–14025. <https://doi.org/10.1029/95jc03307>
- Shetye, S.R., Gouveia, A.D., Shenoi, S.S.C., Sundar, D., Michael, G.S., Nampoothiri, G., 1993. The western boundary current of the seasonal subtropical gyre in the Bay of Bengal. *J. Geophys. Res. Oceans* 98 (C1), 945–954. <https://doi.org/10.1029/92jc02070>
- Shetye, S.R., Shenoi, S.S.C., Gouveia, A.D., Michael, G.S., Sundar, D., Nampoothiri, G., 1991. Wind-driven coastal upwelling along the western boundary of the Bay of Bengal during the southwest monsoon. *Cont. Shelf Res.* 11 (11), 1397–1408. [https://doi.org/10.1016/0278-4343\(91\)90042-5](https://doi.org/10.1016/0278-4343(91)90042-5)
- Sikka, D.R., 1980. Some aspects of the large scale fluctuations of summer monsoon rainfall over India in relation to fluctuations in the planetary and regional scale circulation parameters. *J. Earth Syst. Sci.* 89 (2), 179–195. <https://doi.org/10.1007/bf02913749>
- Sil, S., Chakraborty, A., 2011. Simulation of east India coastal features and validation with satellite altimetry and drifter climatology. *Int. J. Ocean Clim. Syst.* 2 (4), 279–289. <https://doi.org/10.1260/1759-3131.2.4.279>
- Song, H., Miller, A.J., McClatchie, S., Weber, E.D., Nieto, K.M., Checkley Jr., D.M., 2012. Application of a data-assimilation model to variability of Pacific sardine spawning and survivor habitats with ENSO in the California Current System. *J. Geophys. Res. Oceans* 117 (C3). <https://doi.org/10.1029/2011jc007302>
- Thadathil, P., Suresh, I., Gautham, S., Prasanna Kumar, S., Lengaigne, M., Rao, R.R., Neetu, S., Hegde, A., 2016. Surface layer temperature inversion in the Bay of Bengal: main characteristics and related mechanisms. *J. Geophys. Res. Oceans* 121 (8), 5682–5696. <https://doi.org/10.1002/2016jc011674>
- Thangaprakash, V.P., Girishkumar, M.S., Suprit, K., Kumar, N.S., Chaudhuri, D., Dinesh, K., Kumar, A., Shivaprasad, S., Ravichandran, M., Farrar, J.T., Sundar, R., Weller, R., 2016. What controls seasonal evolution of sea surface temperature in the bay of Bengal? Mixed layer heat budget analysis using moored buoy observations along 90°E. *Oceanography* 29 (2), 202–213. <https://doi.org/10.5670/oceanog.2016.52>
- Thushara, V., Vinayachandran, P.N., 2016. Formation of summer phytoplankton bloom in the northwestern Bay of Bengal in a coupled physical-ecosystem model. *J. Geophys. Res. Oceans* 121 (12), 8535–8550. <https://doi.org/10.1002/2016jc011987>
- Tourre, Y.M., White, W.B., 1995. ENSO Signals in Global Upper-Ocean Temperature. *J. Phys. Oceanogr.* 25 (6), 1317–1332. [https://doi.org/10.1175/1520-0485\(1995\)025<1317:esiguo>2.0.co;2](https://doi.org/10.1175/1520-0485(1995)025<1317:esiguo>2.0.co;2)
- Trott, C.B., Subrahmanyam, B., 2019. Detection of intraseasonal oscillations in the Bay of Bengal using altimetry. *Atmos. Sci. Lett.* 175 (7), 4579–4603. <https://doi.org/10.1002/asl.920>
- UNESCO, 1979. *Discharge of Selected Rivers of the World*. UNESCO, Paris.
- Varadachari, V.V.R., 1961. On the process of upwelling and sinking on the east coast of Indi. In: a, Os. Univ. Press, Inst. of Oceanogr. Sci., Wormley, England, Prof. Mahadevan Shastriabdupurti commemoration, 1–27.
- Vinayachandran, P.N., 2009. Impact of physical processes on chlorophyll distribution in the Bay of Bengal. *Geophys. Monogr. Ser.* 71–86. <https://doi.org/10.1029/2008gm000705>
- Vinayachandran, P.N., Mathew, S., 2003. Phytoplankton bloom in the Bay of Bengal during the northeast monsoon and its intensification by cyclones. *Geophys. Res. Lett.* 30, 1572. <https://doi.org/10.1029/2002GL016717>
- Vinayachandran, P.N., Murty, V.S.N., Ramesh Babu, V., 2002. Observations of barrier layer formation in the Bay of Bengal during summer monsoon. *J. Geophys. Res. Oceans* 107. (C12), SRF 19-1SRF 19-9. <https://doi.org/10.1029/2001jc000831>
- Vinayachandran, P.N., Yamagata, T., 1998. Monsoon response of the Sea around Sri Lanka: generation of thermal domes and anticyclonic vortices. *J. Phys. Oceanogr.* 28 (10), 1946–1960. [https://doi.org/10.1175/1520-0485\(1998\)028<1946:mrotsa>2.0.co;2](https://doi.org/10.1175/1520-0485(1998)028<1946:mrotsa>2.0.co;2)
- Vinayachandran, P., Shetye, S., Sengupta, D., Gadgil, S., 1996. Forcing mechanisms of the Bay of Bengal circulation. *Curr. Sci.* 71 (10), 753–763.
- Vinayachandran, P.N., Shetye, S.R., 1991. The warm pool in the Indian Ocean. *Proc. Indian Acad. Sci. (Earth Planet Sci.)* <https://doi.org/10.1007/BF02839431>
- Wang, Q., Kalogiros, J.A., Ramp, S.R., Paduan, J.D., Buzorius, G., Jonsson, H., 2011. Wind stress curl and coastal upwelling in the area of Monterey Bay observed during AOSN-II. *J. Phys. Oceanogr.* 41 (5), 857–877. <https://doi.org/10.1175/2010jpo4305.1>
- Webster, P.J., Moore, A.M., Loschnigg, J.P., Leben, R.R., 1999. Coupled ocean–atmosphere dynamics in the Indian Ocean during 1997–98. *Nature* 401 (6751), 356–360. <https://doi.org/10.1038/43848>
- Wyrtki, K., 1973. *Physical Oceanography of the Indian Ocean*. In: *Ecological Studies*. Springer, Berlin, Heidelberg, 18–36. https://doi.org/10.1007/978-3-642-65468-8_3
- Xu, Y., Wu, Y., Wang, H., Zhang, Z., Li, J., Zhang, J., 2021. Seasonal and interannual variabilities of chlorophyll across the eastern equatorial Indian Ocean and Bay of Bengal. *Prog. Oceanogr.* 198, 102661. <https://doi.org/10.1016/j.pocean.2021.102661>
- Zhang, Z., Pohlmann, T., Chen, X., 2021. Correlation between subsurface salinity anomalies in the Bay of Bengal and the Indian Ocean Dipole and governing mechanisms. *Ocean Sci.* 17 (1), 393–409. <https://doi.org/10.5194/os-17-393-2021>

Available online at www.sciencedirect.com

ScienceDirect

journal homepage: www.journals.elsevier.com/oceanologia

ORIGINAL RESEARCH ARTICLE

Impact of environmental factors on phytoplankton composition and their marker pigments in the northern Adriatic Sea

Elif Eker-Develi^{a,*}, Jean-François Berthon^b, Gary Free^c^a Mersin University, Faculty of Education, Mersin, Turkey^b Joint Research Centre of the European Commission, Ispra, VA, Italy^c CNR, Institute for Electromagnetic Sensing of the Environment, IREA, Rome, Italy

Received 2 February 2022; accepted 19 May 2022

Available online 29 May 2022

KEYWORDSPhytoplankton composition;
Carbon biomass;
HPLC-CHEMTAX,
Adriatic Sea;
Chlorophyll *a*

Abstract Phytoplankton composition, abundance and carbon biomass were investigated at monthly intervals during 2006–2007 at a coastal site, “Acqua Alta” an oceanographic tower, in the northern Adriatic Sea. Results were compared with chlorophyll *a* concentrations of phytoplankton classes attributed by HPLC-CHEMTAX analysis. Changes in the taxonomic structure were associated with environmental parameters. The total carbon biomass of phytoplankton was positively correlated with the temperature and negatively correlated with silicate concentrations. Nutrient concentrations were higher in the winter–spring period than in the summer–autumn period. The highest carbon biomass and abundance of phytoplankton were observed during summer–autumn months. Diatoms were the group that had the highest contribution to the total carbon biomass during the sampling period. Small flagellates, which were the major contributors to the total cell counts were dominant during the summer period. There was a significant correlation between carbon biomass and CHEMTAX-derived Chl *a* values of diatoms and dinoflagellates. However, the total carbon biomass of phytoplankton was not correlated with Chl *a*, which seemed to be related to seasonal changes in the ratios of C:Chl *a* of all tax-

* Corresponding author at: Mersin University, Faculty of Education, Mersin, Turkey.

E-mail address: elif.eker@mersin.edu.tr (E. Eker-Develi).

Peer review under the responsibility of the Institute of Oceanology of the Polish Academy of Sciences.

<https://doi.org/10.1016/j.oceano.2022.05.002>0078-3234/© 2022 Institute of Oceanology of the Polish Academy of Sciences. Production and hosting by Elsevier B.V. This is an open access article under the CC BY-NC-ND license (<http://creativecommons.org/licenses/by-nc-nd/4.0/>).

onomic classes. This ratio was higher during the summer-autumn period (73 ± 33) than during the winter–spring period (17 ± 20).

© 2022 Institute of Oceanology of the Polish Academy of Sciences. Production and hosting by Elsevier B.V. This is an open access article under the CC BY-NC-ND license (<http://creativecommons.org/licenses/by-nc-nd/4.0/>).

1. Introduction

Phytoplankton composition and biomass as well as nutrients define the trophic status of the aquatic environment (Sebastia and Rodilla, 2013). Taxonomic composition is usually assessed by standard or inverted microscopy. Alternatively, a pigment-based approach determined by high-performance liquid chromatography (HPLC) coupled with the CHEMTAX program (Mackey et al., 1996) is often used to categorize phytoplankton groups. While the former is laboursome and requires expertise, the latter necessitates proficiency in HPLC analysis and confirmation with microscopy mainly since some pigments are shared by several taxonomic classes of phytoplankton (Irigoien et al., 2004; Jeffrey and Vesk, 1997; Jeffrey et al. 2011).

The northern Adriatic is very shallow with an average bottom depth of 35 m (Artegiani et al., 1997a) and its circulation is cyclonic with strong jets along the western Adriatic coasts (Artegiani et al., 1997b). There are two major rivers, the Po and Adige, affecting dissolved nutrient concentrations, biological productivity, salinity and stratification in the northwestern section (Bernardi Aubry et al. 2004). The Po River contributes to half of the total freshwater inflow to the northern Adriatic Sea (Degobbi and Gilmartin, 1990; Pizzetti et al., 2015). Coastal waters are dynamic and seasonal stratification may not be observed in the water column due to strong advection (Franco and Michelato, 1992). Short-term meteorological phenomena exert a strong influence on the chemical and biological structure of the ecosystem. Regenerated nutrients are controlled by vertical mixing following depletion of nutrients by spring phytoplankton productivity (Zavatarelli et al., 1998).

The northern Adriatic Sea gradually started to become eutrophic from the 1970s to mid-1980s (Cerino et al., 2019; Giani et al. 2012). However, during 2000–2007 a process of oligotrophication started, probably due to a decline in both freshwater discharge and its phosphorus content (Mozetić et al., 2010; Mozetić et al., 2012). Satellite-derived Chl *a* data obtained from the northern Adriatic Sea basin showed a decrement of $0.11 \text{ mg m}^{-3} \text{ year}^{-1}$ from 1998 to 2007, which corresponds to a 1 mg m^{-3} decrease during the last decade (Mozetić et al., 2010).

Regarding the seasonality of phytoplankton blooms, a key aspect of observations in the northern Adriatic is the alteration in the timing of the dominant blooms. In some studies winter-spring blooms were prominent (Cabrini et al., 2012; Cerino et al. 2019), in other ones spring-summer blooms (Bernardi Aubry et al., 2004; Godrijan et al., 2013; Mozetić et al., 2012; Talaber et al., 2014). In contrast, in the southern Adriatic Sea, phytoplankton blooms occurring in spring were reported by several different studies (Cerino et al., 2012; Drakulović et al., 2012; Krivokapić et al., 2018).

Dominant phytoplankton taxa have also shown some regional differences. In the Gulf of Trieste, N Adriatic, dur-

ing 1986–2017, the phytoplankton community was dominated by nanoflagellates (>60% of abundance) and diatoms (25–31%), which were followed by coccolithophores and dinoflagellates (Cabrini et al., 2012; Cerino et al., 2019; Mozetić et al., 2012). Similarly, in the southern Adriatic, nanoflagellates exceeded the diatoms in abundance (Cerino et al., 2012; Drakulović et al., 2012). On the other hand, in the NW Adriatic, diatoms dominated in terms of both abundance and biomass during the majority of the years between 1990 and 1999 (Bernardi Aubry et al., 2004).

Seasonal changes in the abundance and phytoplankton community composition in the NW and N Adriatic can be summarized as follows: During autumn and early winter nanoflagellates dominate. Diatoms which have high growth rates, peak in the late winter–spring period with increased nutrient concentrations and irradiance and with sustained nutrient supply through river discharge (Bernardi Aubry et al. 2004; Cabrini et al. 2012, Cerino et al. 2019, Mozetić et al. 2012). In summer, reduced freshwater discharge and precipitation cause a decline in nutrient levels and this limits the growth of diatoms. As a result, nano- and dinoflagellates, which can uptake or feed on organic substances and don't require silicate for growth, get the opportunity to increase during this warm period. Occasional increases in the abundance of large size diatoms during the summer is also observed (Bernardi Aubry et al. 2004). The highest abundances of coccolithophores are observed during autumn-winter (Cabrini et al. 2012, Cerino et al. 2019).

Although there are a limited number of previous studies related to marker pigments and phytoplankton abundance in the Adriatic Sea (Krivokapić et al. 2018; Viličić et al. 2008), based on our literature survey, the carbon biomass of taxonomic classes has not been compared with marker pigments in this region. Since phytoplankton are the primary producers and they are the base of the food pyramid, their carbon biomass values can be used to estimate secondary and tertiary production (Grinson et al., 2017) as well as in the estimation of carbon sequestration. In other regions, there are time-series studies, similar to the present investigation, performed in the English Channel (Llewellyn et al., 2005), the Atlantic coast of Spain (Rodríguez et al., 2006) and one recent investigation in the NE Mediterranean Sea (Konucu et al., 2022). Results of these investigations have been used in many different areas including sensing of oceanic carbon pump from space (Brewin et al., 2021; Gazeau et al., 2017; Torres et al., 2020) and modelling studies (Arteaga et al., 2016).

The aim of the present investigation was to observe monthly changes of phytoplankton composition and biomass based on both microscopy and HPLC-CHEMTAX and their relationship with environmental parameters during a two-year period at a coastal site (“Acqua Alta” oceanographic tower from CNR-Italy) located 8 nautical miles off Venice. This study will provide information about trends in phytoplank-

ton species composition, abundance and carbon biomass which are important elements to comprehend impacts of anthropogenic and climate-related forces on the environment. Results of the present investigation will also elucidate the efficiency of using marker pigments as a proxy for phytoplankton carbon biomass and will also help validation of remote sensing data as well as informing modelling studies.

2. Material and methods

Phytoplankton and nutrient (NO_3 , NH_4 , PO_4 and SiO_2) near-surface samples were collected from a platform (Aqua Alta Oceanographic Tower) located in the northwestern Adriatic Sea (12.51°E and 45.31°N , Figure 1) between December 2005 and February 2008 with a 1–3 month interval (Table S1). The bottom depth at this site is 17 meters. Phytoplankton samples were collected in 1 L amber glass bottles and fixed with formaldehyde (buffered with borax) to have a 1.55% final concentration. Samples were left to settle for 1–2 weeks after which the supernatant was siphoned off by thin curved tubes down to 15–20 ml. Phytoplankton and nutrient (NO_3 , NH_4 , PO_4 and SiO_2) near-surface samples were collected from a platform (Aqua Alta Oceanographic

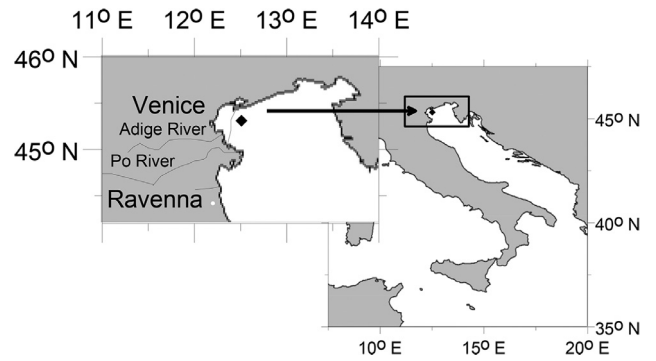


Figure 1 Sampling spot (“Acqua Alta” oceanographic tower) in the northern Adriatic Sea.

Tower) located in the northwestern Adriatic Sea (12.51°E and 45.31°N , Figure 1) between December 2005 and February 2008 with a 1–3 month interval (Table S1). The bottom depth at this site is 17 meters. Phytoplankton samples were collected in 1 L amber glass bottles and fixed with formaldehyde (buffered with borax) to have a 1.55% final concentration. Samples were left to settle for 1–2 weeks af-

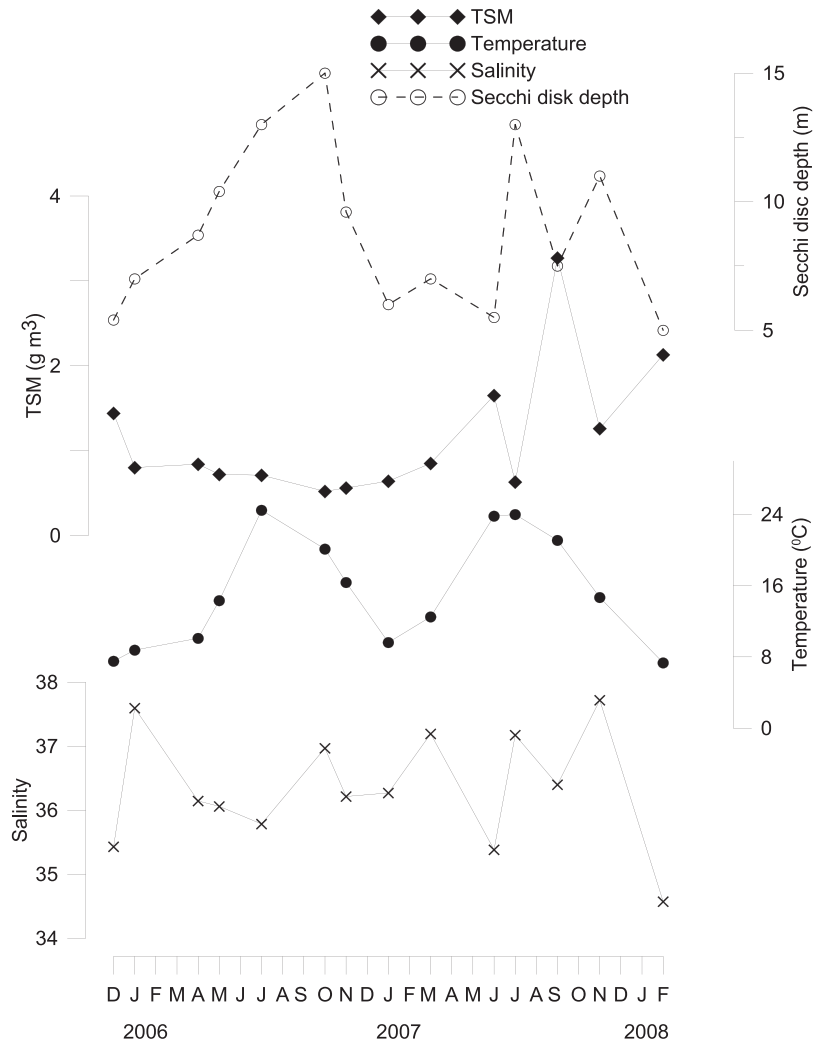


Figure 2 Near surface temperature, salinity, total suspended matter (TSM), and Secchi Depth, measured during phytoplankton sampling.

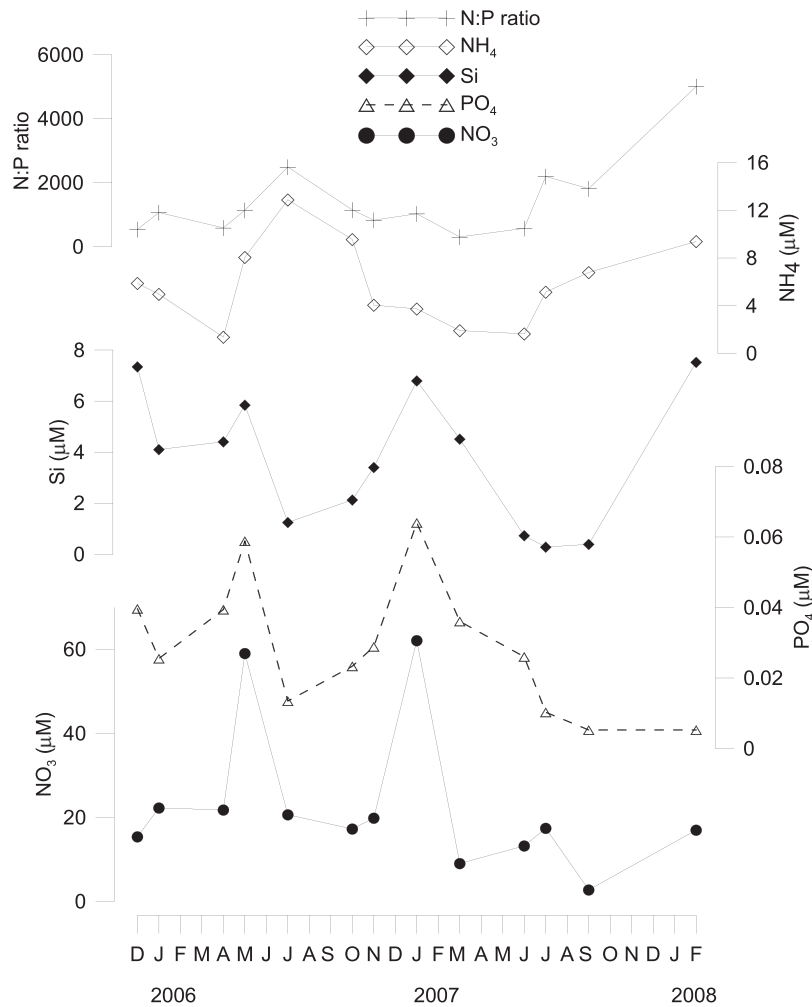


Figure 3 Nutrient concentrations during 2005–2008 in the northern Adriatic Sea.

ter which the supernatant was siphoned off by thin curved tubes down to 15–20 ml. Phytoplankton cells (~400 cells) were counted with a Sedgewick Rafter Cell under a phase-contrast binocular microscope with 200X and 400X magnification (Karlson et al., 2010). Phytoplankton species were identified to the lowest possible taxonomic level based on relevant publications (Balech, 1988; Bérard-Therriault et al., 1999; Cupp, 1943; Dodge, 1982; Hasle, 1997; Massuti and Margalef, 1950; Rampi and Bernhard, 1980; Sournia, 1986; Steidinger and Tangen, 1997; Throndsen 1997).

The biovolume (V) of each cell was calculated from its appropriate morphometric characteristics (i.e. diameter, length and width) (Kovala and Larrance, 1966; Olenina et al., 2006). $1 \mu\text{m}^3$ V was assumed equal to 1 pg wet weight (Gasiunaite et al., 2005; Hillebrand et al., 1999; Wasmund et al. 1998). Carbon biomasses were calculated from the volume of each cell according to the equations of Menden-Deuer et al., (2001) as below;

for diatoms
 for diatoms >3000 μm^3
 for dinoflagellates
 for haptophytes
 for chlorophytes and prasinophytes
 for small flagellates, cryptophytes and cyanobacteria

$$\begin{aligned} \log C &= -0.541 + 0.811 (\log V) \\ \log C &= -0.933 + 0.881 (\log V) \\ \log C &= -0.353 + 0.864 (\log V) \\ \log C &= -0.642 + 0.899 (\log V) \\ \log C &= -1.026 + 1.088 (\log V) \\ \log C &= -0.583 + 0.860 (\log V) \end{aligned}$$

Vertical profiles of sea temperature and salinity were simultaneously obtained using an Idronaut or a SeaBird SBE19+ CTD profiler.

Samples of inorganic nutrients were collected with a Nansen bottle and filtered through $0.45 \mu\text{m}$ GF/C filters and kept frozen at -20°C within 100 mL acid-cleaned high-density polyethylene bottles for a few weeks until analysis. Silicate samples were kept at 4°C until analysis. PO_4 , SiO_2 and NH_4 were analyzed with standard spectrophotometric methods (Eisenrich et al., 1975; Fresenius et al. 1988; Grasshoff et al., 1983). $\text{N-NO}_3+\text{NO}_2$ was measured with an Ion Chromatography (Dionex ICS 1500 for cations, coupled with a DX 500 for anions determination, U.S.A., Pfaff, 1993) and before the analyses, a silver column was used to remove Cl^- ions from the samples. In order to certify measured concentrations a MOOS-1 Seawater Certified Reference Material for Nutrients (for orthophosphate, silicate, nitrate and nitrite) was used. Detection limits of PO_4 , NO_3 , NH_4 and Si

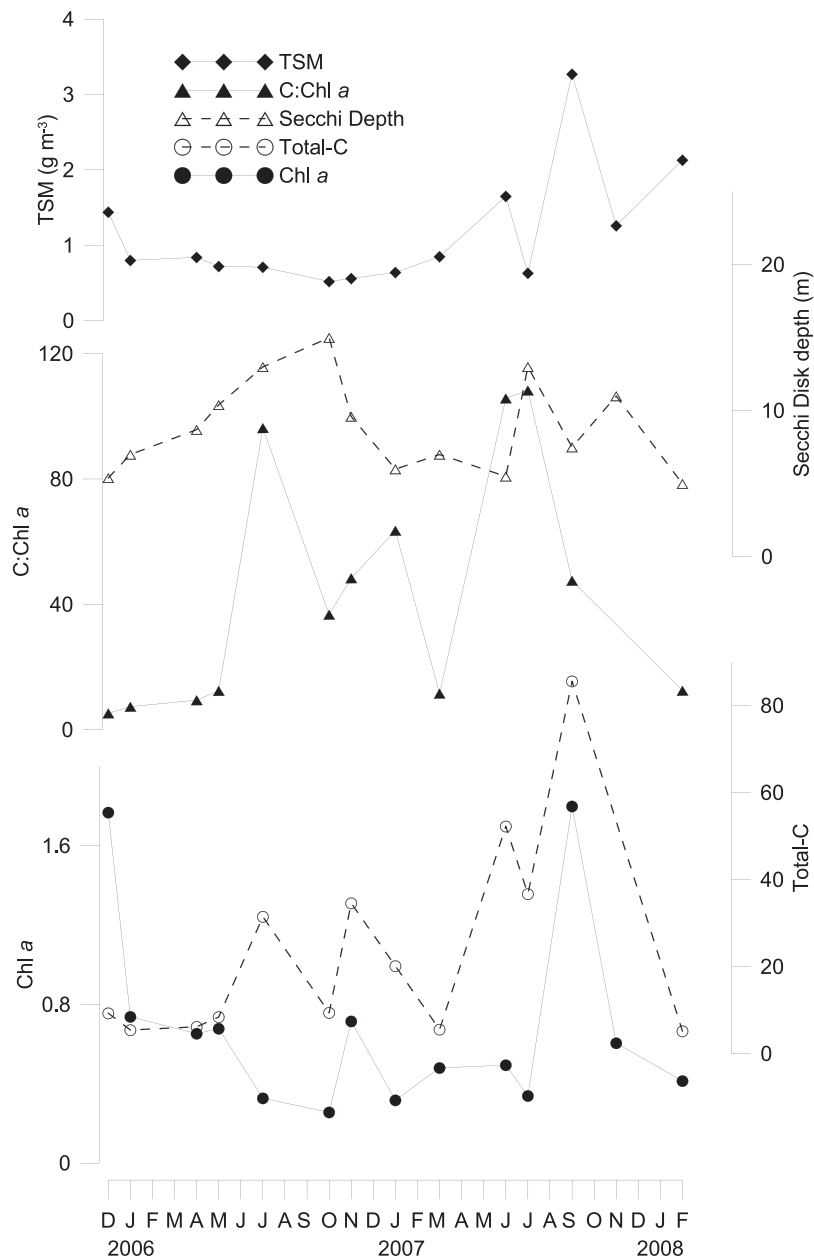


Figure 4 Total carbon biomass of phytoplankton ($\mu\text{g L}^{-1}$), Chl *a* ($\mu\text{g L}^{-1}$) and C:Chl *a* ratios during 2005–2008 in the northern Adriatic Sea.

were $0.02 \mu\text{M}$, $0.32 \mu\text{M}$, $0.11 \mu\text{M}$ and $0.2 \mu\text{M}$ respectively.

Total suspended matter (TSM) concentration was measured according to Van der Linde (1998). Seawater was first passed through $300 \mu\text{m}$ mesh size net and filtered through pre-weighted $47 \text{ mm } \varnothing$ GF/F Whatman filters which were ignited at 450°C and washed with distilled water and dried at 75°C prior to filtration. Filtration volumes ranged between 1.5 and 2.5 L.

2.1. Determination of marker pigments

HPLC pigment analysis was performed following the measurement protocols of the Joint Global Ocean Flux Study (JGOFS, 1994), and by modifying the method presented by Wright et al. (1991). 0.8 to 6 L of seawater was collected

and filtered through 47 mm GF/F Whatman glass fibre filters. The filters were stored in liquid nitrogen for the duration of the campaign and then kept at -80°C until the analysis. A modified version of pigment extraction was applied (Barlow et al., 1997). The filters were thawed and transferred into a plastic Falcon tube containing 3 ml of 100% acetone. They were then sonicated (Sonicator SonoPlus GM2070, Bandelin) in a 0°C water bath for 1 min and left to extract for 24 h at -20°C . Extracts were clarified by filtering them onto $0.45 \mu\text{m}$ Teflon syringe filters and analysed with a Hewlett Packard/Agilent 1100 HPLC system. The HPLC system used comprises a reversed-phase C18 column ($250 \times 4.6 \text{ mm}$, $5 \mu\text{m}$ particle size, Hichrom, with a C18 guard column), an autosampler with thermostat, a diode array detector (DAD), a pumping system and degasser,

data acquisition and analysis software and a three phases solvent gradient. Pigments were identified from both absorbance spectra and retention times from the signals in the DAD detector (405 nm for phaeopigments and 436 nm for chlorophyll pigments and carotenoids). The HPLC system was calibrated using pigment standards from DHI Water & Environment. This method does not permit the separation of divinyl chl *a* and chlorophyll *b* (chl *b*) from monovinyl chl *a* and chl *b*, respectively. It is not capable of fully separating chlorophyll *c1* and chlorophyll *c2* (presented here as chl *c1+c2*) either. $\beta\gamma$, $\beta\epsilon$ and $\beta\beta$ carotenes were not resolved well and their sum was given as β -carotene. The individual pigments measured were thus (Table S2): Chl *a*, peridinin (Peri), diadinoxanthin fucoxanthin (Fuco), alloxanthin (Allo), chl *b*, β -carotene (Caro), diatoxanthin (Dtx), 19'-butanoyloxyfucoxanthin (But), zeaxanthin (Zea), 19'-hexanoyloxyfucoxanthin (Hex) and the degradation product of chl *a*, chlorophyllide *a* (chl *a*).

2.2. CHEMTAX analysis

The CHEMTAX 1.95 software (Mackey et al., 1996), Microsoft Excel version was used to determine phytoplankton taxonomy based on pigments.

The pigments, phytoplankton groups and their abbreviations are shown in Table S2. Seven phytoplankton classes; diatoms, dinoflagellates, haptophytes, cryptophytes, chlorophytes, prasinophytes and cyanobacteria and their marker pigments Fuco, Peri, Hex-fuco, Allo, Chl *b*, Zea and But-Fuco were chosen for CHEMTAX analysis based on microscopy and pigment data (Tables S2 and S3). Among these pigments, Fuco is also present in haptophytes, chrysophytes and raphidophytes; Peri is an unambiguous pigment for dinoflagellates; Hex-fuco is the unique pigment of haptophytes, while Allo is of cryptophytes; Chl *b* is the marker pigment of all green flagellates such as chlorophytes, prasinophytes and euglenophytes; Zea is mainly found in cyanobacteria but also present in some chlorophytes in low quantity (Jeffrey et al., 1997).

A Pigment:Chl *a* ratio matrix for each taxonomic class was obtained from Wright et al. (2009), Mackey et al. (1996) and Schlüter et al. (2000). Output ratios were used as a new input ratio matrix repeatedly until the ratios become stable (Table S3).

The parameters set for the calculations were as follows: ratio limits were set to 500, weighting was 'bounded relative error by pigment', iteration limit = 200, epsilon limit = 0.0001, initial step size = 10, step ratio = 1.3, cutoff step = 200, elements varied = 5, subiterations = 1, weight bound = 30 (Mackey et al., 1996).

2.3. Statistics

In order to assess the impact of environmental factors (temperature, salinity, TSM, nitrate, ammonium, phosphate, silicate) on the carbon biomass, abundance and CHEMTAX derived Chl *a* of phytoplankton groups and the total community, redundancy analysis (RDA) was performed using CANOCO 4.5. RDA was chosen by applying the $\log_{10}(N + 1)$ -transformed carbon biomass and CHEMTAX derived Chl *a* data to detrended correspondence analysis. Since the gradients in the functional structure were below 3 standard

Table 1 Spearman rank correlations between carbon biomass and Chl *a* of phytoplankton groups and environmental parameters. Significant values were indicated as bold. Temp.: Temperature, TSM: Total suspended matter, * $p < 0.05$, ** $p < 0.01$.

	TSM	Secchi disc depth	Temp.	Salinity	PO ₄	NO ₃	NH ₄	Si	Diatom-C	Dino-C	Hapto-C	S. flag.-C	Total-C
TSM (g m ⁻³)	1												
Secchi disc depth (m)	-0.639*	1											
Temp. (°C)	-0.302	0.813**	1										
Salinity (psu)	-0.385	0.009	0.11	1									
PO ₄ (µM)	-0.195	-0.516	-0.366	-0.055	1								
NO ₃ (µM)	-0.571*	0.005	-0.17	0.082	0.468	1							
NH ₄ (µM)	-0.137	0.539	0.165	-0.17	-0.479	-0.016	1						
Si (µM)	0.198	-0.685*	-0.885**	-0.33	0.531	0.253	-0.022	1					
Diatom-C (µg L ⁻¹)	-0.027	0.324	0.654*	0.027	-0.663*	-0.352	0.225	-0.780**	1				
Dino-C (µg L ⁻¹)	0.066	-0.114	0.451	-0.253	0.179	-0.06	-0.132	0.434	0.357	1			
Hapto-C (µg L ⁻¹)	-0.137	0.388	0.632*	0.082	-0.371	-0.231	0.192	-0.610*	0.418	0.066	1		
S. flag.-C (µg L ⁻¹)	0.099	0.219	0.027	-0.363	0.201	-0.082	0.11	0.214	-0.181	0.324	0.324	1	
Total-C (µg L ⁻¹)	-0.132	0.352	0.775**	-0.27	-0.215	-0.258	-0.11	-0.753**	0.786**	0.802**	0.604*	-0.011	1
Total-A (cells L ⁻¹)	-0.115	0.425	0.868**	0.110	-0.289	-0.423	0.027	-0.769**	0.665*	0.516	0.604*	0.236	0.791**
Diatom-Chl <i>a</i> (µg L ⁻¹)	0.407	-0.170	0.288	-0.143	-0.330	-0.505	-0.247	-0.500	*0.571	0.368	0.159	-0.176	0.544
Dino-Chl <i>a</i> (µg L ⁻¹)	0.213	-0.361	-0.209	-0.396	0.209	-0.088	0.088	0.33	0.154	*0.626	-0.176	-0.236	0.258
Hapto-Chl <i>a</i> (µg L ⁻¹)	-0.024	-0.21	-0.126	0.06	0.525	0.817	-0.143	0.181	-0.379	0.099	-0.324	-0.159	-0.104
Chl <i>a</i> (µg L ⁻¹)	0.477	-0.308	-0.248	-0.002	0.077	-0.231	-0.198	0.038	0.038	0.154	-0.363	-0.280	0.022

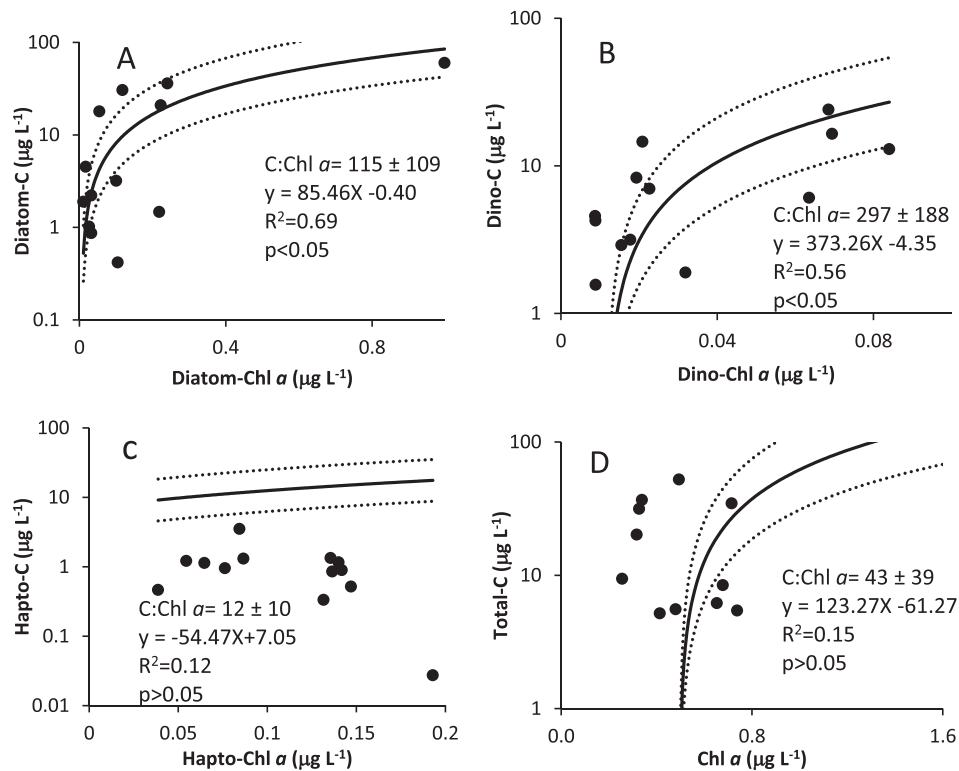


Figure 5 Model II Linear regression of carbon biomass versus CHEMTAX derived Chl a values of (A) diatoms (B) dinoflagellates and (C) haptophytes (D) model II Linear regression of carbon biomass of total community versus Chl a .

deviations (SDs for DCA axis 1: 0.572 and 0.956; DCA axis 2: 0.340 and 0.586 respectively) linear ordination method, RDA was found suitable for our data. Additionally, Spearman rank correlation analysis was performed using SPSS.

3. Results

3.1. Hydrography

The surface temperature follows a clear seasonal cycle with a minimum in winter (6–7°C in December–January) and a maximum during summer (24°C in June–July) (Figure 2). Salinity fluctuated between 35 and 38 psu without showing a clear cycle, being more dependent on the variability of riverine output (in particular, the Po and Tagliamento rivers). High values of Secchi disk depths were typically observed during the summer months and, as expected, were inversely correlated with the total suspended matter concentration ($p < 0.05$, Figure 2; Table 1).

3.2. Seasonal variations in environmental parameters, carbon biomass and Chl a of phytoplankton

Maxima in nitrate ($\sim 60 \mu\text{M}$) and phosphate ($0.06 \mu\text{M}$) concentrations were observed in the winter-spring period (Figure 3). There was not a significant correlation between salinity and nutrients (Table 1). Ammonium concentrations were always lower than nitrate. Molar ratios of N:P changed between 300 and 2500. Silicate concentrations ranged from

0.28 to $7.5 \mu\text{M}$. Nutrient maxima for silicate, nitrate and phosphate typically coincided in the winter–spring period with peak concentrations in May 2006 and January in 2007 (Figure 3).

There was a significant negative correlation ($p < 0.01$) between silicate concentrations and the temperature (Table 1).

The highest carbon biomass of the total phytoplankton community and chlorophyll a were observed in the summer-autumn period during 2005–2008 (Figure 4). Chl a was also high in December 2005 but this did not correspond to a high phytoplankton carbon biomass. These two variables were not correlated with each other ($p > 0.05$, Figure 5). C:Chl a ratios ranged from 5 to 108 (43 ± 39) and reached maximum values in June–July 2006 and 2007 (Figure 4). Carbon biomass and abundance values were much higher in summer–autumn period than in winter–spring (Figures 4 and S1).

Although C:Chl a ratios of all groups appeared to change with seasons (Figure S2), HPLC-CHEMTAX derived chlorophyll a values of diatoms and dinoflagellates were in concert with carbon biomasses of these groups in general. However, the carbon biomass of haptophytes was not concordant with the Chl a of this group (Figure 5). The high carbon biomass of haptophytes in July 2006 (Figure 6) was due to the dominance of the large species *Syracosphaera pulchra*. There was not any correlation between the abundance of haptophytes and Hapto-Chl a either (Figure S3 and regression analysis, $p > 0.05$).

The average contribution of diatoms to the total carbon biomass was $42 \pm 27\%$ and the total carbon biomass of diatoms constituted 60% of the total carbon biomass dur-

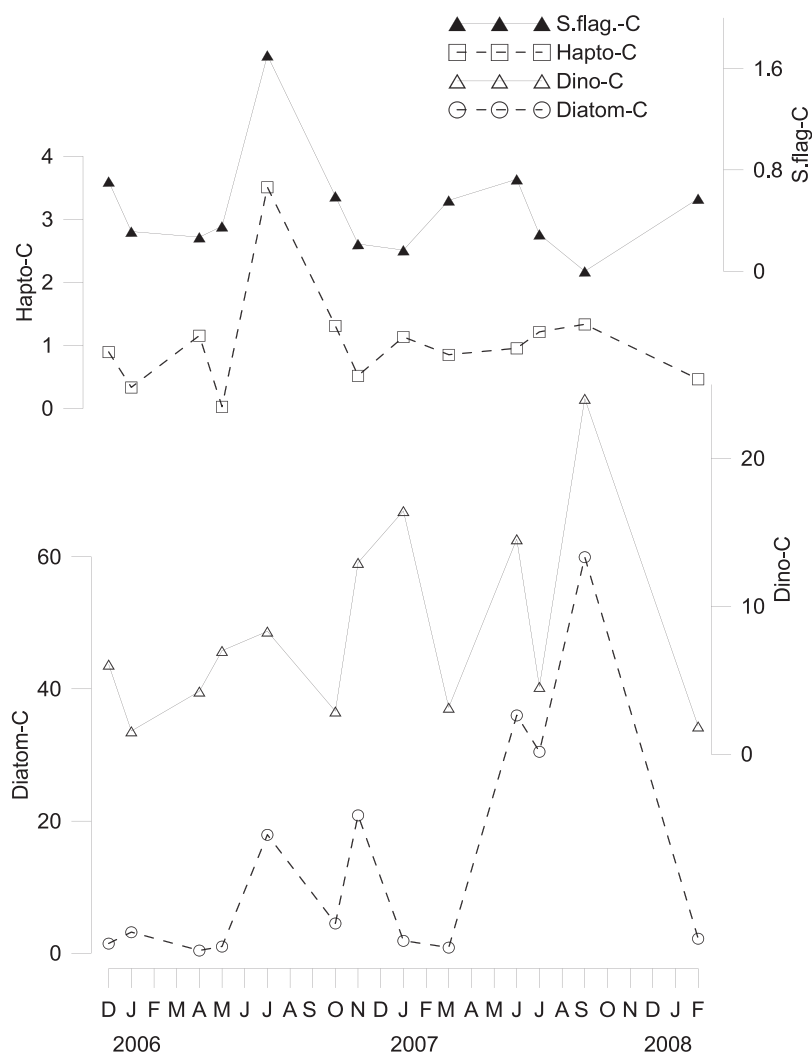


Figure 6 Carbon biomass ($\mu\text{g L}^{-1}$) of main phytoplankton groups during 2005–2008 in the northern Adriatic Sea (Contribution of cryptophytes, prasinophytes and chlorophytes to the carbon biomass based on microscopy was minor).

ing the whole sampling period. This group constituted the highest carbon biomass among other classes (Figure 6). The carbon biomass of diatoms was negatively correlated with both silicate and phosphate concentrations and positively correlated with the temperature (Table 1). According to microscopy results, dinoflagellates were the second most important group in terms of carbon biomass. Haptophytes were the third most important group in terms of carbon biomass based on microscopy.

According to CHEMTAX derived Chl *a* values and marker pigments, dinoflagellates (Peri), cryptophytes (Allo) and green flagellates (prasinophytes and chlorophytes containing Chl *b*) were dominant in the winter (December) of 2005 whereas the dinoflagellates and cyanobacteria (Zea) appeared to be dominant in the winter (February) of 2008 (Figures 7, 8). Marker pigments and Chl *a* of diatoms were higher during the summer–autumn period than in other seasons.

In the redundancy analysis, the first two axes explained 78.1% of the total variability in species data (i.e. carbon biomass) and 97.2% of the total variability in the species-

environment relation (Table S4; Figure 9A). Figure 9A shows that the most important phytoplankton group in terms of carbon biomass is diatoms since it has a longer axis (blue in colour) and is close to the X axis. In addition, based on this figure, the impact of temperature on Diatom-C appears to be positive (arrows are in the same direction) and more important than other parameters since it is longer and closer to the X axis, which explained 85.7% of the total variability in the species-environment relation. Similar to the Spearman Rank Correlation, the RDA1 for carbon biomass was correlated with the temperature ($r = 0.80$) and silicate concentrations ($r = -0.77$) while the RDA2 was related to phosphate and nitrate concentrations ($r = 0.685$ and $r = 0.535$, respectively). However, the correlation was not significant (Monte Carlo test, significance of the first canonical axis, eigenvalue = 0.688, $p = 0.12$, significance of all the canonical axes, trace = 0.803, $p = 0.09$).

According to the second redundancy analysis the first two axes explained 66.5% of the total variability in CHEMTAX derived phytoplankton groups and 96.8% of the total variability in the species-environment relation (Table S4; Figure 9B).

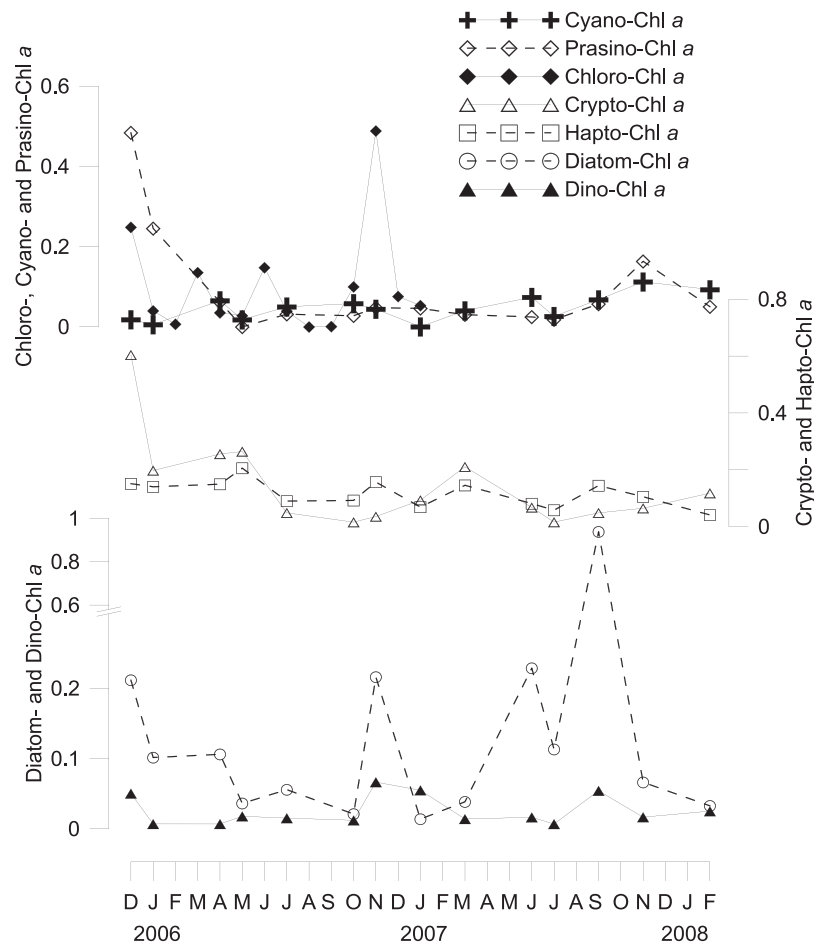


Figure 7 Chl *a* ($\mu\text{g L}^{-1}$) of major phytoplankton groups based on HPLC-CHEMTAX analysis during 2005–2008 in the northern Adriatic Sea.

RDA1 for Chl *a* of the phytoplankton groups was associated with the TSM ($r = 0.672$) and RDA2 was correlated positively with the silicate concentration and negatively with the temperature ($r = 0.729$ and $r = -0.716$). However, the correlation was not significant (Monte Carlo test, significance of the first canonical axis, eigenvalue = 0.504, $p = 0.30$, significance of all the canonical axes, trace = 0.987, $p = 0.23$).

3.3. Species composition

The genus having the highest carbon biomass during the study period was *Chaetoceros* spp. (Table S5), which reached the highest values in the June–July period in 2006 and 2007. *Rhizosolenia*, *Proboscia* and *Pseudosolenia* genera also contributed highly to the total carbon biomass in the summer–autumn periods (July–October). While present all year round, *Cerataulina pelagica* was dominant in June–September 2007. *Guinardia flaccida*, *Leptocylindrus* spp. and *Pseudo-nitzschia* spp. were also dominant during the summer-autumn months. Although present in all the samples, the contribution of *Cylindrotheca closterium* to the total carbon biomass was low. *Skeletonema marinoi* was observed in 30% of the samples (generally in December–January) and its abundance was quite low.

Among the dinoflagellates, *Prorocentrum minimum* was present in all of the samples. It was high in abundance during April–July 2006 and reached the maximum carbon biomass in January 2007. *Gyrodinium* spp., *Gymnodinium* spp. and *Ceratium* spp. were also frequently observed in the samples, especially in summer–autumn. *Gonyaulax* spp. reached high carbon biomass in November 2006 and January 2007.

Emiliania huxleyi was present all year round with maximum abundance in July–September 2007.

4. Discussion

4.1. Environmental parameters

As would be expected, the water temperature was higher in warm summer months than in winter months similar to previous investigations in the northern Adriatic Sea (Bernardi Aubry and Acri 2004, Cerino et al. 2019). In the present study, salinity values fluctuated between 34.5 and 37.5 during the sampling period and there was not an apparent trend of seasonal increase or decrease in salinity (Figure 2). However, in a previous study performed in the inlets of the Gulf of Venice and in the Gulf of Trieste

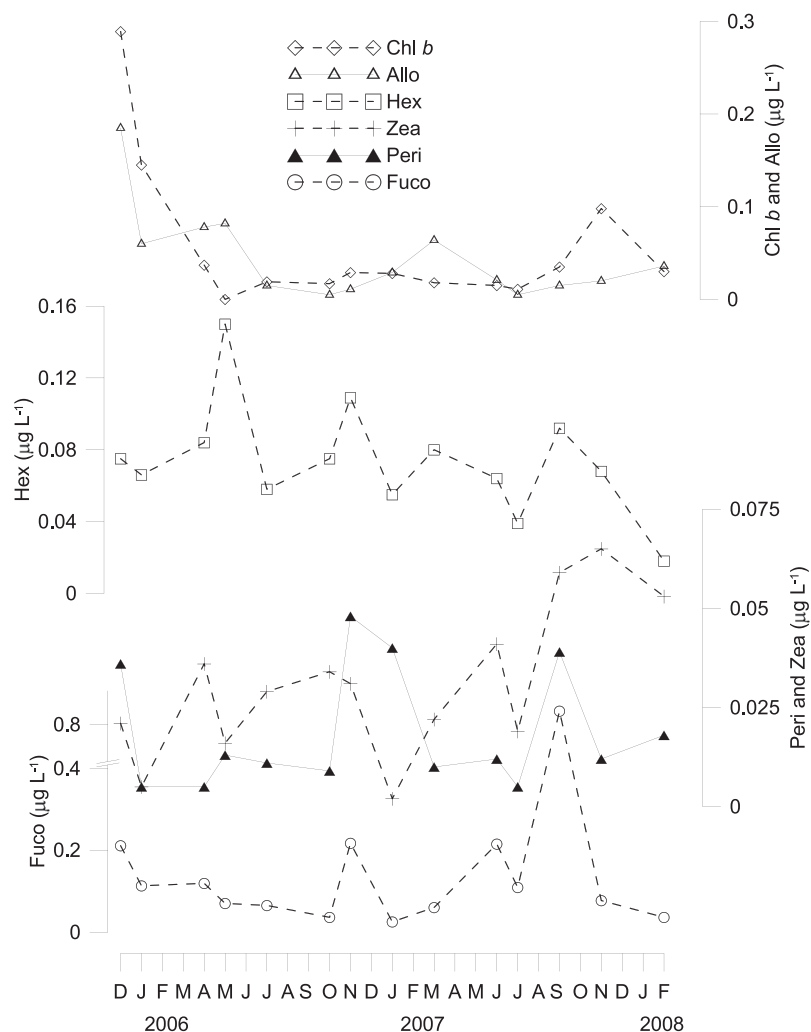


Figure 8 Marker pigments during 2005–2008 in the northern Adriatic Sea.

salinity values have been generally found to be high during cold winter-early spring months (Bianchi et al. 2004, Cerino et al. 2019) and declined with high rates of riverine discharge in the late spring (Degobbi et al. 2000, Penna et al. 2006). Strong vertical mixing and circulation of water in winter months (Marini et al. 2008) must be the cause of high salinity during this cold period.

The highest nutrient concentrations were observed during the winter–spring period (Figure 3). This was also shown by a significant negative correlation between the temperature and silicate concentrations (Table 1) indicating input of nutrients during the cold periods similar to other studies performed in the northern Adriatic Sea (Bernardi Aubry and Acri, 2004; Cerino et al., 2019). Nitrate and phosphate concentrations also increased simultaneously with silicate during 2006–2007 in the present study (Figure 3). However, in contrast to the silicate, the increase in the nitrate and phosphate concentration in December 2006 and February 2008 was not so pronounced.

The maximum DIN concentration observed in the present study ($67 \mu\text{M}$) was close to the highest value measured in the NE and NW Adriatic Sea coast ($\sim 70 \mu\text{M}$, Cerino et al., 2019; Penna et al., 2006, Table 2). The highest phosphate

concentration measured in the present investigation ($0.06 \mu\text{M}$) was much lower than the maximum values attained in other studies (Table 2). Silicate concentrations were also relatively low (average $3.7 \pm 2.6 \mu\text{M}$) in this study. The average of dissolved inorganic nitrogen (DIN) and phosphate during the sampling period was $29 \pm 18 \mu\text{M}$ and $0.03 \pm 0.02 \mu\text{M}$, respectively and the phosphorus seemed to be severely limiting with N/P ratios changing from 303 to 5010 (average: 1439 ± 1258). The global median value of N/P ratio based on a large data set was reported as 22:1 in all major oceans covering the period 1970–2010 (Martiny et al. 2014). Although higher than the global median, averages of N/P ratios in the inlets of Venice Lagoon during 2001–2002 (between 135 ± 118 and 286 ± 199) were lower than the values found in the present study (Bianchi et al. 2004). Very low phosphorus concentrations in this study can be explained with reduced phosphorus discharge by Po River after 1986 as a result of the implementation of new Italian legislation (Totti et al., 2019). However, again an increase in phosphate concentrations have been reported during 2007–2016 period in spite of still low phosphorus outflow from the Po River, probably due to the input of phosphorus from other sources (Totti et al., 2019).

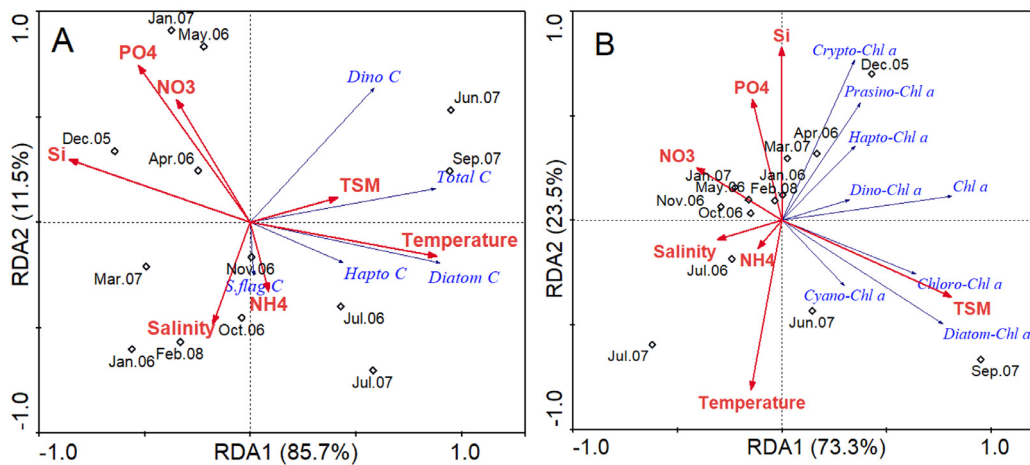


Figure 9 Redundancy analysis between environmental parameters and (A) carbon biomass (B) Chl *a* of main phytoplankton groups.

4.2. Carbon biomass and Chl *a* of phytoplankton and their relation with environmental parameters

Chl *a* concentrations were not congruent with the total carbon biomass of phytoplankton despite the presence of a correlation between CHEMTAX-derived Chl *a* and carbon biomass of diatoms and dinoflagellates (Figure 5). This discrepancy could be related to fixation problems of nanoflagellates with formaldehyde or Lugol’s iodine. For instance, in a study performed in the southern Adriatic Sea, 96% of phytoplankton could not be associated with any taxonomic class in the preserved samples (Cerino et al., 2012). In addition, this inconsistency could also be associated to variations in the marker pigment content of flagellates with changing light intensity, especially photoprotective pigments such as alloxanthin, β -carotene and zeaxanthin (Konucu et al., 2022).

In spite of the presence of a correlation between Chl *a* and carbon biomass of diatoms and dinoflagellates, our graphs showed a variation in C:Chl *a* ratios of diatoms and dinoflagellates similar to other phytoplankton groups during different seasons as well (Figure S2).

As expected, with low nutrient concentrations and high light intensities in the summer period, C:Chl *a* ratios were higher during this warm period than in the winter months (Figure 4). The C:Chl *a* ratio has previously been reported to change between <10 and >200 among distinct phytoplankton groups, species and cell size and under changing light, nutrient and temperature conditions (Finkel, 2001; Geider, 1987; Laws and Bannister, 1980; Sathyendranath et al., 2009).

When marker pigments and the corresponding abundance of diatoms and dinoflagellates were compared, the correlation did not appear ($p > 0.05$) probably due to the variations in pigment content of cells based on their size (Figure S1). Similarly, increases in fucoxanthin and peridinin concentrations did not always correspond to high diatom or dinoflagellate abundance in Boka Kotorska Bay, southeastern Adriatic Sea during 2008–2009 (Krivocapic et al., 2018). However, abundance values of these groups were generally concordant with their marker pigments in a study performed in the Zrmanja Estuary, eastern Adriatic Sea in winter 2000 and summer 2003 (Viličić et al., 2008).

There was not any significant correlation between either abundance or biomass of haptophytes and CHEMTAX assigned Chl *a* of this group in this study. Similarly, the abundance of haptophytes was not coherent with 19’Hexanoyloxyfucoxanthin concentrations in the study of Viličić et al. (2008). The lack of correlation between CHEMTAX associated Chl *a* values and carbon biomass of haptophytes could be related to either the disappearance of non-calcifying haptophyte species (such as *Chrysochromulina* spp.) with regular fixation methods (Konucu et al., 2022) or the presence of the haptophyte marker pigment within some dinoflagellates species (Zapata et al., 2012). Similar to the present study, the coefficient of determination (R^2) values between carbon biomass and CHEMTAX derived Chl *a* values of *Emiliania huxleyi* was weaker ($R^2 = 0.40$) than of diatoms and dinoflagellates ($R^2 = 0.97$ and 0.81) during a coccolithophorid bloom in the Patagonian Shelf (Souza et al., 2012).

Temperature and silicate concentrations appeared as the best predictor variable explaining the variations in carbon biomass of phytoplankton (RDA, Figure 9). The total carbon biomass of phytoplankton was positively correlated with the temperature and negatively correlated with the silicate concentrations. Spearman Rank correlation also showed a similar relationship ($p < 0.01$, Table 1). This showed that phytoplankton carbon biomass and abundance reached higher values (Figures 4, S1) during warm and nutrient-poor periods (Figures 2, 3), based on the results of the present sampling. A negative correlation between silicate concentrations and carbon biomass appears to be due to the dominance of diatoms within the total carbon biomass (60% of total carbon biomass during the study period) and the consumption of silicate by diatoms. Phosphate concentration was also negatively correlated with the carbon biomass of diatoms. As a result, low nutrient concentrations in general during summer must be due to the consumption of nutrients by the phytoplankton community, scarcity of zooplankton (Bernardy Aubry et al., 2012) and low input of freshwater nourishing surface waters (Degobbis et al., 2000). Similar summer blooms of phytoplankton in the northern Adriatic Sea were reported in several previous studies (Bernardi Aubry et al., 2004; Godrijan et al., 2013; Mozetić et al., 2012; Talaber et al., 2014). Fur-

Table 2 Nutrient concentrations measured in distinct studies in the northern Adriatic Sea.

Location	Period	DIN (μM)	NO_3^- (μM)	PO_4^{3-} (μM)	NH_4^+ (μM)	Si (μM)	Chl <i>a</i> ($\mu\text{g L}^{-1}$)	N/P	Secchi disk depth (m)	Source
Gulf of Venice	2006–2008	9.54–67.09	2.75–62.1	0.02–0.06	1.4–12.9	0.28–7.52	0.25–1.8	303–5010	5.4–15	Present study
Gulf of Venice	2001–2002	1.40–41.9	0.0–30.2	0.0–0.4	0.4–10.7	1.4–69.6	0.7–36.7	11–1637	–	Bernardi Aubry and Acri (2004)
Gulf of Venice	1999–2001	0.11–221.5	0.01–197.3	0.01–2.0	–	0.01–115.3	0.01–25.6	–	–	Bernardi Aubry et al. (2006)
NW Adriatic	1990–1999	0.03–382.1	–	0.01–9.4	–	0.01–67.7	0.01–66.3	80–118	0.10–15	Bernardi Aubry et al. (2004)
Gulf of Trieste	2010–2017	0.02–71.3	–	0.01–0.28	–	0.07–40.7	–	–	–	Cerino et al. (2019)
Near to Po River	2001–2002	3.00–50.0	–	0.1–1.0	–	–	–	10–500	–	Degobbis et al. (2005)
Gulf of Trieste	1992	–	1.00–9.0	–	–	1.0–8.0	3.0–13.0	–	4–19	Malej et al. (1995)
NW Adriatic	2001–2002	5.00–70.00	–	0.1–0.55	–	0.01–20.0	5–45	~36–320	0.92–4.15	Penna et al. (2006)
NW Adriatic	2001–2002	2.0–34.2	–	~0.06–0.4	–	5–17.8	~2.96–6.15	135–286	0.5–4.5	Bianchi et al. (2004)
N Adriatic	2009–2010	<3–18.5	–	<0.1	–	0.55–14.7	0.16–2.1	–	–	Talaber et al. (2014)

thermore, a similar inverse relationship between the nutrients and phytoplankton abundance was also observed in the Gulf of Venice and the Gulf of Trieste (Bernardi Aubry and Acri, 2004; Cerino et al., 2019).

High silicate but low nitrate and phosphate concentrations observed in December 2005 and February 2008 must be related to the consumption of nutrients by phytoplankton groups other than diatoms which was shown by high CHEMTAX derived Chl *a* values of chlorophytes, prasinophytes, cryptophytes and dinoflagellates in the former date and by cyanobacteria Chl *a* in the latter date.

High carbon biomass and abundance of phytoplankton during warm summer months did not seem to cause low Secchi disk depths in June–July period (Figures 2, 4, S1) and there was a significant positive correlation between the temperature and Secchi disk depths (Figure 2). Probably other particles in the winter–spring period cause low Secchi disk depths. As expected, there was a significant negative correlation between Secchi Disk depth and TSM concentrations (Table 1).

Despite high nutrient concentrations during the winter–spring period similar to previous studies (Bernardi Aubry and Acri, 2004; Cerino et al., 2019), low phytoplankton abundance and carbon biomass could be related to the increase in abundance of copepods during this season. The abundance of copepods was higher during 1986–2005 than during 1972–1980 in winter–spring in the northern Adriatic Sea (Bernardi Aubry et al., 2012; Conversi et al., 2009; Kamburska and Fonda Umani, 2006, 2009).

In contrast to the present investigation, in the Gulf of Trieste, the phytoplankton annual cycle was characterized by a late winter–early spring peak, which was formed by flagellates and diatoms during 1986–2010 (Cabrini et al., 2012). Another study carried out in the same region in the period 2010–2017 noted maximum abundances in spring (May) and minimum values in winter (Cerino et al., 2019) similar to observations in distinct regions of the northern Adriatic Sea (Bernardi Aubry and Acri, 2012; Mozetic et al., 2012; Totti et al., 2000). In general, diatoms and flagellates (<10 μm in size) were reported to co-dominate during these spring blooms. Flagellates and diatoms were the main components of the abundance in the present study as well (Figure S1). They reached the highest abundance in the June–July period. Based on a long-term study during 2010–2017 in the Gulf of Trieste, phytoplankton abundance started to increase in March and attained the maximum values in May (Cerino et al., 2019). However, in the present study, neither the abundance nor the carbon biomass of phytoplankton was high during the spring (March–May) period (Figures 6, S1).

The diatom genera having the maximal abundances were *Chaetoceros* spp., *Pseudo-nitzschia delicatissima*, *Thalassiosira* sp. and *Cerataulina pelagica* in the present study (Table S5). *Cerataulina pelagica*, *Chaetoceros* spp. and *Pseudo-nitzschia* spp. were the most representative taxa in other studies performed in the northern Adriatic Sea as well (Bernardi Aubry et al., 2012; Cabrini et al. 2012; Mozetić et al., 2010). In addition to the aforementioned species, *Skeletonema marinoi* was also a dominant species in these mentioned studies (Bernardi Aubry et al. 2012; Cabrini et al. 2012; Marić et al., 2012). *Skeletonema marinoi* was observed in low abundance in the present study, and its abundance has declined in the last decade com-

pared to 1972–1999 which has been attributed to a decrease in phosphate concentrations after the Italian law at the end of 1980s restricting agricultural and industrial usage of phosphorus (Cabrini et al., 2012). In contrast, the much more frequent observation of *Chaetoceros* spp. during the winter–spring bloom may indicate oligotrophication of the system since this small-sized genera can grow at limited nutrient concentrations and low N/P ratios (Lagus et al. 2004; Mozetić et al. 2010). It is possible that nutrient limitation even during winter-spring might have led the *Chaetoceros* spp. bloom to be shifted to an earlier period.

Carbon biomass of phytoplankton obtained in July 2006 in the present study ($30 \mu\text{g C L}^{-1}$) was lower than a value calculated in the same period at a station closer to the Po River ($50 \mu\text{g C L}^{-1}$) but higher than at another offshore station in the Adriatic Sea (Pugnetti et al., 2008). The maximum carbon biomass obtained in this study ($85 \mu\text{g C L}^{-1}$) was similar to a maximum value ($80.7 \mu\text{g C L}^{-1}$) calculated in the southern Adriatic Sea during November 2006–June 2008 (Cerino et al., 2012). While the maximum biomass occurred in September 2007 in this study, in the southern Adriatic Sea it was observed in April 2007.

In contrast to other studies, one of the dinoflagellate peaks was observed in the cold January period in 2007 due to the species *Prorocentrum minimum*. The abundance and carbon biomass of diatoms were low in spite of high nutrient concentrations during this sampling period. This could be the reason for the peak abundance of *P. minimum* on this date. Other peaks were in June and September (Figure 6). This species was dominant in the warm period in the Gulf of Trieste during 2009–2010 (Talaber et al., 2014).

In the present study Chl *a* concentrations varied between $0.25 \mu\text{g L}^{-1}$ and $1.80 \mu\text{g L}^{-1}$ (average 0.685 ± 0.49) during the study period, the highest being in December 2005 and September 2007 and the lowest in October 2006 (Figure 4). The first peak in Chl *a* was formed by cryptophytes, prasinophytes, chlorophytes and dinoflagellates. The second peak was constituted of mainly diatoms and dinoflagellates. Chl *a* concentration ranged between 0.16 and $2.1 \mu\text{g L}^{-1}$ in the Gulf of Trieste during 2009–2010 with two peaks in Chl *a* concentrations in summer (June–July) and in late autumn (December) (Talaber et al., 2014). Chl *a* concentrations tended to decrease over the years 1970–2007 in the northern Adriatic Sea probably due to reduced nutrient input via the Po River as a result of environmental regulations (Mozetić et al., 2010). Chl *a* concentrations at the Lagoon inlets of Venice were higher than in our study (Table 2, Bianchi et al., 2004; Bernardi Aubry and Aciri 2004).

In the present investigation during the summer–autumn period diatoms, dinoflagellates and haptophytes dominated. Cryptophytes, prasinophytes, chlorophytes and cyanobacteria were more abundant during the winter-spring period based on marker pigments.

5. Conclusion

Our study showed a good correlation between pigment and microscopy-based results of diatoms and dinoflagellates. These groups were the major components of phytoplankton composition based on our microscopy results. However, according to the pigment results, the contribution of hap-

tophytes to the total chlorophyll *a* appears almost as much as diatoms during the majority of the sampling periods. The role of other flagellates such as cryptophytes and chlorophytes also seemed to be underestimated by microscopy when compared to pigment results. On the other hand, the high abundance of small flagellates observed during the summer months did not correspond to any prominent increase in Chl *b* or alloxanthin which are among the pigments of small flagellates. Some of these flagellates could be possibly heterotrophic.

In this study, the seasonality of phytoplankton abundance was mainly concordant with previous studies performed in the northern Adriatic Sea. While high nutrients but low carbon biomass of phytoplankton during the winter-spring period was observed this contrasted with low nutrient concentrations but high carbon biomass during the summer-autumn period. The temperature and silicate concentrations were the best predictor variables explaining variations in the carbon biomass of phytoplankton. Species composition in the present study was also similar to the previous observations performed in the region. While total carbon biomass of phytoplankton was not correlated with Chl *a* values, which seems mainly related to seasonal changes in C:Chl *a* ratios, CHEMTAX derived Chl *a* values and carbon biomasses of diatoms and dinoflagellates were significantly correlated. The present study is a part of a long-term monitoring investigation carried out with remote sensing and pigment data performed at a platform located in the Venice Lagoon. Thus, this study will provide an opportunity to compare pigment results, remote sensing data and phytoplankton data.

Declaration of competing interest

The authors declare that they have no known competing financial interests or personal relationships that could have appeared to influence the work reported in this paper.

Acknowledgements

This work has been supported by the Joint Research Centre of the European Commission within the CoASTS time-series project led by Giuseppe Zibordi. Acknowledgments are due to Dirk van der Linde for his extensive support in field and laboratory activities and to the personnel of the AAOT site (CNR-Italy) for the continuous support. We thank Fabrizio Sena for performing nutrient analyses. We also thank Erhan Mutlu who helped in statistical analysis.

Supplementary materials

Supplementary material associated with this article can be found, in the online version, at <https://doi.org/10.1016/j.oceano.2022.05.002>.

References

- Arteaga, L., Pahlow, M., Oschlies, A., 2016. Modeled Chl:C ratio and derived estimates of phytoplankton carbon biomass and its

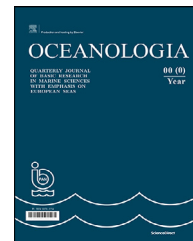
- contribution to total particulate organic carbon in the global surface ocean. *Global Biogeochem. Cy.* 30 (12), 1791–1810. <https://doi.org/10.1002/2016GB005458>
- Artegiani, A., Bregant, D., Paschini, E., Pinardi, N., Raicich, F., Russo, A., 1997a. The Adriatic Sea General Circulation. Part I: Air–Sea Interactions and Water Mass Structure. *JPO* 27, 1492–1514. [https://doi.org/10.1175/1520-0485\(1997\)027\(1492:TASGCP\)2.0.CO;2](https://doi.org/10.1175/1520-0485(1997)027(1492:TASGCP)2.0.CO;2)
- Artegiani, A., Bregant, D., Paschini, E., Pinardi, N., Raicich, F., Pinardi, N., 1997b. The Adriatic Sea General Circulation. Part II: Baroclinic Circulation Structure. *JPO* 27, 1515–1532. [https://doi.org/10.1175/1520-0485\(1997\)027\(1515:TASGCP\)2.0.CO;2](https://doi.org/10.1175/1520-0485(1997)027(1515:TASGCP)2.0.CO;2)
- Balech, E., 1988. Los dinoflagelados del Atlántico Sudoccidental. In: *Publicaciones especiales – Instituto Español de Oceanografía*, 310 pp.
- Barlow, R.G., Cummings, D.G., Gibb, S.W., 1997. Improved resolution of mono- and divinyl chlorophylls a and b and zeaxanthin and lutein in phytoplankton extracts using reverse phase C-8 HPLC. *Mar. Ecol. Prog. Ser.* 161, 303–307. <https://doi.org/10.3354/meps161303>
- Bérard-Therriault, L., Poulin, M., Bossé, L., 1999. *Guide d'identification du phytoplancton marin de l'estuaire et du golfe du Saint-Laurent incluant également certains protozoaires. Les presses scientifiques du CNRC, Ottawa*, 387 pp.
- Bernardi Aubry, F., Aciri, F., 2004. Phytoplankton seasonality and exchange at the inlets of the Lagoon of Venice (July 2001–June 2002). *J. Mar. Syst.* 51, 65–76. <https://doi.org/10.1016/j.jmarsys.2004.05.008>
- Bernardi Aubry, F., Berton, A., Bastianini, M., Socal, G., Aciri, F., 2004. Phytoplankton succession in a coastal area of the NW Adriatic, over a 10-year sampling period 1990–1999. *Cont. Shelf Res.* 24, 97–115. <https://doi.org/10.1016/j.csr.2003.09.007>
- Bernardi Aubry, F., Aciri, F., Bastianini, M., Bianchi, F., Cassin, D., Pungetti, A., Socal, G., 2006. Seasonal and interannual variations of phytoplankton in the Gulf of Venice Northern Adriatic Sea. *Chem. Ecol.* 22, S71–S91. <https://doi.org/10.1080/02757540600687962>
- Bernardi Aubry, F., Cossarini, G., Aciri, F., Bastianini, M., Bianchi, F., Camatti, E., De Lazzari, A., Pugnetti, A., Solidoro, C., Socal, G., 2012. Plankton communities in the Northern Adriatic: patterns and changes over last 30 years. *Estuar. Coast. Shelf Sci.* 115, 125–137. <https://doi.org/10.1016/j.ecss.2012.03.011>
- Bianchi, F., Ravagnan, E., Aciri, F., Bernardi Aubry, F., Boldrin, A., Cassin, D., Turchetto, M., 2004. Variability and fluxes of hydrology, nutrients and particulate matter between the Venice lagoon and the Adriatic Sea. Preliminary results (years 2001–2002). *J. Mar. Syst.* 51, 49–64. <https://doi.org/10.1016/j.jmarsys.2004.05.007>
- Brewin, R.J.W., Sathyendranath, S., Platt, P., Bouman, H., Ciavatta, S., Dall'Olmo, G., Dingle, J., Groom, S., Jonsson, B., Kostadinov, T.S., Kulk, G., Laine, M., Martinez-Vicente, V., Psarra, S., Raitsos, D.E., Richardson, K., Rio, M.H., Rousseaux, C.S., Salisbury, J., Shutler, J.D., Walker, P., 2021. Sensing the ocean biological carbon pump from space: a review of capabilities, concepts, research gaps and future developments. *Earth Sci. Rev.* 217, 103604. <https://doi.org/10.1016/j.earscirev.2021.103604>
- Cabrini, M., Fornasaro, D., Cossarini, G., Lipizer, M., Virgilio, D., 2012. Phytoplankton temporal changes in a coastal northern Adriatic site during the last 25 years. *Estuar. Coast. Shelf Sci.* 115, 113–124. <https://doi.org/10.1016/j.ecss.2012.07.007>
- Cerino, F., Bernardi Aubry, F., Coppola, J., La Ferla, R., Maimone, G., Socal, G., Totti, C., 2012. Spatial and temporal variability of pico-, nano- and micropHYtoplankton in the offshore waters of the southern Adriatic Sea (Mediterranean Sea). *Cont. Shelf Res.* 44, 94–105. <https://doi.org/10.1016/j.csr.2011.06.006>
- Cerino, F., Fornasaro, D., Kralj, M., Giani, M., Cabrini, M., 2019. Phytoplankton temporal dynamics in the coastal waters of the north-eastern Adriatic Sea (Mediterranean Sea) from 2010 to 2017. *Nat. Conserv.* 34, 343–372. <https://doi.org/10.3897/natureconservation.34.30720>
- Conversi, A., Peluso, T., Fonda Umani, S., 2009. The Gulf of Trieste: a changing ecosystem. *J. Geophys. Res.* 114, C03S90. <https://doi.org/10.1029/2008JC004763>
- Cupp, E.E., 1943. Marine Plankton Diatoms of the West Coast of North America. *Bull. Scripps Inst. Oceanogr.* 5, 1–273.
- Degobbi, D., Gilmartin, M., 1990. Nitrogen, phosphorus and silicon budgets for the northern Adriatic Sea. *Oceanol. Acta* 13, 31–45. <https://doi.org/10.1002/2016JC012669>
- Degobbi, D., Precali, R., Ivancic, I., Smoldaka, N., Fuks, D., Kveder, S., 2000. Long-term changes in the northern Adriatic ecosystem related to anthropogenic eutrophication. *Int. J. Environ. Pollut.* 13, 495–533. <https://doi.org/10.1504/IJEP.2000.002332>
- Degobbi, D., Precali, R., Ferrari, C.R., Djakovac, T., Rinaldi, A., Ivancic, I., Gismondi, M., Smoldaka, N., 2005. Changes in nutrient concentrations and ratios during mucilage events in the period 1999–2002. *Sci. Total Environ.* 353, 103–114. <https://doi.org/10.1016/j.scitotenv.2005.09.010>
- Dodge, J.D., 1982. *Marine dinoflagellates of the British Isles. Her Majesty's Stationary Office, London*, 142 pp.
- Drakulović, D., Pestorić, B., Cvijan, M., Krivokapić, S., Vukšanović, N., 2012. Distribution of phytoplankton community in Kotor Bay (south-eastern Adriatic Sea). *Cent. Eur. J. Biol.* 7 (3), 470–486. <https://doi.org/10.2478/s11535-012-0023-6>
- Eisenrich, S.J., Bannerma, R.T., Armstrong, D.E., 1975. A simplified phosphorus analysis technique. *Environ. Lett.* 91, 43–53.
- Finkel, Z.V., 2001. Light absorption and size scaling of light-limited metabolism in marine diatoms. *Limnol. Oceanogr.* 46, 86–94. <https://doi.org/10.4319/lo.2001.46.1.0086>
- Franco, P., Michelato, A., 1992. Northern Adriatic Sea: oceanography of the basin proper and of the western coastal zone. In: Vol-lenweider, R.A., Marchetti, R., Viviani, R. (Eds.), *Marine Coastal Eutrophication. The Science of the Total Environment*. Elsevier Science Publ. B.V., Amsterdam, 35–62.
- Fresenius, W., Quentin, K.E., Schneider, W., 1988. *Water Analysis – A Practical Guide to Physicochemical, Chemical and Microbiological Water Examination and Quality Assurance*. Springer, Berlin, Germany, 830 pp.
- Gasiunaite, Z.R., Cardoso, A.C., Heiskanen, A.S., Henriksen, P., Kauppila, P., Olenina, I., Pilkaitytė, R., Purina, I., Razinkovas, A., Sagertg, S., Schubert, H., Wasmund, N., 2005. Seasonality of coastal phytoplankton in the Baltic Sea: influence of salinity and eutrophication. *Estuar. Coast. Shelf Sci.* 65, 239–252. <https://doi.org/10.1016/j.ecss.2005.05.018>
- Gazeau, F., Sallon, A., Pitta, P., Tsiola, A., Maugendre, L., Giani, M., Celussi, M., Pedrotti, M.L., Marro, S., Guieu, C., 2017. Limited impact of ocean acidification on phytoplankton community structure and carbon export in an oligotrophic environment: Results from two short-term mesocosm studies in the Mediterranean Sea. *Estuar. Coast. Shelf Sci.* 186, 72. <https://doi.org/10.1016/j.ecss.2016.11.016>
- Geider, R.J., 1987. Light and temperature dependence of the carbon to chlorophyll a ratio in microalgae and cyanobacteria: implications for physiology and growth of phytoplankton. *New Phytol.* 106, 1–34. <https://doi.org/10.1111/j.1469-8137.1987.tb04788.x>
- Giani, M., Djakovac, T., Degobbi, D., Cozzi, S., Solidoro, C., Fonda Umani, S., 2012. Recent changes in the marine ecosystem of the northern Adriatic Sea. *Estuar. Coast. Shelf Sci.* 115, 1–13. <https://doi.org/10.1016/j.ecss.2012.08.023>
- Godrijan, J., Marić, D., Tomažič, I., Precali, R., Pfannkuchen, M., 2013. Seasonal phytoplankton dynamics in the coastal waters of

- the north-eastern. J. Sea Res. 77, 32–44. <https://doi.org/10.1016/j.seares.2012.09.009>
- Grasshoff, K., Ehrhardt, M., Kremling, K., 1983. Determination of nutrients. In: *Methods of SeaWater Analysis*. Verlag Chemie GmbH, Weinheim, 125–188.
- Grinson, G., Jayasankar, J., Phiros, S., Shalin, S., 2017. Concept for estimation of secondary and tertiary biomass from primary production. In: *Course Manual Summer School on Advanced Methods for Fish Stock Assessment and Fisheries Management*. Lecture Note Ser. 2/2017. CMFRI, Kochi, 301–307.
- Hasle G. R., Syvertsen E. E. 1997. Marine Diatoms. In: C. R. Tomas (ed.), *Identifying Marine Phytoplankton*. Acad. Press, New York, 276–278.
- Hillebrand, H., Dürselen, C.D., Kirschtel, D., Pollinger, U., Zohary, T., 1999. Biovolume calculation for pelagic and benthic microalgae. J. Phycol. 35, 403–424. <https://doi.org/10.1046/j.1529-8817.1999.3520403.x>
- Irigoin, X., Meyer, B., Harris, R., Harbour, D., 2004. Using HPLC pigment analysis to investigate phytoplankton taxonomy: the importance of knowing your species. Helgol. Mar. Res. 58, 77–82. <https://doi.org/10.1007/s10152-004-0171-9>
- Jeffrey, S.W., Mantoura, R.F.C., Wright, S.W., 1997. *Phytoplankton Pigments in Oceanography: Guidelines to Modern Methods*. UNESCO Publishing, Paris, 37–84.
- Jeffrey, S.W., Wright, S.W., Zapata, M., 2011. Microalgal classes and their signature pigments. In: Roy, S., Llewellyn, C.A., Egeland, E.S., Johnsen, G. (Eds.), *Phytoplankton Pigments: Characterization, Chemotaxonomy and Applications in Oceanography*. Cambridge University Press, Scientific Committee on Oceanic Research (SCOR), 3–76. <https://doi.org/10.1017/cbo9780511732263.004>
- JGOFs (Joint Global Ocean Flux Study), 1994. *JGOFs Protocols for the Joint Global Ocean Flux Study Core Measurements*. JGOFs Report No: 29. Committee on Oceanic Research, 170 pp.
- Kamburska, L., Fonda Umani, S., 2006. Long term copepod dynamics in the Gulf of Trieste. northern Adriatic Sea: recent changes and trends. Clim. Res. 31, 195–203. <https://doi.org/10.3354/cr031195>
- Kamburska, L., Fonda Umani, S., 2009. From seasonal to decadal inter-annual variability of mesozooplankton biomass in the northern Adriatic Sea (Gulf of Trieste). J. Mar. Syst. 78, 490–504. <https://doi.org/10.1016/j.jmarsys.2008.12.007>
- Karlson, B., Godhe, A., Cusack, C., Bresnan, E., 2010. Microscopic and molecular methods for quantitative phytoplankton analysis. In: *Intergovernmental Oceanographic Commission Manuals and Guides*, 55. UNESCO, Paris, France, 5–12.
- Konucu, M., Eker-Develi, E., Örek, H., Başduvar, Ş., Kideys, A.E., 2022. Marker pigments and carbon biomass of phytoplankton on the northeastern Mediterranean Sea coast. J. Exp. Mar. Biol. Ecol. 550, 151718. <https://doi.org/10.1016/j.jembe.2022.151718>
- Kovalá, P.E., Larrance, J.D., 1966. Computation of phytoplankton cell numbers, cell volumes, cell surface and plasma volume per litre from microscopical counts. Univ. Wash. Publ. Oceanogr. 38, 1–21.
- Krivokapić, S., Bosak, S., Viličić, D., Kušpilić, G., Drakulović, D., Pestorić, B., 2018. Algal pigments distribution and phytoplankton group assemblages in coastal transitional environment – Boka Kotorska Bay (South eastern Adriatic Sea). Acta Adriat 59 (1), 35–50. <https://doi.org/10.32582/aa.59.1.3>
- Lagus, A., Suomela, J., Weithoff, G., Heikkilä, K., Helminen, H., Sipura, J., 2004. Species-specific differences in phytoplankton responses to N and P enrichments and the N:P ratio in the Archipelago Sea, northern Baltic Sea. JPR 26, 779–798. <https://doi.org/10.1093/plankt/fbh070>
- Laws, A., Bannister, T.T., 1980. Nutrient- and light-limited growth of *Thalassiosira fluviatilis* in continuous culture, with implications for phytoplankton growth in the ocean. Limnol. Oceanogr. 25, 457–473. <https://doi.org/10.4319/lo.2004.49.6.2316>
- Llewellyn, C.A., Fishwick, J.R., Blackford, J.C., 2005. Phytoplankton community assemblage in the English Channel: a comparison using chlorophyll a derived from HPLC-CHEMTAX and carbon derived from microscopy cell counts. J. Plankton Res. 27, 103–119. <https://doi.org/10.1093/plankt/fbh158>
- Mackey, M.D., Mackey, D.J., Higgins, H.W., Wright, S.W., 1996. CHEMTAX - a program for estimating class abundances from chemical markers: application to HPLC measurements of phytoplankton. Mar. Ecol. Prog. Ser. 144, 265–283. <https://doi.org/10.3354/meps144265>
- Malej, A., Mozetic, P., Maacic, V., Terzic, S., Ahel, M., 1995. Phytoplankton responses to freshwater inputs in a small semi-enclosed gulf Gulf of Trieste, (Adriatic Sea). MEPS 120, 111–121. <https://doi.org/10.3354/meps120111>
- Marić, D., Kraus, R., Godrijan, J., Supić, N., Djakovac, T., Precali, R., 2012. Phytoplankton response to climatic and anthropogenic influences in the north-eastern Adriatic during the last four decades. Estuar. Coast. Shelf Sci. 115, 98–112. <https://doi.org/10.1016/j.ecss.2012.02.003>
- Marini, M., Jones, B.H., Campanelli, A., Grilli, F., Lee, C.M., 2008. Seasonal variability and Po River plume influence on biochemical properties along western Adriatic coast. J. Geophys. Res. 113, C05590. <https://doi.org/10.1029/2007JC004370>
- Martiny A.C., Vrugt J.A., Lomas M.W., 2014. Concentrations and ratios of particulate organic carbon, nitrogen, and phosphorus in the global ocean. Scientific Data 1, 140048. <https://doi.org/10.1038/sdata.2014.48>
- Massuti, M.O., Margalef, R., 1950. Introducción al estudio del plancton Marino. CSIC – patronato Juan de la Cierva de Investigación Científica y Técnica 1–182. <http://hdl.handle.net/10261/160705>
- Menden-Deuer, S., Lessard, E.J., Satterberg, J., 2001. Effect of preservation on dinoflagellate and diatom cell volume and consequences for carbon biomass predictions. Mar. Ecol. Prog. Ser. 222, 41–50. <https://doi.org/10.3354/meps222041>
- Mozetić, P., Solidoro, C., Cossarini, G., Socal, G., Precali, R., Francé, J., Bianchi, F., De Vittor, C., Smolaka, N., Fonda Umani, S., 2010. Recent trends towards oligotrophication of the Northern Adriatic: evidence from chlorophyll a time series. Estuaries Coast. 33, 362–375. <https://doi.org/10.1007/s12237-009-9191-7>
- Mozetić, P., Francé, J., Kogovšek, T., Malej, A., 2012. Plankton trends and community changes in a coastal sea (northern Adriatic): bottom-up vs. top-down control in relation to environmental drivers. Estuar. Coast. Shelf Sci. 115, 138–148. <https://doi.org/10.1016/j.ecss.2012.02.009>
- Olenina I., Hajdu S., Edler L., Andersson A., Wasmund N., Busch S., Göbel J., Gromisz S., Huseby S., Huttunen M., Jaanus A., Kokkonen P., Ledaine I., Niemkiewicz E., 2006. Biovolumes and size-classes of phytoplankton in the Baltic Sea. In: Olenina I., Hajdu S., Edler L., Andersson A., Wasmund N., Busch S., Göbel J., Gromisz S., Huseby S., Huttunen M., Jaanus A., Kokkonen P., Ledaine I., Niemkiewicz E. (Eds.) HELCOM Baltic Sea Environ. Proc. 106, Helsinki, 144 pp.
- Penna, A., Ingarao, C., Ercolessi, M., Rocchi, M., Penna, N., 2006. Potentially harmful microalgal distribution in an area of the NW Adriatic coastline: Sampling procedure and correlations with environmental factors. Estuar. Coast. Shelf Sci. 70, 307–316. <https://doi.org/10.1016/j.ecss.2006.06.023>
- Pfaff, J.D., 1993. *US EPA Method 300.0, Methods for the Determination of Inorganic Substances in Environmental Samples*. EPA-600/R-93-100. NTIS PB94–121811.
- Pizzetti, I., Lupini, G., Bernardi Aubry, F., Aciri, F., Fuchs, B.M., Fazi, S., 2015. Influence of the Po River runoff on the bac-

- terio plankton community along trophic and salinity gradients in the Northern Adriatic Sea. *Mar. Ecol.* 37 (6), 1386–1397. <https://doi.org/10.1111/maec.12355>
- Pugnetti, A., Bazzoni, A.M., Beran, A., Bernardi Aubry, F., Camatti, E., Celussi, M., Coppola, J., Crevatin, E., Del Negro, P., Paoli, A., 2008. Changes in biomass structure and trophic status of the plankton communities in a highly dynamic ecosystem (Gulf of Venice, Northern Adriatic Sea). *Mar. Ecol.* 29, 367–374. <https://doi.org/10.1111/j.1439-0485.2008.00237.x>
- Rampi, L., Bernhard, M., 1980. *Chiave per la Determinazione Delle Peridinee Pelagiche Mediterranee*, C.N.E.N. RT/BIO, (80) 8, 1–193.
- Rodríguez, F., Garrido, J.L., Crespo, B.G., Arbones, B., Figueiras, F.G., 2006. Size-fractionated phytoplankton pigment groups in the NW Iberian upwelling system: impact of the Iberian poleward current. *Mar. Ecol. Prog. Ser.* 323, 59–73. <https://doi.org/10.3354/meps323059>
- Sathyendranath, S., Stuart, V., Nair, A., Oka, K., Nakane, T., Bouman, H., Forget, M.H., Maass, H., Platt, T., 2009. Carbon-to-chlorophyll ratio and growth rate of phytoplankton in the sea. *Mar. Ecol. Prog. Ser.* 383, 73–84. <https://doi.org/10.3354/meps07998>
- Schlüter, L., Møhlenberg, F., Havskum, H., Larsen, S., 2000. The use of phytoplankton pigments for identifying and quantifying phytoplankton groups in coastal areas: testing the influence of light and nutrients on pigment/chlorophyll a ratios. *Mar. Ecol. Prog. Ser.* 192, 49–63. <https://doi.org/10.3354/meps192049>
- Sebastia, M.T., Rodilla, M., 2013. Nutrient and Phytoplankton Analysis of a Mediterranean Coastal Area. *Environ. Manage.* 51, 225–240. <https://doi.org/10.1007/s00267-012-9986-3>
- Sournia, A., 1986. *Atlas du phytoplancton marin. Vol. 1: Cyanophycées, Dictyochophycées, Dinophycées, Raphidophycées*. Centre National de la Recherche Scientifique, Paris.
- Souza, M.S. de, Mendes, C.R.B., Garcia, V.M.T., Pollery, R.C.G., Brotas, V.C., 2012. Phytoplankton community during a coccolithophorid bloom in the Patagonian Shelf: microscopic and high-performance liquid chromatography pigment analyses. *J. Mar. Biol. Assoc. U.K.* 92 (1), 13–27. <https://doi.org/10.1017/S0025315411000439>
- Steidinger, K.A., Tangen, K., 1997. *Dinoflagellates*. In: Tomas, C.R. (Ed.), *Identifying Marine Phytoplankton*. Acad. Press, San Diego, 387–584.
- Talaber, I., Francé, J., Mozetić, P., 2014. How phytoplankton physiology and community structure adjust to physical forcing in a coastal ecosystem. *Phycologia* 53, 74–85. <https://doi.org/10.2216/13-196.1>
- Thronsdon, J., 1997. *The Planktonic Marine Flagellates*. In: Tomas, C.R. (Ed.), *Identifying Marine Phytoplankton*. Acad. Press, San Diego, 591–729.
- Torres, R., Artioli, Y., Kitidis, V., Ciavatta, S., Ruiz-Villarreal, M., Shutler, J., Polimene, L., Martinez, V., Widdicombe, C., Woodward, E.M.S., Smyth T., Fishwick, J., Tilstone, G.H., 2020. Sensitivity of modeled CO₂ air–sea flux in a coastal environment to surface temperature gradients surfactants and satellite data assimilation. *Remote Sens.* 12 (12), 2038. <https://doi.org/10.3390/rs12122038>
- Totti, C., Civitarese, G., Acri, F., Barletta, D., Candelari, G., Paschini, E., Solazzi, A., 2000. Seasonal variability of phytoplankton populations in the middle Adriatic sub-basin. *JPR* 22, 1735–1756. <https://doi.org/10.1093/plankt/22.9.1735>
- Totti, C., Romagnoli, T., Accoroni, S., Coluccelli, A., Pellegrini, M., Campanelli, A., Grilli, F., Marini, M., 2019. Phytoplankton communities in the northwestern Adriatic Sea: Interdecadal variability over a 30-years period (1988–2016) and relationships with meteorological drivers. *J. Mar. Syst.* 193, 137–153. <https://doi.org/10.1016/j.jmarsys.2019.01.007>
- Van der Linde, D., 1998. *Protocol for the determination of total suspended matter in oceans and coastal zone. Technical note No. 1.98.182*. Joint Research Centre, European Commission.
- Viličić, D., Terzić, S., Ahel, M., Burić, Z., Jasprica, N., Carić, M., 2008. Phytoplankton abundance and pigment biomarkers in the oligo-trophic eastern Adriatic estuary. *Environ. Monit. Assess.* 142 (1–3), 199–218. <https://doi.org/10.1007/s10661-007-9920-y>
- Wasmund, N., Nausch, G., Matthäus, W., 1998. Phytoplankton spring blooms in the southern Baltic Sea—spatiotemporal development and long-term trends. *J. Plankton Res.* 20, 1099–1117. <https://doi.org/10.1093/plankt/20.6.1099>
- Wright, S.W., Ishikawa, A., Marchant, H.J., Davidson, A.T., Van Den Enden, R.L., Nash, G.V., 2009. Composition and significance of picophytoplankton in Antarctic waters. *Polar Biol* 32, 797–808. <https://doi.org/10.1007/s00300-009-0582-9>
- Wright, S.W., Jeffrey, S.W., Mantoura, R.F.C., Llewellyn, C.A., Bjoernland, T., Repeta, D., Welschmeyer, N., 1991. Improved HPLC method for the analysis of chlorophylls and carotenoids from marine phytoplankton. *Mar. Ecol. Prog. Ser.* 77, 183–196. <https://doi.org/10.3354/meps077183>
- Zapata, M., Fraga, S., Rodríguez, F., Garrido, J.L., 2012. Pigment-based chloroplast types in dinoflagellates. *Mar. Ecol. Prog. Ser.* 465, 33–52. <https://doi.org/10.3354/meps09879>
- Zavatarelli, M., Raicich, F., Bregant, D., Russo, A., Artegiani, A., 1998. Climatological biogeochemical characteristics of the Adriatic Sea. *J. Mar. Syst.* 18, 227–263. [https://doi.org/10.1016/S0924-7963\(98\)00014-1](https://doi.org/10.1016/S0924-7963(98)00014-1)

Available online at www.sciencedirect.com

ScienceDirect

journal homepage: www.journals.elsevier.com/oceanologia

ORIGINAL RESEARCH ARTICLE

Distribution and characterization of organic matter within the sea surface microlayer in the Gulf of Gdańsk

Abra Penezić^{a,*}, Violetta Drozdowska^{b,*}, Tihana Novak^a,
Blaženka Gašparović^a

^a Division for Marine and Environmental Research, Rudjer Boskovic Institute, 10000, Zagreb, Croatia

^b Physical Oceanography Department, Institute of Oceanology, Polish Academy of Sciences, Sopot, Poland

Received 23 December 2021; accepted 26 May 2022

Available online 8 June 2022

KEYWORDS

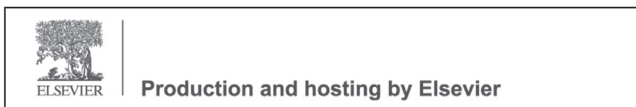
Sea surface microlayer;
Chromophoric dissolved organic matter (CDOM);
Fluorescent organic matter (FDOM);
Surface-active organic substances (SAS);
Marine lipids;
POC

Abstract We present the characterisation and distribution of organic matter (OM) within the sea surface microlayer (SML) and underlying water (ULW) collected in October 2015 at nine stations in the Baltic Sea, Gulf of Gdańsk, encompassing the Vistula River plume. The salinity of >7 throughout the transect indicated Vistula plume was possibly displaced westward by the preceding northerly and easterly winds between 5.7 and 10.7 ms^{-1} during the sampling campaign. Spectral analysis pointed to the highest contribution of aromatic and high molecular weight molecules (lowest spectral slope (S_R) ratios and highest absorption coefficient at 254 nm ($a_{\text{CDOM}}(254)$) at the first two stations near the river mouth, demonstrating a very limited influence of the river plume. Concentrations of surface-active organic substances (SAS) ranged from 0.28 to 0.60 mg L^{-1} in eq. Triton-X-100 in SML, and from 0.22 to 0.47 mg L^{-1} in eq. Triton-X-100 in the ULW, while POC concentrations ranged from 0.27 to 0.84 mg L^{-1} in SML and from 0.20 to 0.37 mg L^{-1} in ULW. Enrichment of SAS and POC detected at the highest wind speeds indicates rapid SML recovery by OM transported from the ULW. Low lipids to POC contribution, on average 5% and 7% in SML and ULW respectively, points to eutrophic conditions. Statistically

* Corresponding authors at: Division for Marine and Environmental Research, Rudjer Boskovic Institute, 10000, Zagreb, Croatia; Physical Oceanography Department, Institute of Oceanology, Polish Academy of Sciences, Sopot, Poland.

E-mail addresses: abra@irb.hr (A. Penezić), drozd@iopan.pl (V. Drozdowska).

Peer review under the responsibility of the Institute of Oceanology of the Polish Academy of Sciences.



<https://doi.org/10.1016/j.oceano.2022.05.003>

0078-3234/© 2023 Institute of Oceanology of the Polish Academy of Sciences. Production and hosting by Elsevier B.V. This is an open access article under the CC BY license (<http://creativecommons.org/licenses/by/4.0/>).

significant negative correlation between S_R and the Lipid:PIG ratio in SML and ULW suggests the production of lower molecular weight OM by phytoplankton living under favourable environmental conditions. Accumulation of lipid reserves triacylglycerols (TG) in the SML indicates more stressful plankton growth conditions compared to ULW.

© 2023 Institute of Oceanology of the Polish Academy of Sciences. Production and hosting by Elsevier B.V. This is an open access article under the CC BY license (<http://creativecommons.org/licenses/by/4.0/>).

1. Introduction

The sea surface microlayer (SML) is an interface between the sea and the atmosphere that affects the processes of mass and energy exchange between the two compartments (Cunliffe et al., 2013; Wurl et al., 2017) and thus affects the global climate. It is defined as the uppermost layer of the sea, up to 1000 μm thick, whose physical and biogeochemical properties differ from those of the underlying water (Hunter, 1997; Zhang et al., 2003). It can be described as a hydrated, gelatinous film in which in-situ produced organic matter (OM) and microorganisms from the deeper layers accumulate along with atmospherically deposited material and pollutants (Engel et al., 2017; Gašparović et al., 1998; Penezić et al., 2021; Robinson et al., 2019; Wurl and Obbard, 2004; Wurl et al., 2017). The formation, thickness and distribution of SML is strongly influenced by meteorological conditions including wind speed (Falkowska, 1999; Liss and Duce, 1997; Stolle et al., 2020). However, it is known that SML recovers quickly after physical disruption (Dragičević and Pravić, 1981; Williams, 1986), mainly through rising bubbles containing organic material adsorbed at the surface (Liss, 1975; Stefan and Szeri, 1999; Woolf, 2005; Wurl et al., 2011). Studies have shown that recovery of SML occurs in all the oceans at wind speeds above average oceanic conditions (Archer and Jacobson, 2005; Sabbaghzadeh et al., 2017; Wurl et al., 2009). Such self-sustainability even at higher sea states, caused by increased bubble fluxes acting as a continuous supply of surface-active material to the SML (Sabbaghzadeh et al., 2017), has strong implications for global air-sea CO_2 exchange. Indeed, the presence of surfactants, which are ubiquitous in the oceans, significantly affects the transport rate of gas across the water surface (Broecker et al., 1978; Frew et al., 1990; Mustaffa et al., 2020; Ribas-Ribas et al., 2017; Tsai et al., 2003; Wurl et al., 2011). Recent studies are beginning to quantify the link between surface-active organic substances (SAS) concentration in SML and gas transfer velocity k_w (Pereira et al., 2016; Rickard et al., 2022).

The marine OM originates mainly from phytoplankton activity, with additional contributions from terrestrial sources through riverine inputs (Gašparović et al., 2011). In coastal waters, especially those under the influence of rivers, increased biological activity leads to increased OM production, with about 70% of dissolved OM being of terrestrial origin (Coble, 2007). A significant portion of marine OM is presented by SAS, consisting of recalcitrant material, such as humic substances, or freshly produced biogenic material, namely carbohydrates, proteins, and lipids (Ćosović et al., 1985; Gašparović et al., 2011). Lipid content in phytoplankton ranges from ≤ 1 to 46% of dry weight

(Romankevich, 1984). Phytoplankton exudates, through direct release or zooplankton grazing, metabolic processes, and cell lysis, are the main source of marine lipids, which vary in composition depending on the phytoplankton community and environmental conditions (Novak et al., 2019).

Lipids are important organic biomarkers used to determine OM sources due to their specific functions in different cell types (Parrish, 1988; Parrish et al., 2000). They are less susceptible to degradation than carbohydrates or proteins. Harvey et al. (1995) found that under oxic conditions carbohydrates are recycled within 15 days, proteins within 41 days, and lipids within 77 days. Saturated lipids have been shown to be highly resistant to degradation. Gašparović et al. (2016, 2018) found an increase in saturated lipids of up to 30-fold from the surface to abyssal depths (4800 m) of the North Atlantic, while at the same time particulate organic carbon decreased by 90%. Membrane lipids, such as phospholipids and glycolipids, are indicators of living organisms, free fatty acids can indicate degradation processes, while the ratio between specific lipid classes can serve as an indicator of organisms' adaptation to changes in environmental conditions (Derieux et al., 1998; Gašparović et al., 2014, 2016; Gerin and Goutx, 1994; Goutx et al., 2003; Novak et al., 2019). Lipids are also an important factor in carbon sequestration in the ocean – their buoyancy contributes to their surface activity, facilitating both their accumulation at the sea surface and their adsorption to sinking particles, which transports them to deeper layers (Gašparović et al., 2016; Novak et al., 2019). Some organic molecules, especially fulvic and humic acids, can absorb light due to their optically active parts, and are referred to as chromophoric dissolved organic matter (CDOM), a class of molecules additionally including fluorescent dissolved organic matter (FDOM), which can emit part of the absorbed light as fluorescence (Drozdowska et al., 2015; Marcinek et al., 2020). As an important optical constituent of seawater, CDOM absorbs primarily in the ultraviolet to the blue spectral region and can absorb up to 90% of solar radiation in the 400–500 nm spectral range in coastal waters, which can affect primary production (Arrigo and Brown, 1996; Belanger et al., 2008; Zhao et al., 2018). Optical characterization methods of OM provide a rapid and reliable way to detect and identify dissolved organic matter (DOM) and additionally give insight into DOM transformation processes (Drozdowska et al., 2017; Stedmon et al., 2003) such as DOM removal through photodegradation or microbial activities (Lei et al., 2020). This is particularly important for coastal areas with intense riverine inputs and high primary production, where optical characterization can help distinguish between DOM of marine and terrestrial origin (Coble, 1996; Drozdowska, 2007; Marcinek et al.,

2020). Biotic and abiotic OM processing at the air–sea interface impacts the ocean carbon cycle (Johannessen et al., 2001) and leads to the formation of volatile organic compounds (VOC), which are potential precursors for secondary organic aerosols (SOA) that strongly influence cloud formation and contribute to Earth's solar radiation balance (Bruggemann et al., 2018; Mayer et al., 2020). The mentioned processes, such as air–water gas exchange, carbon sequestration, VOC formation and others, are of global importance, and are all affected by OM distribution and processing, with different OM classes playing their own important roles in the exchange of energy and matter between the sea and the atmosphere. Therefore, characterization of the marine OM, especially considering the air–sea interface, is essential to deepen our understanding of the feedback between these two largest environmental niches.

In this study, we primarily focused on investigating the links between different organic matter classes within the SML and the underlying water (ULW) at 1 m depth, in the Gulf of Gdańsk, a coastal area in the southern part of the Baltic Sea, influenced by the Vistula River. This study is an extension of the work of Drozdowska et al. (2017), which compared the spectroscopic and fluorescence properties of SML and ULW samples during three different field campaigns (in April 2015, October 2015, and September 2016) collected at the same transect. During the October 2015 campaign, in addition to CDOM and FDOM analysis, additional characterization of OM in the SML and ULW was performed, namely SAS, particulate organic carbon (POC), and particulate lipids and their classes, with the aim of further exploring the specific links between different OM groups and properties, in addition to considering the influence of wind, an important driver of the physical and biogeochemical properties of SML. Thus, the objectives of this study were i) to investigate the properties and spatial distribution of different types of OM in the SML and ULW in a transect in the Gulf of Gdańsk encompassing the Vistula River plume, ii) to identify sources of OM, iii) to identify processes responsible for the distribution of OM and to evaluate the influence of winds on the establishment of SML, and iv) to investigate the relationships between the OM optical properties and OM surface activity.

2. Material and methods

2.1. Study area

The study area included a transect in the southern Baltic Sea, more specifically in the Gulf of Gdańsk, starting at the Vistula River mouth and extending about 47 km toward the open sea (Figure 1, Table S1). The brackish Baltic Sea is characterised by a high water residence time due to poor exchange with the North Sea through the Danish Straits (Szymczak-Żyła et al., 2019). This and its large catchment area make it vulnerable to eutrophication, anoxia, and the impacts of pollutants (Pędziński and Witak, 2019; Szymczak-Żyła et al., 2019). Between the early and late 20th century intensive inputs of nitrogen and phosphorus increased four-fold and eightfold, respectively (Glasby and Szefer, 1998; Larsson et al., 1985), promoting eutrophication, reducing water transparency, and causing a shift from macrophyte- to phytoplankton-dominated systems in some areas of the

Baltic Sea (Andrén, 1999). Vistula River, the longest river in the Baltic Sea catchment, with a length of 1047 km and an average flow of 1080 m³ s⁻¹ (Buszewski et al., 2005), brings the largest amounts of total nitrogen and phosphorus (about 65 and 60%, respectively) (HELCOM, 2018) and, despite recent reductions in nutrient inputs (HELCOM, 2018; Pastuszek et al., 2012), contributes to eutrophication, especially in the Gulf of Gdańsk area. The Gulf of Gdańsk is a highly eutrophic area with large-scale growth of filamentous brown algae, extensive summer blooms of cyanobacteria, and high Chl *a* concentrations (Kruk-Dowgiallo, 1996; Mazur-Marzec et al., 2006). Due to the considerable input of terrestrial OM, which affects its optical and biological properties (Kowalczyk et al., 2006), the Gulf of Gdańsk has also been recognized as a sink for particulate matter of both autochthonous and allochthonous origin (Drozdowska et al., 2002; Drozdowska and Fateyeva, 2013; Maksymowska et al., 2000; Piskozub et al., 1998). The dynamic conditions of this coastal area make it particularly interesting as a study site for the characterisation of different OM classes and their interactions.

2.1.1. Sampling and sample treatment

Sampling was conducted at nine stations (Figure 1) between October 15th and 16th, 2015. The exact locations of the stations, indicated by W1–W9, are given in Table S1. The ULW samples were collected from a depth of 1 m, using a 10 L Niskin water sampler, while the SML samples were collected using a 50 × 50 cm stainless steel Garret net, mesh size 18 (a wire thickness 0.36 mm and the mesh eye size 1 mm), which approximates the thickness of the collected SML to 500 μm. The SML sampling procedure is described in detail in Drozdowska et al. (2017) and in the Supplementary Information (Figure S1). Briefly, samples were collected from onboard the *r/v Oceania*, by vertically immersing the screen and waiting for the microlayer to stabilize before carefully lifting the screen horizontally through the water surface at a speed of approximately 5–6 cm s⁻¹. In windy conditions, it is necessary to hold the ship bow to wind, so that the screw – astern and about 1 m below the water surface – is idling, i.e. spinning slowly, but this does not disturb the stability of the surface water amidships. Exceptionally, during water sampling on this cruise, in high wind conditions, the ship was oriented with its head to the wind to minimize disturbance of the wind field and potential contamination from the ship, while samples were collected from the bow (Sabbaghzadeh et al., 2017; Salter et al., 2011). The shape of the hull of *r/v Oceania*, tapering downwards, allows the surface water to be reached by the Garret Screen from a distance of approximately 1–3 m from the ship's side, further minimizing potential contamination. The samples were poured into polyethylene bottles through a special slit in the screen frame. Aliquots of the collected samples were used for the determination of SAS, which were determined on board immediately after sampling and without filtration. Aliquots collected for absorbance and fluorescence measurements were placed unfiltered in dark containers and stored at 4°C until measurement within 48 h of sampling. Aliquots for particulate lipid measurements were first filtered through a metal mesh with a pore size of 200 μm to avoid sampling organisms larger than phytoplankton and large organic particles. Samples were then filtered through

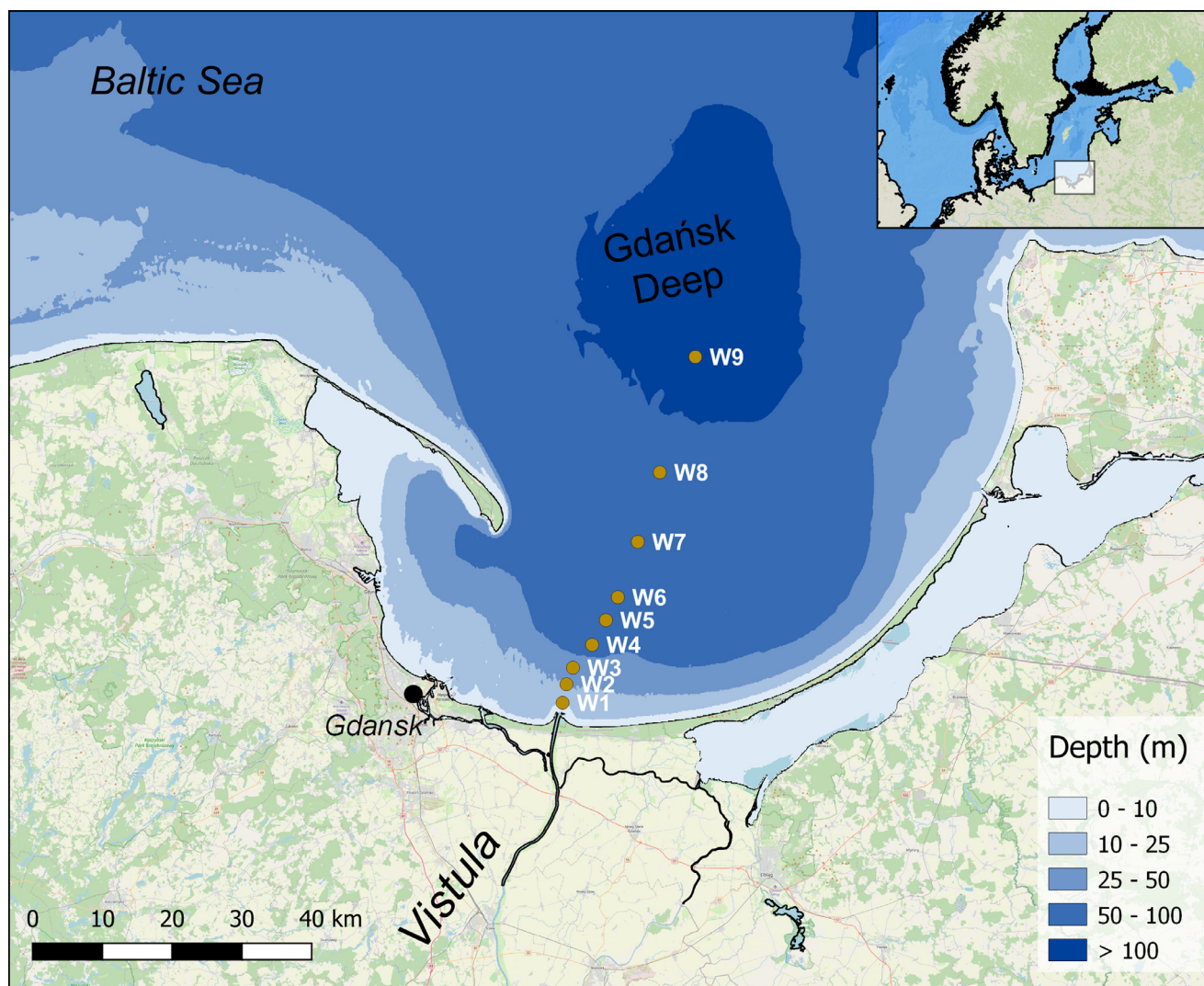


Figure 1 Sampling stations (W1–W9) in the Gulf of Gdańsk, the southern Baltic Sea. Map made with QGIS (QGIS Development Team 2018; <http://qgis.osgeo.org>, accessed on November 12th, 2021).

glass fibre filters with a pore size of $0.7 \mu\text{m}$ (GF/F Whatman, Buckinghamshire, UK). The filters were then placed in cryotubes, frozen in liquid nitrogen and stored at -20°C until analysis. Prior to use, the filters were pre-burned at 450°C for 4 hours to remove possible organic contaminants. The same filter types and storage procedure were used to collect the POC samples. All glassware used for filtration was washed with chromic sulfuric acid and rinsed with ultrapure water (Merck Millipore, Burlington, Massachusetts, USA) to avoid organic contaminants. Salinity and sea surface temperature were measured during sampling at a depth of 0.6–0.9 m, using a CTD probe (SeaBird SBE 49, Bellevue, Washington, USA).

2.1.2. Statistical analysis

Pearson's correlation coefficient matrix was used to test correlations between different parameters, while two-sample t-test was used to test for significant differences between datasets means. Statistical analysis was done in Origin 7 (Origin Lab, USA).

2.2. Organic matter analysis

2.2.1. Particulate organic carbon analysis

POC was determined using an SSM-5000A solid sample module, connected to a TOC-VCPH (Shimadzu, Japan) carbon analyser calibrated with glucose. Samples were acidified with 2 mol L^{-1} HCl, to remove the inorganic carbonate fraction, folded, and placed in alumina ceramic sample boats, followed by drying at 50°C for 12 hours (Giani et al., 2005; Ryba and Burgess, 2002). The samples were then burned at 900°C in a stream of oxygen. The produced CO_2 is detected using a non-dispersive infrared (NDIR) detector. POC concentrations were corrected using measurements of blank filters, which were subjected to the same procedure as the samples. The value obtained by the average filter blank, which includes the instrument blank, is $5 \mu\text{g C L}^{-1}$. The calibration was made with glucose standards in the range between 0 and $200 \mu\text{g}$ organic carbon, giving the reproducibility of the method of 3% and a limit of detection of $5 \mu\text{g C L}^{-1}$.

2.2.2. Chromophoric and fluorescent organic matter analysis

The results of chromophoric and fluorescent analysis of organic matter have already been published in the study by Drozdowska et al. (2017), where more details on the analytical procedures can be found, but are also briefly presented here. Samples collected for CDOM and FDOM analysis were not filtered, to characterise the total OM and to maintain consistency with SAS determination, as it is assumed that filtration removes a significant amount of surfactants (Schneider-Zapp et al., 2013). In previous studies, we observed that the differences between filtered and non-filtered samples were in the short UV and far VIS ranges, but did not cause significant changes in the absorption indices, as these were based on the relative differences between the values of $a_{\text{CDOM}}(\lambda)$ determined between the two affected ranges (Drozdowska et al., 2017). Moreover, filtration affects the fluorescence spectral bands only for the protein-type T component, with the differences being the same for SML and ULW (Drozdowska et al., 2018, 2017). Being aware of the limitations of the methods used, we decided to conduct the measurements on the unfiltered samples but to keep the CDOM and FDOM nomenclature (Drozdowska and Józefowicz, 2015).

Absorbance measurements were carried using a Perkin Elmer Lambda 650 spectrophotometer (Perkin Elmer, Waltham, Massachusetts, USA). The uncertainty of the instrument for the absorbance signal is less than 0.001. For a 10 cm path length quartz cuvette, the systematic error of the measurement on the spectrophotometer is constant and is 0.023 cm^{-1} . The recorded spectral range was between 240 and 700 nm using ultrapure water as the reference signal. The recorded absorbance $A(\lambda)$ spectra were processed to obtain CDOM absorption coefficients curves $a_{\text{CDOM}}(\lambda)$, m^{-1} . Next, a non-linear least-squares fitting method was applied (Stedmon et al., 2000) to calculate the spectral slope coefficient ($S_{\Delta\lambda}$) in two spectral ranges: 275–295 and 350–400 nm, $S_{275-295}$ and $S_{350-400}$, respectively. The ratio of the two spectral slope coefficients, $S_{275-295}$ and $S_{350-400}$, is known as the slope ratio (S_R) and serves as an indicator of the molecular weight and source of OM; higher molecular weight molecules, which are also more likely to be of allochthonous origin, have a low S_R (Helms et al., 2008). The standard deviations (SD) of $S_{275-295}$ and $S_{350-400}$ did not exceed 2% of their values, while the maximum uncertainty of the measurement and SD of S_R did not exceed 6% and 3%, respectively.

Fluorescence excitation emission matrix (EEM) spectra were obtained using a Cary Eclipse scanning spectrofluorometer (Agilent Technologies, Santa Clara, California, USA), with samples measured in a 1 cm path length quartz cuvette. A series of emission scans (280–600 nm at 2 nm resolution) were measured over an excitation wavelength range between 250 and 500 nm in 10 nm increments. To standardize fluorescence intensity measurements to Raman units, RU (Murphy et al., 2010), i.e., to ensure comparability of results, a scan of ultrapure water is performed on each measurement day. The EEM spectrum of the ultrapure water allows control of instrument parameters and to count the energy of the Raman scattering band between 375–425 nm, for the spectrum excited at 350 nm. The calculated value is

used to correct the EEM spectra of the SML and ULW water samples.

2.2.3. Lipid analysis

Lipid material collected on GF/F filters was extracted by using a modified procedure described by Bligh and Dyer (1959), with n-hexadecanone added as an external standard for calculating the sample recovery. The detailed procedure is explained in Gašparović et al. (2014, 2015, 2017) and is briefly presented here. Lipid extracts were evaporated to dryness under a stream of nitrogen and redissolved in 14 to 20 μL of dichloromethane. Aliquots of 2 μL of the redissolved sample were spotted onto silica-coated quartz thin-layer chromatography rods, where the samples were developed in a series of seven developing baths with a mixture of increasingly polar organic solvents. After development, lipids were analysed using a thin layer chromatography – flame ionization detector (TLC-FID) Iatroscan MK-VI (Iatron, Japan) at a hydrogen flow rate of 160 ml min^{-1} and an air flow rate of 2000 ml min^{-1} , and quantified using external calibration with lipid class standards. Each sample was analysed between two and four times. Limits of detection (LODs) were determined as the analyte concentrations corresponding to a signal-to-noise (S/N) ratio of 3. The lipid classes analysed and their LODs are as follows: hydrocarbons (HC), LOD = 0.10 μg ; triacylglycerols (TG), LOD = 0.20 μg ; wax and steryl esters (WE), LOD = 0.10 μg ; fatty acid methyl esters (ME), LOD = 0.22 μg ; ketones (KET), LOD = 0.25 μg ; free fatty acids (FFA), LOD = 0.15 μg ; fatty alcohols (ALC), LOD = 0.20 μg ; 1,3-diacylglycerols (1,3 DG), LOD = 0.33 μg ; sterols (ST), LOD = 0.15 μg ; 1,2-diacylglycerols (1,2 DG), LOD = 0.15 μg ; pigments (PIG), LOD = 0.25 μg ; monoacylglycerols (MG), LOD = 0.15 μg ; monogalactosyldiacylglycerols (MGDG) LOD = 0.23 μg , digalactosyldiacylglycerols (DGDG), LOD = 0.21 μg ; sulfoquinovosyldiacylglycerols (SQDG), LOD = 0.06 μg ; mono- and di-phosphatidylglycerols (PG), LOD = 0.27 μg , phosphatidylethanolamines (PE), LOD = 0.11 μg ; and phosphatidylcholines (PC), LOD = 0.14 μg . The percent recoveries of the samples were calculated from the ratio of the recovered n-hexadecanone mass and the theoretical n-hexadecanone mass originally added to the sample. The recovery averaged $117 \pm 16\%$. The final concentration of particulate lipid (C) was then calculated based on the mass of lipid (m) obtained with the calibration equations, the volume of the sampled seawater (V_{sample}), the percentage of the spotted sample (% spotted), and the lipid recovery (% recovery) using the following equation:

$$C = \frac{\left(\frac{m \times 100}{V_{\text{sample}}}\right) / (\% \text{ spotted})}{\% \text{ recovery}} \times 100 \quad (1)$$

2.2.4. Surface-active substances analysis

Surface-active substances were determined electrochemically by alternating current (AC) voltammetry (Ćosović, 2005; Ćosović and Vojvodić, 1998) using a portable potentiostat (Palmsens, Houten, The Netherlands). The three-electrode system consisted of a hanging mercury drop working electrode, an Ag/AgCl (3M KCl) reference electrode, and a platinum wire counter electrode. Only the capacitive component of the current is measured by AC voltammetry

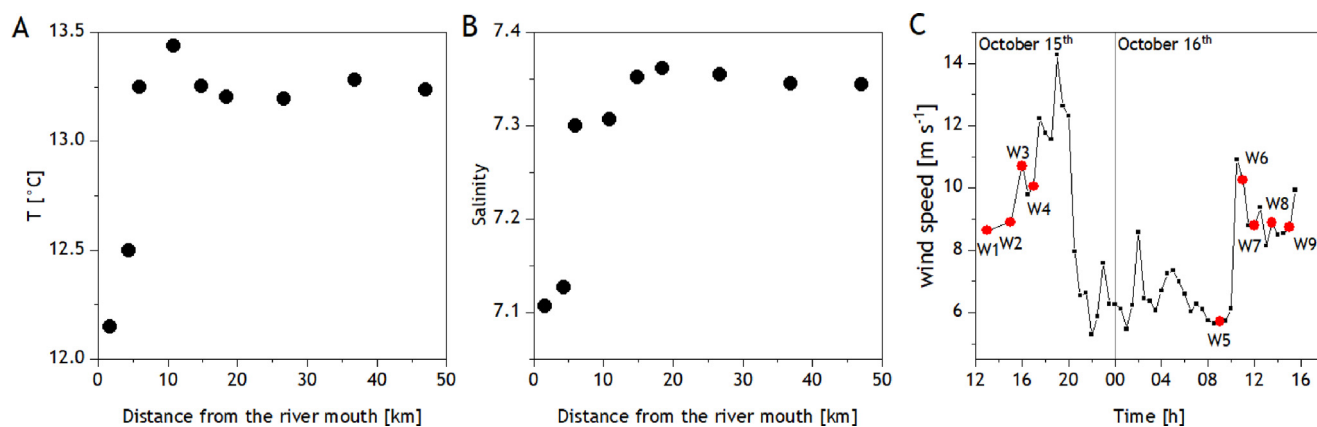


Figure 2 Sea surface temperature (A) and salinity (B), along with average wind speed (C) recorded throughout the field campaign and the transect.

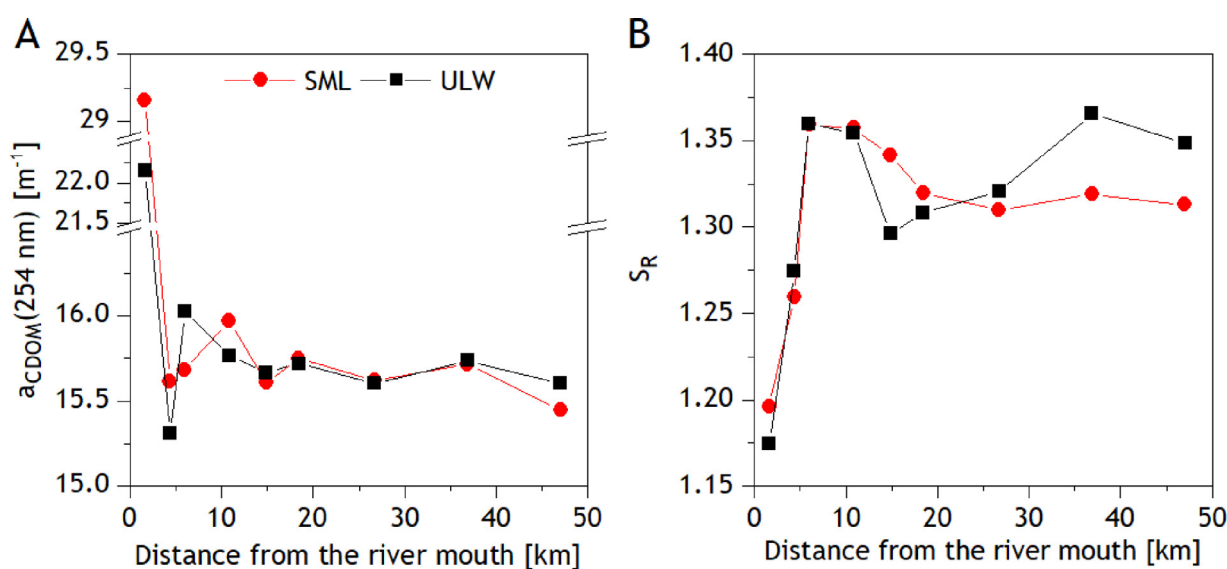


Figure 3 The CDOM absorption coefficient at 254 nm, $a_{\text{CDOM}}(254)$ (A) and spectral slope ratio (S_R) (B) determined for sea surface microlayer (SML) (circles) and underlying water (ULW) (squares) samples.

and the concentration of SAS is estimated from calibration curves obtained with a nonionic surfactant Triton-X-100 (T-X-100), which serves as a good model compound (Frka et al., 2009). Calibration was performed in 0.5 M NaCl, and the determined LOD of the method was 0.07 mg L⁻¹ eq. Triton X-100. The ionic strength of the samples was adjusted to 0.5 M by adding saturated NaCl before the measurements.

3. Results

3.1. Oceanographic parameters

Data on sea surface temperature and salinity, along with wind speed are shown in Figure 2. The lowest temperatures, 12.1 and 12.5°C, were measured at stations W1 and W2, which are closest to the river mouth. Thereafter, a slight increase was observed, and the temperature remained between 13.2 and 13.4°C throughout the transect. Salinity

was lowest near the river mouth at stations W1 and W2, at about 7.1, which is, however, higher than expected for the Vistula Estuary and indicates a strong mixing of the fresh and seawater (Drozdowska et al., 2017; Schiewer and Schernewski, 2002). This was to be expected as meteorological conditions in October 2015 just prior to the field campaign included a strong northerly wind blowing from the open Baltic Sea to the coast of Poland, which changed to predominantly easterly winds throughout the field campaign. The presence of easterly/south-easterly winds and westerly surface currents (Figure S2) may have shifted the Vistula plume to the west of the studied transect. Therefore, the influence of the river was difficult to discern. Only the slightly lower salinity at stations near the river mouth, e.g., W1 and W2, indicated the influence of the Vistula plume. At the times of sampling, which was performed mainly in the afternoon hours (Table S1), wind speed varied between 5.7 m s⁻¹ and 10.7 m s⁻¹ with values mostly above 8.5 m s⁻¹. The lowest wind speed was observed after a calm night between

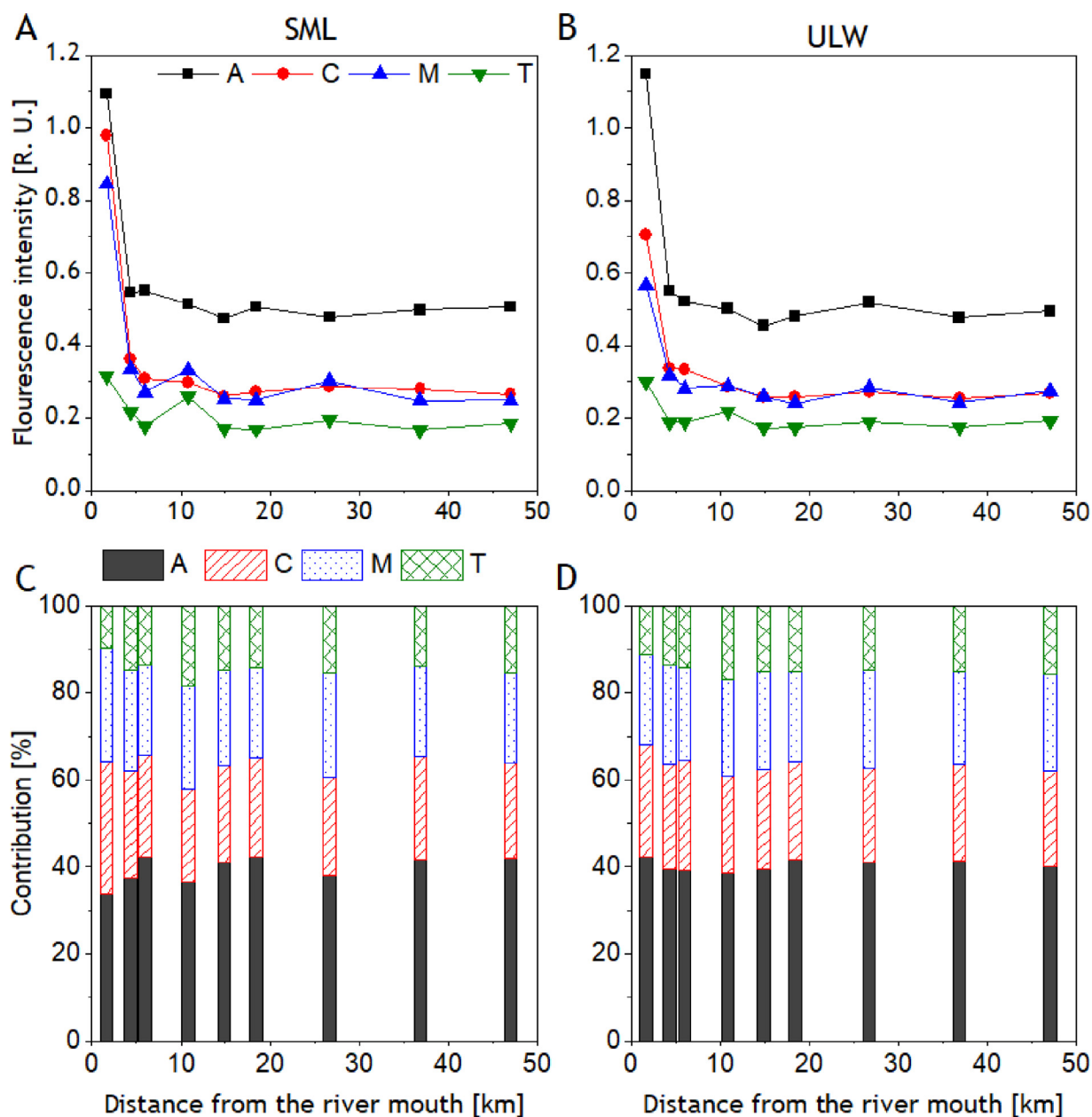


Figure 4 Fluorescence intensities of main FDOM components (A and B) and percentage composition of terrestrial UV humic-like substances (A), terrestrial visible humic-like substances (C), marine humic-like substances (M), and proteinaceous substances (T) (C and D) of the sea surface microlayer (SML) (A and C) and underlying water (ULW) (B and D) throughout the transect.

October 15th and 16th, which resulted in sample W5 being sampled during the calmest conditions of the field campaign (Figure 2).

3.2. Chromophoric organic matter

Based on the UV/VIS spectra of SML and ULW samples, the absorption coefficients at 254 nm ($a_{CDOM}(254)$) were determined (Figure 3), which are specific for aromatic molecules absorbing at this wavelength. The highest $a_{CDOM}(254)$ in SML was determined at station W1, followed by a significant decrease at W2, with the lowest $a_{CDOM}(254)$ determined at station W9, farthest from the Vistula River. A similar distribu-

tion was observed in the ULW, with the highest $a_{CDOM}(254)$ determined at W1, and a significant decrease at W2, which was in fact the lowest observed $a_{CDOM}(254)$ value in the ULW. The slope ratio (S_R) in the SML ranged from 1.20 at station W1 to 1.36 at stations W3 and W4, while in ULW the lowest ratio was also observed at station W1 (1.17) and the highest at W8 (1.37).

Fluorescence intensities and contribution of each component to FDOM composition in the SML and ULW are shown in Figure 4. Fluorescence intensities of the major FDOM components: A, C, M and T, expressed in Raman units (R. U.), are used as proxies of the different FDOM types. Peak A is attributed to terrestrial UV humic-like

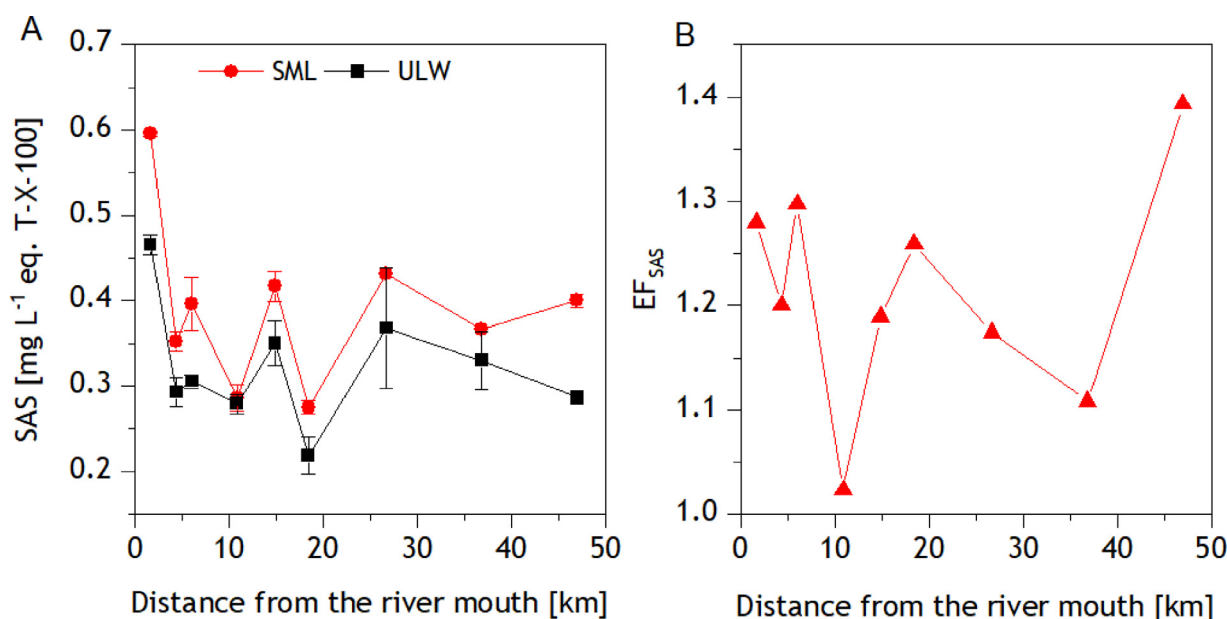


Figure 5 Distribution of surface-active organic substances (SAS) in the sea surface microlayer (SML) (circles) and underlying water (ULW) (squares) (A) and SAS enrichment factors (B) throughout the transect.

substances (ex./em. – excitation and emission – 250/437 nm); peak C represents terrestrial visible-humic like substances (ex./em. 310/429 nm); peak M characterizes marine humic-like substances (ex./em. 300/387 nm) and peak T represents proteinaceous substances (ex./em. 270/349 nm) (Loiselle et al., 2009; Zhang et al., 2013a). The values of the (M+T):(A+C) ratios are given in Table S2. The ratios allow an assessment of the relative contribution of DOM recently produced in situ (M+T) to terrestrial humic substances (A+C), which are characterized by highly complex structures with high molecular weight (Parlanti et al., 2000). Values of the ratio (M+T):(A+C) >1 indicate the predominance of autochthonous DOM, while values of <0.6 indicate allochthonous/anthropogenic DOM (Drozdowska et al., 2015).

The levels of FDOM components were only slightly higher in the SML than in the ULW. The difference between the means in SML and ULW was not statistically significant according to the two-sample t-test. The percent composition of FDOM components varied most within the first 15 km of the transect at stations W1–W4, while in the remainder of the transect the contributions of each component remained fairly constant in both SML and ULW. The contribution of UV humic-like substances (A) averaged 40% in both SML and ULW. In the SML it ranged from 34% at W1 to 42% at W3 and in ULW from 39% at W3 to 42% at W1. Terrestrial visible humic-like substances (C) contributed an average of 24% in the SML and 23% in the ULW to FDOM composition and were highest at W1, near the river mouth, in both SML and ULW. They ranged from 21% at W3 to 30% at W1 in SML, and from 22% at W7 to 26% at W1 in ULW. Marine humic-like substances (M) contributed an average of 22% to the FDOM composition of SML and ULW, ranging from 21% at W9 to 26% at W1 in the SML, and from 21% at W1 to 23% at W2 in the ULW. The contribution of proteinaceous material (T) was distributed differently compared to other components. At station W1, their contribution was lowest in both SML and ULW, 10% and

11%, respectively, while the highest contribution was found at station W4, 18% and 17% in the SML and ULW, respectively. The average contribution of proteinaceous material across the transect was 15% in both SML and ULW.

3.3. Surface-active substances

Concentrations of SAS in the SML and ULW throughout the transect are shown in Figure 5A and listed in Table S2. Concentrations in the SML ranged from 0.28 ± 0.01 mg L⁻¹ to 0.60 ± 0.00 mg L⁻¹ in eq. T-X-100, with an average value of 0.39 ± 0.09 mg L⁻¹ in eq. T-X-100, while in the ULW they ranged from 0.22 ± 0.02 mg L⁻¹ to 0.47 ± 0.01 mg L⁻¹ in eq. T-X-100, with an average value of 0.32 ± 0.07 mg L⁻¹ in eq. T-X-100. The highest concentrations were determined at the river mouth, at station W1, and the lowest at station W6, in both the SML and ULW. A statistically significant positive correlation was found between the concentration of SAS in the SML and in the ULW ($r = 0.937$, $p < 0.001$).

The enrichment factor (EF), defined as the ratio of SAS concentrations determined in the SML and ULW, showed that all SML samples were enriched in SAS (Figure 5B). Enrichment factors ranged from 1.0 to 1.4 (Table 2), with the lowest EF observed at station W4 and the highest at station W9, which is farthest from the river mouth (Figure 5B).

3.4. Particulate organic carbon and particulate lipids

The distribution of POC and particulate lipids in the SML and ULW and the corresponding EFs are shown in Figure 6. The POC value determined at station W4 was extremely low (0.004 mg L⁻¹), suggesting measurement error, and was therefore not considered in further analysis. Table 1 shows the concentrations of total particulate lipids and lipid classes determined in the SML and ULW. POC concentrations

Table 1 Concentrations of particulate total lipids and lipid classes (\pm SD) in the sea surface microlayer (SML) and underlying (ULW) in the analyzed transect.

SML ($\mu\text{g L}^{-1}$)																		
Station	Membrane lipids										Intracellular reserve lipids			Degradation indices				
	Total	HC	ST	PIG	MGDG	DGDG	SQDG	PG	PE	PC	WE	ME	TG	FFA	ALC	1,3 DG	1,2 DG	MG
W1	37.30 \pm 4.07	\pm 1.75	\pm 0.73	\pm 1.14	\pm 1.20	\pm 4.50	\pm 5.09	\pm 3.76	\pm 0.83	\pm 2.13	\pm 0.29	\pm 3.16	\pm 5.76	\pm 0.59	\pm 0.91	\pm 1.38	\pm 0.02	\pm 1.79
	1.79	0.35	0.02	0.04	0.02	0.04	0.23	0.60	0.46	0.12	0.29	0.09	0.02	0.56	0.07	0.01	0.27	0.00
W2	35.80 \pm 2.85	\pm 1.63	\pm 0.73	\pm 3.89	\pm 1.26	\pm 5.12	\pm 4.05	\pm 2.62	\pm 0.81	\pm 1.25	\pm 0.12	\pm 3.39	\pm 5.82	\pm 0.51	\pm 0.45	\pm 1.29	\pm 0.02	\pm 1.82
	0.09	0.14	0.06	0.45	0.07	0.61	0.21	0.04	0.02	0.13	0.05	0.60	0.56	0.05	0.16	0.08	0.00	
W3	28.16 \pm 1.87	\pm 1.35	\pm 0.78	\pm 2.81	\pm 1.61	\pm 2.41	\pm 5.36	\pm 2.07	\pm 0.67	\pm 0.59	\pm 0.23	\pm 3.15	\pm 3.58	\pm 0.58	\pm 0.53	\pm 0.53	\pm 0.05	\pm 1.48
	0.11	0.03	0.10	0.03	0.07	0.38	0.32	0.09	0.06	0.10	0.01	0.24	0.49	0.08	0.05	0.02	0.02	
W4	27.82 \pm 1.75	\pm 1.17	\pm 1.29	\pm 1.67	\pm 1.79	\pm 3.63	\pm 5.35	\pm 2.04	\pm 0.79	\pm 0.54	\pm 0.19	\pm 1.12	\pm 4.69	\pm 0.95	\pm 0.38	\pm 0.44	\pm 0.03	\pm 1.58
	0.02	0.05	0.14	0.06	0.25	0.05	0.71	0.03	0.10	0.21	0.11	0.22	0.42	0.02	0.07	0.03	0.00	
W5	30.65 \pm 4.41	\pm 1.15	\pm 0.70	\pm 1.83	\pm 1.94	\pm 5.70	\pm 4.69	\pm 2.36	\pm 0.85	\pm 0.60	\pm 0.07	\pm 0.83	\pm 3.79	\pm 0.81	\pm 0.43	\pm 0.50	\pm 0.01	\pm 1.94
	0.40	0.03	0.11	0.10	0.20	0.48	1.03	0.10	0.12	0.13	0.02	0.03	0.80	0.08	0.04	0.10	0.00	
W6	33.04 \pm 2.45	\pm 1.13	\pm 0.79	\pm 6.20	\pm 1.56	\pm 5.06	\pm 5.03	\pm 1.86	\pm 0.73	\pm 1.19	\pm 0.05	\pm 1.67	\pm 3.38	\pm 0.62	\pm 0.59	\pm 0.73	\pm 0.01	\pm 1.70
	0.25	0.20	0.13	0.47	0.16	0.39	0.30	0.06	0.01	0.04	0.02	0.13	0.31	0.10	0.07	0.24	0.00	
W7	34.99 \pm 2.21	\pm 1.29	\pm 1.08	\pm 6.23	\pm 1.95	\pm 5.88	\pm 4.19	\pm 2.28	\pm 0.75	\pm 0.78	\pm 0.26	\pm 1.18	\pm 4.83	\pm 0.96	\pm 0.44	\pm 0.67	\pm 0.01	\pm 2.12
	1.18	0.04	0.27	0.14	0.08	0.90	0.34	0.01	0.03	0.16	0.09	0.24	0.39	0.34	0.21	0.07	0.00	
W8	34.20 \pm 2.22	\pm 1.25	\pm 1.08	\pm 4.13	\pm 1.69	\pm 5.78	\pm 5.29	\pm 1.90	\pm 0.96	\pm 0.77	\pm 0.19	\pm 1.10	\pm 5.73	\pm 0.98	\pm 0.42	\pm 0.68	\pm 0.01	\pm 1.69
	0.08	0.06	0.14	0.32	0.06	0.43	0.03	0.17	0.02	0.11	0.13	0.19	0.75	0.01	0.08	0.27	0.00	
W9	31.44 \pm 2.16	\pm 1.35	\pm 0.92	\pm 3.42	\pm 1.80	\pm 5.37	\pm 3.85	\pm 0.95	\pm 0.61	\pm 0.79	\pm 0.36	\pm 2.86	\pm 5.24	\pm 0.61	\pm 0.44	\pm 0.69	\pm <LOD	\pm 1.96
	0.21	0.15	0.38	0.23	0.42	0.84	0.55	0.03	0.09	0.05	0.00	0.05	0.51	0.30	0.01	0.03		

ULW ($\mu\text{g L}^{-1}$)																		
Station	Membrane lipids										Intracellular reserve lipids			Degradation indices				
	Total	HC	ST	PIG	MGDG	DGDG	SQDG	PG	PE	PC	WE	ME	TG	FFA	ALC	1,3 DG	1,2 DG	MG
W1	22.73 \pm 1.54	\pm 1.04	\pm 0.43	\pm 1.10	\pm 0.79	\pm 4.32	\pm 3.33	\pm 3.03	\pm 0.62	\pm 0.62	\pm 0.11	\pm 0.91	\pm 3.31	\pm 0.41	\pm 0.58	\pm 0.54	\pm 0.01	\pm 1.42
	0.05	0.06	0.22	0.02	0.21	0.01	0.26	0.07	0.01	0.06	0.05	0.04	0.61	0.00	0.06	0.28	0.00	
W2	28.66 \pm 1.50	\pm 1.86	\pm 0.47	\pm 1.18	\pm 1.08	\pm 5.07	\pm 3.81	\pm 3.46	\pm 1.00	\pm 0.21	\pm 0.10	\pm 1.81	\pm 5.70	\pm 0.43	\pm 0.29	\pm 0.66	\pm 0.02	\pm 1.61
	0.09	0.11	0.02	0.21	0.14	0.04	0.29	0.48	0.14	0.01	0.03	0.50	0.36	0.08	0.01	0.07	0.00	
W3	25.03 \pm 1.48	\pm 1.06	\pm 1.11	\pm 2.41	\pm 1.64	\pm 2.44	\pm 5.75	\pm 1.72	\pm 0.88	\pm 0.22	\pm 0.18	\pm 1.08	\pm 3.43	\pm 0.91	\pm 0.35	\pm 0.33	\pm 0.05	\pm 1.58
	0.05	0.18	0.01	0.24	0.13	0.55	0.42	0.22	0.03	0.01	0.10	0.19	0.01	0.28	0.05	0.03	0.01	
W4	26.05 \pm 1.47	\pm 1.09	\pm 1.63	\pm 1.81	\pm 1.90	\pm 2.93	\pm 5.36	\pm 2.21	\pm 0.74	\pm 0.24	\pm 0.25	\pm 0.96	\pm 3.66	\pm 0.93	\pm 0.44	\pm 0.42	\pm 0.02	\pm 1.20
	0.15	0.06	0.23	0.08	0.07	0.03	0.04	0.15	0.04	0.02	0.00	0.23	0.24	0.07	0.01	0.01	0.00	
W5	21.50 \pm 1.28	\pm 0.75	\pm 0.85	\pm 1.20	\pm 1.27	\pm 5.11	\pm 4.28	\pm 1.78	\pm 0.63	\pm 0.27	\pm 0.03	\pm 0.62	\pm 2.13	\pm 0.63	\pm 0.23	\pm 0.44	\pm 0.01	\pm 1.86
	0.37	0.19	0.20	0.14	0.10	0.50	0.70	0.09	0.08	0.09	0.04	0.06	0.59	0.09	0.09	0.13	0.00	
W6	28.48 \pm 1.64	\pm 0.90	\pm 0.70	\pm 1.38	\pm 1.84	\pm 5.79	\pm 6.92	\pm 2.28	\pm 0.51	\pm 0.45	\pm 0.16	\pm 0.50	\pm 3.83	\pm 0.73	\pm 0.30	\pm 0.54	\pm 0.01	\pm 2.72
	0.45	0.15	0.22	0.43	0.09	1.39	3.05	0.40	0.02	0.23	0.09	0.08	0.13	0.24	0.18	0.24	0.00	
W7	29.35 \pm 1.69	\pm 1.07	\pm 1.08	\pm 2.78	\pm 1.84	\pm 5.79	\pm 5.57	\pm 2.24	\pm 0.86	\pm 0.20	\pm 0.03	\pm 0.68	\pm 3.86	\pm 1.00	\pm 0.22	\pm 0.44	\pm 0.01	\pm 2.24
	0.53	0.15	0.21	0.18	0.07	0.44	0.39	1.05	0.12	0.15	0.05	0.22	1.07	0.21	0.12	0.05	0.00	
W8	23.26 \pm 1.20	\pm 0.78	\pm 1.27	\pm 1.65	\pm 1.35	\pm 4.05	\pm 3.55	\pm 1.92	\pm 0.51	\pm 0.95	\pm 0.21	\pm 0.43	\pm 3.69	\pm 1.08	\pm 0.25	\pm 0.37	\pm 0.01	\pm 1.36
	0.04	0.11	0.46	0.10	0.05	0.21	0.03	0.14	0.02	0.11	0.03	0.02	0.42	0.07	0.02	0.04	0.00	
W9	30.65 \pm 1.98	\pm 0.88	\pm 1.45	\pm 4.98	\pm 1.82	\pm 6.08	\pm 3.47	\pm 1.15	\pm 0.77	\pm 0.39	\pm 0.13	\pm 1.64	\pm 4.77	\pm 0.57	\pm 0.30	\pm 0.28	\pm <LOD	\pm 2.71
	0.02	0.06	0.04	1.20	0.35	0.71	0.40	0.16	0.17	0.20	0.10	1.24	2.18	0.25	0.06	0.18		

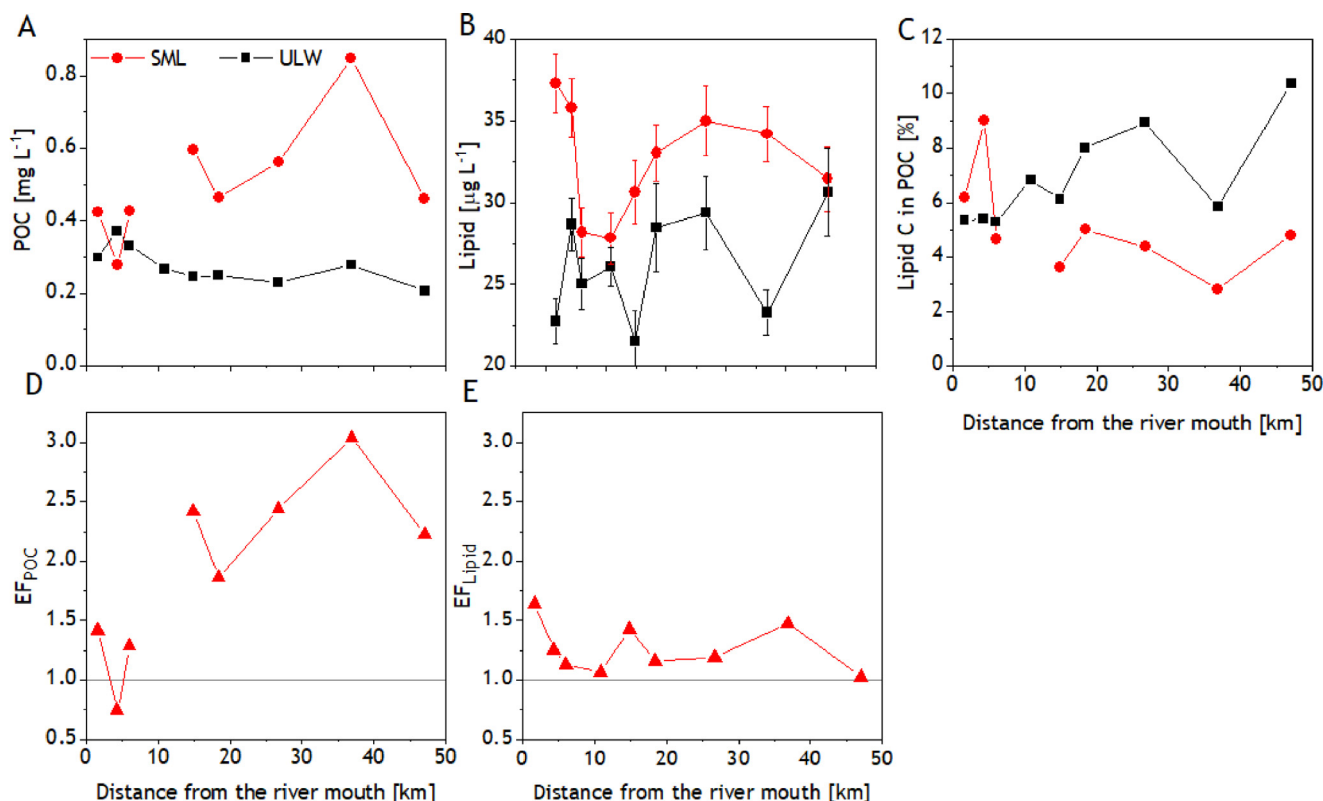


Figure 6 The distribution of particulate organic carbon (POC) (A), particulate lipids (B) and the contribution of particulate lipid carbon to POC (C) in the sea surface microlayer (SML) (circles) and the underlying water (ULW) (squares), along with the enrichment factors (EF) of POC (D) and lipids (E) throughout the transect.

in the SML ranged from 0.27 mg L^{-1} to 0.84 mg L^{-1} , with an average value of $0.51 \pm 0.17 \text{ mg L}^{-1}$, while they were significantly lower in the ULW (two-sample t-test, $p = 0.001$), with an average value of $0.27 \pm 0.05 \text{ mg L}^{-1}$ and ranging from 0.20 mg L^{-1} to 0.37 mg L^{-1} . The lowest POC values in the SML were determined at stations W1–W3, while the highest POC concentrations in the ULW were found at the same stations (1.3–3.0) except station W2 (0.8), with an average enrichment factor of 1.9 ± 0.7 and an increasing trend from the river mouth toward the open sea.

The average concentration of particulate lipids in the SML was $32.60 \pm 3.32 \text{ } \mu\text{g L}^{-1}$, ranging from $27.82 \pm 1.58 \text{ } \mu\text{g L}^{-1}$ to $37.30 \pm 1.79 \text{ } \mu\text{g L}^{-1}$. In the ULW, the average concentration was $26.19 \pm 3.26 \text{ } \mu\text{g L}^{-1}$, much lower than in the SML (two-sample t-test, $p < 0.001$), ranging from $21.50 \pm 1.86 \text{ } \mu\text{g L}^{-1}$ to $30.65 \pm 1.94 \text{ } \mu\text{g L}^{-1}$, with a slightly increasing trend toward the open sea. Particulate lipids were enriched in all SML samples, on average 1.26 ± 0.21 , with the lowest enrichment at station W9 (1.03) and the highest enrichment at station W1 (1.6) (Figure 6). The fraction of particulate lipid carbon in POC ranged from 2.8 to 9.0% (average 5.1%) in the SML and from 5.3 to 10.4% (average 6.9%) in ULW. With the exception of stations W1 and W2, which are closest to the river mouth, the contribution of lipids to POC was higher in the ULW than in the SML, with a statistically significant difference in means, when W1 and W2 are excluded from the analysis (two-sample t-test, $p = 0.003$)

(Figure 6C). The contribution of lipids to POC in the ULW showed an increasing trend toward the open sea.

Lipid classes can be divided into three groups based on their functions. Membrane lipids include the phospholipids (PG, PE and PC) and ST, which are components of planktonic plasma membranes (Cantarero et al., 2020), and the glycolipids (GL): MGDG, DGDG, SQDG, and PIG, which are found in thylakoid membranes and are indicators of autotrophs (Guschina and Harwood, 2009).

Triacylglycerols, WE and ME indicate metabolic reserves of phytoplankton and zooplankton (Arts, 1999). Lipid classes including FFA, ALC, 1,2 DG, 1,3 DG, and MG indicate lipid degradation processes and are referred to as degradation indices (Goutx et al., 2003). The distribution and concentrations of the three groups of lipids are shown in Figure 7. Membrane lipids were the most abundant group, with an average concentration of $19.94 \pm 2.28 \text{ } \mu\text{g L}^{-1}$ in the SML, and $17.78 \pm 2.44 \text{ } \mu\text{g L}^{-1}$ in the ULW. Membrane lipids accounted for an average of $61 \pm 6\%$ of particulate lipids in SML and $68 \pm 4\%$ in ULW, and statistically significant positive correlations were found between the concentrations of PIG ($r = 0.802$, $p = 0.009$), DGDG ($r = 0.677$, $p = 0.045$), SQDG ($r = 0.817$, $p = 0.007$), and PE ($r = 0.768$, $p = 0.015$) in SML and ULW. The average concentration of degradation indices in the SML was $6.79 \pm 1.25 \text{ } \mu\text{g L}^{-1}$, while in the ULW it was $5.35 \pm 0.96 \text{ } \mu\text{g L}^{-1}$, with a statistically significant difference between the two means (two-sample t-test, $p = 0.014$). The degradation indices accounted for an average of $21 \pm 3\%$

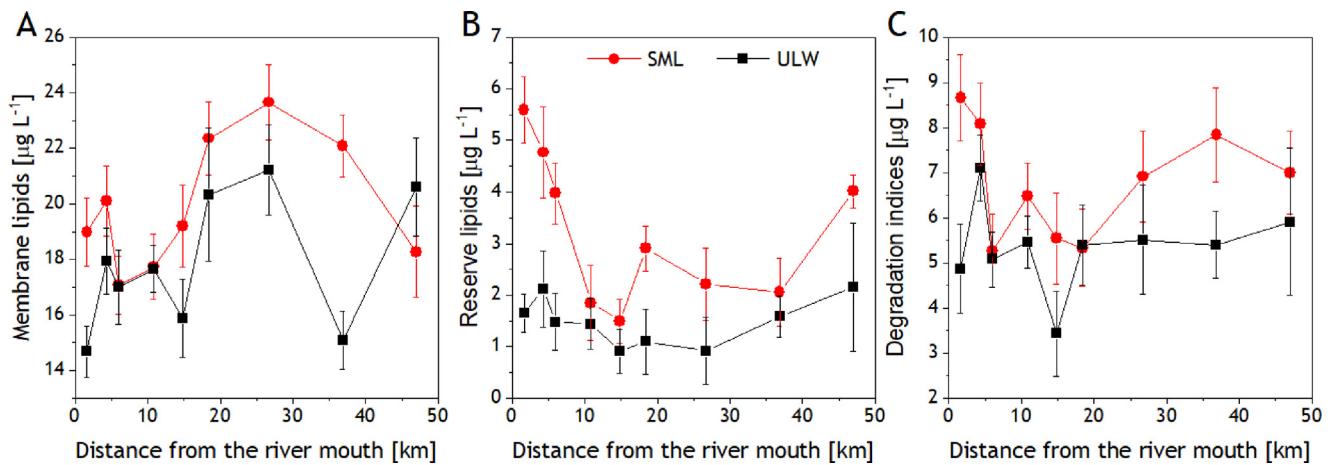


Figure 7 Distribution and concentrations of total membrane lipids (GL, PL, ST and PIG) (A), total reserve lipids (WE, ME and TG) (B) and total degradation indices (FFA, ALC, 1,2 DG, 1,3 DG, MG) (C) in sea surface microlayer (SML) (circles) and underlying water (ULW) (squares) throughout the transect.

and $20 \pm 3\%$ of particulate lipids in SML and ULW, respectively. Statistically significant correlations were found between the concentrations of ALC ($r = 0.762$, $p = 0.017$), 1,3 DG ($r = 0.738$, $p = 0.023$), 1,2 DG ($r = 0.709$, $p = 0.032$), MG ($r = 0.952$, $p < 0.001$) in the SML and ULW.

The lowest concentrations determined were those of reserve lipids, with an average value of $3.21 \pm 1.44 \mu\text{g L}^{-1}$ in the SML and a slightly, but still significantly lower (two-sample t-test, $p = 0.003$) value of $1.48 \pm 0.46 \mu\text{g L}^{-1}$ in the ULW. Reserve lipids accounted for $10 \pm 4\%$ and $6 \pm 2\%$ of the particulate lipids in the SML and ULW, respectively. A statistically significant correlation was found between the concentrations of TG ($r = 0.754$, $p = 0.019$) in SML and ULW.

Hydrocarbons are present in living organisms and account for approximately 1% of the lipid content of marine microorganisms (Sargent et al., 1976). The concentration of hydrocarbons in the particulate fraction ranged from 1.75 to 4.41 $\mu\text{g L}^{-1}$ in the SML and from 1.20 to 1.98 $\mu\text{g L}^{-1}$ in the ULW.

The concentration of glycolipids (MGDS, SQDG and DGDG) increased toward the open sea, especially in the ULW. Oppositely, the concentration of PL in both SML and ULW decreased slightly with distance from the river mouth.

The enrichment in SML was observed for all lipid classes, with reserve lipids showing the highest enrichment, e.g., on average there was 2.9 times more WE in the SML than in the ULW.

Environmental conditions such as nutrient availability, light conditions, and temperature affect the biochemistry of phytoplankton by potentially directing biosynthetic pathways toward the production of different biomolecules, i.e., protein synthesis is favoured under good, non-stressful growth conditions, while lipid synthesis is favoured under stressful conditions (Gašparović et al., 2014, Gerin and Goutx, 1994). The Lipid:Chl *a* ratio (Gerin and Goutx, 1994) is often used to evaluate the biosynthetic pathways of photosynthetic communities. Using particulate pigment (PIG) concentration data, which provide a rough estimate of autotrophic plankton biomass, we calculated the ratio of particulate lipids and PIG in the SML and ULW (Figure 8). The ratio showed a sharp decrease from stations W1–W2 near

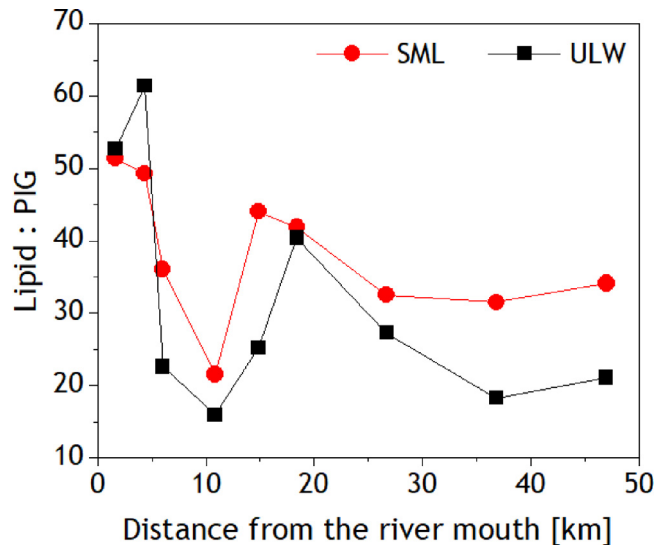


Figure 8 Lipid:PIG ratios in sea surface microlayer (SML) (circles) and underlying water (ULW) (squares) throughout the transect.

the river mouth to stations W3–W4, which are about 5–10 km from the river mouth, after which an increase was observed toward station W5.

The statistically significant negative correlations observed between S_R and the Lipid:PIG ratio in SML ($r = -0.718$, $p = 0.029$) and ULW ($r = -0.795$, $p = 0.010$) (Figure 9) point to a possible relationship between the environmental conditions of phytoplankton growth and the molecular weight of OM produced.

The PE:PG ratios (indicating the predominant bacterial or phytoplankton biomass) (Table S2) ranged from 0.25 to 0.74 in the SML and from 0.33 to 0.91 in the ULW. The highest values were observed at stations W1 and W2 in both SML and ULW, followed by a significant decrease at stations W3 and W4. Wax esters, indicators of zooplankton, were enriched in the SML compared to the ULW (Table 2). The high-

Table 2 Concentration ranges of surface-active organic substances (SAS) and the enrichment factor (EF) ranges in the sea surface microlayer (SML) and underlying water from 1 m depth (ULW), determined in this study, along with results from other similar studies.

Location (sampling method)	SML thickness (μm)	SAS (mg L^{-1} eq. T-X-100)		EF	Reference
		SML	ULW		
Baltic Sea; Vistula plume (metal screen)	~500	0.28–0.60	0.22–0.47	1.0–1.4	This study
Middle Adriatic; coastal (metal screen)	260 \pm 40	0.25 \pm 0.06 – 0.79 \pm 0.54	0.06 \pm 0.02 – 0.30 \pm 0.13	1.4–5.1	Frka et al., 2009
W Atlantic; Mauritania (metal screen)	465 \pm 34	0.22 \pm 0.18	0.16 \pm 0.07	1.5 \pm 0.7	Barthelmess et al., 2021
North Sea (metal screen)	65–80	0.15–1.96	0.09–1.70	0.9–1.6	Rickard et al., 2022
North Sea (metal screen)	65–80	0.08 \pm 0.01 – 0.38 \pm 0.04	0.09 \pm 0.02 – 0.28 \pm 0.01	0.75 \pm 0.17 – 1.90 \pm 0.71	Pereira et al., 2016.
Norwegian Sea; fjords (metal screen)	100–150	0.12–0.21	0.07–0.14	1.21–2.8	Gašparović et al., 2007.
Baltic Sea and North Sea (glass discs)	60–100	0.31 \pm 0.03 – 0.60 \pm 0.63	0.13 \pm 0.03 – 0.49 \pm 0.05	0.9 \pm 0.2 – 3.9 \pm 3.3	Ribas-Ribas et al., 2017
North Sea; Jade bay (glass discs)	~50–80	0.05–0.81	0.20–0.29	0.6–1.0	Rickard et al., 2019
N Atlantic; N Pacific, nearshore (0-2 km) (glass plate)	50–120	0.11–4.99		0.5–5.9	Wurl et al., 2011
N Atlantic; N Pacific, offshore (2-20 km) (glass plate)	50–120	0.11–1.26		0.6–5.0	Wurl et al., 2011
E Pacific; Santa Barbara channel (glass plate)	50 \pm 10	0.21–0.83	0.11 – 0.637	3.6–3.9	Wurl et al., 2009
Atlantic transect 2014 (metal screen)		0.12–1.00	0.10–0.36	0.95–4.52	Sabbaghzadeh et al., 2017
Atlantic transect 2015 (metal screen)		0.12–1.76	0.08–0.91	0.97–3.47	Sabbaghzadeh et al., 2017

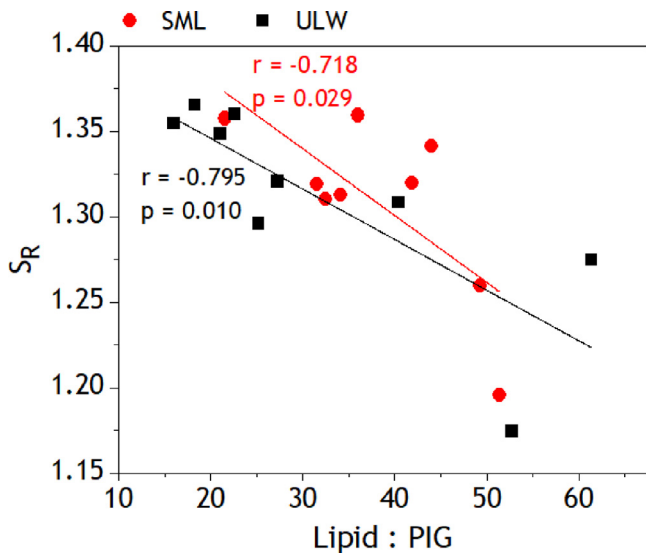


Figure 9 Correlation between the slope ratio (S_R) and the Lipid:PIG ratio for sea surface microlayer (SML) (circles) and underlying water (ULW) (squares) throughout the transect.

est concentration of WE was measured in the SML at station W1, closest to the river mouth.

4. Discussion

4.1. Estimation of river propagation to the Gulf of Gdańsk

In the absence of topographic boundaries, the Vistula Estuary connects freely to the adjacent coastal waters of the Gulf of Gdańsk. The Vistula River plume usually has a horizontal extension of approximately 4–30 km from the river mouth with a thickness between 0.5 and 12 m (Cyberska and Krzywiński, 1988; Grelowski and Wojewodzki, 1996), supplying the Gulf of Gdańsk with terrestrial organic matter. However, the strong northerly winds prior and the easterly winds during the field campaign (Figure S2) caused a strong mixing of the surface waters, probably pushing the Vistula plume westward out of its usual direction (Drozdowska et al., 2017) and increasing salinity to >7 throughout the studied transect. The influence of the river was therefore difficult to discern, and the slight increase in salinity and decrease in temperature from stations W1 and W2 toward the open sea indicated that it was mainly confined to the two stations near the river mouth. As shown by our previous study, which includes this (October 2015) and two other field campaigns (April 2015 and September 2016) along the same transect, the intense mixing of fresh and seawater had an impact on the distribution of OM, based on analysis of its optical properties (Drozdowska et al., 2017). During the April 2015 and September 2016 campaigns, calm, windless sea conditions prevailed, and most importantly, a salinity gradient allowed us to distinguish between coastal waters under the influences of the Vistula River (<7) and seawater (>7), which was not the case during the October 2015 campaign (the

campaign analysed in this study). The most striking differences between April 2015, September 2016 and this campaign were observed for the stations closest to the river mouth. The absorption coefficients $a_{CDOM}(254)$ were higher in April 2015 and September 2016, than in campaign discussed here. The changes in S_R values spanned a range three times larger in April 2015 and September 2016 (Figures 3A, 3B, S3 and S4) (Drozdowska et al., 2017). All FDOM components had significantly higher intensities in both SML and ULW in April 2015 and September 2016 compared to this campaign, especially at stations W1 and W2 (Figures 4 and S5), likely due to calmer weather conditions that allowed for greater influence of riverine material on the surface coastal waters. Fluorescence intensities obtained for this campaign in October 2015, were reasonably comparable to those observed in April 2015 and September 2016 only in waters with salinity >7 , again indicating the very limited influence of the Vistula River and a strong seawater intrusion in October 2015. However, the contribution of the different FDOM components determined in April 2015 and September 2016 was not significantly different from those determined for this campaign, probably because most of the samples in April 2015 and September 2016 actually had salinity >7 .

During the October 2015 campaign, significantly higher $a_{CDOM}(254)$ in the SML and ULW at station W1 compared to all other stations indicate the strongest presence of riverine chromophoric DOM closest to the river mouth, while lower values determined for the two layers at stations W2–W9 indicate the removal of CDOM, probably by photodegradation/transformation (Oberosterer et al., 2008), as well as dilution processes of riverine OM upon entering the Gulf (Pereira et al., 2016). Similar $a_{CDOM}(254)$ absorption coefficient values determined in SML and ULW (Figure 3A) confirmed a well-mixed upper water column, although no statistically significant correlation was found between SML and ULW values.

4.2. Biogeochemistry of SML and ULW

In addition to the optical characterisation from the previous study (Drozdowska et al., 2017), the additional characterization of OM presented in this study helped reveal some biogeochemical processes within the Vistula plume.

The $a_{CDOM}(254)$, an indicator of the presence of aromatic molecules, showed no significant correlation with HC concentrations in SML and ULW, possibly due to the fact that this class of lipids was neither highly aromatic nor of anthropogenic origin, as these mainly have an aromatic structure (Patel et al., 2020). In addition, HC concentrations were below $10 \mu\text{g L}^{-1}$ in both SML and ULW, which is another indication that no significant source of hydrocarbon pollution was present. A slight decrease in $a_{CDOM}(254)$ values with an increasing concentration of SAS observed in the SML, but not in the ULW (Figure S6), suggests that an increase in OM surface activity does not necessarily imply an increase in OM aromaticity, complementing the lack of correlation between $a_{CDOM}(254 \text{ nm})$ and HC.

4.2.1. High wind does not prevent POC accumulation in the SML

Concentrations of POC in our study were comparable to those in other coastal areas (Gašparović et al., 2007,

Penezić et al., 2021, Stolle et al., 2010), but higher than those observed in the Atlantic Ocean (Van Pinxteren et al., 2017). Despite high wind speeds, we observed POC enrichment at all stations except at W2, although no relationship with wind speed was observed. Similar results are obtained by Van Pinxteren et al. (2017), who sampled in both low (2–5) and high ($>5 \text{ m s}^{-1}$) wind conditions. In contrast, Obernosterer et al. (2008) showed a significant negative correlation between POC enrichment in the SML and wind blowing 6 h prior to sampling, where all recorded wind speeds were $<3 \text{ m s}^{-1}$. Stolle et al. (2010), on the other hand, observed the formation of a slick in the southern Baltic Sea at $<2 \text{ m s}^{-1}$ wind speed, which resulted in very high POC concentrations in the SML ($\approx 9 \text{ mg L}^{-1}$), leading to an enrichment factor of up to 26.8.

4.2.2. The active role of surface-active substances in the (re)establishment of SML

The determined concentrations of SAS in the SML and ULW were comparable to those reported by other authors using the same analytical method (calibration with Triton-X-100 as the model compound), for coastal areas, but also for the open sea (Table 2). The same was observed for the enrichment factors, despite different sampling techniques, different locations, weather conditions and different thicknesses of the sampled SML. Despite high wind speeds, SAS were enriched in the SML, although no statistically significant correlation was found between the two parameters. These enrichments confirm the rapid recovery of the SML by transport and accumulation of OM from the subsurface, as observed earlier (Dragičević and Pravić, 1981; Liss, 1975; Wurl et al., 2009; Sabbaghzadeh et al., 2017). This is particularly evident in the case of SAS that have a high affinity for the air/water interface. A high positive correlation was found between SAS concentrations in the SML and ULW, with a similar linear dependence ($\text{SAS}_{\text{ULW}} = 0.690 \times \text{SAS}_{\text{SML}} + 0.052$) as derived by Pereira et al. (2016) ($\text{SAS}_{\text{ULW}} = 0.766 \times \text{SAS}_{\text{SML}} + 0.018$). Our result supports the observation that ULW constantly replenishes SAS in the SML (Cunliffe et al., 2013; Pereira et al., 2016) and reinforces the discussion about the self-sustainability of the SML with respect to its surface activity, even in strong wind conditions.

4.2.3. Lipids, biomarkers of the trophic conditions

Determined concentrations of particulate lipids in ULW ($21.5\text{--}30.6 \mu\text{g L}^{-1}$) and SML ($27.8\text{--}37.3 \mu\text{g L}^{-1}$) are generally lower compared to other studies of mostly more oligotrophic areas (e.g., Penezić et al., 2010 ($47.9 \mu\text{g L}^{-1}$ particulate lipids in SML and $46.4 \mu\text{g L}^{-1}$ in ULW); Triesch et al., 2021 (concentrations of particulate lipids: $36.4\text{--}93.5 \mu\text{g L}^{-1}$ in SML and $61.0\text{--}118.1 \mu\text{g L}^{-1}$ in ULW)). However, lipid enrichments were observed at all stations (Figure 6E).

Significantly higher concentrations of total lipids, reserve lipids, and degradation indices in SML compared to ULW (Figures 6 and 7, Table 1) indicated a richer plankton community in the SML than in the ULW, although non-living OM may have contributed to both POC and lipid pools. This suggests the Baltic SML as the layer of more favourable trophic conditions for plankton development. The SML enrichment

of reserve lipids (Figure 7B) suggests that the plankton in the SML grew under more stressful conditions compared to the ULW, because these lipids are known to accumulate in phytoplankton under adverse environmental conditions, whereas optimal phytoplankton growth usually results in lower lipid cell content (Bourguet et al., 2009; Novak et al., 2019; Sharma et al., 2012). In particular, conditions such as lack of nutrients, as well as an increase in temperature can influence lipid composition and production, which usually leads to an accumulation of lipids (Novak et al., 2018; Sharma et al., 2012). The observed increase in GL concentration with increasing distance from the river mouth, especially evident in the ULW, can be related to the expected decrease in nutrient concentration at greater distance from the Vistula Estuary (Pastuszak et al., 2012) and points to one of the adaptive mechanisms of phytoplankton to low nutrient conditions, namely intensified synthesis of phosphorus- and nitrogen-free molecules such as glycolipids MGDG, SQDG, and DGDG (Frka et al., 2011). On the other hand, the decreasing concentrations of PL with increasing distance from the river mouth indicate a lower availability of phosphorus, since the synthesis of phospholipids depends on P availability.

The trophic conditions of a system can also be indicated by the contribution of particulate lipids to POC, which can exceed 30% in oligotrophic conditions (Frka et al., 2011; Marić et al., 2013; Gašparović et al., 2014). The low contribution of lipids to POC found in this study (Figure 6c), as low as 2.8% and predominantly less than 10%, is more characteristic for eutrophic areas. The change in trophic conditions along the transect was observed by an increasing contribution of lipids in the POC with increasing distance from the river mouth observed in the ULW. In the ULW the contribution of lipid to POC was generally higher than in the SML, especially at stations W3 to W9. The lower contribution of lipids to POC observed in SML suggests that nutrients were more available to phytoplankton in the SML than in the ULW, except at stations close to the river mouth (W1 and W2). This is plausible considering that OM degradation and remineralization are faster in SML due to biotic (bacteria) (Tank et al., 2011; Zhang et al., 2013b) and especially abiotic (photooxidation and autoxidation by free radical-mediated oxidation (Rontani and Belt, 2020)) processes. Higher concentrations of lipid degradation indices in SML (Figure 7c) confirm higher OM degradation and remineralization in this layer, while the presence, but not the enrichment, of bacterial biomarker PE in SML confirms the importance of the simultaneous effects of abiotic OM processing in the SML (Table 2). In addition, according to Reinthaler et al. (2008), bacterial growth in the SML is low and bacterioneuston only maintains its cellular mass, while Stolle et al. (2010) found that the productivity of the bacterioneuston is not, or only weakly, associated with the change in the amount of OM in SML.

4.2.4. OM origin

Statistically significant correlations between the concentrations of PIG, DGDG, SQDG, and PE in SML and ULW, suggest that the ULW was the origin of plankton lipid classes in the SML, rather than the presence of independent plankton populations in the two layers. The enrichment of membrane

lipids (Figure 7A) confirms the enrichment of living plankton in the SML (Derieux et al., 1998).

While PE are the most abundant phospholipids in marine bacteria (Gerin and Goutx, 1993), PG are the major phospholipids in microalgae (Dembitsky and Rozentsvet, 1990; Harwood, 2006). The PE:PG ratio is thus used as an indicator of bacterial or phytoplankton biomass dominance; PE:PG ratios between 0 and 0.3 indicate phytoplankton dominance, and >0.3 bacterial dominance (Gerin and Goutx, 1994). The values of PE:PG ratio, which were mostly above 0.3 in the transect (Table S2), indicate a significant presence of bacteria in both layers (Table S2), while a statistically significant positive correlation between the concentrations of PE in the SML and ULW points to the interconnection of the two layers. The highest ratios observed for W1 and W2 in both SML and ULW indicate the highest bacterial biomass, probably supported by riverine originated OM and nutrients.

The high PIG concentrations detected in both SML and ULW samples at 10 km from the river mouth (station W4, Table 2), indicated rich phytoplankton biomass, most likely due to good growing conditions. The evaluated low Lipid:PIG ratios (Figure 8) suggested reduced lipid accumulation expected for plankton growth under optimal environmental conditions (e.g. Novak et al., 2019). An increase in the contribution of the “T” component in the fluorescence intensities at station W4 from an average of 14% to 18% (Figure 4C and D) in SML and from an average of 15% to 18% in ULW, indicated the presence of freshly produced proteinaceous material, further confirming significant plankton activity at W4. This observation was possible because the measurements were performed in unfiltered samples, which allowed detection of the freshly produced proteinaceous material that tends to form gel-like structures and would otherwise have been retained on the filter (Drozdowska et al., 2018). The highest values of the (M+T):(A+C) ratio (Table S2) observed at station W4 also indicated a slightly higher contribution of OM of marine origin at this station, compared to the other stations, likely due to the assumed increase in primary production.

In addition to indicating the photochemically induced shift in molecular weight (Helms et al., 2008), S_R can also be used as an indicator of phytoplankton biomass, leading to an increase in autochthonous OM that contains a higher proportion of low molecular weight compounds (Santos-Echeandía et al., 2012; Zhang et al., 2013b). A significant increase in S_R at stations W3 and W4 (Figure 3B) also suggested an increase in phytoplankton primary production. The statistically significant negative correlation between S_R and the Lipid:PIG ratio (Figure 9) underlined that primary production was directed toward the production of lower molecular weight OM by phytoplankton growing under favourable environmental conditions.

The lowest observed (M+T):(A+C) ratio that was determined at station W1 in the ULW provided a slight indication of a higher contribution of terrestrial humic substances of high molecular weight. However, based on the (M+T):(A+C) ratios, which averaged 0.57 in the SML and 0.56 in the ULW, OM can only be classified as being of mixed marine and terrestrial/anthropogenic origin (Drozdowska et al., 2015; Osburn et al., 2014). Another indication of the dominance of higher molecular weight terrestrial OM at stations W1 and

W2 was the lowest observed S_R slope ratio determined for the ULW and SML.

Wax esters, primarily reserve lipids of zooplankton with amphiphilic properties, may dominate the reserve lipid pool in freshwater zooplankton (Arts, 1999). The WE detected in our samples most likely originated from the microzooplankton, since the samples were prefiltered with a net with a pore size of 200 μm . The active movement of microzooplankton toward a richer food source in SML resulted in WE having one of the highest enrichments in the SML compared to all other lipid classes analysed.

5. Conclusions

Characterization of OM along the transect in the eutrophic coastal area of the Gulf of Gdańsk, partially encompassing the Vistula River plume, provided insights into the biogeochemical processes affecting the OM distribution in the SML and ULW.

The rapid establishment of SML in strong winds was confirmed by the enrichment of SAS and POC detected even at the highest wind speeds and throughout the transect, while the highly positive, statistically significant correlation between SAS concentrations in the SML and ULW indicated the rapid resupply of SAS in the SML from the ULW.

Due to the wind blowing before and during the campaign, the small influence exerted by the Vistula River within the studied transect was limited to a few kilometres narrow area near the river mouth (stations W1 and somewhat W2), as shown mainly by the optical properties of OM. Station W1 was characterized by the highest values of the absorption coefficient at 254 nm in both SML and ULW, together with the lowest S_R ratios observed at W1 and W2, indicating the highest contribution of aromatic and high molecular weight molecules as well as terrestrial visible humic-like substances, implied by the highest observed fluorescence intensities at W1 and W2. The highest concentrations of total particulate lipids in SML, especially groups comprising reserve lipids and degradation indices, were detected at W1 and W2, pointing to intense degradation processes in the surface microlayer, which was further confirmed by the highest observed PE:PG ratios in the SML and ULW, as an indicator of high bacterial biomass. The enrichment of lipid degradation indices in the SML and the lack of the bacterial biomarker PE enrichment, suggest that OM was subjected to more abiotic (photooxidation and autoxidation) and/or biotic reworking/remineralization processes in the SML than in the ULW. The most intense biological activity was observed at W4, as indicated by the highest PIG concentrations and the lowest Lipid:PIG ratio in the SML and ULW. Analysis of the distribution of the Lipid:PIG ratio led to the observation of a statistically significant negative correlation between the S_R and the Lipid:PIG ratio in both SML and ULW, linking the favourable environmental conditions for phytoplankton growth to the production of lower molecular weight OM.

The complexity of physical, chemical, and biochemical factors, including photochemistry, winds, biological productivity and activity, that determine OM distribution, makes it difficult to show a clear (de)coupling between SML and ULW. However, our observations with respect to specific classes

and groups of OM suggest that the ULW is the major supplier of OM to the SML, leading to its enrichment by some OM classes. The similar distribution in SML and ULW and the lack of “enrichment” of optical indices point to the similar type of material in both layers, which potentially lacks significant surface activity. Thus, the coupling of SML and ULW is highly dependent on the specific properties of the analysed OM as well as external factors. The relationships and dependencies shown here represent a valuable step toward better understanding the biogeochemistry of surface coastal waters.

Declaration of competing interest

The authors declare that they have no known competing financial interests or personal relationships that could have appeared to influence the work reported in this paper.

Acknowledgements

We thank the crew of the r/v *Oceania*. This work was funded by a grant from the Croatian Science Foundation under projects IP-11-2013-8607 and IP-2018-01-3105, and by the Polish National Science Centre contract No. 2021/41/B/ST10/00946. We would also like to thank the reviewers, whose comments and insights deeply helped to improve the quality of the manuscript.

Supplementary materials

Supplementary material associated with this article can be found, in the online version, at <https://doi.org/10.1016/j.oceano.2022.05.003>.

References

- Andrén, E., 1999. Changes in the composition of the diatom flora during the last century indicate increased eutrophication of the Oder estuary, south-western Baltic Sea. *Estuar. Coast. Shelf Sci.* 48 (6), 665–676. <https://doi.org/10.1006/ecss.1999.0480>
- Archer, C.L., Jacobson, M.Z., 2005. Evaluation of global wind power. *J. Geophys. Res. Atmos.* 110, D1110. <https://doi.org/10.1029/2004JD005462>
- Arrigo, K.R., Brown, C.W., 1996. Impact of chromophoric dissolved organic matter on UV inhibition of primary productivity in the sea. *Mar. Ecol. Prog. Ser.* 140, 207–216. <https://doi.org/10.3354/meps140207>
- Arts, M.T., 1999. Lipids in Freshwater Zooplankton: Selected Ecological and Physiological Aspects. In: Arts, M.T., Wainman, B.C. (Eds.), *Lipids in Freshwater Ecosystems*. Springer, New York, NY, 71–90. https://doi.org/10.1007/978-1-4612-0547-0_5
- Barthelmess, E.T., Schütte, F., Engel, A., 2021. Variability of the Sea Surface microlayer Across a filament’s edge and potential influences on gas exchange. *Front. Mar. Sci.* 8, 718384. <https://doi.org/10.3389/fmars.2021.718384>
- Belanger, S., Babin, M., Larouche, P., 2008. An empirical ocean color algorithm for estimating the contribution of chromophoric dissolved organic matter to total light absorption in optically complex waters. *J. Geophys. Res.* 113, C04027. <https://doi.org/10.1029/2007JC004436>
- Bligh, E.G., Dyer, W.J., 1959. A rapid method of total lipid extraction and purification. *Can. J. Biochem. Physiol.* 37, 911–917. <https://doi.org/10.1139/y59-099>
- Bourguet, N., Goutx, M., Ghiglione, J.F., Pujo-Pay, M., Mevel, G., Momzikoff, A., Mousseau, L., Guigue, C., Garcia, N., Raimbault, P., Pete, R., Oriol, L., Lefevre, D., 2009. Lipid biomarkers and bacterial lipase activities as indicators of organic matter and bacterial dynamics in contrasted regimes at the DYFAMED site, NW Mediterranean. *Deep-Sea Res. Pt. II* 56, 1454–1469. <https://doi.org/10.1016/j.dsr2.2008.11.034>
- Broecker, H.-C., Petermann, J., Siems, W., 1978. The influence of wind on CO₂-exchange in a wind-wave tunnel, including the effects of monolayers. *J. Mar. Res.* 36, 595–610.
- Bruggemann, M., Hayeck, N., George, C., 2018. Interfacial photochemistry at the ocean surface is a global source of organic vapors and aerosols. *Nat. Commun.* 9, 2101. <https://doi.org/10.1038/s41467-018-04528-7>
- Buszewski, B., Buszewska, T., Chmarzyński, A., Kowalkowski, T., Kowalska, J., Kosobucki, P., Zbytniewski, R., Namieśnik, J., Kot-Wasik, A., Pacyna, J., Panasiuk, D., 2005. The present condition of the Vistula River catchment area and its impact on the Baltic Sea coastal zone. *Reg. Environ. Chang.* 5, 97–110. <https://doi.org/10.1007/s10113-004-0077-8>
- Cantarero, S.I., Henríquez-Castillo, C., Dildar, N., Vargas, C.A., von Dassow, P., Cornejo-D’Ottone, M., Sepúlveda, J., 2020. Size-Fractionated Contribution of Microbial Biomass to Suspended Organic Matter in the Eastern Tropical South Pacific Oxygen Minimum Zone. *Front. Mar. Sci.* 7, 1–20. <https://doi.org/10.3389/fmars.2020.540643>
- Coble, P.G., 1996. Characterization of marine and terrestrial DOM in seawater using excitation-emission matrix spectroscopy. *Mar. Chem.* 51, 325–346. [https://doi.org/10.1016/0304-4203\(95\)00062-3](https://doi.org/10.1016/0304-4203(95)00062-3)
- Coble, P.G., 2007. *Marine optical biogeochemistry: The chemistry of ocean color*. *Chem. Rev.* 107, 402–418. [10.1021/cr050350+](https://doi.org/10.1021/cr050350+)
- Ćosović, B., Vojvodić, V., Pleše, T., 1985. Electrochemical determination and characterization of surface active substances in freshwaters. *Water Res.* 19, 175–183. [https://doi.org/10.1016/0043-1354\(85\)90196-4](https://doi.org/10.1016/0043-1354(85)90196-4)
- Ćosović, B., Vojvodić, V., 1998. Voltammetric analysis of surface active substances in natural seawater. *Electroanalysis* 10, 429–434. [https://doi.org/10.1002/\(SICI\)1521-4109\(199805\)10:6<429::AID-ELAN429>3.0.CO;2-7](https://doi.org/10.1002/(SICI)1521-4109(199805)10:6<429::AID-ELAN429>3.0.CO;2-7)
- Ćosović, B., 2005. Surface-Active Properties of the Sea Surface Microlayer and Consequences for Pollution in the Mediterranean Sea. *The Handbook of Environmental Chemistry*. Springer <https://doi.org/10.1007/b107150>
- Cunliffe, M., Engel, A., Frka, S., Gašparović, B., Guitart, C., Murrell, J.C., Salter, M., Stolle, C., Upstill-Goddard, R., Wurl, O., 2013. Sea surface microlayers: A unified physicochemical and biological perspective of the air-ocean interface. *Prog. Oceanogr.* 109, 104–116. <https://doi.org/10.1016/j.pocan.2012.08.004>
- Cyberska, B., Krzymiński, W., 1988. Extension of the Vistula River water in the Gulf of Gdańsk. In: *Proc. 16th Conf. Baltic Oceanograph. Instit. Mar. Res., Kiel, Germany*, 290–304.
- Dembitsky, V.M., Rozentsvet, O.A., 1990. Phospholipid composition of some marine red algae. *Phytochemistry* 29, 3149–3152. [https://doi.org/10.1016/0031-9422\(90\)80175-G](https://doi.org/10.1016/0031-9422(90)80175-G)
- Derieux, S., Fillaux, J., Saliot, A., 1998. Lipid class and fatty acid distributions in particulate and dissolved fractions in the north Adriatic Sea. *Org. Geochem.* 29, 5–7. [https://doi.org/10.1016/S0146-6380\(98\)00089-8](https://doi.org/10.1016/S0146-6380(98)00089-8)
- Dragičević, D., Pravdić, V., 1981. Properties of the seawater–air interface: Rates of surface film formation under steady state conditions. *Limnol. Oceanogr.* 26, 492–499. <https://doi.org/10.4319/lo.1981.26.3.0492>
- Drozdowska, V., Babichenko, S., Lisin, A., 2002. Natural water fluorescence characteristics based on lidar investigations of a sur-

- face water layer polluted by an oil film; the Baltic cruise – May 2000. *Oceanologia* 44 (3), 339–354.
- Drozdowska, V., 2007. Seasonal and spatial variability of surface seawater fluorescence properties in the Baltic and Nordic Seas: Results of lidar experiments. *Oceanologia* 49 (1), 59–69.
- Drozdowska, V., Fateyeva, N.L., 2013. Spectrophotometric study of natural Baltic surfactants – results of marine experiment. In: Traczewska, T.M., Hanus-Lorenz, B. (Eds.), *Hydrobiology in Environment Protection*. Oficyna Wydawnicza Politechniki Wrocławskiej, Wrocław, 25–32.
- Drozdowska, V., Józefowicz, M., 2015. Spectrophotometric studies of marine surfactants in the southern Baltic Sea. *Oceanologia* 57 (2), 159–167. <https://doi.org/10.1016/j.oceano.2014.12.002>
- Drozdowska, V., Kowalczyk, P., Józefowicz, M., 2015. Spectrofluorometric characteristics of fluorescent dissolved organic matter in a surface microlayer in the Southern Baltic coastal waters. *J. Eur. Opt. Soc.* 10, 15050. <https://doi.org/10.2971/jeos.2015.15050>
- Drozdowska, V., Wrobel, I., Markuszewski, P., Makuch, P., Raczkowska, A., Kowalczyk, P., 2017. Study on organic matter fractions in the surface microlayer in the Baltic Sea by spectrophotometric and spectrofluorometric methods. *Ocean Sci.* 13, 633–647. <https://doi.org/10.5194/os-13-633-2017>
- Drozdowska, V., Kowalczyk, P., Konik, M., Dzierzbicka-Głowacka, L., 2018. Study on different fractions of organic molecules in the Baltic Sea surface microlayer by spectrophotometric and spectrofluorimetric methods. *Front. Mar. Sci.* 5, 1–12. <https://doi.org/10.3389/fmars.2018.00456>
- Engel, A., Bange, H.W., Cunliffe, M., Burrows, S.M., Friedrichs, G., Galgani, L., Herrmann, H., Hertkorn, N., Johnson, M., Liss, P.S., Quinn, P.K., Schartau, M., Soloviev, A., Stolle, C., Upstill-Goddard, R.C., van Pinxteren, M., Zäncker, B., 2017. The Ocean's vital skin: toward an integrated understanding of the sea surface microlayer. *Front. Mar. Sci.* 4. <https://doi.org/10.3389/fmars.2017.00165>
- Falkowska, L., 1999. Sea surface microlayer: A field evaluation of teflon plate, glass plate and screen sampling techniques. Part 2. Dissolved and suspended matter. *Oceanologia* 41 (2), 223–240.
- Frew, N.M., Goldman, J.C., Dennett, M.R., Johnson, A.S., 1990. Impact of phytoplankton-generated surfactants on air-sea gas exchange. *J. Geophys. Res.* 95, 3337. <https://doi.org/10.1029/jc095ic03p03337>
- Frka, S., Kozarac, Z., Čosović, B., 2009. Characterization and seasonal variations of surface active substances in the natural sea surface micro-layers of the coastal Middle Adriatic stations. *Estuar. Coast. Shelf Sci.* 85, 555–564. <https://doi.org/10.1016/j.ecss.2009.09.023>
- Frka, S., Gašparović, B., Marić, D., Godrijan, J., Djakovac, T., Vojvodić, V., Dautović, J., Kozarac, Z., 2011. Phytoplankton driven distribution of dissolved and particulate lipids in a semi-enclosed temperate sea (Mediterranean): Spring to summer situation. *Estuar. Coast. Shelf Sci.* 93 (4), 290–304. <https://doi.org/10.1016/j.ecss.2011.04.017>
- Gašparović, B., Kozarac, Z., Saliot, A., Čosović, B., Möbius, D., 1998. Physico-chemical characterization of natural and ex-situ reconstructed sea-surface microlayers. *J. Colloid Interface Sci.* 208, 191–202. <https://doi.org/10.1006/jcis.1998.5792>
- Gašparović, B., Plavšić, M., Čosović, B., Saliot, A., 2007. Organic matter characterization in the sea surface microlayers in the subarctic Norwegian fjords region. *Mar. Chem.* 105, 1–14. <https://doi.org/10.1016/j.marchem.2006.12.010>
- Gašparović, B., Djakovac, T., Tepić, N., Degobbis, D., 2011. Relationships between surface-active organic substances, chlorophyll a and nutrients in the northern Adriatic Sea. *Cont. Shelf Res.* 31, 1149–1160. <https://doi.org/10.1016/j.csr.2011.04.010>
- Gašparović, B., Frka, S., Koch, B.P., Zhu, Z.Y., Bracher, A., Lechtenfeld, O.J., Neogi, S.B., Lara, R.J., Kattner, G., 2014. Factors influencing particulate lipid production in the East Atlantic Ocean. *Deep-Sea Res. Pt. I.* 89, 56–67. <https://doi.org/10.1016/j.dsr.2014.04.005>
- Gašparović, B., Kazazić, S.P., Cvitešić, A., Penezić, A., Frka, S., 2015. Improved separation and analysis of glycolipids by latroscan thin-layer chromatography-flame ionization detection. *J. Chromatogr. A* 1409, 259–267. <https://doi.org/10.1016/j.chroma.2015.07.047>
- Gašparović, B., Penezić, A., Lampitt, R.S., Sudasinghe, N., Schaub, T., 2016. Free fatty acids, tri-, di- and monoacylglycerol production and depth-related cycling in the Northeast Atlantic. *Mar. Chem.* 186, 101–109. <https://doi.org/10.1016/j.marchem.2016.09.002>
- Gašparović, B., Kazazić, S.P., Cvitešić, A., Penezić, A., Frka, S., 2017. Corrigendum to “Improved separation and analysis of glycolipids by latroscan thin-layer chromatography–flame ionization detection”. [*J. Chromatogr. A* 1409 (2015) 259267. <https://doi.org/10.1016/j.chroma.2015.07.047>]. *J. Chromatogr. A* 1521. <https://doi.org/10.1016/j.chroma.2017.09.038>
- Gašparović, B., Penezić, A., Frka, S., Kazazić, S., Lampitt, R.S., Holguin, F.O., Sudasinghe, N., Schaub, T., 2018. Particulate sulfur-containing lipids: production and cycling from the epipelagic to the abyssopelagic zones. *Deep-Sea Res. Pt. I* 134, 12–22. <https://doi.org/10.1016/j.dsr.2018.03.007>
- Gerin, C., Goutx, M., 1993. Separation and quantification of phospholipids from marine bacteria with the latroscan mark IV TLC–FID. *J. Planar Chromatogr.* 6, 307–312.
- Gerin, C., Goutx, M., 1994. Latroscan-measured particulate and dissolved lipids in the Almeria-Oran frontal system (Almofront-1, May 1991). *J. Mar. Sys.* 5, 343–360. [https://doi.org/10.1016/0924-7963\(94\)90055-8](https://doi.org/10.1016/0924-7963(94)90055-8)
- Giani, M., Savelli, F., Berto, D., Zangrando, V., Čosović, V., Vojvodić, V., 2005. Temporal dynamics of dissolved and particulate organic carbon in the northern Adriatic Sea in relation to the mucilage events. *Sci. Total Environ.* 353, 126–138. <https://doi.org/10.1016/j.scitotenv.2005.09.062>
- Glasby, G.P., Szefer, P., 1998. Marine pollution in Gdansk Bay, Puck Bay and the Vistula Lagoon, Poland: An overview. *Sci. Total Environ.* 212, 49–57. [https://doi.org/10.1016/S0048-9697\(97\)00333-1](https://doi.org/10.1016/S0048-9697(97)00333-1)
- Goutx, M., Guigue, C., Striby, L., 2003. Triacylglycerol biodegradation experiment in marine environmental conditions: Definition of a new lipolysis index. *Org. Geochem.* 34, 1465–1473. [https://doi.org/10.1016/S0146-6380\(03\)00119-0](https://doi.org/10.1016/S0146-6380(03)00119-0)
- Grelowski, A., Wojewodzki, T., 1996. The impact of the Vistula river on the hydrological conditions in the Gulf of Gdansk in 1994. *Bull. Sea Fish. Inst.* 137, 23–33.
- Guschina, I.A., Harwood, J.L., 2009. Algal lipids and effect of the environment on their biochemistry. In: Kainz, M., Brett, M.T., Arts, M.T. (Eds.), *Lipids in Aquatic Ecosystems*. Springer, New York, 1–24. https://doi.org/10.1007/978-0-387-89366-2_1
- Harvey, H.R., Tuttle, J.H., Bell, J., 1995. Kinetics of phytoplankton decay during simulated sedimentation, Changes in biochemical composition and microbial activity under oxic and anoxic conditions. *Geochim. Cosmochim. Acta* 59, 367–3377. [https://doi.org/10.1016/0016-7037\(95\)00217-N](https://doi.org/10.1016/0016-7037(95)00217-N)
- Harwood, J.L., 2006. Membrane Lipids in Algae. In: Siegenthaler, P.-A., Murata, N. (Eds.), *Lipids in Photosynthesis: Structure, Function and Genetics*. Advances in Photosynthesis and Respiration, vol 6. Springer, Dordrecht, 53–64. https://doi.org/10.1007/0-306-48087-5_3
- HELCOM, 2018. Input of nutrients by the seven biggest rivers in the Baltic Sea region. *Balt. Sea Environ. Proc. No.* 161, 31. <https://www.helcom.fi/wp-content/uploads/2019/08/BSEP163.pdf>
- Helms, J.R., Stubbins, A., Ritchie, J.D., Minor, E.C., Kieber, D.J., Mopper, K., 2008. Absorption spectral slopes and slope ratios as indicators of molecular weight, source, and photobleaching of chromophoric dissolved organic matter. *Limnol. Oceanogr.* 53, 955–969. <https://doi.org/10.4319/lo.2008.53.3.0955>

- Hunter, K.A., 1997. Chemistry of the sea-surface microlayer. In: Liss, P.S., Duce, R.A. (Eds.), *The sea surface and global change*. Cambridge Univ. Press., 287–320.
- Johannessen, S.C., Miller, W.L., 2001. Quantum yield for the photochemical production of dissolved inorganic carbon in seawater. *Mar. Chem.* 76, 271–283. [https://doi.org/10.1016/S0304-4203\(01\)00067-6](https://doi.org/10.1016/S0304-4203(01)00067-6)
- Kowalczyk, P., Stedmon, C.A., Markager, S., 2006. Modeling absorption by CDOM in the Baltic Sea from season, salinity and chlorophyll. *Mar. Chem.* 101, 1–11. <https://doi.org/10.1016/j.marchem.2005.12.005>
- Kruk-Dowgiallo, L., 1996. The role of the filamentous brown algae in the degradation of the underwater meadows the Gulf of Gdańsk. *Oceanol. Stud.* 25, 125–135.
- Larsson, U., Elmgren, R., Wulff, F., 1985. Eutrophication and the Baltic sea: Causes and consequences. *Ambio* 14, 9–14.
- Lei, X., Pan, J., Devlin, A.T., 2020. Variations of the Absorption of Chromophoric Dissolved Organic Matter in the Pearl River Estuary. In *Estuaries and Coastal Zones-Dynamics and Response to Environmental Changes*. IntechOpen. <https://www.intechopen.com/chapters/70692>
- Liss, P.S., 1975. Chemistry of the sea surface microlayer. In: Riley, J.P., Skirrow, G. (Eds.), *Chemical Oceanography*, vol. 2. Academic Press, London, U.K., 193–244.
- Liss, P.S., Duce, R.A. (Eds.), 1997, *The Sea Surface and Global Change*. Cambridge Univ. Press, New York, 519 pp. <https://doi.org/10.1017/CBO9780511525025>
- Loiselle, S.A., Bracchini, L., Dattilo, A.M., Ricci, M., Tognazzi, A., Cózar, A., Rossi, C., 2009. Optical characterization of chromophoric dissolved organic matter using wavelength distribution of absorption spectral slopes. *Limnol. Oceanogr.* 54, 590–597. <https://doi.org/10.4319/lo.2009.54.2.0590>
- Maksymowska, D., Richard, P., Piekarek-Jankowska, H., Riera, P., 2000. Chemical and isotopic composition of the organic matter sources in the Gulf of Gdansk (Southern Baltic Sea). *Estuar. Coast. Shelf Sci.* 51, 585–598. <https://doi.org/10.1006/ecss.2000.0701>
- Marcinek, S., Santinelli, C., Cindrić, A.M., Evangelista, V., Gonnelli, M., Layglon, N., Mounier, S., Lenoble, V., Omanović, D., 2020. Dissolved organic matter dynamics in the pristine Krka River estuary (Croatia). *Mar. Chem.* 225, 103848. <https://doi.org/10.1016/j.marchem.2020.103848>
- Marić, D., Frka, S., Godrijan, J., Tomažić, I., Penezić, A., Djakovac, T., Vojvodić, V., Precali, R., Gašparović, B., 2013. Organic matter production during late summer-winter period in a temperate sea. *Cont. Shelf Res.* 55, 52–65. <https://doi.org/10.1016/j.csr.2013.01.008>
- Mayer, K.J., Wang, X., Santander, M.V., Mitts, B.A., Sauer, J.S., Sultana, C.M., Cappa, C.D., Prather, K.A., 2020. Secondary marine aerosol plays a dominant role over primary sea spray aerosol in cloud formation. *ACS Cent. Sci.* 6, 2259–2266. <https://doi.org/10.1021/acscentsci.0c00793>
- Mazur-Marzec, H., Krężel, A., Kobos, J., Pliński, M., 2006. Toxic *Nodularia spumigena* blooms in the coastal waters of the Gulf of Gdańsk: a ten-year survey. *Oceanologia* 48 (2), 255–273.
- Murphy, K.R., Butler, K.D., Spencer, R.G.M., Stedmon, C.A., Boehme, J.R., Aiken, G.R., 2010. Measurement of dissolved organic matter fluorescence in aquatic environments: An inter-laboratory comparison. *Environ. Sci. Technol.* 44, 9405–9412. <https://doi.org/10.1021/es102362t>
- Mustaffa, N.I.H., Ribas-Ribas, M., Banko-Kubis, H.M., Wurl, O., 2020. Global reduction of in situ CO₂ transfer velocity by natural surfactants in the sea-surface microlayer. *Proc. R. Soc. A* 476, 20190763. <https://doi.org/10.1098/rspa.2019.0763>
- Novak, T., Godrijan, J., Pfannkuchen, D.M., Djakovac, T., Mlakar, M., Baricevic, A., Tanković, M.S., Gašparović, B., 2018. Enhanced dissolved lipid production as a response to the sea surface warming. *J. Mar. Sys.* 180, 289–298. <https://doi.org/10.1016/j.jmarsys.2018.01.006>
- Novak, T., Godrijan, J., Pfannkuchen, D.M., Djakovac, T., Medić, N., Ivančić, I., Mlakar, M., Gašparović, B., 2019. Global warming and oligotrophication lead to increased lipid production in marine phytoplankton. *Sci. Total Environ.* 668, 171–183. <https://doi.org/10.1016/j.scitotenv.2019.02.372>
- Obernosterer, I., Catala, P., Lami, R., Caparros, J., Ras, J., Bricaud, A., Dupuy, C., Van Wambeke, F., Lebaron, P., 2008. Biochemical characteristics and bacterial community structure of the sea surface microlayer in the South Pacific Ocean. *Biogeosciences* 5, 693–705. <https://doi.org/10.5194/bg-5-693-2008>
- Osburn, C.L., Del Vecchio, R., Boyd, T.J., 2014. Physicochemical effects on dissolved organic matter fluorescence in natural waters. In: Coble, P.G., Lead, J., Baker, A., Reynolds, D.M., Spencer, R.G.M. (Eds.), *Aquatic Organic Matter Fluorescence*. Cambridge Univ. Press, New York, 233–277.
- Parlanti, E., Wörz, K., Geoffroy, L., Lamotte, M., 2000. Dissolved organic matter fluorescence spectroscopy as a tool to estimate biological activity in a coastal zone submitted to anthropogenic inputs. *Org. Geochem.* 31, 1765–1781. [https://doi.org/10.1016/S0146-6380\(00\)00124-8](https://doi.org/10.1016/S0146-6380(00)00124-8)
- Parrish, C.C., 1988. Dissolved and particulate marine lipid classes: a review. *Mar. Chem.* 23 (1–2), 17–40. [https://doi.org/10.1016/0304-4203\(88\)90020-5](https://doi.org/10.1016/0304-4203(88)90020-5)
- Parrish, C.C., Abrajano, T.A., Budge, S.M., Helleur, R.J., Hudson, E.D., Pulchan, K., Ramos, C., 2000. Lipid and Phenolic Biomarkers in Marine Ecosystems: Analysis and Applications. In: Wangersky, P.J. (Ed.), *Marine Chemistry. The Handbook of Environmental Chemistry*, vol 5D. Springer, Berlin, Heidelberg https://doi.org/10.1007/10683826_8
- Pastuszak, M., Stålnacke, P., Pawlikowski, K., Witek, Z., 2012. Response of Polish rivers (Vistula, Oder) to reduced pressure from point sources and agriculture during the transition period (1988–2008). *J. Mar. Sys.* 94, 157–173. <https://doi.org/10.1016/j.jmarsys.2011.11.017>
- Patel, A.B., Shaikh, S., Jain, K.R., Desai, C., Madamwar, D., 2020. Polycyclic Aromatic Hydrocarbons: Sources, Toxicity, and Remediation Approaches. *Front. Microbiol.* 11, 562813. <https://doi.org/10.3389/fmicb.2020.562813>
- Peđziński, J., Witak, M., 2019. Evidence of cultural eutrophication of the Gulf of Gdańsk based on diatom analysis. *Oceanol. Hydrobiol. Stud.* 48, 247–261. <https://doi.org/10.2478/ohs-2019-0022>
- Penezić, A., Gašparović, B., Burić, Z., Frka, S., 2010. Distribution of marine lipid classes in salty Rogoznica Lake (Croatia). *Estuar. Coast. Shelf Sci.* 86, 625–636. <https://doi.org/10.1016/j.ecss.2009.11.030>
- Penezić, A., Milinković, A., Bakija Alempijević, S., Žužul, S., Frka, S., 2021. Atmospheric deposition of biologically relevant trace metals in the eastern Adriatic coastal area. *Chemosphere* 283, 131178. <https://doi.org/10.1016/j.chemosphere.2021.131178>
- Pereira, R., Schneider-Zapp, K., Upstill-Goddard, R.C., 2016. Surfactant control of gas transfer velocity along an offshore coastal transect: results from a laboratory gas exchange tank. *Biogeosciences* 13, 3981–3989. <https://doi.org/10.5194/bg-13-3981-2016>
- Piskozub, J., Drozdowska, V., Irczuk, M., 1998. A water Raman extinction lidar system for detecting thin oil spills: preliminary results of field tests. *Oceanologia* 40 (1), 3–10.
- Reinthal, T., Sintes, E., Herndl, G.J., 2008. Dissolved organic matter and bacterial production and respiration in the sea-surface microlayer of the open Atlantic and the western mediterranean sea. *Oceanogr.* 53 (1), 122–136. <https://doi.org/10.4319/lo.2008.53.1.0122>
- Ribas-Ribas, M., Mustaffa, N.I.H., Rahlff, J., Stolle, C., Wurl, O., 2017. Sea surface scanner (S3): A catamaran for high-resolution

- measurements of biogeochemical properties of the sea surface microlayer. *J. Atmos. Ocean. Technol.* 34, 1433–1448. <https://doi.org/10.1175/JTECH-D-17-0017.1>
- Rickard, P.C., Uher, G., Upstill-Goddard, R.C., Frka, S., Mustaffa, N.I.H., Banko-Kubis, H.M., Cvitešić Kušan, A., Gašparović, B., Stolle, C., Wurl, O., Ribas-Ribas, M., 2019. Reconsideration of seawater surfactant activity analysis based on an inter-laboratory comparison study. *Mar. Chem.* 208, 103–111. <https://doi.org/10.1016/j.marchem.2018.11.012>
- Rickard, P.C., Uher, G., Upstill-Goddard, R.C., 2022. Photo-reactivity of surfactants in the sea-surface microlayer and subsurface water of the Tyne estuary, UK. *Geophys. Res. Lett.* 49 (4), e2021GL095469. <https://doi.org/10.1029/2021GL095469>
- Robinson, T.B., Wurl, O., Bahlmann, E., Jürgens, K., Stolle, C., 2019. Rising bubbles enhance the gelatinous nature of the air–sea interface. *Limnol. Oceanogr.* 64, 2358–2372. <https://doi.org/10.1002/lno.11188>
- Romankevich, E.A., 1984. *Geochemistry of Organic Matter in the Ocean*. Springer Berlin, Heidelberg, 334.
- Rontani, J.F., Belt, S.T., 2020. Photo- and autoxidation of unsaturated algal lipids in the marine environment: An overview of processes, their potential tracers, and limitations. *Org. Geochem.* 139, 103941. <https://doi.org/10.1016/j.orggeochem.2019.103941>
- Ryba, A.S., Burgess, R.M., 2002. Effects of sample preparation on the measurement of organic carbon, hydrogen, nitrogen, sulfur and oxygen concentrations in marine sediments. *Chemosphere* 48, 139–147. [https://doi.org/10.1016/s0045-6535\(02\)00027-9](https://doi.org/10.1016/s0045-6535(02)00027-9)
- Sabbaghzadeh, B., Upstill-Goddard, R.C., Beale, R., Pereira, R., Nightingale, P.D., 2017. The Atlantic Ocean surface microlayer from 50°N to 50°S is ubiquitously enriched in surfactants at wind speeds up to 13 m s⁻¹. *Geophys. Res. Lett.* 44, 2852–2858. <https://doi.org/10.1002/2017GL072988>
- Salter, M.E., Upstill-Goddard, R.C., Nightingale, P.D., Archer, S.D., Blomquist, B., Ho, D.T., Huebert, B., Schlosser, P., Yang, M., 2011. Impact of an artificial surfactant release on air-sea gas fluxes during Deep Ocean Gas Exchange Experiment II. *J. Geophys. Res. Oceans* 116, C11016. <https://doi.org/10.1029/2011JC007023>
- Santos-Echeandía, J., Caetano, M., Brito, P., Canario, J., Vale, C., 2012. The relevance of defining trace metal baselines in coastal waters at a regional scale: The case of the Portuguese coast (SW Europe). *Mar. Environ. Res.* 79, 86–99. <https://doi.org/10.1016/j.marenvres.2012.05.010>
- Sargent, J.R., Lee, R.F., Nevenzel, J.C., 1976. Marine waxes. In: Kolattukudy, P.E. (Ed.), *Chemistry and Biochemistry of Natural Waxes*. Elsevier, Amsterdam, 49–91.
- Schiewer, U., Schernewski, G., 2002. Baltic Coastal Ecosystem Dynamics and Integrated Coastal Zone Management. In: Ass, E.-P. (Ed.), *Littoral 2002, Proc. 6th International Symposium, Porto 22–26.9.2002*. Univ. Porto, 115–123.
- Schneider-Zapp, K., Salter, M.E., Mann, P.J., Upstill-Goddard, R.C., 2013. Technical Note: Comparison of storage strategies of sea surface microlayer samples. *Biogeosciences* 10, 4927–4936. <https://doi.org/10.5194/bg-10-4927-2013>
- Sharma, K.K., Schuhmann, H., Schenk, P.M., 2012. High lipid induction in microalgae for biodiesel production. *Energies* 5, 1532–1553. <https://doi.org/10.3390/en5051532>
- Stedmon, C.A., Markager, S., Kaas, H., 2000. Optical properties and signatures of chromophoric dissolved organic matter (CDOM) in Danish coastal waters. *Estuar. Coast. Shelf Sci.* 51, 267–278. <https://doi.org/10.1006/ecss.2000.0645>
- Stedmon, C.A., Markager, S., Bro, R., 2003. Tracing dissolved organic matter in aquatic environments using a new approach to fluorescence spectroscopy. *Mar. Chem.* 82, 239–254. [https://doi.org/10.1016/S0304-4203\(03\)00072-0](https://doi.org/10.1016/S0304-4203(03)00072-0)
- Stefan, R.L., Szeri, A.J., 1999. Surfactant scavenging and surface deposition by rising bubbles. *J. Colloid Interface Sci.* 212, 1–13. <https://doi.org/10.1006/jcis.1998.6037>
- Stolle, C., Nagel, K., Labrenz, M., Jürgens, K., 2010. Succession of the sea-surface microlayer in the coastal Baltic Sea under natural and experimentally induced low-wind conditions. *Biogeosciences* 7, 2975–2988. <https://doi.org/10.5194/bg-7-2975-2010>
- Stolle, C., Ribas-Ribas, M., Badewien, T.H., Barnes, J., Carpenter, L.J., et al., 2020. The Milan Campaign: Studying diel light effects on the air-sea interface. *Bull. Am. Meteorol. Soc.* 101, 146–166. <https://doi.org/10.1175/BAMS-D-17-0329.1>
- Szymczak-Żyła, M., Krajewska, M., Witak, M., Ciesielski, T.M., Ardelan, M.V., Jenssen, B.M., Goslar, T., Winogradow, A., Filipkowska, A., Lubecki, L., Zamojska, A., Kowalewska, G., 2019. Present and Past-Millennial Eutrophication in the Gulf of Gdańsk (Southern Baltic Sea). *Paleoceanogr. Paleoclimatology* 34, 136–152. <https://doi.org/10.1029/2018PA003474>
- Tank, S.E., Lesack, L.F.W., Gareis, J.A.L., Osburn, C.L., Hesslein, R.H., 2011. Multiple tracers demonstrate distinct sources of dissolved organic matter in lakes of the Mackenzie delta, western Canadian arctic. *Limnol. Oceanogr.* 56 (4), 1297–1309. <https://doi.org/10.4319/lo.2011.56.4.1297>
- Triesch, N., van Pinxteren, M., Frka, S., Spranger, T., Hoffmann, E.H., Gong, X., Wex, H., Schulz-Bull, D., Gašparović, B., Herrmann, H., 2021. Concerted measurements of lipids in seawater and on submicron aerosol particles at the Cape Verde Islands: biogenic sources, selective transfer and high enrichments. *Atmos. Chem. Phys.* 21, 4267–4283. <https://doi.org/10.5194/acp-21-4267-2021>
- Tsai, W.-T., Lui, K.-K., 2003. An assessment of the effects of seasurface surfactant on global atmosphere-ocean CO₂ flux. *J. Geophys. Res.* 108, 3127–3143. <https://doi.org/10.1029/2000JC000740>
- Van Pinxteren, M., Barthel, S., Fomba, K.W., Müller, K., Von Tümpling, W., Herrmann, H., Thomsen, L., 2017. The influence of environmental drivers on the enrichment of organic carbon in the sea surface microlayer and in submicron aerosol particles—measurements from the Atlantic Ocean. *Elementa: Science of the Anthropocene* 5, 35. <https://doi.org/10.1525/elementa.225>
- Williams, P.M., Carlucci, A.F., Henrichs, S.M., Van Fleet, E.S., Horri-gan, S.G., Reid, F.M.H., Robertson, K.J., 1986. Chemical and microbiological studies of sea-surface films in the Southern Gulf of California and off the West Coast of Baja California. *Mar. Chem.* 19, 17–98. [https://doi.org/10.1016/0304-4203\(86\)90033-2](https://doi.org/10.1016/0304-4203(86)90033-2)
- Woolf, D.K., 2005. Bubbles and their role gas exchange. In: Liss, P.S., Duce, R.A. (Eds.), *The Sea Surface and Global Change*. Cambridge Univ. Press, U. K, 173–205.
- Wurl, O., Obbard, J.P., 2004. A review of pollutants in the sea-surface microlayer (SML): A unique habitat for marine organisms. *Mar. Pollut. Bull.* 48, 1016–1030. <https://doi.org/10.1016/j.marpolbul.2004.03.016>
- Wurl, O., Miller, L., Röttgers, R., Vagle, S., 2009. The distribution and fate of surface-active substances in the sea-surface microlayer and water column. *Mar. Chem.* 115, 1–9. <https://doi.org/10.1016/j.marchem.2009.04.007>
- Wurl, O., Wurl, E., Miller, L., Johnson, K., Vagle, S., 2011. Formation and global distribution of sea-surface microlayers. *Biogeosciences* 8, 121–135. <https://doi.org/10.5194/bg-8-121-2011>
- Wurl, O., Ekau, W., Landing, W.M., Zappa, C.J., 2017. Sea surface microlayer in a changing ocean – A perspective. *Elem. Sci. Anthropocene* 5, 31. <https://doi.org/10.1525/elementa.228>
- Zhang, Z., Liu, L., Liu, C., Cai, W., 2003. Studies on the sea surface microlayer: II. The layer of sudden change of physical and chemical properties. *J. Colloid Interf. Sci.* 264, 148–159. [https://doi.org/10.1016/S0021-9797\(03\)00390-4](https://doi.org/10.1016/S0021-9797(03)00390-4)
- Zhang, Y., Liu, X., Osburn, C.L., Wang, M., Qin, B., Zhou, Y., 2013a. Photobleaching Response of Different Sources of Chromophoric

- Dissolved Organic Matter Exposed to Natural Solar Radiation Using Absorption and Excitation-Emission Matrix Spectra. *PLoS One* 8, e77515. <https://doi.org/10.1371/journal.pone.0077515>
- Zhang, Y., Liu, X., Wang, M., Qin, B., 2013b. Compositional differences of chromophoric dissolved organic matter derived from phytoplankton and macrophytes. *Org. Geochem.* 55, 26–37. <https://doi.org/10.1016/j.orggeochem.2012.11.007>
- Zhao, J., Cao, W., Xu, Z., Ai, B., Yang, Y., Jin, G., Wang, G., Zhou, W., Chen, Y., Chen, H., Sun, Z., 2018. Estimating CDOM concentration in highly turbid estuarine coastal waters. *J. Geophys. Res.-Oceans* 123, 5856–5873. <https://doi.org/10.1029/2018JC013756>

Available online at www.sciencedirect.com

ScienceDirect

journal homepage: www.journals.elsevier.com/oceanologia

ORIGINAL RESEARCH ARTICLE

Contaminant transport in the surf zone

David A. Chin*

Department of Chemical, Environmental, and Materials Engineering, University of Miami, Coral Gables, FL, USA

Received 7 April 2022; accepted 9 June 2022

Available online 21 June 2022

KEYWORDS

Dispersion;
Surf zone;
Turbulent diffusion;
Waves

Abstract Dispersion of dissolved contaminants introduced at various locations within and just outside the surf zone are investigated. It is shown that the Longuet-Higgins model of surf-zone hydrodynamics adequately describes the distribution of longshore currents measured at the laboratory scale. Relations are derived between the longitudinal and transverse dispersion coefficients and the influencing parameters. The maximum longitudinal dispersion coefficients are associated with tracer releases near the breaker line, and longitudinal dispersion coefficients generally increase with travel time for distances up to at least 10 surf-zone widths. In contrast, transverse dispersion coefficients remain relatively constant for increasing travel time. The longitudinal and transverse dispersion coefficients can be significantly influenced by assumed values of local turbulent diffusion and cross-shore shear dispersion.

© 2022 Institute of Oceanology of the Polish Academy of Sciences. Production and hosting by Elsevier B.V. This is an open access article under the CC BY-NC-ND license (<http://creativecommons.org/licenses/by-nc-nd/4.0/>).

1. Introduction

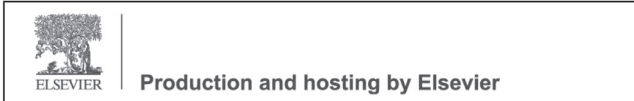
The hydrodynamics of waves and currents in the surf zone are of interest due to their effect on shoreline erosion, sediment transport, and the performance of coastal structures. Waves and currents are also important in determining the

transport of contaminants that are either discharged into the surf zone, or advected into the surf zone from further offshore. The strategic location of contaminant discharges and other point sources in high-dilution surf-zone environments have the potential to reduce the adverse effects on beach water quality, and to control the locations of high-impact areas within the surf zone. Nearshore wave-induced drift (via Stokes drift and wave-breaking) along with wind induced surface drift are potentially major mechanisms that lead to the shoreline stranding of oil (Novelli et al., 2020). Advective and diffusive transport within the surf zone have been largely ignored when considering the shoreline impact of buoyant ocean-outfall discharges of domestic wastewater that are advected towards the shore under the influence of onshore winds. In these cases, it has been common practice to use measured offshore velocities along with assumptions of spatial homogeneity to predict shoreline impact (e.g.,

* Corresponding author at: Department of Chemical, Environmental, and Materials Engineering, University of Miami, Coral Gables, FL, 33146, USA.

E-mail address: dchin@miami.edu

Peer review under the responsibility of the Institute of Oceanology of the Polish Academy of Sciences.



Koh, 1988), ignoring the fact that nearshore currents will be mostly in directions parallel of the shoreline, and advection and transport will be influenced by nearshore velocity shear and mixing associated with breaking waves. The primary objective of the present investigation is to quantify the mixing characteristics of contaminants that are introduced at various locations within and just outside the surf zone.

2. Background

Nearshore currents and tracer transport are influenced by a variety of factors, such as bathymetry, shoreline geometry, the presence of offshore structures, wave spectra, wave-breaking characteristics, and locations of the tracer sources. Key processes influencing the characteristics of waves and currents in the nearshore zone are refraction, diffraction, shoaling, and energy loss due to wave breaking. Waves approaching a shoreline are mostly irregular in that they consist of a combination of waves with different wave heights, frequencies, and propagation directions. In principle, irregular waves can be considered as a linear combination of regular (monochromatic) waves, with the distribution of wave heights versus frequency and direction being represented by a wave spectrum. Hence, the study of the behavior of regular monochromatic waves is fundamental to the study of irregular waves. Most generalized studies of the hydrodynamics in the surf zone assume simplified two-dimensional bathymetries, with plane beaches and beaches with offshore bars being the most common. The study of plane beaches is particularly attractive since it only requires one parameter – the slope – to fully characterize the beach. Whereas previous studies have mostly focused on nearshore hydrodynamics, tracer transport in the surf zone has received much less attention. Such studies have mostly consisted of dye-releases at a few locations in the surf zone, and then using these measurements to estimate bulk mixing coefficients within the surf zone. However, these studies have not resolved spatial variations of mixing within the surf zone nor the relation between discharge location and mixing characteristics. The present study investigates the mixing of dissolved tracers released into the surf zone where both regular and irregular waves obliquely propagate towards plane beaches. The primary objectives of the study are to identify quantitative relations between the mixing parameters, beach and wave characteristics, and tracer discharge locations.

3. Governing equations

As regular waves approach a plane beach at an oblique angle, the key processes are shoaling, refraction, wave setup, and the generation of longshore currents caused by breaking waves. Tracers injected into the nearshore zone are advected by the induced longshore current and diffused by small-scale turbulent fluctuations within the velocity field. Shear dispersion caused by cross-shore circulation can also be an influential transport process. The governing equations used to describe longshore currents induced by breaking waves are given below.

Wave transformation, setup, and currents. The governing equations that relate incident waves to the generation of longshore currents are as follows:

$$\text{Shoaling : } \frac{\partial}{\partial x}(E_w c_g \cos \theta) = E_l \quad (1)$$

$$\text{Refraction : } \frac{\sin \theta}{c} = \text{constant} \quad (2)$$

$$\text{Wave setup : } \rho g(h + \eta) \frac{\partial \eta}{\partial x} = -\frac{\partial S_{xx}}{\partial x} \quad (3)$$

$$\text{Longshore current : } \tau_b + \frac{\partial}{\partial x} \left[\rho \nu_e (h + \eta) \frac{\partial v}{\partial x} \right] = \frac{\partial S_{xy}}{\partial x} \quad (4)$$

where x is the coordinate measured normal to the shoreline; y is the coordinate measured along the shoreline; E_w is the energy density of the wave, which is equal to $\rho g H^2 / 8$ where ρ is the water density, g is the gravity constant, and H is the wave height; c_g is the group velocity of the wave; θ is the direction of wave propagation relative to the beach normal; E_l is the energy loss rate in breaking or broken waves; c is the phase speed of the wave; h is the still-water depth; η is the mean water-surface elevation relative to the still-water surface elevation; S_{xx} and S_{xy} are components of the radiation stress; τ_b is the bottom shear stress caused by the longshore wave-induced current; ν_e is the eddy viscosity; and v is the longshore current generated by breaking and broken waves. The governing equations given by Equations (1)–(4) along with various constitutive relations are solved simultaneously to estimate the wave heights and longshore wave-induced currents. Using this approach, Equations (1) and (2) are solved for the wave height $H(x)$ as a function of distance from the shore, and Equations (3) and (4) use the calculated wave-height distribution, $H(x)$, to estimate the radiation-stress components, S_{xx} and S_{xy} , and solve for the alongshore current distribution $v(x)$.

Transport in the nearshore zone. The wave-induced velocity field consists of both a large-scale mean component and a small-scale random turbulent-diffusion component. The large-scale mean component, $v(x)$, is estimated by the solution of Equations (3) and (4), and the turbulent-diffusion component can be locally represented by a normally distributed random velocity with a mean of zero and a standard deviation of $\sqrt{2\epsilon} / \Delta t$, where ϵ is the turbulent diffusion coefficient. Hence, the velocity field V can be expressed in terms of its components as:

$$V_y = v(x) + N\left(0, \sqrt{\frac{2\epsilon_y}{\Delta t}}\right), \quad V_x = N\left(0, \sqrt{\frac{2\epsilon_x}{\Delta t}}\right) \quad (5)$$

where V_x and V_y are the offshore and alongshore components of the velocity, respectively, $v(x)$ is the alongshore component of the mean velocity, $N(\mu, \sigma)$ is a normal random variable with a mean of μ and a standard deviation of σ , and ϵ_x and ϵ_y are the components of the turbulent diffusion coefficient in the x and y directions, respectively. Using the velocity field defined by Equation (5), the Lagrangian transport of a mass, M , instantaneously released at a given location is described at each time step, Δt , by

$$\mathbf{x}_2 = \mathbf{x}_1 + V \Delta t \quad (6)$$

where x_1 and x_2 are the starting and ending coordinates, respectively, of a released tracer particle. For an instantaneous release of tracer mass at a given point, the advection steps are repeated up the time $t = n\Delta t$ with n_{sim} repeated simulations, and the variances of the tracer-particle distribution in the coordinate directions at time t are given by

$$\begin{aligned} \sigma_x^2(t) &= \frac{1}{n_{sim}} \sum_{i=1}^{n_{sim}} [x_i(t) - \bar{x}(t)]^2, \\ \sigma_y^2(t) &= \frac{1}{n_{sim}} \sum_{i=1}^{n_{sim}} [y_i(t) - \bar{y}(t)]^2 \end{aligned} \quad (7)$$

where $(x_i(t), y_i(t))$ are the coordinates of a particle in simulation i at time t , and $(\bar{x}(t), \bar{y}(t))$ is the mean location of all particles at time t . The relations given by Equation (7) can be used to estimate the components of the effective dispersion coefficient (K_x, K_y), which are defined by

$$K_x = \frac{\sigma_x^2}{2t}, \quad K_y = \frac{\sigma_y^2}{2t} \quad (8)$$

The resulting concentration distribution can be derived from the distribution of particle locations using the relation

$$\bar{c}(x_j, y_j, t) = \frac{M}{n_{sim} h_j \Delta x \Delta y} n_j(t) \quad (9)$$

where $\bar{c}(x_j, y_j, t)$ is the average concentration over a volume element centered at (x_j, y_j) at time t , Δx and Δy are the dimensions of the volume element in the x and y directions, respectively, h_j is the depth of water within the volume element, and $n_j(t)$ is the number of particles within the volume element at time t . In the case of a continuous release from the same discharge location as an instantaneous release, and in the same ambient velocity field, the resulting concentration distribution can be obtained from Equation (9) by superposition, which yields

$$\bar{c}_c(x_j, y_j, t) = \frac{\dot{M} \Delta t}{n_{sim} h_j \Delta x \Delta y} \sum_{k=1}^n n_j(k \Delta t) \quad (10)$$

where $\bar{c}_c(x_j, y_j, t)$ is the average concentration over a volume element centered at (x_j, y_j) at time $t = n\Delta t$, and \dot{M} is the mass release rate from the continuous source.

4. Implementation

A variety of assumptions are necessary of obtain an analytic solution to Equations (1)–(4) that can be used to estimate the mean longshore current $v(x)$. The assumptions used in this study are described below.

4.1. Shoaling and refraction

The shoaling and refraction processes described by Equations (1) and (2) are generally divided into two stages: before wave breaking and after wave breaking.

Before wave breaking. Before wave breaking, the energy loss rate E_l during wave propagation is negligible; however, a relation between wave height and water depth needs to be specified. The main complicating factor is that linear wave theory is seldom strictly applicable up to the breaker

line. Assuming linear conditions before wave breaking, the wave height, $H(x)$, at any distance x from the shoreline is given by a combination of Equations (1) and (2) which lead to (Komar, 1998)

$$\frac{H(x)}{H_0} = \sqrt{\frac{c_{g0} \cos \theta_0}{c_g \cos \theta}}, \quad \text{where } c_g = \frac{g}{\omega} \left[\tanh kh + \frac{kh}{\cosh^2 kh} \right] \quad (11)$$

where H_0 and θ_0 are the wave height and direction approaching the sloped beach, c_g is the local group velocity, and c_{g0} is the group velocity of the waves approaching the beach. The effect of wave nonlinearities is to increase the wave height above that predicted by Equation (11). As alternatives to Equation (11), a variety of nonlinear shoaling theories have been proposed (e.g., Rienecker and Fenton, 1981; Shuto, 1974). According to Shuto (1974), nonlinear effects should be taken into account for $Ur \geq 30$, where Ur is the local Ursell number, defined as $Ur = gHT^2/h^2$, where T is the wave period. Rienecker and Fenton (1981) developed a higher order wave model using up to 16 terms in a Fourier expansion of the wave equation, and this model was shown to provide a reasonable approximation of the wave height up to the time of wave breaking. In this study, the shoaling relation given by Equation (11) was assessed by comparing predicted pre-breaking wave heights with laboratory measurements.

Wave breaking. Waves are typically assumed to break when the ratio of the wave height, H , to the water depth, h , exceeds a critical value called the breaker coefficient, γ_b . Typical values of γ_b are in the range of 0.4–1.2, although γ_b is frequently cited as being in the range of 0.76–0.88. There is some evidence that γ_b is a function of the beach slope, S , with increasing γ_b corresponding to increasing S (Battjes, 1974; Thornton and Guza, 1986). However, even for a given beach slope, γ_b can be highly variable; for example, for a slope of 10% values of γ_b in the range of 0.68–1.18 have been reported (Galvin and Eagleson, 1964). Additional dependency of γ_b on the deepwater wave steepness, H_0/L_0 , has also been indicated, and an empirical relation between γ_b , S , and H_0/L_0 has been suggested (Weggel, 1972) and used to describe wave-height transformation in the surf zone (Dally, 1990). The assumed value of γ_b has a direct influence on the distance from shore at which waves break, which then influences the wave-induced velocity distribution. In the present study, γ_b was used as a calibration parameter, and values of γ_b were varied to yield the best match between theory and measurements of wave-induced longshore velocity profiles.

After wave breaking. After wave breaking, both the form of the energy loss function, E_l , and the relation between wave height and water depth are uncertain. Longuet-Higgins (1970a) simplified this uncertainty by assuming that, after breaking, the wave height remains proportional to the water depth, with the proportionality factor being equal to γ_b . For plane beaches, this means that the wave height declines approximately linearly between the breaker line and the shoreline. Laboratory measurements indicate that this approximation is reasonable (Sun and Tao, 2003; Yan et al., 2021); however, this approximation is less applicable for beach slopes on the order of 1% or less. For smaller beach slopes, multiple wave breaking and shoaling cycles

are prevalent, with γ_b for broken waves being less than that for breaking waves (Yan et al., 2021). A parametric model for nonlinear wave shoaling was proposed and validated by Kweon and Goda (1997), with a notable feature of this model being that the wave height is roughly proportional to the water depth after wave breaking, with the proportionality factor being around 0.4. Wave heights after wave breaking influence the radiation-stress gradients that are used to determine the longshore velocity profile via Equation (4). In the present study, radiation-stress gradients consistent with a linear decline in wave height between the breaker line and the shoreline were assumed.

4.2. Wave-induced longshore current

Analytic longshore flow models for plane beaches using Equation (4) were originally proposed by Bowen (1969) and Longuet-Higgins (1970b). The key differences between these models are: (1) Bowen (1969) assumed a linear proportionality between the bottom shear stress and the wave-induced velocity (compared with a quadratic relation assumed by Longuet-Higgins), and (2) Bowen (1969) assumed a constant eddy viscosity in the surf zone (compared with an eddy viscosity that goes to zero as the coastline is approached assumed by Longuet-Higgins). In this study, the alongshore velocity distribution is assumed to be described by the Longuet-Higgins (1970b) model, in which the bottom shear stress, τ_b , radiation-stress gradient, $\partial S_{xy}/\partial x$, and eddy viscosity, ν_e , in Equation (4) are specified as follows:

$$\begin{aligned} \tau_b &= \frac{2}{\pi} \alpha_0 C_D \rho v \sqrt{gh}, & \frac{\partial S_{xy}}{\partial x} &= \frac{5}{4} \alpha_0^2 \rho (gh)^{3/2} S \left(\frac{\sin \theta}{c} \right), \\ \nu_e &= N \rho x \sqrt{gh} \end{aligned} \quad (12)$$

where α_0 is a constant that is approximately equal to 0.41; C_D is the bottom-drag coefficient; v is the alongshore velocity; c is the local phase speed, which is equal to \sqrt{gh} in shallow water; N is a dimensionless constant that is estimated to be within the range of 0–0.016; and x is the perpendicular distance from the shoreline. Using the relations in Equation (12) with Equations (1)–(4), the velocity distribution is given by (Longuet-Higgins, 1970b):

$$\frac{v}{V} = \begin{cases} \varphi_1 \cdot (x^*)^{p_1} + \varphi_2 \cdot x^*, & 0 < x^* \leq 1 \\ \varphi_3 \cdot (x^*)^{p_2}, & 1 < x^* < \infty \end{cases} \quad (13)$$

where $x^* = x/x_b$ is the normalized distance perpendicular to the shoreline, φ_1 , φ_2 , and φ_3 are functions of the parameters p_1 , p_2 , and P as given by

$$\begin{aligned} \varphi_1 &= \frac{p_2 - 1}{p_1 - p_2} \left(\frac{1}{1 - 2.5P} \right), & \varphi_2 &= \frac{p_1 - p_2}{p_2 - 1} \varphi_1, \\ \varphi_3 &= \frac{p_1 - 1}{p_2 - 1} \varphi_1 \end{aligned} \quad (14)$$

where p_1 and p_2 are functions of the single parameter, P , where

$$p_1 = -\frac{3}{4} + \left(\frac{9}{16} + \frac{1}{P} \right)^{\frac{1}{2}}, \quad p_2 = -\frac{3}{4} - \left(\frac{9}{16} + \frac{1}{P} \right)^{\frac{1}{2}} \quad (15)$$

The combination of Equations (13)–(15) give the velocity distribution in the nearshore zone, $v(x)$, as a function of P ,

x_b , and V . In the Longuet-Higgins (1970b) formulation, P and V can be expressed in terms of other parameters as

$$P = \frac{\pi SN}{2\alpha_0 C_D}, \quad V = \frac{5\pi\alpha_0 S}{8C_D} \sqrt{gh_b} \sin \theta_b \quad (16)$$

where h_b and θ_b are the still-water depth and wave angle, respectively, at the breaker line. Of the three parameters (P , V , and x_b) that control the longshore velocity distribution, P measures the relative importance of cross-shore momentum transfer (quantified by the eddy viscosity), V is representative scale of the longshore velocity, and x_b is the distance from the shore to the breaker line. Although the Longuet-Higgins (1970b) formulation presented here assumes that turbulent fluctuations are the primary mechanism of cross-shore momentum transfer, Svendsen and Puetrevu (1994) have shown that cross-shore circulation caused by breaking waves can be a much greater source of cross-shore momentum transfer than turbulent velocity fluctuations. This shear-dispersion mechanism can be effectively accounted for in the Longuet-Higgins (1970b) model by increasing the value of N in Equation (12), which is included in the P parameter. The longshore velocity distribution given by Equation (13) is subsequently compared with several laboratory-measured wave-induced velocity profiles.

Other considerations. On planar beaches, wave-basin and field measurements roughly confirm a local maximum longshore velocity within the surf zone, with the longshore velocity decreasing rapidly to zero near the shoreline, and gradually decaying to zero over a distance 0.5–2 times the surf-zone width beyond the region of wave breaking (Longuet-Higgins, 1970b). In non-planar beaches, the presence of sand bars or irregular bathymetry can introduce several velocity maxima in the vicinity of sand bar crests, velocity minima in troughs, and a significant non-zero flow close to the shoreline (Ruessink et al., 2001).

4.3. Turbulent diffusion

The components of the local turbulent diffusion coefficient in the cross-shore (x) and longshore (y) directions, ϵ_x and ϵ_y , respectively, can be taken as being proportional to the maximum wave induced orbital velocity and the maximum particle displacement (based on shallow-water wave theory). Using these proportionalities and assuming isotropy, the components of the local turbulent diffusion coefficients can be expressed in the following form (Bowen and Inman, 1974; Thornton, 1970):

$$\epsilon_x = \epsilon_y = \epsilon_t = \alpha \left(\frac{Hg}{c} \right)^2 T_0 \quad (17)$$

where α is a proportionality constant, H is the local wave height, g is the gravity constant; c is the local phase speed, and T_0 is the wave period. The local value of the turbulent diffusion coefficient, ϵ_t , can be scaled by its value at the breaker line, denoted by ϵ_{tb} , which is calculated using Equation (17) with $H=H_b$ and $c=c_b \approx \sqrt{gh_b}$, where the “b” subscript indicates breaker-line values, shallow water conditions are assumed, and T_0 is taken as being invariant in the surf zone. Under these conditions, ϵ_{tb} , is given by

$$\epsilon_{tb} = \alpha \left(\frac{H_b g}{c_b} \right)^2 T_0 \rightarrow \epsilon_{tb} = \alpha \frac{H_b^2 T_0 g}{h_b} \quad (18)$$

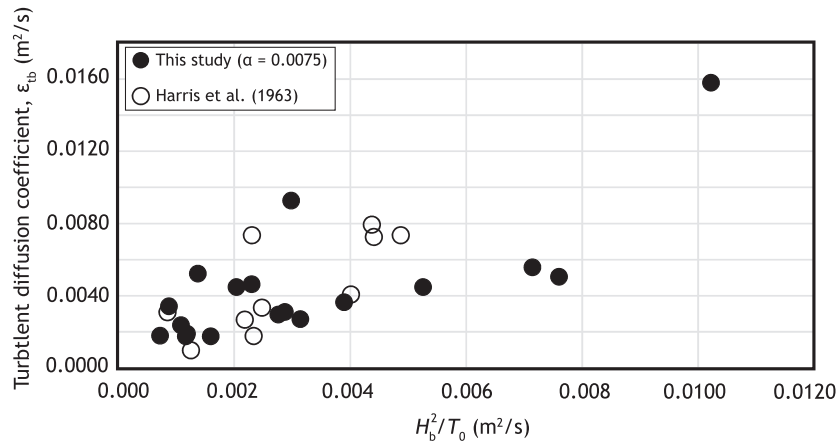


Figure 1 Local turbulent diffusion coefficients.

To determine an appropriate value of α , values of ϵ_{tb} were calculated using Equation (18) with wave-basin measurements used in this study, and these estimated values of ϵ_{tb} were compared with the laboratory-scale values of the turbulent diffusion coefficient reported by Harris et al. (1963). To determine the best match, values of α were varied in increments of 0.0025, and $\alpha = 0.0075$ was found to provide the best agreement between ϵ_{tb} calculated with Equation (18) and the Harris et al. (1963) data. These data are compared in Figure 1, where ϵ_{tb} is plotted as a function of H_b^2/T_0 , which is the format originally presented by Harris et al. (1963). It is relevant to note that taking ϵ_{tb} as proportional to H_b^2/T_0 is consistent with Equation (18), where gravity controls the relation between the length and time scales such that $H_b/T_0^2 \sim g$. Cross-shore mixing is primarily influenced by both wave-induced turbulence and shear dispersion associated with cross-shore circulation induced by breaking waves. Pearson et al. (2009) have shown that, for waves normal to the shoreline, cross-shore dispersion is the primary contributor to cross-shore mixing. However, with the effect of shear dispersion taken into account and taking $H_b/T_0^2 \sim g$ it can be shown that the added effect of shear dispersion can be represented by an increased value of α in Equation (18).

Upscaling laboratory results. Wave-basin experiments are generally scaled for Froude similarity between laboratory-scale and full-scale (field) conditions. Imposing Froude similarity, the time-scale ratio, T_r , is related to the length-scale ratio, L_r , by

$$T_r = \sqrt{L_r} \tag{19}$$

Therefore, if the wave-basin dimensions are 1/16 times the corresponding full-scale dimensions, then the laboratory-scale time scale is 1/4 times the time scale in the field; this also means that the laboratory-scale wave period must be 1/4 times the corresponding period in the field. Froude scaling also implies that the ratio of the full-scale diffusion coefficient to the lab-scale diffusion coefficient should be equal to $L_r^2/T_r = L_r^{1.5}$. Since both ϵ_{tb} and $H_b^2 T_0 g/h_b$ in Equation (18) have the same scaling, then the factor α is expected to be scale invariant, which means that the value of α found at the lab scale should be applicable at the field scale. This hypothesis was tested using

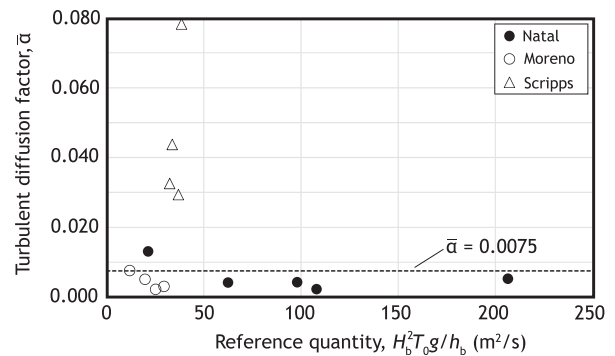


Figure 2 Field-scale turbulent diffusion factors.

the field data shown in Table 1, where data for the Moreno and Scripps sites were reported by Inman et al. (1971), and data for the Natal site were reported by Harris et al. (1963). For each site and experiment number (#), Table 1 shows the wave period (T_0), characteristic wave height at breaking (H_b), water depth at breaking (h_b), incident angle (θ_b), estimated cross-shore and longshore turbulent diffusion coefficients (ϵ_x and ϵ_y , respectively), the reference quantity ($H_b^2 T_0 g/h_b$), the ratios of cross-shore and longshore diffusion coefficients to $H_b^2 T_0 g/h_b$ (α_x and α_y , respectively), and the ratio of the averaged diffusion coefficient to $H_b^2 T_0 g/h_b$ ($\bar{\alpha}$). The data shown in Table 1 indicate that α is anisotropic, with highly anisotropic results being reported at the Scripps site, and less anisotropic results reported at the Moreno site. The incident angle is likely a factor influencing the isotropy of turbulent diffusion, with normally incident waves (i.e., $\theta_b = 0^\circ$) creating the most anisotropic diffusion coefficients. However, for all the laboratory data used in this study, the incident angle was 30° , which should increase the isotropy of the turbulent diffusion coefficient and provides some justification for assuming isotropic turbulent diffusion for the cases considered in this study. Recognizing that the turbulent-diffusion coefficient, α , at the lab scale corresponds to $\bar{\alpha}$ at the field scale, scale invariance of α would be supported if $\bar{\alpha} \approx \alpha$, regardless of the value of $H_b^2 T_0 g/h_b$. The relation between $\bar{\alpha}$ and $H_b^2 T_0 g/h_b$ at the field sites is shown in Figure 2, where the lab-derived value of

Table 1 Field results.

Site	#	T_0 (s)	H_b (m)	h_b (m)	θ_b (°)	ϵ_x (m ² /s)	ϵ_y (m ² /s)	$H_b^2 T_0 g / h_b$ (m ² /s)	α_x (-)	α_y (-)	$\bar{\alpha}$ (-)
Moreno	93	13.6	0.15	0.119	43	0.08	0.03	25.2	0.003	0.001	0.002
	95	14.3	0.14	0.093	3	0.11	0.07	29.5	0.004	0.002	0.003
	97	14.3	0.08	0.045	3	0.12	0.08	19.7	0.006	0.004	0.005
	104	11.7	0.11	0.117	0	0.12	0.06	11.9	0.010	0.005	0.008
Scripps	107	11.7	0.46	0.657	0	2	0.17	37.0	0.054	0.005	0.029
	109	11.7	0.42	0.6	0	2.8	0.15	33.7	0.083	0.004	0.044
	112	11.1	0.42	0.592	0	2	0.11	32.4	0.062	0.003	0.033
Natal	129	12.2	0.46	0.657	1	5.9	0.13	38.5	0.153	0.003	0.078
	1	12	1.37	1.07	0	1.08	-	206.5	0.005	-	0.005
	2	10	1.07	1.04	0	0.24	-	108.0	0.002	-	0.002
	3	8	0.91	1.05	0	0.26	-	62.4	0.004	-	0.004
	4	10	1.22	1.49	0	0.42	-	98.0	0.004	-	0.004
	5	8	0.61	1.37	0	0.28	-	21.3	0.013	-	0.013

$\alpha = 0.0075$ is also shown. It is apparent from these results that there is fair agreement between $\bar{\alpha}$ and $\alpha = 0.0075$ at the Moreno and Natal sites, with $\bar{\alpha} \gg 0.0075$ at the Scripps site. There is no conclusive reason for the discrepancy at the Scripps site, although increased cross-shore shear dispersion at this site could account for this effect. Taken together, the results shown in Figure 2 provide fair support for the scale invariance assertion for α . Note that the values of $H_b^2 T_0 g / h_b$ in the lab-scale experiments are in the range of 0.21–1.2, which is around two orders of magnitude smaller than the values of $H_b^2 T_0 g / h_b$ at the field scale, hence a scale invariance finding for α is quite impressive.

Dye and drifter studies. Several dye and drifter studies have been performed in the surf zone to quantify turbulent diffusion coefficients. These studies generally confirm that the surf zone is a region of intense mixing, and that, in the absence of rip currents, diffusion and advective transport tend to retain tracers within the surf zone (Clarke et al., 2007). Clarke et al. (2007) reported cross shore local diffusion coefficients of around 1 m²/s, and local longshore diffusion coefficients of around 0.1 m²/s; outside the surf zone, diffusion coefficients were reported as 0.03 m²/s. Based on observed dye dilution, Inman et al. (1971) obtained cross-shore diffusion coefficients in the range of 0.08–5.9 m²/s, and alongshore diffusion coefficients in the range of 0.03–0.17 m²/s. Spydell et al. (2007) used surface drifters to study dispersion in the surf zone, although dispersion of surface drifters is not representative of the dispersion of a tracer that is dissolved in the water column. The Spydell et al. (2007) results showed that, after initial isotropy, the alongshore dispersion is much greater than the cross-shore dispersion. Sun and Tao (2006) performed dye-release studies in a laboratory wave basin and concluded that the dye discharged inside the surf-zone will transport approximately parallel to the shoreline under the action of waves, while the dye transport outside the surf-zone is hardly affected by wave action. It was also shown that the effect of waves on pollutant transport was greater for beaches with lesser slopes. Takewaka et al. (2003) reported on a field-scale instantaneous dye release just offshore of the main breaker line, where the dye was tracked by airborne video from a height of approximately 200 meters. As expected, the re-

leased dye mostly moved parallel to the shoreline, with the dye closer to shore moving faster, and the dye patch having an inclined elliptical shape. The cross-shore mixing rate increased as the breaker line was approached. Dye studies adjacent to a plane beach reported by Harris et al. (1963) showed that for normally incident waves cross-shore dispersion can be dominant with minimal alongshore translation; for oblique waves, alongshore advection and dispersion within the narrow surf-zone band was observed. Grant et al. (2005) reported longitudinal dispersion coefficients in the range of 40–80 m²/s where the mean longshore current was around 30 cm/s, and the width of the surf zone was on the order of 50 m.

5. Dimensional analysis

The primary objective of the present study is to identify relations that can be used to quantify the dispersion of contaminants released in and around the surf zone. Contaminant transport is primarily influenced by both the distribution of mean velocity and velocity fluctuations due to turbulence, with turbulence-induced transport parameterized by the turbulent diffusion coefficient. Dispersion coefficients are macroscopic parameters that can be used in conventional advection-dispersion models to calculate concentrations resulting from released contaminants. The dispersion-coefficient components of most interest are the components normal and parallel to the shoreline, denoted by K_x and K_y , respectively. The functional relationship between the dispersion-coefficient components and the influencing variables can be expressed as follows:

$$K_x \text{ or } K_y = f_1(x_0, x_b, P, V, t, \epsilon_{tb}) \quad (20)$$

where x_0 is the release location, x_b is the breaker-line location, P is the velocity-profile shape parameter, V is the average longshore velocity, t is the time since release, and ϵ_{tb} is the characteristic turbulent diffusion coefficient, which is taken to be the turbulent diffusion coefficient at the breaker line. In accordance with the Longuet-Higgins (1970b) model of wave-generated alongshore velocity given by Equation (13), the velocity distribution is determined by

the parameters P , x_b , and V . Using the Buckingham pi theorem, Equation (20) can be expressed in the following non-dimensional form:

$$\frac{K_x}{Vx_b} = f_{2x}\left(\frac{x_0}{x_b}, P, \frac{Vt}{x_b}, \frac{\epsilon_{tb}}{Vx_b}\right), \quad \frac{K_y}{Vx_b} = f_{2y}\left(\frac{x_0}{x_b}, P, \frac{Vt}{x_b}, \frac{\epsilon_{tb}}{Vx_b}\right) \quad (21)$$

The components of the normalized longitudinal dispersion coefficients can be defined as $K_x^* = K_x/(Vx_b)$ and $K_y^* = K_y/(Vx_b)$; the normalized discharge location relative to the breaker line as $x_0^* = x_0/x_b$; the normalized time since release as $t^* = tV/x_b$, which is also a measure of the along-shore mean advection distance relative to x_b ; and the normalized turbulent diffusion coefficient as $\epsilon_{tb}^* = \epsilon_{tb}/(Vx_b)$. Combining Equation (18) with the definition of ϵ_{tb}^* yields

$$\epsilon_{tb}^* = \alpha \frac{gH_b^2 T_0}{Vx_b h_b} \quad (22)$$

For any given scenario, H_b , T_0 , h_b , x_b , and V can be estimated from site conditions; however, α must be specified based on the characteristic value derived from lab-scale or field-scale experiments. Expressing Equation (21) in terms of the normalized variables yields

$$K_x^* = f_{2x}(x_0^*, P, t^*, \epsilon_{tb}^*), \quad K_y^* = f_{2y}(x_0^*, P, t^*, \epsilon_{tb}^*) \quad (23)$$

Determination of empirical relations corresponding to the functional relations given by Equation (23) are key outcomes of this investigation.

6. Data analyses

The data used in this study were obtained from measurements in wave basins that were reported by others. These data included measurements of longshore velocities caused by waves obliquely impacting a shoreline. In some cases, corresponding measurements of wave heights as a function of distance from the shoreline were also available. Using these data, the present study was conducted in two stages. In the first stage, the measured longshore velocity distributions were compared to the Longuet-Higgins (1970b) distribution, henceforth called the LH distribution, and the best-fit theoretical distributions were identified. In the second stage, Lagrangian particle tracking was used along with the best-fit velocity distributions to determine the dispersion coefficients, and the quantitative dependencies expressed in Equation (23).

7. Longshore velocity distributions

The longshore velocity distributions used in this study were mostly derived from laboratory measurements reported by Sun and Tao (2003), Sun and Tao (2006), and Yan et al. (2021). These experiments were all performed at Dalian University of Technology in China, with the investigators affiliated with Dalian University of Technology, Tianjin University, and Beijing Normal University. These academic institutions are all located in the vicinity of the Bohai Sea, which receives discharge from the Yellow River in North China. The reported research is mostly focused on and motivated by conditions in Bohai Bay, located within the Bohai Sea.

Sun and Tao (2003) experiments. The wave basin used by Sun and Tao (2003) was 42.6 m long and 24.0 m wide, the beach was placed at a 30° angle to the incoming waves, and the beach extended 18 m normal to the shoreline. Two beach slopes were investigated, 1% (1:100) and 2.5% (1:40), and the corresponding still-water depths at the beginning of the beach slopes were 18.0 cm and 45.0 cm, respectively. Both regular and irregular waves were studied, with periods of 1.0 s and 1.5 s, and characteristic wave heights of 3 cm and 5 cm were used. A few dye-release experiments were also conducted in the wave basin, using both instantaneous and continuous releases. This study was published in Chinese.

Sun and Tao (2006) experiments. The same experimental setup as reported in Sun and Tao (2003) was used. Results were given for a beach slope of 1%, a wave period of 1 s, regular waves with a height of 7 cm, and irregular waves with an average height of 5 cm. Pollutant transport was recorded by tracking the released dye using a video camera placed at 8 m above the water surface, although the dye-release results were not reported in this paper.

Yan et al. (2021) experiments. The wave basin used by Yan et al. (2021) was 55 m long, 32 m wide, and 0.8 m deep, with the waves being generated by a piston-type wave maker having 70 paddles. The beach geometry was the same as that of Sun and Tao (2003), with the beach at a 30° angle to the incoming waves, and the beach extending 18 m normal to the shoreline. Two beach slopes were investigated, 1% and 2.5%, and the corresponding still-water depths at the beginning of the beach slopes were 18.0 cm and 45.0 cm, respectively. The incident waves included both regular and irregular waves with periods of 1.0 s, 1.5 s, and 2.0 s, and three wave heights for each wave period. Despite the similarity of experimental setup with that of Sun and Tao (2003), Yan et al. (2021) made no reference to the earlier study.

Other measurements. Aside from the above experimental data, one additional data set was derived from experiments reported by Visser (1982) performed at the Delft University of Technology; these results were also reported by Larson et al. (1991). The Visser (1982) experiments were done in a wave basin that was approximately 17 m long and 34 m wide, with a snake-type generator that produced only regular waves. The beach was placed at a 15.4° angle to the incoming waves, the beach slope was approximately 10%, and the approach waves had a period of 1 second. In addition to the data generated in the aforementioned wave-basin experiments, several earlier laboratory measurements have also been reported in the open literature (e.g., Brebner and Kamphuis, 1963; Gavin and Eagleson, 1964; Putnam et al., 1949; Saville, 1950).

7.1. Fitted velocity distributions

The beach slope (S), wave period (T), and approach wave height (H_0), for each of the data sets used in this study are shown in Table 2. Data sets 1 and 102 are from Sun and Tao (2003), data sets 2 and 201 are from Sun and Tao (2006), data sets 3–24 and 26–30 are from Yan et al. (2021), and data set 25 is from Visser (1982). Wave types “R” and “I” in Table 2 refer to regular and irregular waves, respectively. For the irregular waves, Sun and Tao (2003) reported the

Table 2 Parameters of velocity distributions.

Set #	Type	S (%)	T (s)	H_0 (cm)	γ_b (-)	x_b (m)	P (-)	V (cm/s)
1	R	1	1.0	3.0	0.70	4.93	0.017	9.6
102	I	1	1.0	3.0	0.65	5.25	0.151	7.3
2	R	1	1.0	7.0	0.87	9.94	0.142	11.6
201	I	1	1.0	5.0	0.71	7.55	0.167	8.7
3	R	1	2.0	7.0	0.79	9.77	0.023	8.5
14	R	2.5	1.0	8.6	0.77	4.39	0.038	19.2
15	R	1	1.0	4.9	0.69	7.61	0.001	7.8
16	R	1	1.0	6.0	0.70	8.92	0.035	7.8
17	R	1	1.5	4.9	0.70	7.90	0.001	7.9
18	R	1	1.5	5.3	0.68	8.64	0.016	8.4
19	R	1	2.0	4.6	0.66	7.95	0.001	7.8
25	R	10	1.0	8.9	0.65	1.33	0.676	38.0
26	I	1	1.5	2.9	0.47	6.99	0.016	6.3
27	I	2.5	1.0	5.6	0.57	3.94	0.140	11.9
28	I	1	1.0	3.7	0.54	7.39	0.35	6.7
29	I	1	1.5	3.6	0.51	7.89	0.025	7.2
30	I	1	2.0	3.6	0.54	7.75	0.032	7.1

average wave height but did not report the spectral characteristics, Sun and Tao (2006) reported average wave heights and used the Wen spectrum (Wen and Yu, 1984), and Yan et al. (2021) reported root-mean-square wave heights and used the JONSWAP spectrum (Hasselmann et al., 1973). For each set of velocity-profile measurements, values of x_b , P , and V were found that provide the best least-squares fit between the measurements and the LH velocity profile. In the fitting process, values of x_b were generated indirectly by first specifying a breaking coefficient, γ_b , and then calculating x_b by applying the linear theory of wave shoaling and refraction on the planar beach. This approach served not only to specify x_b , but also to provide a rough estimate of the breaking coefficient that corresponds to the given regular-wave experimental parameters. If wave-height measurements corresponding to the alongshore velocity measurements were available, the calculated value of x_b was compared with the observed value of x_b , which provided a useful assessment of the complete LH model, which includes the assumption that wave pre-breaking heights in the surf zone can be described by linear theory, and that post-breaking wave heights are proportional to the still-water depth.

8. Results

The values of x_b , P , and V that provide the best fit to the observed longshore velocity profiles are shown in Table 2, and the corresponding fitted longshore velocity distributions and measured velocity profiles are shown in Figure 3 for regular waves, and Figure 4 for irregular waves. Comparisons of the LH-model velocity distributions with measured data show fairly close agreement in both regular and irregular wave environments. These results provide support for the functional relation in Equation (13), in which the velocity distribution is entirely parameterized by x_b , P , and V . Although approximation of the measured data by theoretical (LH) distributions seems reasonable, deviations oc-

cur which can be partially attributed to experimental variability as well as the more complex conditions that occur with low beach slopes, where multiple wave-breaking conditions can exist. In the present study, the best-fit theoretical velocity distributions are subsequently used in the dispersion simulations, where shear dispersion is expected to be the dominant mixing mechanism for tracers released into the nearshore environment. In this context, the theoretical velocity distributions shown in Figures 3 and 4 adequately represent the predominant velocity shears in the nearshore zone.

Wave heights. For the three regular-wave cases in which corresponding velocity measurements and wave heights were reported, the linear-theory wave heights corresponding to values of x_b used in the best-fit velocity distribution are compared with the wave-height measurements in Figure 5. For data sets 1 and 25 there is good agreement between the measurements and the linear-theory wave heights (solid line) corresponding to the observed velocity distribution, while for data set 3 there is not good agreement. The pre-breaking linear-theory wave-height distribution was also estimated by varying γ_b to find the best agreement between measured and theoretical wave heights, and these best-fit wave-height distributions are shown as a dash-dot line in Figure 5. It is apparent that values of γ_b can be found that yield wave-height distributions that adequately represent the observed wave-height distributions using linear theory. Collectively, comparative evaluation of corresponding wave-height and longshore velocity measurements indicate that the LH model of wave-heights and corresponding longshore velocity profiles might be approximately valid in some cases (two of the three in the present study). Notably, the Ursell numbers (at breaking) for data sets 1, 3, and 25 were estimated as 130, 307, and 39 respectively, with an Ursell number of 30 sometimes being cited as the upper limit for the application of linear theory (Tsai et al., 2005). Aside from discrepancies in the theoretical and measured pre-breaking wave heights, it is apparent from Figure 5 that the approximation that post-breaking wave heights decrease linearly to zero at the shoreline is a reasonable approximation. It is important to keep in mind that discrepancies in the theoretical and measured wave heights do not invalidate the fitted theoretical velocity distributions, which are purely a functional fit.

9. Dispersion in the nearshore zone

Laboratory measurements of tracer dispersion with corresponding measurements of longshore velocities are very limited. The only laboratory measurements that could be found were those reported by Sun and Tao (2003), who presented plots of the visible outlines of dye plumes at fixed times after initial release. These results were previously utilized by Winckler et al. (2013) to assess their dispersion-theory formulation, which was based on solving the advection-diffusion equation. The dispersion results reported by Sun and Tao (2003) correspond to the measured longshore velocities in data set 1, and so for comparative purposes the particle-tracking simulations in this study were implemented using the LH velocity profile that best fit the velocity measurements (see Figure 3).

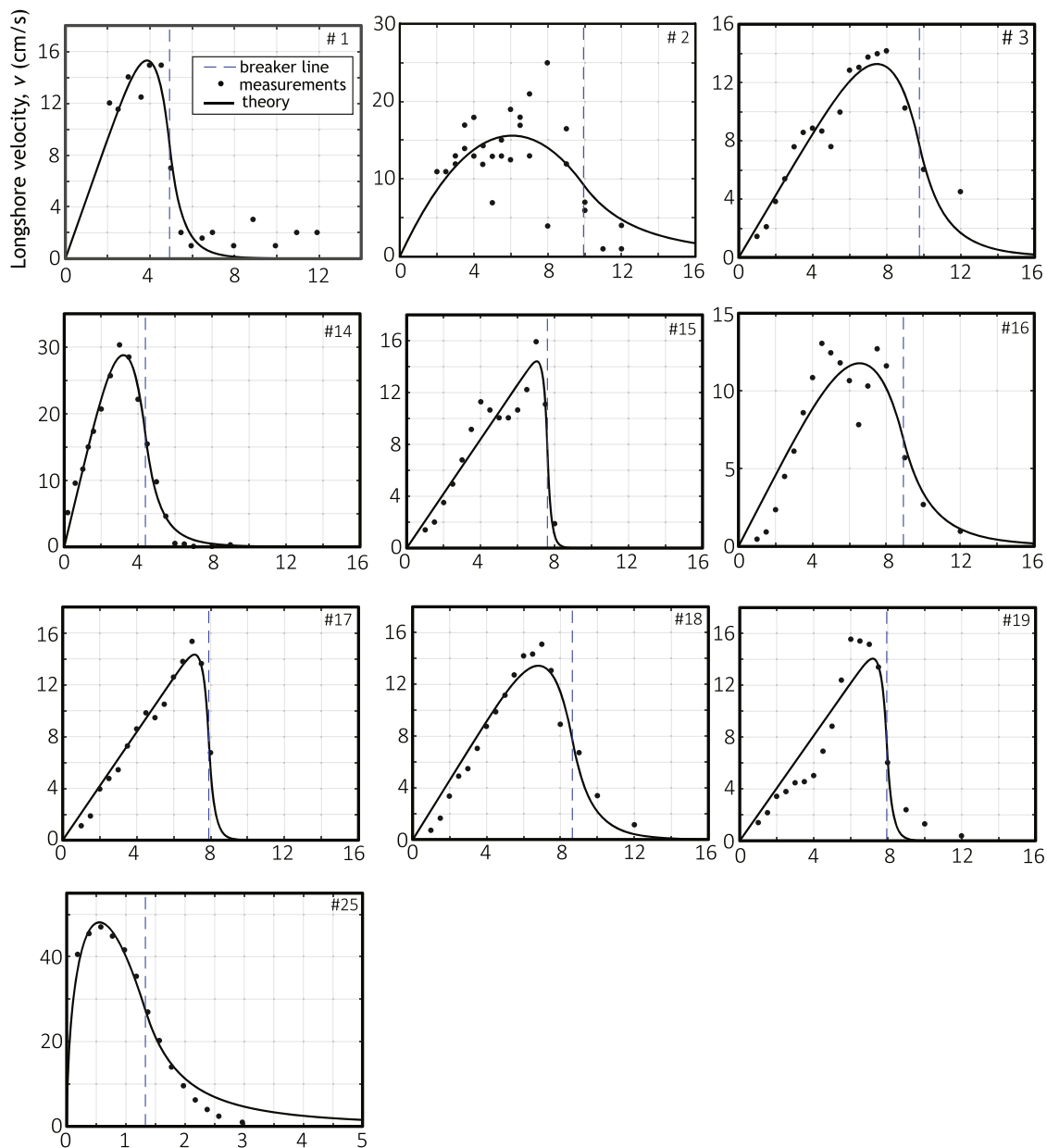


Figure 3 Velocity distributions with regular incident waves.

Instantaneous release. Comparison of the simulated tracer plume with the corresponding plume outline reported by Sun and Tao (2003) is shown in Figure 6a for an instantaneous release after 50 seconds. A difficulty with this comparison is identifying the concentration contour that corresponds to the plume outline reported by Sun and Tao (2003). For the simulation, the reference concentration, c_{0i} , was defined by

$$c_{0i} = \frac{M}{\Delta x \Delta y \Delta z_0} \quad (24)$$

where M is the released mass, Δx and Δy are the concentration-grid cell dimensions in the x and y coordinate directions, and Δz_0 is the still-water depth at the release location. In this study, $M=1$ kg, $\Delta x=\Delta y=0.25$ m, and $\Delta z_0=0.05$ m, and the plotted concentration contours in Figure 6a correspond to 1%, 0.1%, and 0.01% of

c_{0i} . The comparison between the reported and simulated instantaneous-release plumes in Figure 6a shows the center of the simulated plume being located further downstream than reported by Sun and Tao (2003). This finding was also observed by Winckler et al. (2013), and the discrepancy was attributed to the dye likely being released at a low-velocity location within the water column, since the reported longshore advection of the dye is inconsistent with the reported velocity measurements. Notably, the Winckler et al. (2013) advection-diffusion calculations also included the Stokes drift estimated using linear theory, which caused their predicted plume location to be closer to the shoreline than was observed. The present study neglects the Stokes drift, since it is uncertain under nonlinear conditions, and did not appear to be a significant process in the wave-basin. The dominance of shear dispersion is readily apparent from the shape of the simulated plume in Figure 6a, where the

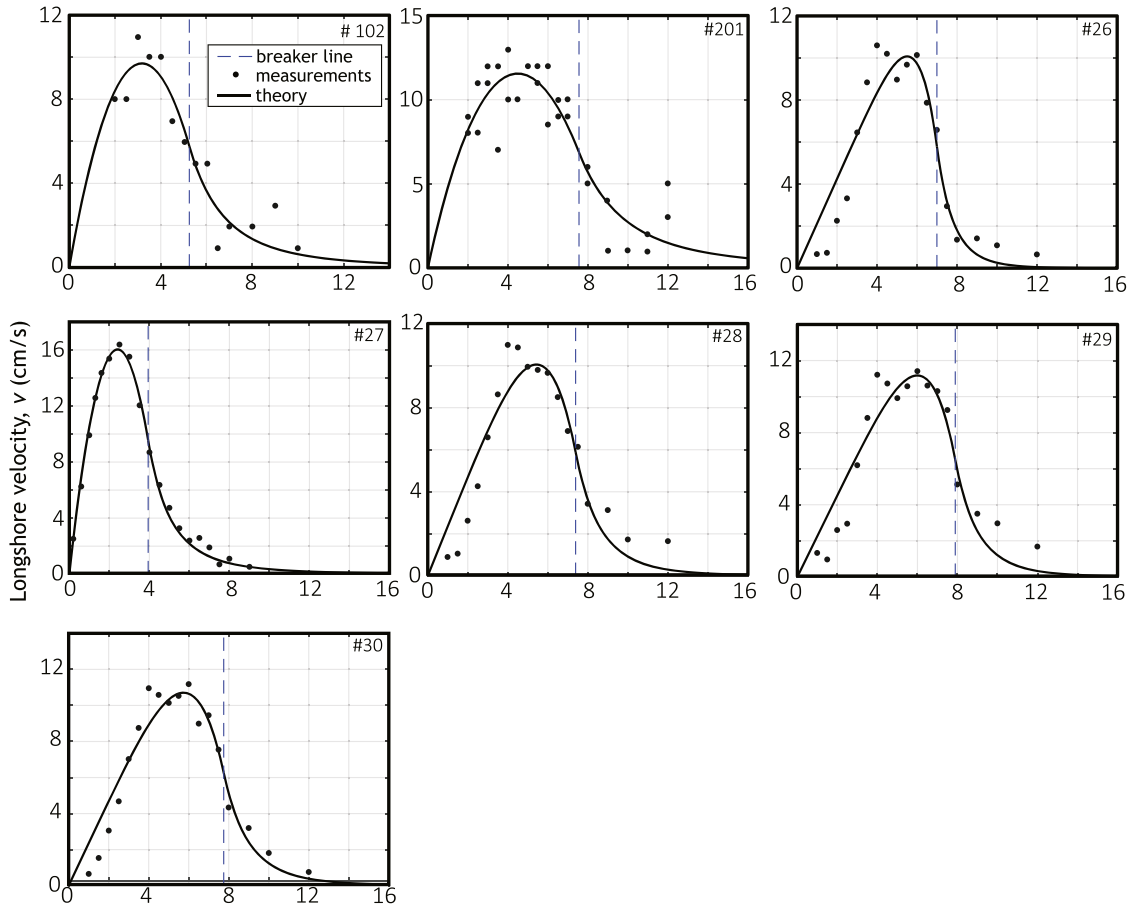


Figure 4 Velocity distributions with irregular incident waves.

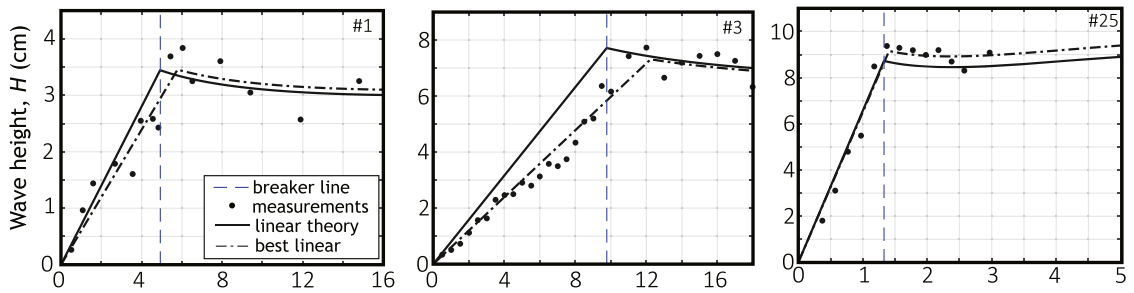


Figure 5 Wave heights with regular incident waves.

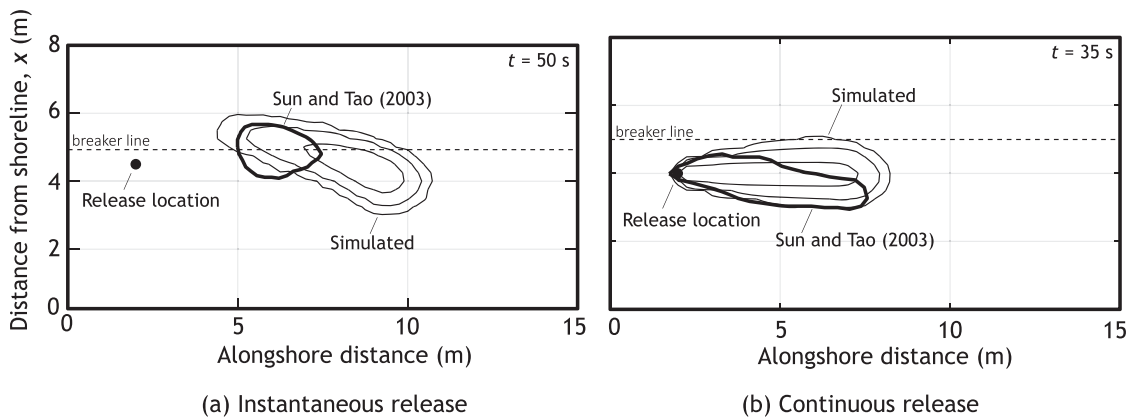


Figure 6 Comparison with dispersion observations: (a) instantaneous release; and (b) continuous release.

differential advection of the tracer is strongly influenced by the shear in the velocity profile. It is also readily apparent from the simulated plume that the effective longshore dispersion coefficient is much greater than the effective cross-shore dispersion coefficient.

Continuous release. For the continuous release, the reference concentration, c_{0c} , was defined by

$$c_{0c} = \frac{\dot{M}t}{\Delta x \Delta y \Delta z_0} \quad (25)$$

where \dot{M} is the mass release rate, t is the time of the simulation, and the other variables have the same definitions as for the instantaneous release. In this study, $\dot{M} = 1$ kg/s, $\Delta x = \Delta y = 0.25$ m, $\Delta z_0 = 0.13$ m, $t = 35$ s, and the concentration contours shown in Figure 6b correspond to 1%, 0.1%, and 0.01% of c_{0c} . The unreported concentration associated with the plume outline given by Sun and Tao (2003) again limits the comparison with the simulations; however, the reported outline of the plume from a continuous release is consistent with that of the simulated plume. Collectively, the results presented here provide a reasonable assurance that the dispersion simulations used in this study can provide an adequate representation of surf-zone dispersion for a given velocity field.

9.1. Dispersion coefficients

Dispersion coefficients were calculated in the cross-shore and longshore directions in accordance with the definitions given in Equation (8). Dispersion coefficients are generally expected to increase as a function of time, since with increasing time the plume increases in size and encompasses a wider variety of local velocities and turbulent diffusion coefficients. As indicated in the functional relations in Equation (23), for any given longshore-velocity-profile (quantified by P), the normalized components of the dispersion coefficient (K_x^* and K_y^*) depend on the normalized time since release (t^*), normalized release location (x_0^*), and normalized characteristic turbulent diffusion coefficient (ϵ_{tb}^*).

9.1.1. Temporal variation of dispersion coefficients

To facilitate analysis of the temporal variation of K_x^* and K_y^* , the turbulent-diffusion factor, α , was fixed as 0.0075, which was shown previously (in Figures 1 and 2) to be consistent with measurements of turbulent diffusion at both the laboratory and field scale. The values of K_x^* and K_y^* at dimensionless times (t^*) of 1, 5, and 10 were selected to assess the temporal evolution of the components of the dispersion coefficient. These normalized advection times correspond to mean longshore advection distances from the contaminant source on the order of x_b , $5x_b$, and $10x_b$, respectively. These selected reference times and corresponding distances were strategic, in that rip currents typically occur at longshore intervals of $5-10x_b$, and so dispersion coefficients over travel distances greater than $10x_b$ would be of lesser practical interest since such plumes would likely be intersected by rip currents.

Longshore dispersion. The normalized longitudinal dispersion coefficient, K_y^* , for normalized times since release (t^*) equal to 1, 5, and 10 are shown in Figure 7a for normalized release locations, $x_0^* (= x_0/x_b)$, in the range of 0–2. The results in Figure 7a are for data sets 17, 14, and

201, which have velocity shape parameters (P) of 0.001, 0.038, and 0.167, respectively. These data sets were chosen purposely, since longitudinal dispersion is controlled by velocity shear, and maximum velocity shear is inversely proportional to the magnitude of P . The results in Figure 7a demonstrate the following characteristics: (1) K_y^* increases with time regardless of release location, (2) the maximum value of K_y^* typically corresponds to release locations at distances on the order of $1.0-1.1x_b$ from the shoreline, which are at or just outside the breaker line, and (3) as time increases, K_y^* versus release location, x_0^* , typically has a double-peaked shape, with a nearshore lower peak at around $0.3x_b$, and a higher peak at around $1-1.1x_b$. The lower nearshore peak occurs where the presence of the shoreline begins to significantly influence the longshore dispersion, and the higher peak occurs near where the shear in the longshore velocity is the highest, which is near the breaker line. The maximum value of K_y^* at any time since release generally depends on the magnitude of the velocity shear, as measured by P . The maximum values of K_y^* (considering all release locations) as a function of P for various times since release are shown in Figure 8a. These results confirm the assertion that higher values of K_y^* are associated with higher shears in the mean longshore velocity, which correspond to lower values of P . From the results shown in Figure 8, K_y^* is in the approximate ranges of 0.04–0.2, 0.1–0.9, and 0.2–1.6 for t^* equal to 1, 5, and 10, respectively.

Cross-shore dispersion. Temporal variations of the normalized cross-shore dispersion coefficient, K_x^* , are shown in Figure 7b. It is apparent from these results that: (1) K_x^* values are generally less than 0.012, which makes $K_x^* \cong K_y^*$ for $t^* \leq 1$, and $K_x^* \ll K_y^*$ for $t^* \gg 1$, and (2) except for release locations in the vicinity of the breaker line (where $x_0^* = 1$), values of K_x^* are approximately independent of time. For releases near the breaker line, K_x^* values tend to slightly decrease over time. This atypical behavior is primarily because the K_x^* is proportional to $(Hg/c)^2 T_0$, which peaks at the breaker line. Consequently, releases from near the breaker line generally extend over regions with lower local values of $(Hg/c)^2 T_0$, thereby reducing the average K_x^* over time. The maximum values of K_x^* (considering all release locations) as a function of P for various times since release are given in Figure 8b. These results show that K_x^* is approximately independent of velocity shape parameter, P , which is an expected result since cross-shore mixing is primarily controlled by turbulent diffusion.

9.1.2. Role of turbulent diffusion

The growth of K_x^* and K_y^* as a function of time, as shown in Figure 7, is conditioned on a turbulent diffusion factor, α , of 0.0075, which is consistent with both laboratory- and field-scale measurements. However, the adequacy of using $\alpha = 0.0075$ in all beach and wave configurations is unresolved, along with the appropriate formulation for representing the spatial variability of turbulent diffusion and cross-shore shear dispersion in the surf zone. To partially assess the influence of the magnitude of turbulent diffusion and cross-shore shear dispersion on the longshore and cross-shore dispersion coefficients, the turbulent diffusion factor, α , was varied in the range of 0.00025–0.625, and the maximum values of K_x^* and K_y^* (considering all release locations) was determined for each value of α .

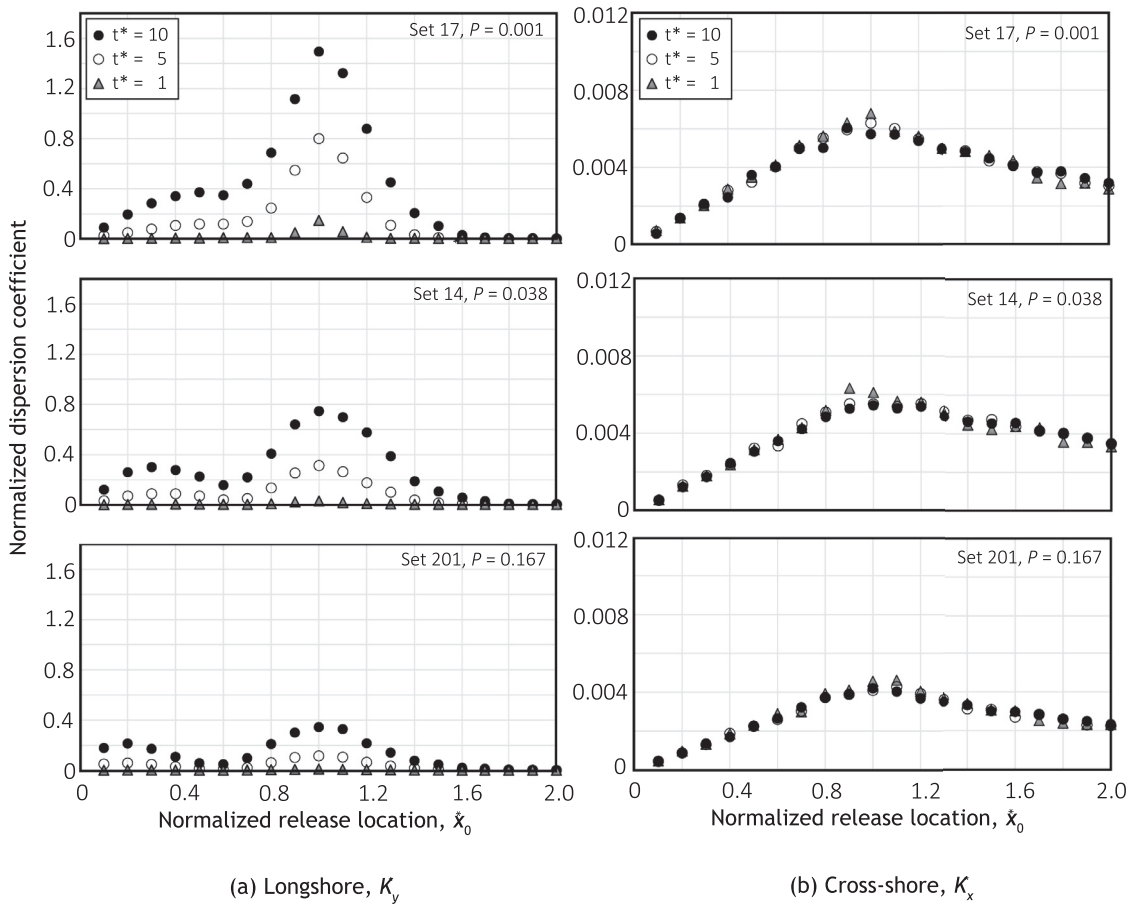


Figure 7 Temporal variation of normalized dispersion coefficients as a function of release location.

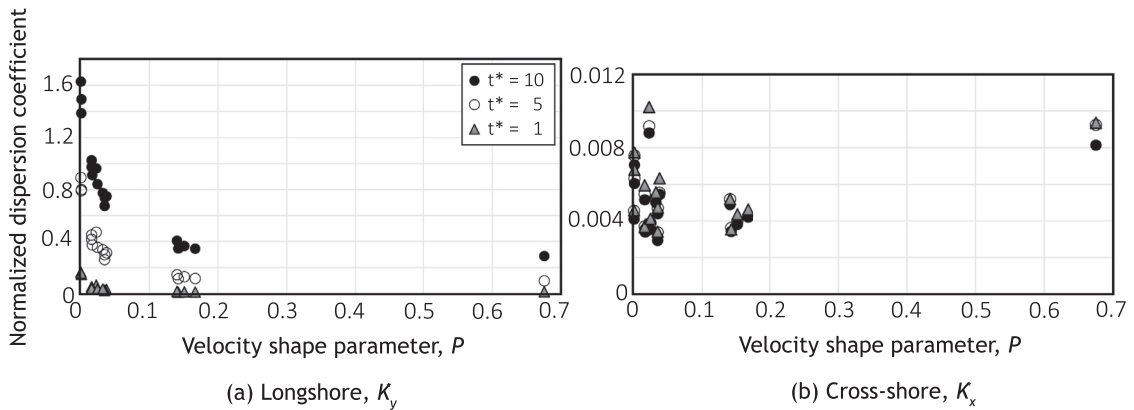


Figure 8 Maximum dispersion coefficient as a function of the velocity shape parameter.

Effect on longshore dispersion. The maximum normalized longshore dispersion coefficient, K_y^* , for any release location, as a function of the turbulent diffusion factor, α , is shown in Figure 9a. It is apparent from these results that the maximum value of K_y^* depends on the magnitude of turbulent-diffusion factor, α . For t^* values of 5 and 10, the maximum values of K_y^* typically occur for α in the range of 0.001–0.1. For $t^* = 1$, the maximum values of K_y^* monotonically increase with increasing α , which is a manifestation of the dominance of turbulent diffusion in longitudinal dispersion at early times since tracer release.

The magnitude of the maximum value of K_y^* , for all values of α , is significantly influenced by the longshore velocity profile, as characterized by the parameter P . The maximum value of K_y^* declines with increasing values of P , which corresponds to K_y^* decreasing with decreasing velocity shear.

Effect on cross-shore dispersion. The maximum normalized cross-shore dispersion coefficient, K_x^* , for any release location, as a function of the turbulent-diffusion factor, α , is shown in Figure 9b. The effect of α on cross-shore dispersion, K_x^* , shows approximately the same trend for all values of t^* , with K_x^* monotonically increasing with increasing val-

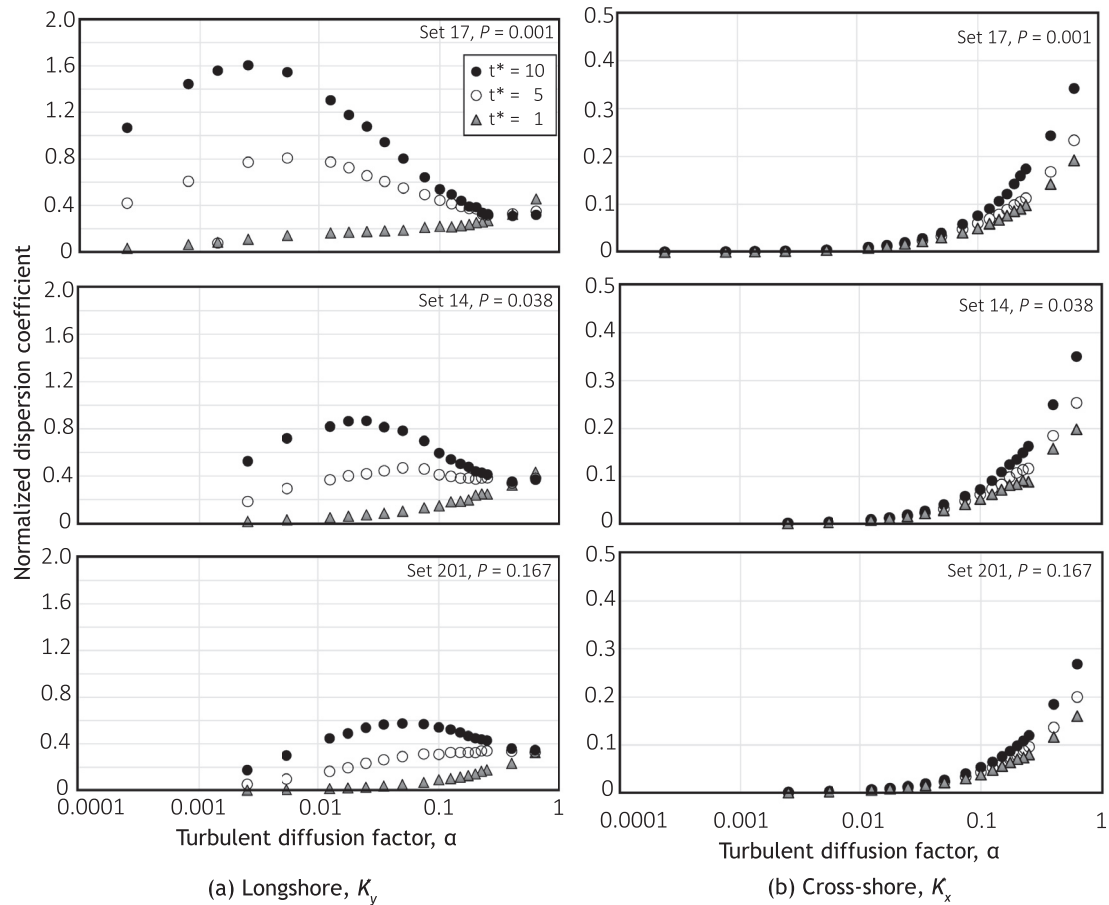


Figure 9 Normalized dispersion coefficients as a function of local turbulent diffusion.

ues of α . This reflects the fact that turbulent diffusion is the dominant mechanism of cross-shore dispersion.

10. Conclusions

This study provides advances in both the understanding and the predictability of contaminant dispersion in the surf zone of planar beaches and provides directions for future research. The hydrodynamics of the surf zone can be studied using laboratory-scale wave basins by imposing Froude similarity to relate the length and time scales in a wave basin to the corresponding scales in the field. Measurements of longshore velocities induced by both regular and irregular waves obliquely approaching planar beaches in wave basins were analyzed and, where available, wave heights corresponding to the measured velocity profiles were also considered. It is shown that the Longuet-Higgins (1970b) model of surf-zone hydrodynamics adequately describes the distribution of longshore currents measured at the laboratory scale. However, the adequacy of the Longuet-Higgins (1970b) model in predicting corresponding wave heights and longshore currents is limited to Ursell numbers less than around 100, which exceeds the limit of 30 normally associated with linear theory. The maximum longitudinal dispersion coefficients result from tracer releases near the breaker line, and longitudinal dispersion co-

efficients increase with travel time for distances up to at least 10 surf-zone widths. Transverse dispersion coefficients remain relatively constant for increasing travel time. It is notable that the longitudinal and transverse dispersion coefficients can be significantly influenced by local turbulent diffusion and cross-shore shear dispersion, so adequate estimation of these quantities is important, and further research in this area is needed.

Declaration of competing interest

The authors declare that they have no known competing financial interests or personal relationships that could have appeared to influence the work reported in this paper.

References

Battjes, J., 1974. Surf similarity. In: *Proceedings of the Fourteenth International Conference on Coastal Engineering*. American Society of Civil Engineers, New York, 466–480.
 Bowen, A., 1969. The generation of longshore currents on a plane beach. *J. Mar. Res.* 27, 206–215.
 Bowen, A., Inman, D., 1974. Nearshore mixing due to waves and wave-induced currents. *Rapports et Proces-verbaux des Reunions. Conseil International pour l'Exploration de la Mer* 167, 6–12.

- Brebner, A., Kamphuis, J., 1963. Model tests on the relationship between deep-water wave characteristics and longshore currents. Queens University, Kingston, Ontario C.E. Research Report No. 31.
- Clarke, L., Ackerman, D., Largier, J., 2007. Dye dispersion in the surf zone: Measurements and simple models. *Cont. Shelf Res.* 27, 650–669. <https://doi.org/10.1016/j.csr.2006.10.010>
- Dally, W., 1990. Random breaking waves: a closed-form solution for planar beaches. *Coastal Eng.* 14, 233–263.
- Galvin Jr., C., Eagleson, P., 1964. Experimental Study of Longshore Currents on a Plane Beach. Hydrodynamics Laboratory, Department of Civil Engineering, Massachusetts Institute of Technology, Cambridge, Massachusetts. Tech. Rep. No. 63.
- Grant, S., Kim, J., Jones, B., Jenkins, S., Wasyl, J., Cudaback, C., 2005. Surf zone entrainment, along-shore transport, and human health implications of pollution from tidal outlets. *J. Geophys. Res.* 110. <https://doi.org/10.1029/2004JC002401>
- Harris, T., Jordaan, J., McMurray, W., Verwey, C., Anderson, F., 1963. Mixing in the Surf Zone. *Int. J. Air Water Pollut.* 7, 649–667.
- Hasselmann, K., Barnett, T., Bouws, E., Carlson, H., Cartwright, D., Enke, K., Ewing, J., Gienapp, H., Hasselmann, D., Kruseman, P., Meerburg, A., Muller, P., Olbers, D., Richter, K., Sell, W., Walden, H., 1973. Measurements of wind-wave growth and swell decay during the Joint North Sea Wave Project (JONSWAP). *Erganzung zur Deut. Hydrogr. Z., Reihe A* 8 (12), 1–95.
- Inman, D., Tait, R., Nordstrom, C., 1971. Mixing in the surf zone. *J. Geophys. Res.* 76 (15), 3493–3514.
- Koh, R., 1988. Shoreline Impact from Ocean Waste Discharges. *J. Hydraulic Eng.* 114 (4), 361–376.
- Komar, P., 1998. *Beach Processes and Sedimentation*, 2nd edn., Prentice Hall, Upper Saddle River, New Jersey, 544 pp.
- Kweon, H.-M., Goda, Y., 1997. A Parametric Model for Random Wave Deformation by Breaking on Arbitrary Beach Profiles. In: *Proceedings, 25th International Conference on Coastal Engineering*, September 2–6, 1996. American Society of Civil Engineers, Orlando, Florida, 261–274.
- Larson, M., Kraus, N., 1991. Numerical Model of Longshore Current for Bar and Trough Beaches. *J. Waterw. Port C.* 17 (4), 326–347.
- Longuet-Higgins, M., 1970a. Longshore Currents Generated by Obliquely Incident Sea Waves, 1. *J. Geophys. Res.* 75 (33), 6778–6789.
- Longuet-Higgins, M., 1970b. Longshore Currents Generated by Obliquely Incident Sea Waves, 2. *J. Geophys. Res.* 75 (33), 6790–6801.
- Novelli, G., Guigand, C., Boufadel, M., Ozgökmen, T., 2020. On the transport and landfall of marine oil spills, laboratory and field observations. *Mar. Pollut. Bull.* 150, 110805. <https://doi.org/10.1016/j.marpolbul.2019.110805>
- Pearson, J.M., Guymet, I., West, J.R., Coates, L.E., 2009. Solute Mixing in the Surf Zone. *J. Waterw. Port C.* 135 (4), 127–134. <https://doi.org/10.1061/ASCE0733-950X2009135:4127>
- Putnam, J., Munk, W., Traylor, M., 1949. The prediction of longshore currents. *EOS T.-Am. Geophys. Un.* 30, 337–345.
- Rienecker, M., Fenton, J., 1981. A Fourier approximation method for steady water waves. *J. Fluid Mech.* 104, 119–137.
- Ruessink, B., Miles, J., Feddersen, F., Guza, R., Elgar, S., 2001. Modeling the alongshore current on barred beaches. *J. Geophys. Res.* 106, 22451–22463.
- Saville, T., 1950. Model study of sand transport along an infinitely long straight beach. *EOS T.-Am. Geophys. Un.* 31, 555–565.
- Shuto, N., 1974. Nonlinear long waves in a channel of varied section. *Coast. Eng. Jpn.* 17, 1–12.
- Spydell, M., Feddersen, F., Guza, R., Schmidt, W., 2007. Observing surf-zone dispersion with drifters. *J. Phys. Oceanogr.* 37, 2920–2939. <https://doi.org/10.1175/2007JPO3580.1>
- Sun, T., Tao, J., 2003. Numerical modeling and experimental verification of pollutant transport under waves in the nearshore zone. *Acta Oceanol. Sin.* 25 (3), 104–112.
- Sun, T., Tao, J., 2006. Numerical simulation of pollutant transport acted by wave for a shallow water sea bay. *Int. J. Numer. Method. Fluid.* 51, 469–487.
- Svendsen, I.A., Putrevu, U., 1994. Nearshore mixing and dispersion. *Proc. R. Soc. Lond. A* 445, 561–576. <https://doi.org/10.1098/rspa.1994.0078>
- Takewaka, S., Misaki, S., Nakamura, T., 2003. Dye Diffusion Experiment in a Longshore Current Field. *Coast. Eng. J.* 45 (3), 471–487.
- Thornton, E., 1970. Variation of longshore currents across the surf zone. In: *Proceedings of the 12th Conference on Coastal Engineering*. American Society of Civil Engineers, Washington, DC, 291–308.
- Thornton, E., Guza, R., 1986. Surf Zone Longshore Currents and Random Waves: Field Data and Models. *J. Phys. Oceanogr.* 16, 1165–1178.
- Tsai, C.-P., Chen, H.-B., Hwung, H.-H., Huang, M.J., 2005. Examination of empirical formulas for wave shoaling and breaking on steep slopes. *Ocean Eng.* 32, 469–483.
- Visser, P., 1982. The proper longshore current in a wave basin. Department of Civil Engineering, Delft University of Technology, Delft, Netherlands Technical Report No. 82-1.
- Weggel, J., 1972. Maximum Breaker Height. *J. Waterway. Div. - ASCE* 98 (WW4), 529–548.
- Wen, S., Yu, Z.W., 1984. *Theories and Calculation Principle for Ocean Waves* (in Chinese). Science Press, Beijing, China.
- Winckler, P., Liu, P.L.-F., Mei, C.C., 2013. Advective Diffusion of Contaminants in the Surf Zone. *J. Waterw. Port C Ocean Eng.* 139 (6), 437–454.
- Yan, S., Zou, Z., Shen, L., Wang, Y., 2021. Calculation Model for Multiple Breaking Waves and Wave-Induced Currents on Very Gentle Beaches. *J. Waterw. Port C. Div.* 147 (5), 04021017. [https://doi.org/10.1061/\(ASCE\)WW.1943-5460.0000643](https://doi.org/10.1061/(ASCE)WW.1943-5460.0000643)

Available online at www.sciencedirect.com

ScienceDirect

journal homepage: www.journals.elsevier.com/oceanologia

ORIGINAL RESEARCH ARTICLE

Habitat suitability models of five keynote Bulgarian Black Sea fish species relative to specific abiotic and biotic factors

Ivelina Zlateva*, Violin Raykov, Violeta Slabakova, Elitsa Stefanova, Kremena Stefanova

Institute of Oceanology “Fridtjof Nansen”, Bulgarian Academy of Sciences, Varna, Bulgaria

Received 17 December 2021; accepted 9 June 2022

Available online 22 June 2022

KEYWORDS

Habitat suitability;
Spatial distribution;
MaxEnt;
Biotic interactions;
Abiotic variables;
Black Sea

Abstract Over the past few years, predicting species spatial distributions has been recognized as a powerful tool for studying biological invasions in conservation biology and planning, ecology, and evolutionary biology. Species spatial distribution models (SDMs) are used extensively for assessing the effects of changes in habitat suitability, the impacts of climate change, and the realignment of the existing conservation priorities. SDMs relate known patterns of species occurrences to a specific set of environmental conditions. Accordingly, we have used MaxEnt SDM tool in order to provide habitat suitability models of 5 keynote fish species: European sprat (*Sprattus sprattus* L.), red mullet (*Mullus barbatus*, L.), horse mackerel (*Trachurus mediterraneus*, L.), bluefish (*Pomatomus saltatrix*, L.) and whiting (*Merlangius merlangus*, L.), inhabiting the Bulgarian region of the Black Sea. Presence-only (PO) data collected by pelagic surveys performed between 2017 and 2019 was further utilized to link known species occurrence localities with selected abiotic factors, such as surface sea temperature and salinity, dissolved oxygen, and speed of currents. Biotic interactions were also considered for fitting the patterns of habitat suitability models. The SDMs, obtained from the present research study, prove to have satisfactory predictive accuracy to be further implemented for conservation measures and planning, stock management policy-making, or ecological forecasting.

© 2022 Institute of Oceanology of the Polish Academy of Sciences. Production and hosting by Elsevier B.V. This is an open access article under the CC BY-NC-ND license (<http://creativecommons.org/licenses/by-nc-nd/4.0/>).

* Corresponding author at: Institute of Oceanology “Fridtjof Nansen”, Bulgarian Academy of Sciences, Varna, Bulgaria.

E-mail address: ibikarska@yahoo.com (I. Zlateva).

Peer review under the responsibility of the Institute of Oceanology of the Polish Academy of Sciences.



Production and hosting by Elsevier

1. Introduction

The Black Sea has been identified as one of the most vulnerable ecosystems on the globe, affected by discharges from land-based sources on the territories of the central and eastern European countries along the river Danube (Zaitsev, 2008). Under anthropogenic and natural affects, the Black Sea ecosystem experienced dramatic structural and functional changes in the '80s (Daskalov, 2002; Ivanov and Beverton, 1985; Keskin et al., 2017; Pauly et al., 1998, 2002). Excessive overfishing, eutrophication, and the introduction of invasive species (Caddy, 2008; Prodanov, et al., 1997; Zaitsev and Maev, 1997) were reported as key factors in the disruption of the ecosystem structure and the significant loss of biodiversity.

The overexploitation of the top-predatory pelagic species led to an increase in populations of small planktivorous pelagic species, and the fisheries have therefore shifted towards the small pelagic species (Pauly et al., 1998; Pauly and Watson, 2005). At the regional level, the Black Sea fisheries in the past years have been reduced to: anchovy (*Engraulis encrasicolus*), European sprat (*Sprattus Sprattus*), Mediterranean horse mackerel (*Trachurus mediterraneus*), flathead grey mullet (*Mugil Cephalus*), bonito (*Sarda sarda*); bluefish (*Pomatomus saltatrix*); red mullet (*Mullus barbatus*), piked dogfish (*Squalus acanthias*), thornback ray (*Raja clavata*), turbot (*Psetta maxima*), gobies (*Gobiidae*), veined rapa whelk (*Rapana venosa*) and sand gaper (*Mya arenaria*).

Bulgaria has, since 2007, been applying the Total Allowable Catch (TAC), and Maximum Sustainable Yield (MSY) regimes only for turbot (*Psetta maxima*) and European sprat (*S. sprattus*), with the sprat stock being assessed as exploited below its sustainable level, while the status of the other commercially targeted and bycatch species still remains poorly known. As a whole, about 75% of the assessed Black Sea stocks are persistently reported to be fished at biologically unsustainable levels, regardless of the conservation and technical measures introduced to avoid overfishing to ensure sustainable exploitation (FAO, 2020).

The latter indicates the need for local and regional stock management improvements and the introduction of more advanced methods in terms of conservation and conservation planning, specifically in light of the growing global threat of climatic changes.

The purpose of the present study is to create predictive habitat suitability models of 5 keynote species for the Bulgarian Black Sea fisheries: European sprat (*S. sprattus*), red mullet (*M. barbatus*) and whiting (*M. merlangus*) (considered shared/transboundary stocks), are showing no clear migratory pattern, and horse mackerel (*T. mediterraneus*) and bluefish (*P. saltatrix*) whose presence was systematically recorded in the study area at a seasonally adjusted rate as part of their natural migration pattern. The implementation of these models for conservation, stock management, and policy-making will address specific stock assessments' shortcomings and may serve as a base for the adoption of spatially oriented measures toward achieving sustainable stock management and biodiversity protection.

In principle, stock management relies on scientific advice for optimal exploitation levels, based on stock assessments

in which a population model is fitted to the available data and utilized to forecast the possible consequences of applying various fishing mortality levels. Stock assessment models provide estimates of MSY; however, they take into consideration only biological factors while assuming an invariant environment. Another limitation of the models is that they do not incorporate information for the spatial distribution of the stocks, which may be the species' response to environmental variability or distribution shifts related to developmental stages (Watson et al., 2022).

Reliable and exhaustive information on patterns in spatial distribution and the actual geographic extent of a given species or ecological system have been recognized as essential prerequisites in planning for its successful management or conservation (Clément et al., 2014; Lawler et al., 2011). Identification of areas of higher abundances of a given species could therefore help ensure the proper maintenance of ecological processes (Clément et al., 2014), prioritize the existing conservation and stock management strategies, and furthermore support the introduction of new successful strategies.

Over the past few years, spatial distribution modeling (SDM) has been applied to a broad range of problems, including conservation biology and planning, management decision, and policy-making (Guisan and Thuiller, 2005; Srivastava et al., 2019; Zimmermann et al., 2010). From such a perspective, SDM is presently one of the most effective instruments in assessing the spatial conservation status of biodiversity (Cayuela et al., 2009) and is seen as an effective tool to provide an understandable measure of the species' habitat preferences for a specific environment (Guisan and Thuiller, 2005; Zimmermann et al., 2010).

SDMs are predictive tools that utilize occurrence locations of known species and analyze them in direct contrast to a series of environmental layers by the implementation of a set of statistical algorithms designed to demonstrate the impact of the environment on species presence/absence distribution patterns (Coops et al., 2009; Elith and Leathwick, 2009; Guisan and Thuiller, 2005; Zimmermann et al., 2010).

The habitat suitability models presented in this paper were fitted with MaxEnt package software Version 3.4.4. (Phillips et al., 2017), in an effort to identify the areas of a high probability of occurrence and make a valuable contribution to the existing knowledge as to the actual spatial distribution of species, and develop a deeper understanding of the suite of environmental variables characterizing their habitat suitability. The resultant SDMs predictive performance was evaluated by the area under the ROC (receiver operating characteristic) curve (AUC) metrics, and the probabilities of species occurrence were cross-validated with the species field-measured biomass to rationalize the models' implementation in conservation planning, stock management or ecological forecasting.

2. Material and methods

2.1. Spatial distribution modeling software

The MaxEnt software package was selected as one of the most frequently used for correlative models (Merow et al.,

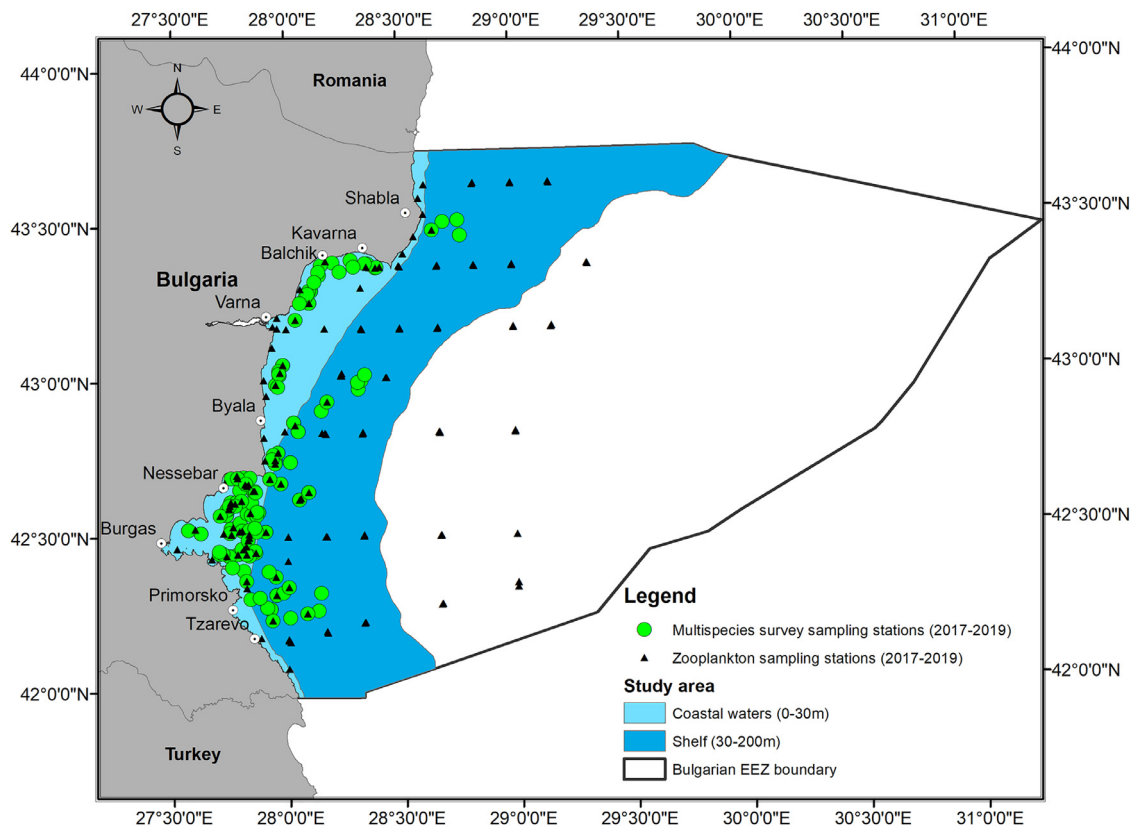


Figure 1 The study area – Bulgarian Black Sea coastal and shelf waters (light and dark blue areas). The multispecies survey sampling sites (green dots), with the all-species data records used for the modeling, models cross-validation with field-measured biomasses, and for the sprat biomass digital layer. The mesozooplankton sampling stations (black triangles) are used for the mesozooplankton biomass digital layer.

2013). It is a presence-only based statistical algorithm that has been successfully applied to model the biogeographic distributions of species in different parts of the world. The model input data is a list of species presence locations along with a set of environmental predictors across a user-defined spatial extent that is divided into grid cells. MaxEnt extracts a sample of background locations, contrasts it against the presence locations, and generates a probability estimate of species presence (or relative environmental suitability) that varies from 0 (lowest) to 1 (highest) (Phillips et al., 2006).

2.2. Study area

The study area (Figure 1) was reduced to Bulgarian Black Sea coastal and shelf waters due to the inclusion of biotic interactions in the models. Sprat biomass and mesozooplankton biomass data were spatially limited; therefore, their incorporation as predictors predisposed a reduction in the study area relative to the spatial extent where high-resolution data was available.

2.3. Selection of abiotic and biotic variables as model predictors

The environmental variables were selected in accordance with *a priori* known impact extent and ecological concepts associated with species preferences to a specific environment and those affecting the biomass and recruitment vari-

ability (Clavel-Henry et al., 2020; Mackenzie et al., 2008; Maureaud et al., 2019; Pécuchet et al., 2015; Rose et al., 2019; Schickele et al. 2021; Smoliński, 2019). Furthermore, in view of the availability of the environmental data sources, the surface sea temperature, salinity, dissolved oxygen, and the speed of the currents were selected as the most relevant predictors.

Although the latter refers only to the abiotic environment, some biotic interactions were also selected as model predictors, since the inclusion of species biotic interactions were also expected to have a significant effect on species actual and potential distribution. The present study makes particular reference to those biotic interactions that are consistent with the species feeding ecology (as proxies for competition for food and predator-prey interactions) (Bal et al., 2020; Ceyhan et al., 2007; Georgieva and Daskalov, 2019; Georgieva et al., 2019; Mihneva et al., 2015; Onay and Dalgic, 2019; Yankova et al., 2008). Mesozooplankton biomass was selected and incorporated as a predictor variable in the model for all the species under consideration, while sprat biomass was further included as an exclusive predictor for horse mackerel, whiting, and bluefish models only.

2.4. Species presence data

Species PO localities data were derived from pelagic surveys (Figure 1) carried out in the 2017–2019 period (6 expedi-

tions: autumn 2017, 2 expeditions in the autumn of 2018, spring 2019, and autumn 2019). The latter was initially designed for sprat stock assessments and further adapted (since 2017) to examine bycatch composition and provide analysis and relative swept area abundance/biomass indices for other commercially important species such as horse mackerel, red mullet, bluefish, and whiting.

Surveys' sampling design covered the Bulgarian Black Sea coastal (0–30 m) and shelf area (30–200 m), and each expedition surveyed a random selection of 36 to 38 sampling sites, providing a good resolution of presence-absence records of the species within the study area. The species data matrix (response matrix) was thus constructed by accounting for the PO localities records (440 records in total – n=156 for sprat; n=102 for whiting, n=51 for horse mackerel, n=97 for red mullet, and n=34 for the bluefish model).

2.5. Mesozooplankton data

A total of 619 samples were collected at more than 100 sampling sites (Figure 1) over the 2017–2019 period by closing plankton Juday net, 0.1 m² mouth opening area, 150 μm mesh size, starting at 2 meters above the bottom or oxygen minimum zone to the surface at integral sampling layers or districted layers depending on the water stratification and thermocline depth (Aleksandrov et al., 2020). Before sample preservation, the gelatinous species (*Aurelia aurita*, *Pleurobrachia pileus*, *Mnemiopsis leidyi*, *Beroe ovata*) were removed, rinsed, measured, and counted on board (Shiganova et al., 2021). The samples were preserved in a final 4% formalin solution buffered to pH 8–8.2 with disodium tetraborate (borax) (Na₂B₄O₃ * 10H₂O) (Aleksandrov et al., 2020). In the laboratory, the samples were settled before being divided into sub-samples. A Bogorov's chamber was used for quantitative assessment (abundance and biomass calculation) and qualitative (taxonomic structure) processing of sub-samples (Aleksandrov et al., 2020). The sub-samples were examined through the use of an Olympus SZ30 Stereoscopic Zoom Microscope. The taxa of Cladocera, Copepoda, Appendicularia, and Chaetognatha were identified at the species level. All other taxa were identified to phylum, class, or order levels. Biomass values as wet weight were estimated based on the number of individuals and the individual weight given per taxon and size class in Petipa (1959).

2.6. Digital data layers used for fitting SDMs

All predictor variables were uploaded in MaxEnt in the form of digital layers and further utilized to fit the SDMs. The Black Sea monthly mean environmental data layers (near-surface temperature (temp), salinity (sal), dissolved oxygen (do), and eastward seawater velocity (cu_uo)) for April to December over the 2017–2019 period (corresponding with the period when the survey expeditions were carried out) were obtained from Copernicus Marine Environmental Service (CMEMS) data portal (<https://marine.copernicus.eu/>). CMEMS provides re-analyzed monthly hydrophysical and biogeochemical fields for the Black Sea. The products are generated in gridded format by numerical simulation models (the hydrodynamic NEMO (Madec, 2016) and the biogeo-

chemical BAMHBI (Capet et al., 2016; Grégoire et al., 2008; Grégoire and Soetaert, 2010)), which embodies the assimilated in situ and satellite data for the Black Sea profile. The final products are oceanographic data layers in netCDF format with a spatial resolution of 0.037° × 0.028°, covering the entire Black Sea region, providing monthly mean values per model cell.

The datasets were imported into an ArcGIS 10.2 and re-sampled to a 0.037° × 0.037° uniform grid via the nearest neighbor assignment method. The monthly means of each variable over the period of interest were arithmetically averaged to acquire their three annual mean values. Finally, the grid cells of each three mean annual layers inside the region of interest were extracted in ESRI ASCII grid format.

ESRI ASCII grids of sprat biomass (sprat_2) and mesozooplankton biomass (zoo2) with a spatial resolution of 0.037° × 0.037° were generated by using the Inverse Distance Weighting (IDW) function of ArcGIS 10.2. The grid cells inside the relevant region of interest were extracted consistently with the spatial extent of environmental data layers.

2.7. Evaluation and validation of SDMs performance and applicability

The SDMs were cross-validated with ten replicate model runs for an adequate assessment of their predictive performance. Following the analysis of MaxEnt Jackknife tests as to the variables' importance in the training gain, test gain, and area under the ROC curve (AUC) for the test samples, the predictors in the initially suggested model structure were reduced to those that provided best training data fit and predictive performance.

To ensure that the models proposed are effective for conservation and stock management purposes, SDMs validation was conducted as to whether the higher predicted relative probabilities are associated with areas where the studied species occur in high abundances or densities. In order to facilitate conclusive evidence, MaxEnt predicted habitat suitability grid was overlaid with the field-measured biomass grid for all localities used in fitting the training data models.

3. Results

3.1. Evaluation of SDMs predictive performance

All model fits were assessed as performing better than a random model would (S1 Figures 1–5). Their predictive performance was evaluated by AUC metrics (Table 1)

MaxEnt grid output (maps) for the predictive habitat suitability models (Figure 2a–e) use a color scale to indicate the predictive probability of the most favorable environment for the species under study, with red indicating the highest possible probability of suitable conditions, green indicating conditions equal to those where species were found, and lighter shades of blue corresponding to the low predicted probability of suitable environment (Phillips, 2017).

Table 1 SDMs predictive performance assessment metrics by species (average test data AUC metrics for replicated runs).

Species SDM	Avg. test AUC for replicated runs	Standard deviation
sprat (<i>Sprattus sprattus</i>)	0.861	0.047
whiting (<i>Merlangius merlangus</i>)	0.869	0.05
horse mackerel (<i>Trachurus mediterraneus</i>)	0.933	0.037
red mullet (<i>Mullus barbatus</i>)	0.876	0.042
bluefish (<i>Pomatomus saltatrix</i>)	0.926	0.04

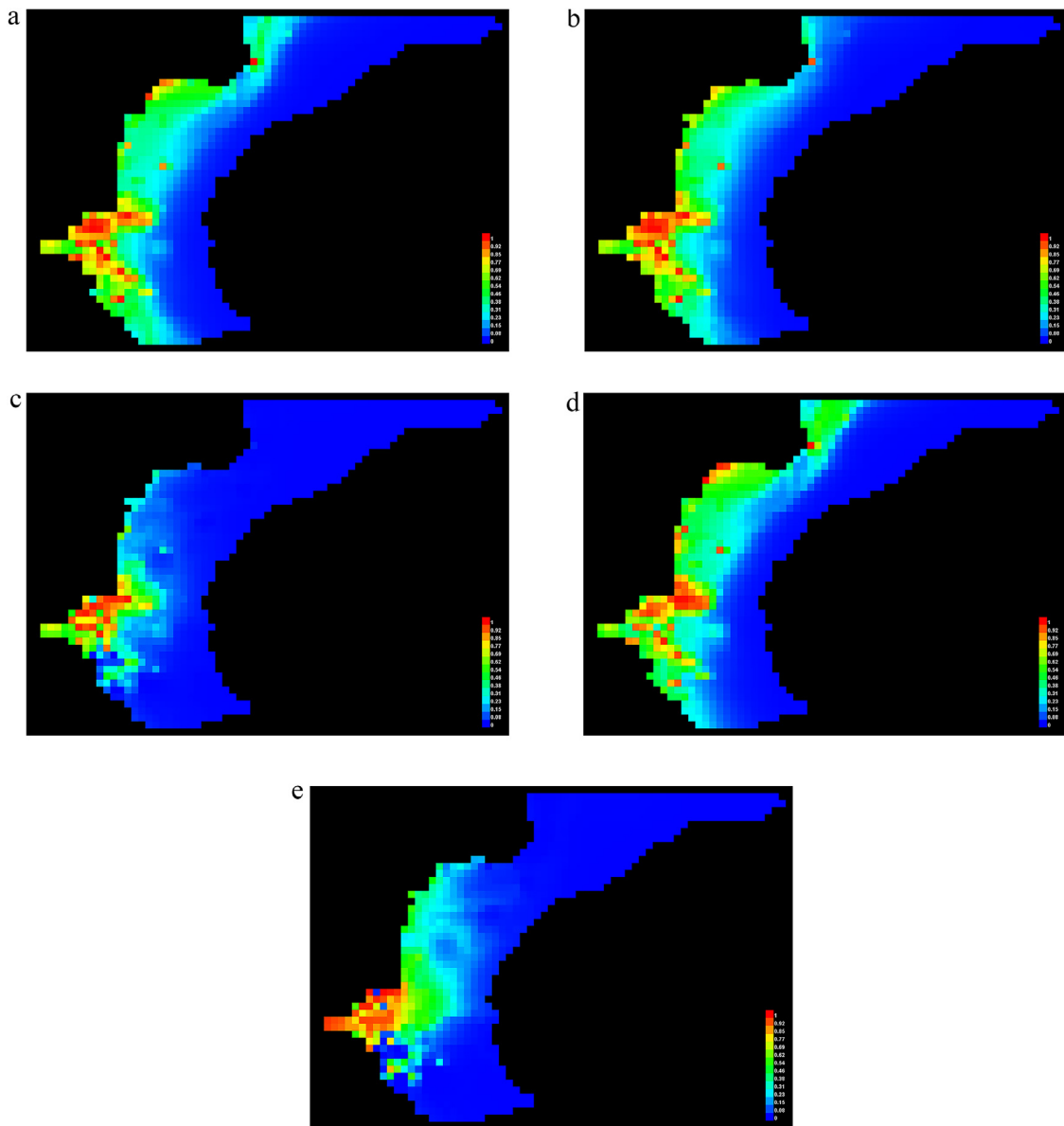


Figure 2 MaxEnt Habitat suitability maps (point-wise mean and standard deviation of the 10 replicate Maxent runs) of a) sprat (*Sprattus sprattus*); b) whiting (*Merlangius merlangus*); c) horse mackerel (*Trachurus mediterraneus*); d) red mullet (*Mullus barbatus*) and e) bluefish (*Pomatomus saltatrix*) in the Bulgarian Black Sea coastal and shelf waters.

Table 2 Environmental and biotic variables percentage contribution for fitting the training data models by species (percentage contributions >10% are marked in bold).

Species	Salinity (sal) [%]	Temperature (temp) [%]	Dissolved oxygen (do) [%]	Currents speed (cu_uo) [%]	Mesozooplankton biomass (zoo2) [%]	Sprat biomass (sprat_2) [%]
sprat	49.3	10.7	4.3	-	35.7	-
whiting	46.3	11.2	2.4	-	40.1	-
horse mackerel	32	-	13.7	-	43.6	10.7
red mullet	57.5	-	-	5.9	36.7	-
bluefish	53.5	-	25.9	0.2	-	20.3

3.2. Analysis of variables' importance in fitting the training data models and comparison of Jackknife plots of variables' importance for best training and test data fit

MaxEnt provides statistical outcomes for the contribution of predictor variables in fitting the training data models (Table 2).

Regularized training gain and test AUC Jackknife plots analyses (S1.Figures 6–15) highlighted that for the large majority of the studied species (sprat, whiting, horse mackerel and red mullet), the environmental predictor with the highest gain (if used separately), was mesozooplankton biomass, and it thus appears to have the most useful information by itself, whereas the environmental variable that decreases the gain the most if omitted was salinity. Hence, it represents the most information that was not present in the other predictor variables incorporated into the model structure. Subsequently, the Jackknife test on AUC data showed that mesozooplankton biomass generalizes better than salinity in predicting test data localities. Bluefish model Jackknife plots analysis (S1.Figure 14 and S1.Figure 15) indicated that the environmental variable with the highest information gain, when used in isolation, was salinity, while the environmental variable that decreased the gain the most if omitted was dissolved oxygen, which therefore appears to have the most information that was not present in the other variables included in the model.

The test results also point to the conclusion that the speed of the current has little to no influence at all on fitting training and test data models with respect to the vast majority of the studied species. However, their exclusion from the red mullet and bluefish model's structure did not improve or, more precisely, rather reduced the overall predictive performance of the models.

3.3. SDMs validation

MaxEnt predicted habitat suitability grid was overlaid with the field-measured biomass for all localities used in fitting the training data models to validate the expected association of the highest probabilities of occurrence of the studied species with areas where the species performance is evidently high (Figure 3 and S1.Figure 16–19).

Observed, was a clear spatial overlap between the two grids – field-measured biomass and MaxEnt predicted probabilities.

4. Discussion and conclusions

4.1. Presence only or presence-absence data?

Species observation data resolution and quality may have a substantial effect on the model performance and, respectively, on the accuracy of the predictions. Species presence-absence data records are often scarce and incomplete and are habitually influenced by uncertainties caused by various sources of error, bias, or inaccuracy that need to be addressed (Bryn et al., 2021). However, the inclusion of absence data is highly recommended to ensure that the model's predictions are reliable, though the absence localities inclusion is only reasonable in case of availability of repetitive observations that the species is not present in the studied area or location. The latter may also refer to unsuitable environmental conditions, seasonal migration, or migration related to developmental stages (Lobo et al., 2010). In general, SDM has been developed to use both PO or presence-absence (PA) data (Brotons et al., 2004); however, generalization as to whether methods using PA or PO data along with pseudo-absence data or background locations yields better results in predicting species distribution seem hardly conceivable. Few case studies, however, highlight that when working with PO data, particular attention must be paid to the sampling design for uninformed background or pseudo-absence data, as they may lead to erroneous modeling results (Bryn et al., 2021; Støa et al., 2018; Stokland et al., 2011).

In line with the latter considerations, it is important to note that the SDMs presented in this paper used MaxEnt background (or pseudo-absences) defaults. Basically, the background locations are being built by contrasting the presences against background locations where presence/absence is unmeasured, and MaxEnt further contrasts the environmental conditions at the background locations with those at observed presence locations (Merow et al., 2013). The default background locations option was considered acceptable, accounting for the focus of the present case study, which is related to identifying the actual and potential future spatial distribution of the studied species with desired predictive accuracy at the geographical extent where the species are reachable, rather than studying species habitat suitability in the absence of dispersal limitations or introduction to a new geographical area.

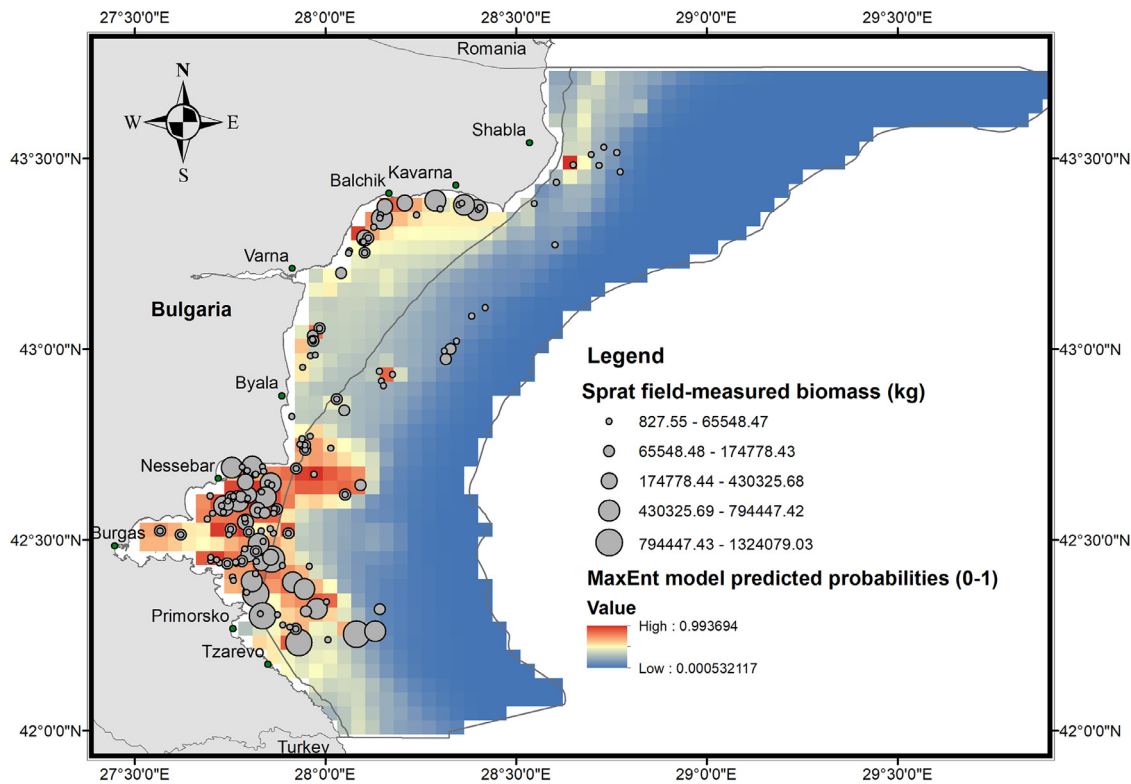


Figure 3 MaxEnt model-predicted probabilities grid vs. field-measured biomass grid of *Sprattus sprattus* in the Bulgarian Black Sea coastal and shelf waters during the survey expeditions carried out in the 2017–2019 period.

4.2. Model conceptualization and predictive performance

Many studies report that the predictive performance of SDMs is more reliable if biotic interactions are carefully examined and incorporated as predictors (Bueno de Mesquita et al., 2016; Flores-Tolentino et al., 2020; Giannini et al., 2013; Lany et al., 2017; Leach et al., 2016; Preuss and Padiá, 2021), rather than those based solely on abiotic variables as they are more likely to overestimate distributions, specifically for species strongly restricted by their biotic interactions (Flores-Tolentino et al., 2020; Godsoe et al., 2017). On the contrary, other studies report that the inclusion of biotic interactions, especially in joint-species distribution and climate envelop models, can lead to misinterpretation of the models when expanded to the macroecological level as they are viewed as having a limited spatial extent within the structure of their biotic interactions unless a suitable proxy can be incorporated in these models (Araújo and Luoto, 2007; Dormann et al., 2018). Nevertheless, the very selection of suitable quantitative proxies, for inferring possible biotic interactions to be included in the model as predictors, remain challenging. This might be linked to the fact that biotic interactions are integrally complex, and it is not always clear what information is relevant for each species in order for their effect on the community composition to be properly identified (Godsoe et al., 2017).

As our modeling results show, both biotic and abiotic factors play an equally important role in fitting the training data models for sprat, whiting, and red mullet, and furthermore, it is biotic interactions that are of utmost importance for predicting the localities of the various species. The lat-

ter is in complete agreement with the premise that biotic predictors significantly improve habitat suitability models for species strongly restricted by their biotic interactions. Conversely, as for fitting the migratory species habitat suitability models, the abiotic variables take major priority for fitting both training and test data, thus demonstrating strong specific preferences for the abiotic environment. In addition, bluefish and horse mackerel predicted suitability overlaps with the corresponding areas of the highest predicted suitability for sprat and whiting, which can easily be justified by their clear patterns of movement and species migration. This complex behavior enables animals to exploit many temporally productive and spatially discrete habitats to maximize survival and reproduction success and avoid adverse environmental conditions (Lennox et al., 2016).

To prevent eventual misinterpretation of the model, we propose a spatial extent limited to the geographic space that provides a plentiful supply of research data on the selected biotic interactions. Species co-existence and predator-prey interactions, as well as competition for food, were represented only by mesozooplankton biomass and one of the most abundant species biomasses (sprat) as both were considered a suitable proxy, and the spatial resolution of data was satisfactory in terms of interpolation error. An attempt was made for the introduction of a digital layer of combined small pelagic species biomass indices in fitting the bluefish model as a predictor variable, though the resolution of PO data for horse mackerel was not satisfactory enough in terms of data interpolation error, and the inclusion of such layer would probably introduce an unnecessary bias in predicting habitat suitability.

On the whole, many underlying processes remained unaccounted for in terms of species biotic interactions and abiotic environment due to the selection of a relatively simple model structure; however, the overall SDMs performance proved to be satisfactory regardless of their generalization and possible robustness.

4.3. Model validation and applicability for stock management and conservation

In conservation planning and stock management, species abundance is deliberated as the most informative quantitative expression when assessing species stock status, distribution, diversity, and population trends and dynamics (Brown, 1984; Sparre and Venema, 1998; Williams and Araújo, 2000). The major concern for the application of SDMs as a means of establishing conservation measures and setting up conservation priorities relates to the fact that the predicted relative probabilities of species occurrence may not necessarily reflect abundances (Clément et al., 2014; Williams and Araújo, 2000). The latter indicated the need to identify and validate the possible relationship between occurrence probabilities and abundance indices. On the other hand, SDMs are generally expected to reflect the niche requirements of the species and the environmental conditions that are associated with higher species performance (Thuiller et al., 2010), and correspondingly, habitats with a perceived increase in species occurrence frequencies are more likely to be associated with higher abundances (Hernandez et al., 2006). However, they may also be indicative of reproductive biology processes, response to habitat variations, feeding ecology, or migration patterns.

Accordingly, a validation of the predicted probabilities with the field-measured biomass of the species under consideration in the present study was conducted, and the cross-validation results showed a good spatial overlap. In general, the proposed models tend to demonstrate considerable accuracy in predicting the areas related to higher species performance for all the studied species and, therefore, can be successfully applied for conservation planning and/or the introduction of spatially oriented stock management measures. On that account, the bluefish and horse mackerel models must be considered only seasonally where both species are present in the Bulgarian Black Sea waters as part of their natural migration route.

Expansion of the proposed SDMs at a regional level may significantly contribute to the conservation planning and improved ecological forecasting for the entire Black Sea ecosystem. It is evident, though, that the models using only climatic variables as predictors may lead to significant uncertainty when analyzing species distribution, and the fact that biotic interaction data is spatially limited makes its incorporation at a regional level even more challenging.

Implementation of chlorophyll *a* satellite data in fish forecasting models has generally proven to be successful in identifying species favorable habitats (Druon, 2017; Mansor et al., 2001). Accordingly, the SDMs obtained from the present study can be further advanced to predict habitat suitability for the entire Black Sea region through the use of chlorophyll *a* satellite data as habitat-specific characteristics relative to known presence/absence localities of

the species as a proxy to biotic interactions at a macro-ecological level and more precise identification of fish productivity zones.

Acknowledgments

Species sampling data source:

Project no. BG 14MFOP001-3.003-0001-C01, "Collection, management and use of data for the purposes of scientific analysis and implementation of the Common Fisheries Policy for the period 2017–2019", funded by the Maritime Affairs and Fisheries Program, co-financed by the European Union through the European Maritime and Fisheries Fund.

Project no. BG 14MFOP001-3.003-0001-C02, "Collection, management and use of data for the purposes of scientific analysis and implementation of the Common Fisheries Policy for the period 2020–2021", funded by the Maritime Affairs and Fisheries Program, co-financed by the European Union through the European Maritime and Fisheries Fund.

Zooplankton sampling data source:

The study has been partly supported by the Ministry of Environment and Waters (Agreements for the period 2012–2017), the Ministry of Education and Science (MES) of Bulgaria, contract no. 83530/20.07.2018, eMS BSB319, the National Science Program: "Environmental Protection and Reduction of Risks of Adverse Events and Natural Disasters".

Supplementary materials

Supplementary material associated with this article can be found, in the online version, at <https://doi.org/10.1016/j.oceano.2022.06.002>.

References

- Aleksandrov, B., Arashkevich, E., Gubanova, A., Korshenko, A., 2020. Black Sea monitoring guidelines: mesozooplankton. Dnipro, Seredniak T.K., 34 pp.
- Araújo, M.B., Luoto, M., 2007. The importance of biotic interactions for modeling species distributions under climate change. *Global Ecol. Biogeogr.* 16 (6), 743–753. <https://doi.org/10.1111/j.1466-8238.2007.00359.x>
- Bal, H., Telat, Y., Dilek, T., 2020. Diet composition of bluefish *Pomatomus saltatrix* (Linnaeus, 1766) in the Sea of Marmara. *Bull. Mar. Sci.* 9 (1), 46–50. <https://doi.org/10.33714/masteb.675929>
- Brotans, L., Thuiller, W., Araújo, M.B., Hirzel, A.H., 2004. Presence-absence versus presence-only modeling methods for predicting bird habitat suitability. *Ecography* 27 (4), 437–448. <https://doi.org/10.1111/j.0906-7590.2004.03764.x>
- Brown, J.H., 1984. On the relationship between abundance and distribution of species. *Am. Nat.* 124 (2), 255–279. <https://doi.org/10.1086/284267>
- Bryn, A., Bekkby, T., Rinde, E., Gundersen, H., Halvorsen, R., 2021. Reliability in distribution modeling—A synthesis and step-by-step guidelines for improved practice. *Front. Ecol. Evol.* 9, 658713. <https://doi.org/10.3389/fevo.2021.658713>
- Bueno de Mesquita, C.P., King, A.J., Schmidt, S.K., Farrer, E.C., Suding, K.N., 2016. Incorporating biotic factors in species dis-

- tribution modeling: are interactions with soil microbes important? *Ecography* 39 (10), 970–980. <https://doi.org/10.1111/ecog.01797>
- Caddy, J.F., 2008. Recent experience and future options for fisheries assessment and management in the Black Sea: A GFCM perspective. In: General Fisheries Commission for the Mediterranean. Meeting document GFCM/XXXII/2008/Dma, 4, 72–76.
- Capet, A., Meysman, F.J., Akoumianaki, I., Soetaert, K., Grégoire, M., 2016. Integrating sediment biogeochemistry into 3D oceanic models: a study of benthic-pelagic coupling in the Black Sea. *Ocean Model.* 101, 83–100. <https://doi.org/10.1016/j.ocemod.2016.03.006>
- Cayuela, L., Golicher, D.J., Newton, A.C., Kolb, M., De Albuquerque, F.S., Arets, E.J.M.M., Alkemade, J.R.M., Perez, A.M., 2009. Species distribution modeling in the tropics: problems, potentialities, and the role of biological data for effective species conservation. *Trop. Conserv. Sci.* 2 (3), 319–352. <https://doi.org/10.1177/194008290900200304>
- Ceyhan, T., Akyol, O., Ayaz, A., Juanes, F., 2007. Age, growth, and reproductive season of Bluefish (*Pomatomus saltatrix*) in the Marmara region. Turkey. *ICES J. Mar. Sci.* 64 (3), 531–536. <https://doi.org/10.1093/icesjms/fsm026>
- Clavel-Henry, M., Piroddi, C., Quattrocchi, F., Macias, D., Christensen, V., 2020. Spatial Distribution and Abundance of Mesopelagic Fish Biomass in the Mediterranean Sea. *Front. Mar. Sci.* 7, 1136. <https://doi.org/10.3389/fmars.2020.573986>
- Clément, L., Catzeflis, F., Richard-Hansen, C., Barrioz, S., de Thoisy, B., 2014. Conservation interests of applying spatial distribution modeling to large vagile Neotropical mammals. *Trop. Conserv. Sci.* 7 (2), 192–213. <https://doi.org/10.1177/194008291400700203>
- Coops, N.C., Waring, R.H., Schroeder, T.A., 2009. Combining a generic process-based productivity model and a statistical classification method to predict the presence and absence of tree species in the Pacific Northwest. USA. *Ecol. Model.* 220 (15), 1787–1796. <https://doi.org/10.1016/j.ecolmodel.2009.04.029>
- Daskalov, G.M., 2002. Overfishing drives a trophic cascade in the Black Sea. *Mar. Ecol. Prog. Ser.* 225, 53–63. <https://doi.org/10.3354/meps225053>
- Dormann, C.F., Bobrowski, M., Dehling, D.M., Harris, D.J., Hartig, F., Lischke, H., Moretti, M.D., Pagel, J., Pinkert, S., Schleuning, M., Schmidt, S.I., Sheppard, C.S., Steinbauer, M.J., Zeuss, D., Kraan, C., 2018. Biotic interactions in species distribution modeling: 10 questions to guide interpretation and avoid false conclusions. *Global Ecol. Biogeogr.* 27 (9), 1004–1016. <https://doi.org/10.1111/geb.12759>
- Druon, J.N., 2017. Ocean Productivity index for Fish in the Arctic: First assessment from satellite-derived plankton-to-fish favourable habitats, EUR 29006 EN, JRC109947. Publications Office of the European Union, Luxembourg, 24. <https://doi.org/10.2760/28033>
- Elith, J., Leathwick, J.R., 2009. Species distribution models: ecological explanation and prediction across space and time. *Annu. Rev. Ecol. Evol. S.* 40, 677–697. <https://doi.org/10.1146/annurev.ecolsys.110308.120159>
- FAO, 2020. The State of Mediterranean and Black Sea Fisheries. General Fisheries Commission for the Mediterranean, Rome, Italy, 172 pp. <https://doi.org/10.4060/cb2429en>
- Flores-Tolentino, M., García-Valdés, R., Saénz-Romero, C., Ávila-Díaz, I., Paz, H., Lopez-Toledo, L., 2020. Distribution and conservation of species is misestimated if biotic interactions are ignored: the case of the orchid *Laelia speciosa*. *Sci. Rep.* 10 (1), 1–14. <https://doi.org/10.1038/s41598-020-63638-9>
- Georgieva, Y.G., Daskalov, G.M., 2019. Shift in growth of an apex marine predator: Bluefish *Pomatomus saltatrix* (L., 1766) (Perciformes: Potamonidae) in relation to changes in feeding. *Acta Zool. Bulgar.* 71 (1), 63–72.
- Georgieva, Y.G., Daskalov, G.M., Klayn, S.L., Stefanova, K.B., Stefanova, E.S., 2019. Seasonal diet and feeding strategy of horse mackerel *Trachurus mediterraneus* (Steindachner, 1868) (Perciformes: Carangidae) in the South-Western Black Sea. *Acta Zool. Bulgar.* 71, 201–210.
- Giannini, T.C., Chapman, D.S., Saraiva, A.M., Alves-dos-Santos, I., Biesmeijer, J.C., 2013. Improving species distribution models using biotic interactions: a case study of parasites, pollinators and plants. *Ecography* 36 (6), 649–656. <https://doi.org/10.1111/j.1600-0587.2012.07191.x>
- Godsoe, W., Franklin, J., Blanchet, F.G., 2017. Effects of biotic interactions on modeled species' distribution can be masked by environmental gradients. *Ecol. Evol.* 7 (2), 654–664. <https://doi.org/10.1002/ece3.2657>
- Grégoire, M., Raick, C., Soetaert, K., 2008. Numerical modeling of the central Black Sea ecosystem functioning during the eutrophication phase. *Prog. Oceanogr.* 76 (3), 286–333. <https://doi.org/10.1016/j.pcean.2008.01.002>
- Grégoire, M., Soetaert, K., 2010. Carbon, nitrogen, oxygen and sulfide budgets in the Black Sea: A biogeochemical model of the whole water column coupling the oxic and anoxic parts. *Ecol. Model.* 221 (19), 2287–2301. <https://doi.org/10.1016/j.ecolmodel.2010.06.007>
- Guisan, A., Thuiller, W., 2005. Predicting species distribution: offering more than simple habitat models. *Ecol. Lett.* 8 (9), 993–1009. <https://doi.org/10.1111/j.1461-0248.2005.00792.x>
- Hernandez, P.A., Graham, C.H., Master, L.L., Albert, D.L., 2006. The effect of sample size and species characteristics on performance of different species distribution modeling methods. *Ecography* 29 (5), 773–785. <https://doi.org/10.1111/j.0906-7590.2006.04700.x>
- Ivanov, L., Beverton, R.J.H., 1985. In: *The fisheries resources of the Mediterranean Pt. 2: Black Sea*, FAO, 60, 147 pp.
- Keskin, C., Ulman, A., Zyllich, K., Raykov, V., Daskalov, G.M., Pauly, D., Zeller, D., 2017. The marine fisheries in Bulgaria's Exclusive Economic Zone, 1950–2013. *Front. Mar. Sci.* 4 (53), 1–10. <https://doi.org/10.3389/fmars.2017.00053>
- Lany, N.K., Zarnetske, P.L., Gouhier, T.C., Menge, B.A., 2017. Incorporating context dependency of species interactions in species distribution models. *Integr. Comp. Biol.* 57 (1), 159–167. <https://doi.org/10.1093/icb/ix057>
- Lawler, J.J., Wiersma, Y.F., Huettmann, F., 2011. Using species distribution models for conservation planning and ecological forecasting. In: Drew, C.A., Wiersma, Y.F., Huettmann, F. (Eds.), *Predictive species and habitat modeling in landscape ecology*. Springer, New York, 271–290. https://doi.org/10.1007/978-1-4419-7390-0_14
- Leach, K., Montgomery, W.I., Reid, N., 2016. Modeling the influence of biotic factors on species distribution patterns. *Ecol. Model.* 337, 96–106. <https://doi.org/10.1016/j.ecolmodel.2016.06.008>
- Lennox, R.J., Chapman, J.M., Souliere, C.M., Tudorache, C., Wikelski, M., Metcalfe, J.D., Cooke, S.J., 2016. Conservation physiology of animal migration. *Conserv. Physiol.* 4 (1), cov072. <https://doi.org/10.1093/conphys/cov072>
- Lobo, J.M., Jiménez-Valverde, A., Hortal, J., 2010. The uncertain nature of absences and their importance in species distribution modeling. *Ecography* 33 (1), 103–114. <https://doi.org/10.1111/j.1600-0587.2009.06039.x>
- MacKenzie, B.R., Horbowy, J., Köster, F.W., 2008. Incorporating environmental variability in stock assessment: predicting recruitment, spawner biomass, and landings of Sprat (*Sprattus sprattus*) in the Baltic Sea. *Can. J. Fish. Aquat. Sci.* 65 (7), 1334–1341. <https://doi.org/10.1139/F08-051>
- Madec, G., 2016. NEMO – The OPA9 Ocean Engine: Note du Pole de Modelisation Institut Pierre-Simon Laplace No. 27, <https://www.ipsl.fr>

- nemo-ocean.eu/wp-content/uploads/NEMO_book.pdf (last access 11 November 2021).
- Mansor, S., Tan, C.K., Ibrahim, H.M., Shariff, A.R.M., 2001. Satellite fish forecasting in south China sea. 22nd Asian Conference on Remote Sensing 5 (9).
- Maureaud, A., Hodapp, D., van Denderen, P.D., Hillebrand, H., Gislason, H., Spaanheden Dencker, T., Beukhof, E., Lindegren, M., 2019. Biodiversity–ecosystem functioning relationships in fish communities: biomass is related to evenness and the environment, not to species richness. *Proc. R. Soc. B.* 286 (1906), 20191189. <https://doi.org/10.1098/rspb.2019.1189>
- Merow, C., Smith, M.J., Silander Jr, J.A., 2013. A practical guide to MaxEnt for modeling species' distributions: what it does, and why inputs and settings matter. *Ecography* 36 (10), 1058–1069. <https://doi.org/10.1111/j.1600-0587.2013.07872.x>
- Mihneva, V., Raykov, V., Stefanova, K., Grishin, A., 2015. Sprat feeding in front of the Bulgarian Black Sea coast. In: 12th International Conference on the Mediterranean Coastal Environment, MEDCOAST, 2015, 431–442.
- Onay, H., Dalgic, G., 2019. Seasonal changes in the food spectrum and day-time rhythm of feeding in red mullet *Mullus barbatus* (Linnaeus, 1758) in the Southeast Black Sea. *Fresenius Environ. Bull.* 28 (4), 2671–2678.
- Pauly, D., Christensen, V., Dalsgaard, J., Froese, R., Torres Jr, F., 1998. Fishing down marine food webs. *Science* 279 (5352), 860–863. <https://doi.org/10.1126/science.279.5352.860>
- Pauly, D., Christensen, V., Guénette, S., Pitcher, T.J., Sumaila, U.R., Walters, C.J., Watson, R., Zeller, D., 2002. Towards sustainability in world fisheries. *Nature* 418 (6898), 689–695. <https://doi.org/10.1038/nature01017>
- Pauly, D., Watson, R., 2005. Background and interpretation of the 'Marine Trophic Index' as a measure of biodiversity. *Philos. T. Roy. Soc. B.* 360 (1454), 415–423. <https://doi.org/10.1098/rstb.2004.1597>
- Pécuchet, L., Nielsen, J.R., Christensen, A., 2015. Impacts of the local environment on recruitment: a comparative study of North Sea and Baltic Sea fish stocks. *ICES J. Mar. Sci.* 72 (5), 1323–1335. <https://doi.org/10.1093/icesjms/fsu220>
- Petipa, T.S., 1959. On average weight of main forms of zooplankton. *Annals of Sevastopol Biological Station* (5) 13–24.
- Phillips, S.J., 2017. A brief tutorial on Maxent, http://biodiversityinformatics.amnh.org/open_source/maxent/ (last accessed on 18.01.2021).
- Phillips, S.J., Anderson, R.P., Dudík, M., Schapire, R.E., Blair, M.E., 2017. Opening the black box: An open-source release of Maxent. *Ecography* 40 (7), 887–893. <https://doi.org/10.1111/ecog.03049>
- Phillips, S.J., Anderson, R.P., Schapire, R.E., 2006. Maximum entropy modeling of species geographic distributions. *Ecol. Model.* 190 (3–4), 231–259. <https://doi.org/10.1016/j.ecolmodel.2005.03.026>
- Preuss, G., Padiál, A.A., 2021. Increasing reality of species distribution models of consumers by including its food resources. *Neotrop. Biol. Conserv.* 16 (3), 411–425. <https://doi.org/10.3897/neotropical.16.e64892>
- Prodanov, K., Mikhailov, K., Daskalov, G., Maxim, C., Chaschchin, A., Arkhipov, A., Shyakhov, V., Ozdamar, E., 1997. Environmental management of fish resources in the Black Sea and their rational exploitation. In: *GFCM Studies and Reviews*, 68. FAO, Rome, 178 pp.
- Rose, K.A., Gutiérrez, D., Breitburg, D., Conley, D., Craig, J.K., Halley, E., Froehlich, R., Kripa, J.V., Mbaye, B.C., Mohamed, K.S., Padua, S., Prema, D., 2019. Impacts of ocean deoxygenation on fisheries. In: Laffoley, D., Baxter, J.M. (Eds.), *Ocean deoxygenation: Everyone's problem – Causes, impacts, consequences and solutions*. IUCN Gland, Switzerland, 562 pp.
- Schickele, A., Goberville, E., Leroy, B., Beaugrand, G., Hattab, T., Francour, P., Raybaud, V., 2021. European small pelagic fish distribution under global change scenarios. *Fish. Fish.* 22 (1), 212–225. <https://doi.org/10.1111/faf.12515>
- Shiganova, T.A., Anninsky, B., Finenko, G.A., Kamburska, L., Mutlu, E., Mihneva, V., Stefanova, K., 2021. Black Sea Monitoring Guidelines. In: *Macroplankton (Gelatinous plankton)*. Dnipro, Seredniak T.K., 38 pp.
- Smoliński, S., 2019. Incorporation of optimal environmental signals in the prediction of fish recruitment using random forest algorithms. *Can. J. Fish. Aquat. Sci.* 76 (1), 15–27. <https://doi.org/10.1139/cjfas-2017-0554>
- Sparre, P., Venema, S.C. 1998. Introduction to tropical fish stock assessment, Part 1. Manual. FAO Fisheries Technical Paper. No. 306.1, Rev. 2. Rome, FAO, 407 pp.
- Srivastava, V., Lafond, V., Griess, V.C., 2019. Species distribution models (SDM): applications, benefits and challenges in invasive species management. *CAB Rev.* 14 (20), 1–13. <https://doi.org/10.1079/PAVSNNR201914020>
- Støa, B., Halvorsen, R., Mazzoni, S., Gusarov, V.I., 2018. Sampling bias in presence-only data used for species distribution modeling: theory and methods for detecting sample bias and its effects on models. *Sommerfeltia* 38, 1–53. <https://doi.org/10.2478/som-2018-0001>
- Stokland, J.N., Halvorsen, R., Støa, B., 2011. Species distribution modeling – effect of design and sample size of pseudo-absence observations. *Ecol. Model.* 222, 1800–1809. <https://doi.org/10.1016/j.ecolmodel.2011.02.025>
- Thuiller, W., Albert, C.H., Dubuis, A., Randin, C., Guisan, A., 2010. Variation in habitat suitability does not always relate to variation in species' plant functional traits. *Biol. Lett.* 6 (1), 120–123. <https://doi.org/10.1098/rsbl.2009.0669>
- Watson, J.W., Boyd, R., Dutta, R., Vasdekis, G., Walker, N.D., Roy, S., Everitt, R., Hyder, K., Sibly, R.M., 2022. Incorporating environmental variability in a spatially-explicit individual-based model of European sea bass. *Ecol. Model.* 466, 109878, 1–11. <https://doi.org/10.1016/j.ecolmodel.2022.109878>
- Williams, P.H., Araújo, M.B., 2000. Using probability of persistence to identify important areas for biodiversity conservation. *P. Roy. Soc. B-Biol.* 267 (1456), 1959–1966. <https://doi.org/10.1098/rspb.2000.1236>
- Yankova, M.H., Raykov, V.S., Frateva, P.B., 2008. Diet composition of horse mackerel, *Trachurus mediterraneus ponticus* Aleev, 1956 (Osteichthyes: Carangidae) in the Bulgarian Black Sea waters. *Türk. J. Fish. Aquat. Sc.* 8 (2), 321–327.
- Zaitsev, Y., 2008. An introduction to Black Sea ecology. Smil. Publ. Agency Ltd., Odessa, 228 pp.
- Zaitsev, Y., Mamaev, V., 1997. Marine Biological Diversity in the Black Sea: a Study of Change and Decline. Call number. DP(05)/B627/v.3. Black Seas Environmental Series. United Nations Publ, New York, USA, 208 pp.
- Zimmermann, N.E., Edwards Jr, T.C., Graham, C.H., Pearman, P.B., Svenning, J.C., 2010. New trends in species distribution modeling. *Ecography* 33 (6), 985–989. <https://doi.org/10.1111/j.1600-0587.2010.06953.x>

Available online at www.sciencedirect.com

ScienceDirect

journal homepage: www.journals.elsevier.com/oceanologia

ORIGINAL RESEARCH ARTICLE

Physical control on the inter-annual variability of summer dissolved nutrient concentration and phytoplankton biomass in the Indian sector of the Southern Ocean

Jenson Vilayil George*, Ravidas Krishna Naik, Narayanapillai Anilkumar, Prabhakaran Sabu, Shramik Maruti Patil, Rajani Kanta Mishra

National Centre for Polar and Ocean Research, Goa, India

Received 1 October 2021; accepted 16 June 2022

Available online 1 July 2022

KEYWORDS

Indian sector of the Southern Ocean;
Chlorophyll-*a*;
Nutrients;
Winter mixing;
Sea ice;
Fronts

Abstract To understand the role of physical processes and their interannual variability on the dissolved nutrient concentration and phytoplankton biomass distribution, field data collected in the Indian sector of the Southern Ocean (ISSO) during the austral summer of 2009–2011 are used. In the subtropical zone, macronutrients were limited ($N:P < 1$, $N:Si < 1$, $Si:P \approx 1$) and the phytoplankton biomass variability was mainly governed by the mesoscale eddy activity associated with the Agulhas Return Current. High nutrient low chlorophyll condition prevailed in the sub-Antarctic zone and further south. A South-North gradient of the upper layer dissolved SiO_2 was higher than that of NO_3 . The sub-Antarctic zone was characterized by the highest $N:Si$ ratio (>4) and it was associated with the enhanced draw down of silicate due to the winter/spring diatom blooms in the region. The chlorophyll-*a* (CHL) concentration in the Polar Frontal Zone was low ($\sim 0.2 \text{ mg m}^{-3}$) in 2009 and 2010 but it was high (0.5 mg m^{-3}) in 2011. This increase in CHL in 2011 was due to the supply of dissolved iron from the strong winds and subsequent mixing during the winter of 2010. Further, the increased CHL values in the Antarctic zone (0.5 mg m^{-3}) in 2011 compared to 2009 and 2010 could be due to the increased sea ice

* Corresponding author at: National Centre for Polar and Ocean Research, Ministry of Earth Sciences, Goa, India.

E-mail address: jenson@ncpor.res.in (J.V. George).

Peer review under the responsibility of the Institute of Oceanology of the Polish Academy of Sciences.



melting associated with positive Southern Annular Mode. The increased phytoplankton biomass in the summer of 2011 coincides with an increase in nitrate utilization (N:P \approx 13) compared to 2009 and 2010. Observations showed that ISSO frontal zones are characterized by inter-annual variability in terms of nutrient utilization and phytoplankton biomass production.

© 2022 Institute of Oceanology of the Polish Academy of Sciences. Production and hosting by Elsevier B.V. This is an open access article under the CC BY license (<http://creativecommons.org/licenses/by/4.0/>).

1. Introduction

The Southern Ocean plays a crucial role in the global carbon cycle, as this region is an important atmospheric carbon dioxide sink (Gruber et al., 2019). However, the Southern Ocean cannot reach its potential for atmospheric carbon uptake because of the inefficiency of the biological pump; it is a high nutrient – low chlorophyll (HNLC) region. Major reasons for the observed HNLC are the iron stress (Boyd and Ellwood, 2010; Martin et al., 1990), light limitation (Mitchell et al., 1991; Nelson and Smith, 1991), deep mixing (Taylor et al., 2013), and grazing pressure (Dubischar and Bathmann, 1997). The Indian sector of the Southern Ocean (ISSO; 20°E–110°E, 40°S–70°S) is also not different and follows an HNLC pattern. Satellite-derived austral summer climatology of surface chlorophyll-*a* (CHL) suggests low surface CHL concentration of 0.2 mg m⁻³ (Figure 1a) in the ISSO. However, the exceptions to the HNLC condition with CHL 0.5 mg m⁻³ are observed in the regions where physical control of the phytoplankton biomass is dominating. Examples of such regions are the vicinity of the Subtropical Front (STF), the waters near the Kerguelen and Crozet Islands, downstream the bathymetric features, and coastal waters influenced by the seasonal ice retreat (Anilkumar et al., 2015; Moore and Abbott, 2000). In a climate change scenario, the change in physical control not only affects the phytoplankton biomass but also the higher trophic level biodiversity and fisheries which have large commercial value (Deppeler and Davidson, 2017).

Apart from being a CO₂ sink, the Southern Ocean also regulates global primary productivity by supplying nutrients to low latitude oceans via the formation and transportation of mode and intermediate waters in the subtropical and sub-Antarctic region (Demuyne et al., 2020; Sarmiento et al., 2004). The nutrient characteristics of the mode and intermediate waters are determined by the biogeochemistry in the formation region which is further influenced by the physical control (Henley et al., 2020; Moore et al., 2018). The Southern Ocean comprises different biophysical zones with the boundary marked by fronts (Longhurst, 2010, Orsi et al. 1995). Unlike the Atlantic and Pacific sectors of the Southern Ocean, ISSO has a complex frontal system with individual branches of fronts merging and diverging by the peculiarities of bottom topography and the presence of Agulhas Return Current (Figure 1a; Belkin and Gordon, 1996; Kostianoy et al., 2004; Park et al., 1993). Though the fronts merge to form a wide front, different physical processes dominate each of these frontal zones.

The northernmost front in the ISSO is the STF, which is the boundary between warm-saline, nutrient-poor Subtropical Surface Water in the north and cooler, fresher,

nutrient-rich Sub-Antarctic Surface Water in the south. Agulhas Return Current flows parallel or juxtaposed to the STF (Lutjeharms and Ansorge, 2001). The region between Agulhas Return Current and STF is known as the Subtropical Frontal Zone (STFZ). Owing to the presence of Agulhas Return Current, which is dynamically very unstable, STFZ in the ISSO is characterized by high eddy kinetic energy (Figure 1b; Ansorge and Lutjeharms, 2005). High mesoscale eddy activity in the STFZ causes intermittent and short-lived CHL blooms and control dissolved nutrient characteristics of the region (George et al., 2018; Llido et al., 2005).

The Sub-Antarctic Frontal Zone (SAFZ) is the region between STF and Sub-Antarctic Front (SAF). SAFZ in the ISSO is characterized by the presence of major islands, Crozet and Kerguelen (Figure 1c). The interaction of the Antarctic Circumpolar Current (ACC) with these islands supplies micro-nutrients like iron to the offshore HNLC waters through the sediments deposited on the continental margins (Blain et al., 2001; Planquette et al., 2007; Sanial et al., 2014). However, the deep regions of the SAF of ISSO are less productive due to the prevalent iron stress. Even though the ISSO is characterized by high macronutrient concentration, the SAF region can be silicate limited in the austral summer (Parli et al., 2020). The silicate limitation is mainly controlled by the northward advection of silicate-limited water from the south, where the proliferation of diatoms reduced the silicate (Sarmiento et al., 2004). A recent study by Demuyne et al. (2020) pointed out that in short time scales (1–10 years), physical processes like advection and entrainment play a dominant role in the silicate limitation rather than the ambient biology.

Polar Frontal Zone (PFZ) is the region between SAF and Polar Front (PF). Generally, in austral summer, PFZ waters are not light limited with Photosynthetically Active Radiation (PAR) typically greater than 32 Einstein m⁻² day⁻¹ (Figure 1c, Venables and Moore, 2010). However, the presence of high wind stress patch (~0.2 Pa) centered at 50°S (Figure 1d) along with convective mixing may result in deep mixed layers, which can eventually decrease the light availability for phytoplankton and result in low phytoplankton biomass. The meridional migration of this high wind belt due to Southern Annular Modes controls the northward Ekman transport of deep water, affecting the phytoplankton distribution and dissolved nutrients (Hoppema et al., 2003).

The region south of PF to coastal waters of Antarctica is known as the Antarctic Zone (AZ). One of the characteristics of the AZ is the Antarctic divergence, where upwelling of Upper Circumpolar Deep Water (UCDW) brings dissolved micro and macronutrients into the surface layer affecting the phytoplankton biomass and dissolved nutrient inventory (Hoppema et al., 2003). The annual formation and dissipa-

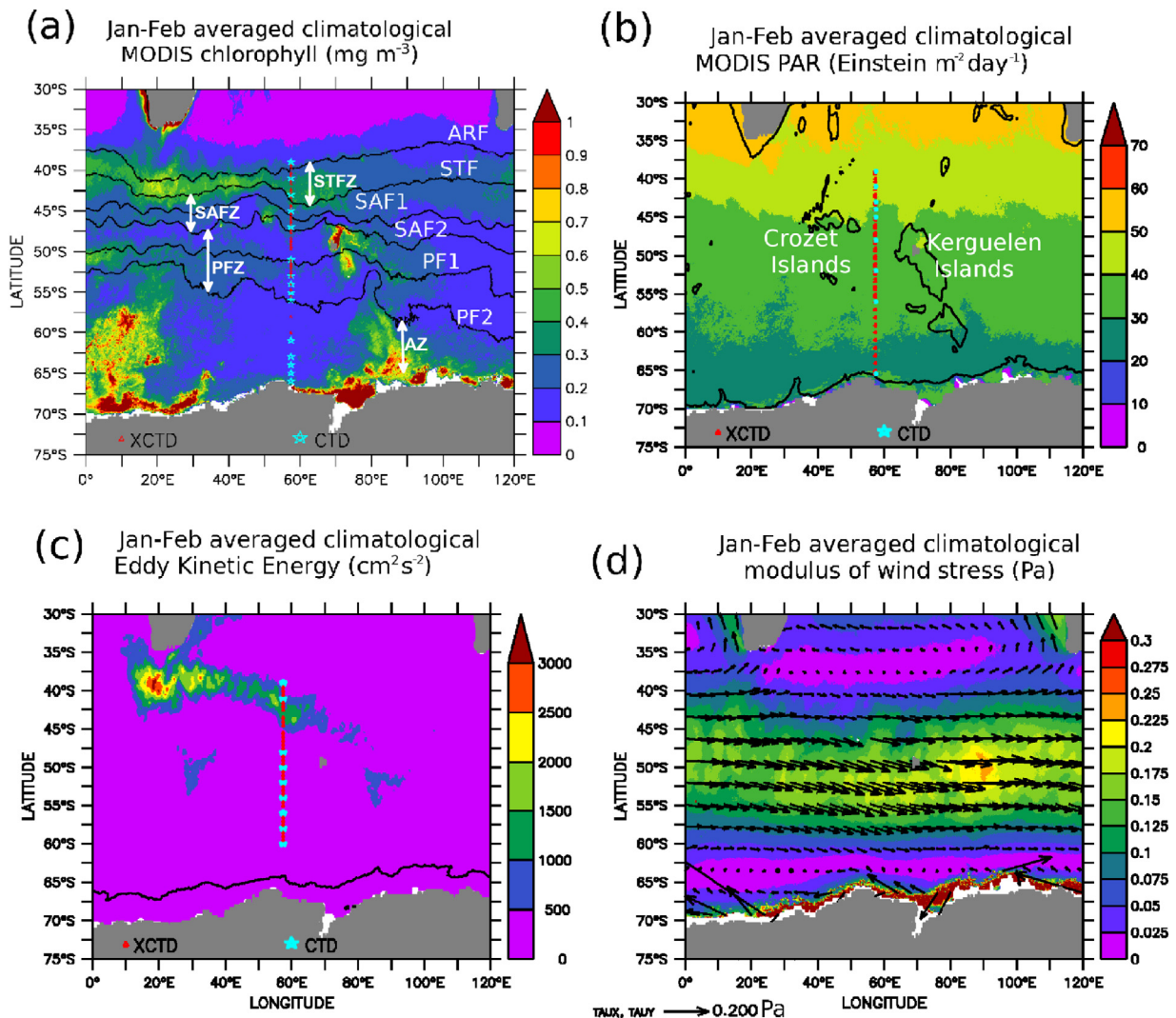


Figure 1 January–February averaged climatology of (a) MODIS CHL (mg m^{-3}). Black contours represent climatological frontal locations derived from sea surface temperature (GHRSSST). The ARF, STF, SAF1, SAF2, PF1 and PF2 represented from north to south by 18, 14, 10, 7.5, 4.5, and 2.5°C temperature contours, respectively. Frontal zones are also demarcated. (b) Photosynthetically active radiation (PAR, $\text{Einstein m}^2 \text{ day}^{-1}$). The black contour lines represent the 2000 m depth isobath derived from the etopo20 data set. (c) Eddy Kinetic Energy (EKE, $\text{cm}^2 \text{ s}^{-2}$). The black contour lines represents the climatological sea ice limit (15% sea ice fraction). (d) QuikSCAT modulus of wind stress (Pa). Vectors represent zonal and meridional wind stress. CTD/XCTD locations during SOE2009, SOE2010, SOE2011 are marked as light blue star/red triangles in the panel a, b, and c, respectively.

tion of sea ice and the distinct seasonal surface water mass transformations (Williams et al., 2008) make the AZ waters a physically dynamic area of the ISSO. The observed high phytoplankton biomass ($\text{CHL } 0.5 \text{ mg m}^{-3}$, Figure 1a) in the Antarctic coastal waters is due to the elevated levels of micronutrients (mainly iron) in the coastal waters as a result of glacial melting (Park et al., 1998). The sea ice melt also creates buoyant melt waters, which can enhance the irradiance levels by rapidly shoaling the mixed layer, resulting in elevated phytoplankton biomass (Briggs et al., 2018).

Though the recent decade saw an increase in exploration of the Southern Ocean, studies mostly focused on the Pacific and Atlantic sectors of the Southern Ocean. Indian Sector of the Southern Ocean was largely under-sampled, especially the basic biogeochemical parameters. Present manuscript assesses the physical control on the phytoplankton biomass,

nutrient concentrations, and its interannual variability during the summer of 2009–2011 in the ISSO, one of the least studied sectors of the Southern Ocean.

2. Data and methods

Hydrographic data collected during the Southern Ocean expeditions SOE2009 (from 19 February 2009 to 20 March 2009), SOE2010 (31 January 2010 to 1 March 2010), SOE2011 (from 1 February 2011 to 2 March 2011) were used to understand the physical control on the distribution of CHL and macronutrient concentrations in the ISSO. In 2009, the expedition was carried out onboard *r/v Akademik Boris Petrov*, and the subsequent expeditions were conducted onboard oceanographic *r/v Sagar Nidhi*. The CTD used during

Table 1 Instruments used for measuring different parameters during the expeditions to the Southern Ocean.

Cruise	Parameters	Instruments
SOE2009	Temperature/salinity	CTD MARK III-B (Neil Brown Instrument Systems, Inc.) XCTD-1 (TSK, Japan)
SOE2010	Dissolved Nutrients	UV-vis spectrophotometer (Perkin-Elmer)
	Chlorophyll concentration	UV-vis spectrophotometer (Perkin-Elmer)
SOE2011	Temperature/salinity	Seacat SBE21 portable CTD (Sea-Bird Electronics, USA) XCTD-3 (TSK, Japan)
	Dissolved Nutrients	UV-vis spectrophotometer (Perkin-Elmer)
	Chlorophyll concentration	UV-vis spectrophotometer (Perkin-Elmer)
	Temperature/salinity	SBE 911 plus system (Sea-Bird Electronics, USA) XCTD-3 (TSK, Japan)
	Dissolved Nutrients	Autoanalyser (Skalar 107 Analytical Sanplus 8505 Interface v3.05)
	Chlorophyll concentration	Turner Designs AU-10 Fluorometer

SOE2009 was MARK III-B (Neil Brown Instrument Systems, Inc.). During SOE2010, it was Seacat SBE21 portable CTD (Sea-Bird Electronics, USA) attached to the IDRONUT water sampler, and during SOE2011, CTD used was SBE 911 plus system (Sea-Bird Electronics, USA). The temperature and conductivity accuracy for all these CTD systems were $\pm 0.001^\circ\text{C}$ and $\pm 0.0001 \text{ S m}^{-1}$, respectively. Expendable CTD (XCTD) was also used between the CTD stations during the expeditions. The CTD/XCTD sampling locations are given in Figure 1. During SOE2009, XCTD-1 (TSK, Japan) was used, and during SOE2010/SOE2011 XCTD-3 (TSK, Japan) was used. The accuracy of XCTD temperature, conductivity, and depth is $\pm 0.02^\circ\text{C}$, $\pm 0.0003 \text{ S m}^{-1}$, and $\pm 2\%$ of depth, respectively. The XCTD profiles were quality controlled by following the guidelines in the CSIRO Cookbook (Bailey et al., 1994; George and Anilkumar, 2022). The salinity data from the CTD/XCTD were calibrated against water samples analyzed using a high-precision salinometer (Guildline AUTOSAL).

Seawater samples were collected from standard depths (0, 10, 20, 30, 50, 75, 100, and 120 m) with General Oceanics Niskin samplers (5 L) fitted on a rosette along with the CTD. Nutrient analysis was carried out following the standard methods (Grasshoff et al., 1983). Seawater subsamples were collected in 250 ml Nalgene bottles and kept frozen at -20°C till the nutrient analysis. Prior to the analysis, the samples were thawed and brought to room temperature. A UV-vis spectrophotometer (Perkin-Elmer) was used to analyze the nitrate, phosphate, and silicate during SOE2009 and SOE2010. In 2011, nutrients were analyzed onboard using an autoanalyser (Skalar 107 Analytical Sanplus 8505 Interface v3.05). CHL analyses were carried out following the standard procedures (Strickland and Parsons, 1972). Water samples for CHL analysis were filtered through GF/F filter (pore size $0.7 \mu\text{m}$). After the filtration, the filters were immediately transferred to an amber color glass tube with 10 ml of 90% acetone. The filter was crushed with the help of a glass rod and kept overnight in the freezer for extraction. The next day, the suspension is transferred into the cuvette and measured using a fluorometer/spectrophotometer. In 2009 and 2010, CHL analysis was made using a UV-vis spectrophotometer (Perkin-Elmer). While in 2011, the CHL anal-

ysis was carried out using Turner Designs AU-10 Fluorometer. The details of parameters and instruments used during the cruises are given in Table 1.

In order to understand the austral summer surface CHL distribution in ISSO, January–February average climatology of CHL is derived from the monthly MODIS data from July 2002 to September 2013. The monthly climatology of a variable is the mean of monthly values of the variable over a specified period. The climatological frontal location was obtained from the climatology of sea surface temperature calculated using GHRSSST data (October 2003 to October 2013). Climatological photosynthetically active radiation (PAR) was derived from MODIS data from July 2002 to September 2013. Climatology of eddy kinetic energy (EKE, $\text{cm}^2 \text{ s}^{-2}$) was calculated from AVISO, SSALTO/DUACS delayed time geostrophic velocity anomaly from September 1999 to August 2013. The climatological sea ice limit (15% sea ice fraction) was derived from SSM/I sea ice fraction from January 2003 to September 2013. QuikSCAT modulus of wind stress (Pa) data from August 1999 to October 2009 has been used to calculate the monthly climatology. For the time series analysis, we used Navy Fleet Numerical Meteorology and Oceanography Center (FNMOC; <https://oceanview.pfeg.noaa.gov/thredds/dodsC/FNMOC>) wind products. Variability of surface ocean currents was inferred from Ocean Surface Current Analysis Real-Time (OSCAR) data (https://podaac.jpl.nasa.gov/dataset/OSCAR_L4_OC_third-deg). The MLD is calculated as the depth at which the density is greater by 0.03 kg m^{-3} from the density value at 10 m depth.

Monthly products of total CHL concentration, nitrate, iron, MLD, and contribution of major functional phytoplankton types to total CHL for the February month from 2009 to 2011 were obtained from the NASA Ocean Biogeochemical model (NOBM; <https://giovanni.gsfc.nasa.gov/giovanni/>). The global NOBM model is coupled with the circulation and radiative model. The biogeochemical component of the model comprises 4 phytoplankton taxonomic groups: diatoms, cyanobacteria, chlorophytes, and coccolithophores. Further details of the model can be found in Gregg and Casey (2007). The data were with half-degree resolution from 40°S to 66°S along 57.5°E . Temperature/salinity

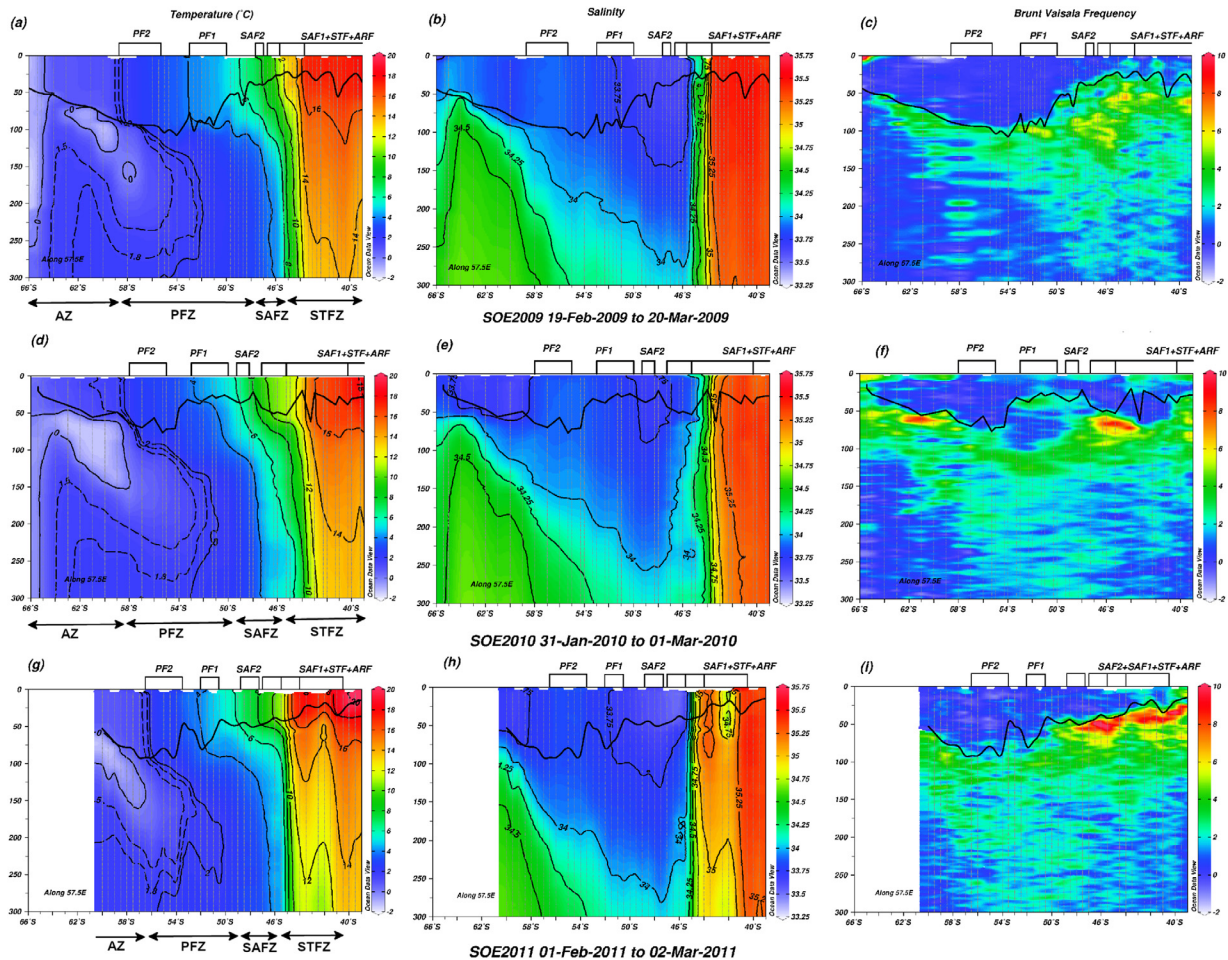


Figure 2 The vertical section along 57.5°E of (a) temperature (b) salinity and (c) Brunt Vaisala frequency during SOE2009; (d) temperature (e) salinity and (f) Brunt Vaisala Frequency during SOE2010; (g) temperature (h) salinity and (i) Brunt Vaisala frequency during SOE2011. The thick black line represents the mixed layer depth.

data from ARGO floats (https://www.nodc.noaa.gov/argo/floats_data.html) is also used to understand the thermohaline variability in the study region.

2.1. Frontal structure during the observation period

Frontal structure during the cruises was identified using the surface temperature criterion (ARF: 19–17°C, STF: 17–11°C, SAF1: 11–9°C, SAF2: 7–6°C, PF1: 5–4°C, PF2: 3–2°C) of Anilkumar et al. (2015). The frontal location identified by the surface temperature criterion closely matched with the locations identified by subsurface temperature contours and salinity characteristics (figure not shown) detailed in Table 1 of Anilkumar et al. (2015). Consistent with the previous studies (Anilkumar et al., 2006, 2014; Dong et al., 2006), during the observation period, both SAF and PF were branched as their northern (SAF1 and PF1, respectively) and southern fronts (SAF2 and PF2, respectively) as seen in Figure 2. Along 57.5°E, the Agulhas return Front (ARF), STF, and SAF1 were merged to form a wide front extending from 39°S to 47°S. Earlier studies by Park et al. (1993), Sparrow et al. (1996), and Kostianoy et al. (2004) also noted

a merged front in this region. The Southern Ocean is divided into frontal zones, distinct regions with relatively uniform thermohaline and biogeochemical characteristics bounded by the fronts (Figures 2 and 3; Orsi et al. 1995). The merged ARF and STF region is the STZ. The SAZ is from the south of STF to SAF2, and the PFZ is from the south of SAF2 to PF2. South of PF2 is the AZ. Different biogeochemical conditions and physical processes dominate in each of these frontal zones.

3. Results

3.1. Hydrography during SOE2009, SOE2010 and SOE2011

3.1.1. Thermohaline structure

Most of the observations presented in this manuscript were carried out during February–March and therefore represented the late austral summer conditions of the study region. Latitude-depth sections of temperature (Figure 2a,d, and g) and salinity (Figure 2b,e, and h) collected during the Southern Ocean expeditions SOE2009, SOE2010, and

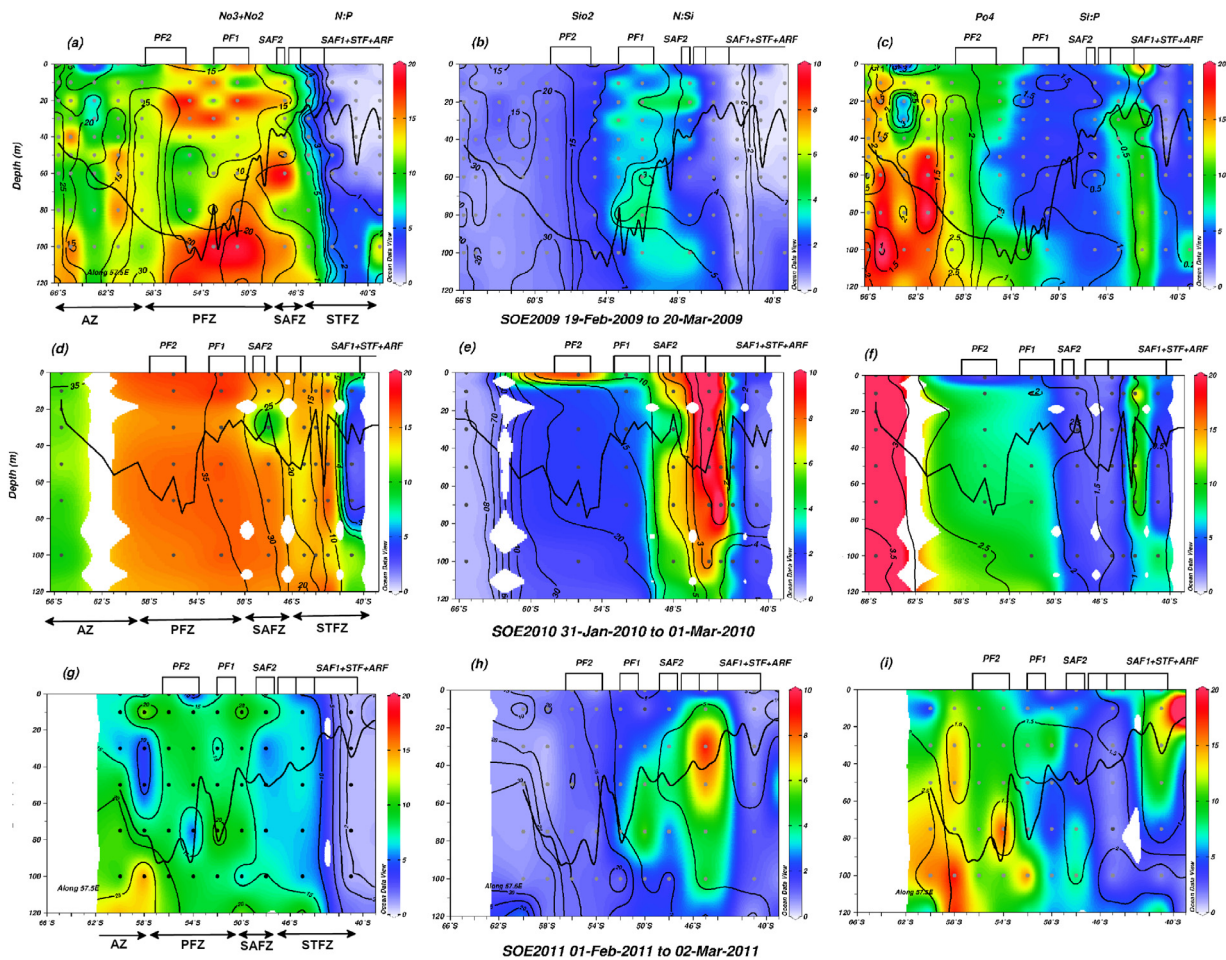


Figure 3 The vertical section along 57.5°E of (a) N:P (color bar) overlaid by NO₃+NO₂ contour (b) N:Si (color bar) overlaid by SiO₂ contour and (c) Si:P (Color bar) overlaid by PO₄ contour during SOE2009; (d) N:P (color bar) overlaid by NO₃+NO₂ contour (e) N:Si (color bar) overlaid by SiO₂ contour and (f) Si:P (Color bar) overlaid by PO₄ contour during SOE2010; (g) N:P (color bar) overlaid by NO₃+NO₂ contours (h) N:Si (color bar) overlaid by SiO₂ contours and (i) Si:P (Color bar) overlaid by PO₄ contours during SOE2011. The thick black line represents the mixed layer depth.

SOE2011 show the frontal structure of the region. During SOE2011, the merged frontal system of ARF+STF+SAF1 was compact (from 41°S to 47°S) compared to SOE2009 and SOE2010 (from 39°S to 47°S). SAF2 location was centered at 48°S during all the expeditions. During SOE2009 and SOE2010, PF1 was observed between 50°S and 53°S. However, during SOE2011, PF1 was confined to 51°S–52°S. While the extent of PF2 (55°S to 59°S) was similar during SOE2009 and SOE2010, it was compact and shifted northward (54°S to 57°S) in SOE2011.

Major water masses observed in the upper 300 m water column from 40°S to 66°S were the sub-Tropical surface water (T12°C, S35.1 psu), sub-Antarctic surface water (T9°C, S34 psu), and the Antarctic surface water (T5°C, S34 psu). The water with a temperature of less than 4°C and salinity of 34 psu observed below the up-sloping 34 psu isohaline from SAF to the south suggests the upwelling of Circumpolar Deep Water (CDW). A temperature minimum layer with values ranging between –2°C and 1.5°C was located 50–200 m south of 50°S in the study region during SOE2009, SOE2010, and SOE2011 (Figure 2a,d, and g). Below this layer, the temperature gradually increased by ~2°C up

to 300 m and then exhibited isothermal characteristics further down. From Figure 2, it is clear that there is an inter-annual variability in the austral summer frontal structure and thermohaline characteristics in the study region.

The latitude-depth Brunt Vaisala frequency sections (Figure 2c,f, and i) suggest that the STZ and SAZ were characterized by a shallow (~30 m) mixed layer and high static stability below the mixed layer depth. In the PFZ, the water column was less stable, and the mixed layer deepened up to ~100 m. Further south in the AZ, the mixed layer was shallow (20–50 m). One stark difference noticed in the PF1 during the SOE2010 was its shallow mixed layer (~20 m) compared to SOE2009 and SOE2011 (~80 m).

3.1.2. Nutrient distribution

In general, nitrate+nitrite (NO₃+NO₂), silicate (SiO₂), and phosphate (PO₄) concentrations in the upper 120 m increased from ARF to AZ (Figure 3). During SOE2009, from ARF to AZ, the concentration of NO₃+NO₂, SiO₂, and PO₄ ranged between 0.1–31 μM, 0.2–40 μM, and 0.1–3.5 μM, respectively (Figure 3a,b and c). Compared to SOE2009, during SOE2010, NO₃+NO₂, SiO₂, and PO₄ concentrations

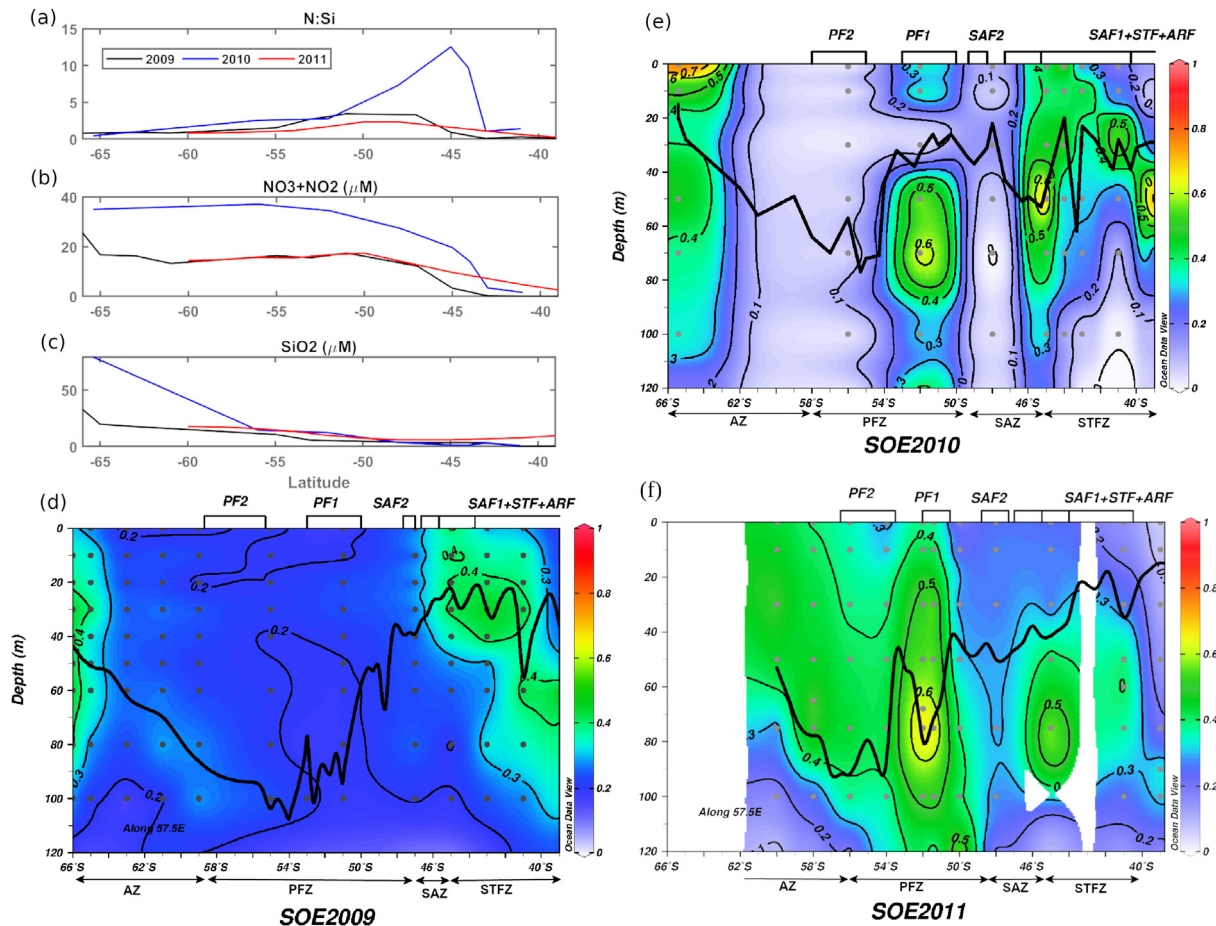


Figure 4 Mixed layer averaged nutrient properties during SOE2009, SOE2010 and SOE2011, (a) N:Si (b) NO_3+NO_2 concentration (μM) and (c) SiO_2 concentrations (μM). The chlorophyll section along 57.5°E during (d) SOE2009 (e) SOE2010 and (f) SOE2011.

were higher and varied between 2–36 μM , 1–85 μM , and 0.2–3.6 μM , respectively (Figure 3c,d and e). During SOE2011, the NO_3+NO_2 concentrations were higher than 1 μM , and it increased from ARF (1.5 μM) to PF2 (25 μM) (Figure 3g). Throughout the cruise track, silicate concentration was higher than $\sim 1 \mu\text{M}$, and it increased from ARF (2 μM) to the southernmost station at 60°S ($\sim 38 \mu\text{M}$, Figure 3h). The phosphate concentration was lower than 1 μM in the STF region, and further south, it increased up to 3 μM (Figure 3i). In terms of upper layer SiO_2 distribution, PF acted as a transition region, where towards its north, SiO_2 values were less than 6 μM , and towards its south, SiO_2 values reached up to 80 μM (Figure 3b,e, and h).

Overall N:P ratio from ARF to PF2 increased from 1 to 18 and then decreased to 10 in Antarctic coastal waters (Figure 3a,d, and g). Similarly, N:Si ratio also increased from ARF to SAF2 (1– ~ 10) and then decreased to 1 at 66°S (Figure 3b,e, and h). Si:P ratio generally increased from ARF to Antarctic coastal waters (Figure 3c,f, and i). Figure 4a,b and c show the mixed layer average of N:Si ratio, NO_3+NO_2 and SiO_2 concentrations respectively in the study region. Even though the general pattern of nutrient ratios was similar during all the cruises, absolute values showed strong inter-annual variability. The highest N:Si ratio was observed in the SAZ. During SOE2009, N:Si values reached up to 3, and in SOE2010 10, and in SOE2011 about 2.

An important feature in the meridional section of nutrient concentration is the latitudinal gradient of nitrate and silicate concentrations with high values in the south and low values in the north (Figure 4b and c). While the nitrate concentration decreases mildly towards the north, the silicate concentration shows strong gradients across the PF region (55°S – 50°S). This difference in the meridional decrease of upper layer nitrate and silicate concentration is also observed in other Southern Ocean sectors. SAF regions (48°S – 43°S) also observed substantial depletion of silicate with respect to nitrate. The observed vertical CHL distribution during the cruises was further analyzed to understand the role of ambient phytoplankton biomass on the nutrient ratios.

3.1.3. Chlorophyll-a distribution

CHL distribution along 57.5°E during SOE2009 and SOE2010 (Figure 4c and d, respectively) was similar to climatology (Figure 1a), with elevated surface CHL concentration ($\sim 0.4 \text{ mg m}^{-3}$) in the STFZ and coastal waters of Antarctica. In the SAZ and PFZ, the upper 120 m was characterized by low CHL concentration ($\sim 0.2 \text{ mg m}^{-3}$). However, CHL in the PFZ during SOE2010 was anomalously low, with a concentration 0.1 mg m^{-3} (Figure 4d). In contrary to SOE2009 and SOE2010, during SOE2011, at the PFZ and AZ, the CHL concentration was high ($\sim 0.5 \text{ mg m}^{-3}$) in the upper water column

(Figure 4e), and the STZ and SAZ region was characterized by low CHL concentrations ($\sim 0.2 \text{ mg m}^{-3}$), except in the deep CHL maximum (DCM). During all the cruises, prominent DCM ($\sim 0.6 \text{ mg m}^{-3}$) was noticed in the STZ. The surface distribution of CHL concentration was consistent with that derived from the satellite (Figure 5 a,b, and c).

3.2. Eddies, winds, and surface currents

The alternating patches of positive and negative sea level anomalies and overlaid geostrophic velocity anomaly vectors suggest that during SOE2009, SOE2010, and SOE2011, the ARF and STF region was characterized by high mesoscale eddy activity (Figure 5d,e and f, respectively). Even though the intensity of eddies reduced towards the south, the presence of both positive and negative sea level anomaly patches was observed in the PF regions.

Winds in the ISSO are typically westerlies from the ARF to PF, with the core lying at $50\text{--}55^\circ\text{S}$ (Figure 6a,b and c). However, winds turn to easterlies in the coastal regions. The wind pattern results in subtropical convergence north of the PF and polar divergence south of the PF. At the coast, easterlies result in downwelling. Strong inter-annual variability was noticed in terms of strength and location of the core of the westerly. In the summer of 2009 and 2011, the core of westerly was $\sim 55^\circ\text{S}$, whereas during 2011, it was $\sim 50^\circ\text{S}$. During SOE2009, the high wind stress patch was $\sim 0.4 \text{ Pa}$, whereas in 2010 and 2011 it was $\sim 0.25 \text{ Pa}$. The eddy-populated region of the ARF+STF frontal region was characterized by weak wind stress ($\sim 0.15 \text{ Pa}$, (Figure 6a,b and c)).

One of the important features observed in the OSCAR surface currents is the strong (0.8 m s^{-1}) Agulhas Return Current (Figure 6d,e and f). There are two prominent current regions in ISSO, the eastward flowing ARC in the ARF+STF region and ACC in the polar frontal region. Mesoscale variability in the ARF+STF region, represented here by sea surface height anomalies, aligns with the ARC core (Figure 6d,e and f).

3.3. NASA Ocean Biogeochemical Model (NOBM)

The NOBM February surface CHL (Figure 7a) data along 57.5°E captured major features observed in the in-situ CHL data (Figure 4). ARF+STF merged frontal regions, and the coastal areas were CHL productive. Elevated surface CHL was noted in the PF region in 2011. MLD from NOBM (Figure 7b) also matched the general pattern inferred from the CTD/XCTD data (Figure 2), where MLD is shallow in both the ARF+STF region and the coastal Antarctic region. Deepest MLD was noticed in the PF region; however, the MLD in NOBM data was overestimated. The latitudinal variation of nitrate in the NOBM data (Figure 7c) was also consistent with in situ data (Figure 3a,d, and g), with macronutrient-limited ARF+STF and high nutrients further south.

Iron concentrations were increased consistently from ARF to coastal regions along 57.5°E (Figure 7d). However, the PF region and further south exhibited enhanced iron concentration during 2011. Diatoms were the major functional group that contributed to the total CHL in the SAF and further south (Figure 7e). However, in the ARF+STF re-

gions, coccolithophores were the major contributors to the phytoplankton biomass (Figure 7f).

4. Discussion: Physical control of the phytoplankton biomass and dissolved nutrients

CHL concentration is considered as a proxy for phytoplankton biomass (Huot et al., 2007). The variability of CHL and macronutrient concentration both in time and space noted in the ISSO warrants a detailed discussion. Physical processes control the phytoplankton biomass mainly by influencing nutrient and light availability. Major physical processes affecting the surface macronutrients concentration are associated with the supply of nutrients from the deeper layer and its subsequent horizontal transport. Different physical processes dominate each frontal zone; thus, the response of phytoplankton biomass and nutrient concentration is also different. Variation in the N/P/Si ratio from its canonical Redfield values (16:1:16; Redfield (1963)) is instrumental in understanding the changes in the species composition and/or physiological adaptation of particular species to ambient environmental conditions (Giddy et al., 2012). In the following sections, we will discuss the dominating physical processes in each frontal zones and their control on the phytoplankton biomass and dissolved macronutrient concentrations.

4.1. The subtropical zone

In all of the hydrographic sections occupied along 57.5°E , ARF was merged with STF (Figure 2). The CHL concentration showed considerable variability in this merged frontal region (STZ) between the cruises (Figure 4c,d and e). This is the region in the ISSO where prominent DCMs are noted. STZ is macronutrient-limited (Figure 3) compared to other fronts in the ISSO (Gandhi et al., 2012; George et al., 2018; Jasmine et al., 2009; Naik et al. 2015) and any supply of the nutrients can elevate the CHL concentration. This region is known for its high mesoscale eddy activity (George et al., 2018; Sabu et al., 2015) and intermittent short-lived CHL blooms, especially during the austral spring and summer (Llido et al., 2005). The presence of mesoscale eddies can be seen in the undulation of isotherms and sea level anomalies as well (Figure 2a,d,g, and Figure 5d,e,f).

Eddies can influence the CHL distribution by displacing the phytoplankton (stirring, trapping) or by modifying the nutrient and light conditions (Dawson et al., 2018; Frenger et al., 2018). The mesoscale activity in this region is reflected in the CHL distribution as the cyclonic eddies bring up nutrients to surface, which can advect further east and regulate the CHL concentration (Kahru et al., 2007). On the other hand, anticyclonic eddies pile up nutrient-limited surface water and reduce the CHL concentration (McGillicuddy et al., 1998). Furthermore, submesoscale processes at the outer edge of anticyclonic eddies cause vertical advection of nutrients and increase the CHL concentration (Strass et al., 2002). Thus, the CHL variability noted in the STZ is associated with the eddies.

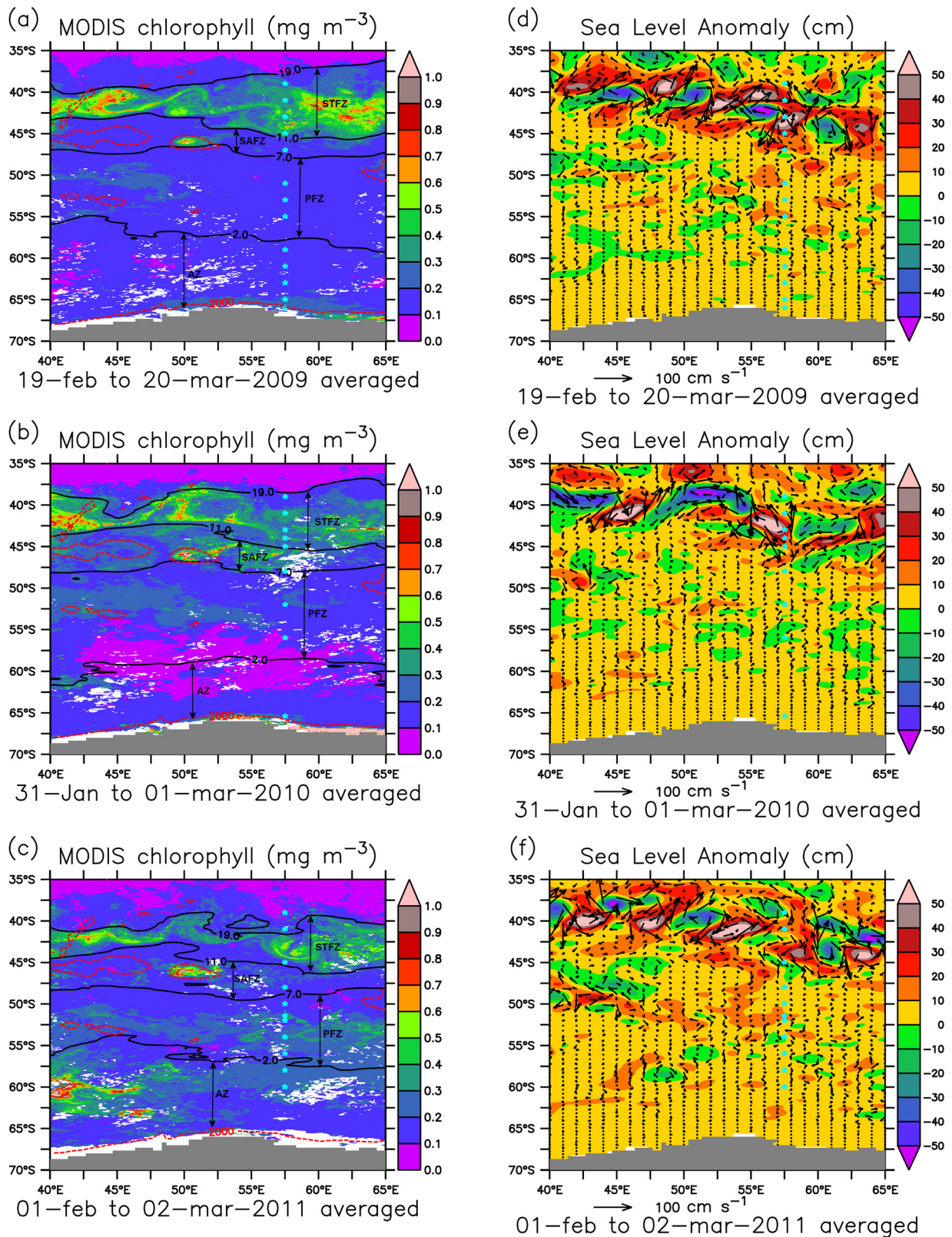


Figure 5 The 8 day composite MODIS CHL overlaid by the GHRSSST sea surface temperature both averaged over the cruise period of (a) SOE2009 (b) SOE2010 (c) SOE2011. The weekly AVISO merged sea level anomaly overlaid by geostrophic velocity anomalies both averaged over the cruise period of (d) SOE2009 (e) SOE2010 (f) SOE2011. The light blue stars represent the CHL station during the respective cruises. The red dashed contour depicts the 2000 m depth isobath derived from etopo20 data.

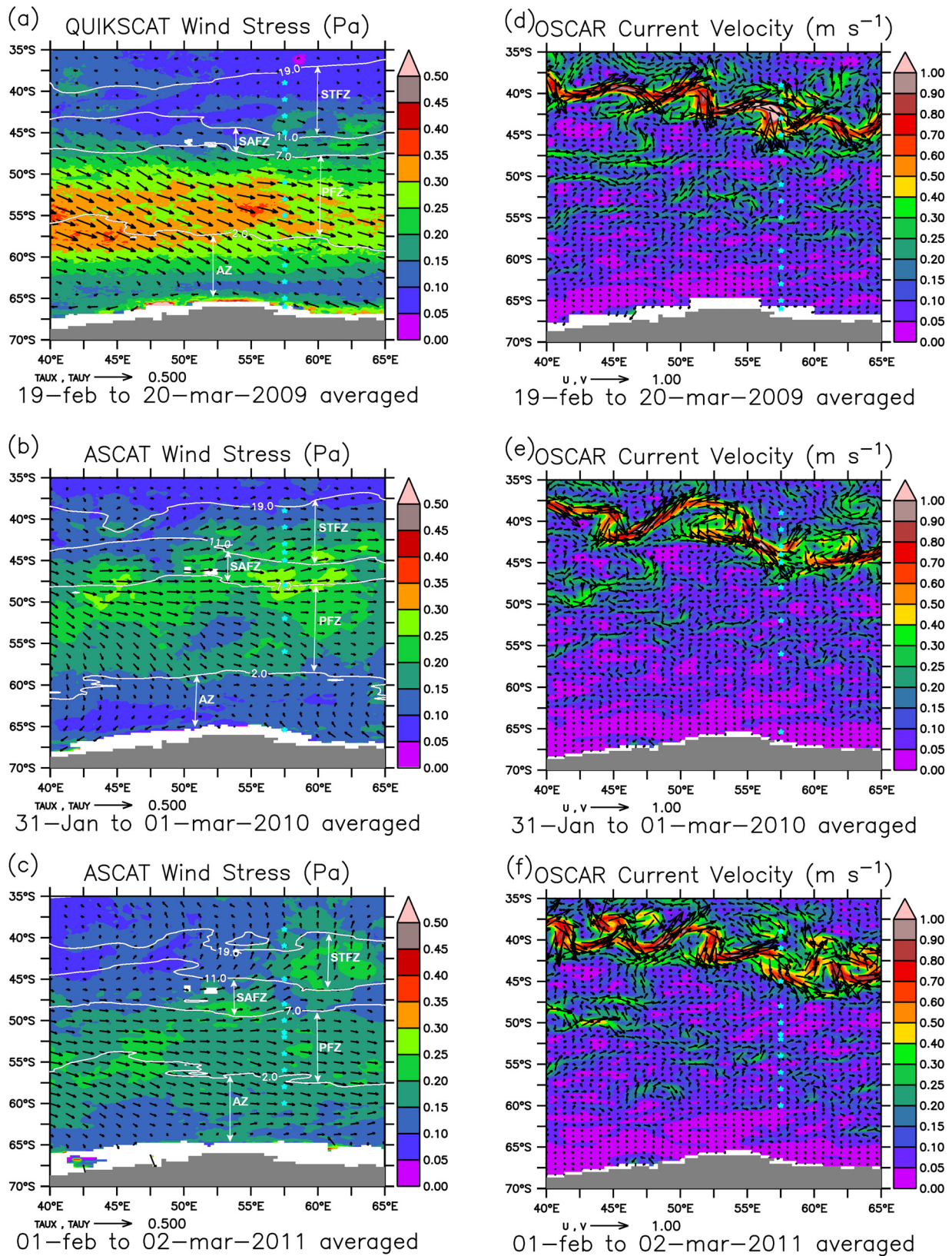


Figure 6 QUIKSCAT modulus of wind stress, overlaid by the wind stress components averaged over the cruise period of (a) SOE2009. ASCAT modulus of wind stress overlaid by the wind stress component averaged over the cruise period of (b) SOE2010 (c) SOE2011. OSCAR current velocity (m s^{-1}) overlaid by the velocity components averaged over the cruise period of (d) SOE2009 (e) SOE2010 (f) SOE2011. The sky blue star represents the station locations during the respective cruises.

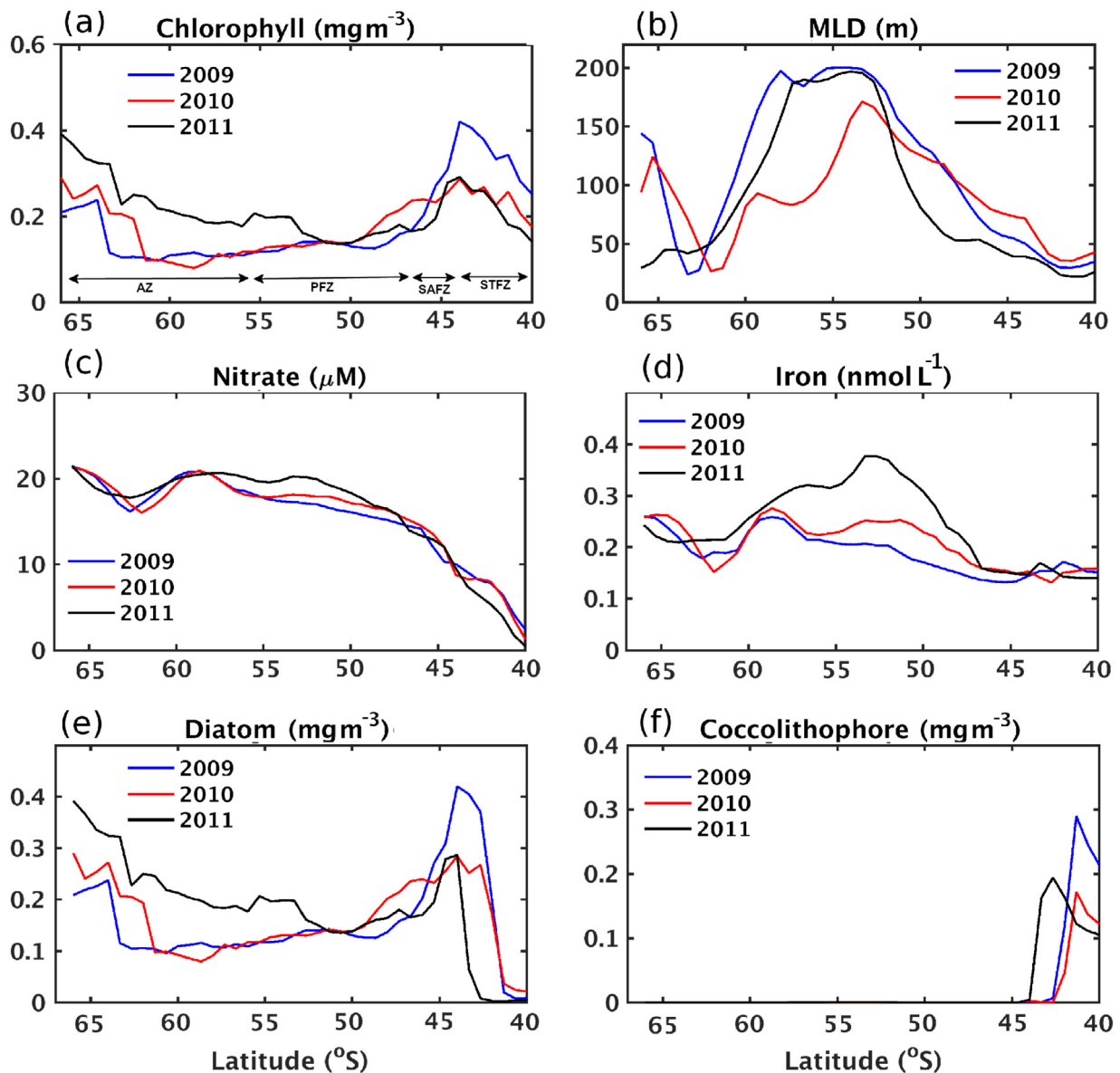


Figure 7 NOBM February data along 57.5°E in 2009 to 2011 (a) chlorophyll-a (b) mixed layer depth (c) nitrate (d) iron (e) diatom (f) coccolithophore.

The increased CHL production is further supported by the shallow MLD and increased stratification in the region (Figure 2). Wind stress is also weak (~0.15 Pa) in this merged frontal region, aiding the shallow mixed layer and increased stratification (Figure 6a,b and c). From the OSCAR currents, it is clear that the eddies in the STZ region are mainly due to the baroclinic instability of eastward flowing strong (0.8 m s⁻¹) ARC (Figure 6d, e and f; Backeberg et al., 2012; Beal et al., 2011; Lutjeharms and Ansong, 2001). The MODIS CHL distribution during the cruises also showed the filamentous meandering nature of the ARC (Figure 5a,b and c) aligned with the Agulhas Return Current (Figure 6d,e and f). Thus, the inter cruise variability noted in CHL in the STZ region was mainly tied up with the ARC and the associated eddy generation.

4.2. The sub-Antarctic zone

Compared to STZ, in the SAZ, the number of eddies was less across the cruise transects (Figure 5d,e and f). Stratification was weaker in the SAZ than in the STZ (Figure 2). The MLD also showed a gradual increase from STF to SAF2 (~20 m to ~50 m), thus creating a possible light limitation for individual phytoplankton cell. The offshore regions of SAZ (away from the Crozet Islands) are always less CHL productive (Figure 5a,b and c), mainly because of the lack of iron supply due to the deep bottom topography. The increased CHL concentration is expected in the waters surrounding the Crozet Islands and the Southwest Indian Ridge, where the depth is less than 2000 m. Satellite images showed a patch of high CHL north of the Crozet Is-

lands, which is in concurrence with Planquette et al. (2007). Pollard et al. (2002) pointed out that the interaction of waters flowing close to the Crozet Islands (which carries dissolved iron of island origin) with waters that are coming far from the islands results in a patchy dissolved iron distribution and hence the CHL.

Nutrient concentration of upper ocean waters of SAZ+STZ during late summer are of global importance since these are the regions of Antarctic Intermediate Water (AAIW) and Sub-Tropical Mode Water (STMW) formation, which eventually exported out of the Southern Ocean to ventilate at the surface layers of mid and low-latitude oceans (Demuynck et al., 2020; Sarmiento et al., 2004). Dissolved nutrient characteristics in the SAZ are mostly governed by the northward Ekman transport of nutrient-rich upwelled water from the south (Demuynck et al., 2020; Marinov et al., 2006). Previous studies showed that the advected water from the south is low in silicate concentration compared to nitrate, as the diatom species dominated in those waters are hyper silicified and export the silicate to deep water through the sinking of thick frustules (Assmy et al., 2013; Smetacek et al., 2002). The diatom uses silicon to build external skeletons (frustule) of silicon dioxide around the cell. During early summer, larger diatoms can dominate, and when their frustules settle down, silicate limitation can occur. Physiological adaptation of plankton cells under iron limitation can further increase the export of biogenic silica relative to nitrogen and phosphorus from the surface to deeper waters (Pichevin et al., 2014). Though this explains the strong latitudinal gradient observed in the silicate values compared to nitrate (Figure 4b and c), this does not explain the peak in N:Si noted at the northern part of the SAZ (Figure 4a).

The time series of satellite CHL data (Figure 8a) showed that during both 2010 and 2011 June–October, CHL blooms were present at $\sim 45^\circ\text{S}$. The subsequent summer was characterized by N:Si > 4 in the SAZ. During 2009, there were no winter/spring CHL blooms centered at $\sim 45^\circ\text{S}$, and in the following summer, the N:Si ratio was < 4 (Figure 3b,e,h). The NOBM data further indicated that CHL blooms observed in the satellite data set mainly consisted of diatoms (data not shown). It appears that during late summer when the stations occupied in SOE2010 and SOE2011, diatoms may have extracted Si down to limiting levels and N:Si values increased to 4. It has to be noted that even in the iron replete conditions, Southern Ocean diatoms are more silicified than the tropical variants (Timmermans et al., 2004).

Previous studies also pointed out that along with the iron limitation, SAZ can be silicate limited as well (Boyd et al., 2010; Hadfield, 2011). Silicate concentration observed in the SAZ was less than $10 \mu\text{M}$ (Figure 3b,e and h), which can be limited for the diatoms (Boyd, 2002; Hadfield, 2011; Nelson et al., 2001), the major phytoplankton group in the SAZ (Figure 7e). NOBM data during February 2009, 2010, and 2011 on suggested iron concentration values was also lower in SAF compared to PF (Figure 7d). Thus, in the SAZ, the phytoplankton production is assumed to be hampered by the co-limitation of iron and silicate. Previous studies further support this hypothesis that in late summer the SAZ region is dominated by coccolithophores rather than the diatoms in the ISSO (Mendes et al., 2015; Shramik et al., 2013). Our observations suggest that in the SAZ, the supply of nutrients

during winter and the drawdown of nutrients in the consecutive summer play an important role in deciding which phytoplankton communities dominate. A change in dominating phytoplankton species influences the potential of the Southern Ocean as an atmospheric CO_2 sink, and the dissolved nutrient characteristics of newly formed water masses which will be eventually exported to low latitude oceans.

4.3. The polar frontal zone

Climatologically, pelagic ISSO is a less productive region with a CHL concentration of approximately 0.2 mg m^{-3} (Figure 1a). Major features observed in the late summer of 2009–2011 were the anomalously low CHL ($\sim 0.1 \text{ mg m}^{-3}$) in the PF2 region during SOE2010 and the elevated CHL ($\sim 0.4 \text{ mg m}^{-3}$) in the PFZ (Figure 4c,d, and e) during SOE2011. The observed inter-annual variability in phytoplankton biomass was reflected in nutrient concentrations and nutrient ratios. The summer of 2010 was characterized by the highest N:P value (~ 15), indicating low nitrate utilization, whereas the summer of 2011 N:P values was the lowest (~ 13), suggesting higher nitrate utilization (Figure 3a,d, and g).

Wind stress has an important role in the CHL distribution in the Southern Ocean as it can change the MLD, which in turn alters the light condition for individual phytoplankton cells (Venables and Moore, 2010). The late summer is typically characterized by low surface PAR ($\sim 24 \text{ Einstein m}^{-2} \text{ day}^{-1}$; Figure 8b). A deeper MLD can cause light limitation for the phytoplankton. Compared to SOE2010, during SOE2011, the MLD in the PF was deeper, but the CHL concentration was higher (0.4 mg m^{-3}). The CHL observation does not show a correspondence with the MLD. This suggests that light limitation due to the deepening of the MLD may not be the discerning factor for the observed anomalous CHL concentration observed during SOE2010 and SOE2011.

QuikSCAT wind stress during the SOE2009 suggests a comparatively high stress (0.35 Pa) patch centered at 55°S (Figure 6a). During SOE2010, the high wind stress patch shifted northwards and was centered at 50°S (Figure 6b). Compared to SOE2009, the wind stress was reduced as well ($\sim 0.25 \text{ Pa}$). However, during SOE2011, the high wind stress patch became further weak (0.2 Pa) compared to that during SOE2009 and SOE2010 and was centered at 55°S . The Southern Annular Mode (SAM) governs the north–south movement of the westerly wind belt that circles Antarctica (Sallée et al., 2010). During the positive SAM period, the belt of strong westerly winds contracts towards Antarctica. Conversely, during the negative SAM event, expansion of the belt of strong westerly winds towards the equator occurs. Time series of wind stress averaged over 55°E – 60°E showed that during SOE2010, the negative SAM shifted the westerly wind belt further northward (Figure 8c), and the northward Ekman transport reduced (Figure 8d). Wind stress curl suggested positive values at the PFZ, suggesting Ekman pumping (Figure 8e), which induces downwelling. Upwelling in the deep open ocean HNLC region is important because it is the major supply mechanism of micronutrients (Boyd and Ellwood, 2010). Thus, the weakening of the westerly wind belt and its northward shift due to negative SAM might have resulted in the anomalously low CHL production at PFZ during SOE2010.

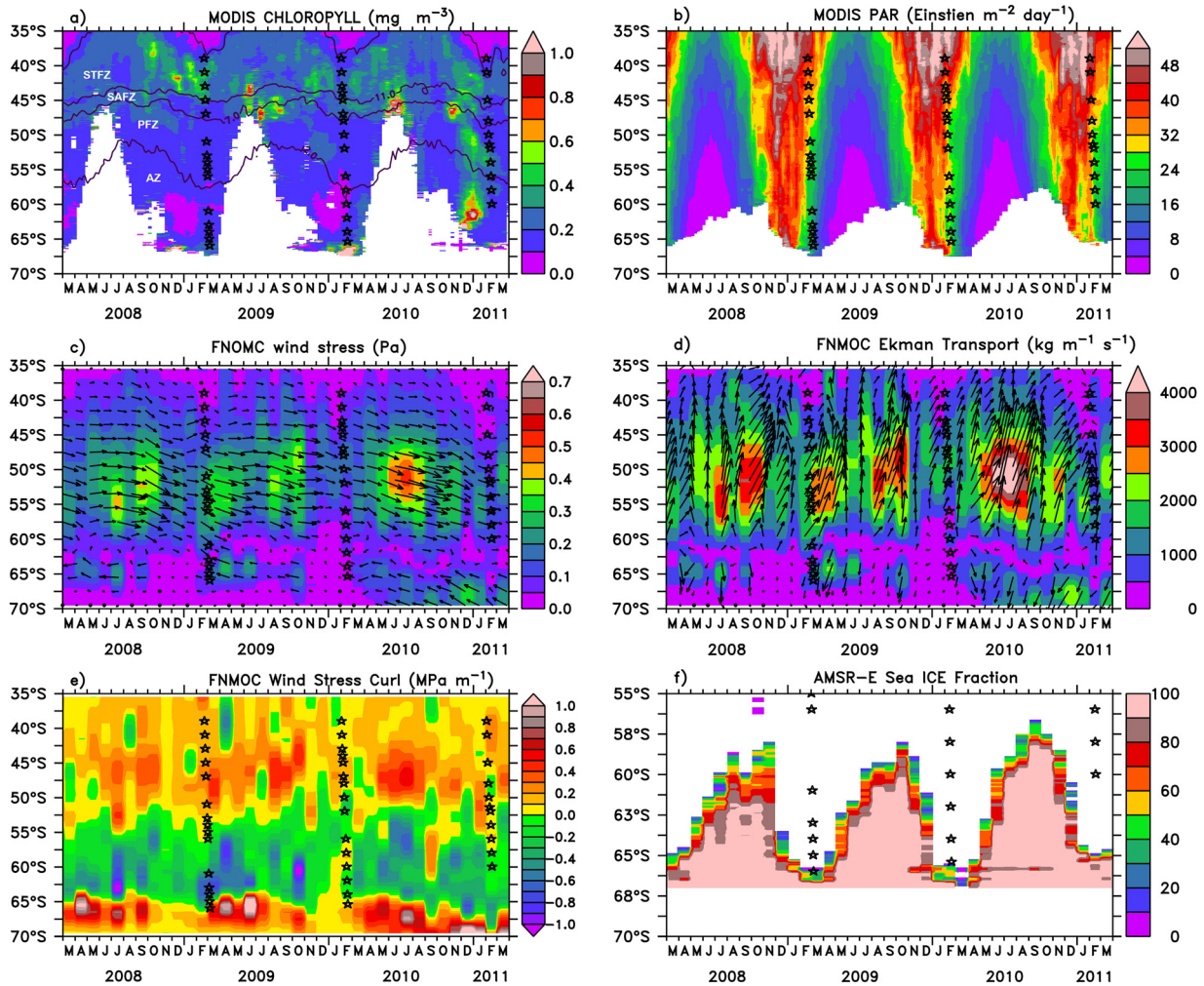


Figure 8 The time series of 55°E–60°E averaged (a) MODIS chlorophyll-*a* concentration (b) MODIS photosynthetically active radiation (c) FNMOC blended wind stress (d) FNMOC Ekman transport (e) FNMOC wind stress curl, and (f) AMSR-E sea ice fraction along 57.5°E. The station location is represented as stars. The frontal zones in (a) is demarcated based on sea surface temperature (GHRSS) contours.

Winter mixing and upwelling can also contribute to subsequent CHL production in summer (Tagliabue et al., 2014). Lack of iron supply and biological consumption typically depletes the iron concentrations in the upper ocean, but the remineralization of organic matter keeps the iron concentration higher in the subsurface waters (Boyd and Ellwood, 2010; Boyd et al., 2012; Frew et al., 2006). The time series of wind stress averaged over 55°E–60°E shows that wind stress was 0.4 Pa during June–September 2010 (Figure 8c). However, wind stress was less than 0.4 Pa during June–September of 2008 and 2009. The strong wind in June–September of 2010 resulted in strong northward Ekman transports between 60°S and 45°S (Figure 8d). The time series of wind stress also suggests Ekman upwelling between 65°S and 55°S (Figure 8e). Thus, the deep winter mixing due to the strong winter wind stress in 2010 can increase MLD to subsurface dissolved iron reservoirs and cause the supply of dissolved iron to surface. To verify this hypothesis, we analyzed three ARGO floats that were present around our study region in 2008, 2009, and 2010 (Figure 9). It can be seen that in general, June–September MLD deepened from 100

m to 200 m and then further reduced to 100 m by December. During 2008 and 2009, MLD was in general less than 200 m and subsurface warm (2°C saline (34 psu) CDW) was further away from the MLD (Figure 9a and b). In contrast, during 2010, the MLD reached up to 220 m in September and stayed there till November and the warm-saline CDW was close to the base of MLD during this period. Previous studies from the Atlantic sector of the Southern Ocean showed that upwelling and northward transport of dissolved iron-enriched CDW causes elevated production in the polar frontal zone (Hoppema et al., 2003; Tagliabue et al., 2012). Thus, the enhanced winter mixing and subsequent supply of dissolved iron in the CDW perhaps resulted in the summer elevated CHL concentration in the PFZ. To further understand the processes of winter supply of dissolved iron and its utilization by phytoplankton in the summer, more measurements of bioavailable iron are necessary in the ISSO.

The increased phytoplankton biomass production during SOE2011 further resulted in high nitrate consumption and low N:P and N:Si values (Figures 3, 4a,b). The lowest phytoplankton biomass has been observed in 2010, mainly due

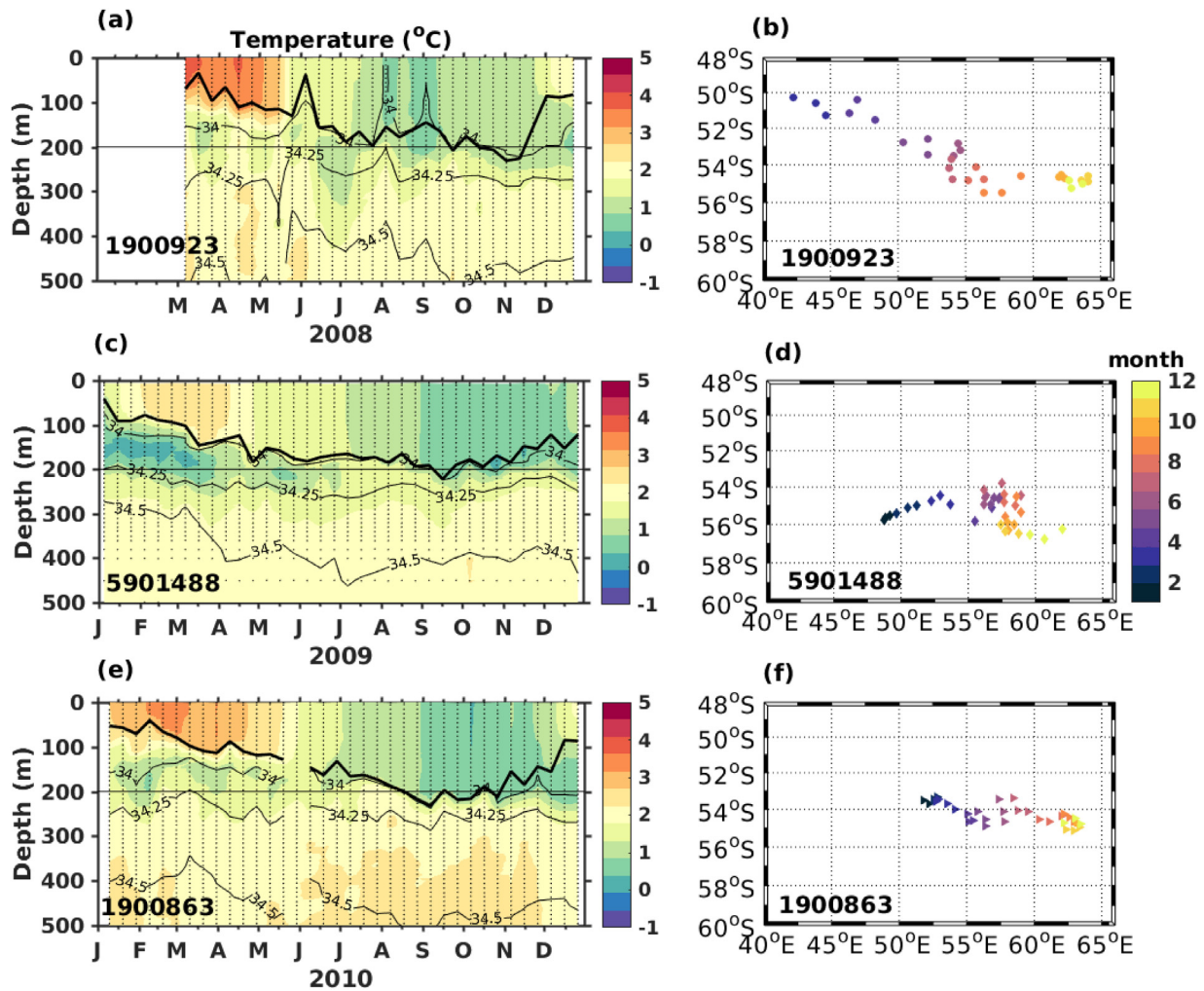


Figure 9 The time series of temperature (color bar) and salinity (contour) of three ARGO floats in (a) 2008 (float No. 1900923) (c) 2009 (float No. 5901488) (e) 2010 (float No. 1900863). Thick black lines represent the mixed layer depth. The corresponding locations of ARGO profiles are given in (b), (d), and (f), respectively.

to the lack of supply of iron to the euphotic zone and the corresponding N:P and N:Si values were the highest. Previous studies (Milligan and Harrison, 2000; Ryan-Keogh et al., 2018) suggested that iron limitation in combination with the low light condition can result in a lack of photosynthetically derived reductant in phytoplankton and in-turn excretion of excess nitrate and nitrite in the phytoplankton cell back into the water column.

4.4. Antarctic zone

Most of the AZ is the seasonal ice zone where winter sea ice extends from the coast to 56°S and melts during consecutive summers, limiting the sea ice to the coast (Figure 8f). Phytoplankton biomass production is closely related to sea ice variability (Anilkumar et al., 2014). The temperature-minimum layer, also known as winter water (WW), observed during the summer has a close relationship with the wintertime condition (Yuan et al., 2004). WW is the remnant of the mixed layer of the previous winter capped by seasonal warming and freshening. The WW is associated with ice melt and freshening in the ISSO. Cooler WW was observed during

SOE2011 than in SOE2010 and SOE2009 (Figure 10a), which indicates a colder winter in 2010. The lowest salinity of WW noticed during SOE2011, compared to SOE2009 and SOE2010 (Figure 10b) further suggests increased sea ice melting. Deepest WW was also noticed in SOE2011 (Figure 10c) indicating an increased presence of sea ice in the winter of 2010. Time series of AMSRE-Sea ice fraction (Figure 8f) also suggests enhanced sea ice during 2010.

Sabu et al. (2014) suggested that the increased sea ice in 2010 was an artifact of positive SAM and La Niña events. Sea ice drift overlaid on the SSM/I sea ice concentration (Figure 10d,e, and f) further showed that the sea ice drift piled the sea ice in the study region. Holm-Hansen et al. (2005) observed that the low productive pelagic regions of AZ can have a strong DCM in the upper part of the temperature minimum layer where dissolved iron from sea ice melt is present. The lack of such DCM during SOE2009 and SOE2010 suggests that WW was not a source of iron. However, during SOE2011, the sea ice drifted from the east and may have iron in the sea ice melt resulting in increased CHL concentration. However, iron measurements are required to verify this hypothesis. During winter, sea ice

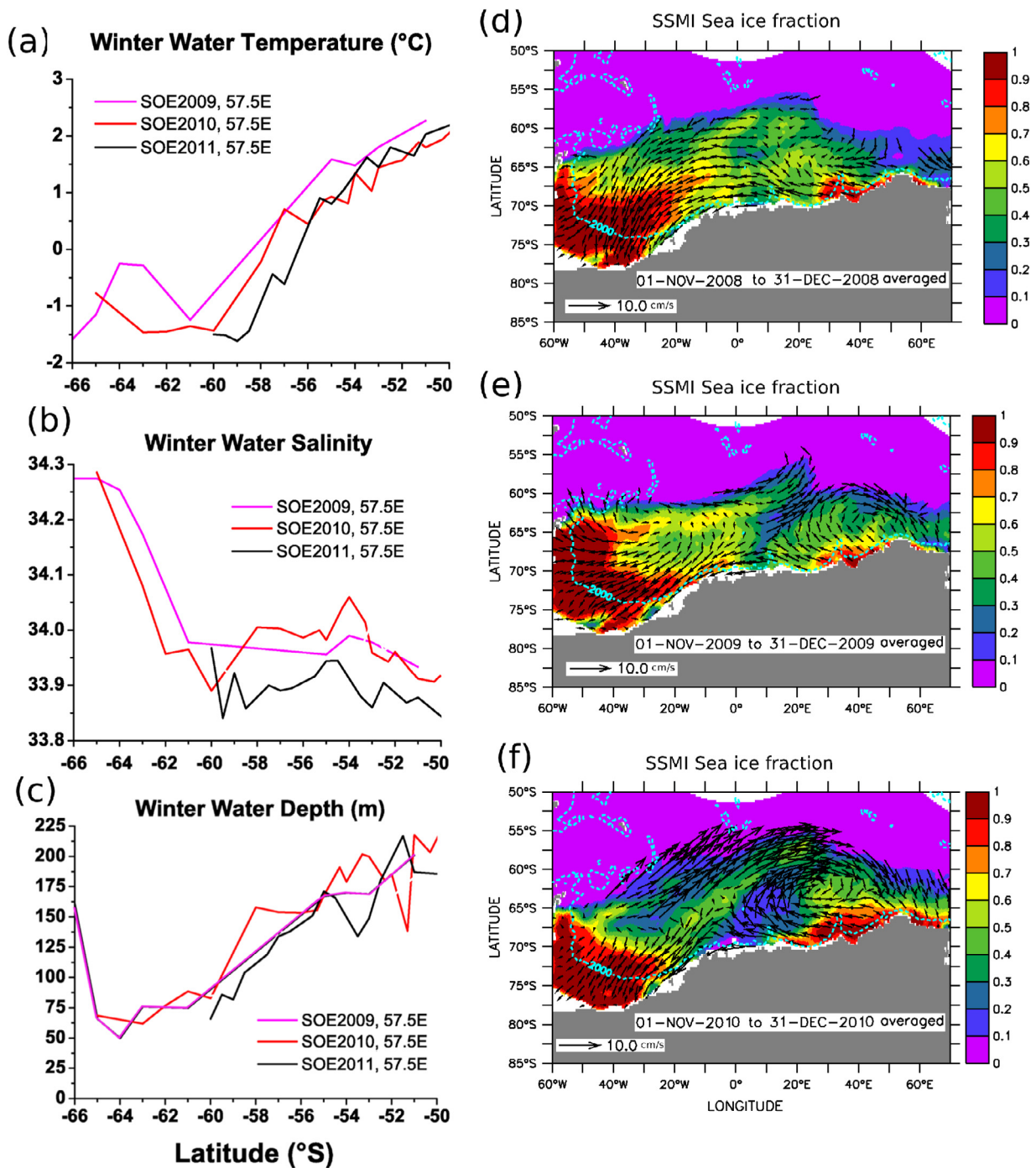


Figure 10 Winter water core properties (a) temperature (°C) (b) salinity (c) depth (m). SSMI sea ice fraction overlaid by the sea ice drift vectors averaged over (d) 2008 November–December (e) 2009 November–December and (f) 2010 November–December.

accumulates aeolian deposits (Gao et al., 2003), which are subsequently released during ice melt. Other mechanisms for iron accumulation in sea ice involve bioaccumulation through the algal growth at the base of sea ice, nucleation during the formation of ice, scavenging of particles, sieving of iron particles, etc. (de Jong et al., 2013; Lannuzel et al., 2016).

The elevated levels of micronutrients in the coastal waters as a result of glacial melting may stimulate the signif-

icant phytoplankton blooms in the ISSO (Park et al., 1998). A high in situ concentration of CHL was observed in the coastal waters of Antarctica during SOE2009 and SOE2010 (0.4 mg m^{-3} ; Figure 4c,d, and e). The averaged satellite CHL data for the cruise period also showed high concentrations of CHL (0.8 mg m^{-3}) in the coastal region during SOE2009 and SOE2010 (Figure 5a and b). Taylor et al. (2013) have suggested that sea ice melting increased the stability of the water column resulting in shallow MLD and favoring the el-

evated CHL. During SOE2009 and SOE2010, the MLD noted in the coastal waters were 50 m and 20 m, respectively (Figure 2), thus favoring SOE2010 as more CHL productive ($\sim 0.7 \text{ mg m}^{-3}$) than SOE2009 ($\sim 0.4 \text{ mg m}^{-3}$, Figure 4c,d, and e).

Upwelling of nutrient rich upper circumpolar deep water (UCDW) in the Antarctic zone is the main supply of nutrients in the region. The upwelled UCDW is further transported northward and southward as the upper and lower branches of meridional overturning circulation before the complete utilization of dissolved nutrients by phytoplankton (Marinov et al., 2006). Coastal waters of Antarctica were characterized by elevated dissolved silicate with values up to $85 \mu\text{M}$ and nitrate concentration up to $36 \mu\text{M}$. Dissolution of biogenic silica in cold waters and flux of dissolved silicate by upwelling, Ekman advection and vertical mixing are the reason for the elevated dissolved Silicate concentration in the coastal waters (Nelson et al., 1991). Because of the elevated dissolved silicate values, N:Si values were typically less than 1 and Si:P values were ~ 20 in the coastal waters (Figure 3c,f, and i).

5. Conclusion

The hydrographic data collected during SOE2009, SOE2010, and SOE2011 in the ISSO is used to understand the physical forcing on phytoplankton biomass distribution and macronutrient utilization in the study region. From the data analysis, it is clear that the frontal zones are not always characterized by elevated CHL. There is a considerable inter-annual variability existing in the CHL and dissolved macronutrient concentration and distribution. The study showed that SO fronts are dynamic systems, and the CHL is regulated by various physical processes. In the STZ region, high mesoscale activity due to the presence of ARC mainly regulate the CHL concentration. STZ region appears to be macronutrient-limited.

In the SAZ and further south, the ocean is characterized by HNLC. Reduced CHL concentration in SAZ is attributed to the iron and silicate co-limitation. Previous studies have suggested the advection of silicate limited surface water (due to the silicate drawdown by diatoms) from the south to the SAZ (Demuyne et al., 2020; Marinov et al., 2006; Weir et al., 2020). Our observation also suggested strong depletion of silicate from AZ to SAZ. Further, it has been noticed that the highest N:Si values (~ 4) were observed in the northern part of the SAZ, and it was associated with winter/spring CHL blooms noted in the SAF region. This bloom may have exported the Si to the limiting level and this along with iron stress resulted in the low CHL concentration in the consecutive summer. The duration and number of CHL bloom events in the SAF region governed the macronutrient ratios. For a better understanding of the change in phytoplankton species between winter and summer, more wintertime observations are required in the Southern Ocean. At present, most of the biogeochemical observations in the ISSO are skewed to summer.

Strong year-to-year variability has been noticed in the CHL concentration in the PFZ. The summer of 2011 was characterized by high phytoplankton biomass (CHL $\sim 0.5 \text{ mg m}^{-3}$). This increase in CHL was mainly attributed to the

winter mixing which reduced the iron stress. In contrary to the summer of 2011, during 2010, PFZ region was less productive probably due to the northward migration of the wind belt associated with negative SAM. The inter-annual variability noticed in phytoplankton biomass production and supply of micronutrients through the physical processes also altered the nutrient concentrations and the nutrient ratios. During the summer of 2011, N:P and N:Si values were less than what was observed during the summer of 2010, a manifestation of higher nitrate drawdown compared to silicate. Macronutrient concentration and ratios observed during the late summer in the PFZ and SAZ region have global importance, as these regions are the formation sites of AAIW and STMW, respectively, during the consecutive winter. AAIW and SMW are exported out of the SO to the low latitudes and become the major source of nutrients for the ambient primary production (Demuyne et al., 2020; Sarmiento et al., 2004).

In the AZ, increased sea ice advected from the east during the previous winter caused elevated CHL concentration during SOE2011. However, the very low CHL concentration noted in SOE2010 and SOE2009 suggests that the presence of WW or more melting of sea ice does not always result in CHL elevation; rather, the input of iron to the system is regulating the CHL. The supply of iron from sea ice also depends on the origin of the sea ice.

Declaration of competing interest

The authors declare that they have no known competing financial interests or personal relationships that could have appeared to influence the work reported in this paper.

Acknowledgements

This work was supported by the Ministry of Earth Sciences, Government of India. We are thankful to Director, NCPOR for the constant support. The authors also would like to thank the vessel management cell and the ship staff of both *r/v Sagar Nidhi* and *r/v Akademik Boris Petrov* for the successful completion of Indian expedition to Southern Ocean 2009, 2010 and 2011. The in-situ data sets used in this study are available from NCPOR data bank. This is NCPOR contribution number J-15/2022-23.

References

- Anilkumar, N., Chacko, R., Sabu, P., Pillai, H.U., George, J.V., Achuthankutty, C., 2014. Biological response to physical processes in the Indian ocean sector of the southern ocean: a case study in the coastal and oceanic waters. *Environ. Monit. Assess.* 186, 8109–8124. <https://doi.org/10.1007/s10661-014-3990-4>
- Anilkumar, N., George, J., Chacko, R., Nuncio, N., Sabu, P., 2015. Variability of fronts, fresh water input and chlorophyll in the Indian ocean sector of the southern ocean. *N. Z. J. Mar. Freshwater Res.* 49, 20–40. <https://doi.org/10.1080/00288330.2014.924972>
- Anilkumar, N., Luis, A.J., Somayajulu, Y., Babu, V.R., Dash, M., Pednekar, S., Babu, K., Sudhakar, M., Pandey, P., 2006. Fronts, water masses and heat content variability in the western Indian sector

- of the southern ocean during austral summer 2004. *J. Mar. Syst.* 63, 20–34. <https://doi.org/10.1016/j.jmarsys.2006.04.009>
- Ansorge, I.J., Lutjeharms, J.R., 2005. Direct observations of eddy turbulence at a ridge in the southern ocean. *Geophys. Res. Lett.* 32. <https://doi.org/10.1029/2005GL022588>
- Assmy, P., Smetacek, V., Montresor, M., Klaas, C., Henjes, J., Strass, V.H., Arrieta, J.M., Bathmann, U., Berg, G.M., Breitbarth, E., et al., 2013. Thick-shelled, grazer-protected diatoms decouple ocean carbon and silicon cycles in the iron-limited Antarctic Circumpolar Current. *Proc. Natl. Acad. Sci.* 110, 20633–20638. <https://doi.org/10.1073/pnas.1309345110>
- Backeberg, B.C., Penven, P., Rouault, M., 2012. Impact of intensified indian ocean winds on mesoscale variability in the Agulhas system. *Nat. Clim. Change.* 2, 608–612. <https://doi.org/10.1038/nclimate1587>
- Bailey, R., Gronell, A., Phillips, H., Tanner, E., Meyers, G., 1994. Quality control cookbook for xbt data (expendable bathythermograph data). version 1.1.
- Beal, L.M., De Ruijter, W.P., Biastoch, A., Zahn, R., 2011. On the role of the Agulhas system in ocean circulation and climate. *Nature* 472, 429–436. <https://doi.org/10.1038/nature09983>
- Belkin, I.M., Gordon, A.L., 1996. Southern ocean fronts from the greenwich meridian to tasmania. *J. Geophys. Res. - Oceans* 101, 3675–3696.
- Blain, S., Tréguer, P., Belviso, S., Bucciarelli, E., Denis, M., Desabre, S., Fiala, M., Jézéquel, V.M., Le Fèvre, J., Mayzaud, P., Marty, J.-C., Razouls, S., 2001. A biogeochemical study of the island mass effect in the context of the iron hypothesis: Kerguelen islands, Southern Ocean. *Deep-Sea Res. Pt. I*, 48, 163–187. [https://doi.org/10.1016/S0967-0637\(00\)00047-9](https://doi.org/10.1016/S0967-0637(00)00047-9)
- Boyd, P.W., 2002. Environmental factors controlling phytoplankton processes in the Southern Ocean. *J. Phycol.* 38, 844–861. <https://doi.org/10.1046/j.1529-8817.2002.t01-1-01203.x>
- Boyd, P.W., Ellwood, M.J., 2010. The biogeochemical cycle of iron in the ocean. *Nat. Geosci.* 3, 675–682. <https://doi.org/10.1038/ngeo964>
- Boyd, P.W., Strzepek, R., Chiswell, S., Chang, H., DeBruyn, J.M., Ellwood, M., Keenan, S., King, A.L., Maas, E.W., Nodder, S., Sander, S.G., 2012. Microbial control of diatom bloom dynamics in the open ocean. *Geophys. Res. Lett.* 39 (18). <https://doi.org/10.1029/2012GL053448>
- Boyd, P.W., Strzepek, R., Fu, F., Hutchins, D.A., 2010. Environmental control of open-ocean phytoplankton groups: Now and in the future. *Limnol. Oceanogr.* 55, 1353–1376. <https://doi.org/10.4319/lo.2010.55.3.1353>
- Briggs, E.M., Martz, T.R., Talley, L.D., Mazloff, M.R., Johnson, K.S., 2018. Physical and Biological Drivers of Biogeochemical Tracers Within the Seasonal Sea Ice Zone of the Southern Ocean From Profiling Floats. *J. Geophys. Res. - Oceans* 123, 746–758. <https://doi.org/10.1002/2017JC012846>
- Dawson, H.R., Stratton, P.G., Gaube, P., 2018. The unusual surface chlorophyll signatures of southern ocean eddies. *J. Geophys. Res. - Oceans* 123, 6053–6069. <https://doi.org/10.1029/2017JC013628>
- de Jong, J., Schoemann, V., Maricq, N., Mattielli, N., Langhorne, P., Haskell, T., Tison, J.L., 2013. Iron in land-fast sea ice of McMurdo Sound derived from sediment resuspension and wind-blown dust attributes to primary productivity in the Ross Sea, Antarctica. *Mar. Chem.* 157, 24–40. <https://doi.org/10.1016/j.marchem.2013.07.001>
- Demuynck, P., Tyrrell, T., Naveira Garabato, A., Moore, M.C., Martin, A.P., 2020. Spatial variations in silicate-to-nitrate ratios in Southern Ocean surface waters are controlled in the short term by physics rather than biology. *Biogeosciences* 17, 2289–2314. <https://doi.org/10.5194/bg-17-2289-2020>
- Deppeler, S.L., Davidson, A.T., 2017. Southern Ocean phytoplankton in a changing climate. *Front. Mar. Sci.* 4, 40. <https://doi.org/10.3389/fmars.2017.00040>
- Dong, S., Sprintall, J., Gille, S.T., 2006. Location of the Antarctic polar front from AMSR-E satellite sea surface temperature measurements. *J. Phys. Oceanogr.* 36, 2075–2089. <https://doi.org/10.1175/JPO2973.1>
- Dubischar, C.D., Bathmann, U.V., 1997. Grazing impact of copepods and salps on phytoplankton in the Atlantic sector of the Southern Ocean. *Deep Sea Res. Pt. II* 44, 415–433.
- Frenger, I., Münnich, M., Gruber, N., 2018. Imprint of Southern Ocean eddies on chlorophyll. *Biogeosciences* 15, 4781–4798. <https://doi.org/10.5194/bg-2018-70>
- Frew, R.D., Hutchins, D.A., Nodder, S., Sanudo-Wilhelmy, S., Tovar-Sanchez, A., Leblanc, K., Hare, C.E., Boyd, P.W., 2006. Particulate iron dynamics during FeCycle in subantarctic waters south-east of New Zealand. *Global Biogeochem. Cy.* 20. <https://doi.org/10.1029/2005GB002558>
- Gandhi, N., Ramesh, R., Laskar, A., Sheshshayee, M., Shetye, S., Anilkumar, N., Patil, S.M., Mohan, R., 2012. Zonal variability in primary production and nitrogen uptake rates in the southwestern Indian Ocean and the Southern Ocean. *Deep-Sea Res. Pt. I* 67, 32–43. <https://doi.org/10.1016/j.dsr.2012.05.003>
- Gao, Y., Fan, S.M., Sarmiento, J.L., 2003. Aeolian iron input to the ocean through precipitation scavenging: A modeling perspective and its implication for natural iron fertilization in the ocean. *J. Geophys. Res. Atmos.* 108. <https://doi.org/10.1029/2002JD002420>
- George, J.V., Anilkumar, N., 2022. High-frequency noise and depth error associated with the XCTD/XBT profiles in the Indian Ocean sector of Southern Ocean and southwestern tropical Indian Ocean. *J. Earth Syst. Sci.* 131 (1), 1–13. <https://doi.org/10.1007/s12040-021-01789-7>
- George, J.V., Anilkumar, N., Nuncio, M., Soares, M.A., Naik, R.K., Tripathy, S.C., 2018. Upper layer diapycnal mixing and nutrient flux in the subtropical frontal region of the Indian sector of the Southern Ocean. *J. Mar. Syst.* 187, 197–205. <https://doi.org/10.1016/j.jmarsys.2018.07.007>
- Grasshoff, K., Ehrhardt, M., Kremling, K., 1983. *Methods of Seawater Analysis.* Verlag Chem., Weinheim, 600 pp.
- Gregg, W.W., Casey, N.W., 2007. Modeling coccolithophores in the global oceans. *Deep Sea Res. Pt. II* 54 (5–7), 447–477. <https://doi.org/10.1016/j.dsr2.2006.12.007>
- Giddy, I.S., Swart, S., Tagliabue, A., 2012. Drivers of non-redfield nutrient utilization in the atlantic sector of the southern ocean. *Geophys. Res. Lett.* 39. <https://doi.org/10.1029/2012GL052454>
- Gruber, N., Landschützer, P., Lovenduski, N.S., 2019. The variable Southern Ocean carbon sink. *Annu. Rev. Mar. Sci.* 11, 159–186. <https://doi.org/10.1146/annurev-marine-121916-063407>
- Hadfield, M.G., 2011. Expected and observed conditions during the sage iron addition experiment in subantarctic waters. *Deep Sea Res. Pt. II* 58, 764–775. <https://doi.org/10.1016/j.dsr2.2010.10.016>
- Henley, S.F., Cavan, E.L., Fawcett, S.E., Kerr, R., Monteiro, T., Sherrill, R.M., Bowie, A.R., Boyd, P.W., Barnes, D.K., Schloss, I.R., Marshall, T., 2020. Changing biogeochemistry of the Southern Ocean and its ecosystem implications. *Front. Mar. Sci.* 581. <https://doi.org/10.3389/fmars.2020.00581>
- Holm-Hansen, O., Kahru, M., Hewes, C.D., 2005. Deep chlorophyll a maxima (dcms) in pelagic Antarctic waters. ii. relation to bathymetric features and dissolved iron concentrations. *Mar. Ecol. Prog. Ser.* 297, 71–81. <https://doi.org/10.3354/meps297071>
- Hoppema, M., de Baar, H.J., Fahrback, E., Hellmer, H.H., Klein, B., 2003. Substantial advective iron loss diminishes phytoplankton production in the Antarctic Zone. *Global Biogeochem. Cy.* 17. <https://doi.org/10.1029/2002GB001957>
- Huot, Y., Babin, M., Bruyant, F., Grob, C., Twardowski, M., Claustre, H., 2007. Does chlorophyll a provide the best index of phytoplankton biomass for primary productivity studies? *Biogeosci. Discuss.* 4, 707–745.

- Jasmine, P., Muraleedharan, K., Madhu, N., Devi, C.A., Alagarsamy, R., Achuthankutty, C., Jayan, Z., Sanjeevan, V., Sahayak, S., 2009. Hydrographic and productivity characteristics along 45°E longitude in the southwestern Indian Ocean and Southern Ocean during austral summer 2004. *Mar. Ecol. Prog. Ser.* 389, 97–116. <https://doi.org/10.3354/meps08126>
- Kahru, M., Mitchell, B., Gille, S., Hewes, C., Holm-Hansen, O., 2007. Eddies enhance biological production in the Weddell-Scotia confluence of the Southern Ocean. *Geophys. Res. Lett.* 34. <https://doi.org/10.1029/2007GL030430>
- Kostianoy, A.G., Ginzburg, A.I., Frankignoulle, M., Delille, B., 2004. Fronts in the Southern Indian Ocean as inferred from satellite sea surface temperature data. *J. Mar. Syst.* 45, 55–73. <https://doi.org/10.1016/j.jmarsys.2003.09.004>
- Lannuzel, D., Vancoppenolle, M., Van der Merwe, P., De Jong, J., Meiners, K.M., Grotti, M., Nishioka, J., Schoemann, V., 2016. Iron in sea ice: Review and new insights. *Elem. Sci. Anth.* 4. <https://doi.org/10.12952/journal.elementa.000130>
- Llido, J., Garon, V., Lutjeharms, J., Sudre, J., 2005. Event-scale blooms drive enhanced primary productivity at the subtropical convergence. *Geophys. Res. Lett.* 32. <https://doi.org/10.1029/2005GL022880>
- Longhurst, A.R., 2010. *Ecological geography of the sea*. Elsevier.
- Lutjeharms, J., Ansorge, I., 2001. The agulhas return current. *J. Mar. Syst.* 30, 115–138. [https://doi.org/10.1016/S0924-7963\(01\)00041-0](https://doi.org/10.1016/S0924-7963(01)00041-0)
- Marinov, I., Gnanadesikan, A., Toggweiler, J., Sarmiento, J.L., 2006. The Southern Ocean biogeochemical divide. *Nature* 441, 964–967. <https://doi.org/10.1038/nature04883>
- Martin, J.H., Gordon, R.M., Fitzwater, S.E., 1990. Iron in Antarctic waters. *Nature* 345, 156–158.
- McGillicuddy, D., Robinson, A., Siegel, D., Jannasch, H., Johnson, R., Dickey, T., McNeil, J., Michaels, A., Knap, A., 1998. Influence of mesoscale eddies on new production in the Sargasso sea. *Nature* 394, 263–266. <https://doi.org/10.1038/28367>
- Mendes, C.R.B., Kerr, R., Tavano, V.M., Cavalheiro, F.A., Garcia, C.A.E., Dessai, D.R.G., Anilkumar, N., 2015. Cross-front phytoplankton pigments and chemotaxonomic groups in the Indian sector of the Southern ocean. *Deep Sea Res. Pt. II* 118, 221–232. <https://doi.org/10.1016/j.dsr2.2015.01.003>
- Milligan, A.J., Harrison, P.J., 2000. Effects of non-steady-state iron limitation on nitrogen assimilatory enzymes in the marine diatom THALASSIOSIRA WEISSFLOGII (BACILLARIOPHYCEAE). *J. Phycol.* 36, 78–86. <https://doi.org/10.1046/j.1529-8817.2000.99013.x>
- Mitchell, B.G., Brody, E.A., Holm-Hansen, O., McClain, C., Bishop, J., 1991. Light limitation of phytoplankton biomass and macronutrient utilization in the Southern Ocean. *Limnol. Oceanogr.* 36, 1662–1677.
- Moore, J.K., Abbott, M.R., 2000. Phytoplankton chlorophyll distributions and primary production in the Southern Ocean. *J. Geophys. Res. - Oceans* 105, 28709–28722.
- Moore, J.K., Fu, W., Primeau, F., Britten, G.L., Lindsay, K., Long, M., Doney, S.C., Mahowald, N., Hoffman, F., Randonson, J.T., 2018. Sustained climate warming drives declining marine biological productivity. *Science* 359 (6380), 1139–1143. <https://doi.org/10.1126/science.aao6379>
- Naik, R.K., George, J.V., Soares, M.A., Devi, A., Anilkumar, N., Roy, R., Bhaskar, P.V., Murukesh, N., Achuthankutty, C.T., 2015. Phytoplankton community structure at the juncture of the Agulhas Return Front and Subtropical Front in the Indian Ocean sector of Southern Ocean: Bottom-up and top-down control. *Deep Sea Res.* 233–239. <https://doi.org/10.1016/j.dsr2.2015.01.002>, Pt II118
- Nelson, D.M., Ahern, J.A., Herlihy, L.J., 1991. Cycling of biogenic silica within the upper water column of the Ross Sea. *Mar. Chem.* 35, 461–476. [https://doi.org/10.1016/S0304-4203\(09\)90037-8](https://doi.org/10.1016/S0304-4203(09)90037-8)
- Nelson, D.M., Brzezinski, M.A., Sigmon, D.E., Franck, V.M., 2001. A seasonal progression of Si limitation in the Pacific sector of the Southern Ocean. *Deep Sea Res. Pt. II* 48, 3973–3995. [https://doi.org/10.1016/S0967-0645\(01\)00076-5](https://doi.org/10.1016/S0967-0645(01)00076-5)
- Nelson, D.M., Smith Jr, W., 1991. Sverdrup revisited: Critical depths, maximum chlorophyll levels, and the control of southern ocean productivity by the irradiance-mixing regime. *Limnol. Oceanogr.* 36, 1650–1661. <https://doi.org/10.4319/lo.1991.36.8.1650>
- Orsi, A.H., Whitworth III, T., Nowlin Jr, W.D., 1995. On the meridional extent and fronts of the Antarctic Circumpolar Current. *Deep-Sea Res. Pt. I* 42, 641–673.
- Park, Y.H., Charriaud, E., Fioux, M., 1998. Thermohaline structure of the antarctic surface water/winter water in the indian sector of the Southern Ocean. *J. Mar. Syst.* 17, 5–23.
- Park, Y.H., Gamberoni, L., Charriaud, E., 1993. Frontal structure, water masses, and circulation in the crozet basin. *J. Geophys. Res. Oceans* 98, 12361–12385.
- Parli, B.V., Dessai, D.R., Anilkumar, N., Chacko, R., Pavithran, S., 2020. Meridional variations in N* and Si* along 57°30' E and 47°E transects in the indian sector of the Southern Ocean during austral summer 2011. *Deep Sea Res. Pt. II* 178, 104846. <https://doi.org/10.1016/j.dsr2.2020.104846>
- Pichevin, L., Ganeshram, R., Geibert, W., Thunell, R., Hinton, R., 2014. Silica burial enhanced by iron limitation in oceanic upwelling margins. *Nat. Geosci.* 7, 541–546. <https://doi.org/10.1038/ngeo2181>
- Planquette, H., Statham, P.J., Fones, G.R., Charette, M.A., Moore, C.M., Salter, I., Nedelec, F.H., Taylor, S.L., French, M., Baker, A., Mahowald, N., Jickells, T.D., 2007. Dissolved iron in the vicinity of the Crozet islands. *Southern Ocean. Deep Sea Res. Pt. II* 54, 1999–2019. <https://doi.org/10.1016/j.dsr2.2007.06.019>
- Pollard, R., Lucas, M., Read, J., 2002. Physical controls on biogeochemical zonation in the Southern Ocean. *Deep Sea Res. Pt. II* 49, 3289–3305. [https://doi.org/10.1016/S0967-0645\(02\)00084-X](https://doi.org/10.1016/S0967-0645(02)00084-X)
- Redfield, A.C., 1963. The influence of organisms on the composition of seawater. *The sea* 2, 26–77.
- Ryan-Keogh, T.J., Thomalla, S.J., Mtshali, T.N., van Horsten, N.R., Little, H.J., 2018. Seasonal development of iron limitation in the sub-Antarctic zone. *Biogeosciences* 15, 4647–4660. <https://doi.org/10.5194/bg-15-4647-2018>
- Sabu, P., Anilkumar, N., George, J.V., Chacko, R., Tripathy, S., Achuthankutty, C., 2014. The influence of air–sea–ice interactions on an anomalous phytoplankton bloom in the Indian Ocean sector of the Antarctic zone of the southern ocean during the austral summer, 2011. *Polar Sci.* 8, 370–384. <https://doi.org/10.1016/j.polar.2014.08.001>
- Sabu, P., George, J.V., Anilkumar, N., Chacko, R., Valsala, V., Achuthankutty, C., 2015. Observations of watermass modification by mesoscale eddies in the subtropical frontal region of the Indian Ocean sector of Southern Ocean. *Deep Sea Res. Pt. II* 118, 152–161. <https://doi.org/10.1016/j.dsr2.2015.04.010>
- Sallée, J., Speer, K., Rintoul, S., 2010. Zonally asymmetric response of the southern ocean mixed-layer depth to the Southern Annular Mode. *Nat. Geosci.* 3, 273–279. <https://doi.org/10.1038/ngeo812>
- Sanial, V., van Beek, P., Lansard, B., d'Ovidio, F., Kestenare, E., Souhaut, M., Zhou, M., Blain, S., 2014. Study of the phytoplankton plume dynamics off the crozet islands (southern ocean): A geochemical-physical coupled approach. *J. Geophys. Res. - Oceans* 119, 2227–2237. <https://doi.org/10.1002/2013JC009305>
- Sarmiento, J.L., Gruber, N., Brzezinski, M., Dunne, J., 2004. High-latitude controls of thermocline nutrients and low latitude biological productivity. *Nature* 427, 56–60. <https://doi.org/10.1038/nature02127>

- Shramik, P., Rahul, M., Suhas, S., Sahina, G., 2013. Phytoplankton abundance and community structure in the Antarctic polar frontal region during austral summer of 2009. *Chin. J. Oceanol. Limnol.* 31, 21–30. <https://doi.org/10.1007/s00343-013-1309-x>
- Smetacek, V., Klaas, C., Menden-Deuer, S., Rynearson, T.A., 2002. Mesoscale distribution of dominant diatom species relative to the hydrographical field along the Antarctic Polar Front. *Deep Sea Res. Pt. II* 49, 3835–3848. [https://doi.org/10.1016/S0967-0645\(02\)00113-3](https://doi.org/10.1016/S0967-0645(02)00113-3)
- Sparrow, M.D., Heywood, K.J., Brown, J., Stevens, D.P., 1996. Current structure of the South Indian ocean. *J. Geophys. Res. – Oceans* 101, 6377–6391.
- Strass, V.H., Garabato, A.C.N., Pollard, R.T., Fischer, H.I., Hense, I., Allen, J.T., Read, J.F., Leach, H., Smetacek, V., 2002. Mesoscale frontal dynamics: shaping the environment of primary production in the Antarctic Circumpolar Current. *Deep Sea Res. Pt. II* 49, 3735–3769. [https://doi.org/10.1016/S0967-0645\(02\)00109-1](https://doi.org/10.1016/S0967-0645(02)00109-1)
- Strickland, J.D.H., Parsons, T.R., 1972. *A Practical Hand Book of Seawater Analysis*, 2nd edn. *Fish. Res. Board Canada Bull.*, 167, 310.
- Tagliabue, A., Mtshali, T., Aumont, O., Bowie, A., Klunder, M., Roychoudhury, A., Swart, S., 2012. A global compilation of dissolved iron measurements: focus on distributions and processes in the Southern Ocean. *Biogeosciences* 9. <https://doi.org/10.5194/bg-9-2333-2012>
- Tagliabue, A., Sallée, J.B., Bowie, A.R., Lévy, M., Swart, S., Boyd, P.W., 2014. Surface-water iron supplies in the Southern Ocean sustained by deep winter mixing. *Nat. Geosci.* 7, 314–320. <https://doi.org/10.1038/ngeo2101>
- Taylor, M.H., Losch, M., Bracher, A., 2013. On the drivers of phytoplankton blooms in the Antarctic marginal ice zone: A modeling approach. *J. Geophys. Res. - Oceans* 118, 63–75. <https://doi.org/10.1029/2012JC008418>
- Timmermans, K.R., Van Der Wagt, B., De Baar, H.J., 2004. Growth rates, half saturation constants, and silicate, nitrate, and phosphate depletion in relation to iron availability of four large, open-ocean diatoms from the Southern Ocean. *Limnol. Oceanogr.* 49, 2141–2151. <https://doi.org/10.4319/lo.2004.49.6.2141>
- Venables, H., Moore, C.M., 2010. Phytoplankton and light limitation in the southern ocean: Learning from high-nutrient, high-chlorophyll areas. *J. Geophys. Res. – Oceans* 115. <https://doi.org/10.1029/2009JC005361>
- Weir, I., Fawcett, S., Smith, S., Walker, D., Bornman, T., Fietz, S., 2020. Winter biogenic silica and diatom distributions in the Indian Sector of the Southern Ocean. *Deep-Sea Res. Pt. I* 166, 103421. <https://doi.org/10.1016/j.dsr.2020.103421>
- Williams, G., Nicol, S., Raymond, B., Meiners, K., 2008. Summer-time mixed layer development in the marginal sea ice zone off the Mawson coast. East Antarctica. *Deep Sea Res. Pt. II* 55, 365–376. <https://doi.org/10.1016/j.dsr.2007.11.007>
- Yuan, X., Martinson, D.G., Dong, Z., 2004. Upper ocean thermohaline structure and its temporal variability in the southeast Indian Ocean. *Deep-Sea Res. Pt. I* 51, 333–347. <https://doi.org/10.1016/j.dsr.2003.10.005>

Available online at www.sciencedirect.com

ScienceDirect

journal homepage: www.journals.elsevier.com/oceanologia

ORIGINAL RESEARCH ARTICLE

Effects of different conditions on particle dynamics and properties in West-Estonian coastal areas

Mirjam Uusõue^{a,*}, Martin Ligi^a, Tiit Kutser^b, François Bourrin^c,
Kristi Uudeberg^a, Kersti Kangro^a, Birgot Paavel^b

^a Tartu Observatory, University of Tartu, Tartumaa, Estonia

^b Estonian Marine Institute, University of Tartu, Tallinn, Estonia

^c CEFREM, UMR 5110 CNRS, UPVD, Perpignan Cedex, France

Received 24 April 2021; accepted 27 June 2022

Available online 13 July 2022

KEYWORDS

Suspended particulate matter;
Inherent optical properties;
Backscattering ratio;
Particle size distribution;
Aggregation

Abstract Satellite sensors are used to monitor water on a large scale. One of the key variables defining the water-leaving signal is suspended particulate matter (SPM) and thus it is important to understand its properties to improve remote sensing algorithms. However, only a few studies investigating the variability of SPM properties (concentration, nature and size) under different seasonal, weather and geographical conditions have been carried out in the Baltic Sea. We focused on relatively shallow areas (maximum depth of 10 m) where there is strong sediment transport by rivers and resuspension of the particles by wave action and advection by currents. Eleven field campaigns were conducted using a set of instruments measuring inherent optical properties, auxiliary data, and, in Pärnu Bay, also particle size distributions. The results showed that the SPM concentrations, particulate absorption, mass-specific particulate scattering, and backscattering varied temporally and spatially from 5.5–19.6 g m⁻³, 0–5.62 m⁻¹, 0.08–1.45 m² g⁻¹, and 0.0009–0.25 m² g⁻¹, respectively. The spectral backscattering ratio, which in general is considered to be constant in bio-optical remote sensing algorithms, was actually wavelength-dependent and varied between 0.005 and 0.09 depending on the origin of the particles (organic or mineral matter), particle size distribution, weather conditions, and location. *In situ* particle size measurements in coastal waters of Pärnu Bay also showed that

* Corresponding author at: Tartu Observatory, University of Tartu, Observatooriumi 1, Tõravere, 61602 Tartumaa, Estonia.

E-mail addresses: mirjam.uusoue@ut.ee (M. Uusõue), martin.ligi@ut.ee (M. Ligi), tiit.kutser@ut.ee (T. Kutser), francois.bourrin@univ-perp.fr (F. Bourrin), kristi.uudeberg@gmail.com (K. Uudeberg), kersti.kangro@ut.ee (K. Kangro), birgot.paavel@ut.ee (B. Paavel).
Peer review under the responsibility of the Institute of Oceanology of the Polish Academy of Sciences.



<https://doi.org/10.1016/j.oceano.2022.06.006>

0078-3234/© 2022 Institute of Oceanology of the Polish Academy of Sciences. Production and hosting by Elsevier B.V. This is an open access article under the CC BY-NC-ND license (<http://creativecommons.org/licenses/by-nc-nd/4.0/>).

resuspended fine clay particles agglomerated into flocs of $>30 \mu\text{m}$ in the brackish waters of the Baltic Sea having random shapes and different sizes.

© 2022 Institute of Oceanology of the Polish Academy of Sciences. Production and hosting by Elsevier B.V. This is an open access article under the CC BY-NC-ND license (<http://creativecommons.org/licenses/by-nc-nd/4.0/>).

List of acronyms and abbreviations used in this study

SPM	Suspended particulate matter, g m^{-3}
SPIM	Suspended particulate inorganic matter, g m^{-3}
SPOM	Suspended particulate organic matter, g m^{-3}
IOP	Inherent optical properties
$a(\lambda)$	Spectral absorption coefficient, m^{-1}
$a_{tot}(\lambda)$	Spectral absorption coefficient with pure water absorption added, m^{-1}
$a_p(\lambda)$	Spectral particulate absorption coefficient, m^{-1}
$b(\lambda)$	Spectral scattering coefficient, m^{-1}
$b_p^*(\lambda)$	Spectral mass-specific scattering coefficient, $\text{m}^2 \text{g}^{-1}$
$c(\lambda)$	Spectral attenuation coefficient, m^{-1}
$b_b(\lambda)$	Spectral backscattering coefficient, m^{-1}
$b_{bp}^*(\lambda)$	Spectral mass-specific backscattering coefficient, $\text{m}^2 \text{g}^{-1}$
$\tilde{b}_{bp}(\lambda)$	Spectral backscattering ratio
PSD	Particle size distribution, μm
j	Junge exponent
Rrs	Remote sensing reflectance
CDOM	Coloured dissolved organic matter
$a_{CDOM}(\lambda)$	Spectral CDOM absorption coefficient at a specific wavelength, m^{-1}
S_{CDOM}	Slope of CDOM absorption, nm^{-1}
β	Volume scattering function
Chl- a	Chlorophyll- a , mg m^{-3}
TVC	Total volume concentration, $\mu\text{L L}^{-1}$
D	Particle diameter, μm
D50	Median particle size, μm

1. Introduction

Suspended particulate matter (SPM) is an important water constituent because it increases turbidity and affects light penetration in the water column. Consequently, it affects the water quality and living conditions of water organisms. For example, it is easier for prey to hide from predators when the SPM concentrations are higher. On the other hand, it is more difficult for them to find food if water is full of inedible particles (Hecht and van der Lingen, 1992). The SPM is composed of organic matter (phytoplankton, organic detritus) and mineral particles (detrital sediments). Their properties differ from each other considerably and therefore, the water reflectance may vary a lot depending on the type and size of the particles.

The SPM originates from different sources: biological production, fluvial input, erosion, and aerosol deposition. The amount of SPM coming from one source may vary significantly. For example, the amount of SPM in river deltas

varies notably depending on the river discharge during the dry season, wet season, and flood episodes. The data about river discharge and sediment flux variability during these events has been well studied for large rivers such as the Rhône River (Sadaoui et al., 2016; Sakho et al., 2019), the Amazon River (Filizola and Guyot, 2009), etc. It was difficult to find this data for smaller rivers because it has not been collected or accessible via open sources.

The SPM concentrations can be measured with different methods: gravimetric measurements from *in situ* water samples (direct measurement; Neukermans et al., 2012), the transformation of the acoustic signal obtained by acoustic Doppler current profilers (indirect measurement Callede et al., 2009), and SPM concentrations derived from the optical turbidity measurements (indirect measurement; Kari et al., 2017). The SPM concentrations can be also estimated remotely by using satellite imagery of the surface layer and bio-optical algorithms created for SPM retrieval (Forget and Ouillon, 1998; Holyer, 1978; Ligi et al., 2017; Sydor, 1980). In addition, it is also reasonable to measure other particle properties to gain insights into the SPM and its influence on the water environment and remote sensing signal. The number of sophisticated instruments capable of measuring the optical properties of particles is increasing, (e.g. LISST instruments series by Sequoia Scientific). For example, *in situ* spectrophotometers can be used to measure the spectral absorption coefficient, $a(\lambda)$, and attenuation coefficient, $c(\lambda)$, from which the spectral scattering coefficient, $b(\lambda)$, is calculated (Ohi et al., 2008; Sun et al., 2017; Twardowski et al., 1999). Other instruments (e.g. WET Labs ECO-VSF3) can be used to measure the volume scattering function, β , from which the spectral backscattering coefficient, $b_b(\lambda)$, is retrieved (Sullivan et al., 2013).

Easily measurable parameters can be used as proxies to retrieve parameters that are difficult to measure. For instance, the scattering and backscattering by particles in suspension correlate with the mass concentration of the particles as a first approximation. It is indirectly related to particles size distribution, and the proportions of organic and inorganic fractions (Reynolds et al., 2016; Woźniak et al., 2018). Indeed, the light scattering by particles depends on their composition, refraction index, size, and shape. Another important parameter that has been studied is the spectral backscattering ratio, $\tilde{b}_{bp}/b_p(\lambda)$ which is the ratio of spectral backscattering to scattering. For Case I waters (optical properties are dominated by phytoplankton, related coloured dissolved organic matter (CDOM) and degraded detritus) it is described with a smooth linear function based on theory and models (Whitmire et al., 2007). For Case II waters (optical properties are dominated by phytoplankton and also by sediments and CDOM), the situation is more complicated and this parameter cannot be described with a simple function as at different wavelengths it is differently influenced by water constituents (Chami et al., 2005; Mckee and Cunning-

ham, 2005; Slade and Boss, 2015). In remote sensing algorithms and bio-optical models, $b_{bp}/b_p(\lambda)$ is sometimes considered to be constant (Stramska et al., 2000). For example, Kirk (1981) showed that a value of 0.019 is valid for the majority of moderately turbid coastal waters. In reality, this parameter is related to different particle properties such as their origin. Thus, mineral particles which have higher refractive indices than organic particles, have also higher $b_{bp}/b_p(\lambda)$ (Boss et al., 2004). In addition, the parameter $b_{bp}/b_p(\lambda)$ is also impacted by both the particle size distribution (PSD) and shape (Aas et al., 2005). A higher $b_{bp}/b_p(\lambda)$ indicates smaller particles.

The PSDs, which are the concentrations (in volume or number) of particles within different size classes (Qiu et al., 2016), have been measured in laboratories for a long time using sieving, pipette, and hydrometric methods (Gee and Or, 2002). Unfortunately, these methods are time-consuming and difficult to adapt *in situ*. Thus, new laser diffraction methods have been established. They facilitate the measurement of the size distributions in water samples in the laboratory (Faé et al., 2019). The size distributions could be measured directly *in situ* in coastal waters based on the combination of laser diffractometers and underwater cameras (Davies and Nepstad, 2017; Many et al., 2016). The PSDs are described using the power law approximation or “Junge-type” distributions, where j is the Junge exponent (Babin et al., 2003), if the particles are of mineral origin and the PSD slopes could be estimated. The steeper the slope is or the higher the j exponents are, the higher the concentration of small particles. The smaller the j exponents are, the higher the concentration of big particles or flocs and the flatter is the slope (Buonassissi and Dierssen, 2010; Junge, 1963). Based on these models, the PSDs correlate with other parameters, such as the b_{bp} slope (Kostadinov et al., 2009; Slade and Boss, 2015) and $b_{bp}/b_p(\lambda)$ (Ulloa et al., 1994). It means, that indirectly they can be used in remote sensing of SPM. The remote sensing reflectance, R_{rs} , is directly proportional to the ratio of backscattering to absorption ($b_b(\lambda)$ and $a(\lambda)$, respectively), which in turn depends on the particulate and dissolved constituents of the seawater (Gordon et al., 1975; Morel and Prieur, 1977; Whitmire et al., 2007).

As flocs and small single particles have different sedimentation rates, they impact both, the water column turbidity and water optical properties differently, in particular single particles have the greatest impact on light scattering (Mikkelsen et al., 2006). In addition, particles that agglomerate into flocs may incorporate heavy metals that are released into the water column after disaggregation induced by disturbances, such as trawling or storms (Palanques et al., 1995).

The Baltic Sea is unique, with brackish water and high inflows of rivers, compared to its surface area. These rivers bring in large amounts of CDOM, especially to the coastal areas. (Kowalczyk, 1999). In summer, strong cyanobacterial blooms occur due to high nutrient concentrations (Bianchi et al., 2000; Kahru et al., 1994). The SPM is usually dominated by organic particles except in some conditions in coastal areas when mineral particles dominate (Woźniak et al., 2011). Remote sensing studies have demonstrated that the Baltic Sea is an extraordinarily complex study object, where SPM concentrations in water cannot

be retrieved by using standard remote sensing and bio-optical algorithms (Darecki et al., 2003; Ohde et al., 2007; Toming et al., 2017). Therefore, there is a strong need to determine the properties of SPM that allow generation of regional algorithms. Until now, only a few studies of the optical properties of SPM have been carried out (Berthon and Zibordi, 2010; Freda, 2012; Kratzer and Moore, 2018; Kutser et al., 2009; Paavel et al., 2011; Woźniak et al., 2011, 2018).

The main aim of our study was to find optical fingerprints of different SPM characteristics which allow retrieving these with remote sensing algorithms in the future. Firstly, spatio-temporal variability of the water constituent characteristics was studied. Secondly, the origin and characteristics of SPM were investigated. Finally, the variability of optical properties between three Estonian bays was analysed.

2. Study area

The Baltic Sea is a shallow semi-enclosed brackish water body with low water exchange with the Atlantic Ocean and with high freshwater inflow from rivers.

Three Estonian bays (Pärnu, Matsalu, and Haapsalu) on the eastern coast of the Baltic Sea were studied because they have a strong flux of particles from river discharge. In addition, due to their shallowness, they are strongly affected by resuspension by waves and currents. Pärnu Bay is located on the west coast of Estonia (Figure 1). Because of its openness to strong westerly winds, the bay's water level and salinity fluctuations are irregular.

The mean depth of the bay is 4.7 m (maximum of 8 m), with salinity of 3–5 PSU, and current velocity of 4–11 cm s⁻¹ (maximum of 90 cm s⁻¹). The characteristic bay bottom type is varved clay on top of which are Holocene sediments like fine sand (>0.063 mm diameter), clay and mud (<0.063 mm diameter; Kartau et al., 2011). Pärnu Bay is strongly influenced by the inflow from the Pärnu River (144 km long; mean discharge of 64 m³ s⁻¹; the catchment area of 6920 km², one of the largest in Estonia). Furthermore, wind-derived resuspension of sediments from the shallow bottom results in high concentrations of suspended particles in the water column (Paavel et al., 2011). The Pärnu River also provides high quantities of CDOM (Paavel et al. (2011) showed that with high river discharge, the CDOM absorption at 380 nm could attend 31.8 m⁻¹) making Pärnu Bay an optically complex system. Human factors and urbanization also affect the water quality as the river mouth is in the city of Pärnu (~40000 inhabitants) which is the fourth largest city in Estonia. The city of Pärnu with its sandy beaches is among the most popular summer tourism locations in Estonia and therefore the monitoring of the water quality is vital. Pärnu Bay belongs to one of the three coastal locations where the water samples are collected twice per month by the Estonian National Monitoring Program. Additionally, local environmental agencies have collected long time series of background data (river discharge, rain amount). Facts, that Pärnu Bay is a complex water body with highly variable conditions and that there is access to additional data for more thorough analyses made it the best location to run our study with additional optical measurements.

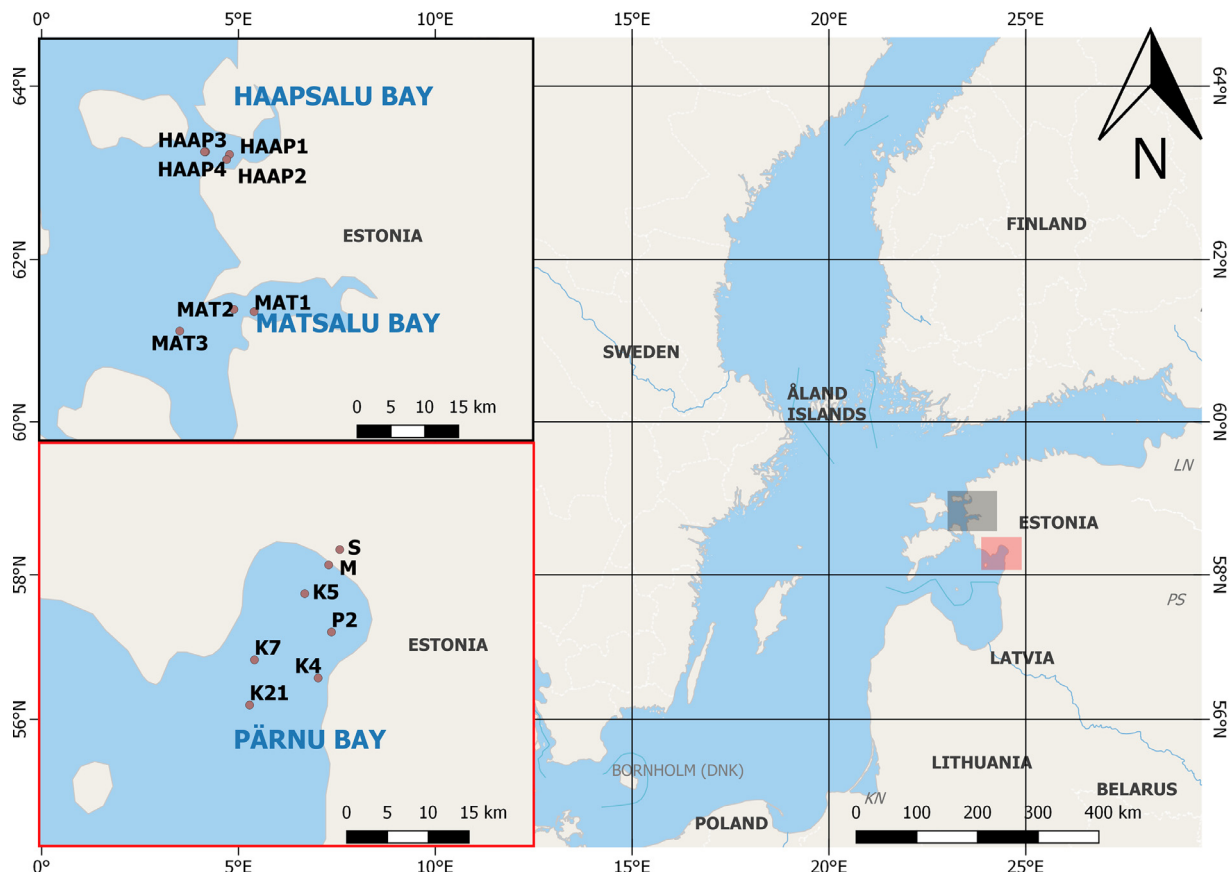


Figure 1 Locations of all measurement stations in the Estonian coastal waters. Matsalu Bay and Haapsalu Bay (top) and Pärnu Bay (bottom).

Matsalu Bay belongs to the Matsalu National Park, which is a well-known natural reserve for the protection of more than 250 bird species (KKA, 2016). Due to the rules of the natural reserve, human activities in this area are limited. Matsalu Bay is a very shallow bay with an average depth of only 1.5 m and the maximum depth of 3.5 m. Similarly to Pärnu Bay, the influence of the Kasari River is remarkable as it brings a large quantity of CDOM (Kutser et al. (2009) measured CDOM absorption values exceeding 30 m^{-1} at 420 nm) and a smaller amount of SPM to the bay. The colour of the water is predominantly brown, and the Secchi depth varies between 0.2–3.5 m. The increase in SPM in Matsalu Bay is mainly prevented by the reed belt.

Haapsalu Bay unlike Matsalu Bay and similarly to Pärnu Bay is also strongly influenced by human activities. It is the most important peloid (therapeutically used mud) depository in Estonia. According to official surveys, it was the bay with the poorest water quality in Estonia, in 2015 (EEA, 2015), mainly due to the pollution (originating from the city of Haapsalu) and discharge of nutrient-rich sediments. Due to the very shallow (~3 m deep) and sectioned area, the water mixing is poor and pollutants remain in the sediments.

3. Methods and data

Four field campaigns were conducted in Pärnu Bay during which optical data, such as the spectral absorption, atten-

uation, scattering, and backscattering coefficients ($a(\lambda)$, $c(\lambda)$, $b(\lambda)$, $b_b(\lambda)$, respectively), and PSD (only in August 2018), were measured using a variety of profiling instruments (Table 1). Generally, the water column was well mixed during all field campaigns and therefore, the median spectra of all above-mentioned parameters were used in this study. Still, the stratification was observed at the river mouth stations (Figure 2).

Fieldwork was carried out in 2017 and 2018 during different seasons to test various conditions. Water samples were collected from the surface layer (between the surface and 0.5 m depth) and stored in dark and cold for less than 10 h before filtering. Optical instruments utilised different sampling intervals; therefore, the data were coupled by using the pressure-dependent depth measured by the instrument measuring conductivity, temperature, depth (CTD) and time. Additional optical measurements were conducted by the Estonian Marine Institute of the University of Tartu in Haapsalu and Matsalu bays in 2012, 2013, 2016, and 2018 (7 campaigns altogether).

The background data, such as the discharges of the Pärnu and Kasari River, and rainfall amounts, were obtained respectively from the Estonian Environment Agency (www.keskkonnaagentuur.ee) and Estonian Weather Service (www.ilmateenistus.ee). The campaign days in July 2017 (daily river discharge = $12 \text{ m}^3 \text{ s}^{-1}$, wind = $1.8\text{--}5 \text{ m s}^{-1}$) and May 2018 (daily river discharge = $22 \text{ m}^3 \text{ s}^{-1}$, wind = $4\text{--}7 \text{ m s}^{-1}$) were sunny and calm. A strong river discharge was

Table 1 Details of fieldworks in studied bays including date, area, station (St), instruments and background data.

Field work day	Area	Station	Instruments	Wind speed (m s^{-1})	Wave height (m)	River discharge ($\text{m}^3 \text{s}^{-1}$)
21.07.2012	Matsalu Bay	MAT1, MAT2, MAT3	Wet Labs AC-S, ECO-BB3, ECO-VSF3, Seabird CTD, water samples	-	0.3	32
24.07.2013	Haapsalu Bay	HAAP1, HAAP2, HAAP3	Wet Labs AC-S, ECO-BB3, ECO-VSF3, Seabird CTD water samples	6	0.4	-
25.07.2013	Matsalu Bay	MAT1, MAT2, MAT3	Wet Labs AC-S, ECO-BB3, ECO-VSF3, Seabird CTD water samples	1–2	0.1	2
31.05.2016	Haapsalu Bay	HAAP1, HAAP2	Wet Labs AC-S, ECO-BB3, ECO-VSF3, Seabird CTD Water samples	6	0.3	-
14.09.2016	Haapsalu Bay	HAAP3	Wet Labs AC-S, ECO-BB3, ECO-VSF3, Seabird CTD water samples	-	0.005	-
12.10.2016	Haapsalu Bay	HAAP4	Wet Labs AC-S, ECO-BB3, ECO-VSF3, Seabird CTD water samples	1.5	-	-
07.07.2017	Pärnu Bay	M, K5, K4, K7, K21	Wet Labs AC-S, ECO-BB3, ECO-VSF3, Seabird CTD, water samples	1.8–5	0.1	12
17.04.2018	Pärnu Bay	M, K5, K4, K7, K21	Wet Labs AC-S, ECO-BB3, ECO-VSF3, Seabird CTD, water samples	1–5	0.2	117
15.05.2018	Pärnu Bay	M, K5, K4, K7, K21	Wet Labs AC-S, ECO-BB3, ECO-VSF3, Seabird CTD, water samples	4–7	0.3	22
17.07.2018	Matsalu and Haapsalu Bay	MAT1, MAT2 HAAP1, HAAP6	Wet Labs AC-S, ECO-BB3, ECO-VSF3, Seabird CTD, water samples	4–8	0.5	1
28.08.2018	Pärnu Bay	M, K5, K4, K7, K21, P2, S	Wet Labs AC-S, ECO-BB3, ECO-VSF3, Seabird CTD, water samples, Sequoia Sci LISST-100X Type-C	3–4.5 (23.08 13)	0.4 (26.08 1)	7

observed in April 2018 (rainy, daily river discharge = $117 \text{ m}^3 \text{ s}^{-1}$, wind = $1–5 \text{ m s}^{-1}$). The field campaign in August 2018 was carried out shortly after a period with strong westerly wind, which led to high waves and mixing of the water column (west wind $23.08 = 13 \text{ m s}^{-1}$, waves = 40 cm, daily river discharge = $7 \text{ m}^3 \text{ s}^{-1}$). The measurement stations in Pärnu Bay are shown in Figure 1. Five of the stations were used during the first three campaigns and seven stations during the last campaign (including stations S and P2).

3.1. *In situ* optical data

3.1.1. Spectral absorption, attenuation, and scattering coefficients

The profiles of absorption and attenuation coefficients, $a(\lambda)$, and, $c(\lambda)$, were measured using the WET Labs AC-S (www.seabird.com) between 402–722 nm. The data were calculated according to four steps recommended in the user manual (WET Labs, 2011).

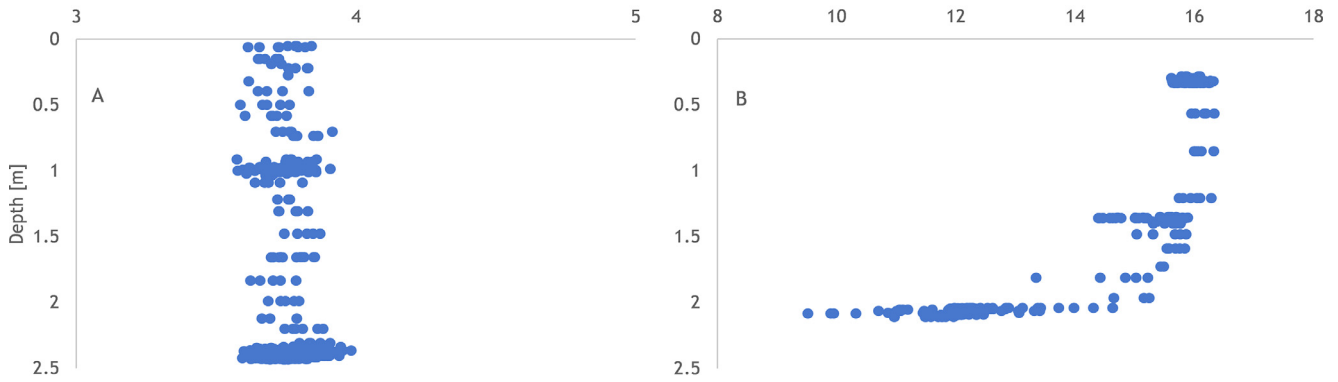


Figure 2 Particulate absorption coefficients (a_p) profiles measured at 412 nm. A: example of mixed water at the station K7 in July 2017 and B: example of stratified waters at the river mouth station M in April 2018.

- 1) The average $a(\lambda)$ and $c(\lambda)$ blank spectra, measured with milliQ water before the fieldwork, were subtracted from the raw $a(\lambda)$ and $c(\lambda)$ spectra measured during the field work. All spectra were interpolated to the same wavelength values (402–722 nm, 2 nm step).
- 2) $a(\lambda)$ and $c(\lambda)$ were corrected using Eq. (1) to eliminate the temperature and salinity effects of the brackish water of the Baltic Sea.

$$ac_{tsc}(\lambda) = ac_{interp}(\lambda) - [\Psi_t * (T - Tr) + \Psi_s * S], \quad (1)$$

where $ac_{tsc}(\lambda)$ represents the salinity- and temperature-corrected absorption or attenuation coefficient at a specific wavelength, respectively; $ac_{interp}(\lambda)$ is the blank-corrected raw absorption or attenuation coefficient at a specific wavelength; and Ψ_t and Ψ_s are the spectral temperature- and salinity-dependent constants, respectively, which were obtained from Sullivan et al. (2006). The Tr is the instrument reference temperature in °C from the device configuration file. The salinity of distilled water is not included in the equation because it is zero and thus negligible. The parameters T and S are the temperature and salinity measured by the CTD, respectively.

- 3) The next step was to compute the total spectral absorption coefficients, $a_{tot}(\lambda)$, by applying the scattering correction to the salinity- and temperature-corrected $a(\lambda)$ and adding pure water $a(\lambda)$ (Pope and Fry, 1997) obtained from Pegau et al. (2003) using Eq. (2):

$$a_{tot}(\lambda) = \frac{a_{tsc}(\lambda) - a_{tsc}(715)}{c_{tsc}(715) - a_{tsc}(715)} * (c_{tsc}(\lambda) - a_{tsc}(\lambda)) + a_{purewater}(\lambda), \quad (2)$$

where $a_{tot}(\lambda)$ is the total spectral absorption coefficient, $a_{tsc}(\lambda)$ and $c_{tsc}(\lambda)$ are the temperature- and salinity-corrected absorption and attenuation coefficients at a specific wavelength calculated using Eq. (1). 715 nm is a reference wavelength in the near-infrared range (Leymarie et al., 2010), and $a_{purewater}(\lambda)$ is the absorption of pure water at a specific wavelength (Pope and Fry, 1997).

- 4) The particulate absorption coefficients, $a_p(\lambda)$, were calculated by subtracting the CDOM absorption, $a_{CDOM}(\lambda)$ from $a_{tsc}(\lambda)$ using Eq. (3). As the $a_{CDOM}(\lambda)$ values (details in 3.2) were measured from the surface water samples, the $a_{tsc}(\lambda)$ values were also taken as an average of the

first 50 cm of surface water.

$$a_p(\lambda) = a_{tsc}(\lambda) - a_{CDOM}(\lambda), \quad (3)$$

where $a_p(\lambda)$ is the particulate absorption at a specific wavelength, $a_{tsc}(\lambda)$ is the temperature- and salinity-corrected absorption coefficient at a specific wavelength and $a_{CDOM}(\lambda)$ is the CDOM absorption at a specific wavelength.

- 5) The spectral particulate scattering coefficients, $b_p(\lambda)$, were calculated from $a_{tsc}(\lambda)$ and $c_{tsc}(\lambda)$ using Eq. (4).

$$b_p(\lambda) = c_{tsc}(\lambda) - a_{tsc}(\lambda), \quad (4)$$

where $b_p(\lambda)$ is the spectral particulate scattering coefficient at a specific wavelength and $c_{tsc}(\lambda)$ and $a_{tsc}(\lambda)$ are the temperature- and salinity-corrected attenuation and absorption coefficients at a specific wavelength, respectively.

- 6) The mass-specific scattering coefficients, $b_p^*(\lambda)$, were retrieved by dividing $b_p(\lambda)$ and SPM concentration using Eq. (5).

$$b_p^*(\lambda) = \frac{b_p(\lambda)}{SPM}, \quad (5)$$

where $b_p^*(\lambda)$ is the mass-specific scattering coefficient at a specific wavelength, $b_p(\lambda)$ is the particulate scattering at a specific wavelength and SPM is the concentration of suspended particulate matter.

3.1.2. Backscattering

The β , which was used to calculate the $b_{bp}(\lambda)$, was measured with WET Labs ECO-BB3 and ECO-VSF3 meters (www.seabird.com). The ECO-BB3 meter measures β at an angle of 124° and at 3 wavelengths (412, 595, and 715 nm). ECO-VSF3 measures β at 3 angles (100°, 125°, and 150°) and 3 wavelengths (470, 532, and 660 nm). However, as post-fieldwork calibration showed issues with BB3 at 595 nm, these values were removed from the analysis. The $b_{bp}(\lambda)$ was calculated according to instructions in the instrument user manuals (WET Labs, 2010, 2007). Based on the combination of these instruments, $b_{bp}(\lambda)$ spectra at six wavelengths could be obtained.

The $b_{bp}(\lambda)$ measured with ECO-BB3 were calculated using four steps:

- 1) Corrected β values were obtained using Eq. (6) and $a_{tsc}(\lambda)$ calculated in Section 3.1.1.

$$\beta_{cor}(\lambda) = \beta_{measured}(\lambda) * e^{0.0391 * a_{tsc}(\lambda)}, \quad (6)$$

where $\beta_{cor}(\lambda)$ is the corrected volume scattering function at a specific wavelength, $\beta_{measured}(\lambda)$ is the raw volume scattering function at a specific wavelength, and $a_{tsc}(\lambda)$ is the salinity/temperature corrected spectral absorption at a specific wavelength.

- 2) The β value of pure water was obtained using Eq. (7) established by Morel (1974).

$$\beta_w(\lambda) = 1.38 * \left(\frac{\lambda}{500}\right)^{-4.32} * \left(1 + \frac{0.35S}{37}\right) * 10^{-4} * \left[1 + \cos^2\left(\frac{124^\circ}{1 + \delta}\right)\right], \quad (7)$$

where $\beta_w(\lambda)$ is the volume scattering function of pure water at a specific wavelength, S is the salinity, and $\delta = 0.09$.

- 3) The β parameter of particles was calculated using Eq. (8) by subtracting the β value of pure water from the corrected β .

$$\beta_p(\lambda) = \beta_{cor}(\lambda) - \beta_w(\lambda), \quad (8)$$

where $\beta_p(\lambda)$ is the volume scattering function of the particles at a specific wavelength, $\beta_{cor}(\lambda)$ is the corrected volume scattering function at a specific wavelength, and $\beta_w(\lambda)$ is the volume scattering function of water at a specific wavelength.

- 4) The $b_{bp}(\lambda)$ was calculated using Eq. (9):

$$b_{bp}(\lambda) = 2\pi * X * \beta_p(\lambda), \quad (9)$$

where $b_{bp}(\lambda)$ is the spectral particulate backscattering coefficient at a specific wavelength, $X = 1.1$ is a factor determined by Boss and Pegau (2001) and recommended in ECO-BB3 sensor user manual, and $\beta_p(\lambda)$ is the volume scattering of particles at a specific wavelength.

The $b_b(\lambda)$ of ECO-VSF3 were calculated using four steps:

- 1) The raw data were corrected using Eq. (10) and $a_{tsc}(\lambda)$:

$$\beta_{cor}(\lambda) = \beta(\theta) * e^{(L * a_{tsc}(\lambda))}, \quad (10)$$

where $\beta_{cor}(\lambda)$ is the corrected volume scattering function at a specific wavelength, $\beta(\theta)$ is the volume scattering function at a viewing angle in radians (100, 125, and 150 rad calculated from degree units), L is the path length provided by the instrument manufacturer ($L = 0.0314$ for $\theta = 100$, $L = 0.0441$ for $\theta = 125$, and $L = 0.0804$ for $\theta = 150$), and $a_{tsc}(\lambda)$ is the salinity/temperature corrected spectral absorption coefficient at a specific wavelength.

- 2) Solid angles were computed using Eq. (11) and $\beta_{cor}(\lambda)$ values and fitted with a cubic polynomial (the fourth value for the π angle is 0):

$$x(100^\circ, 125^\circ, 150^\circ) = \beta_{cor}(\lambda) * 2 * \pi * \sin(\theta), \quad (11)$$

where x represents solid angles of 100°, 125°, and 150° and $\beta_{cor}(\lambda)$ is the corrected volume scattering function at a specific wavelength.

The results were integrated from $\pi/2$ to π to obtain the total backscattering of the whole hemisphere.

- 3) $b_{bp}(\lambda)$ were computed using Eq. (12), that is, by subtracting the total scattering of seawater from the total backscattering coefficient:

$$b_{bp}(\lambda) = b_b(\lambda) - \frac{0.0029308 * \left(\frac{\lambda}{500}\right)^{-4.24}}{2}, \quad (12)$$

where $b_{bp}(\lambda)$ is the particulate backscattering coefficient at a specific wavelength and $b_b(\lambda)$ is the total backscattering coefficient at a specific wavelength.

- 4) Mass-specific backscattering coefficients, $b_{bp}^*(\lambda)$, were computed by dividing $b_{bp}(\lambda)$ and SPM, using Eq. (13).

$$b_{bp}^*(\lambda) = \frac{b_{bp}(\lambda)}{SPM}, \quad (13)$$

where $b_{bp}^*(\lambda)$ is the mass-specific particulate backscattering coefficient at a specific wavelength, $b_{bp}(\lambda)$ is the particulate backscattering coefficient at a specific wavelength, and SPM is the suspended particulate matter concentration.

3.1.3. Backscattering ratio

The $b_{bp}/b_p(\lambda)$ was calculated using Eq. (14), that is, by dividing $b_{bp}(\lambda)$ by the corresponding $b_p(\lambda)$ value at a specific wavelength. The interpolation of b_p was required for two wavelengths (595 and 715 nm).

$$b_{bp}/b_p(\lambda) = \frac{b_{bp}(\lambda)}{b_p(\lambda)}, \quad (14)$$

where $b_{bp}/b_p(\lambda)$ is the spectral backscattering ratio at a specific wavelength, $b_{bp}(\lambda)$ is the spectral particulate backscattering coefficient at a specific wavelength, and $b_p(\lambda)$ is the spectral particulate scattering coefficient at a specific wavelength.

3.2. Water samples and sediment analyses

Water samples were collected from the surface layer at 0.5 m depth and from the bottom layer (only in August 2018) following ISO 5667-3 (International Organization for Standardization, 2018), filtered, and analysed at the laboratory following ISO 10260 (International Organization for Standardization, 1992). The SPM, suspended particulate inorganic matter (SPIM), suspended particulate organic matter (SPOM), and chlorophyll-*a* (Chl-*a*) concentrations as well as the absorption coefficients of coloured dissolved organic matter $a_{CDOM}(\lambda)$ were determined from the samples.

The concentration of SPM was measured gravimetrically (precision of weights 0.01 mg) after filtration of the measured volume of water through Whatman GF/F filters. The filters were in prior pre-combusted at 550°C for 30 min, then washed with MilliQ water, then dried at 103–105°C for 1h and finally pre-weighed. The inorganic fraction SPIM was measured after combustion at 550°C for 30 minutes. The organic fraction SPOM was determined by subtracting SPIM from SPM (ESS, 1993). To determine the Chl-*a* concentrations, the water samples were filtered using GF/F filters. The chlorophyll pigments were extracted with 5 mL of 96% ethanol and measured with a Perkin ELMER Lambda 35 UV/VIS spectrophotometer (www.perkinelmer.com). Finally, the method reported by Jeffrey and Humphrey (1975) was applied to calculate the Chl-*a* concentrations.

To obtain the spectral absorption of coloured dissolved organic matter $a_{CDOM}(\lambda)$, the samples were filtered through GF/F filters and the filtrate was filtered through a Millipore filter with a pore size of 0.2 μm .

The $a_{CDOM}(\lambda)$ was measured with a spectrophotometer (either Perkin ELMER Lambda 35 UV/VIS or Hitachi U-3010 UV/VIS in the range 350–750 nm) in filtrate, in a 10 cm cuvette against distilled water and corrected for residual scattering according to the method described by Lindell et al. (1999). In this study, the values of $a_{CDOM}(412)$ were used because it is the wavelength of ECO-BB3 and OLCI sensor of Sentinel-3. The slope of CDOM absorption (S_{CDOM}) was calculated between 350 and 550 nm (Nima et al., 2019). Bottom sediment samples were collected with a Van Veen grab sampler (www.vanwalt.com) in August 2018 to visually observe the bottom sediment types and carry out grain size distribution analyses in the laboratory with LISST-100X (Sequoia Sci.; described in detail in chapter 3.3).

3.3. In situ and laboratory particle data

Particle Size Distributions were measured with a particle size analyser sensor (Sequoia Scientific LISST-100X Type C, 1 Hz; www.sequoiasci.com). The LISST-100X sensor uses a 670 nm laser-beam and ring-detector with 32 logarithmically spaced rings that perceive raw small-angle scattering of the beam by suspended particles which is converted into volumic concentration of particles by inversion matrix (Agrawal and Pottsmith, 2000). The sensor measures PSDs in 32 logarithmically spaced size classes, optical transmission at 670 nm, optical volume scattering function (VSF), and attenuation coefficient. For the default “Spherically Shaped Particles” method, the particle size classes are ranging from 2.5 (lower limit) to 500 μm (upper limit) and for the “Randomly Shaped Particles” inversion matrix based on Mie’s theory, the particle size classes are ranging from 1.90 (lower limit) to 381 μm (upper limit). The last method was used for the data analyses. The instrument was deployed to measure the PSDs at the surface and in the bottom layer at each station. The processing of the raw data was done with the LISST-SOP software (www.sequoiasci.com) and parameter calculations with the MATLAB software (www.mathworks.com). Subsequently, normalised volume concentrations were computed for each of the 32 size classes. Extreme size classes, such as 1.9–4 μm and 250–380 μm , exhibited extremely high values in all samples ($>100 \mu\text{g mL}^{-1}$). Therefore we assumed that they were “rising tails” due to the presence of smaller or bigger particles outside the measurement range and we eliminated them before calculating the normalised volume concentration (frequency) of the particles, median particle size (D50), and Junge distribution (j ; refer to Eq. (15) Many et al., 2016; Mikkelsen et al., 2005).

The PSDs of the surface and bottom water samples were then measured in the laboratory using the same LISST-100X sensor. Before the analysis, the water samples were treated in an ultrasound bath (High-Power Ultrasonic Cleaner, Cole-Parmer®, www.coleparmer.com) for 180 s at a frequency of 42 kHz. Based on this treatment, it could be determined if the big particles observed in *in situ* measurements are unique particles or aggregates of small particles. The bottom sediment samples from the stations K5, K21, K4, and

S, extracted with the Van Veen grab sampler were diluted in water, analysed in the laboratory using the same LISST-100X sensor, and used as references (PSDs) for resuspended particles from the sea bottom.

The total volume concentrations (TVCs) of the particles were calculated by summing the volume concentrations of all size classes row by row. Normalised volume concentrations (frequencies) were calculated by dividing the volume concentrations of each size class by the TVC row by row.

To compute the Junge exponent, j , the particle number per size class was derived from normalised LISST-100X volume concentrations by dividing them by an elementary spherical volume. We assumed that the relationship between the particle number and particle size of mineral particles (the majority of particles during the August storm) can be expressed by a power law shown in Eq. (15) (Buonassissi and Dierssen, 2010; Many et al., 2016):

$$n(D) = D^{-j}, \tag{15}$$

where n is the number of particles in $\text{L}^{-1}\mu\text{m}^{-1}$, D is the particle diameter in μm , and j is the Junge distribution of the PSD.

The median particle size D50 was computed to detect groups of particles in the water. It shows that half of the particles in the water are smaller than D50 and half of the particles are larger than D50.

3.4. Correlation factors

To better estimate the relationships between the optically active components concentrations and optical properties of particles, the correlations factors such as RMSE (Root Mean Square Error), NRMSE (Normalized Root Mean Square Error), MBE (Mean Bias Error), and NMBE (Normalized Mean Bias Error) were computed following the Eq. (16), (17), (18), and (19), respectively:

$$RMSE = \sqrt{\frac{\sum_{i=1}^n (x_{calculated} - x_{measured})^2}{n}}, \tag{16}$$

$$NRMSE = \frac{RMSE}{\text{mean}(\sum_{i=1}^n x_{measured})}, \tag{17}$$

$$MBE = \sum_{i=1}^n \frac{(x_{calculated} - x_{measured})}{n}, \tag{18}$$

$$NMBE = \frac{MBE}{\text{mean}(\sum_{i=1}^n x_{measured})}, \tag{19}$$

where, the $x_{calculated}$ is the variable estimated from the linear equation, the $x_{measured}$ is the variable measured *in situ* and n is the number of data points.

4. Results

4.1. Concentrations of water constituents

The temporal and spatial variations of SPM, SPIM, SPOM, and Chl-*a* in the three turbid Estonian bays (Pärnu, Matsalu and Haapsalu) are shown in Figure 3. SPM varied between 6.75 and 19.6 g m^{-3} in Pärnu Bay (Figure 3A). Among the

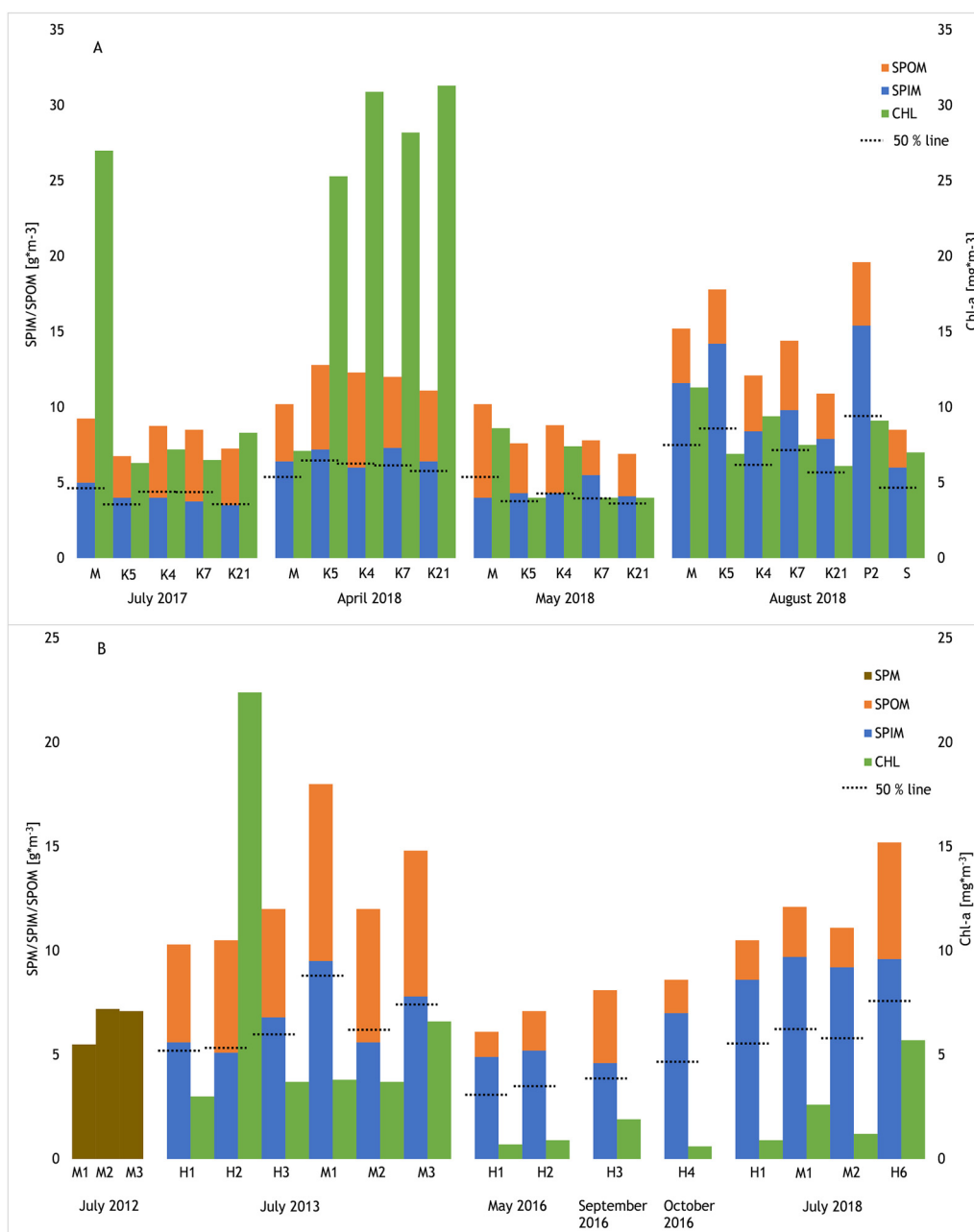


Figure 3 The concentrations of suspended particulate matter (SPM), suspended particulate inorganic matter (SPIM), suspended particulate organic matter (SPOM) and CHL (Chl-*a* – Chlorophyll-*a*). One orange + blue stacked column is equal to the SPM concentration with dotted lines showing the 50% concentration of SPM. A: Pärnu Bay four campaigns and B: Haapsalu (H) and Matsalu (M) bays six campaigns. For the July 2012 campaign, only SPM values were available and therefore presented differently.

four campaigns, the concentrations were the lowest ($\sim 7\text{--}8\text{ g m}^{-3}$) in July 2017 and May 2018. At the same time, the SPM concentrations were slightly higher at the river mouth station M than inside Pärnu Bay, that is, 9.25 and 10.2 g m^{-3} , respectively. The highest SPM concentrations of all campaigns were obtained in August 2018 ($12\text{--}19.6\text{ g m}^{-3}$). The SPM concentrations were highly variable throughout the campaigns and ranged from 5.5 to 15.2 g m^{-3} in Matsalu and Haapsalu bays (Figure 3B). The highest concentrations were observed in July 2013 and the lowest concentrations in July 2012, both in Matsalu Bay.

In general, the SPOM part in the SPM was relatively lower than SPIM part, except for May when it was 1.5 times higher than SPIM at station M. A notably high difference between SPIM and SPOM was observed in August when SPIM was more than two times higher than SPOM. SPIM part in SPM was clearly higher in Matsalu and Haapsalu bays, except in July 2013, when the amount of SPIM was similar to SPOM.

The Chl-*a* concentrations varied between 3.95 and 32.28 mg m^{-3} in Pärnu Bay. The highest Chl-*a* values of all campaigns were observed in April 2018 ($25\text{--}32.28\text{ mg m}^{-3}$) except near the river mouth station M (7 mg m^{-3}). The low-

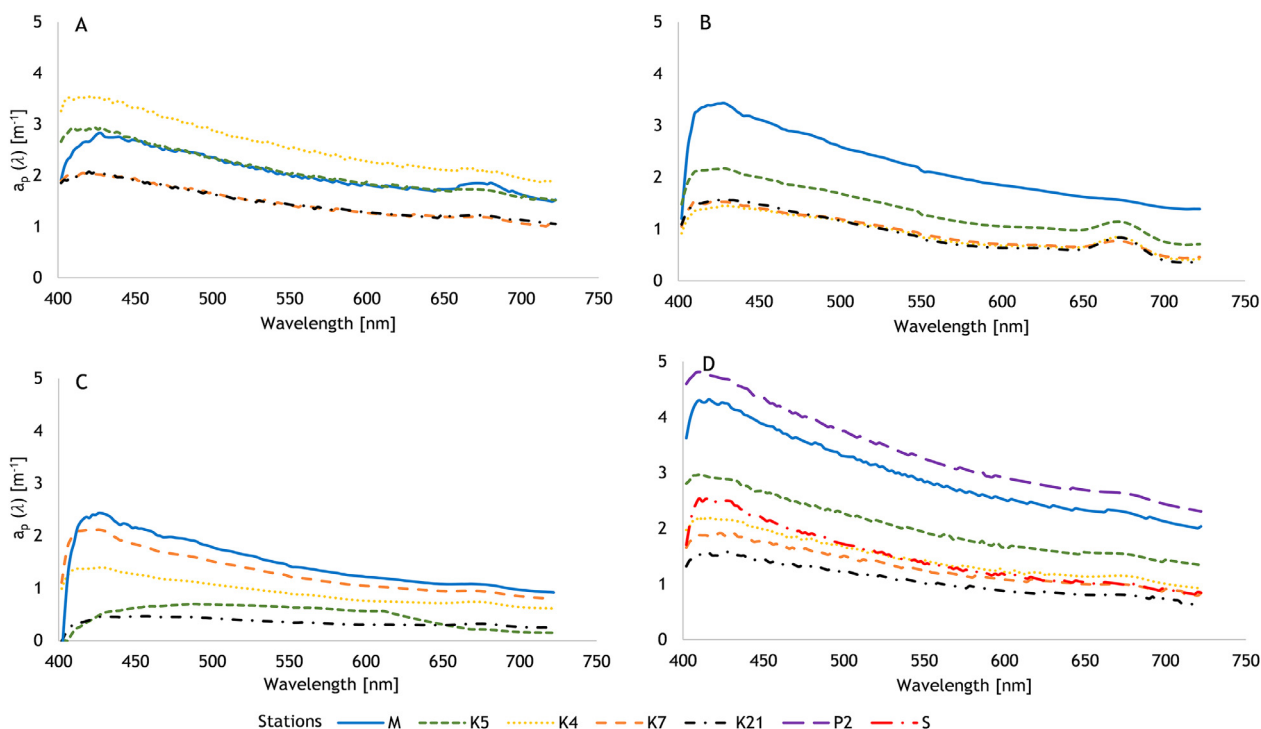


Figure 4 Spectral particulate absorption coefficients, $a_p(\lambda)$, measured in Pärnu Bay: (A) July 2017, (B) April 2018, (C) May 2018, and (D) August 2018.

est Chl-*a* values were observed in May 2018 (3.71–7.43 mg m⁻³). Generally, the Chl-*a* amounts were higher in the river mouth station M. In July, they were three times higher in station M than in the other stations of that campaign (27 mg m⁻³ compared to <9 mg m⁻³). Chl-*a* concentrations varied between 0.6 and 22.4 mg m⁻³ in Haapsalu and Matsalu bays. The maximum amount of Chl-*a* was observed in Haapsalu Bay in July 2013 (22.4 mg m⁻³) and the lowest amounts in spring and autumn 2016 (0.6–1.9 mg m⁻³).

The values of CDOM absorption at 402 nm ($a_{CDOM}(402)$) ranged from 1.38 to 14.08 m⁻¹ in Pärnu Bay. The highest $a_{CDOM}(402)$ were observed in the river mouth station M, where the maximum values were 12.65 and 14.08 m⁻¹ in April and May 2018, respectively. S_{CDOM} varied between 0.016 and 0.019 nm⁻¹. The slope value was 0.016 nm⁻¹ in station S and station M of four campaigns. S_{CDOM} was more elevated in the offshore stations with the maximum value of 0.019 nm⁻¹.

4.2. Inherent optical properties

4.2.1. Particulate absorption coefficients

The $a_p(\lambda)$ also varied temporarily and spatially in Pärnu Bay. The largest variations were observed in the blue part of the spectrum (Figure 4), which is influenced by both phytoplankton and organic matter absorption. Altogether, $a_p(\lambda)$ peaks varied between 0.40 and 4.69 m⁻¹ at 424–430 nm for the four campaigns. $a_p(\lambda)$ spectra were generally elevated in the station M, close to the river mouth and stayed low offshore, in the stations K21, K4. $a_p(\lambda)$ had a steep increase of values between 400 and 420 nm in the river mouth station M and the river station S. The highest $a_p(\lambda)$ were observed in August 2018, near the river mouth (Figure 4D).

The $a_p(\lambda)$ obtained at Haapsalu and Matsalu bays varied between 0.16 and 5.62 m⁻¹ (Figure 5). $a_p(\lambda)$ variability was highest in summer and stayed stable during spring and autumn measurements (< 0.7 m⁻¹). $a_p(\lambda)$ in Matsalu and Haapsalu bays were lower than in Pärnu Bay.

4.2.2. Mass-specific particulate scattering coefficients

The $b_p^*(\lambda)$ of Pärnu Bay also varied temporarily and spatially. Typically, the spectrum exhibits a decreasing trend, with higher values at 402 nm and lower values at 722 nm. In this case, only the same wavelengths that were available for $b_{pp}^*(\lambda)$ were used (412, 470, 532, 660, 712 nm). $b_p^*(\lambda)$ peak values at 412 nm varied between 0.28 and 1.17 m² g⁻¹. The highest $b_p^*(\lambda)$ of all expeditions were observed in July 2017 (Figure 6A) in the middle of the bay at stations K5 (1.2 m² g⁻¹) and K4 (1.1 m² g⁻¹; a place where dredged sediments are dumped). The lowest $b_p^*(\lambda)$ of all expeditions were observed at the outer part of the bay, at the station K21, 0.2 and 0.3 m² g⁻¹ in May (Figure 6C) and April 2018 (Figure 6B), respectively. In April and August 2018, $b_p^*(\lambda)$ was most elevated in the near river mouth station M. The seasonal variability of $b_p^*(\lambda)$ at one station was remarkable. For example, at station K4, the coefficient varied between 0.3 and 1.1 m² g⁻¹ at 412 nm.

The $b_p^*(\lambda)$ of Haapsalu and Matsalu bays varied between 0.098 and 1.45 m² g⁻¹ (Figure 7). The $b_p^*(\lambda)$ were highly variable in Haapsalu Bay during the summer period. They stayed low and stable in spring and autumn (0.1–0.2 m² g⁻¹).

4.2.3. Mass-specific particulate backscattering coefficients

The $b_{bp}^*(\lambda)$ values obtained at five different wavelengths (412, 470, 532, 660, and 715 nm) varied seasonally, geo-

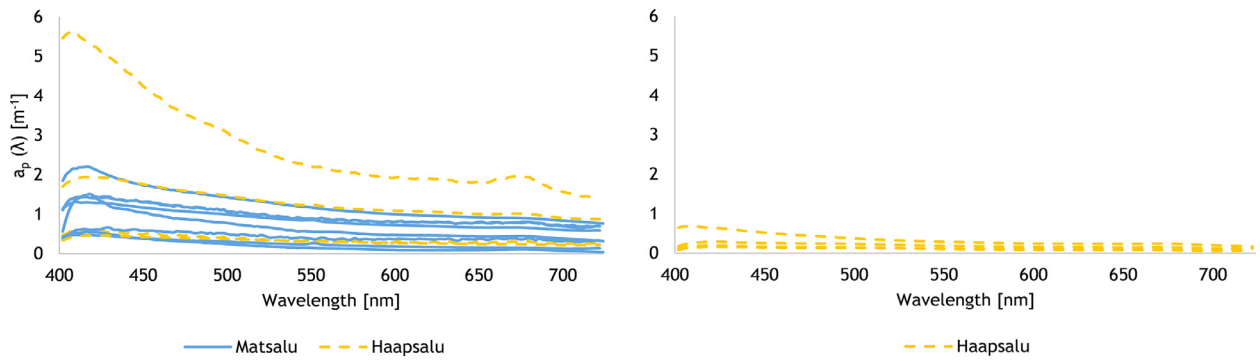


Figure 5 Spectral particulate absorption coefficients, $a_p(\lambda)$, measured at Matsalu and Haapsalu bays in 2012, 2013, 2016, and 2018: (A) summer and (B) spring and autumn.

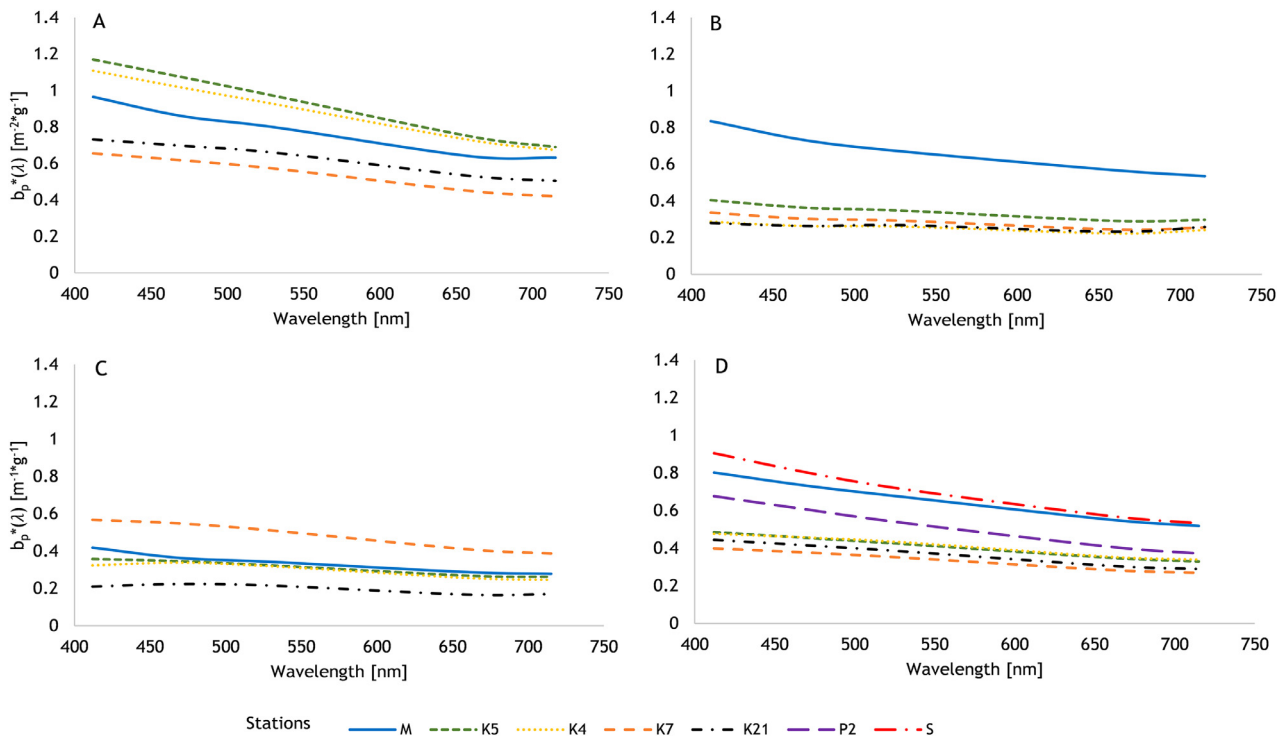


Figure 6 Mass-specific spectral particulate scattering coefficients, $b_p^*(\lambda)$, measured in Pärnu Bay: (A) July 2017, (B) April 2018, (C) May 2018, and (D) August 2018.

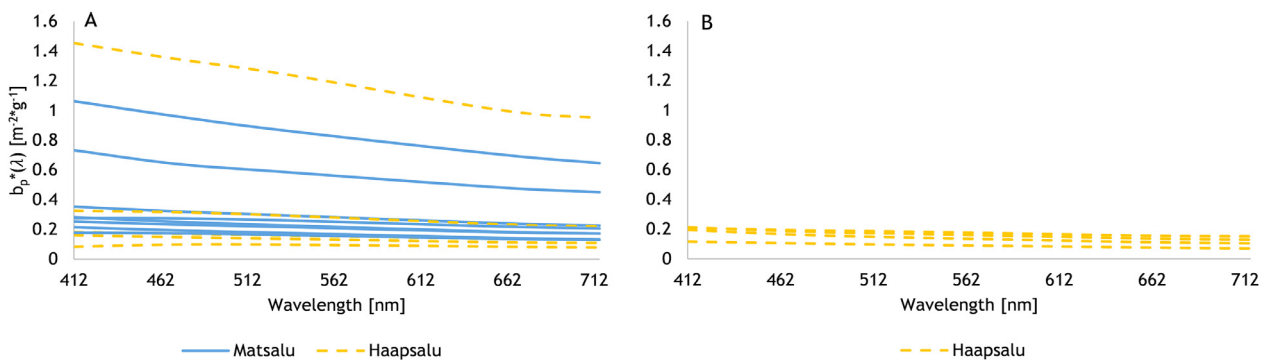


Figure 7 Mass-specific spectral particulate scattering coefficients, $b_p^*(\lambda)$, measured in Matsalu and Haapsalu bays in 2012, 2013, 2016, and 2018: (A) summer and (B) spring and autumn.

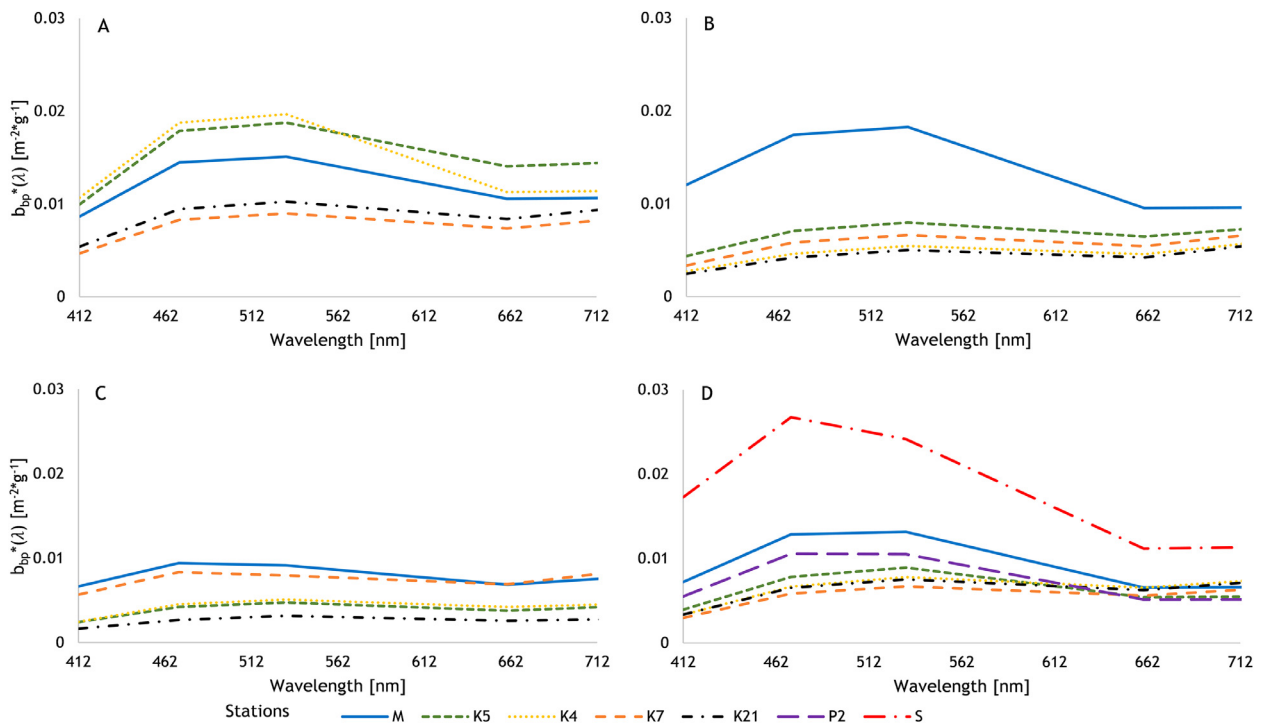


Figure 8 Mass-specific spectral particulate backscattering coefficients, $b_{bp}^*(\lambda)$, measured in Pärnu Bay in (A) July 2017, (B) April 2018, (C) May 2018, and (D) August 2018.

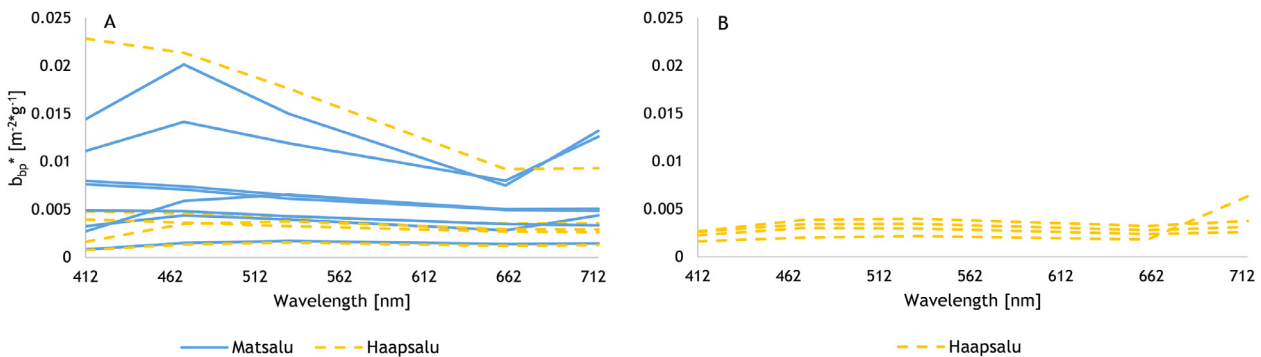


Figure 9 Mass-specific spectral particulate backscattering coefficients, $b_{bp}^*(\lambda)$, measured in Matsalu and Haapsalu bays in 2012, 2013, 2016, and 2018: (A) summer and (B) spring and autumn.

graphically, and spectrally. The peak values ranged from 0.003 to 0.027 $\text{m}^2 \text{g}^{-1}$ (Figure 8). The highest $b_{bp}^*(\lambda)$ were observed near the river mouth station M and in the river station S, except in July 2017 when the elevated $b_{bp}^*(\lambda)$ were in the middle of the bay. The highest $b_{bp}^*(\lambda)$ of all expeditions was observed in August 2018 (Figure 8D) at the river station S (0.026 $\text{m}^2 \text{g}^{-1}$ at 470 nm). Rounded spectra with peak at 470 and 532 nm were observed at the stations K4, K5, M in July 2017 (Figure 8A) and at the station M in April (Figure 8B) and August 2018. Rounded spectra with a peak at 470 nm were observed at stations M and K7 in May 2018 as well as at stations S and P2 in August 2018. In the other stations, the spectra shapes were more stable with the highest values at 532 nm.

The $b_{bp}^*(\lambda)$ obtained at Haapsalu and Matsalu bays varied between 0.0015 and 0.023 $\text{m}^2 \text{g}^{-1}$ (Figure 9). The largest variations of the $b_{bp}^*(\lambda)$ were also registered during the sum-

mer, with maximum coefficients ranging from 0.001 to 0.023 $\text{m}^2 \text{g}^{-1}$. The $b_{bp}^*(\lambda)$ were low and in the similar range also in spring and autumn ($\sim 0.02 \text{m}^2 \text{g}^{-1}$) at Haapsalu Bay. The $b_{bp}^*(\lambda)$ spectra had also diverse shapes. Some spectra had descending motion in summer. Some spectra of Matsalu Bay had peaks at 470 and 712 nm. The spectra of Haapsalu Bay were stable at all wavelengths, the exception was only one spectrum with a peak at 712 nm.

4.3. Backscattering ratio

The $b_{bp}/b_p(\lambda)$ obtained for Pärnu Bay varied and were wavelength-dependent. The spectral shapes of $b_{bp}/b_p(\lambda)$ were similar to $b_{bp}^*(\lambda)$, but in the case of the $b_{bp}/b_p(\lambda)$ the values during one campaign were more similar and there was less variability at the lower wavelengths. $b_{bp}/b_p(\lambda)$ peak values varied between 0.017 and 0.034. The spectra

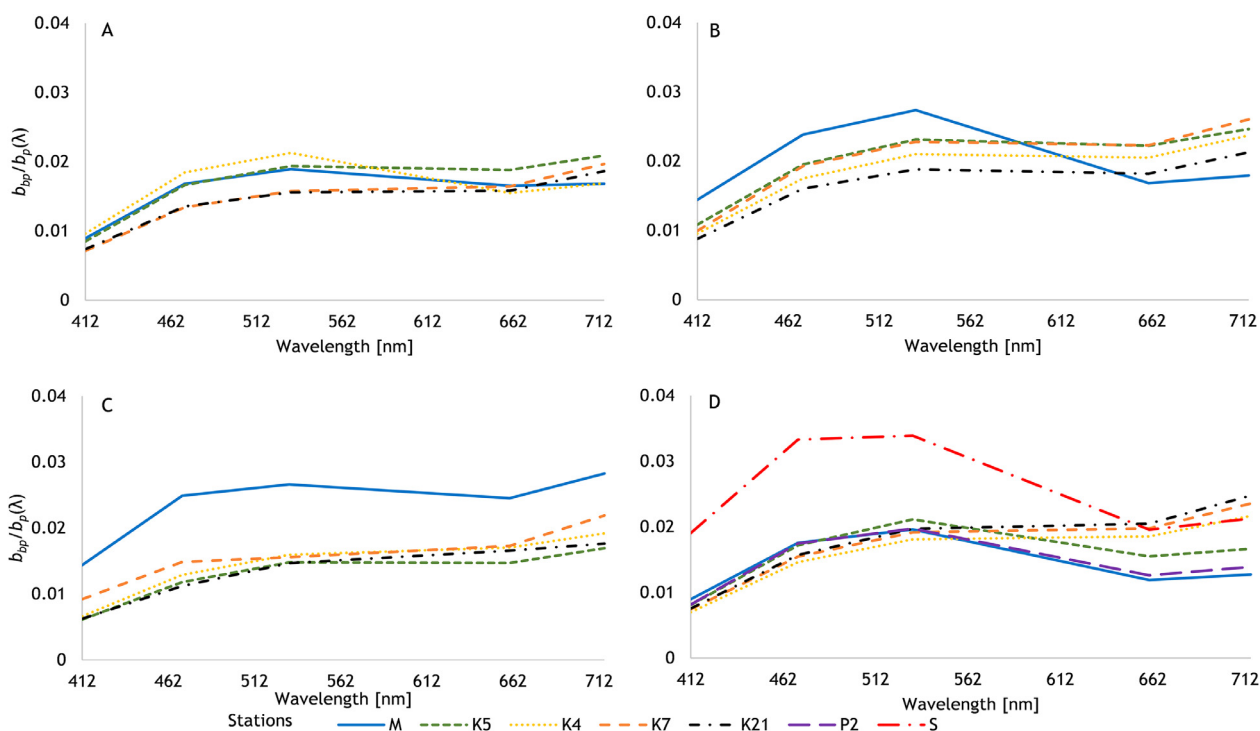


Figure 10 Spectral particulate backscattering ratios, $b_{bp}/b_p(\lambda)$, calculated for Pärnu Bay in (A) July 2017, (B) April 2018, (C) May 2018, and (D) August 2018.

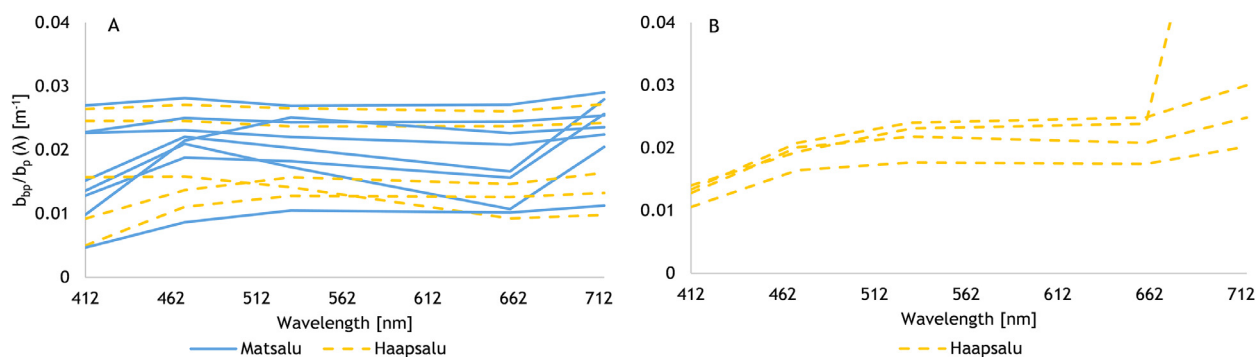


Figure 11 Particulate backscattering ratios, $b_{bp}/b_p(\lambda)$, calculated for Haapsalu and Matsalu bays in 2012, 2013, 2016, and 2018: (A) summer and (B) spring and autumn.

recorded in July 2017 (Figure 10A) were similar to each other. Generally, the highest $b_{bp}/b_p(\lambda)$ were observed close to the river mouth, in station M, except in July 2017 when the spectra recorded were in the similar range. The highest $b_{bp}/b_p(\lambda)$ of all the expeditions was observed at the river station S with the value of 0.034 in August 2018 (Figure 10D). The shapes of the spectra also differed. Arch-shaped spectra, with higher $b_{bp}/b_p(\lambda)$ at lower wavelengths between 470 and 532 nm, were observed at the river mouth station M in July 2017, April 2018 (Figure 10B), May 2018 (Figure 10C) and at the stations close to the river, M, K5, P2, in August 2018. The station S that was inside the river had a peak at 470 nm in August 2018.

The $b_{bp}/b_p(\lambda)$ obtained for Haapsalu, Matsalu, and Pärnu bays were mostly in the same range and varied between

0.01 and 0.1 (Figure 11). The highest ratio (0.1) was obtained in Haapsalu Bay in spring. The variability was more apparent during the summer period in both bays. Note that, the $b_{bp}/b_p(\lambda)$ spectra had quite diverse shapes. For some spectra, the peaks were at 470 and 712 nm while some others declined in values towards higher wavelengths. However, there were also $b_{bp}/b_p(\lambda)$ spectra which were stable at all wavelengths.

4.4. Variability of the sediment

Sediment samples were collected from Pärnu Bay during the August 2018 campaign. Our results showed (Figure 12) that the bottom sediment of stations S and M (inside the Pärnu River and close to its mouth, respectively) were composed of fine-grained anoxic black mud (size < 10 μm). The bot-

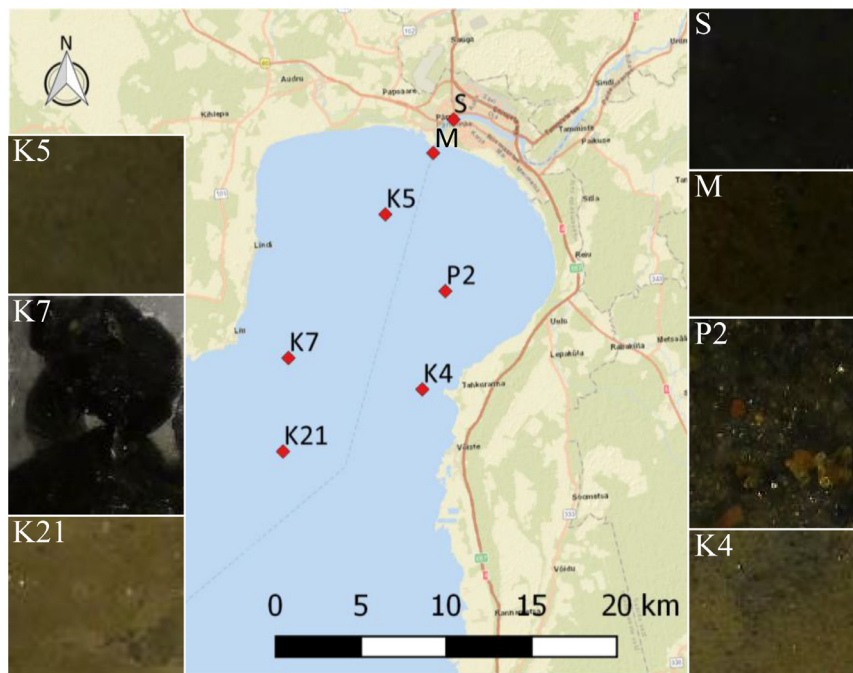


Figure 12 Map representing the bottom sediment types in Pärnu Bay after the extraction of sediments during the August 2018 campaign.

Table 2 Total volume concentrations (TVCs), Junge parameters (j), R^2 related to j , and median particle sizes (D50) derived from *in situ* LISST-100X measurements and disaggregated grain size measurements (DIGS) in August 2018.

Station	<i>In situ</i>				DIGS			
	TVC [$\mu\text{l L}^{-1}$]	j	D50 [μm]	R^2	TVC [$\mu\text{l L}^{-1}$]	j	D50 [μm]	R^2
Surface M	10.11	3.44	6.41	0.98	2.12	4.73	2.75	0.96
Surface K5	23.71	2.47	21.04	0.98	3.33	4.14	4.82	0.95
Surface K4	16.29	2.61	16.06	0.97	2.55	4.22	4.38	0.93
Surface K7	10.49	2.88	12.11	0.97	2.16	4.34	4.78	0.95
Surface K21	7.39	2.86	11.80	0.98	1.83	4.25	4.95	0.92
Surface P2	12.07	2.70	18.41	0.99	1.64	3.94	5.20	0.93
Surface S	5.66	3.16	7.25	0.98	1.30	4.69	3.43	0.95
Bottom S	26.28	2.78	14.74	0.99	2.69	4.86	3.06	0.96

tom was covered with brownish clay mud at stations K5 and K21, (size 2–50 μm). The south-eastern side of the bay was sandy, with coarse sand in the dredged sediment disposal area (station P2; size 20–200 μm) and fine sand farther in the south (station K4; size 5–200 μm). Gravels of the size of several cm were extracted from station K7. Additionally, large quantities of fine-grained (<63 μm) clay were observed at Pärnu Bay, and they dominated the resuspended sediments.

4.5. Particle size distributions

In situ PSD measurements were conducted in August 2018 after a couple of days of strong westerly wind ($>13 \text{ m s}^{-1}$) which caused a strong mixing of the water mass. The *in situ* PSDs and volume concentrations at the surface and in the bottom layers were similar. Therefore, only surface layer

measurements are shown in Figure 13, except for station S, where surface and bottom layers differed.

PSD spectra were observed logarithmically between 4 and 250 μm without the “rising tails” by using the frequency that shows what is the quantity (in %) of particles from total concentration in each size class. All spectra had a mode for particles $> 200 \mu\text{m}$ even above the muddy areas. Similarities were observed between the adjacent stations. For stations M and S (surface) in the river mouth and river, a flat mode was observed between 5 and 40 μm . Near the outer part of the bay at the stations K4, K7, and K21 the main mode was at 20–30 μm . For station K5, the high mode was at 20 μm and the frequency stayed at the high level (4–6 %) for the mode between 20 and 250 μm . The spectrum of the bottom of the river station S resembled the spectrum of station K5, having the flat mode between 20 and 250 μm .

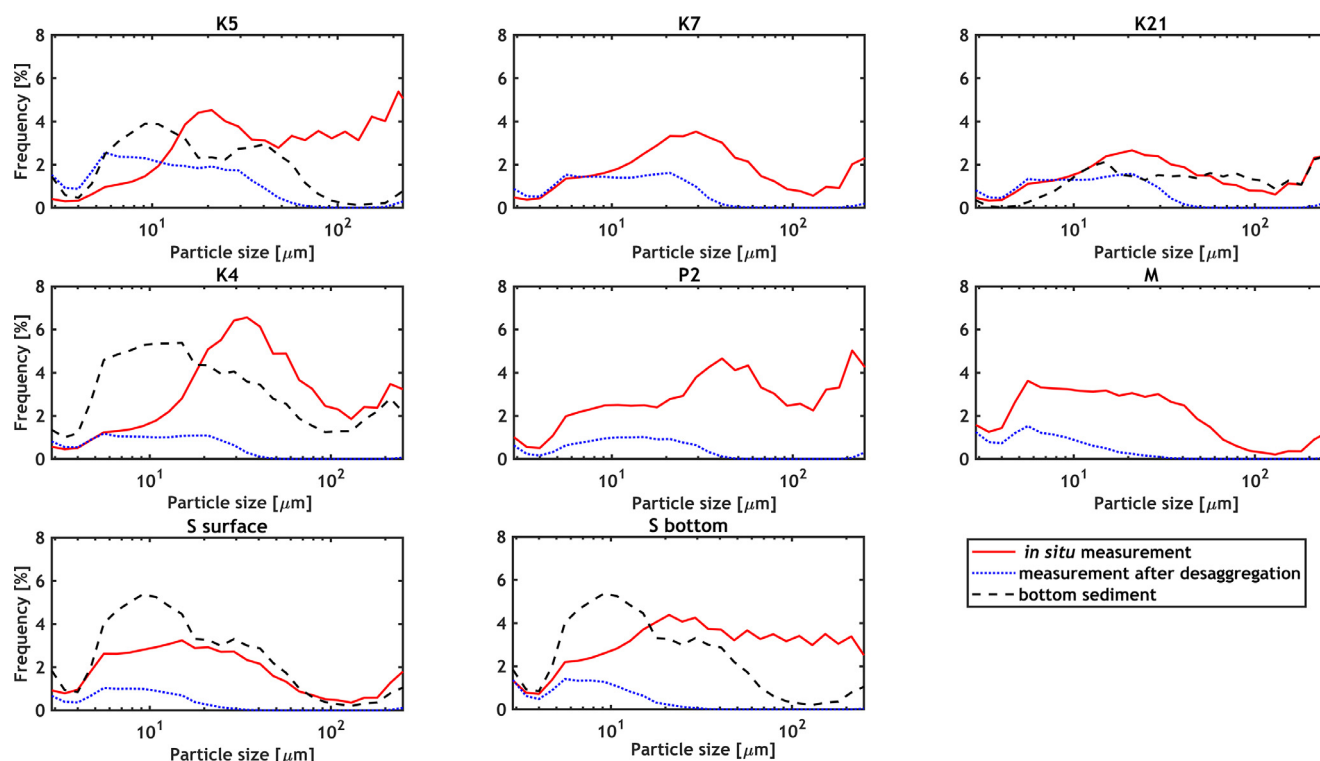


Figure 13 Particle size distributions (PSD) per size class in Pärnu Bay measured on August 28, 2018. Measurements were also carried out in the laboratory after sonication of the water samples and diluted bottom sediments.

The results of the laboratory experiment showed that after the treatment of the samples in the ultrasound bath, the obtained particle size spectra differed from the spectra measured *in situ* in all studied stations. Disaggregated particle spectra contained fewer particles than *in situ* measured spectra. In both, the river station S surface and bottom samples and the station M sample, the main mode was $<10 \mu\text{m}$. For the rest of the stations (K5, K4, K7, K21, and P2) a flat mode between 5 and 20–30 μm was observed. Note, that particles between 30 and 250 μm were absent for all the stations. For stations K5, K4, and S the bottom sediment samples PSD spectra, measured as the reference spectra of suspended sediments had a mode of around 10 μm . For the station K21, the PSD spectrum was wider, having a flat mode between 20 and 250 μm .

For the *in situ* data the correlation between j and D50 was good ($R^2 = 0.89$, $n=8$). Table 2 shows that R^2 were close to 1, which indicates that the particles size distribution followed Junge distribution. j ranged from 2.47 to 2.88 inside the bay. Higher values of j (3.16 and 3.44) were obtained at the surface stations – station S in the river and at station M in the river mouth, respectively. The same trend was observed also for the distribution of D50. Half of the particles of the surface stations M and S (river mouth and inside the river) were small (6.41 and 7.25 μm , respectively), whereas the D50 variability inside the bay was higher (11.80–21.04 μm). After the disaggregation by sonication, the values of j increased ~ 1.5 times, varying between 3.94 and 4.86. The maximum values of j were obtained at the river mouth station M and for the bottom sample at the river station S, 4.73 and 4.94, respectively.

The D50 values after disaggregation were very small (2.75–5.20 μm). The lowest D50 values were determined at the surface station M and the bottom sample of station S, 2.75 and 3.06, respectively. The D50 values obtained inside the bay were one and half times higher than near the river mouth and inside the river.

4.6. Relationships between water constituents

The correlations between parameters, SPM and SPIM/SPOM, SPOM and Chl-*a*, SPIM/SPOM and inherent optical properties (IOPs), were analysed (Table 3).

The correlation between SPIM and SPM was very good for the entire dataset, with $R^2 = 0.90$. The correlation coefficient between SPOM and SPM was $R^2 = 0.08$, although it increased when the data were divided according to seasons. The R^2 value between SPM and SPOM was 0.71 in July 2017 and April 2018 and 0.88 in May 2018. The correlation between SPOM and the Chl-*a* concentration was good in April 2018, with an R^2 value of 0.47, and very good in May 2018, with an R^2 value of 0.90. The correlation between SPIM and SPM was poor in July 2017, April 2018, and May 2018 ($R^2 < 0.37$) and very good in August 2018 ($R^2 = 0.98$). Very good correlations were observed also between the Chl-*a* and $a_{tot}(\lambda)$ and $b_p(\lambda)$ at 402 nm in April 2018, with R^2 values of 0.99. The relationship between b_{bp}/b_p at 412 nm and the Chl-*a* was consistently very good ($R^2 = 0.98$). The best correlations between the SPIM and b_{bp}/b_p were observed at 660 nm in August 2018, with a corresponding R^2 value of 0.63. The best correlations between b_{bp}/b_p and SPOM were

Table 3 Relationships between water constituents – suspended particulate matter (SPM), suspended particulate inorganic matter (SPIM), suspended particulate organic matter (SPOM), chl-*a* (chlorophyll-*a*) – and inherent optical properties – total absorption coefficient (a_{tot}), particulate absorption coefficient (a_p), particulate scattering coefficient (b_p), particulate backscattering ratio (b_{bp}/b_p) with some statistical parameters, root mean squared error (RMSE), normalised root mean squared error (NRMSE), mean bias error (MBE), normalised mean bias error (NMBE), R^2 . N shows the number of variables.

Correlation	Linear correlation	RMSE (*Unit)	NRMSE [%]	MBE (*Unit)	NMBE [%]	R^2	p-value	n
SPIM: SPM	SPM = 0.99 * SPIM + 4.17	1.08	0.13	-0.03	-0.004	0.99	<0.005	22
SPOM: SPM	SPM = 0.87 * SPOM + 7.29	5.90	0.69	-5.88	-0.69	0.08	0.21	22
SPOM: SPM (July 2017)	SPM = 1.06 * SPOM + 3.80	0.51	0.06	0.007	0.0008	0.71	0.07	5
SPOM: SPM (April 2018)	SPM = 0.91 * SPOM + 7.12	0.50	0.04	-0.008	-0.0006	0.71	0.07	5
SPOM: SPM (May 2018)	SPM = 0.78 * SPOM + 5.28	0.40	0.04	-0.02	-0.002	0.88	0.018	5
SPOM: Chl- <i>a</i> (April 2018)	Chl- <i>a</i> = 7.22 * SPOM - 11.71	6.53	0.26	0.03	0.001	0.47	0.20	5
SPOM: Chl- <i>a</i> (May 2018)	Chl- <i>a</i> = 1.36 * SPOM + 0.40	0.60	0.08	-0.03	-0.0004	0.91	0.012	5
SPIM: SPM (July 2017)	SPM = 1.13 * SPIM + 3.50	0.75	0.09	0.02	0.003	0.38	0.27	5
SPIM: SPM (April 2018)	SPM = 0.74 * SPIM + 6.78	0.85	0.07	-0.03	-0.002	0.16	0.50	5
SPIM: SPM (May 2018)	SPM = -0.66 * SPIM + 11.16	1.10	0.12	0.01	0.001	0.10	0.61	5
SPIM: SPM (August 2018)	SPM = 1.12 * SPIM + 2.34	0.52	0.04	0.006	0.0005	0.98	<0.005	7
a_{tot} at 402 nm: Chl- <i>a</i> (April 2018)	Chl- <i>a</i> = -2.91 * a_{tot} + 45.12	0.63	0.02	-0.007	-0.0002	1	<0.005	5
b_p at 402 nm: Chl- <i>a</i> (April 2018)	Chl- <i>a</i> = -3.91 * b_p + 45.70	0.94	0.02	-0.007	-0.0002	0.99	<0.005	5
SPIM: b_{bp}/b_p at 660 nm (August 2018)	$b_{bp}/b_p(660) = -0.001 * SPIM + 0.03$	0.002	0.11	-0.0003	-0.02	0.64	0.03	7
SPOM: b_{bp}/b_p at 660 nm (July 2017)	$b_{bp}/b_p(660) = -0.001 * SPOM + 0.02$	0.001	0.04	0.0001	0.005	0.67	0.09	5
SPOM: b_{bp}/b_p at 660 nm (May 2018)	$b_{bp}/b_p(660) = 0.002 * SPOM + 0.01$	0.002	0.12	-0.0001	-0.007	0.66	0.09	5
Chl- <i>a</i> : b_{bp}/b_p at 412 nm (April 2018)	$b_{bp}/b_p(412) = -0.0002 * Chl-a + 0.01$	0.0005	0.04	-0.0004	-0.04	0.98	0.001	5
a_p at 440 nm: Chl- <i>a</i> (April 2018)	Chl- <i>a</i> = -13.071 * a_p + 49.698	1.80	0.06	-0.001	-	0.96	0.003	5
a_p at 675 nm: Chl- <i>a</i> (April 2018)	Chl- <i>a</i> = -28.975 * a_p + 54.125	2.71	0.1	-0.0005	-	0.91	0.01	5
b_{bp}/b_p at 470 nm: b_{bp}/b_p at 660 nm (May 2018)	$b_{bp}/b_p(660) = 0.65 * b_{bp}/b_p(470) + 0.008$	0.001	0.05	-0.0001	-0.001	0.95	0.005	5
SPOM/Chl- <i>a</i> : b_{bp}/b_p at 660 nm (April 2018)	$b_{bp}/b_p(660) = -0.001 * SPOM/Chl-a + 0.02$	0.002	0.08	-0.0001	-0.002	0.42	0.24	5

* Unit SPM = g m⁻³, Chl-*a* = mg m⁻³, $b_{bp}/b_p(\lambda)$ = unitless

observed in July 2017 at 660 nm ($R^2 = 0.67$) and in May 2018 at 660 nm ($R^2 = 0.66$). a_p at 440 nm representing the blue part of the spectra and at 675 nm representing the red part of the spectra were correlated with SPM and Chl-*a*. The best correlations ($R^2 = 0.96$ and 0.92) were observed between Chl-*a* and a_p at 440 and 675 nm, respectively, in April 2018. The R^2 between SPM and a_p at both wavelengths were slightly higher (0.51–0.6) than between Chl-*a* and a_p (0.39–0.49) for other expeditions. No correlation was found in July 2017 for either of the parameters. The best correlation between the SPOM/Chl-*a* ratio and b_{bp}/b_p at 660 nm was observed in April 2018, when $R^2 = 0.42$. For the other expeditions, the correlation was close to zero.

5. Discussion

5.1. Spatio-temporal variability of water constituents' characteristics

5.1.1. Variability of the SPM and Chl-*a* concentrations

Pärnu Bay is a very dynamic waterbody, that is influenced by the resuspension of the bottom sediment due to wind and waves as well as by the inflow of the Pärnu River. The resuspended water constituents, which could vary in type and amount within short distances and time intervals, have a strong impact on the light penetration in the water col-

umn and thus also on the water quality, ecosystems, and remote sensing signal. Thus, their characteristics such as the variability of concentrations and correlations need to be investigated in detail. For that aim, we conducted four campaigns in the bay and collected samples from five to seven stations during each campaign covering the centre part of the bay, the edges, the offshore part and the outflow of the Pärnu River. These campaigns were conducted during variable conditions and the obtained results were compared to those measured during previous campaigns in the close-by Haapsalu and Matsalu bays. The correlations between different parameters indicate which are the dominant substances in the water. The suspended particles in the water are phytoplankton if SPM and Chl-*a* are in good correlation. Inversely, if the correlations are not good, the suspended particles are mostly of mineral origin. The SPM concentrations were the highest after strong wind events and at the river mouth station M for all campaigns, indicating that both, the Pärnu River discharge and wind contributed to high concentrations of SPM in the water column. [Martinez-Vicente et al. \(2010\)](#) tested the correlations between SPM and SPOM/SPIM/Chl-*a* in the English Channel and found that the SPM and SPOM correlations were weak due to the seasonal variability of the constituents of SPOM but the relationships of the parameters increased after being analysed separately for each season. Our results showed that in Pärnu Bay, suspended particles were mainly dominated by mineral particles. There was a poor correlation between the entire dataset of SPM and SPOM. However, when the relationships between SPM and SPOM were studied separately depending on the campaign, they improved, with R^2 values reaching 0.70, indicating seasonal dependency. There were three local phytoplankton blooms during our study. In April 2018, the Chl-*a* concentrations inside the bay were around 30 mg m^{-3} except in the Pärnu River mouth, where the Pärnu River exported large quantities of CDOM into the bay, causing low amount of phytoplankton. The river inflow was insignificant in July 2017 ($12 \text{ m}^3 \text{ s}^{-1}$) and thus, only slightly higher SPM concentrations were observed at station M close to the river mouth. Simultaneously, the Chl-*a* concentrations were three times higher at station M than inside the bay, referring to the local phytoplankton bloom. For Haapsalu and Matsalu bays the Chl-*a* concentrations were very low except at one of the Haapsalu bays' stations in July 2013 (22.4 mg m^{-3}) indicating a small local bloom. High SPM concentrations ($12\text{--}15 \text{ g m}^{-3}$) with a bigger fraction of mineral particles were induced by a stronger wind phenomenon in July 2018.

During the four campaigns in Pärnu Bay, the SPM concentrations varied between 4.25 and 19.6 g m^{-3} . We also studied previously published SPM concentrations, to gain better knowledge to assess the dynamics of SPM in Pärnu Bay. [Paavel et al. \(2011\)](#) demonstrated that the SPM concentrations varied between 3.7 and 49 g m^{-3} in the summer of 2006 and 2007. The highest concentrations were partially correlated with the peat export from the harbour. In comparison, the SPM concentrations in 1991 ranged from 11 to 38 g m^{-3} , and thus, they remained slightly lower than in the summer of 2006 and 2007 but at the same time, they stayed much higher than those which were observed during the present study. The average SPM concentrations measured in Pärnu Bay from 2008 to 2010 had similar variations to those which were measured in 2017 and 2018 (SPM varied

between 9.4 and 24.3 g m^{-3}). The results indicated that the SPM concentrations generally remained the same during the past years, except during peat transport (with many spills). However, the SPM concentrations (up to 90 g m^{-3}) at the near-shore stations, which differ from traditional monitoring stations, were measured from April to November 2012 ([Lauringson, 2013](#)). Such values were neither observed during our fieldwork nor during monitoring in deeper water. These higher concentrations were probably due to the shallowness of the water where particles could not resettle because of the intense resuspension. However, we should keep in mind that, it is difficult to get an overview of the dynamics with *in situ* data only.

The conditions observed during *in situ* measurements in Pärnu Bay were compared with our previous work. In [Uudeberg et al. \(2020\)](#) water type classification-based approach was applied to Sentinel-3 sensor Ocean and Land Colour Instrument (OLCI) cloud and ice-free images of Pärnu Bay from 2017 to 2018 after the processing with C2RCC atmospheric correction processor. For that approach, 5 water-type classes were created (Clear, Moderate, Turbid, Very Turbid, Brown) based on the reflectance spectra features. After testing diverse SPM algorithms, the best working algorithm was selected for each water-type class. A suitable water-type class was assigned to each satellite image water pixel and was processed with the selected algorithm. The remote sensing results match the concentrations observed during our fieldwork campaigns. Note, that three phenomena were identified using satellite data ([Figure 14](#)) ([Randla et al., 2018](#)). Firstly, during calm conditions, the SPM concentrations were the highest near the shore ([Figure 14A,C](#)). Secondly, the higher concentrations of suspended matter close to the river mouth could indicate the influence of the river ([Figure 14B](#)). However, the rain and snowmelt bring CDOM rather than SPM into the bay. Therefore, before the SPM can be properly valued, the CDOM high absorbing influence needs to diminish. Thirdly, storm periods could be characterised by very high SPM concentrations for the entire bay ([Uudeberg et al., 2019](#)). [Figure 14D–E](#) shows that during and after the storm the conditions could change very fast. In our case, the SPM concentrations decreased significantly within days.

Many episodes with stronger wind occur throughout the year in Pärnu Bay, causing the resuspension of sediments from the bottom. The amount of suspended particles in the water column is also influenced by the Pärnu River, which has a higher discharge after the rain and snowmelt periods. These factors reduce water transparency. The variations of the quantities of suspended matter strongly depend on the weather conditions but also on the type of particles present in the bottom of the bay and in the river flow.

5.1.2. Variability of inherent optical properties

The study of IOPs is important to see what type of particles are in suspension in the water column and how are they influencing the underwater light field. The IOPs and mass-specific IOPs, such as the $a_p(\lambda)$, $b_p^*(\lambda)$, and $b_{sp}^*(\lambda)$, tended to vary spatially and temporarily.

The good correlations between the Chl-*a* concentrations and $b_p(\lambda)$ and $a_{tot}(\lambda)$ in April 2018 indicate the high absorption and scattering by phytoplankton, confirming that the main source affecting the light field during that pe-

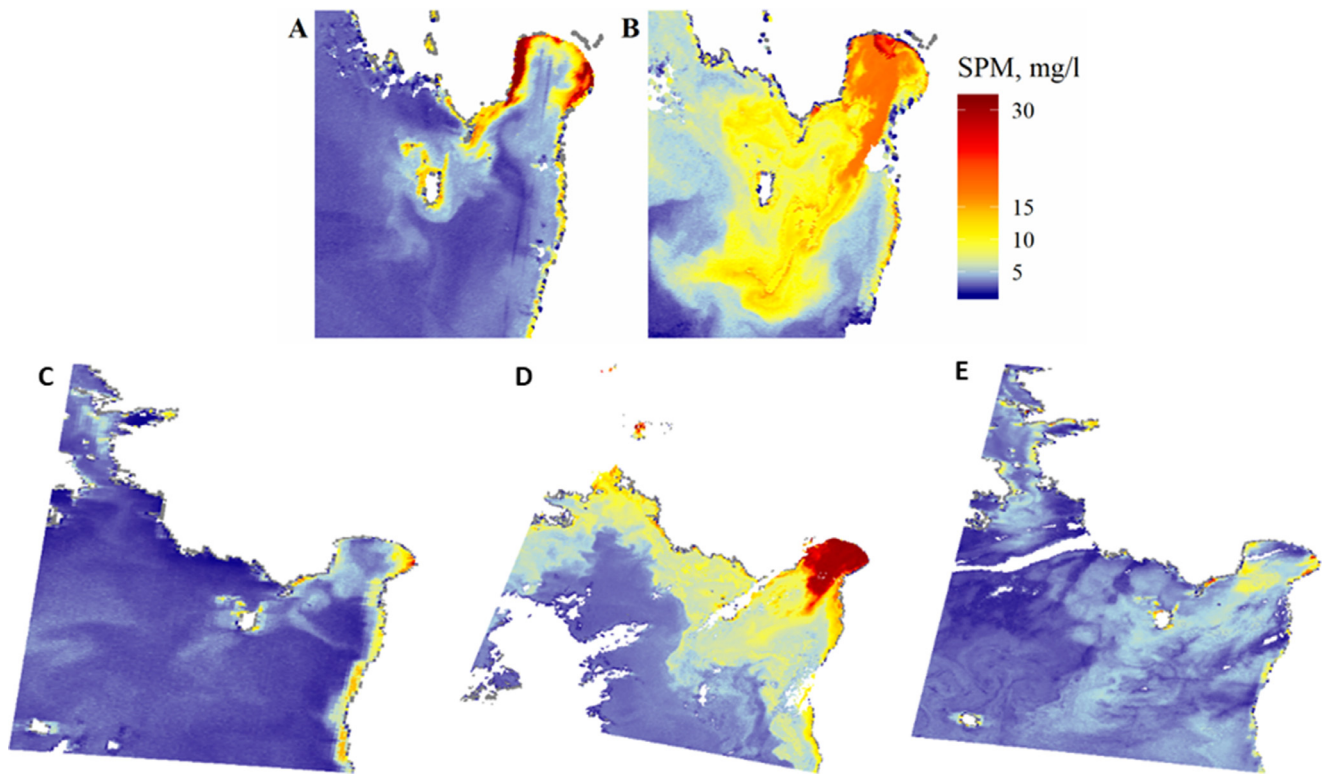


Figure 14 Suspended particulate matter maps of Pärnu Bay derived from Sentinel-3 OLCI L1 images processed with water-type based approach. A) Calm conditions on 31.05.2018. B) River outflow and stronger wind conditions on 17.09.2017. C) Calm conditions six days prior to the storm on 17.06.2018. D) One day after the storm on 23.06.2018. E) Six days after the storm when the situation of SPM has returned to the state of before the storm on 28.06.2018.

riod was phytoplankton spring bloom inside the bay. The $a_p(\lambda)$ were mostly the highest at the river mouth station M, indicating that the light-absorbing particles were brought into the bay mainly by the Pärnu River. The high variability of $a_p(\lambda)$ amongst all expeditions, especially in August 2018 was caused by the various SPM concentrations and compositions. The correlations between $a_p(440\text{ nm})$ and SPM/Chl-*a*, $a_p(675\text{ nm})$ and SPM/Chl-*a* showed that in May and August 2018, SPM was dominating the particulate absorption. Inversely, in April 2018, the high amount of algal particles was present, forming a phytoplankton bloom. The visible peaks at 675 nm on the $a_p(\lambda)$ spectra indicated also the high absorption by phytoplankton. This was also the case for station M at the river mouth in July 2017. The steep slopes visible on the blue part of the $a_p(\lambda)$ spectra at station M in April and May 2018 were induced by the dominance of the absorption by CDOM. This could be assumed because the CDOM absorption was high and similar to measured and corrected absorption at 402 to 406 nm, then diminished fast. The real values of a_{CDOM} at this station were 12.65 and 14.08 m^{-1} , respectively, caused by high river inflow bringing high quantities of CDOM into Pärnu Bay. The S_{CDOM} values were lower and the similar level for all measurements in the river mouth station M and the river station S indicating the same origin of the CDOM. The values increased towards offshore. Our S_{CDOM} values coincided with previous studies. For example, Harvey et al. (2015) showed that the values of S_{CDOM} between 0.015 and 0.017 nm^{-1} are typical for the brackish Baltic Sea. The balance between

terrestrial and autochthone CDOM is leaning in favour of the latter as we move away from the inner bay, as expected (Kowalczyk, 1999).

The R^2 of correlations between SPIM and SPM, SPIM and $b_{bp}/b_p(660)$ were high in August (0.98 and 0.64, respectively), indicating that during a wind event suspended particles were dominated by the mineral fraction, coming from the resuspension of bottom sediments. For all campaigns, the coefficients of IOPs and concentrations of the substances were higher near the shore and diminished towards the outer part of the bay. This could be the result of the gradient from shallow nearshore water to deeper offshore water where the influence of the wind on the bottom sediments and the influence of the Pärnu River are negligible.

The highest $b_{bp}^*(\lambda)$ values were observed near the river mouth during all expeditions, showing that not only phytoplankton but also the SPIM affected the backscattering in these areas. The $b_p^*(\lambda)$ spectra followed the same tendencies. Both parameters had the lowest values inside the bay in April and May 2018 indicating that SPIM had a lower impact on the scattering and backscattering than phytoplankton. Arch-shaped $b_{bp}^*(\lambda)$ spectra with higher $b_{bp}^*(\lambda)$ at lower wavelengths between 470 and 532 nm were observed, mostly close to the river mouth in Pärnu Bay. Kutser et al. (2001) showed with model simulations that such shapes of backscattering are possible and then measured similar spectral shapes in lake Tuusula. They were caused by high quantities of cyanobacteria. This contradicts our results in some cases. For example, the Chl-*a* concen-

trations were lower and SPOM concentrations were significantly lower than the SPIM concentrations in August 2018. However, the Chl-*a*, SPOM concentrations, and CDOM absorption were higher close to the river mouth than at the outer part of the bay. Insufficient correction of the effects of high CDOM values on backscattering spectra could be responsible for the rounded shapes of the spectra. The IOPs of Pärnu Bay and those obtained for Haapsalu and Matsalu bays showed the same tendencies. The $a_p(\lambda)$, $b_p^*(\lambda)$, and $b_{bp}^*(\lambda)$ were low at Haapsalu Bay in spring and autumn compared to those in summer, indicating low Chl-*a* and SPM concentrations. This could be caused by the fact that Haapsalu Bay is a closed environment with little water exchange and movement. Neukermans et al. (2012) studied the $b_{bp}^*(\lambda)$ at 650 nm in coastal and offshore areas of Europe and French Guyana, where $b_{bp}^*(\lambda)$ varied between 0.04 and 0.014 m² g⁻¹. Their results showed that waters dominated by mineral particles backscattered up to 2.4 times more per unit dry mass ($b_{bp}^*(\lambda) = 0.012$ m² g⁻¹) than waters dominated by organic particles ($b_{bp}^*(\lambda) = 0.005$ m² g⁻¹). The organic particle dominance was not that evident in Pärnu Bay, because in the areas where mineral particles were not visibly dominating the SPM, the concentrations of SPIM and SPOM were rather equal. The closest wavelength from Pärnu Bay to the wavelength used by Neukermans was 660 nm where the $b_{bp}^*(\lambda)$ varied between 0.003 and 0.013 m² g⁻¹. The lowest values, less than 0.005 m² g⁻¹ were observed in April and May 2018. The $b_{bp}^*(\lambda)$ values were higher than 0.005 m² g⁻¹ in July 2017 and August 2018. The proportion of organic matter was similar to the proportion of the mineral matter in April and May. The proportion of mineral matter was higher than organic matter in July and August. Therefore, our results were in accordance with the Neukermans study. The $b_{bp}/b_p(\lambda)$ were higher in autumn and spring, which is probably due to the variable origin of the particles or size distribution effect. The increase in the phytoplankton amount and the SPM resuspension due to the shallow bottom or water level decrease may have caused the higher variability at Matsalu Bay during the summer. The presence of phytoplankton and organic matter and their impact on light backscattering may have led to the arch-shape of the $b_{bp}^*(\lambda)$ spectra recorded at Haapsalu and Matsalu bays.

5.1.3. Variability of the particulate backscattering ratio

In our study area, b_{bp}/b_p were ranging from 0.01 to 0.027 at 660 nm with the minimum and maximum $b_{bp}/b_p(\lambda)$ over all wavelengths being from 0.005 to 0.031. Twardowski et al. (2001) modelled the $b_{bp}/b_p(\lambda)$ values and found that they stayed between 0.002 and 0.03 under natural oceanic conditions. The highest $b_{bp}/b_p(\lambda)$ of Estonian coastal waters were observed at 470 or 532 nm, giving the spectra an arch-shape, at the river mouth stations or river-close stations (up to 0.031). McKee and Cunningham (2005) observed the values of $b_{bp}/b_p(\lambda)$ between 0.01 and 0.04. They had plotted the b_{bp}/b_p at 470 against b_{bp}/b_p at 676 nm and found that $b_{bp}/b_p(\lambda)$ were higher at lower wavelengths. The $b_{bp}/b_p(\lambda)$ that was higher in the blue than in the red showed that the scattering phase function is generally wavelength dependent. In Pärnu Bay, the correlation was good only in May, with $R^2 = 0.96$ and at the individual stations (M, S). Considering the findings of

McKee and Cunningham (2005), the $b_{bp}/b_p(\lambda)$ should have been higher at lower wavelengths in May, but the spectra shapes of our results showed that it was not the case. The observations from other expeditions, having very low R^2 , contribute to this understanding. Snyder et al. (2008) measured the b_{bp}/b_p at 550 nm and it varied between 0.005 and 0.06 at the US coast. He concluded that the wavelength dependency of $b_{bp}/b_p(\lambda)$ varied from site to site and within each site. We observed that there was high variability of $b_{bp}/b_p(\lambda)$ between Pärnu, Haapsalu and Matsalu bays with some dependency in Haapsalu and Matsalu bays where the spectra clearly decreased with increasing wavelength.

5.2. Origin and characteristics of SPM

5.2.1. Composition of the bottom sediment

Sediments are resuspended from the sea bottom by wave action and currents. Fine sediments remain in the water column longer than large particles which are heavier and resettle fast. Therefore, it is important to determine the composition of the bottom sediment.

The bottom sediment samples were extracted only in Pärnu Bay and the results were in accordance with previous research (Hendrikson and Ko, 2016). They showed that the bottom sediment in Pärnu Bay is mainly composed of a fine layer of sand and aleurite (0.004–0.063 mm), which was deposited on varved clay that formed under-ice lake conditions in front of a retreating glacier. These fine particles can be easily resuspended by waves.

The previous research shows that the bottom sediments at Haapsalu and Matsalu bays are similar to those at Pärnu Bay. Matsalu Bay comprises high quantities of medium-grained and fine-grained sand in the outer and nearshore parts of the bay (Lutt and Kask, 1980). A tongue of fine-grained and coarse-grained siltstone extends from the Kasari River mouth to the centre of the basin. In addition, morainic sediment has been found in a small area on the southern coast of Matsalu Bay and small quantities of rocks are located near the coast. The bottom sediment at Haapsalu Bay also has a glacial origin (Jõelett, 2016). Varved clays are covered by aleurite mud and sand. This indicates that the suspended particles in all three bays have the same origin and similar properties. In the satellite images of Pärnu Bay, resuspension can be observed near the coast due to the shallow bottom, presence of clay, and wave dynamics.

If the bottom composition is known, then we can derive the types of particles resuspended in the water column. The properties of these particles affect the underwater light field and thus were studied in detail.

5.2.2. Origin of the particles

The measurements of SPM showed that mostly mineral fraction was dominating the SPM in Pärnu, Haapsalu and Matsalu bays (Figure 3). Theoretically, the values of $b_{bp}/b_p(\lambda)$ can be used as approximations to the origin of the particles. It has been reported that the particles are dominated by organic matter and minerals if $b_{bp}/b_p(\lambda)$ is ~ 0.005 and ~ 0.02 , respectively (Tao et al., 2018). $b_{bp}/b_p(\lambda)$ were between 0.007 at 412 nm and 0.031 at 470 nm in Pärnu Bay in August 2018. These observations were supported by the different SPIM and SPOM concentrations of the water samples collected

during the August campaign. The SPIM concentrations were higher than the SPOM concentrations. However, the analyses of the water samples did not confirm these trends for all samples because organic and mineral matter sometimes was present at a 50:50 ratio. Therefore, the correlations between $b_{bp}/b_p(\lambda)$ and the SPIM and SPOM concentrations were plotted to determine which matter affects the light scattering the most. The best correlations for SPIM were in August 2018. Probably, this was due to the higher mineral fraction because of the sediment resuspension by the storm. For SPOM, the highest correlations were in July 2017 and May 2018, where the organic fraction was higher than SPIM. The best wavelength for these correlations was 660 nm. The best correlation between b_{bp}/b_p at 412 nm and the Chl-*a* concentrations was obtained in April 2018 when there was a phytoplankton bloom.

The seasonal correlations were compared with those obtained in a similar, larger-scale study in the Baltic Sea where [Simis et al. \(2017\)](#) analysed the seasonality of the inherent optical properties. They discovered that season-specific correlations exist between $b_{bp}/b_p(532)$ and SPM. The weakest correlations were obtained for the SPIM, suggesting the absence of mineral matter. Their results differ from ours ([Section 4.6](#)). An important factor shaping the results is the measurement location. Their measurements were conducted in the open sea where the concentration of SPIM is usually negligible and phytoplankton and its degradation products dominate in the SPM. There were periods where phytoplankton dominated in the SPM, but mostly mineral particles transported by rivers, currents or resuspended by waves were dominating in the SPM. Therefore, the results obtained in the open sea and near the coast give different outcomes.

[Snyder et al. \(2008\)](#) plotted the SPOM/Chl-*a* ratio against the b_{bp}/b_p at 550 nm. They did not find correlations between these parameters. We plotted the same ratio against b_{bp}/b_p at the closest wavelength, 532 nm. The correlations weren't good except in April when $R^2 = 0.42$. We could assume that in April, mostly organic particles (phytoplankton) in SPM were dominating the backscattering.

5.2.3. Particles size distributions in Pärnu Bay

Parameter $b_{bp}/b_p(\lambda)$ also depends on the particle size. The smaller the particle size is, the larger $b_{bp}/b_p(\lambda)$ and vice versa. In our study, the b_{bp}/b_p spectra exhibit high values at 595 nm (>0.02) and the best correlations with SPM were obtained at 660 nm. In August, mineral matter dominated the suspended particles. The size of the particles in Pärnu Bay in August, ranged from 4 to 250 μm . After the disaggregation experiment, only particles with sizes ranging from 4 to 30 μm remained in the solution. This shows that fine particles were resuspended by waves but later agglomerated into bigger aggregates.

Aggregation phenomena in the brackish waters of the Baltic Sea have not been studied. Previous studies showed that flocculation occurs in areas with high salinity gradients at the mouths of large rivers ([Many et al., 2016](#); [Wolanski and Gibbst, 1995](#)), in the Arctic due to the salinity gradient and high SPM concentrations ([Meslard et al., 2018](#)), and in areas influenced by organic matter ([Lee et al., 2019](#)). We observed that particles may aggregate in areas with very low salinity and low concentrations of organic matter. The

aggregates could not have been transported by the organic-rich Pärnu River because in the river the particles were small.

As shown above, fine particles agglomerated into bigger aggregates with random shapes. [Figure 13](#) indicates the percentage of particles of each size class before and after disaggregation. Based on the D50 values before sonication, half of the particles were smaller than 6–21 μm , implying the presence of large numbers of small particles and higher variability of particles of bigger size classes. The D50 values after sonication were significantly smaller (3–5 μm), showing that bigger particles/aggregates disaggregated into smaller particles. The diminishing volume concentrations of the solution after sonication may be due to the destruction of plankton colonies by the ultrasound treatment ([Holm et al., 2008](#)). The presence of large phytoplankton cells could have led to the measuring of “rising tails” before and after the sonication.

The Junge distribution shows the partition of aggregates and small particles in areas with SPM dominated by mineral particles. We could use this approach because mineral particles dominated the water in August 2018 and the fitting of the PSD slopes had correlations close to 1. [Bader \(1970\)](#) showed that a high distribution ($j \sim 4$) indicates a high proportion of small particles, a low distribution ($j \sim 2.4$) indicates a high proportion of large particles, and $j \sim 3$ represents a “normal” distribution. In this study, the j values ranged from 2.5 to 2.9 inside the bay, indicating a high proportion of large particles or aggregates approaching a “normal” distribution. Inside the river, j was 3.16 and 3.44, representing a “normal” distribution. After the sonication, j varied between 3.94 and 4.86, representing a high proportion of small particles and confirming the disaggregation. Most of the particles in the reference PSD spectra of the bottom sediments were $<10 \mu\text{m}$, confirming this hypothesis. The large flocs have diverse complex shapes, sizes ($<250 \mu\text{m}$), densities, as shown in previous studies ([Many et al., 2016](#); [Spencer et al., 2021](#), etc). Single particles have a small uniform size ($<10 \mu\text{m}$) and their shape is close to a circle. This means that larger flocs have a more complex effect on the light scattering and backscattering than single particles.

6. Conclusions

The aim of this paper was to study the dynamics of particle concentrations, the origin of particles, and variability of optical properties such as $a_p(\lambda)$, $b_p^*(\lambda)$, $b_{bp}^*(\lambda)$, and $b_{bp}/b_p(\lambda)$ as well as the particle size distributions of the suspended particulate matter in Estonian coastal areas to determine how these parameters interact with each other. For this purpose, four campaigns were conducted in the spring and summer of 2017–2018 under different conditions (calm/storm, phytoplankton bloom presence/absence, coastal/offshore area of the bay) in Pärnu Bay. Data from previous optical measurements from Haapsalu and Matsalu Bays (7 campaigns) were analysed together with Pärnu Bay data. The concentrations and optical characteristics of the SPM varied significantly both in time and space in Pärnu Bay and other areas. A particle aggregation phenomenon was observed in the brackish water of Pärnu Bay. It has not been

seen previously. The parameter $b_{bp}/b_p(\lambda)$ correlated with the particle origin and reflected the effects of SPIM and SPOM on the backscattering of light. The SPOM and phytoplankton clearly dominated the backscattering in the calm conditions and during the phytoplankton bloom in spring, while SPIM clearly dominated the backscattering during the August storm. In remote sensing algorithms, $b_{bp}/b_p(\lambda)$ is often considered to be constant because backscattering measurements are rather scarce. Our results show that $b_{bp}/b_p(\lambda)$ is wavelength-dependent, particle size-, and origin-dependent and cannot be considered as constant. This indicates that the situation in coastal waters is more complex and the particle properties and scattering phenomena must be considered to generate better remote sensing algorithms for complex waters.

Declaration of competing interest

The authors declare that they have no known competing financial interests or personal relationships that could have appeared to influence the work reported in this paper.

Acknowledgments

We thank the Tartu Observatory and Estonian Marine Institute water remote sensing groups for collecting the data. This research was supported by the European Union's Horizon 2020 Research and Innovation Program (grant number 730066) and the Estonian Research Council (grant numbers PUTJD719, PRG302, and PSG 10).

Supplementary materials

Supplementary material associated with this article can be found, in the online version, at <https://doi.org/10.1016/j.oceano.2022.06.006>.

References

- Aas, E., Høkedal, J., Sørensen, K., 2005. Spectral backscattering coefficient in coastal waters. *Int. J. Remote Sens.* 26, 331–343. <https://doi.org/10.1080/01431160410001720324>
- Agrawal, Y.C., Pottsmith, H.C., 2000. Instruments for particle size and settling velocity observations in sediment transport. *Mar. Geol.* 168, 89–114. [https://doi.org/10.1016/S0025-3227\(00\)00044-X](https://doi.org/10.1016/S0025-3227(00)00044-X)
- Babin, M., Morel, A., Fournier-Sicre, V., Fell, F., Stramski, D., 2003. Light scattering properties of marine particles in coastal and open ocean waters as related to the particle mass concentration. *Limnol. Oceanogr.* 48, 843–859. <https://doi.org/10.4319/lo.2003.48.2.0843>
- Bader, H., 1970. The hyperbolic distribution of particle sizes. *J. Geophys. Res.* 75, 2822–2830. <https://doi.org/10.1029/JC075i015p02822>
- Berthon, J.F., Zibordi, G., 2010. Optically black waters in the northern Baltic Sea. *Geophys. Res. Lett.* 37, 1–6. <https://doi.org/10.1029/2010GL043227>
- Bianchi, T.S., Engelhaupt, E., Westman, P., Andrén, T., Rølf, C., Elmgren, R., 2000. Cyanobacterial blooms in the Baltic Sea:

- Natural or human-induced? *Limnol. Oceanogr.* 45, 716–726. <https://doi.org/10.4319/lo.2000.45.3.0716>
- Boss, E., Pegau, W.S., 2001. Relationship of light scattering at an angle in the backward direction to the backscattering coefficient. *Appl. Opt.* 40, 5503. <https://doi.org/10.1364/AO.40.005503>
- Boss, E., Pegau, W.S., Lee, M., Twardowski, M., Shybanov, E., Korotaev, G., 2004. Particulate backscattering ratio at LEO 15 and its use to study particle composition and distribution. *J. Geophys. Res.* 109, 1–10. <https://doi.org/10.1029/2002JC001514>
- Buonassissi, C.J., Dierssen, H.M., 2010. A regional comparison of particle size distributions and the power law approximation in oceanic and estuarine surface waters. *J. Geophys. Res. Ocean.* 115, 1–12. <https://doi.org/10.1029/2010JC006256>
- Callede, J., Kosuth, P., Loup, J., Guimarães, S., Callede, J., 2009. Discharge determination by Acoustic Doppler Current Profilers (ADCP): a moving bottom error correction method and its application on the River Amazon at Óbidos correction method and its application on the River. *Hydrolog. Sci. J.* 45 (6), 911–924. <https://doi.org/10.1080/0262666009492392>
- Chami, M., Shybanov, E.B., Churilova, T.Y., Khomenko, G.A., Lee, M.E., Martynov, O.V., Berseneva, G.A., Korotaev, G.K., 2005. Optical properties of the particles in the Crimea coastal waters (Black Sea). *J. Geophys. Res.* 110, 1–17. <https://doi.org/10.1029/2005JC003008>
- Darecki, M., Weeks, A., Sagan, S., Kowalczyk, P., Kaczmarek, S., 2003. Optical characteristics of two contrasting Case 2 waters and their influence on remote sensing algorithms. *Cont. Shelf Res.* 23, 237–250. [https://doi.org/10.1016/S0278-4343\(02\)00222-4](https://doi.org/10.1016/S0278-4343(02)00222-4)
- Davies, E.J., Nepstad, R., 2017. In situ characterisation of complex suspended particulates surrounding an active submarine tailings placement site in a Norwegian fjord. *Reg. Stud. Mar. Sci.* 16, 198–207. <https://doi.org/10.1016/j.risma.2017.09.008>
- EEA, 2015. The European environment - state and outlook 2015: synthesis report. Copenhagen. <https://doi.org/10.2800/944899>
- ESS, 1993. ESS Method 340.2. Total suspended solids, mass balance (dried at 103–105° C), volatile suspended solids (Ignited at 550°C). *Environ. Sci. Sect.* 189–192.
- Faé, G.S., Montes, F., Bazilevskaya, E., Añó, R.M., Kemanian, A.R., 2019. Making Soil Particle Size Analysis by Laser Diffraction Compatible with Standard Soil Texture Determination Methods. *Soil Sci. Soc. Am. J.* 83, 1244–1252. <https://doi.org/10.2136/sssaj2018.10.0385>
- Filizola, N., Guyot, J.L., 2009. Suspended sediment yields in the Amazon basin: an assessment using the Brazilian national data set 3215, 3207–3215. <https://doi.org/10.1002/hyp>
- Forget, P., Ouillon, S., 1998. Surface suspended matter off the Rhone river mouth from visible satellite imagery. *Oceanol. Acta* 21, 739–749. [https://doi.org/10.1016/S0399-1784\(99\)80003-6](https://doi.org/10.1016/S0399-1784(99)80003-6)
- Freda, W., 2012. Spectral dependence of the correlation between the backscattering coefficient and the volume scattering function measured in the southern Baltic Sea. *Oceanologia* 54 (3), 355–367. <https://doi.org/10.5697/oc.54-3.355>
- Gee, G.W., Or, D., 2002. 2.4 Particle-Size Analysis. John Wiley & Sons, Ltd, 255–293. <https://doi.org/10.2136/sssabookser5.4.c12>
- Gordon, H.R., Brown, O.B., Jacobs, M.M., 1975. Computed Relationships Between the Inherent and Apparent Optical Properties of a Flat Homogeneous Ocean. *Appl. Opt.* 14, 417. <https://doi.org/10.1364/ao.14.000417>
- Harvey, E.T., Kratzer, S., Andersson, A., 2015. Relationships between colored dissolved organic matter and dissolved organic carbon in different coastal gradients of the Baltic Sea. *Ambio* 44, 392–401. <https://doi.org/10.1007/s13280-015-0658-4>
- Hecht, T., van der Lingen, C.D., 1992. Turbidity-induced changes in feeding strategies of fish in estuaries. *South African J. Zool.* 27, 95–107. <https://doi.org/10.1080/02541858.1992.11448269>

- Hendrikson&Ko, 2016. Pärnu maakonnaga piirneva mereala maakonnaplaneering II köide. Pärnu.
- Holm, E.R., Stamper, D.M., Brizzolara, R.A., Barnes, L., Deamer, N., Burkholder, J.A.M., 2008. Sonication of bacteria, phytoplankton and zooplankton: Application to treatment of ballast water. *Mar. Pollut. Bull.* 56, 1201–1208. <https://doi.org/10.1016/j.marpolbul.2008.02.007>
- Holyer, R.J., 1978. Toward universal multispectral suspended sediment algorithms. *Remote Sens. Environ.* 7, 323–338. [https://doi.org/10.1016/0034-4257\(78\)90023-8](https://doi.org/10.1016/0034-4257(78)90023-8)
- Jeffrey, S.W., Humphrey, G.F., 1975. New spectrophotometric equations for determining chlorophylls a, b, c1 and c2 in higher plants, algae and natural phytoplankton. *Biochem. und Physiol. der Pflanz.* 167, 191–194. [https://doi.org/10.1016/S0015-3796\(17\)30778-3](https://doi.org/10.1016/S0015-3796(17)30778-3)
- Jõelet, A., 2016. Ülevaade Haapsalu Tagalahe piirkonna geoloogilistest tingimustest seoses kavandatava Noarootsi püsiühendusega. Tartu.
- Junge, C.E., 1963. *Air Chemistry and Radioactivity*. Academic Press, New York.
- Kahru, M., Horstmann, U., Rud, O.E., 1994. Satellite detection of increased cyanobacteria blooms in the Baltic Sea: Natural fluctuation or ecosystem change? | Semantic Scholar. *Ambio* 23, 469–472.
- Kari, E., Kratzer, S., Beltrán-Abaunza, J.M., Harvey, E.T., Vaičiūtė, D., 2017. Retrieval of suspended particulate matter from turbidity—model development, validation, and application to MERIS data over the Baltic Sea. *Int. J. Remote Sens.* 38, 1983–2003. <https://doi.org/10.1080/01431161.2016.1230289>
- Kartau, K., Soomere, T., Tonisson, H., 2011. Quantification of sediment loss from semi-sheltered beaches: a case study of Valgerand Beach, Pärnu Bay, the Baltic Sea. *J. Coast. Res.* 100–104.
- Kirk, J.T., 1981. Estimation of the scattering coefficient of natural waters using underwater irradiance measurements. *Aust. J. Mar. Freshw. Res.* 32, 533–539.
- KKA, 2016. *Matsalu rahvuspark*. Penijõe.
- Kostadinov, T.S., Siegel, D.A., Maritorena, S., 2009. Retrieval of the particle size distribution from satellite ocean color observations. *J. Geophys. Res. Ocean.* 114, 1–22. <https://doi.org/10.1029/2009JC005303>
- Kowalczyk, P., 1999. Seasonal variability of yellow substance absorption in the surface layer of the Baltic Sea. *J. Geophys. Res. Ocean.* 104, 30047–30058. <https://doi.org/10.1029/1999jc900198>
- Kratzer, S., Moore, G., 2018. Inherent optical properties of the Baltic Sea in comparison to other seas and oceans. *Remote Sens.* 10. <https://doi.org/10.3390/rs10030418>
- Kutser, T., Herlevi, A., Kallio, K., Arst, H., 2001. A hyperspectral model for interpretation of passive optical remote sensing data from turbid lakes. *Sci. Total Environ.* 268, 47–58. [https://doi.org/10.1016/S0048-9697\(00\)00682-3](https://doi.org/10.1016/S0048-9697(00)00682-3)
- Kutser, T., Hiire, M., Metsamaa, L., Vahtmäe, E., Paavel, B., Aps, R., 2009. Field measurements of spectral backscattering coefficient of the Baltic Sea and boreal lakes. *Boreal Environ. Res.* 14, 305–312.
- Kutser, T., Paavel, B., Metsamaa, L., Vahtmä, E., 2009. Mapping coloured dissolved organic matter concentration in coastal waters. *Int. J. Remote Sens.* 30, 5843–5849. <https://doi.org/10.1080/01431160902744837>
- Lauringson, V., 2013. Pärnu lahe seisundi parandamine tehislise rифide abil 1. etapp. Tartu.
- Lee, B.J., Kim, J., Hur, J., Choi, I.H., Toorman, E.A., Fettweis, M., Choi, J.W., 2019. Seasonal Dynamics of Organic Matter Composition and Its Effects on Suspended Sediment Flocculation in River Water. *Water Resour. Res.* 55, 6968–6985. <https://doi.org/10.1029/2018WR024486>
- Leymarie, E., Doxaran, D., Babin, M., 2010. Uncertainties associated to measurements of inherent optical properties in natural waters. *Appl. Opt.* 49, 5415–5436.
- Ligi, M., Kutser, T., Kallio, K., Attila, J., Koponen, S., Paavel, B., Soomets, T., Reinart, A., 2017. Testing the performance of empirical remote sensing algorithms in the Baltic Sea waters with modelled and in situ reflectance data. *Oceanologia* 59 (1), 57–68. <https://doi.org/10.1016/j.oceano.2016.08.002>
- Lindell, T., Pierson, D., Premazzi, G., Zilioti, E., 1999. Manual for monitoring European lakes using remote sensing techniques.
- Lutt, J., Kask, J., 1980. *Matsalu lahe põhjasetted*. *Loodusvaatlusi* 1978 (1), 166–178.
- Many, G., Bourrin, F., Durrieu de Madron, X., Pairaud, I., Gangoiff, A., Doxaran, D., Ody, A., Verney, R., Menniti, C., Le Berre, D., Jacquet, M., 2016. Particle assemblage characterization in the Rhone River ROFI. *J. Mar. Syst.* 157, 39–51. <https://doi.org/10.1016/j.jmarsys.2015.12.010>
- Martinez-Vicente, V., Land, P.E., Tilstone, G.H., Widdicombe, C., Fishwick, J.R., 2010. Particulate scattering and backscattering related to water constituents and seasonal changes in the Western English Channel. *J. Plankton Res.* 32, 603–619. <https://doi.org/10.1093/plankt/fbq013>
- Mckee, D., Cunningham, A., 2005. scattering phase function and its implication for modeling radiance transfer in shelf seas. *Appl. Opt.* 44, 126–135.
- Meslard, F., Bourrin, F., Many, G., Kerhervé, P., 2018. Suspended particulate dynamics and fluxes in an Arctic fjord (Kongsfjorden, Svalbard). *Estuar. Coast. Shelf Sci.* 204, 212–224. <https://doi.org/10.1016/j.ecss.2018.02.020>
- Mikkelsen, O.A., Hill, P.S., Milligan, T.G., 2006. Single-grain, microfloc and macrofloc volume variations observed with a LISST-100 and a digital floc camera. *J. Sea Res.* 55, 87–102. <https://doi.org/10.1016/j.seares.2005.09.003>
- Mikkelsen, O.A., Hill, P.S., Milligan, T.G., Chant, R.J., 2005. In situ particle size distributions and volume concentrations from a LISST-100 laser particle sizer and a digital floc camera c, 1959–1978. <https://doi.org/10.1016/j.csr.2005.07.001>
- Morel, A., 1974. Optical properties of pure water and pure sea water. *Opt. Asp. Oceanogr.* 1–24.
- Morel, A., Prieur, L., 1977. Analysis of variations in ocean color. *Limnol. Oceanogr.* 22, 709–722. <https://doi.org/10.4319/lo.1977.22.4.0709>
- Neukermans, G., Ruddick, K., Loisel, H., Roose, P., 2012. Optimization and quality control of suspended particulate matter concentration measurement using turbidity measurements. *Limnol. Oceanogr. Methods* 10, 1011–1023. <https://doi.org/10.4319/lom.2012.10.1011>
- Nima, C., Frette, Ø., Hamre, B., Stamnes, J.J., Chen, Y.C., Sørensen, K., Norli, M., Lu, D., Xing, Q., Muyimbwa, D., Ssenyonga, T., Stamnes, K.H., Erga, S.R., 2019. CDOM absorption properties of natural water bodies along extreme environmental gradients. *Water (Switzerland)* 11, 1–19. <https://doi.org/10.3390/w11101988>
- Ohde, T., Siegel, H., Gerth, M., 2007. Validation of MERIS Level-2 products in the Baltic Sea, the Namibian coastal area and the Atlantic Ocean. *Int. J. Remote Sens.* 28, 609–624. <https://doi.org/10.1080/01431160600972961>
- Ohi, N., Makinen, C.P., Mitchell, R., Moisan, T.A., 2008. Absorption and Attenuation Coefficients Using the WET Labs ac-s in the Mid-Atlantic Bight: Field Measurements and Data Analysis.
- Paavel, B., Arst, H., Metsamaa, L., Toming, K., Reinart, A., 2011. Optical investigations of CDOM-rich coastal waters in Pärnu Bay. *Est. J. Earth Sci.* 60, 102–112. <https://doi.org/10.3176/earth.2011.2.04>
- Palanques, A., Diaz, J.I., Farran, M.L., 1995. Contamination of heavy metals in the suspended and surface sediment of the Gulf of Cadiz (Spain): The role of sources, currents, pathways and sinks. *Oceanol. Acta* 18, 469–477.
- Pegau, S., Zaneveld, J.R.V., Mitchell, G.B., Mueller, J.L., Kahru, M.,

- Wieland, J., Stramska, M., 2003. Ocean Optics Protocols For Satellite Ocean Color Sensor Validation, Revision 4. Volume IV: Inherent Optical Properties: Instruments, Characterizations, Field Measurements and Data Analysis Protocols. Goddard Space Flight Space Center, Greenbelt, MD. <https://doi.org/10.25607/OBP-64>
- Pope, R.M., Fry, E.S., 1997. Absorption spectrum (380–700 nm) of pure water II Integrating cavity measurements. *Appl. Opt.* 36, 8710. <https://doi.org/10.1364/AO.36.008710>
- Qiu, Z., Sun, D., Hu, C., Wang, S., Zheng, L., Huan, Y., Peng, T., 2016. Variability of particle size distributions in the Bohai Sea and the Yellow Sea. *Remote Sens.* 8. <https://doi.org/10.3390/rs8110949>
- Randla, M., Uudeberg, K., Ligi, M., Bourrin, F., Kutser, T., 2018. Heljumi omaduste ja dünaamika varieerumine Pärnu lahes. *Eesti Kaugseirepäev, Tõravere, Estonia.*
- Reynolds, R.A., Stramski, D., Neukermans, G., 2016. Optical backscattering by particles in Arctic seawater and relationships to particle mass concentration, size distribution, and bulk composition. *Limnol. Oceanogr.* 61, 1869–1890. <https://doi.org/10.1002/lno.10341>
- Sadaoui, M., Ludwig, W., Bourrin, F., Raimbault, P., 2016. Controls, budgets and variability of riverine sediment fluxes to the Gulf of Lions (NW Mediterranean Sea). *J. Hydrol.* 540, 1002–1015. <https://doi.org/10.1016/j.jhydrol.2016.07.012>
- Sakho, I., Dussouillez, P., Delanghe, D., Hanot, B., 2019. Suspended sediment flux at the Rhone River mouth (France) based on ADCP measurements during flood events.
- Simis, S.G.H., Ylöstalo, P., Kallio, K.Y., Spilling, K., Kutser, T., 2017. Contrasting seasonality in optical/biogeochemical properties of the Baltic Sea. *PLoS One* 12, 1–31. <https://doi.org/10.1371/journal.pone.0173357>
- Slade, W.H., Boss, E., 2015. Spectral attenuation and backscattering as indicators of average particle size. *Appl. Opt.* 54, 7264–7277.
- Snyder, W.A., Arnone, R.A., Davis, C.O., Goode, W., Gould, R.W., Ladner, S., Lamela, G., Rhea, W.J., Stavn, R., Sydor, M., Weidemann, A., 2008. Optical scattering and backscattering by organic and inorganic particulates in U.S. coastal waters. *Appl. Opt.* 47, 666–677. <https://doi.org/10.1364/AO.47.000666>
- Spencer, K.L., Wheatland, J.A.T., Bushby, A.J., Carr, S.J., Droppo, I.G., Manning, A.J., 2021. A structure–function based approach to floc hierarchy and evidence for the non-fractal nature of natural sediment flocs. *Sci. Rep.* 11, 1–10. <https://doi.org/10.1038/s41598-021-93302-9>
- Stramska, M., Stramski, D., Mitchell, B.G., Mobley, C.D., 2000. Estimation of the absorption and backscattering coefficients from in-water radiometric measurements. *Limnol. Oceanogr.* 45, 628–641. <https://doi.org/10.4319/lo.2000.45.3.0628>
- Sullivan, J.M., Twardowski, M.S., Ronald, J., Zaneveld, V., Moore, C.C., 2013. 6 Measuring optical backscattering in water. <https://doi.org/10.1007/978-3-642-21907-8>
- Sullivan, J.M., Twardowski, M.S., Zaneveld, J.R.V., Moore, C.M., Barnard, A.H., Donaghay, P.L., Rhoades, B., 2006. Hyperspectral temperature and salt dependencies of absorption by water and heavy water in the 400–750 nm spectral range. *Appl. Opt.* 45, 5294. <https://doi.org/10.1364/AO.45.005294>
- Sun, D., Chen, S., Qiu, Z., Wang, S., Huan, Y., He, Y., 2017. Second-order variability of inherent optical properties of particles in Bohai Sea and Yellow Sea: Driving factor analysis and modeling 1266–1287. <https://doi.org/10.1002/lno.10503>
- Sydor, M., 1980. Remote sensing of particulate concentrations in water. *Appl. Opt.* 19, 2794. <https://doi.org/10.1364/ao.19.002794>
- Tao, J., Hill, P.S., Boss, E.S., Milligan, T.G., 2018. Variability of Suspended Particle Properties Using Optical Measurements Within the Columbia River Estuary 6296–6311. <https://doi.org/10.1029/2018JC014093>
- The International Organization for Standardization, 2018. ISO 5667-3: 2018 Water Quality—Sampling—Part 3: Preservation and Handling of Water Samples. Geneva, Switzerland.
- The International Organization for Standardization, 1992. ISO 10260: 1992 Water quality—Measurement of Biochemical Parameters—Spectrometric Determination of the Chlorophyll-a Concentration. Geneva, Switzerland.
- Toming, K., Kutser, T., Uiboupin, R., Arikas, A., Vahter, K., Paavel, B., 2017. Mapping water quality parameters with Sentinel-3 Ocean and Land Colour Instrument imagery in the Baltic Sea. *Remote Sens.* 9. <https://doi.org/10.3390/rs9101070>
- Twardowski, M.S., Boss, E., Macdonald, J.B., Pegau, W.S., Barnard, A.H., Zaneveld, J.R.V., 2001. A model for estimating bulk refractive index from the optical backscattering ratio and the implications for understanding particle composition in case I and case II waters. *J. Geophys. Res.* 106, 14129. <https://doi.org/10.1029/2000JC000404>
- Twardowski, M.S., Sullivan, J.M., Donaghay, P.L., Zaneveld, J.R.V., 1999. Microscale quantification of the absorption by dissolved and particulate material in coastal waters with an ac-9. *J. Atmos. Ocean. Technol.* 16, 691–707. [https://doi.org/10.1175/1520-0426\(1999\)016\(0691:MQOTAB\)2.0.CO;2](https://doi.org/10.1175/1520-0426(1999)016(0691:MQOTAB)2.0.CO;2)
- Ulloa, O., Sathyendranath, S., Platt, T., 1994. Effect of the particle-size distribution on the backscattering ratio in seawater. *Appl. Opt.* 33, 7070–7077.
- Uudeberg, K., Aavaste, A., Kõks, K.L., Ansper, A., Uusõue, M., Kangro, K., Ansko, I., Ligi, M., Toming, K., Reinart, A., 2020. Optical water type guided approach to estimate optical water quality parameters. *Remote Sens.* 12. <https://doi.org/10.3390/rs12060931>
- Uudeberg, K., Randla, M., Arikas, A., Soomets, T., Toming, K., Reinart, A., 2019. Underwater light field changes in Pärnu Bay influenced by weather phenomena and captured by Sentinel-3 (oral presentation). *Bio-Optical and Remote Sensing Workshop.*
- WET Labs, 2011. ac Meter Protocol Document. Philomath.
- WET Labs, 2010. Scattering Meter ECO-BB9, User's Guide. Philomath.
- WET Labs, 2007. ECO-VSF3: Three-angle, Three-wavelength Volume Scattering Function Meter [WWW Document]. User's Guid URL.
- Whitmire, A.L., Boss, E., Cowles, T.J., Pegau, W.S., 2007. Spectral variability of the particulate backscattering ratio. *Opt. Express* 15, 7019–7031. <https://doi.org/10.1029/2005JC003008>
- Wolanski, E., Gibbst, R.J., 1995. Flocculation of Suspended Sediment in the Fly River Estuary, Papua New Guinea. *J. Coast. Res.* 11, 754–762.
- Woźniak, S.B., Meler, J., Lednicka, B., Zdun, A., Stoń-Egiert, J., 2011. Inherent optical properties of suspended particulate matter in the southern Baltic Sea. *Oceanologia* 53 (3), 691–729. <https://doi.org/10.5697/oc.53-3.691>
- Woźniak, S.B., Sagan, S., Zabłocka, M., Stoń-Egiert, J., Borzycka, K., 2018. Light scattering and backscattering by particles suspended in the Baltic Sea in relation to the mass concentration of particles and the proportions of their organic and inorganic fractions. *J. Mar. Syst.* 182, 79–96. <https://doi.org/10.1016/j.jmarsys.2017.12.005>

Available online at www.sciencedirect.com

ScienceDirect

journal homepage: www.journals.elsevier.com/oceanologia

ORIGINAL RESEARCH ARTICLE

Noctiluca blooms intensify when northwesterly winds complement northeasterlies in the northern Arabian Sea: Possible implications

Nittala S. Sarma^{a,*}, Sanjiba Kumar Baliarsingh^b, Sudarsana Rao Pandi^c,
Aneesh Anandrao Lotliker^b, Alakes Samanta^b

^a Marine Chemistry Laboratory, Andhra University, Visakhapatnam, India

^b Indian National Centre for Ocean Information Services, Ministry of Earth Sciences, Govt. of India, Hyderabad, India

^c National Centre for Polar and Ocean Research, Ministry of Earth Sciences, Govt. of India, Vasco-da-Gama, Goa, India

Received 5 October 2021; accepted 27 June 2022

Available online 10 July 2022

KEYWORDS

Noctiluca scintillans;
Harmful Algal Bloom;
Phytoplankton;
Iron fertilization;
HYSPLIT back
trajectories;
Bloom model

Abstract Wind systems are known as nutrient sources playing significant roles in the oceanic realm and global climate oscillations. This study explores, for the first time, the effect of winds on the winter blooms of the mixotrophic dinoflagellate, the green variant of *Noctiluca scintillans* (NSG) in the northern Arabian Sea. When the NSG abundance was lower (i.e., $< \sim 10000$ cells l^{-1}), it was coupled to silicic acid (H_4SiO_4), on which diatoms (phytoplankton) in turn depended. At higher abundance (i.e., $NSG > \sim 10000$ cells l^{-1}), H_4SiO_4 and H_4SiO_4 :DIN (dissolved inorganic nitrogen) ratio fell. The NSG was then intensely green and chlorophyll-*a* richer, attributed to a change in the mode of NSG's nutrition from heterotrophy to autotrophy-dominance. The back-trajectory model revealed that the winds were mostly northeasterly (NE) initially (during February) and were north-westerly (NW) towards the end of winter (March). Separately for the NE and NW winds, the NSG abundance was 10655 ± 18628 and 28896 ± 46225 cells l^{-1} , respectively. The H_4SiO_4 :DIN ratio correspondingly reached < 0.2 and ≥ 0.4 . The NSG was modelled with high significance ($p < 0.001$, $N = 33$) versus the NE and NW wind speeds. Thus, while the NE winds deepened the mixed layer and caused nutrient enrichment and phytoplankton production, the NW winds facilitated the recovery of the H_4SiO_4 :DIN ratio and economical

* Corresponding author at: Marine Chemistry Laboratory, Andhra University, Visakhapatnam, 530003, India.

E-mail address: sarmanittala@gmail.com (N.S. Sarma).

Peer review under the responsibility of the Institute of Oceanology of the Polish Academy of Sciences.



use of H_4SiO_4 for phytoplankton production. It is hypothesized that this process is helped by iron input from NW desert winds during the latter part of winter when the NSG blooms intensify.
 © 2022 Institute of Oceanology of the Polish Academy of Sciences. Production and hosting by Elsevier B.V. This is an open access article under the CC BY-NC-ND license (<http://creativecommons.org/licenses/by-nc-nd/4.0/>).

1. Introduction

Noctiluca scintillans (NS) is a dinoflagellate classified under Harmful Algal Blooms (HAB) due to its potential toxicity and invasive ability by which it dominates an ecosystem (Goes et al., 2020). NS occurs in two variants/ecotypes, namely the green NS (NSG) and the red NS (NSR), at different spatial-temporal scales in accordance with specific preferences of environmental conditions (Harrison et al., 2011). NSR exhibits a heterotrophic mode of nutrition while NSG exhibits mixotrophy. During heterotrophy, both NS variants feed on a variety of diets, including other (than NS) phytoplankton, fish eggs, and small zooplankton. Among phytoplankton, diatoms are the principal prey of NS (Gomes et al., 2018; Zhang et al., 2016). On the other hand, NS has only a few predators, such as jellyfish and salps, which undermines the energy transfer in the marine environment (Gomes et al., 2014). NS proliferation in the ecosystem poses a risk of substantial economic loss as they consume the species occurring in the food chain for the commercially important fish species (Padmakumar et al., 2010).

In recent decades, blooms of NSG have been noticed more frequently and in greater intensities in the global oceans (Harrison et al., 2011; Piontkovski et al., 2021; Turkoglu et al., 2013). The northern Arabian Sea (NAS), one of the most productive basins of the world ocean, experiences episodic blooms of NSG, especially during the tropical winter (Gomes et al., 2014; Madhu et al. 2012; Pandi et al., 2020). During the winter months (January–March), the open ocean region of the NAS gets enriched in nutrients by convective mixing due to the densification of the cooled surface water with the deeper water (Madhupratap et al., 1996). The surface barrier layer forming in the NAS is thin and weak due to the higher salinity of surface water, unlike in typical seas of lower saline surface water than sub-surface water, and hence yields more easily to winter convective forces (Balachandran et al., 2008). In addition to nutrient entrainment due to convective mixing, several other environmental factors play a pivotal role in preparing the conducive bed for bloom formation and sustenance in the NAS.

The knowledge gathered so far has revealed that the episodic NSG blooms in the NAS are attributable to a complex interplay of ambient physical, chemical, biological, and meteorological conditions (Baliarsingh et al., 2018; Lakshmi et al., 2021; Lotliker et al., 2018; Prakash et al., 2017; Sarma et al., 2019; Smitha et al. 2022). On an important note, these conditions occur during the latter half of February and the first half of March, which is the transition time between the north-east (winter) monsoon and the south-west (summer) monsoon, a co-incident time when the Western India Coastal Current (WICC) reaches the NAS in its north-ward journey along the continental slope

(Shetye et al., 1991). A web of controls influences the NSG blooms and makes it challenging to identify the core causes of the bloom formation, timing, abundance variation, and dynamics. Water temperature, nutrient stoichiometry, i.e., Si:N ratio, the mixed layer depth, and prey availability have been identified as controlling factors in different studies cited above. On the other hand, the surface meteorological factors e.g., the wind vector, which is a significant forcing during the seasonal transition, was not examined earlier and could be a primary influencer (compared to the in situ conditions, which are secondary i.e., consequential factors), on the NSG prevalence.

Winds transport land-borne dust rich in crucial nutrient elements, e.g., iron. The global climate is known to be modulated by iron transported through wind-borne dust from land (Burgay et al., 2021; Maher et al., 2010). For instance, dust from the Saharan desert is believed to provide most of the iron present in the Atlantic Ocean and fertilize the Amazon rainforest (Rizzolo et al., 2017). Along with iron (Fe), the other essential nutrients of the dust are dissolved inorganic phosphorus (DIP), nitrate (NO_3), and ammonium (NH_4), which are reported to induce algal blooms in the East China Sea (Tian et al., 2020, 2018). In a mesocosm study over the South China Sea, strong aerosol loadings were observed to relieve nitrogen and trace metal limitations for the growth of phytoplankton, e.g., diatoms (Guo et al., 2012). In the context of the Arabian Sea, it has also been postulated that without the input of aeolian transported iron during the summer monsoon, the productivity would be reduced by half of the presently estimated (Guieu et al., 2019). Iron-limitation has also been advocated in the NAS (Guieu et al., 2019; Moffet et al., 2015; Naqvi et al., 2010). The intensely upwelling western Arabian Sea is reported as chronically Fe-deficient in experiments and models (Kone et al., 2009; Moffet et al., 2015). These studies support the hypothesis that winds may be a key factor in the NSG blooms in the NAS, and the objective of the present study was to examine this hypothesis.

2. Material and methods

2.1. Field survey

Field surveys were carried out in the northeastern Arabian Sea (NEAS) during two expeditions (campaigns) onboard the Ministry of Earth Sciences (MoES), Government of India's Fishery Oceanographic Research Vessel (FORV) *Sagar Sampada* (SS) cruises. The first campaign (Campaign-1, hereafter C#1, cruise no. SS348) was conducted at stations 1 to 10 during 4–16 March 2016. The second campaign (Campaign-2, hereafter C#2, cruise no. SS356) was conducted at stations 11–15 during 9–20 February 2017

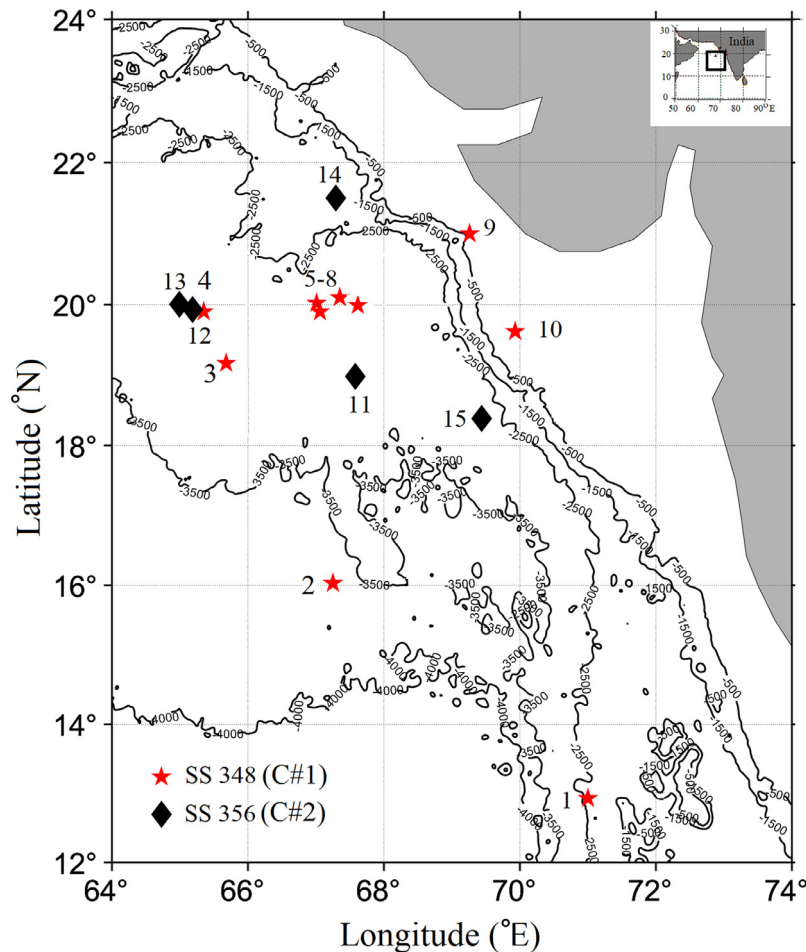


Figure 1 Study area and station locations during campaign-1 (C#1, cruise ID: SS348, stations 1–10) and campaign-2 (C#2, cruise ID: SS356, stations 11–15). Inset shows the study region in the northeastern Arabian Sea (contours: bathymetry, in meters).

(Figure 1). The stations 1 to 12 were occupied during the daytime and were sampled once. The stations 13, 14, and 15 were occupied continuously over >3 days each, and observations were made at regular intervals of 4 hrs. (station 13) and 6 hrs. (stations 14 and 15). At these stations, sampling times from 0100 hrs. to 1300 hrs. were common.

2.2. Meteorological observation and analysis

Meteorological parameters were recorded using an Automatic Weather Station (AWS) installed onboard the vessel. The sensors of the AWS used for recording the meteorological parameters were wind speed-direction (Ultrasonic Gill, 1405-PK-68), air pressure (Setra, 270), air temperature (Vaishala, HMP60), relative humidity (Vaishala, HMP60), and rain gauge (RM Young, 50203). The air mass back-trajectories were generated using the Hybrid Single-Particle Lagrangian Integrated Trajectory (HYSPLIT) model of the National Oceanic and Atmospheric Administration (NOAA, 2021; Rolph et al. 2017; Stein et al. 2015).

2.3. Oceanographic observation and analysis

For recording water temperature and salinity, a Conductivity-Temperature-Depth (CTD) profiler (Sea-Bird,

19Plus) was used. Water samples were collected from the surface (–1 m) using a Niskin Rosette sampler. The Mixed Layer Depth (MLD) was defined as the depth at which the water temperature is 1°C less than the surface (Kumar and Narvekar 2005).

For surface phytoplankton, water samples were collected gently from the undisturbed sea surface using a clean Nalgene bucket (15 litres), sub-sampled in plastic (Nalgene), and fixed with Lugol’s iodine-buffered formaldehyde solution. After an overnight standing, the clear supernatant was decanted, and an aliquot (1 ml) of the phytoplankton concentrate was quantitatively enumerated. The phytoplankton identification and census counts were carried out using trinocular compound microscopes (Nikon Eclipse, E600, Labomed, LX-400). The identification of phytoplankton species was done microscopically by referring to the standard identification keys (Tomas, 1997). Both the steps of collection of seawater samples and the phytoplankton census counts were done in duplicate. Therefore, for each sample, $2 \times 2 = 4$ values were available, which were agreed within $\pm 10\%$ and were averaged.

The first sub-sample of seawater drawn from the Niskin water sampler was for the fixing of dissolved oxygen (DO) by Winkler reagents. The estimation of DO was done by the titrimetric method (Grasshoff et al., 1999). The next sub-sample was drawn for chlorophyll-*a* (chl-*a*). Seawater

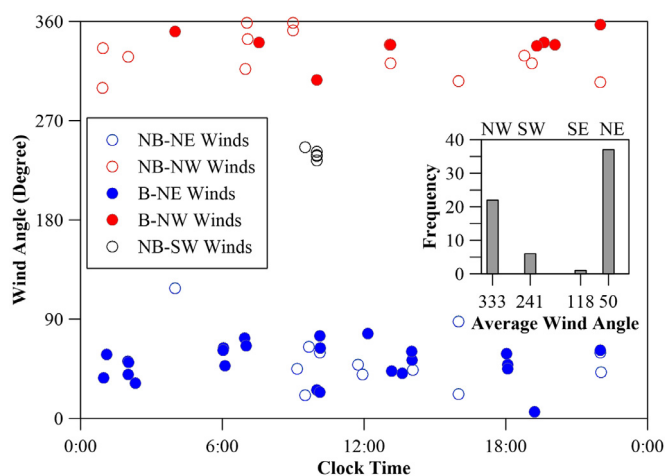


Figure 2 Wind angles with reference to the north at the time of sampling (B: bloom, NSG present, NB: non-bloom, NSG absent). The inset shows their frequency in the distribution of wind.

(1 litre) was filtered immediately through 47 mm diameter GF/F filters ($\sim 0.7 \mu\text{m}$ pore size), and the filter pad was soon soaked in 90% acetone and kept in a refrigerator (4°C) overnight for pigment extraction. Subsequently, the filter pad containing tubes was centrifuged at 4000 rpm. The chl-*a* concentration of the centrifugates was quantified fluorometrically (Turner Designs, Trilogy, C#1) and spectrophotometrically (Thermo Scientific, Evolution 201, C#2).

The seawater filtrates were used for estimating inorganic nutrients nitrite (NO_2), NO_3 , NH_4 , DIP, and silicic acid (H_4SiO_4) using spectrophotometric methods (Grasshoff et al., 1999). For all spectrophotometric determinations of nutrients, a UV-Visible double beam spectrophotometer (Thermo Scientific, Evolution 201) was used. Dissolved inorganic nitrogen (DIN) was computed as the sum of NO_2 , NO_3 , and NH_4 .

2.4. NSG data range categorization

The NSG abundance was considered as falling into four ranges, from its relationships with various biogeochemical constituents, especially H_4SiO_4 (see Results section). They are (i) NSG-N in which NSG was nil ($N = 28$), (ii) NSG-L of low abundance i.e., ≤ 1230 (or, $< \sim 1000$ cells l^{-1} ($N=5$)) (iii) NSG-M of medium abundance i.e., ≤ 22600 (or, < 25000 cells l^{-1} ($N = 23$)), and (iv) NSG-H of high abundance i.e., ≥ 46000 (or, $> \sim 25000$ cells l^{-1} ($N = 6$)).

2.4.1. Phytoplankton indices

The diatoms: dinoflagellates ratio has been used as a phytoplankton community index to assess as well as predict the health of ecosystems, dietary preferences, and biodiversity changes (Teixeira et al., 2016; Tett et al., 2008; Wasmund et al., 2017). The ratio is high in natural, healthy ecosystems and falls rapidly when dinoflagellates increase due to anthropogenic factors. In laboratory experiments, Bi et al. (2021) have shown that diatoms enjoy a competitive superiority at high nutrient concentrations and that the ecosystem moves towards dinoflagellates superiority at very high temperatures and nutrient concentrations. In this study, the Diatoms: (Diatoms+Dinoflagellates other than NSG) ratio (hereafter Diatoms: (Diatoms+Dinoflagellates

ratio) was computed instead of the diatoms: dinoflagellates ratio. This was because in quite a few samples ($N = 6$), dinoflagellates were nil and, in a few others, their abundances were small compared to diatoms and resulted in outlier (average $\pm 3 \times \sigma$, where σ is the standard deviation) ratios. With the new ratio, the degrees of freedom (number of cases minus 1) remained high, and the correlations were better in terms of statistical significance.

The Cyanophyceae e.g., *Trichodesmium* species, are also associated with the NSG blooms, and are its potential feed (Harrison et al., 2011, and references therein). *Trichodesmium* is a N_2 fixer and has a large concentration of iron in its cells, a characteristic considered an ecological indicator (Kustka et al., 2003; Whittaker et al., 2011). *Trichodesmium* blooms where iron is non-limiting, e.g., in large parts of the Atlantic (Chappel et al., 2012; Moore et al., 2009) except when phosphate is limiting (Mills et al., 2004). In the NAS where phosphate is present as an ‘excess nutrient’ (over the Redfieldian phosphate calculated from nitrate, Kumar et al., 2017) and hence non-limiting, it is hypothesized that the dinoflagellates: cyanophyceae ratio can potentially proxy dissolved iron limitation. Again, since in many samples cyanophyceae were nil ($N = 35$), the Dinoflagellates other than NSG: (Dinoflagellates other than NSG+Cyanophyceae) ratio (hereafter Dinoflagellates: (Dinoflagellates+Cyanophyceae) ratio) was calculated, as in the case of Diatoms: (Diatoms+Dinoflagellates) ratio.

2.5. Statistical tests

The statistical tests e.g., Pearson correlation coefficients and regressions were done in a spreadsheet program (Microsoft Excel). The significance of r was obtained from ‘Quick p Value’ from Pearson (R) Score Calculator (socscistatistics.com).

3. Results

3.1. Wind characteristics and the origin of winds

The winds were blowing at various angles ($6\text{--}359^\circ$ with reference to the north). The wind angles were averaged for the

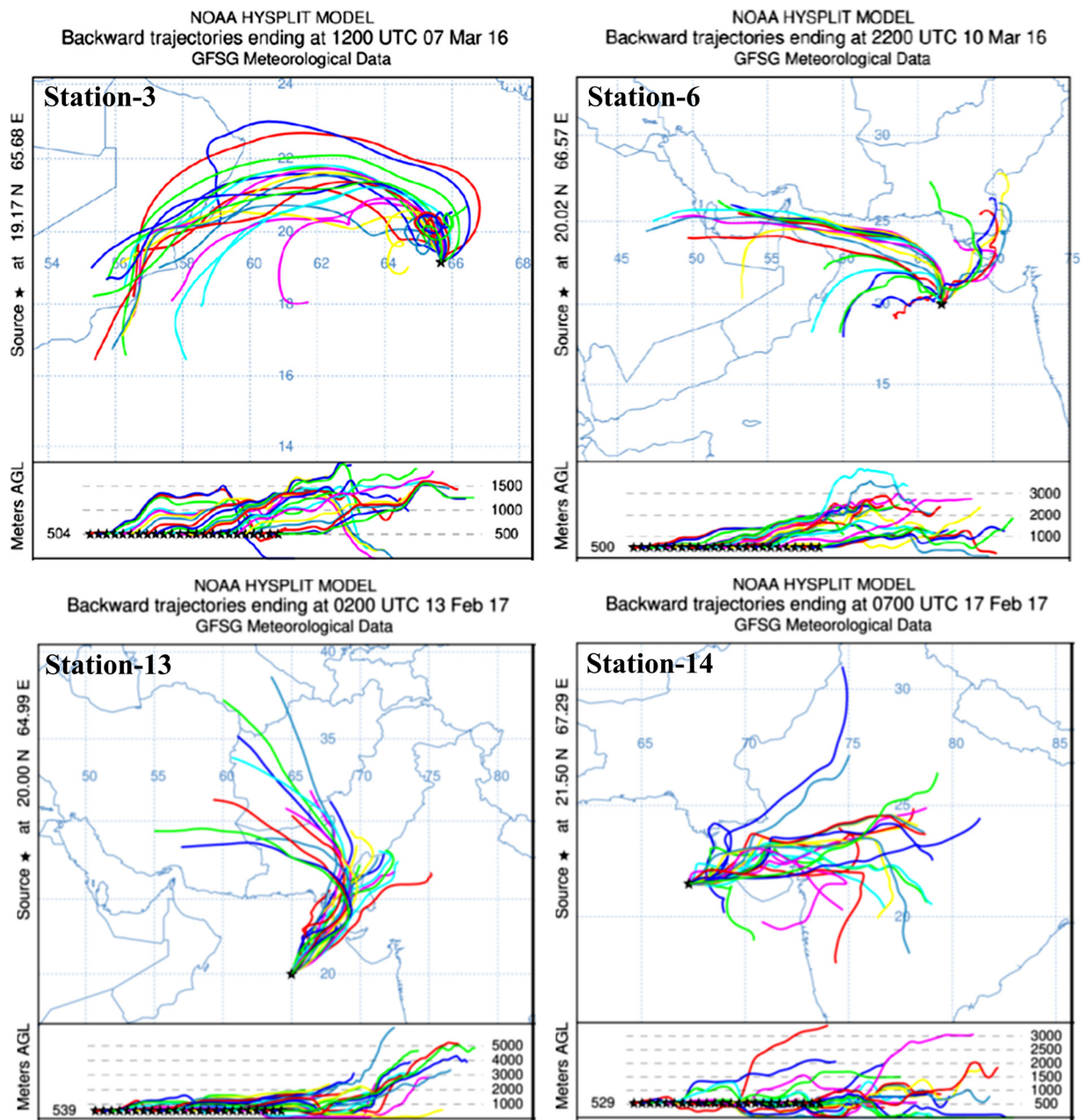


Figure 3 Backward wind trajectories simulated by HYSPLIT model (NOAA) for the 0.5 to 4 km above ground for 3-hour intervals from 72 hours preceding the measurement time at a) Station 3, b) Station 6, c) Station 13 and d) Station14 where NSG blooms occurred. The upper panels are the full back-trajectories of the air masses and the lower panels show the height at different time intervals of the corresponding trajectory. The abscissa (longitude) and ordinate (latitude), in degrees East and North, respectively are embedded.

four quadrants northeast (NE, 0–90°), southeast (SE, 90–180°), southwest (SW, 180–270°), and northwest (NW, 270–360°). Most of the winds were in the NE (range: 6–88°, average, 50°; 60% of the 60 observations) and NW (300–359°, 333°, 30%) (Figure 2) quadrants. The remaining (234–246°, 241°, 10%) were SW originated. In view of the discrete directions of the winds, their associated properties were examined for each direction of the wind vector. Relative humidity (RH) was 7.4% or 7.2% higher in the NW than the NE winds depending on whether NSG was present or not. The RH is a significant discriminator ($p < 0.05$; hereafter, whenever significant at $p < 0.05$, the value is not mentioned) between

the NE and NW winds. During the NW winds, the barometric pressure decreased. The decrease was highly consistent when there was no NSG. The NE winds were faster (34%) than NW winds when NSG was present but slower (11%) than the SW winds when NSG was absent (Table 1).

For identifying the source regions of the NW winds, the back-trajectories of winds were constructed by the HYSPLIT model of the NOAA at altitudes > 0.5 up to 4 km. The upper wind source diagrams at all stations for the sampling durations revealed that during C#2, the winds were synoptically mainly NE, and during C#1, mainly NW. The typical simulations at some of the stations at the time of the survey are

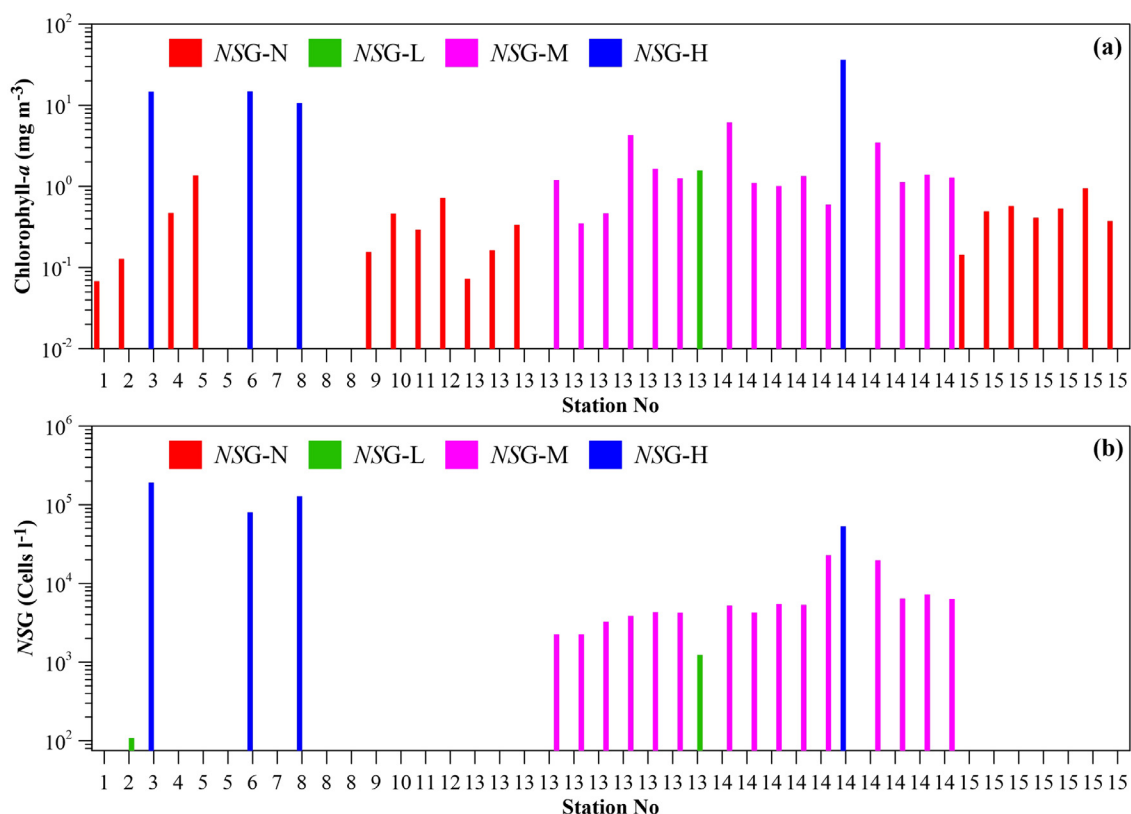


Figure 4 a) Chlorophyll-a (chl-a) estimated in the particulates of selected samples at the stations 1 to 15 (NSG-N, NSG-L, NSG-M and NSG-H are NSG abundances of nil, up to 1230, up to 22600, and more than 46000 cells l⁻¹, respectively), and b) NSG abundance of the samples collected during daytime (6AM to 7PM).

Table 1 Atmospheric and oceanographic characteristics significantly different between NE, NW and SW winds.

Parameter (unit)	NSG-L/M/H			NSG-N			
	average±SD		P value*	average±SD		P value*	average±SD
	NE	NW		Nil-NE	Nil-NW		
No. of observations (N)	26	7	26/7	10	11	10/11	6
Wind direction (°)	50±16	337±15	<0.00001	45±15	332±18	<0.00001	241±5
Wind Speed (m s ⁻¹)	6.3±2.5	4.7±1.0	<0.1	5.9±2.1	6.5±1.6	-	6.8±1.01
Compass (°)	266±98	171±101	0.0318	266±74	199±60	<0.1	123±179
Air temperature (°C)	25.3±1.2	25.9±1.0	-	25.3±1.7	26.4±0.8	<0.1	26.9±0.2
Relative humidity (%)	69.8±9.0	77.2±5.6	0.0468	62.2±11.2	69.4±4.1	<0.1	73.6±1.1
Barometric pressure (mbar)	1014.9±1.4	1014.7±1.2	-	1012.5±1.1	1010.7±1.3	<0.001	1013.5±0.2
SST (°C)	25.08±0.86	25.14±0.84	-	25.84±1.30	26.96±0.36	0.0187	26.61±0.35
SSS (psu)	36.45±0.17	36.41±0.16	-	36.33±0.37	35.87±0.31	0.0117	36.41±0.35
MLD (m)	97.42±22.4	73.7±28.0	0.0245	73.3±34.8	65.7±17.3	-	39±26.50
NO ₂ ⁻ (μM)	0.48±0.20	0.34±0.24	-	0.31±0.30	0.05±0.02	0.0108	0.19±0.32
NO ₃ ⁻ (μM)	4.16±1.48	3.49±2.34	-	2.13±1.94	0.53±0.36	0.0196	0.89±1.13
DIN (μM)	5.09±1.43	4.68±1.71	-	3.13±1.81	1.35±1.30	0.0283	2.97±1.40
H ₄ SiO ₄ (μM)	1.85±0.96	2.84±0.68	0.0153	1.52±1.17	1.37±1.40	-	2.70±0.61
Diat:(Diat+Dino)	0.87±0.1	0.82±0.2	0.0293	0.8±0.8	0.8±0.1	-	0.7±0.2

* P Values <0.1 only are given; - P > 0.1; NE – northeasterly winds; NW – northwesterly winds; SW – southwesterly winds; NSG – *Noctiluca scintillans* Green, N/L/M/H – nil/low/medium/high i.e., non-detectable, <~1000, <~25000 and >25000 cells l⁻¹ of NSG; SST – Sea Surface Temperature, SSS – Sea Surface Salinity, MLD – Mixed Layer Depth, DIN – Dissolved Inorganic nitrogen (NO₂⁻+NO₃⁻+NH₄⁺), Diat – Diatoms, Dino – Dinoflagellates without NSG.

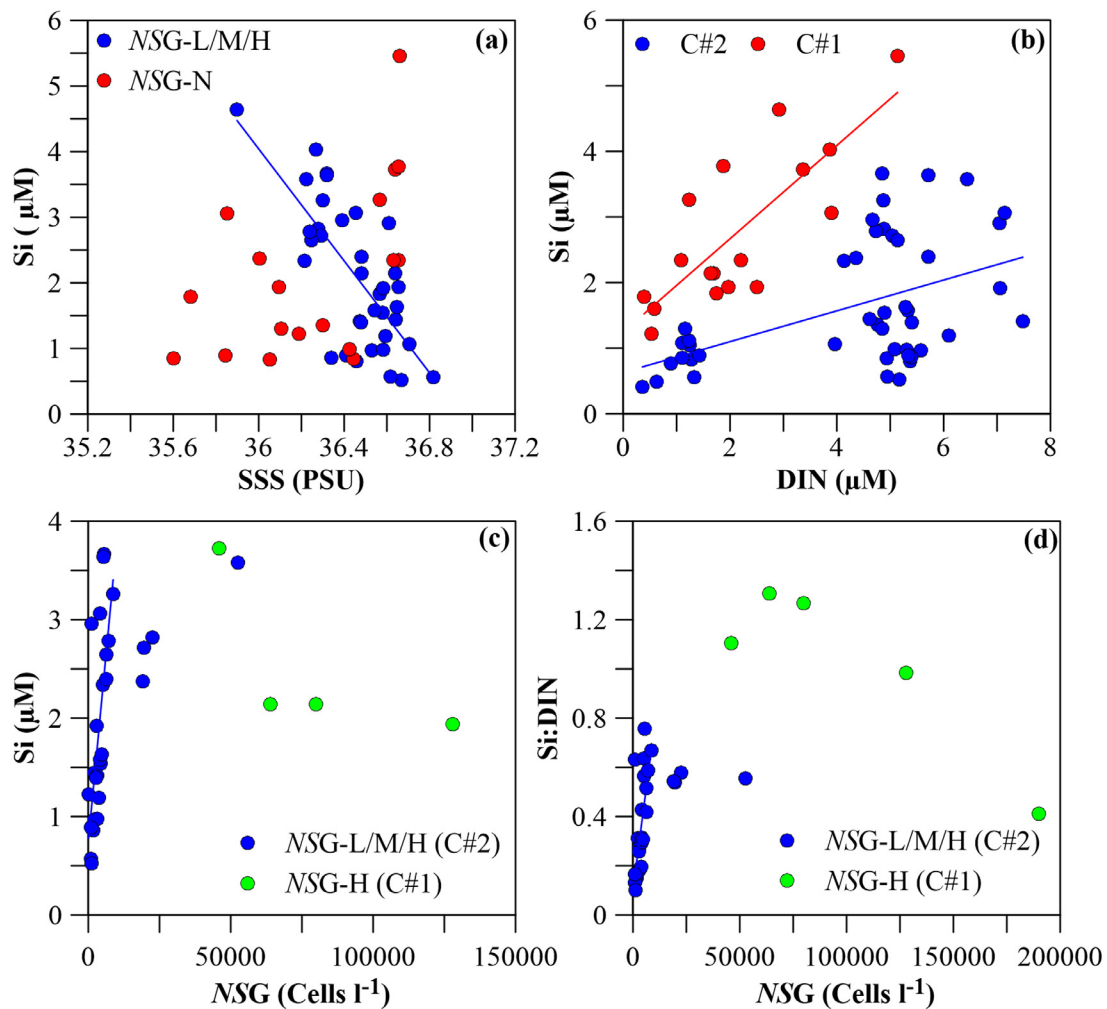


Figure 5 Relationships of silicon (silicic acid) with a) Sea Surface Salinity (SSS), b) Dissolved Inorganic Nitrogen (DIN, $\text{NO}_2^- + \text{NO}_3^- + \text{NH}_4^+$), c) the green *Noctiluca scintillans* (NSG) abundance, and d) relationship of Si:DIN ratio with NSG abundance. The *p* values of all regression lines are: <0.0001 , and the *N* values are 34 (a, NSG-L/M/H), 17 (b, C#2), 24 (c, NSG-L/M, C#2) and 22 (d, C#2, NSG-L/M). The *p* and *N* values of the regression line are 0.014 and 6 in d, C#1, NSG-H (note: the regression lines in (c) and (d) are for $\text{NSG} < 10,000 \text{ cells l}^{-1}$; see text).

presented in Figure 3. The simulations indicated the winds as originating from both NW and NE (Figure 3a, Station 3 and Figure 3b, Station 13 on Day-1 of occupation) or mostly from NW (Figure 3c, Station 6 and Figure 3d, Station 13, Day-2). Unique water column characteristics that supported distinguishing the ecosystem as either NE winds-affected or NW winds-affected, at significance level $p < 0.05$ were the MLD, H_4SiO_4 when NSG was present, and Sea Surface Temperature (SST), Sea Surface Salinity (SSS), and DIN when NSG was absent (Table 1). The winds' physical characteristics, namely speed and temperature also distinguished but at moderate significance ($p < 0.1$) (Table 1).

3.2. Water column characteristics

3.2.1. Nutrient stoichiometry

DIN had a highly significant ($p < 0.0001$, $R^2 = 0.71$, $N=55$) linear relationship with DIP across the different abundance ranges of NSG: $\text{IP} = 0.0781 \cdot \text{DIN} + 0.1582$ (Figure S2), which

revealed that there was a background IP concentration of $0.17 \mu\text{M}$ and that the DIN:DIP ratio was 13.2.

3.2.2. Chl-*a* and the different ranges of NSG

Chl-*a* ranged from close to nil (0.07 mg m^{-3}) to 36.17 mg m^{-3} (Figure 4). Samples of high NSG abundance, i.e., between 46000 and 190000 cells l^{-1} , were visibly green and had $\text{chl-}a \geq 10.6 \text{ mg m}^{-3}$ (4 samples). They were designated as the NSG-H group. A majority of the NSG-H occurrences were associated with NW winds. Samples having $\text{chl-}a < 6.2 \text{ mg m}^{-3}$ were associated with a moderate abundance of NSG ($\leq 22600 \text{ cells l}^{-1}$, NSG-M), and those having $< 1.4 \text{ mg m}^{-3}$ were associated with a low abundance of NSG ($\leq 1230 \text{ cells l}^{-1}$, NSG-L) or nil abundance (NSG-N).

3.2.3. NSG abundance and its relation to silicon distribution

The NSG occurred in a total of 33 samples, of which 13 were collections at night, i.e., 7 PM to 6 AM (Figure 4b shows

only the day samples' data). Six of the 16 stations, i.e., Stations 2, 3, 6, and 8 of C#1 and Stations 13 and 14 of C#2 had NSG. The NSG-L range ($N = 5$) was at Stations 2, 13, and 14. Of these three, Station 2 is at $< \sim 16^\circ\text{N}$ latitude (Figure 1), and is considered as south of the NEAS' southern limit which is about 19°N (Dwivedi et al., 2012). At both stations 13 and 14, NSG-M, which was the most common, occurred. The NSG-H range occurred at Stations 3, 6, and 8 as well as once at Station 14.

H_4SiO_4 correlated negatively with SSS highly significantly when NSG was present (NSG-L/M/H). The distribution was scattered in NSG-N samples (Figure 5a). Si correlated significantly with DIN during C#1 but not during C#2 (Figure 5b). Si increased linearly versus $\log(\text{NSG})$ highly significantly in the NSG-L/M range up to $\sim 10,000$ cells l^{-1} . The NSG-H samples had more NSG than predicted by the linear model of the NSG-L/M range (Figure 5c). In order to understand better how the NSG abundance was changing with both Si and DIN, the Si:DIN ratio was plotted on NSG abundance. The relationship between the two parameters changed in different abundance ranges (Figure 5d). During C#2, the Si:DIN ratio increased from 0.1 up to 0.77 versus NSG abundance with a highly significant positive correlation again up to $\sim 10,000$ cells l^{-1} of NSG-M range). At higher abundances of NSG-M ($> 10,000$) and NSG-H, the Si:DIN ratio decreased to the 0.54–0.55 range. During C#1, the Si:DIN ratio decreased linearly from 2.29 to 0.41 at 190,000 cells l^{-1} with a significant correlation coefficient. The water column characteristics thus did not reveal any common criterion by which the abundance of NSG could be related. The role of winds was examined further.

3.3. NSG's relation to meteorological factors

The measured parameters occurring in association with each direction of the wind are detailed in Table 1. The NSG average abundance was higher during NW winds (7 samples, 33284 cells l^{-1}) than during NE winds (26 samples, 17148 cells l^{-1}) (Table 1). The south-westerly winds (6 occurrences, C#1) were associated with nil NSG (Table 1). The air temperature (AT) had a highly significant positive correlation with NSG abundance (Figure 6a). RH $> 70\%$ held a weak negative relationship with $\log(\text{NSG})$ ($p < 0.05$, $N = 18$) (Figure S3a). Total phytoplankton (TPP, all phytoplankton including NSG), however, held positive relationships with RH separately for the NE ($p < 0.002$, $N = 36$) and NW winds (< 0.05 , 18) Figure S3b). Wind speed had an overall highly significant negative relationship with NSG abundance (Figure 6b).

3.4. Wind as an affecting vector

3.4.1. Water column characteristics

The average SST and SSS were not significantly different between NE and NW winds in the NSG-L/M/H samples. However, they were significantly different in the NSG-N samples being lower (1.12°C) and higher (0.46 PSU), respectively, during NE and NW winds, respectively (Table 1). The MLD was significantly deeper by ~ 26 meters with NE winds than NW winds. NO_2^- and NO_3^- were higher during NE winds, while ammonium was higher during NW winds. Significant

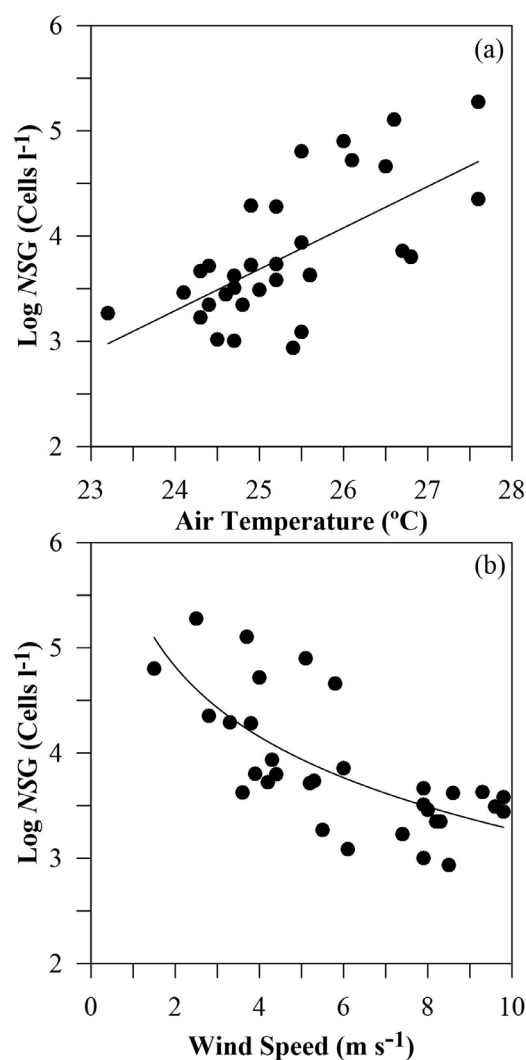


Figure 6 Wind as a non-vector: a) green *Noctiluca scintillans* (NSG) versus air temperature (AT), and b) wind speed. The p and N values of the regression lines are < 0.00001 and 33 respectively in both a) and b).

enrichment of H_4SiO_4 and DIP happened during NW winds. DO did not differ significantly between NE and NW winds in NSG samples, although it was somewhat higher during NW winds than during NE winds (by $13.4 \mu\text{M}$) (Table 2). Depending on the direction i.e., NE or NW, the winds had significant negative or positive relationships with the Si:DIN ratio (Figure 7a).

3.4.2. Phytoplankton indices

When the winds were NE, the abundance of dinoflagellates (other than NSG), hereafter referred to as Dinoflagellates, increased (Figure 7b), and the Diatoms: (Diatoms+Dinoflagellates) ratio decreased (Figure 7c). The Dinoflagellates: (Dinoflagellates+Cyanophyceae) ratio also increased but less significantly (Figure 7d). The TPP abundance was inversely related to NW wind speed with high significance ($p < 0.0001$, $N = 18$) but not related to NE wind speed (Figure S4).

Table 2 Average±Standard deviation of atmospheric, biogeochemical and phytoplankton characteristics associated with winds of different directions (NE, NW and SW).

Parameter (unit)	NSG-L/M/H		NSG-N		
	NE	NW	NE	NW	SW
No. of observations (N)	26	7	10	11	6
Rainfall (cm 24 hrs ⁻¹)	1.9±2.1	1.6±0.5	3±2.1	1.6±1.4	2±0
Long Wave Radiation (W m ⁻²)	370.1±17.6	374.4±15.3	367.5±22.4	385.1±16.4	399.8±5.0
Short Wave Radiation (W m ⁻²)	275.1±339.0	198.7±332.9	283.6±291.5	283.6±415.9	563.5±190.8
IP (μM)	0.61±0.37	1.05±1.19	0.55±0.58	0.27±0.06	0.28±0.09
NH ₄ ⁺ (μM)	0.47±0.95	0.85±1.13	0.69±0.82	0.78±1.45	1.80±0.82
Si:DIN	0.46±0.45	0.67±0.27	0.95±1.36	1.08±0.58	1.01±0.36
DO (μM)	206.2±12.1	210.7±9.9	194.9±30.9	208.3±13.3	198.6±7.9
Chl- <i>a</i> (mg m ⁻³)	3.23±7.28	3.73±3.59	0.87±1.25	0.56±0.35	0.57±0.35
NSG (cells l ⁻¹)	10655±18628	28896±46225	0	0	0
Diatoms (cells l ⁻¹)	24834±29385	20853±18664	6306±8595	6845±4251	2025±815
Dinoflagellates (cells l ⁻¹)	3469±4240	1295±1732	565	1117±841	1163±1317
Cyanobacteria (cells l ⁻¹)	537±836	554±617	290	53±123	37
Silicoflagellates (cells l ⁻¹)	0	na	23	129±214	0
TPP-NSG (cells l ⁻¹)	28840±32265	22702±20094	7184	8144±4894	3240
Diat:Dino	4.36±3.1	6.56±3.6	4.2±4.2	4.4±1.4	10.2±15.3
Dino:Cyano	3.4±3	4±2.8	4.1±4.1	4±0	5.0±5.6
Diat:(Diat+Dino)	0.87±0.1	0.82±0.2	0.8±0.8	0.8±0.1	0.7±0.2
Dino:(Dino+Cyano)	0.88±0.2	0.88±0.2	0.8±0.8	1±0	0.9±0.2

NSG – *Noctiluca scintillans* Green, N/L/M/H – nil/low/medium/high i.e., non-detectable, <~1000, <~25000 and >25000 cells l⁻¹, respectively of NSG; NE – northeasterly winds; NW – northwesterly winds; SW – southwesterly winds; IP – Inorganic Phosphorus; na: not applicable; DIN – Dissolved Inorganic Nitrogen (NO₂⁻+NO₃⁻+NH₄⁺); DO – Dissolved Oxygen; Chl-*a* – Chlorophyll-*a*; TPP – Total phytoplankton; Diat – Diatoms; Dino – Dinoflagellates without NSG; Cyano – Cyanophyceae.

3.5. Time-series study

3.5.1. Role of dissolved oxygen

A high-resolution study of the dynamics taking place was made by a time-series investigation at station 13, where NSG was absent on day-1 but was present later, and at station 14 where NSG occurred in all samplings through its 3.5 days of continuous occupation. The DO concentration was 206.8±9.6 μM and 205.3±12.5 μM at stations 13 and 14, respectively. The DO showed a marginal under-saturation being 97.5±4.8% and 97.4±6.4% saturated, respectively.

3.5.2. The role of winds

During the C#2 campaign, the SST increased steeply with NW wind speed and gently with NE winds with highly significant correlations (Figure 8a). A comparison between stations 13 and 14 showed similarities as well as differences. The similarity was of the Si:DIN ratio, which correlated significantly with the salinity of their combined data (Figure 8b). This inverse linear distribution is similar to the SSS-Si distribution in the NSG-L/M/H samples (Figure 5a). The difference between stations 13 and 14 was in the relationships between air temperature (AT), SST, and SSS. At station 13, SSS correlated highly significantly with AT and less significantly with SST (Figure 8c). At Station 14, versus SSS, the AT was scattered but the SST correlated significantly (Figure 8d).

As summarized in Table 3, the winds at Station 13 were all NE (19 observations), and at Station 14, both NE (8) and NW (5). The NE winds were cooler (by 1.2°C), less humid (by ~17.7%), and faster (by 4.1 m s⁻¹) at Station 13

than at Station 14. At Station 14, the NW wind speed was faster by 1.1 m s⁻¹ than the NE winds (Table 3), contrary to the general trend (Table 1). The SSS range was broader and the maximum SSS higher at Station 13 (36.1 to 36.7 PSU, Figure 9a) compared to Station 14 (36.2–36.6 PSU, Figure 9b). The profile of SST varied less at Station 13 (variation, 0.3°C; range, 24.8 to 25.1) than at Station 14 (1.3, 24.2 to 25.5) Figure S5a,b). At Station 13, the NSG, after appearing (at 1860 cells l⁻¹) as the Day-2 began (0100 hrs. on 12 February 2017), initially decreased (to 1700 cells l⁻¹ at 0500 hrs.) but rose in abundance steadily at about 60–70 cells l⁻¹ before crashing towards the end of the station’s occupation (Figure 9a). A similar profile was followed by NSG at station 14, except that the rate of increase of NSG was about an order of magnitude higher and the peak (52600 cells l⁻¹) that crashed was mid-way of the station’s occupation (Figure 9b).

3.6. Empirical Model for NSG based on wind vector and SST

Multiple linear regression models were attempted involving the NE and NW winds as 2 different (dependent) meteorological variables and as a third variable, the SST, which is an oceanographic variable. The Eq. (1) fitted the data of the NSG-L/M/H samples with highly significant regression statistics (Table 4). Another model (Eq. (2)) in which the wind direction (NE/NW) was not distinguished had less significant statistics (Table 4). In Eq. (1), the NE wind speed is nil when the wind is from NW, and NW wind speed is nil when the

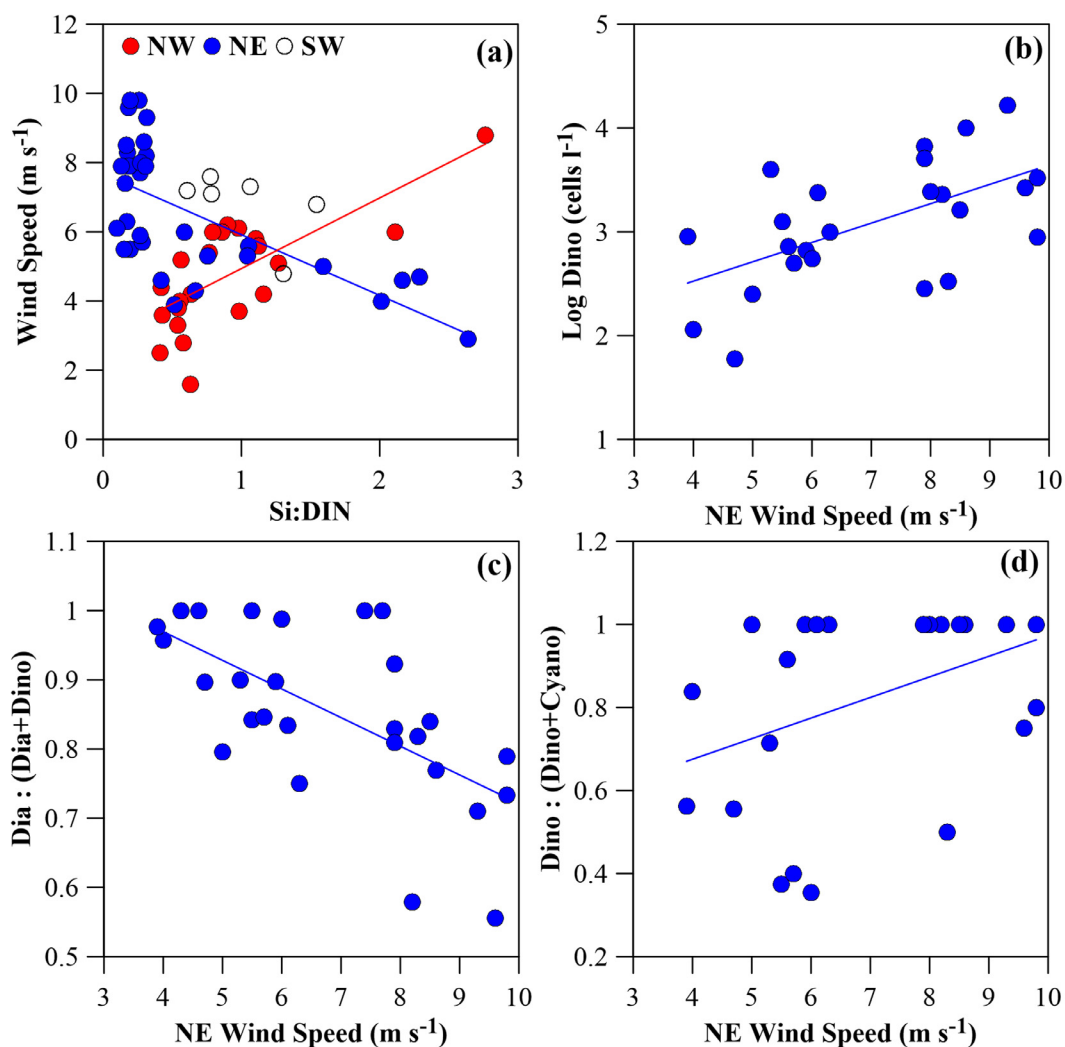


Figure 7 Wind as a vector: a) Wind speed on Si:DIN ratio, and changes during northeast (NE) wind of b) Log(Dinoflagellates, dino), and the two phytoplankton indices i.e., ratio of c) diatoms (diat) to the sum of diatoms and dinoflagellates and d) dinoflagellates to the sum of dinoflagellates and cyanophyceae (cyano). The p and N values of the regression lines are 33 (NE winds) and 18 (NW winds) in (a), 24 in (b), 27 in (c). The values are 0.027 and 22 respectively in (d).

Table 3 Wind parameters at the Time Series Stations, Station 13 and Station 14.

Station Unit	Wind direction	N	Wind speed (m s ⁻¹)	Wind angle Degrees from north	Air temperature (°C)	Relative humidity (%)	Barometric pressure (mbar)	Rainfall (cm day ⁻¹)
Station 13	NE	19	7.7	53	24.5	62.3	1015.1	2.9
Station 14	NE	8	3.6	45	25.7	79.9	1014.2	0.6
Station 14	NW	5	4.7	340	25.7	79.7	1015.2	1.6

*N= number of observations; NE= northeasterly winds; NW= northwesterly winds.

wind is from NE.

$$NSG = -1268682 + 52979 \times SST - 5615 \times NE \text{ wind speed} - 8132 \times NW \text{ wind speed} \quad (1)$$

$$NSG = -1252445 + 52116 \times SST - 5150 \times \text{wind speed} \quad (2)$$

4. Discussion

In the NAS, during the winter season (January–March), the MLD penetrates to deeper than 80 m due to a net heat loss resulting in buoyancy loss for the surface water (Prasad, 2004), with which the negative relationship between MLD and SST (Figure S1a) agrees.

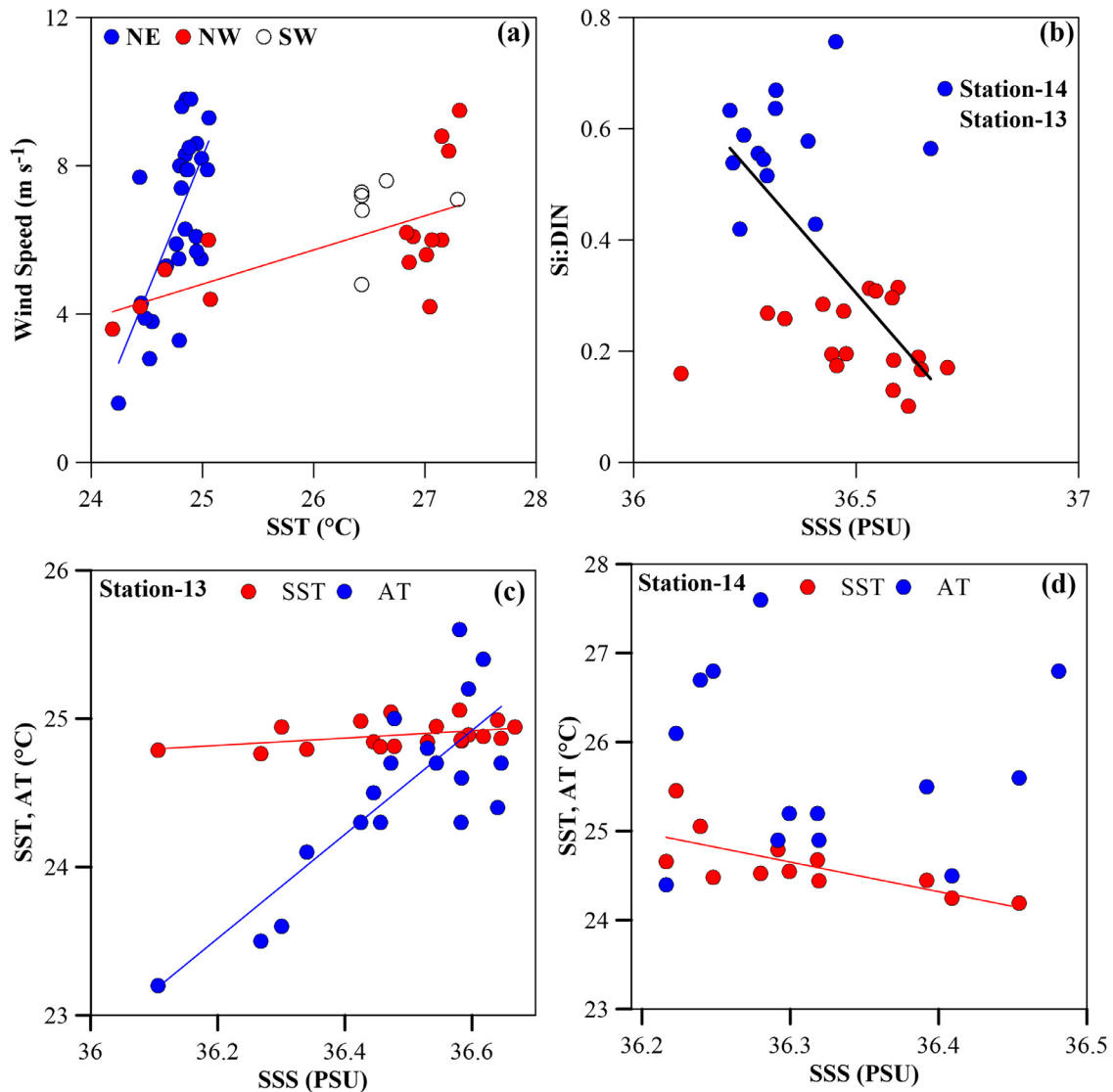


Figure 8 Influence of wind at stations 13 and 14. a) Sea Surface Temperature (SST) as a function of the North-East (NE) and North-West (NW) wind speeds, and the variation against Sea Surface Salinity (SSS) versus, b) Si:DIN ratio and SST and Air Temperature (AT) at c) Station 13, and d) Station 14. The p and N values of the regression lines are < 0.0001, 31 (NE winds), <0.001, 18 (NW winds) in (a), < 0.0001, 31 in (b), < 0.0001, 21 (AT) and 0.091, 17 (SST) in (c) and 0.008, 12 in (d), respectively.

Table 4 Statistics associated with the (multiple linear) Regression models (Eq. (1) and Eq. (2)) for NSG abundance.

Statistic	Eq. (1) (wind speed as vector)	Eq. (2) (wind speed as non-vector)
No. of observations	33	33
Multiple R	0.9267	0.9192
Adjusted R ²	0.8441	0.8346
Standard Error	16253	16737
Significance of Intercept	8×10^{-12}	1.33×10^{-11}
Significance of SST* as a dependent variable	2.22×10^{-12}	3.68×10^{-12}
Significance of NE wind speed as a dependent variable	6.85×10^{-5}	1.93×10^{-4}
Significance of NW wind speed as a dependent variable	6.62×10^{-4}	

SST= Sea Surface Temperature; NE= northeasterly winds; NW= northwesterly winds; Eq. (1), $NSG = -1268682 + 52979 \times SST - 5615 \times NE \text{ wind speed} - 8132 \times NW \text{ wind speed}$; Eq. (2), $NSG = -1252445 + 52116 \times SST - 5150 \times \text{Wind speed}$.

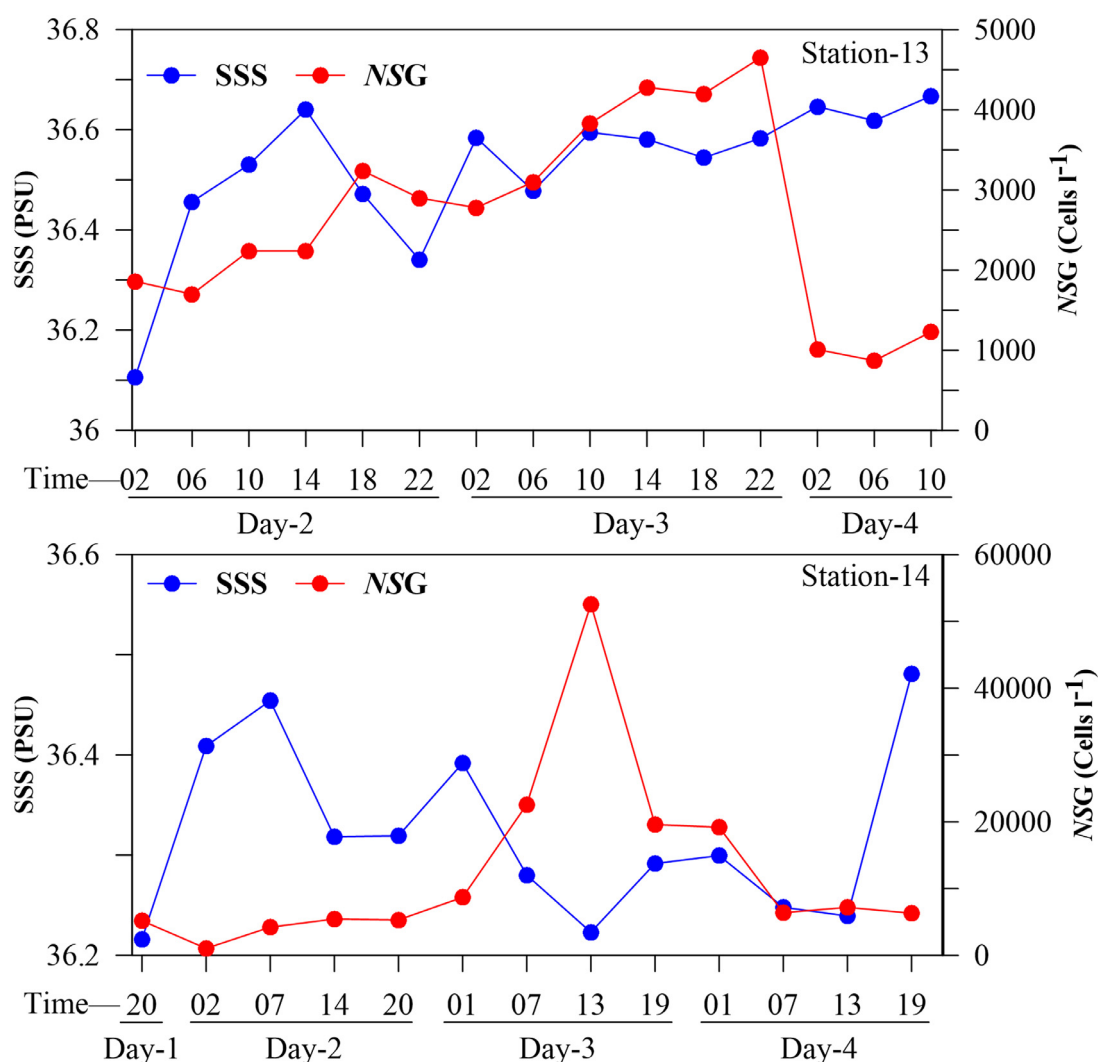


Figure 9 The change of Sea Surface Salinity (SSS) and green *Noctiluca scintillans* (NSG) during the continuous occupation of a) Station 13 (at 4 hour intervals from 10 hr on Day-1 to 10 hour on Day-4), and b) Station 14 (at 6 hr intervals from 20 hours on Day-1 to 19 hours on Day-4).

4.1. Implication of silicon

There was an inverse linear relationship between salinity and H_4SiO_4 in samples in which NSG occurred (Figure 5a). This indicates that a significant portion of H_4SiO_4 was being contributed by less saline water in these samples. In the eastern Arabian Sea, the WICC water of lower salinity (< 36.2 PSU) than the local Arabian Sea High Saline Water (salinity ~ 36.5 PSU, water temperature, $26.8^\circ C$; Prasanna Kumar and Prasad, 1999) flows. During its northward transit along the continental slope, the WICC reaches the NEAS by late winter (Shankar et al., 2015; Shetye et al., 1991). The WICC water is richer in Si being fed by the headwaters of the Bay of Bengal (Prasanna Kumar et al., 2004). This resulted in a gradual shallowing of the mixed layer from C#2 (February) to C#1 (March), proposed by Sarma et al. (2019) as the driver of NSG blooms.

As shown in the Si (Figure 5c) and Si:DIN plots (Figure 5d), the Si:DIN ratio fell (to 0.58) even as H_4SiO_4

had a moderately high concentration (of $2.82 \mu M$) while the NSG-M abundance reached an abundance of 22600 cells l^{-1} at station 14 (during C#2). The ratio remained so (0.57) even when Si increased to $3.58 \mu M$. The fall in Si:DIN ratio from the previously rising trend (Figure 5d) indicates that the diatoms were using the nutrient at a greater ratio (Hutchins and Bruland, 1998; Timmermans et al., 2004) when the NSG abundance increased from 19200 cell l^{-1} ($\log(NSG) = 4.28$ in Figure 5c) onwards. Thus, at $NSG > 19200$ cells l^{-1} during C#2 and all NSG-H samples of C#1, the proliferation of NSG occurred much beyond the available Si (and diatoms) could support.

The NSG-H samples had very high chl-*a* (10.6 to 36.2 $mg\ m^{-3}$) and were intensely green in colour. When stressed for food, NSG is known to activate autotrophy through its prymnesiophyte (green algae) endosymbiont *Protoeuglena noctilucae* (Harrison et al., 2011) as an alternate source of nutrition. Consumption of NO_3^- by the endosymbiont then would increase the Si:DIN ratio in association with NSG-H.

Once this autotrophy-dominant stage is reached, Si may not be a limiting nutrient element for the production of diatoms as proposed (Sarma et al., 2019; Xiang et al., 2019).

The difference between the NE and NW winds was significant ($p = 0.015$) for H_4SiO_4 (Table 1). The WICC was reasoned as the source of H_4SiO_4 earlier from Figure 5a. The WICC is a pole-ward moving current moving against the NE monsoon winds, being driven by a pressure gradient that exists due to a combination of local and remote forcings (Shetye et al., 1994, 2008). A weakening of (the opposing) NE winds could increase the signature of the WICC when the NW winds were strong. Moreover, as the Si:DIN ratio was conservative (with respect to salinity) versus the combined data of stations 13 and 14 (Figure 8b), the role of WICC on the NSG blooms may have extended from the WICC-proximate region (Station 14) to the distal region (Station 13) in the NEAS.

Thus, the question that came up was why did Si concentration remain high (average, $\sim 2.3 \mu\text{M}$) in the NSG-H samples, and why were the diatoms not able to utilize it to multiply further? Was any other essential nutrient missing? These questions favor iron (Fe) as the missing nutrient element. In productive ecosystems such as NEAS during winter, continuous diatom production could lead to dissolved iron (Fe) exhaustion before other nutrients e.g., Si; and iron limitation has been reported in the NAS (Moffet et al., 2015; Naqvi et al., 2010; Sharada et al., 2020).

4.2. Wind influenced phytoplankton indices in the evolving NSG ecosystem

Dinoflagellates increased consistently with NE wind speed (Figure 7b) while MLD got deeper. The accompanying higher nutrient entrainment at the surface should have, to the contrary, advantaged the diatoms. Windy conditions have been inferred to be behind the increased dominance of diatoms over dinoflagellates in the Mediterranean Sea (Stephanie et al., 2012). The exceptional behavior seems to be due to the food preference for diatoms over dinoflagellates (Kiorboe and Titelman, 1998). The dietary choice of NSG may be a trade-off between maximizing food and nutrient intake and minimizing the energy cost of handling different prey (Zhang et al., 2016). The absence of any trend during NW winds (when NSG-H occurs), may be because the shortage of food in comparison to its requirement leaves no choice to the NSG-H.

The Diatoms:(Diatoms+Dinoflagellates) ratio not only distinguished the NE and NW winds significantly (Table 1) but also held a significant negative relationship with NE wind speed (and not NW wind speed) (Figure 7c). The Diatoms:(Diatoms+Dinoflagellates) ratio thus appears as a useful ecological index in the NEAS, as in the case of the Diatoms: Dinoflagellates ratio (Teixeira et al., 2016; Tett et al., 2008; Wasmund et al., 2017). The positive relationship of NE wind speed with the dinoflagellates: (dinoflagellates + cyanophyceae) ratio (Figure 7d) was also significant ($p < 0.05$). It may be indicating that the cyanophyceae appear increasingly as the NE wind slows, i.e., when MLD is shallow, the surface is warmer and has a lower nutrient concentration. The N_2 -fixing cyanophyceae are known to gain an advantage at low NO_3^- (Duce et al.,

2008). However, as the ratio was of similar magnitude in the NE and NW winds (average, 0.88, Table 2) and did not significantly distinguish the two winds, further studies are needed in its support before it can unequivocally be proposed as an ecological indicator.

4.3. Support for the role of winds from earlier studies

Vikebo et al. (2019) found an overwhelming 60% role for wind intensity in the onset time of spring phytoplankton (in terms of chl-*a*) bloom. In the northern Arabian Sea, Dwivedi et al. (2006) observed coupling between phytoplankton blooms and the strength of the NE monsoon wind. But this should be applicable only at lower NSG abundances (up to NSG-M range when the wind speed is limited up to $\sim 6 \text{ m s}^{-1}$, Figure 6b), as observed by Miyaguchi et al. (2006). At higher wind speeds, NS blooms are prevented due to physical stress (Tsai et al., 2018). The dual role of winds in phytoplankton blooms is quite well established. For example, Fitch and Moore (2007) found 5 m s^{-1} as a threshold below which the bloom was facilitated and above which it was retarded.

4.4. Origin and nature of NW winds

The back-trajectories of winds constructed by the HYSPLIT model of the NOAA of the air parcels at altitudes >0.5 up to 4 km indicated that during C#2, the winds were synoptically mostly NE and mostly NW during C#1 (Figure 3). The HYSPLIT model simulations are extensively used and valued for their real-time performance (Rolph et al. 2017; Stein et al. 2015), e.g., source apportioning the African dust (Escudero et al., 2011), and hence dependable.

4.4.1. The likely role of the Afro-Asian dust belt on the northwesterly winds

February-March is a time when the northeasterly trade winds are dominant in the northern Arabian Sea (Dwivedi et al., 2006). Northwesterly winds are also known over the NAS (Chaichitehrani and Allahdadi, 2018) during this time but their impact on the climatology and marine biogeochemistry is not known well. The Arabian desert storms known as Shamal form primarily in summer and winter, and the latter is particularly strong, occurring as 2–5 days episodes with wind speed up to $\sim 20 \text{ m s}^{-1}$ and strengthened by the western disturbances from the Mediterranean, which create a cold front (Yu et al., 2016). Satellite images have shown the shamal wind to advect with its leading storm edge extending up to even Mumbai in India. Satellite observations have also shown that, on a global scale, the dominant sources of natural mineral dust aerosols, located in the dust belt of the Afro-Asian region, leave their imprint along its trajectory that includes the northern Arabian Sea (and Northern India) and up to the Tarim Basin in China (Herman et al. 1997; Torres et al. 1998). The two distinct sources of the cooler (and drier) northeastern winds and the warmer (and wetter) dusty northwestern winds could be affecting the winter ecosystem of the northern Arabian Sea in a subtly distinguishable way.

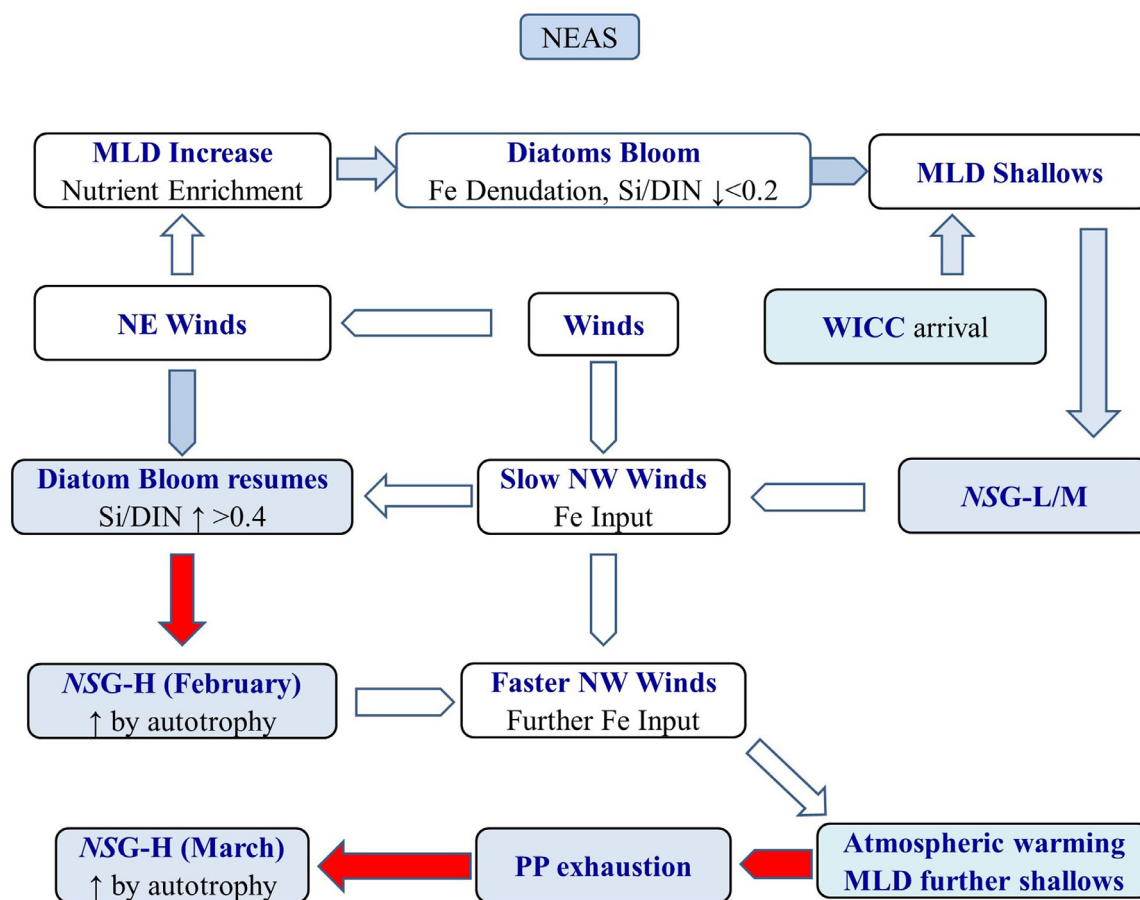


Figure 10 A scheme of the blooms' formation of the green *Noctiluca scintillans* (NSG) in the northeastern Arabian Sea (NEAS), synthesizing the results of this and earlier studies (no fill: atmosphere-driven flux or phytoplankton production; blue-fill: ocean-driven process; red-fill: NSG bloom; text within the boxes is the outcome and its causative process). MLD: Mixed Layer Depth, PP: Phytoplankton other than NSG, NW: North-West, NE: North-East, WICC: Western India Coastal Current, DIN: Dissolved Inorganic Nitrogen.

4.4.2. Role for iron in NSG blooms during NW winds

The arguments presented above support the hypothesis that winds are a key factor in the intensification of NSG blooms. When NW winds constituted a significant portion of the overall wind structure, diatoms used Si more economically, leading to a higher Si:DIN ratio in the water. On the other hand, during NE winds, diatoms fixed more silicon so that Si:DIN ratio fell, leading to Si-stress. The atmospheric dust and aerosols transported by the NE and NW winds to the NAS during the winter and spring inter-monsoon originate from the Pakistan/Iran/Arabian Peninsula belt and the Thar desert/the Indus River alluvial plain, respectively (Bikkina et al., 2020; Pease et al., 1998). The Fe/Al ratio of these two sources is not significantly different and similar to the crustal average (Kumar et al., 2020). However, fractionation taking place during transit has been shown to induce a change in the physical, chemical, and mineralogical composition of the particles (Baker and Jickells, 2006; Trapp et al., 2010). During the faster (and nearer to source region) NE winds, the particles are likely coarser and may be contributing less bioavailable Fe compared to the NW winds as in the Atlantic Ocean for which the Fe solubility was observed as $\sim 10\%$ during faster winds versus up to 80% during slower winds (Trapp et al., 2010). Further, the distinctly

higher RH during NW than NE winds could be promoting a higher Fe input, as has been observed for wet deposition over dry deposition (Suresh et al., 2021). Unlike Fe in the water column, which is mostly in the form of insoluble complexes and hence not bioavailable (Shi et al., 2010), this fresh source introduces bioavailable Fe (Rubin et al., 2011), which can fuel enhanced diatom production. The dissolved iron sourcing from aerosols may not increase its inventory substantially in the mixed-layer as its release is not sustained; however, its initial rapid release takes place making it bioavailable (Boyd et al., 2010).

4.5. A probable mechanism of the formation of NSG blooms: a synthesis

Various sea surface characteristics have been proposed so far as leading to the formation of NSG blooms (Goes et al., 2020; Gomes et al., 2014; Harrison et al., 2019; Lotiker et al., 2018; Prakash et al., 2017; Sarma et al., 2019). They do not explain the hydrographic and regional preferences as well as the timing of the NSG blooms within the NEAS at various intensities satisfactorily. For example, a temperature range of $25\text{--}30^\circ\text{C}$ is reported as preferred

by NSG worldwide (Harrison et al., 2011), and $\sim 25^{\circ}\text{C}$ in the NEAS (Lotliker et al., 2018). This study has shown that greater abundances occurred at SST of $\sim 27^{\circ}\text{C}$ than at 25°C . Similarly, discontinuation of Si renewal at the sea surface due to the shallowing of the mixed layer upon the WICC arrival has been suggested as proving the trigger for NSG blooms (Sarma et al., 2019). But this study has shown that during the NSG-H phase of higher abundance, Si was higher and the Si:DIN ratio more favourable than during NSG-M phase of lower abundance.

A synthesis based on the results on winds (this study) and of the earlier works on the likely sequence of events leading to the formation of NSG blooms is shown in Figure 10. During February (latter half of northeast monsoon, C#2), when the mixed layer was still deep, the surface entrainment of nutrients caused diatoms to bloom, but the diatoms were soon disadvantaged due to the advancement of WICC and the shoaling of mixed layer shallower than the silicicline (Sarma et al., 2019). The Si:DIN (dissolved inorganic nitrogen) ratio fell to <0.2 due to progressive exhaustion of iron (Fe) since diatoms are forced to consume more Si per unit C fixed (Timmermans et al., 2004). Since the regeneration of Si is slower and takes place at greater depths than N, the fall in Si:DIN ratio could have been sustained because of the shallowed mixed layer. But as the plot of MLD on Si:DIN was highly scattered, even cruise-wise, i.e., separately for C#1 and C#2, this assertion could not be verified.

With the diatoms disadvantaged, the opportunist NSG arrives to prey on the diatom stock. The advantage shifts between diatoms and NSG quite a few times due to the alternating deepening and shallowing of MLD by the influence of WICC and the influence of winds varying between NE and NW. When the cooler NE winds prevailed, the surface moved towards uniformity and a deeper mixed layer which advantages the diatoms, but this advantage was lost progressively due to the exhaustion of Fe.

The WICC sources Si needed for the production of diatoms but not soluble iron, i.e., Fe(II) as the water was not sub-oxic. The NW winds input Fe by which diatoms initially gained an advantage but soon, due to stratification as the NW winds were warmer, the advantage shifted to NSG. During C#2 when the NW winds were weaker, the role of the deficiency of iron became more apparent from the NSG abundances of 22600 cells l^{-1} onwards i.e., when the Si:DIN ratio dropped to 0.58. During C#1 when the NW winds were stronger, the role (deficiency) of the deficiency of iron became more apparent at the NSG abundances of 64000 cells l^{-1} , i.e., when the Si:DIN ratio fell to 1.31, and further to 0.41 at an NSG abundance of 190000 cells l^{-1} .

5. Conclusion

The study demonstrates a clear role of the winds and their direction in the formation and intensification of the blooms of the green variant of *Noctiluca scintillans* (NSG) in the northeastern Arabian Sea (NEAS) during late winter (February–March). During February of 2017 (field campaign, C#2), the winds were mostly northeastern (NE) due to the influence of the winter monsoon. The NE winds are cool, drive convection in the upper water column and thereby surface entrainment of nutrients followed by phytoplank-

ton (diatom) production. The NW winds are warm, and their temperature increased steeply with speed (by 3 degrees C over an increase from 4 to 10 m s^{-1} wind speed). The NW winds drive stratification and arrest nutrient input at the surface from the water column but input the crucial micronutrient iron. Wind speed and its direction, i.e., whether NE or SW can be useful as parameters to estimate NSG abundance confidently using the equation:

$$\text{NSG} = -1268682 + 52979 \times \text{SST} - 5615 \times \text{NE wind speed} - 8132 \times \text{NW wind speed},$$

where NSG abundance is in cells l^{-1} , SST is in $^{\circ}\text{C}$ and wind speed is in m s^{-1} .

Silicic acid (H_4SiO_4) and the Si:DIN ratio (DIN = dissolved inorganic nitrogen, $\text{NO}_2^- + \text{NO}_3^- + \text{NH}_4^+$) divided the NSG abundances into 3 ranges namely <1000 cells l^{-1} (NSG-L), up to 22600 (NSG-M) and 46000–190000 cells l^{-1} (NSG-H). The growth of NSG accompanied increases of Si and Si:DIN ratios up to the NSG-M range. Further growth of NSG-M to NSG-H was accompanied by a fall of Si and Si:DIN ratios. This meant that H_4SiO_4 although present (due to WICC) was not utilized for diatom production. The missing nutrient that prevented diatom production was hypothesized as iron. Depending on the phytoplankton abundance (NSG-M abundance) at the time of iron deficiency and the quantum of iron input which depends on the strength of the NW wind, NSG's further proliferation happened. During February, the NW winds were weaker, and the maximum abundance of NSG-H was 52600 cells l^{-1} . During March, the NW winds were strong and more frequent, and the maximum abundance of NSG-H was 190000 cells l^{-1} . The proliferation is by autotrophy of NSG through its endosymbiont with the help of other nutrients like nitrate and phosphate in which the seawater is replete.

The inverse linear relationship between NE wind speed and Diatoms: (Diatoms + Dinoflagellates other than NSG) ratio indicated that diatoms were better preferred as food over dinoflagellates. The (weak) positive relationship with the (Dinoflagellates other than NSG): (Dinoflagellates (other than NSG) + Cyanophyceae) ratio indicated that cyanophyceae were likely preferred over dinoflagellates as food for the NSG.

The time-series studies at Stations 13 and 14 revealed the effects of the two wind sources. At Station 13, its NE winds did not transport iron, nor was the WICC proximate to supply Si, and thus had limited NSG-M. At Station 14, its dual (NE + NW) winds and proximity to WICC provided twin benefits – of H_4SiO_4 enrichment by WICC and iron replenishment by the NW winds. At Station 13, air temperature, which is the essential driver for the loss of surface water buoyancy and a deepening of the ML, led to its linear relationship with sea surface salinity (SSS). But at Station 14 the winter cooling by the NE winds is overwhelmed by the warming caused by the NW winds leading to surface stratification and salinity increase so that it was the SST that related to SSS.

The role attributed earlier to iron as a potentially limiting nutrient element in the northern Arabian Sea is thus observed in the form of the link between the NSG blooms and the wind direction. We do not argue that iron limitation is secular in the NAS but hypothesize that under conditions of intense winter diatom blooms, local exhaustion of iron happens before Si and that its replenishment by the NW

winds provides a trigger for the already existing but devoid of prey NSG to form intense blooms, aided by its autotrophic advantage.

Authors' contributions

N.S.S. conceived the hypothesis, carried out data processing, initial data plotting, and drafted the manuscript; A.A.L. conceptualized, executed, and conducted the cruise; S.K.B., A.A.L., S.R.P., and A.S. carried out onboard observations, operated sampling gears, handled samples; S.R.P. carried out chemical analyses, S.K.B. carried out algal taxonomy, prepared final versions of graphical illustrations, provided necessary inputs for the main text, and carried out editorial formatting. N.S.S. and A.A.L. reviewed the final version of the manuscript and approved it.

Funding

This work was supported by INCOIS provided project grant under SATCORE program (to NSS F&A:XII:D2:023) and CSIR-HRDG Research Associateship (to SRP, 09/002 (510)/2016 EMR-I).

Data availability

The authors confirm that the data supporting the findings of this study are available within the article and full numerical data will be provided on reasonable request.

Conflict of competing interest

The authors declare that they have no competing interests.

Acknowledgments

The authors gratefully acknowledge the NOAA Air Resources Laboratory (ARL) for the provision of the HYSPLIT transport and dispersion model and/or READY website (<https://www.ready.noaa.gov>) used in this publication. We thank the two anonymous reviewers and editor for their valuable comments/suggestions, which helped in improving this paper. The authors thank the Directors of INCOIS and NCPOR for their encouragement, the CMLRE (MoES) for the ship facility, and the crew and other scientists for onboard cooperation. NSS thanks Andhra University for laboratory facilities and Honorary Professorship. This is a joint contribution of Andhra University, INCOIS (contribution no 462), and NCPOR (contribution no J-24/2022-23).

Supplementary materials

Supplementary material associated with this article can be found, in the online version, at <https://doi.org/10.1016/j.oceano.2022.06.004>.

References

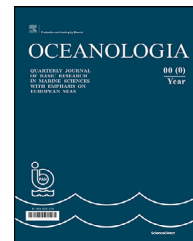
- Baker, A.R., Jickells, T.D., 2006. Mineral particle size as a control on aerosol iron solubility. *Geophys. Res. Lett.* 33, L17608.
- Balachandran, K.K., Laluraj, C.M., Jyothibabu, R., Madhu, N.V., Muraleedharan, K.R., Vijay, J.G., Maheswaran, P.A., Ashraff, T.T.M., Nair, K.K.C., Achuthankutty, C.T., 2008. Hydrography and biogeochemistry of the north western Bay of Bengal and the north eastern Arabian Sea during winter monsoon. *J. Mar. Syst.* 73, 76–86.
- Baliarsingh, S.K., Lotliker, A.A., Sudheesh, V., Samanta, A., Das, S., Vijayan, A.K., 2018. Response of phytoplankton community and size classes to green *Noctiluca* bloom in the northern Arabian Sea. *Mar. Pollut. Bull.* 129 (1), 222–230.
- Bi, R., Cao, Z., Ismar-Rebitz, S., Sommer, U., Zhang, H., Ding, Y., Zhao, M., 2021. Responses of Marine Diatom-Dinoflagellate Competition to Multiple Environmental Drivers: Abundance, Elemental and Biochemical Aspects. *Front. Microbiol.* 12, 731786.
- Bikkina, P., Sarma, V.V.S.S., Kawamura, K., Bikkina, S., Kunwar, B., Sherin, C.K., 2020. Chemical characterization of wintertime aerosols over the Arabian Sea: Impact of marine sources and long-range transport. *Atmos. Environ.* 239, 117749.
- Boyd, P.W., Mackie, D.S., Hunter, K.A., 2010. Aerosol iron deposition to the surface ocean—Modes of iron supply and biological responses. *Mar. Chem.* 120 (1), 128–143.
- Burgay, F., Spolaor, A., Gabrieli, J., Cozzi, G., Turetta, C., Vallelonga, P., Barbante, C., 2021. Atmospheric iron supply and marine productivity in the glacial North Pacific Ocean. *Clim. Past.* 17, 491–505.
- Chaichitehrani, C., Mohammad, N.A., 2018. Overview of wind climatology for the Gulf of Oman and the Northern Arabian Sea. *Am. J. Fluid Dyn.* 8 (1), 1–9.
- Chappell, P.D., Moffett, J.W., Hynes, A.M., Webb, E.A., 2012. Molecular evidence of iron limitation and availability in the global diazotroph *Trichodesmium*. *ISME J* 6, 1728–1739.
- Duce, R.A., LaRoche, J., Altheimer, K., Arrigo, K.R., Baker, A.R., Capone, D.G., et al., 2008. Impacts of atmospheric anthropogenic nitrogen on the open ocean. *Science* 320, 893–897.
- Dwivedi, R.M., Chauhan, R., Solanki, H.U., Raman, M., Matondkar, S.G.P., Madhu, V.R., Meenakumari, B., 2012. Study of ecological consequence of the bloom (*Noctiluca miliaris*) in offshore waters of the Northern Arabian Sea. *Indian J. Geo-Mar. Sci.* 41 (4), 304–313.
- Dwivedi, R.M., Raman, M., Parab, S., Matondkar, S.G.P., Nayak, S., 2006. Influence of northeasterly trade winds on intensity of winter bloom in the Northern Arabian Sea. *Curr. Sci.* 90 (10), 1397–1406.
- Escudero, M., Stein, A.F., Draxler, R.R., Querol, X., Alastuey, A., Castillo, S., Avila, A., 2011. Source apportionment for African dust outbreaks over the Western Mediterranean using the HYSPLIT model. *Atmos. Res.* 99, 518–527.
- Fitch, D.T., Moore, J.K., 2007. Wind speed influence on phytoplankton bloom dynamics in the Southern Ocean Marginal Ice Zone. *J. Geophys. Res.* 112, C08006.
- Goes, J.I., Tian, H., Gomes, H.d.R., et al., 2020. Ecosystem state change in the Arabian Sea fueled by the recent loss of snow over the Himalayan-Tibetan Plateau region. *Sci. Rep.* 10, 7422.
- Gomes, H.d.R., McKee, K., Mile, A., Thandapu, S., Al-Hashmi, K., Jiang, X., Goes, J.I., 2018. Influence of light availability and prey type on the growth and photo-physiological rates of the mixotroph *Noctiluca scintillans*. *Frontiers Mar. Sci.* 5.
- Gomes, H.d.R., Goes, J.I., Matondkar, S.G.P., Buskey, E.J., Basu, S., Parab, S., Prasad, T.G., 2014. Massive outbreaks of *Noctiluca scintillans* blooms in the Arabian Sea due to spread of hypoxia. *Nat. Commun.* 5, 4862.
- Grasshoff, K., Kremling, K., Ehrhardt, M., 1999. Methods of seawater analysis. Verlag Chemie, Weinheim, 632 pp.

- Guieu, C., Muchamad, A., Olivier, A., Nathalie, B., Marina, L., Christian, E., Zouhair, L., 2019. Major impact of dust deposition on the productivity of the Arabian Sea. *Geophys. Res. Letts.* 46.
- Guo, C., Yu, J., Ho, T.-Y., Wang, L., Song, S., Kong, L., Liu, H., 2012. Dynamics of phytoplankton community structure in the South China Sea in response to the East Asian aerosol input. *Biogeosci.* 9, 1519–1536.
- Harrison, P., Piontkovski, S., Al-Hashmi, K., 2019. Overview of decadal ecosystem changes in the western Arabian Sea and the occurrence of Algal blooms. *J. Agri. Mar. Sci.* 23 (1), 11.
- Harrison, P.J., Furuya, K., Glibert, P.M., Xu, J., Liu, H.B., Yin, K., Lee, J.H.W., Anderson, D.M., Gowen, R., Al-Azri, A.R., Ho, A., 2011. Geographical distribution of red and green *Noctiluca scintillans*. *Chin. J. Oceanol. Limnol.* 29, 807–831.
- Herman, J.R., Bhartia, P.K., Torres, O., Hsu, C., Sefstor, C., Celarier, E., 1997. Global distribution of UV-absorbing aerosols from Nimbus7/TOMS data. *J. Geophys. Res.* 102 (D14), 16911–16922.
- Hutchins, D.A., Bruland, K.W., 1998. Iron-limited diatom growth and Si:N uptake ratios in a coastal upwelling regime. *Nature* 393, 561–564.
- Kiorboe, T., Titelman, J., 1998. Feeding, prey selection and prey encounter mechanisms in the heterotrophic dinoflagellate *Noctiluca scintillans*. *J. Plankton Res.* 20 (8), 1615–1636.
- Koné, V., Aumont, O., Lévy, M., Resplandy, L., 2009. Physical and Biogeochemical Controls of the Phytoplankton Seasonal Cycle in the Indian Ocean: A Modeling Study. *Indian Ocean Biogeochemical Processes and Ecological Variability Geophysical Monograph Series 185*. Am. Geophys. Union.
- Kumar, A., Suresh, K., Rahaman, W., 2020. Geochemical characterization of modern aeolian dust over the Northeastern Arabian Sea: Implication for dust transport in the Arabian Sea. *Sci. Total Environ.* 729, 138576.
- Kumar, P.K., Singh, A., Ramesh, R., Nallathambi, T., 2017. N₂ Fixation in the Eastern Arabian Sea: Probable Role of Heterotrophic Diazotrophs. *Front Mar. Sci.* 4.
- Kumar, S.P., Narvekar, J., 2005. Seasonal variability of the mixed layer in the central Arabian Sea and its implication on nutrients and primary productivity. *Deep Sea Res. Pt. II* 52 (14–15), 1848–1861.
- Kustka, A.B., Sanudo-Wilhelmy, S.A., Carpenter, E.J., Capone, D., Burns, J., Sunda, W.G., 2003. Iron requirements for dinitrogen- and ammonium-supported growth in cultures of *Trichodesmium* (IMS 101): comparison with nitrogen fixation rates and iron: carbon ratios of field populations. *Limnol. Oceanogr.* 48, 1869–1884.
- Lakshmi, R.S., Prakash, S., Lotliker, A.A., Baliarsingh, S.K., Samanta, A., Mathew, T., Chatterjee, A., Sahu, B.K., Nair, T.M., 2021. Physicochemical controls on the initiation of phytoplankton bloom during the winter monsoon in the Arabian Sea. *Scientific Reports* 11, 13448.
- Lotliker, A.A., Baliarsingh, S.K., Trainer, V.L., Wells, M.L., Wilson, C., Bhaskar, T.U., Samanta, A., Shahimol, S.R., 2018. Characterization of oceanic *Noctiluca* blooms not associated with hypoxia in the northeastern Arabian Sea. *Harmful Algae* 74, 46–57.
- Madhu, N.V., Jyothibabu, R., Maheswaran, P.A., Jayaraj, K.A., Achuthankutty, C.T., 2012. Enhanced chlorophyll-*a* and primary production in the northern Arabian Sea during the spring intermonsoon due to green *Noctiluca scintillans* bloom. *Mar. Biol. Res.* 8 (2), 182–188.
- Madhupratap, M., Kumar, S.P., Bhattathiri, P.M.A., Kumar, M.D., Raghukumar, S., Nair, K.K.C., Ramaiah, N., 1996. Mechanism of the biological response to winter cooling in the northeastern Arabian Sea. *Nature* 384, 549–552.
- Maher, B.A., Prospero, J.M., Mackie, D., Gaiero, D., Hesse, P.P., Balkanski, Y., 2010. Global connections between aeolian dust, climate and ocean biogeochemistry at the present day and at the last glacial maximum. *Earth-Sci. Rev.* 99 (1–2), 61–97.
- Mills, M.M., Ridame, C., Davey, M., La Roche, J., Geider, R.J., 2004. Iron and phosphorus co-limit nitrogen fixation in the eastern tropical North Atlantic. *Nature* 429, 292–294.
- Miyaguchi, H., Fujiki, T., Kikuchi, T., Kuwahara, V.S., Toda, T., 2006. Relationship between the bloom of *Noctiluca scintillans* and environmental factors in the coastal waters of Sagami Bay, Japan. *J. Plankton Res.* 28 (3), 313–324.
- Moffett, J.W., Vedamati, J., Goepfert, T.J., Pratihary, A., Gauns, M., Naqvi, S.W.A., 2015. Biogeochemistry of iron in the Arabian Sea. *Limnol. Oceanogr.* 60 (5), 1671–1688.
- Moore, C.M., Mills, M.M., Achterberg, E.P., et al., 2009. Large-scale distribution of Atlantic nitrogen fixation controlled by iron availability. *Nat. Geosci.* 2, 867–871.
- National Oceanographic and Atmospheric Administration (NOAA), 2021. http://cimss.ssec.wisc.edu/clavr/amato/Amato_T_Evan/Arabian_0208.html, “Arabian Sea dust storm AVHRR images”.
- Naqvi, S.W.A., Moffett, J.W., Gauns, M.U., Narvekar, P.V., Pratihary, A.K., Naik, H., Ahmed, S.I., 2010. The Arabian Sea as a high-nutrient, low-chlorophyll region during the late southwest monsoon. *Biogeosciences* 7 (7), 2091–2100.
- Padmakumar, K.B., SreeRanjima, G., Fanimol, C.L., Menon, N.R., Sanjeevan, V.N., 2010. Preponderance of heterotrophic *Noctiluca scintillans* during a multi-species diatom bloom along the southwest coast of India. *Int. J. Oceans Oceanogr.* 4 (1), 55–63.
- Pandi, S.R., Baliarsingh, S.K., Lotliker, A.A., Sarma, N.S., Tripathy, S.C., 2020. Empirical relationships for remote sensing reflectance and *Noctiluca scintillans* cell density in the northeastern Arabian Sea. *Mar. Poll. Bull.* 161.
- Pease, P.P., Tchakerian, V.P., Tindale, N.W., 1998. Aerosols over the Arabian Sea: geochemistry and source areas for aeolian desert dust. *J. Arid Environ.* 39 (3), 477–496.
- Piontkovski, S.A., Serikova, I.M., Evstigneev, V.P., Prusova, I.Y., Zagorodnaya, Y.A., Al-Hashmi, K.A., Al-Abri, N.M., 2021. Seasonal blooms of the dinoflagellate algae *Noctiluca scintillans*: regional and global scale aspects. *Reg. Stud. Mar. Sci.* 44, 101771.
- Prakash, S., Roy, R., Lotliker, A., 2017. Revisiting the *Noctiluca scintillans* paradox in northern Arabian Sea. *Curr. Sci.* 113 (7), 1429–1434.
- Prasad, T.G., 2004. A comparison of mixed-layer dynamics between the Arabian Sea and Bay of Bengal: One-dimensional model results. *J. Geophys. Res. - Oceans* 109 (3), 1–15.
- Prasanna Kumar, S., Prasad, T.G., 1999. Formation and spreading of Arabian Sea high-salinity water mass. *J. Geophys. Res. - Oceans* 104 (C1), 1455–1464.
- Prasanna Kumar, S., Narvekar, J., Kumar, A., Shaji, C., Anand, P., Sabu, P., Rijomon, G., Josia, J., Jayaraj, K.A., Radhika, A., Nair, K.K.C., 2004. Intrusion of the Bay of Bengal water into the Arabian Sea during winter monsoon and associated chemical and biological response. *Geophys. Res. Lett.* 31, L15304.
- Rizzolo, J.A., Barbosa, C.G.G., Borillo, G.C., Godoi, A.F.L., Souza, R.A.F., Andreoli, R.V., Manzi, A.O., Sá, M.O., Alves, E.G., Pöhlker, C., Angelis, I.H., Ditas, F., Saturno, J., Moran-Zuloaga, D., Rizzo, L.V., Rosário, N.V., Pauliquevis, T., Santos, R.M.N., Yamamoto, C.I., Andreae, M.O., Artaxo, P., Taylor, P.E., Godoi, R.H.M., 2017. Soluble iron nutrients in Saharan dust over the central Amazon rainforest. *Atmos. Chem. Phys.* 17, 2673–2687.
- Rolph, G., Stein, A., Stunder, B., 2017. Real-time environmental applications and display system. *READY. Environ. Model. Software* 95, 210–228.
- Rubin, M., Berman-Frank, I., Shaked, Y., 2011. Dust- and mineral-iron utilization by the marine dinitrogen-fixer *Trichodesmium*. *Nature Geosci* 4, 529–534.

- Sarma, V.V.S.S., Patil, J.S., Shankar, D., Anil, A.C., 2019. Shallow convective mixing promotes massive *Noctiluca scintillans* bloom in the northeastern Arabian Sea. *Mar. Poll. Bull.* 138, 428–436.
- Shankar, D., Remya, R., Vinayachandran, P.N., Chatterjee, A., Behara, A., 2015. Inhibition of mixed-layer deepening during winter in the northeastern Arabian Sea by the West India Coastal Current. *Clim. Dyn.* 47, 1049–1072.
- Sharada, M.K., Kalyani, C.D., Swathi, P.S., 2020. Iron limitation study in the North Indian Ocean using model simulations. *J. Earth. Syst. Sci.* 129, 93.
- Shetye, S.R., Gouveia, A.D., Shenoi, S.S.C., Michael, G.S., Sundar, D., Almeida, A.M., Santanam, K., 1991. The coastal current off western India during the northeast monsoon. *Deep Sea Res* 38 (12), 1517–1529.
- Shetye, S.R., Gouveia, A.D., Shenoi, S.S.C., 1994. Circulation and water masses of the Arabian Sea. *Proc. Indian Acad. Sci. (Earth Planet. Sci.)* 103 (2), 107–123.
- Shetye, S.R., Iyyappan, S., Shankar, D., Sundar, D., Seelam, J., Mehra, P., Desai, R.G.P., Pednekar, P.S., 2008. Observational evidence for remote forcing of the West India Coastal Current. *J. Geophys. Res.* 113.
- Shi, D., Xu, Y., Hopkinson, B.M., Morel, F.M.M., 2010. Effect of ocean acidification on iron availability to marine phytoplankton. *Science* 327, 676–679.
- Smitha, B.R., Sanjeevan, V.N., Padmakumar, K.B., Hussain, M.S., Salini, T.C., Lix, J.K., 2022. Role of mesoscale eddies in the sustenance of high biological productivity in North Eastern Arabian Sea during the winter-spring transition period. *Sci. Total Environ.* 809, 151173.
- Stein, A.F., Draxler, R.R., Rolph, G.D., Stunder, B.J.B., Cohen, M.D., Ngan, F., 2015. NOAA's HYSPLIT atmospheric transport and dispersion modeling system. *Bull. Amer. Meteor. Soc.* 96, 2059–2077.
- Stephanie, L., Hinder, S.L., Hays, G.C., Edwards, M., Roberts, E.C., Walne, A.W., Gravenor, M.B., 2012. Changes in marine dinoflagellate and diatom abundance under climate change. *Nature Clim. Change* 1–5.
- Suresh, K., Kumar, A., Ramaswamy, V., Prakash Babu, C., 2021. Seasonal variability in aeolian dust deposition fluxes and their mineralogical composition over the Northeastern Arabian Sea. *Int. J. Environ. Sci. Technol.*
- Teixeira, H., Berg, T., Uusitalo, L., Fűrhaupter, K., Heiskanen, A.-S., Mazik, K., et al., 2016. A catalogue of marine biodiversity indicators. *Front. Mar. Sci.* 3, 207.
- Tett, P., Carreira, C., Mills, D.K., Leeuwen, v.S., Foden, J., Brennan, E., Gowen, R.J., 2008. Use of a phytoplankton community index to assess the health of coastal waters. *ICES J. Mar. Sci.* 65, 1475–1482.
- Tian, R., Chen, J., Sun, X., Li, D., Liu, C., Weng, H., 2018. Algae explosive growth mechanism enabling weather-like forecast of harmful algal blooms. *Sci. Rep.* 8, 9923.
- Tian, R., Lin, Q., Li, D., Zhang, W., Zhao, X., 2020. Atmospheric transport of nutrients during a harmful algal bloom event. *Reg. Stud. Mar. Sci.* 34, 101007.
- Timmermans, K.R., Wagt, B vd, de Baar, H.J.W., 2004. Growth rates, half-saturation constants, and silicate, nitrate, and phosphate depletion in relation to iron availability of four large, open-ocean diatoms from the Southern Ocean. *Limnol. Oceanogr.* 49 (6), 2141–2151.
- Tomas, C.R., 1997. *Identifying Marine Phytoplankton*. Academic Press, USA, 858 pp.
- Torres, O., Bhartia, P.K., Herman, J.R., Ahmad, Z., Gleason, J., 1998. Derivation of aerosol properties from satellite measurements of backscattered ultraviolet radiation: theoretical basis. *J. Geophys. Res.* 103, 17,099–17,110.
- Trapp, J.M., Millero, F.J., Prospero, J.M., 2010. Trends in the solubility of iron in dust-dominated aerosols in the equatorial Atlantic trade winds: Importance of iron speciation and sources. *Geochem. Geophys. Geosyst.* 11, Q03014.
- Tsai, S.F., Wu, L.Y., Chou, W.C., Chiang, K.P., 2018. The dynamics of a dominant dinoflagellate, *Noctiluca scintillans*, in the subtropical coastal waters of the Matsu archipelago. *Mar. Poll. Bull.* 127, 553–558.
- Turkoglu, M., 2013. Red tides of the dinoflagellate *Noctiluca scintillans* associated with eutrophication in the Sea of Marmara (The Dardanelles, Turkey). *Oceanologia* 55 (3), 709–732.
- Vikebo, F.B., Strand, K.O., Sundby, S., 2019. Wind intensity is key to phytoplankton spring bloom under climate change. *Front. Mar. Sci.* 6, 1–9.
- Wasmund, N., Kownacka, J., Göbel, J., Jaanus, A., Johansen, M., Jurgensone, I., Lehtinen, S., Powilleit, M., 2017. The diatom/dinoflagellate index as an indicator of ecosystem changes in the Baltic Sea. Principle and handling instruction. *Front. Mar. Sci.* 4, 22.
- Whittaker, S., Bidle, K.D., Kustka, A.B., Falkowski, P.G., 2011. Quantification of nitrogenase in *Trichodesmium* IMS 101: implications for iron limitation of nitrogen fixation in the ocean. *Environ. Microbiol. Rep.* 3, 54–58.
- Xiang, C., Tan, Y., Zhang, H., Liu, J., Ke, Z., Li, G., 2019. The key to dinoflagellate (*Noctiluca scintillans*) blooming and outcompeting diatoms in winter off Pakistan, northern Arabian Sea. *Sci. Total Environ.* 694, 133396.
- Yu, Y., Notaro, M., Kalashnikova, O.V., Garay, M.J., 2016. Climatology of summer Shamal wind in the Middle East. *J. Geophys. Res. Atmos.* 121, 289–305.
- Zhang, S., Liu, H., Guo, C., Harrison, P.J., 2016. Differential feeding and growth of *Noctiluca scintillans* on monospecific and mixed diets. *Mar. Ecol. Prog. Ser.* 549, 27–40.

Available online at www.sciencedirect.com

ScienceDirect

journal homepage: www.journals.elsevier.com/oceanologia

ORIGINAL RESEARCH ARTICLE

Dynamics of trace metals in sediments of a seasonally hypoxic coastal zone in the southeastern Arabian Sea

Dayana Mathew^a, Thundiyl Raju Gireeshkumar^{a,*}, Kareekunnan Shameem^b,
 Camey Monica Furtado^a, Kanneth Satheesan Arya^a,
 Pallikkoottathil Balakrishnan Udayakrishnan^c,
 Kizhakkepat Kalathil Balachandran^a

^a CSIR – National Institute of Oceanography, Regional Centre, Kochi, India

^b Inter University Centre for Development of Marine Biotechnology, School of Marine Sciences, Cochin University of Science and Technology, Kochi, India

^c CSIR – National Institute of Oceanography, Regional Centre, Mumbai, India

Received 10 February 2021; accepted 27 June 2022

Available online 14 July 2022

KEYWORDS

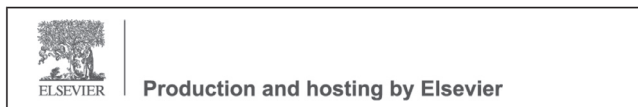
Geochemistry;
 Trace metals;
 Upwelling;
 Hypoxia;
 Organic matter;
 Bioavailability

Abstract This study examined the effect of water column hypoxia on the distribution and geochemical fractionation of trace metals in the seasonally hypoxic coastal environment in the southeastern Arabian Sea. Water and surface sediments were collected fortnightly from the Alappuzha mud bank between April and August 2016, which covered the pre-upwelling and upwelling seasons. The water column was warm and well-oxygenated during April–May. During June–August, the incidence of cold and hypoxic water indicated strong coastal upwelling prevailed in the entire study domain. The Fe and Mn content in sediments gradually decreased, because of the reductive dissolution and subsequent release of metals under hypoxia. The concentration of metals such as Ni, Zn and V decreased substantially under oxygen deficiency, whereas Cr showed marked enrichment in sediments. Although the geochemical forms of trace metals

* Corresponding author at: CSIR – National Institute of Oceanography, Regional Centre, Kochi, 682 018, India. Phone: +914842390814; fax: +914842390618.

E-mail address: gkumar@nio.org (T.R. Gireeshkumar).

Peer review under the responsibility of the Institute of Oceanology of the Polish Academy of Sciences.



<https://doi.org/10.1016/j.oceano.2022.06.007>

0078-3234/© 2022 Institute of Oceanology of the Polish Academy of Sciences. Production and hosting by Elsevier B.V. This is an open access article under the CC BY-NC-ND license (<http://creativecommons.org/licenses/by-nc-nd/4.0/>).

displayed the dominance of residual fractions (inert), the reactive non-residual metal forms (exchangeable, Fe/Mn-(oxy)hydroxide, and organic matter/sulphide bound) showed considerable variability under hypoxia. The shift from Fe/Mn-(oxy)hydroxide bound to organic matter and sulphide bound was evident during hypoxia. Cr exhibited a strong affinity towards organic matter and sulphide, and Pb and Zn showed relatively high association towards the Fe/Mn-(oxy)hydroxide phase. Even with such a phase shift induced by the hypoxic conditions, the concentrations of these metals remained within the normal background levels, indicating the pristine nature of the mud bank environment.

© 2022 Institute of Oceanology of the Polish Academy of Sciences. Production and hosting by Elsevier B.V. This is an open access article under the CC BY-NC-ND license (<http://creativecommons.org/licenses/by-nc-nd/4.0/>).

1. Introduction

Coastal regions experiencing upwelling can be considered ideal sites to understand dissolved oxygen control over the accumulation of trace elements and organic matter (Castillo et al., 2018). Sediments deposited under coastal upwelling areas accumulate many bioactive and redox-sensitive trace metals (Bonning et al., 2004, 2005; Nameroff et al., 2002). Metals exist in sediments in different phases (e.g., organic matter-bound, Fe/Mn-(oxy)hydroxides bound, carbonates, sulphides, and residual) based on the prevailing environmental conditions and affinity of metals towards various carrier phases (Dang et al., 2015; Malandrino et al., 2009). Even though most of these metals (Fe, Mn, Zn) are involved in metabolic processes, trace metals are of particular concern owing to their persistence, bioavailability, and toxicity (Dhanakumar et al., 2013).

Metal fractions in the coastal environment are mainly controlled/regulated by organic matter/organic ligands (Canfield, 1994; Chakraborty et al., 2016; Helmond et al., 2018; Zhang et al., 2014), Fe and Mn-(oxy)hydroxides, and the rate of formation of authigenic minerals (Canfield, 1994; Chakraborty et al., 2016; Helmond et al., 2018). The degradation of organic matter in a water column is more efficient in oxygenated conditions than in hypoxic or anoxic conditions (Henrichs and Reeburgh, 1987; Jahnke et al., 1982), which leads to the enrichment of organic matter bound metals in the sediments (Boning et al., 2009; Helmond et al., 2018; Munoz et al., 2012). Periodic hypoxia or anoxia in the sediment-water interface can alter the sedimentary redox conditions, causing repeated dissolution and re-precipitation of metals bound to Fe/Mn-(oxy)hydroxides (Chakraborty et al., 2016, 2018). Hypoxic bottom water decreases oxygen penetration to the sediment. It decreases electron acceptors, accelerating the release of metals from sediments, and enhancing their potential bioavailability (Eggleton and Thomas, 2004; van der Geest and Leon Paumen, 2008). Thus, depending on the biogeochemical variability across the sediment-water interface (such as dissolved oxygen, pH, grain size, and organic matter), the sediments may act as a sink or source of metals (Atkinson et al., 2007; Gleyzes et al., 2002). Metals can thus enter the food chain in the aquatic environment and become available for accumulation in biota.

Coastal upwelling and mud banks are two concurrent coastal oceanographic phenomena operating along the southwest coast of India. The southwest coast of India ex-

periences basin-wide coastal upwelling during the southwest monsoon season (June–September) when the cold, nutrient-rich, and oxygen-depleted waters are brought to the surface, thereby significantly enhancing the biological production (Gupta et al., 2016; Naqvi et al., 2000). Mud banks are unique seasonal oceanographic phenomena occurring during the southwest monsoon season at specific locations along the southwest coast of India. They appear as semi-circular patches of calm nearshore waters (water depth 10 m) when the rest of the coastal environment is highly turbulent due to high monsoonal waves (height = 2–5 m). A fluid mud layer at the bottom of mud banks continuously attenuates the incident waves to create a calm environment conducive to fishing (Gireeshkumar et al., 2020; Jyothibabu et al., 2018). The coastal waters become productive during the upwelling period, showing a substantial increase in the abundance and biomass of phytoplankton and zooplankton (Arunpandi et al., 2017; Karnan et al., 2017; Madhu et al., 2020, 2021). A shift in the dominance of microbes based on their preferences to sustain low oxygen conditions was also observed (Anas et al., 2018; Parvathi et al., 2019).

Varying levels of dissolved oxygen in the sediment-water interface from the pre-upwelling and upwelling period (well-oxygenated to hypoxic) influence the geochemical partitioning of trace metals. Mud banks can be considered a natural mesocosm to understand the trace metal cycling and biogeochemical processes operating under seasonal oxygen deficiency. Nearshore hypoxia triggers the reductive dissolution of metal oxides, resulting in influxes of trace metals to the overlying water column, which may significantly impact the water column productivity and ecosystem functioning. Understanding the labile metal fractions or potential bioavailability of trace metals in nearshore sediments is crucial for the sustainable development of the coastal environment, especially in specialised coastal systems such as mud banks (Prasannakumar et al., 2018). This time-series monitoring of the Alappuzha mud bank from April (pre-upwelling) to August (upwelling) portrays the transition of a coastal environment (sediment) from normoxic to suboxic condition (Gireeshkumar et al., 2017; Mathew et al., 2019, 2020), which may have a significant influence on the dynamics of trace metals. This study focuses on the variations in trace metal concentrations and their geochemical forms under varying redox conditions in surface sediments to describe the factors influencing metal cycling in this dynamic nearshore region.

2. Material and methods

2.1. Study area

The study region considered herein is situated on the southwest coast of India; it is influenced by the Asian monsoon characterised by seasonally reversing winds and coastal circulation. The west coast of India resembles an eastern-boundary-type upwelling environment during the southwest monsoon (Naqvi et al., 2009) when the surface current flows equatorward. Upwelling brings oxygen-poor, nutrient-rich subsurface waters to the coastal region, which turn hypoxic by late summer due to exhaustion of oxygen by heterotrophic microorganisms (Naqvi et al., 2010). The eastern Arabian Sea is the only region where upwelling occurs with high freshwater inputs. A low salinity lens on the surface also contributes to the development and sustenance of intense oxygen deficiency at considerably shallow depths. Hypoxia in the bottom waters significantly affects the geochemistry of the sediment, and a corresponding decrease in the Fe and Mn concentration proportional to oxygen depletion was observed in the study region (Mathew et al., 2019, 2022).

2.2. Time-series sampling from the study domain

Fortnightly observations were made at three locations (M1, M2, and M3) in and around the Alappuzha mud banks covering the pre-upwelling (April to May) and upwelling (June to August) seasons of 2016. Station M2 (water depth = 7 m) represents the Alappuzha mud bank (tranquil waters with a fluid mud layer at the bottom), while station M1 (water depth = 7 m) is a non-mud bank region located 7 km north of M2. Station M3 is situated at a water depth of 13 m (Figure 1). A CTD profiler (SBE 19 plus) was used to record the salinity (accuracy of ± 0.0005 S/m in terms of conductivity) and temperature (accuracy of $\pm 0.0005^\circ\text{C}$). Water samples were collected at all stations at every 3 m intervals using a 5 L Niskin sampler and sub-sampled to measure dissolved oxygen (DO). Sediments were collected using a Van Veen grab (0.04 m²). Several deployments per station were performed to reduce bias due to the washout of supernatant water and possible disturbance of the surface sediment during the grab operation, obtaining well-preserved sediment samples. The surface layer (1–3 cm) was carefully skimmed off using a pre-cleaned scoop and transferred to a clean high-density polyethylene (HDPE) bottle in an inert atmosphere. The samples were stored in ice till analysis.

2.3. Laboratory analysis

2.3.1. Dissolved oxygen and bulk sediment characteristics

Dissolved oxygen was analysed using Winkler's method with an automatic titration system (Metrohm 865 Dosimat plus) following standard procedure with a detection limit of 2 μM (Grasshoff et al., 1999). Sediment texture was determined following pipette analysis (Folk, 1980) using wet sediments following treatment with 1 M HCl and H₂O₂ (30%) to remove carbonates and organic matter. Sediment samples were washed with distilled water, dried at 50°C, weighed,

and treated with sodium hexametaphosphate (overnight) to disperse the sediment particles, and separated following pipette analysis. Vacuum-dried samples were powdered with a mortar and pestle. For total organic carbon (TOC) analysis, sediments were pre-treated with 1 M HCl (for removal of carbonates), washed with deionised water (to remove salts), and freeze-dried. TOC, total nitrogen (TN), and total sulphur (TS) were determined using a Vario EL III CHNS Analyzer with detection limits of 0.07%, 0.01%, and 0.01%, respectively. The sediment samples (0.3 g) for total metal analysis were digested with a mixture of extra-pure acids, HNO₃-HCl-HF (7:2:1), in a microwave digester (Milestone Ethos Easy). After cooling, the extract was filtered and diluted to 50 ml. Metal concentrations (Fe, Mn, Zn, Ni, Co, Cr, Pb, Cd, and V) were determined using an inductively coupled plasma-optical emission spectrometer (ICP-OES; Thermo Scientific i-CAP 7000 Series). Triplicate analyses were conducted, and the average values were reported as total metal concentrations. The accuracy of trace metal analysis was validated using standard reference material for marine and estuarine sediments (BCSS-1) from the National Research Council of Canada. The recoveries were within the acceptable range ($\pm 5\%$).

2.3.2. Metal fractionation

Sequential extraction was performed using a three-stage modified procedure recommended by Rauret et al. (1999). Solid-phase trace metals are classified into four geochemical forms, namely, water-soluble, exchangeable, and associated with carbonates (Exch), reducible trace metals associated with Fe/Mn hydroxides (Red), trace metals associated with organic matter, and sulphide (Oxi) and metals incorporated into the structural component of the sediment or residual fraction (Res). The sequential extraction method used in this study is described in detail by Nemati et al. (2011).

Freeze-dried and homogenised sediment samples were extracted with glacial acetic acid for 16 hours to extract exchangeable fractions. For a reducible fraction (Red), the residue from step 1 was resuspended in 0.5 M hydroxyl ammonium hydrochloride (pH 1.5) for 16 hours. The oxidisable fractions (Oxi) were extracted by treating the residue from step 2 with H₂O₂, evaporated, and treated with 1 M ammonium acetate solution (pH 2) and shaken for 16 hours. The obtained residue was finally subjected to microwave-assisted tri-acid digestion (Milestone Ethos Easy, USA) using a mixture of HNO₃: HCl: HF (7:2:1) to extract the residual fraction (Red). All extraction was conducted on end over a shaker at 25°C, and the subsequent residue was washed with deionised water to remove traces of the solvent mixture. All fractions were analysed using a graphite furnace atomic absorption spectrophotometer (GFAAS; Thermo Scientific iCE 3000 Series, GFS 35). A certified reference material (BCR 701, Sigma Aldrich, USA) was used to ensure the accuracy of the sequential extraction. The recovery was checked by comparing the total trace metal data with the sum of metal concentrations obtained from each sequential extraction step. The recoveries for both the methods mentioned above were within the acceptable range ($\pm 5\%$). Triplicate extractions were performed, and the average values were reported.

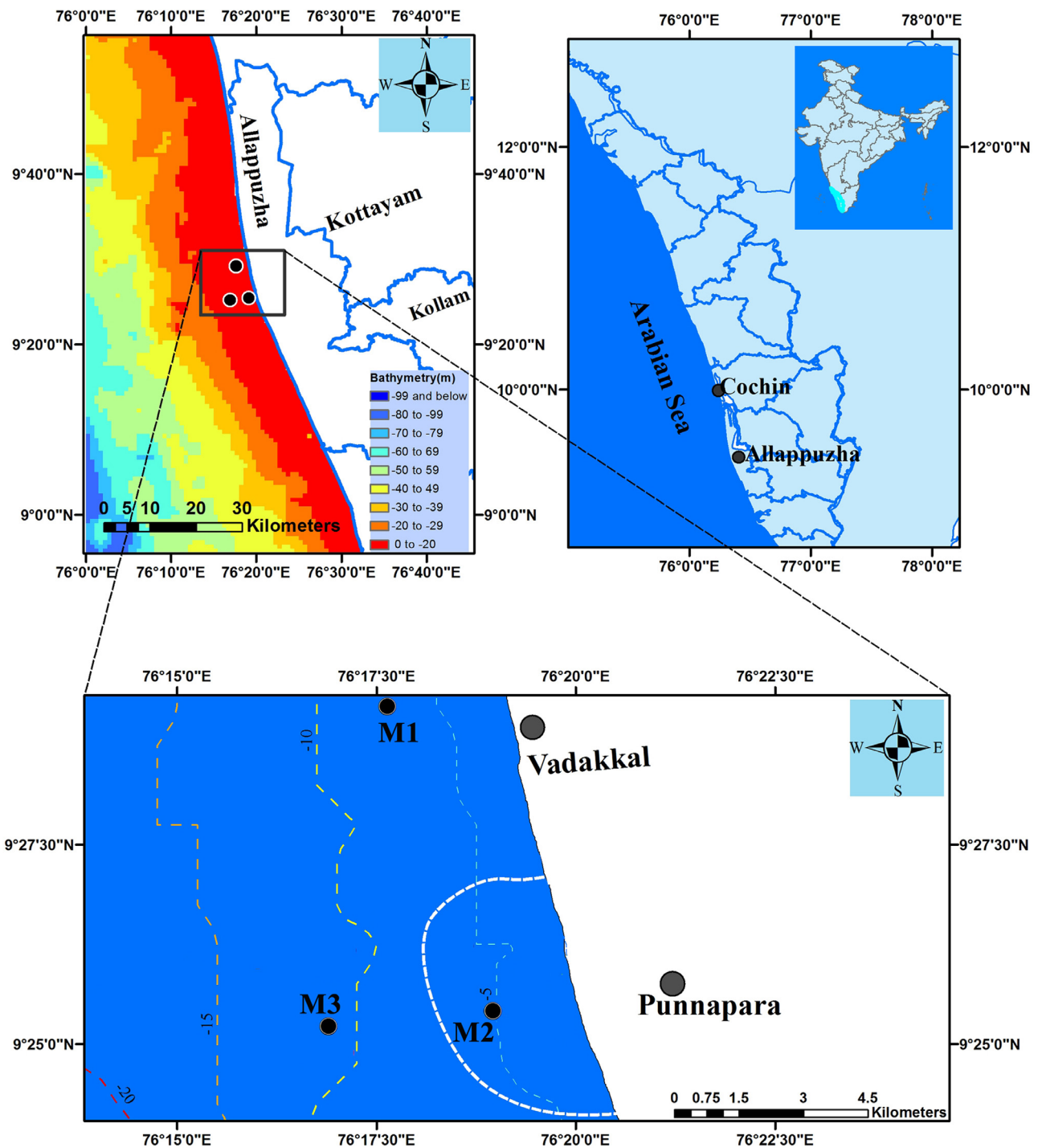


Figure 1 Map of the study region showing locations of sampling stations (M1, M2, and M3) in Allappuzha mud banks. The discontinuous white line indicates the approximate boundary of the persistent mud bank site. The red dots (upper left panel) reported mud bank locations along the southwest coast of India.

3. Results

3.1. Upwelling-induced nearshore hypoxia

The water column temperature data displayed the incursion of cold subsurface water with time, which indicates upwelling (Figure 2a). The water column remained warm on

the surface (32°C) and well mixed till the end of May. The strengthening of south-westerly winds was associated with the upwelling of relatively cold (26°C) bottom waters at M3 on 2 June 2016, which gradually progressed to the coastal locations (M1 and M2). The subsurface water temperature decreased by 3°C during the initial phase of upwelling, and it further intensified as the southwest monsoon progressed.

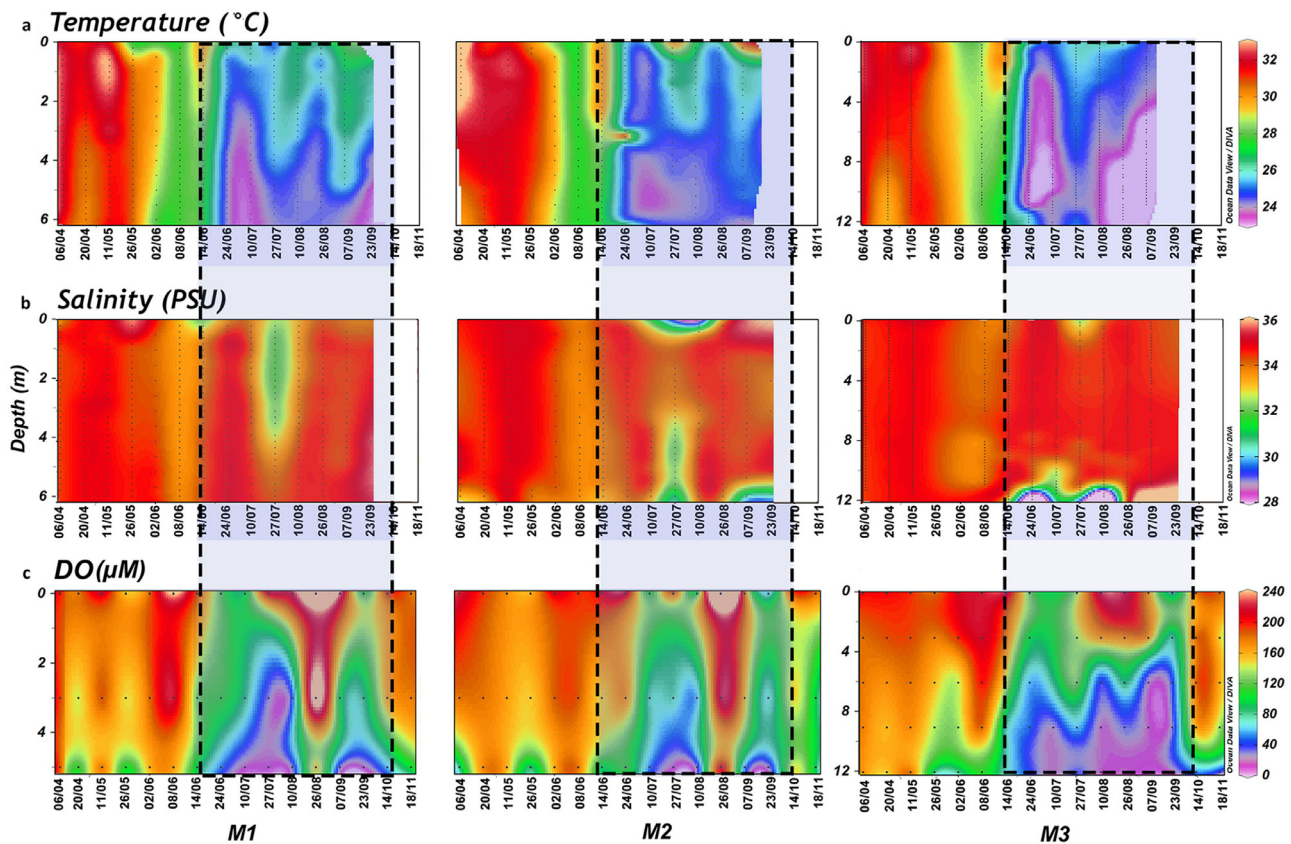


Figure 2 Vertical profiles of temperature (a), salinity (b) and dissolved oxygen (c) during the study period.

The time evolution of water column DO indicates a progressive decline in the concentration and devolvement of water column hypoxia in tandem with the upward propagation of colder waters (Figure 2a). The DO of bottom water was <math><40 \mu\text{M}</math> below the well-oxygenated surface layer (i.e., 2 m below the surface layer at M1 and M2, and 4 m below at M3) during the southwest monsoon and sustained throughout the study period (Figure 2c).

3.2. Bulk sedimentary characteristics

The dominance of clay (>80%) over silty-clay fractions was the characteristic change associated with the formation of mud banks and a fluid mud layer, just above the sediment bed, especially at M2 (Figure 3a). The mud bank formation also coincided with the enrichment of TOC ($2.79\% \pm 0.21\%$), TN ($0.37\% \pm 0.02\%$), TS ($0.9\% \pm 0.16\%$) and TP ($0.21\% \pm 0.08\%$) in sediments (Figure 3b).

3.3. Trace metals in sediments

Iron was the most dominant metal in mud bank sediments and exhibited a significant positive correlation with DO ($r=0.45, p<0.05$) (Supplementary material Table S1). Fe concentration showed a considerable decrease during the southwest monsoon, especially at M3. The removal of Mn was more pronounced (Mn vs DO $r=0.57, p<0.01$; Supplementary material Table S1) during hypoxia when its pre-monsoon levels ($138\text{--}150 \mu\text{g/g}$) decreased considerably to

$70\text{--}74 \mu\text{g/g}$ during the peak monsoon period (Figure 4). Ni, V, and Zn were positively correlated with DO ($p<0.05$) and had the lowest values during hypoxia ($37.12\text{--}81.13 \mu\text{g/g}$, $79.21\text{--}96.87 \mu\text{g/g}$, and $45.72\text{--}67.91 \mu\text{g/g}$, respectively). Cr ($136.11\text{--}242.82 \mu\text{g/g}$) was enriched during hypoxia, whereas Co ($11.00\text{--}14.53 \mu\text{g/g}$), Pb ($12.15\text{--}23.53 \mu\text{g/g}$), and Cd ($0.12\text{--}0.37 \mu\text{g/g}$) did not show any variations (Figure 5).

3.4. Trace metal fractionation

The abundance of different geochemical forms of trace metals varied significantly during the well-oxygenated and hypoxic periods. Different trace metals exhibited a heterogeneous response to the hypoxia at the sediment-water interface. The lithogenic fraction was predominant among the geochemical forms of all trace metals considered herein (Ni: 76–87%; Zn: 69–86%; Cr: 60–83%, Co: 82–92%; Pb: 53–94%). The labile form of Ni exhibited a high affinity towards organic matter (oxidisable; 12–23%), followed by the reducible fraction (<1%) (Figure 6). Among the bioavailable forms of Zn, the reducible fraction accounted for 5–15% of total Zn. It decreased gradually, whereas the oxidisable fraction, (4 to 25% of total Zn), demonstrated an increasing trend during hypoxia (Figure 7a). Pb did not display a seasonal trend; however, its geochemical forms, especially major labile forms (reducible and oxidisable) varied with DO. The reducible fraction was dominant among the labile

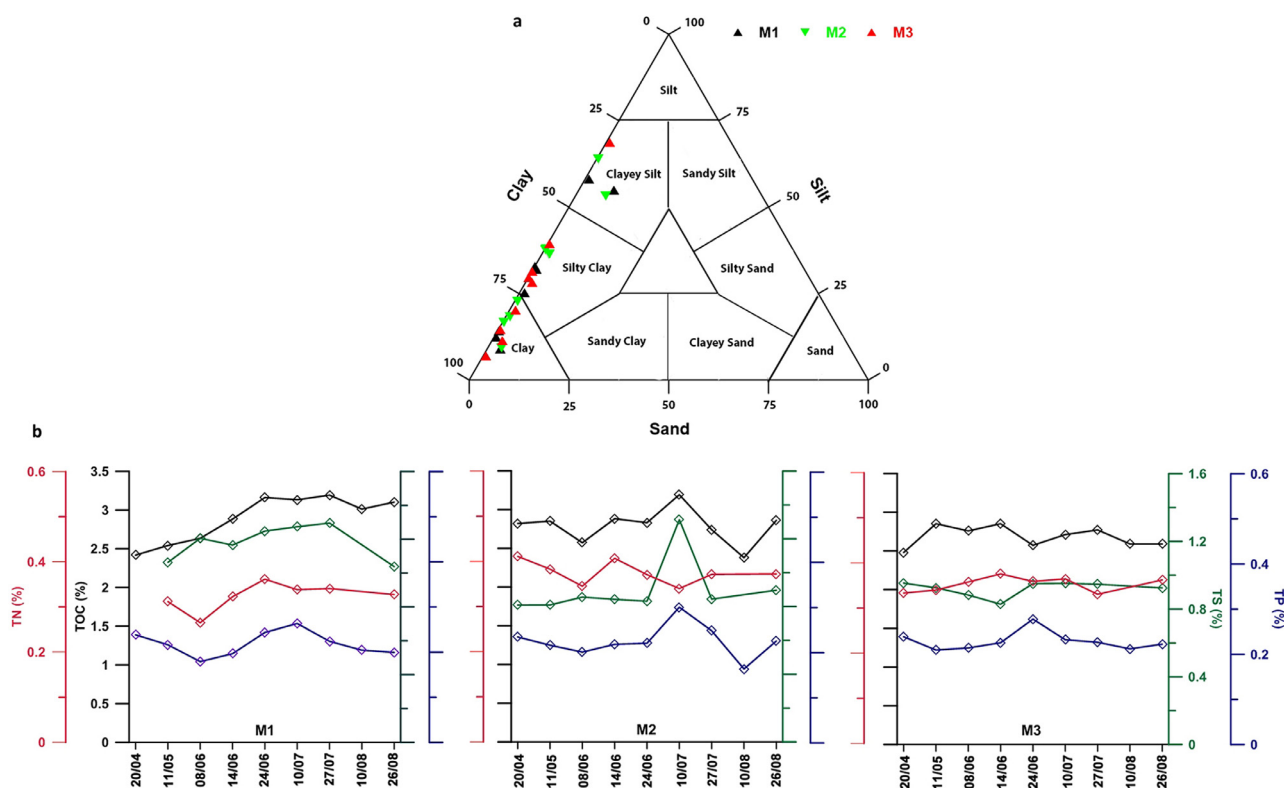


Figure 3 Distribution of sand, silt and clay in surface sediments (a), distribution of Total Organic Carbon (TOC) (b), Total Nitrogen (TN), Total Sulfur (TS) and Total Phosphorus (TP) in surface sediments of the Alappuzha mud bank.

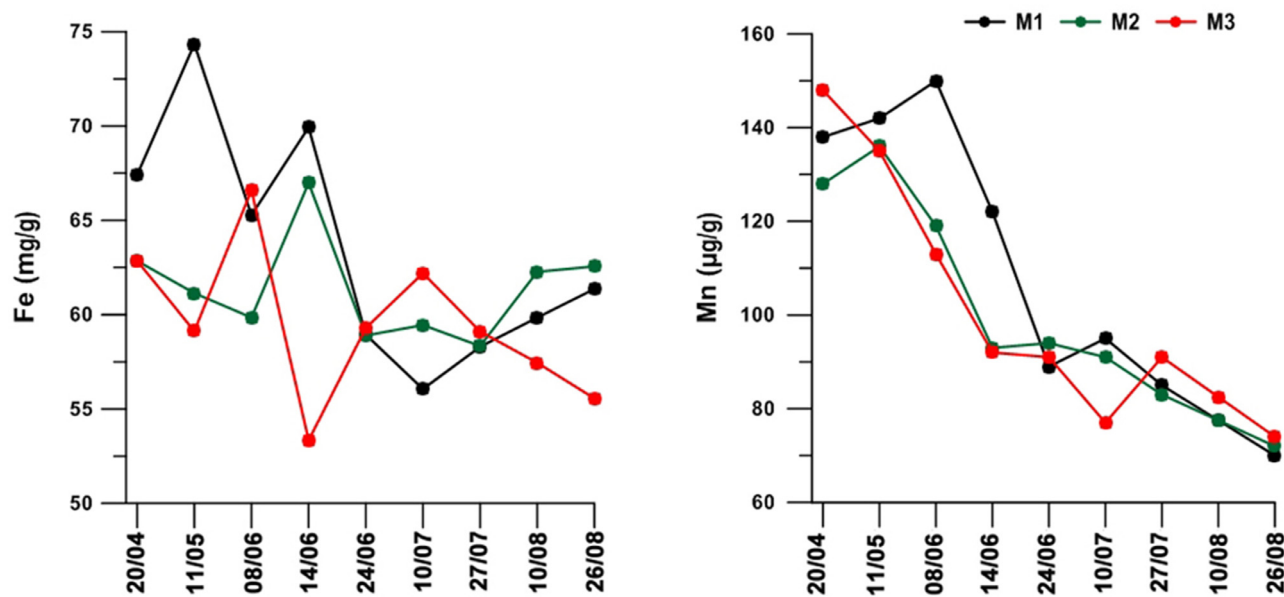


Figure 4 Seasonal variability of Fe and Mn in surface sediments.

forms (1 to 38%), and the oxidisable fraction accounted for 5–14% of total Pb (Figure 7b).

Cr showed significant enrichment during hypoxia and displayed a similar trend to the metals mentioned above. Its reducible fraction (1–13% of total Cr) decreased grad-

ually during the upwelling (hypoxic) period. In contrast, the oxidisable fraction (15–27% of total Cr) increased during the bottom water hypoxia (Figure 8a). For Co, the reducible fraction was lower, contributing 0–6% of total Co, and the oxidisable fraction contributed 7–13% of total Co

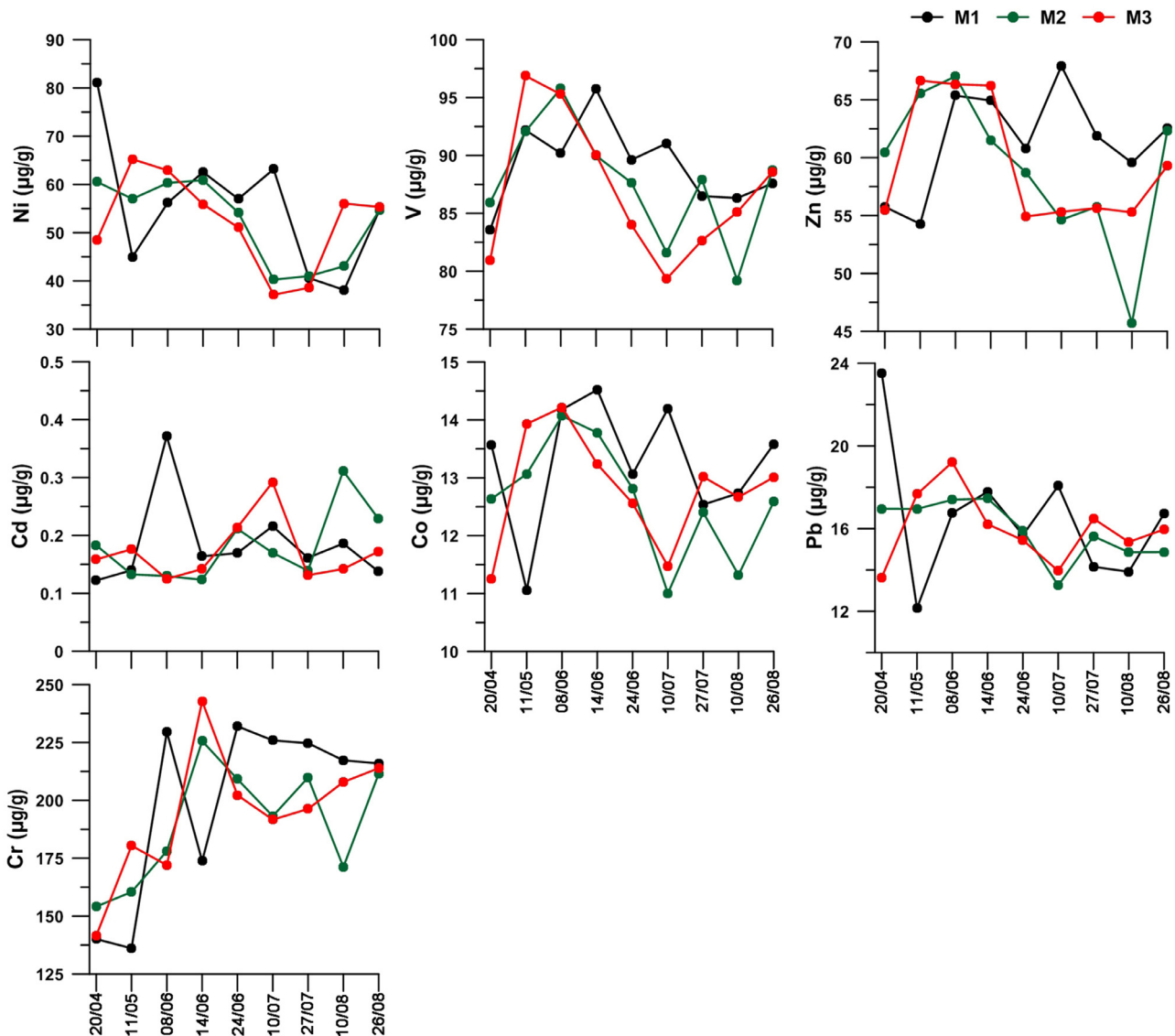


Figure 5 Distribution of trace metals in surface sediments of the Alappuzha mud bank.

(Figure 8b). The exchangeable fraction was considerably low for all the trace metals (Ni < 1%, V < 6%, Zn < 2%, Cr < 1%, Co < 1%, and Pb < 1%).

4. Discussion

Upwelling was persistent in the study region from June onwards, which brought hypoxic waters (<62 µM) to the subsurface layer in the shallow depths (Gireeshkumar et al., 2017; Mathew et al., 2019), and it was sustained for a long period, especially at M3. The low salinity lens in the surface waters formed through intense precipitation in the coastal zone led to strong thermohaline stratification and contributed to the sustenance of severe oxygen deficiency at considerably shallow depths (Naqvi et al., 2006; Naqvi and Unnikrishnan, 2009). The development of water column hypoxia, nutrient enrichment, and high primary productivity in mud bank has been investigated in previous studies (Gireeshkumar et al., 2017; Mathew et al., 2019). The study

region experienced relatively weak winds (<5 m/s) during pre-upwelling (April to May), while considerably strong winds (6–7 m/s) were prevalent during the onset of the southwest monsoon (Smitha et al., 2014). There was substantial rainfall over the study region (average of 7.7 ± 5.8 mm/day) during the monsoon period, with a significant peak during June (average of 15.1 ± 5.8 mm/day) (Madhu et al., 2021). The formed mud banks acted as a calm region even during monsoon due to the thick fluid mud layer, which decreased the wave energy (Jyothibabu et al., 2018; Shynu et al., 2017).

The redox condition of the sediment and adsorbing/scavenging phases such as clay minerals, Fe/Mn-(oxy)hydroxides and organic ligands are the main influencing factors of trace metal accumulation in the sediments (Zhang et al., 2014). Therefore, the main variables explaining metal dynamics are organic enrichment, oxygen, and sediment texture. In mid-June, dissolved oxygen values in the subsurface waters decreased considerably, reaching the lowest (<20 µM) in the study region

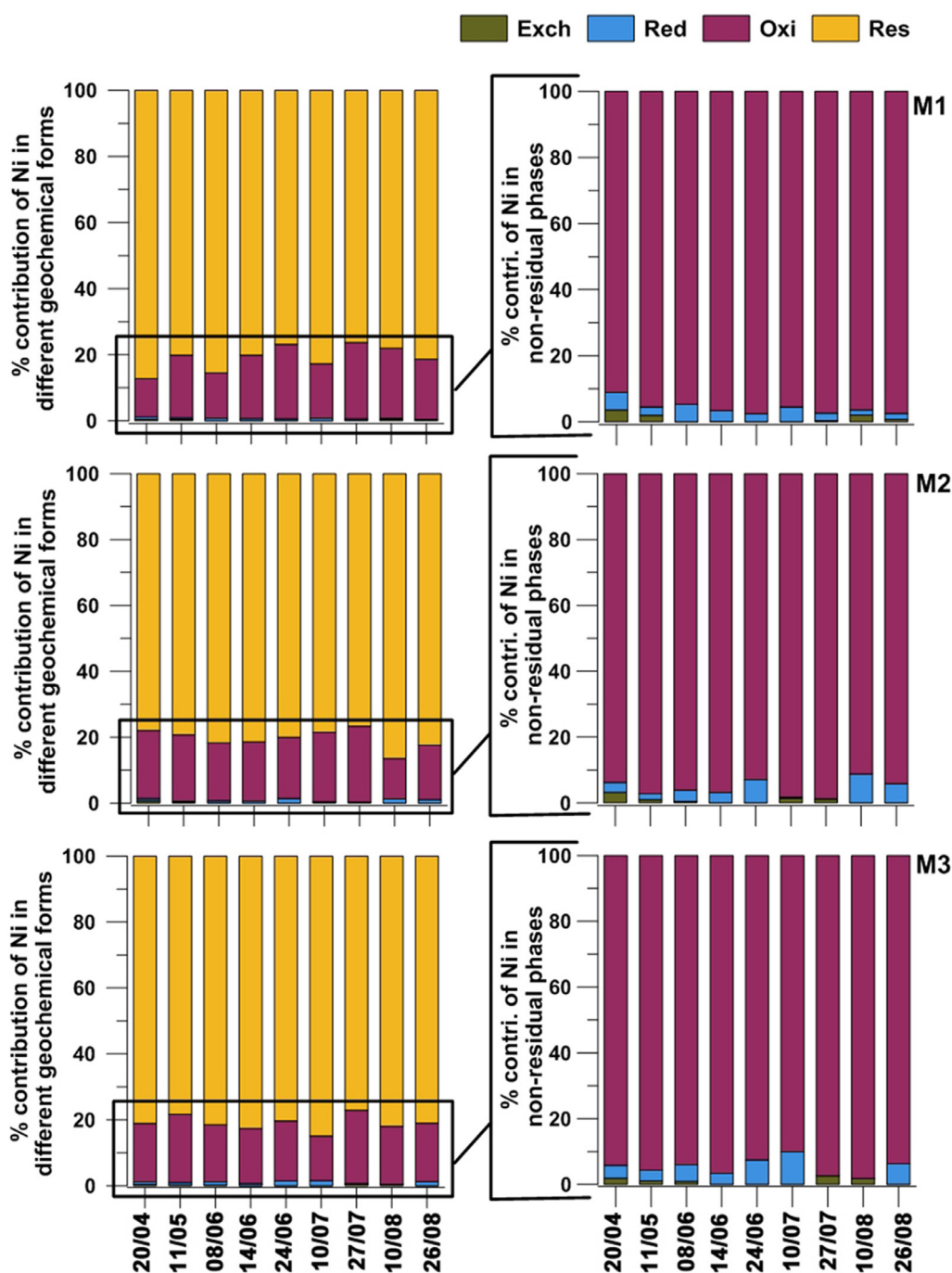


Figure 6 Geochemical forms of Ni in surface sediments.

during July. The offshore station M3 continued to remain hypoxic thereafter (July–September), whereas its incursion towards the shallow depths of the mud bank (M1 and M2) occurred only during severe atmospheric depressions (Muraleedharan et al., 2017). The chlorophyll *a*, and nutrients data obtained in this study is already presented in Gireeshkumar et al. (2017) and Mathew et al. (2019). Chlorophyll-*a* content was low ($<3 \text{ mg/m}^3$) during May and June (especially in the offshore M3 station), and it increased to high concentrations ($>12 \text{ mg/m}^3$) by the end-July due to the nutrient injection through upwelling. Di-

noflagellate blooms were also reported in the study region from August onwards (Madhu et al., 2020, 2021), and subsequent decomposition of organic matter increased the oxygen demand of already oxygen-deficient water. Mudbank sediments are mostly clayey and have high metal binding capacity due to the large surface area (Horowitz and Elrick, 1987; McCave, 1984).

Fe concentration in this study (average of $6.35 \pm 0.61 \text{ wt.}\%$) is much higher than the continental margin ($2.92 \pm 0.78 \text{ wt.}\%$) and the suboxic region ($3.42 \pm 1.08 \text{ wt.}\%$) around the world (Raiswell and Canfield, 1998), which is unique

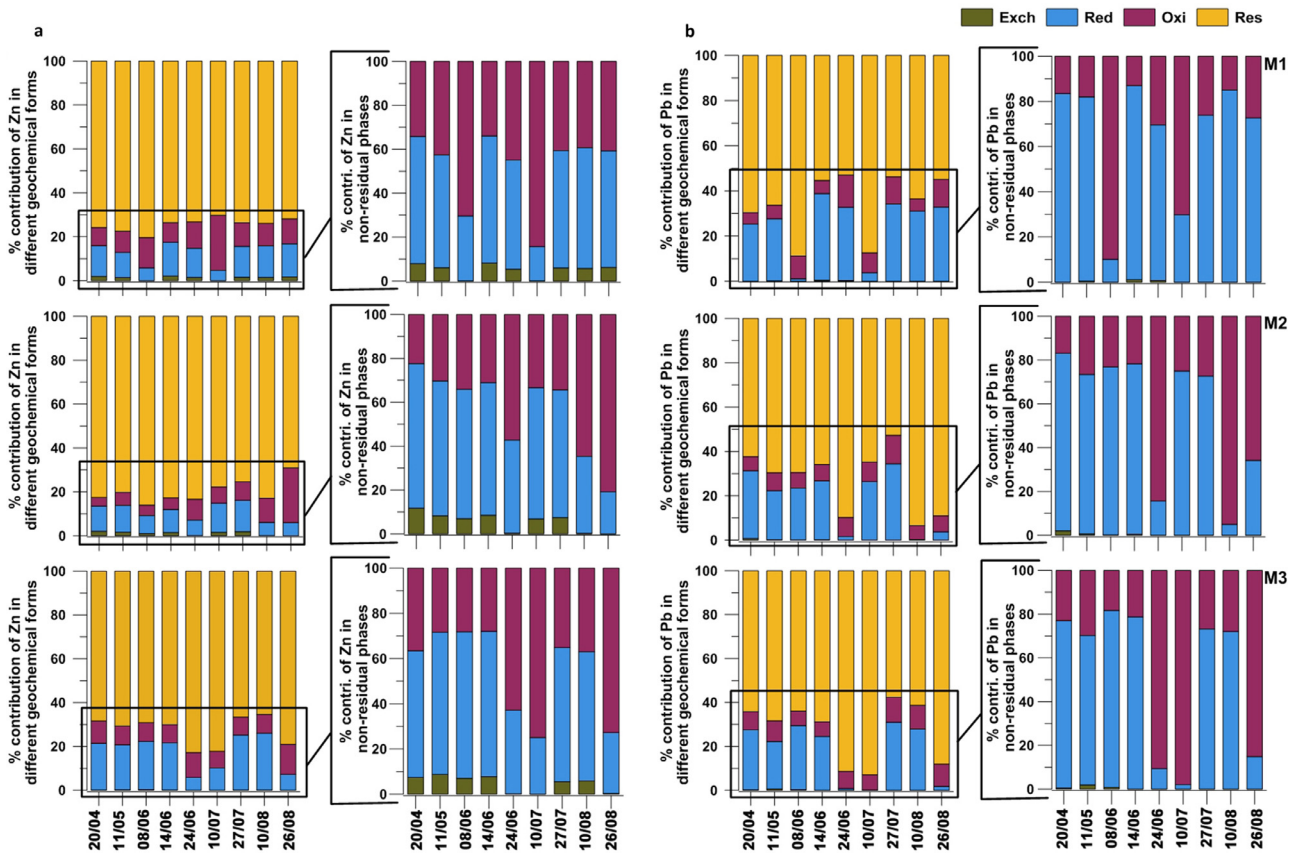


Figure 7 Geochemical forms of Zn (a) and Pb (b) in surface sediments.

to the mud banks (Mathew et al., 2020, 2022). Dissolved oxygen exhibited significant positive correlations with Mn ($r=0.57$, $p<0.01$) and Fe ($r=0.45$, $p<0.05$) (Supplementary Material, Table S1). Mn occurs in sediments as discrete oxide particles, coatings on particles, and Mn^{2+} adsorbed on organic materials (Feely et al., 1982; Graham et al., 1976). In the surface sediment, Fe and Mn concentration decreased proportionally to the decrease in oxygen content, and it was characterised by a more pronounced decrease in Mn concentration (Figure 4). When the overlying water column was well oxygenated, oxygen in the sediment surface was used for the oxidation of organic matter. In contrast, reduction of Mn^{4+} to Mn^{2+} occurred in the deeper layers to release electrons that diffused and re-oxidised Mn^{2+} to Mn^{4+} on the surface (Froelich et al., 1979; Schulz et al., 2006). However, hypoxia favours the reduction of Mn^{4+} to Mn^{2+} , which in turn releases into the water column, decreasing Mn concentrations in the surface sediments. The re-oxidation rate of Fe is higher than that of Mn, and the diffusive flux of Fe from the deeper layers through the dissolution of Fe-(oxy)hydroxides could be re-precipitated even during mild oxygen deficiency (Jensen et al., 1995; Krom and Berner, 1980; Slomp et al., 1996). The temporal variations of Fe and Mn during hypoxic/suboxic events indicated that metal oxide reduction is a significant pathway of organic matter mineralisation in sediments (Berg et al., 1998; Canfield et al., 1993; Thamdrup and Canfield, 1996; Vandieken et al., 2006).

Sedimentary trace metals exhibited different seasonal features concerning the oxygen deficiency in the water column. A marked reduction of Zn, V, and Ni, corresponding to hypoxia ($r=0.43$, 0.45 , and 0.43 respectively, $p<0.05$) (Supplementary Material, Tables S1 and S2), indicated the association of these metals with Fe/Mn-(oxy)hydroxides. The reductive dissolution of this primary binding phase during hypoxic events might dislodge the scavenged metals to the overlying water column or convert metals into more soluble sulphide forms (Chakraborty et al., 2018; Gallon et al., 2004; Schaller et al., 1997). In contrast, Cr enrichment was evident during the same period; Cr enrichment under reducing conditions has been established (Guo et al., 1997) as reduced Cr (III) is more stable than Cr (VI). A slight decrease in total Cr values during peak upwelling indicated the reductive dissolution of Red-Cr corresponding to oxygen deficiency (especially at M2 and M3).

4.1. Trace metal fractionation in sediments

The non-residual forms of Ni predominated by Oxi-Ni (Figure 6) showed a close correlation with TOC ($r=0.66$; $p<0.01$, Supplementary Material, Table S2), indicating that organic matter is the major controlling factor for bioavailability. Ni is involved in the enzymes participating in photoautotrophic production (especially in diatoms); therefore, in most highly productive upwelling zones (Peru, Namibia,

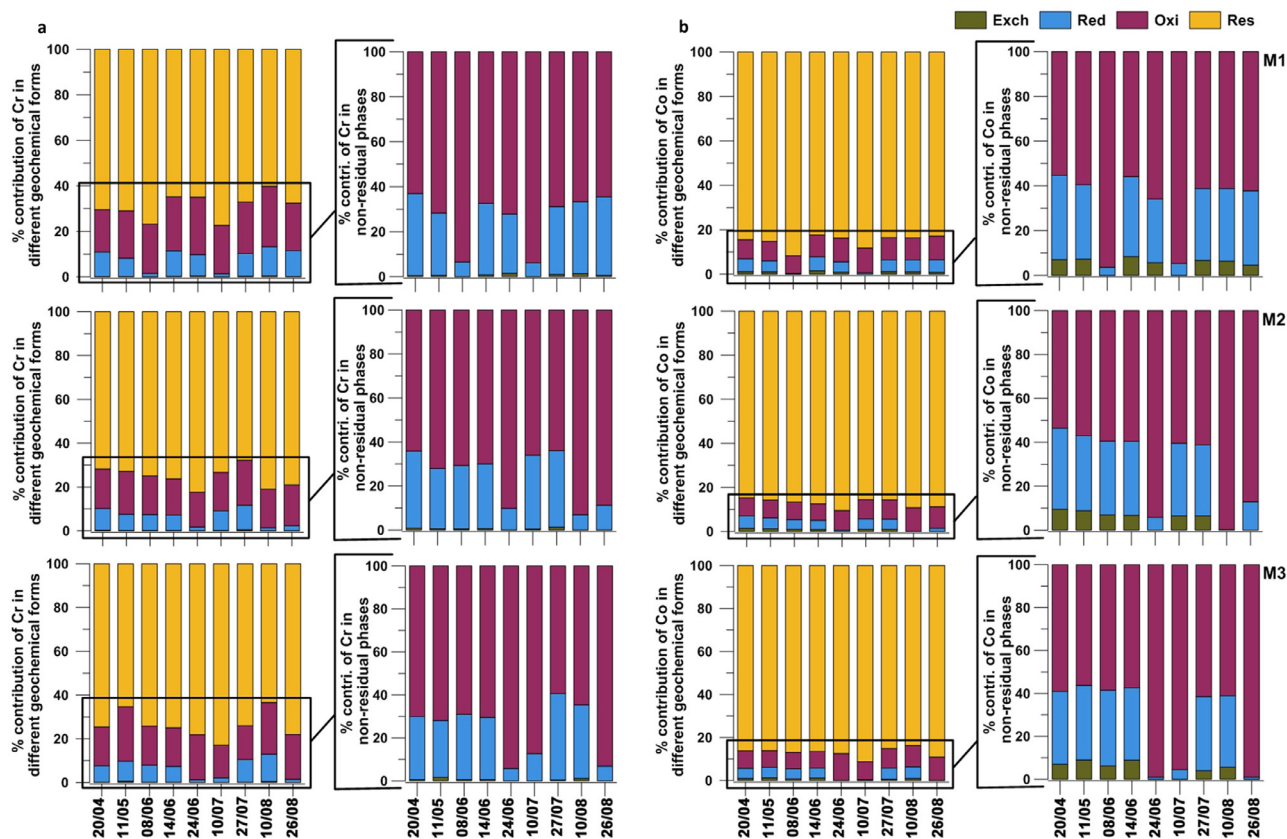


Figure 8 Geochemical forms of Cr (a) and Co (b) in surface sediments.

Chile, and the Gulf of California), a close association between Ni and organic matter has been observed, and it is often considered a reliable indicator of organic matter sinking flux (Boning et al., 2015; Twining et al., 2012). Red-Ni displayed a significant negative correlation with Exch-Ni ($r = -0.52$; $p < 0.05$) (Supplementary Material, Table S2), which may be due to the reductive dissolution of Ni during hypoxia and subsequent release into the pore water or the overlying water column.

Among the non-residual fractions, Pb was more concentrated ($>30\%$) in the reducible form (Figure 7b), indicating its dependence on Fe/Mn-(oxy)hydroxide (Belzile et al., 1989; Chakraborty et al., 2015). Under the oxic condition, Pb forms stable complexes with Fe/Mn-(oxy)hydroxides, whereas hypoxic conditions lead to the dissolution of metal oxides releasing Pb in the reducible form (Chakraborty et al., 2016, 2018; Gallon et al., 2004). Red-Pb content decreased considerably during persistent hypoxia (24 June–10 July). Subsequent hypoxia for a short duration showed a spike in this fraction, which may be due to the re-precipitation of authigenic Fe-oxides (poorly crystalline oxides) with high scavenging capacity. The significant correlation of Fe with Exch-Pb ($r = 0.88$, $p < 0.01$, Supplementary Material, Table S3) substantiates the loss of Pb in exchangeable form by dissolution and its association with organic matter/sulphide. Similarly, non-residual Zn was mainly concentrated in the reducible fraction (Fe/Mn-(oxy)hydroxides), followed by oxidisable and exchangeable

fractions (Figure 7a). Both reducible and exchangeable fractions of Zn were low during intense hypoxia, which may be attributed to their weak adsorption as a coating to metal oxides. However, an increase in Oxi-Zn could be attributed to the adsorption of released Zn to oxidisable phases. The positive correlation of Oxi-Zn with chlorophyll *a* ($r = 0.48$, $p < 0.05$, Supplementary Material, Table S1) suggests an increased association of Zn with freshly derived organic matter during enhanced biological productivity.

Under the oxic condition, Cr (IV) (chromate ion, $H_xCrO_4^{-2+x}$) is thermodynamically stable (Richard and Bourg, 1991), and it prefers to bind with organic phases and gets weakly adsorbed to Fe/Mn-(oxy)hydroxides. Approximately 20% of the metal concentration (30–50 $\mu\text{g/g}$) was bound in this fraction (Oxi-Cr), and it increased gradually with upwelling intensity, especially at M1 (Figure 8a). However, Red-Cr decreased considerably corresponding to decreasing DO values (Chakraborty et al., 2018) owing to the reduction of Fe/Mn-(oxy)hydroxides. Oxi-Cr exhibited a significant positive correlation with TS ($r = 0.52$, $p < 0.01$) (Supplementary Material, Table S4). Under reducing conditions, the rapid reduction of highly soluble Cr (IV) (Guha et al., 2001; James, 2002) to less mobile Cr (III) occurs, which is favoured by the presence of organic matter (Chakraborty et al., 2018), sulphide, and Fe (II) (Schaller et al., 1997). The association of reduced chromium with iron sulphide (Lakatos et al., 2002) is also probable. Thereby, stable Cr (III) forms dominant in sediments dur-

ing peak upwelling, leading to the enrichment of overall Cr concentration (Figure 8b). The non-residual fraction of Co prefers to adsorb on the surface of Fe/Mn-(oxy)hydroxides (Chakraborty et al., 2012) and organic matter, while Oxi-Co showed a significant positive correlation with clay ($r=0.48$, $p<0.05$) and a negative correlation with DO ($r = -0.54$, $p < 0.05$, Supplementary Material, Table S5).

In marine ecosystems, metal contamination harms flora and fauna. Total metal concentrations, except for Cr and Ni, in mud bank sediments are substantially below the threshold limits (for instance, Pb concentration is 20 $\mu\text{g/g}$, while the threshold limit is 60 $\mu\text{g/g}$) specified by sediment quality guidelines (SQGs) (MacDonald et al., 1996; SEPA, 2002). Under reducing conditions, Cr (III) predominant in the sediment is rarely found in the dissolved form, and it cannot easily pass-through cell membranes, while the major component of Ni is in the residual fraction. This clearly shows that even though Cr and Ni concentrations in clayey mud bank sediments are high, their potential bioavailability is limited.

Benthic fauna in oxygen-deficient zones exhibit morphological and physiological adaptations to maximise oxygen uptake (Childress and Seibel, 1998; Levin, 2003), they generally show reduced diversity and biomass under oxygen deficiency (Levin et al., 2009; Rowe 1971). On the west coast of India, under oxygen deficiency, standing stock of macrobenthos, species number and diversity of polychaetes were decreased (Joydas and Damodaran, 2014); furthermore, substantially low benthic biomass has been reported from 20 m depth contours along the southwest coast of India (Jeyaraj et al., 2007). Therefore, the enrichment of toxic organic matter-bound metals (especially Cr and Ni) may not pose any large-scale impact on benthic fauna due to its low biomass and abundance in the mud bank sediments.

5. Conclusions

This study investigated seasonal variations and geochemical fractionation of trace metals in the surface sediments of a seasonally hypoxic (upwelling) coastal environment to understand hypoxia-induced changes in trace metal fractions. The incidence of cold and hypoxic waters indicated strong coastal upwelling in the study region during the southwest monsoon. The reduction in the concentrations of Fe and Mn during hypoxia periods indicated the dissolution of Fe/Mn-(oxy)hydroxides in the surface sediments. Concentrations of trace metals such as Ni, V, and Zn decreased gradually in sediments, while that of Cr was considerably enriched. Geochemical fractionation revealed that these variations follow their preference for binding sites during hypoxia. Ni and Cr exhibited strong affinities towards organic matter and sulphides. Pb and Zn were characterised by their relatively high affinity towards the Fe/Mn-(oxy)hydroxide phase under hypoxia. Reductive dissolution of reducible fractions led to decreased Ni, Zn, V, and Pb levels. Stable Cr (III) bound to organic matter was enriched, though all values were within threshold limits. Hypoxia in the sediment-water interface shifts the Fe/Mn-(oxy)hydroxide bound metals to organic matter and sulphide bound, which is relatively more bioavailable. However, it possesses less/no harm to the biota due to the low trace metal concentration in the

sediment, the dominance of stable forms, and the relatively fewer benthic fauna during the oxygen deficiency. However, the labile fractions can affect biota in future if (i) the metal concentrations increase due to anthropogenic activities or (ii) the intensity of hypoxia continues to increase.

Declaration of competing interest

The authors declare that they have no known competing financial interests or personal relationships that could have appeared to influence the work reported in this paper.

Acknowledgements

The authors thank the facilities and the support provided by the Director, National Institute of Oceanography and the Scientist in Charge, Regional Centre-Kochi. We appreciate the services rendered by our colleagues of CSIR-NIO in carrying out the field sampling successfully. We thank the Ministry of Earth Sciences (MoES), India, for the funding (Grant numbers: MoES/36/OOIS/Extra/22/2016 dated 25/02/2019). Kanneth Satheesan Arya acknowledges the Department of Science and Technology (DST) for providing him DST-INSPIRE Fellowship. The critical comments given by the Editor and anonymous reviewers have considerably helped to improve the clarity of the manuscript. We thank Editingindia for proofreading our manuscript for English grammar and usage. This is NIO contribution No.10352

Supplementary materials

Supplementary material associated with this article can be found, in the online version, at <https://doi.org/10.1016/j.oceano.2022.06.007>.

References

- Anas, A., Sheeba, V.A., Jasmin, C., Gireeshkumar, T.R., Mathew, D., Krishna, K., Nair, S., Muraleedharan, K.R., Jayalakshmy, K.V., 2018. Upwelling induced changes in the abundance and community structure of archaea and bacteria in a recurring mud bank along the southwest coast of India. *Reg. Stud. Mar. Sci.* 18, 113–121. <https://doi.org/10.1016/j.rsma.2018.01.006>
- Arunpandi, N., Jyothibabu, R., Jagadeesan, L., Gireeshkumar, T.R., Karnan, C., Naqvi, S.W.A., 2017. Noctiluca and copepods grazing on the phytoplankton community in a nutrient-enriched coastal environment along the southwest coast of India. *Environ. Monit. Assess.* 189. <https://doi.org/10.1007/s10661-017-6061-9>
- Atkinson, C.A., Jolley, D.F., Simpson, S.L., 2007. Effect of overlying water pH, dissolved oxygen, salinity and sediment disturbances on metal release and sequestration from metal contaminated marine sediments. *Chemosphere* 69, 1428–1437.
- Belzile, N., DeVitre, R.R., Tessier, A., 1989. In situ collection of diagenetic iron and manganese oxyhydroxides from natural sediments. *Nature* 340, 376–377.
- Berg, P., Risgaard-Petersen, N., Rysgaard, S., 1998. Interpretation of measured concentration profiles in sediment pore water. *Limnol. Oceanogr.* 43, 1500–1510.

- Böning, P., Brumsack, H., Böttcher, M., Schnetger, B., Kriete, C., Kallmeyer, J., Borchers, S., 2004. Geochemistry of Peruvian near-surface sediments. *Geochim. Cosmochim. Acta* 68, 4429–4451. <https://doi.org/10.1016/j.gca.2004.04.027>
- Böning, P., Cuypers, S., Grunwald, M., Schnetger, B., Brumsack, H.J., 2005. Geochemical characteristics of Chilean upwelling sediments at ~36°S. *Mar. Geol.* 220 (1–4), 1–21. <https://doi.org/10.1016/j.margeo.2005.07.005>
- Böning, P., Brumsack, H.J., Schnetger, B., Grunwald, M., 2009. Trace element signatures of Chilean upwelling sediments at 36°S. *Mar. Geol.* 259, 112–121.
- Böning, P., Shaw, T., Pahnke, K., Brumsack, H., 2015. Nickel as indicator of fresh organic matter in upwelling sediments. *Geochim. Cosmochim. Acta* 162 (1), 99–108. <https://doi.org/10.1016/j.gca.2015.04.027>
- Canfield, D.E., 1994. Factors influencing organic carbon preservation in marine sediments. *Chem. Geol.* 114, 315–329.
- Canfield, D.E., Thamdrup, E., Hansen, J. W., 1993. The anaerobic degradation of organic matter in Danish coastal sediments: Iron reduction, manganese reduction, and sulfate reduction. 57, 3867–3883.
- Castillo, A., Valdés, J., Sifeddine, A., Vega, S.E., Díaz-Ochoa, J., Marambio, Y., 2018. Evaluation of redox-sensitive metals in marine surface sediments influenced by the oxygen minimum zone of the Humboldt Current System, Northern Chile. *Int. J. Sediment Res.* 34 (2), 178–190. <https://doi.org/10.1016/j.ijsrc.2018.08.005>
- Chakraborty, P., Jayachandran, S., Chakraborty, S., 2018. Chromium speciation in the sediments across the oxygen minimum zone, western continental margin of India. *Geol. J.* 54 (3), 1132–1140. <https://doi.org/10.1002/gj.3214>
- Chakraborty, P., Babu, P.V.R., Sarma, V.V., 2012. A study of lead and cadmium speciation in some estuarine and coastal sediments. *Chem. Geol.* 217–225, 294–295. <https://doi.org/10.1016/j.chemgeo.2011.11.026>
- Chakraborty, P., Chakraborty, S., Jayachandran, S., Madan, R., Sarkar, A., Linsy, P., Nath, B.N., 2016. Effects of bottom water dissolved oxygen variability on copper and lead fractionation in the sediments across the oxygen minimum zone, western continental margin of India. *Sci. Total Environ.* 1052–1061, 566–567. <https://doi.org/10.1016/j.scitotenv.2016.05.125>
- Chakraborty, P., Ramteke, D., Chakraborty, S., 2015. Geochemical partitioning of Cu and Ni in mangrove sediments: Relationships with their bioavailability. *Mar. Pollut. Bull.* 93, 194–201. <https://doi.org/10.1016/j.marpolbul.2015.01.016>
- Childress, J.J., Seibel, B.A., 1998. Life at stable low oxygen levels: adaptations of animals to oceanic oxygen minimum layers. *J. Exp. Biol.* 201, 1223–1232.
- Dang, D.H., Lenoble, V., Durrieu, G., Omanović, D., Mullet, J.U., Mounier, S., Garnier, C., 2015. Seasonal variations of coastal sedimentary trace metals cycling: insight on the effect of manganese and iron (oxy)hydroxides, sulphide and organic matter. *Mar. Pollut. Bull.* 92 (1–2), 113–124.
- Dhanakumar, S., Murthy, K.R., Solaraj, G., Mohanraj, R., 2013. Heavy-Metal Fractionation in Surface Sediments of the Cauvery River Estuarine Region, Southeastern Coast of India. *Environ. Contam. Toxicol.* 64. <https://doi.org/10.1007/s00244-013-9886-4>
- Eggleton, J., Thomas, K.V., 2004. A review of factors affecting the release and bioavailability of contaminants during sediment disturbance events. *Environment International* 30, 973–980.
- Feely, R.A., Chester, A.J., Paulson, A.J., Larrance, J.D., 1982. Relationships Between Organically Bound Cu and Mn in Settling Particulate Matter and Biological Processes in a Subarctic Estuary 1. *Estuaries* 5, 74–80.
- Folk, R.L., 1980. Petrology of sedimentary rocks. Hemphill Publ. Co., Austin, Texas, 78703, 184 pp.
- Froelich, P.N., Klinkhammer, G.P., Bender, M.L., Luedtke, N.A., Heath, G.R., Cullen, D., Dauphin, P., Hammond, D., Hartman, B., Maynard, V., 1979. Early oxidation of organic matter in pelagic sediments of the eastern equatorial Atlantic: suboxic diagenesis. *Geochim. Cosmochim. Acta* 43, 1075–1090. [https://doi.org/10.1016/0016-7037\(79\)90095-4](https://doi.org/10.1016/0016-7037(79)90095-4)
- Gallon, C., Tessier, A., Gobeil, C., Torre, M.C.A., 2004. Modeling diagenesis of lead in sediments of a Canadian Shield lake. *Geochim. Cosmochim. Acta* 68, 3531–3545. <https://doi.org/10.1016/j.gca.2004.02.013>
- Gireeshkumar, T.R., Mathew, D., Pratihary, A.K., Naik, H., Narvekar, K.U., Araujo, J., Balachandran, K.K., Muraleedharan, K.R., Thorat, B., Nair, M., Naqvi, S.W.A., 2017. Influence of upwelling induced near shore hypoxia on the Alappuzha mud banks, South West Coast of India. *Cont. Shelf Res.* 139, 1–8. <https://doi.org/10.1016/j.csr.2017.03.009>
- Gireesh Kumar, T.R., Dayana Mathew, Udaykrishnan, P.B., Shameem, K., Fahad Fathin, K.P., Furtado, C.M., Deepulal, P.M., Nair, M., Balachandran, K.K., 2020. Montmorillonite and phosphorus enrichment in sediments as the causative factor for the formation of mud banks along the southwest coast of India. *Reg. Stud. Marine Sci.* Vol. 40, 101517. <https://doi.org/10.1016/j.rsma.2020.101517>
- Gleyzes, C., Tellier, S., Astruc, M., 2002. Fractionation studies of trace elements in contaminated soils and sediments: a review of sequential extraction procedure. *Trends Anal. Chem.* 21, 451–467.
- Graham, W.F., Bender, L., Klinkhammer, G.P., 1976. Manganese in Narragansett Bay. *Limnol. Oceanogr.* 21, 665–673.
- Grasshoff, K., Ehrhardt, M., Kremling, K., 1999. *Methods of Sea Water Analysis*. VCH, Weinheim, Germany, 159–196.
- Guha, H., Saiers, J.E., Brooks, S., Jardine, P., Jayachandran, K., 2001. Chromium transport, oxidation, and adsorption in manganese-coated sand. *J. Contam. Hydrol.* 49 (3), 311–334.
- Guo, T., Delaune, R.D., Patrick, W.H., 1997. In: *The influence of sediment redox chemistry on chemically active forms of arsenic, cadmium, chromium, and zinc in estuarine sediment*, Vol. 23. Pergamon Press, 305–316.
- Gupta, G.V.M., Sudheesh, V., Sudharma, K.V., Saravanane, N., Dhanya, V., Dhanya, K.R., Lakshmi, G., Sudhakar, M., Naqvi, S.W.A., 2016. Evolution to decay of upwelling and associated biogeochemistry over the southeastern Arabian Sea shelf. *Biogeosciences* 121 (1), 159–175. <https://doi.org/10.1002/2015JG003163>
- Helmond, N.A.G.M., Van, Jilbert, T., Slomp, C.P., 2018. Hypoxia in the Holocene Baltic Sea: Comparing modern versus past intervals using sedimentary trace metals. *Chem. Geol.* 493, 478–490. <https://doi.org/10.1016/j.chemgeo.2018.06.028>
- Henrichs, S.M., Reeburgh, W.S., 1987. Anaerobic mineralisation of marine sediment organic matter: rates and the role of anaerobic processes in the oceanic carbon economy. *Geomicrobiol. J.* 5, 191–237.
- Horowitz, A.J., Elrick, K., 1987. The relation of stream sediment surface area, grain size and composition to trace element chemistry. *Appl. Geochemistry* 2.
- Jahnke, R.A., Emerson, S.R., Murray, J.W., 1982. A model of oxygen reduction, denitrification, and organic matter mineralisation in marine sediments 1. *Limnol. Oceanogr.* 27 (4), 610–623.
- James, B.R., 2002. Chemical transformations of chromium in soils: Relevance to mobility, bio-availability and remediation. The International Chromium Development Association The chromium file, no. 8 Available at.
- Jayaraj, K.A., Jayalakshmi, K.V., Saraladevi, K., 2007. Influence of environmental properties on macrobenthos in the northwest Indian Shelf. *Environ. Monit. Assess.* 127, 459–475.
- Jensen, H.S., Mortensen, P.B., Andersen, F.O., Jensen, A., 1995.

- Phosphorus cycling in a coastal marine sediment, Aarhus Bay, Denmark. *Limnol. Oceanogr.* 36, 908–917.
- Joydas, T.V., Damodaran, R., 2014. Infaunal macrobenthos of the oxygen–minimum zone on the Indian western continental shelf. *Mar. Ecol.* 35, 22–35.
- Jyothibabu, R., Balachandran, K.K., Jagadeesan, L., Karnan, C., Arunpandi, N., Naqvi, S.W.A., Pandiyarajan, R.S., 2018. Mud Banks along the southwest coast of India are not too muddy for plankton. *Sci. Rep.* 8, 1–13.
- Karnan, C., Jyothibabu, R., Manoj Kumar, T.M., Balachandran, K.K., Arunpandi, N., Jagadeesan, L., 2017. Seasonality in autotrophic mesoplankton in a coastal upwelling-mud bank environment along the southwest coast of India and its ecological implications. *Cont. Shelf Res.* 146, 1–12. <https://doi.org/10.1016/j.csr.2017.08.006>
- Krom, M.D., Berner, R.A., 1980. Adsorption of phosphate in anoxic marine sediments. *Limnol. Oceanogr.* 25, 797–806.
- Lakatos, J., Brown, S.D., Snape, C.E., 2002. Coals as sorbents for the removal and reduction of hexavalent chromium from aqueous waste streams. *Fuel* 81, 691–698.
- Levin, L.A., 2003. Oxygen minimum zone benthos: Adaptation and community response to hypoxia. *Oceanogr. Mar. Biol. Ann. Rev.* 41, 1–45.
- Levin, L.A., Ekau, W., Gooday, A.J., Jorissen, F., Middelburg, J.J., Naqvi, S.W.A., Neira, C., Rabalais, N.N., Zhang, J., 2009. Effect of natural and human-induced hypoxia on coastal benthos. *Biogeosciences* 6, 2063–2098.
- Madhu, N.V., Anil, P., Gireeshkumar, T.R., Muraleedharan, K.R., Kiran, K., Vishal, C.R., 2020. Phytoplankton characterisation in the Alappuzha mud banks during the pre-/post phases of a red-tide, *Prorocentrum shikokuense* Hada. *Reg. Stud. Mar. Sci.* 40, 101486. <https://doi.org/10.1016/j.rsma.2020.101486>
- Madhu, N.V., Anil, P., Meenu, P., Gireeshkumar, T.R., Muraleedharan, K.R., Rehitha, T.V., Dayana, M., Vishal, C.R., 2021. Response of coastal phytoplankton to upwelling induced hydrological changes in the Alappuzha mud bank region, southwest coast of India. *Oceanologia* 63 (2), 261–275. <https://doi.org/10.1016/j.oceano.2021.02.001>
- Malandrino, M., Abollino, O., Buoso, S., Casalino, C.E., Gasparon, M., Giacomino, A., La Gioia, C., Mentasti, E., 2009. Geochemical characterisation of Antarctic soils and lacustrine sediments from Terra Nova Bay. *Microchem. J.* 92 (1), 21–31.
- Mathew, D., Gireeshkumar, T.R., Balachandran, K.K., Udayakrishnan, P.B., Shameem, K., Deepulal, P.M., Nair, M., Madhu, N.V., Muraleedharan, K.R., 2020. Influence of hypoxia on phosphorus cycling in Alappuzha mud banks, southwest coast of India. *Reg. Stud. Mar. Sci.* 34, 101083. <https://doi.org/10.1016/j.rsma.2020.101083>
- Mathew, D., Gireeshkumar, T.R., Udayakrishnan, P.B., Muraleedharan, K.R., Madhu, N.V., Nair, M., Revichandran, C., Balachandran, K.K., 2019. Inter-annual variations in the hydrochemistry of Alappuzha mud banks, southwest coast of India. *Cont. Shelf Res.* 177, 42–49. <https://doi.org/10.1016/j.csr.2019.03.008>
- Mathew, D., Gireeshkumar, T.R., Udayakrishnan, P.B., Shameem, K., Nayana, P.M., Deepulal, P.M., Sarath, R., Nair, M., Jaleel, A.K.U., Balachandran, K.K., 2022. Geochemical speciation of iron under nearshore hypoxia: A case study of Alappuzha mud banks, southwest coast of India. *Cont. Shelf Res.* 238. <https://doi.org/10.1016/j.csr.2022.104686>
- McCave, 1984. Size spectra and aggregation of suspended particles in the deep ocean. *Deep Sea Res. Pt. A* 31 (4), 329–352.
- MacDonald, D.D., Scottcarr, R., Calder, F.D., Long, E.R., Ingersoll, C.G., 1996. Development and evaluation of sediment quality guidelines for Florida coastal waters. *Ecotoxicology* 5, 253–278. <https://doi.org/10.1007/BF00118995>
- Munoz, P., Dezileau, L., Cardenas, L., Sellanes, J., Lange, C.B., Inostroza, J., Muratli, J., Salamance, M.A., 2012. Geochemistry of trace metals in shelf sediments affected by seasonal and permanent low oxygen conditions off central Chile, SE Pacific (~36°S). *Cont. Shelf Res.* 33, 51–68.
- Muraleedharan, K.R., Dinesh Kumar, P.K., Prasanna Kumar, S., Srijith, B., John, S., Naveen Kumar, K.R., 2017. Observed salinity changes in the Alappuzha mud bank, southwest coast of India and its implication to hypothesis of mudbank formation. *Cont. Shelf Res.* 137, 39–45. <https://doi.org/10.1016/j.csr.2017.01.015>
- Naqvi, S.W.A., Jayakumar, D.A., Narvekar, P.V., Naik, H., 2000. Increased marine production of N₂O due to intensifying anoxia on the Indian continental shelf. *Nature* 408, 346–349.
- Naqvi, S.W.A., Bange, H.W., Farias, L., Monteiro, P.M.S., Scranton, M.I., Zhang, J., 2010. Coastal hypoxia /anoxia as a source of CH₄ and N₂O. *Biogeosciences Discuss.* 6, 9455–9523. <https://doi.org/10.5194/bgd-6-9455-2009>
- Naqvi, S.W.A., Naik, H., Jayakumar, A., Pratihary, A. K., Narvekar, G., Kurian, S., Agnihotri, R., Shailaja, M. S., Narvekar, P. V. 2009. Seasonal Anoxia Over the Western Indian Continental Shelf. In: *Indian Ocean Biogeochemical Processes and Ecological Variability*, Wiggert, J.D., Hood, R.R., Naqvi, S.W.A., Brink, K.H., Smith, S.L. (Eds.), Vol. 185, Amer. Geophys. Union, Washington, 333–346.
- Naqvi, S.W.A., Naik, H., Pratihary, A., D'Souza, W., Narvekar, P.V., Jayakumar, D.A., Devol, A.H., Yoshinari, T., Saino, T., 2006. Coastal versus open ocean denitrification in the Arabian Sea. *Biogeosciences* 3 (4), 621–633.
- Naqvi, S.W.A., Unnikrishnan, A.S., 2009. Hydrography and Biogeochemistry of the Coastal Ocean. In: *Surface Ocean–Lower Atmosphere Processes*, Le Quére, C., Saltzman, E.S. (Eds.), Geophys. Monogr. Ser. Vol. 187, Amer. Geophys. Union, Washington, 233–250. <https://doi.org/10.1029/2008GM000771>
- Nameroff, T., Balistrieri, L., Murray, W., 2002. Suboxic trace metals geochemistry in the Eastern Tropical North Pacific. *Geochim. Cosmochim. Ac.* 66 (7), 1139–1158.
- Nemati, K., Bakar, N.K.A., Abas, M.R., Sobhanzadeh, E., 2011. Speciation of heavy metals by modified BCR sequential extraction procedure in different depths of sediments from Sungai Buloh, Selangor, Malaysia. *J. Hazard. Mater.* 192, 402–410. <https://doi.org/10.1016/j.jhazmat.2011.05.039>
- Parvathi, A., Jasna, V., Aswathy, V.K., Nathan, V.K., Aparna, S., Balachandran, K.K., 2019. Microbial diversity in a coastal environment with co-existing upwelling and mud-banks along the southwest coast of India. *Mol. Biol. Rep.* <https://doi.org/10.1007/s11033-019-04766-y>
- Prasanna Kumar, S., Dinesh Kumar, P.K., Muraleedharan, K.R., George, G., Mathew, D., Kripa, V., Jeyabaskaran, R., Ramiah, N., Gopalakrishnan, A., Naqvi, S.W.A., 2018. Mudbanks and fisheries along the Kerala coast-myth and reality. *Curr. Sci. India* 4, 773–778.
- Raiswell, R., Canfield, D.E., 1998. Sources of iron for pyrite formation in marine sediments. *Am. J. Sci.* 298, 219–245. <https://doi.org/10.2475/ajs.298.3.219>
- Rauret, G., López-Sánchez, J.F., Sahuquillo, A., Rubio, R., Davidson, C., Ure, A., Quevauviller, P. 1999. Improvement of the BCR three step sequential extraction procedure prior to the certification of new sediment and soil reference materials. *J. Environ. Monit.* (1), 57–61. <https://doi.org/10.1039/a807854h>
- Richard, F.C., Bourg, A.C.M., 1991. Aqueous geochemistry of Cr: A review. *Water Res.* 25 (7), 807–816.
- Rowe, G.T., 1971. Benthic biomass in the Pisco, Peru upwelling. *Investigación Pesquera* 35, 127–135.
- Schaller, T., Transportation, S., Board, S., Wehrli, B., 1997. Sedimentary profiles of Fe, Mn, V, Cr, As and Mo as indicators of benthic redox conditions in Baldeggersee Sedimentary profiles of Fe, Mn, V, Cr, As and Mo as indicators of benthic redox conditions in Baldeggersee. *Aquatic Sci.* 59, 345–361. <https://doi.org/10.1007/BF02522363>

- Schulz, H.D., Zabel, M., Schulz, H.D., 2006. *Marine Geochemistry*, 2nd Edn., Springer, 593 pp.
- Shynu, R., Rao, V. P., Samiksha, S.V., Vethamony, P., Naqvi, S.W.A., Kessarkar, P.M., Babu, M.T., Dineshkumar, P.K., 2017. Estuarine, Coastal and Shelf Science Suspended matter and fluid mud off Alleppey, southwest coast of India. *Estuar. Coast. Shelf Sci.* 185, 31–43.
- SEPA (State Environmental Protection Administration of China), 2002. *Marine Sediment Quality (GB 18668–2002)*. Standards Press of China, Beijing.
- Slomp, C.P., Van der Gaast, S.J., Van Raaphorst, W., 1996. Phosphorus binding by poorly crystalline iron oxides in North Sea sediments. *Mar. Chem.* 52, 55–73. [https://doi.org/10.1016/0304-4203\(95\)00078-X](https://doi.org/10.1016/0304-4203(95)00078-X)
- Smitha, A., Joseph, K.A., Jayaram, C., Balchand, A.N., 2014. Upwelling in the southeastern Arabian Sea as evidenced by Ekman mass transport using wind observations from OCEANSAT-II Scatterometer.
- Thamdrup, B., Canfield, D.E., 1996. Pathways of carbon oxidation in continental margin sediments off central Chile. *Limnol. Oceanogr.* 41, 1629–1650.
- Twining, B.S., Baines, S.B., Vogt, S., Nelson, D.M., 2012. Role of diatoms in nickel biogeochemistry in the ocean. *Global Biogeochem. Cy.* 26, 1–9. <https://doi.org/10.1029/2011GB004233>
- Van der Geest, H.G., Leon Paumen, M., 2008. Dynamics of metal availability and toxicity in historically polluted floodplain sediments. *Sci. Total Environ.* 406, 419–425.
- Vandieken, V., Nickel, M., Jørgensen, B.B., 2006. Carbon mineralisation in Arctic sediments northeast of Svalbard: Mn(IV) and Fe(III) reduction as principal anaerobic respiratory pathways. *Mar. Ecol. Prog. Ser.* 322, 15–27. <https://doi.org/10.3354/meps322015>
- Zhang, X.W., Kong, L.W., Li, J., 2014. An investigation of alternations in Zhanjiang clay properties due to atmospheric oxidation. *Géotechnique* 64 (12), 1003–1009.

Available online at www.sciencedirect.com

ScienceDirect

journal homepage: www.journals.elsevier.com/oceanologia

ORIGINAL RESEARCH ARTICLE

Seasonal assessment of the trophic status in the coastal waters adjoining Tuticorin harbor in relation to water quality and plankton community in the Gulf of Mannar, India

Rengasamy Subramaniyan Sathishkumar^{a,b}, Arumugam Sundaramanickam^{a,*},
Ajit Kumar Mohanty^b, Gouri Sahu^b, Thangavelu Ramesh^a,
Kumar Balachandar^c, Ajith Nithin^a, Parthasarathy Surya^a,
Krishnan Silambarasan^c

^a Centre of Advanced Study in Marine Biology, Annamalai University, Parangipettai, Tamil Nadu, India

^b Radiological and Environment Safety Division, Indira Gandhi Centre for Atomic Research, Kalpakkam, Tamil Nadu, India

^c Fishery Survey of India, Beach Road, Visakhapatnam, Andhra Pradesh, India

Received 21 June 2021; accepted 21 July 2022

Available online 5 August 2022

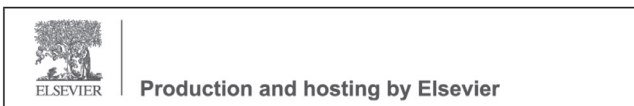
KEYWORDS

Algal bloom;
Eutrophication;
Plankton diversity;
Southeast coast of
India;
Trichodesmium;
TRIX

Abstract Seasonal variations in hydrography, trophic status, and plankton community structure were studied along the Tuticorin coastal waters (TCWs) in the Gulf of Mannar (GoM). Samples were collected in 2015 and 2016 to analyze physico-chemical (temperature, pH, salinity, suspended particulate matter (SPM), dissolved oxygen (DO), nutrients, etc.) and biological parameters (chlorophyll-*a*, phytoplankton, and zooplankton). The trophic index (TRIX) and eutrophication index (EI) were calculated to describe the eutrophication status of TCWs. Temperature, pH, salinity, DO, and SPM showed seasonality due to the impact of the northeast monsoon. A massive bloom of *Trichodesmium erythraeum* was observed, with a visible impact on water quality and the plankton community. The cluster and principal component analysis indicated the bloom event as a distinct phenomenon. ANOVA results showed significant seasonal variations rather than spatial variations. According to the trophic indices, the area had a low trophic level in 2015 and a high trophic level in 2016. The Tuticorin inshore waters had the

* Corresponding author at: Centre of Advanced Study in Marine Biology, Annamalai University, Parangipettai, Tamil Nadu, India.
E-mail addresses: rssathishphd@gmail.com (R.S. Sathishkumar), fish_lar@yahoo.com (A. Sundaramanickam).

Peer review under the responsibility of the Institute of Oceanology of the Polish Academy of Sciences.



<https://doi.org/10.1016/j.oceano.2022.07.002>

0078-3234/© 2022 Institute of Oceanology of the Polish Academy of Sciences. Production and hosting by Elsevier B.V. This is an open access article under the CC BY-NC-ND license (<http://creativecommons.org/licenses/by-nc-nd/4.0/>).

highest TRIX and EI values during the dominance of cyanobacteria bloom in the post-monsoon 2016. The trophic indices had a positive relationship with phytoplankton abundance but showed an inverse relation with zooplankton abundance. The overall range of the TRIX index (3.18–5.96) indicated that the environment was oligotrophic to eutrophic, and EI values (0.72–21.61) indicated that the state of coastal waters was moderate to poor. This study states that periodic monsoonal flow and frequent algal bloom events have a significant impact on the GoM coastal waters.

© 2022 Institute of Oceanology of the Polish Academy of Sciences. Production and hosting by Elsevier B.V. This is an open access article under the CC BY-NC-ND license (<http://creativecommons.org/licenses/by-nc-nd/4.0/>).

1. Introduction

The richness and productivity of marine ecosystems can be assessed by investigating the hydrographical features (Rajasegar, 2003). Typically, coastal regions are the most affected marine ecosystems that receive a large concentration of nutrients from freshwater runoff and effluents from artificial sources (McLusky and Elliott, 2004; Sarma et al., 2013). However, increasing nutrient concentrations can cause eutrophication (Newton et al., 2003) which further leads to a biological phenomenon, like the algal bloom events (Domingues et al., 2011). Among the nutrients, overloading of nitrogen and phosphorus from diverse sources can alter the biogeochemistry of oceans and increased primary production is the most common effect that is expected to happen in the water environment (Smith et al., 1999). The human population, livestock, and terrestrial use are major contributors to nitrogen (N) and phosphorus (P) loading into aquatic ecosystems (Smith et al., 1999). These, both parameters (N and P), are considered as crucial criteria for assessing the trophic status of any aquatic ecosystem (Vollenweider et al., 1998). Currently, aquatic ecosystems are routinely assessed for their health and trophic status using a variety of indices to identify anthropogenic stressors and natural hazards (Jørgensen et al., 2010; Rath et al., 2018; Srichandan et al., 2019). For example, several parameters such as dissolved oxygen (DO), annual phosphate concentration, dissolved inorganic nitrogen (DIN), and chlorophyll-*a* (chl-*a*) have been proposed as indicators for water body classification (EEA, 1999; OECD, 1982). However, more complex statistical methods, imitation models, and trophic levels are most extensively used to assess water quality.

Many investigators have employed TRIX to assess the trophic levels of the Black Sea (Moncheva et al., 2001), Aegean Sea (Penna et al., 2004), Algarve, South Portugal (Coelho et al., 2007), Aegean, Eastern Mediterranean (Primpas and Karydis, 2011), Adriatic Sea, Italy (Fiori et al., 2016), coastal waters of northeastern Mediterranean (Tugrul et al., 2019), and Iranian Caspian Sea (Kucuksezgin et al., 2019; Nasrollahzadeh et al., 2008), North Yellow Sea, Shandong Peninsula (Yang et al., 2020). In India, very few reports have evaluated trophic status by using TRIX (Hardikar et al., 2021; Jayachandran and Nandan, 2012; Rajaneesh et al., 2015; Rath et al., 2018; Srichandan et al., 2019). These studies were mostly confined to the Kerala, Karnataka, Maharashtra, and Odisha coasts of India. Despite numerous studies that reported the plankton and water quality of the Gulf of Man-

nar (GoM) (Asha and Diwakar, 2007; Balakrishnan et al., 2017; Bharathi et al., 2018; Rajendran et al., 2018; Sathishkumar et al., 2021), none of the studies so far have evaluated the trophic indices for this region. Similarly, the eutrophication index (EI) is a popular method for measuring the level of eutrophication in coastal water ecosystems, and it has been used in various coastal waters (Kucuksezgin et al., 2019; Pavlidou et al., 2015; Tugrul et al., 2019). Its application in the coastal environment has not been reported so far from Indian waters. Considering the above, the present study mainly aims to evaluate the eutrophication status of the Tuticorin coastal waters (TCWs) in various seasons using TRIX and EI. Subsequently, the relationship of TRIX and EI with the plankton (phyto- and zooplankton) community will also be assessed to find out the conduciveness of the ecosystem for plankton distribution.

2. Material and methods

2.1. Study area

Gulf of Mannar (GoM) is a large shallow bay in the Indian Ocean, the first biosphere reserve in India, declared by UNESCO in 1989. The GoM contains large fish resources, which is an economically unavoidable fish trading region in southern India. The study area of Tuticorin (Lat. 8°48'21"N; Long. 78°9'18"E) is situated in the GoM, and it is one of the most economically important coastal cities in southern Tamil Nadu, India (Figure 1). This coastal region is seriously affected by many anthropogenic factors through sewage and various industrial discharges from seafood processing, chemical, petroleum, and fertilizer industries, a thermal power plant, aquaculture ponds, salt pans, etc. (Raj Chandar and Rejeesh Kumar, 2012). This coastal city contains a major harbor, namely V.O.C port (formerly Tuticorin Port). It is an active port for the trade of many materials like coals, oils, urea, chemicals, food and cosmetics materials, etc. In general, this coastal region experiences four seasons per annum comprising the post-monsoon/POM (January to March), summer/SUM (April to June), pre-monsoon/PRM (July to September) and monsoon/MON (October to December).

2.2. Hydrological sampling methods

The coastal water survey was carried out seasonally at six different stations along two transects in the Tuticorin coast (Figure 1). Transects one and two were located near Tu-

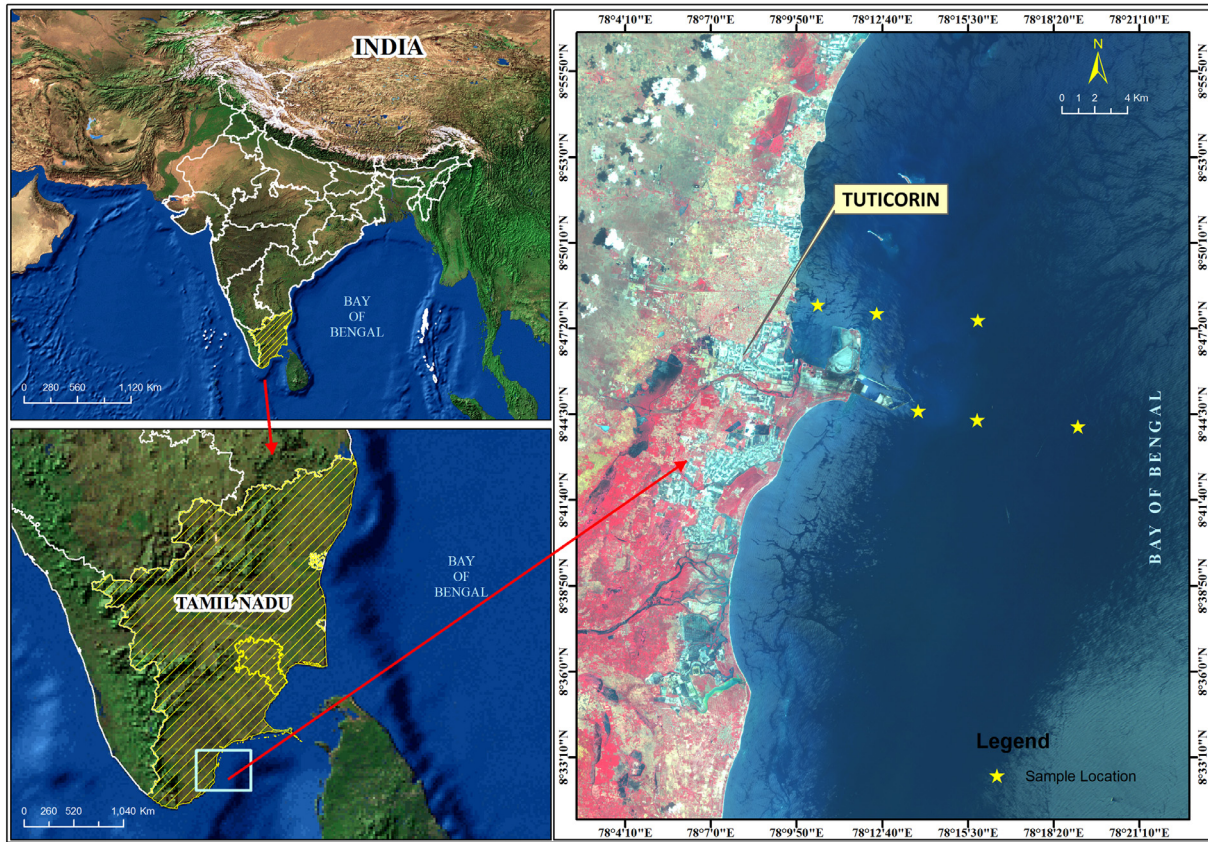


Figure 1 The map depicts the study area (TCWs) and sampling locations in the Gulf of Mannar.

Table 1 Details of the sampling locations and water depths at Tuticorin coastal waters during the study period (2015–2016).

Transect	Sampling location	Maximum depth (m)	Latitude	Longitude
Transect 1	Tuticorin old harbour (TOH)	6	8°48'18"N	78°10'47"E
		11	8°48'18"N	78°12'14"E
		17	8°48'18"N	78°16'16"E
Transect 2	Tuticorin new harbour (TNH)	12	8°44'45"N	78°14'22"E
		19	8°44'45"N	78°16'44"E
		24	8°44'45"N	78°19'30"E

ticorin’s old harbor and new harbor, respectively. Table 1 contains information about the sampling locations in more detail. The coastal sampling was conducted for eight consecutive seasons in 2015 and 2016. The surface water was collected using a Niskin water sampler. Seawater temperature (SWT) was recorded by a mercury thermometer with an accuracy of $\pm 0.1^{\circ}\text{C}$. The pH values were tested by a pre-calibrated portable pH tester (± 0.1 accuracy) (pH tester Eutech Instruments, Mode pH Testr10). Salinity was recorded using a calibrated digital Refractometer (ATAGO-Japan, Model PAL-1). For DO, the samples were collected using glass stopper bottles and fixed on the sampling site following Winkler’s method revised by Strickland and Parsons (1972). For nutrient estimation, water samples were collected in one-liter pre-cleaned polypropylene bottles, kept in an icebox, and transported to the laboratory. Later,

the collected water samples were passed through Whatman ($0.45\ \mu\text{m}$) filter paper by using Millipore 4 bar Vacuum / Pressure Pump, 220V/ 50Hz. Besides, the used filter paper was placed in a hot air oven at $40^{\circ}\text{C} \pm 5^{\circ}\text{C}$ (until dry) to measure suspended particulate matter (SPM). Filtered water samples were utilized for the analysis of dissolved micro-nutrients such as nitrite, nitrate, inorganic phosphate (IP), silicate, ammonia, total nitrogen (TN), and total phosphate (TP). Standard methods were followed to analyze all the above nutrients (Grassoff et al., 1999). In addition, one liter of surface water was collected in a dark polypropylene container and transported to the laboratory with the help of an icebox for chlorophyll-*a* (chl-*a*) estimation. The pigment extraction method was adopted for the chl-*a* measurement by using 90% acetone. Extracted samples were then kept in a refrigerator (20 hrs) under dark conditions, and then the pigment

concentration was measured with a UV–VIS spectrophotometer using 1 cm cells at 630 nm, 645 nm, and 665 nm using the standard method (Strickland and Parsons, 1972). All of the above analyses (nutrients and pigments) were performed with a SHIMADZU UV-1800 spectrophotometer made in Singapore.

2.3. Plankton sampling and analyses

The phytoplankton and zooplankton samples were collected with one replicate in the surface waters of the Tuticorin coast by using 55- μm and 200- μm mesh nets, respectively. The collected plankton samples were preserved immediately in diluted formalin solution (2% for phytoplankton and 4% for zooplankton) for qualitative and quantitative studies. An inverted microscope was used for both plankton identifications. For phytoplankton, the counting was done by the sedimentation method as described by Sukhanovo (1978) (unit measurement: cells L^{-1}), and the species-level identifications were made by using standard works of Al-Kandari et al. (2009), Santhanam et al. (1987), Smith (1977), Subramanyan (1946), and Venkataraman (1939). Similarly, for zooplankton, the counting was done by following standard procedures (Omori and Ikeda, 1984). Proper counting of the subsamples was done and recorded on the datasheets and expressed as nos. m^{-3} . Identification of the zooplankton was made using standard literature (Conway et al., 2003; Dakin and Colefax, 1940; Goswami, 2004; Kasthurirangan, 1963; Perumal et al., 1998; Wickstead, 1965).

2.4. Estimation of TRIX and EI indices

The trophic index (TRIX) is a commonly used index to classify the coastal environment (Volleinweider et al., 1998). It categorizes the seawater environment into oligotrophic, mesotrophic, and eutrophic habitats based on the concentration of water parameters (Volleinweider et al., 1998). In TRIX, four parameters such as total nitrogen (TN), total phosphorus (TP), chlorophyll-*a* (chl-*a*), and dissolved oxygen percentage ($\text{D}\%O_2$) are used in a linear combination to assess the coastal water status (Penna et al., 2004; Vollenweider et al., 1998). The trophic and eutrophication status of the TCWs were assessed employing the TRIX (Vollenweider et al., 1998) and EI (Primpas et al., 2010) (Table 2). TRIX is a useful technique to categorize the status of the water environment for an understandable application (Vollenweider et al., 1998). The following equation was used to derive the TRIX index:

$$\text{TRIX} = [\log_{10}(\text{Chl-}a) \times (\text{D}\%O_2) \times (\text{TN}) \times (\text{TP}) + a] / b$$

where Chl-*a*: chlorophyll-*a*, $\text{D}\%O_2$: the percentage deviation of dissolved oxygen from the saturation level, TN: total nitrogen ($\mu\text{g L}^{-1}$), TP: total phosphorus ($\mu\text{g L}^{-1}$), the parameters $a = 1.5$ and $b = 1.2$ are constant coefficients for fix the minimal limit of the index and also to fix the scale value at <10 has proposed by Giovanardi and Vollenweider (2004).

The eutrophication index (EI) was estimated by the following formulation (Primpas et al., 2010):

$$\text{EI} = [(0.279 \times \text{CPO}_4^{3-}) + (0.261 \times \text{CNO}_3^-) + (0.296 \times \text{CNO}_2^-) + (0.275 \times \text{CNH}_4^+) + (0.261 \times \text{CChl-}a)]$$

Where; CPO_4^{3-} , CNO_3^- , CNO_2^- , CNH_4^+ and CChl-*a* are the concentrations (μM) of phosphate, nitrate, nitrite, ammonia, and chlorophyll-*a* ($\mu\text{g L}^{-1}$), respectively. The comprehensive stages and ranges of eutrophication in different coastal ecosystems are described elsewhere (Kucuksezgin et al., 2019; Pavlidou et al., 2015) (Table 2).

2.5. Statistical analyses

Data obtained from this study are demonstrated in box plots and contour graphs created with the Grapher (ver. 4) and Surfer (ver. 13) software packages, respectively. XLSTAT pro was used to perform multivariate analyses such as principal component analysis (PCA), cluster analysis (CA), Pearson correlation matrix, and two-way ANOVA. Furthermore, various indices such as Margalef's species richness (D), Pielou's evenness (J'), and Shannon-Wiener diversity index (H') were calculated using PRIMER software (Ver. 6.1) to assess the state of the biological community (phytoplankton and zooplankton).

3. Results

3.1. Hydrological variables

The box plots visualizing the seasonal and annual trend of physicochemical variables in TCWs between 2015 and 2016 are given in Figure 2 and Figure 3. The seasonal mean values of the obtained data are shown in Table 1S. In the present investigation, the surface water temperature (SWT) fluctuated between 28.0°C to 34.3°C. Comparatively, the high temperature was experienced in the summer (SUM) season, while the low temperature was noticed in the monsoon (MON) season (Figure 2). The ANOVA test for SWT revealed significant variation from season to season ($p < 0.05$). The pH values varied from 7.9 to 8.4 (Figure 2), where the corresponding limits were recorded during POM-16 and SUM-15 respectively. The pH trend was similar to temperature; however, the above range indicated that the water was alkaline during the study. Salinity differed from 30.0 to 35.8 (Figure 2), where the corresponding lowest and highest values were noted during MON and SUM seasons in 2016, respectively. Salinity and temperature expressed a notable positive correlation ($r = 0.778$; $p < 0.0001$) with each other proving their covariance nature (Tables 3 and 4). In the present study, the DO concentrations decreased from 6.25 mg L^{-1} to 3.83 mg L^{-1} (Figure 2). The highest concentration of DO was found in MON 2016, while the lowest concentration was found in POM 2016. Suspended particulate matters (SPM) varied widely between 15.10 and 94.63 mg L^{-1} (Figure 2). In 2015 and 2016, the highest SPM concentrations were found in the POM and SUM seasons, respectively. According to the correlation matrix, salinity ($r = -0.373$; $p < 0.009$), phytoplankton density ($r = -0.271$; $p < 0.062$), and phytoplankton diversity ($r = -0.458$; $p < 0.001$) were seemed negative correlations with the SPM (Tables 3 and 4).

3.2. Nutrient dynamics

Nitrite concentration varied significantly ($p < 0.05$) between 0.029 and 0.958 $\mu\text{M L}^{-1}$ (Figure 2). In our study, peak ni-

Table 2 Some methodological tools for assessing the trophic status of coastal waters.

Methods	Threshold	Units	Trophic status
Dissolved Inorganic Nitrogen ^a	<6.5	μM	Good (Oligotrophic)
	6.5–9.0	μM	Fair (Mesotrophic)
	9.0–16.0	μM	Poor (Mesotrophic to eutrophic)
	>16.0	μM	Bad (Eutrophic)
Dissolved Inorganic Phosphorus ^a	<0.5	μM	Good (Oligotrophic)
	0.5–0.7	μM	Fair (Mesotrophic)
	0.7–1.1	μM	Poor (Mesotrophic to eutrophic)
	>1.1	μM	Bad (Eutrophic)
Chlorophyll- <i>a</i> ^b	<2.0	μg L ⁻¹	Oligotrophic
	2.1–2.9	μg L ⁻¹	Oligotrophic to mesotrophic
	3.0–6.9	μg L ⁻¹	Mesotrophic
	7.0–9.9	μg L ⁻¹	Mesotrophic to eutrophic
	>10	μg L ⁻¹	Eutrophic
Trophic Index (TRIX) ^{c,d,e}	<2	Unit	Excellent (Ultra-oligotrophic)
	2–4	Unit	High (Oligotrophic)
	4–5	Unit	Good (Mesotrophic)
	5–6	Unit	Moderate (Mesotrophic to eutrophic)
	6–8	Unit	Poor (Eutrophic)
Eutrophication Index (EI) ^{f,g}	<0.04	Unit	High
	0.04–0.38	Unit	Good
	0.38–0.85	Unit	Moderate
	0.85–1.51	Unit	Poor
	>1.51	Unit	Bad

^a EEA (1999)

^b OECD (1982)

^c Vollenweider et al. (1998)

^d Giovanardi and Vollenweider (2004)

^e Penna et al. (2004)

^f Pavlidou et al. (2015)

^g Kucuksezgin et al. (2019).

trite concentration was witnessed during the monsoon season (2015), while the least concentration was witnessed in the POM season of 2016. In this study, the nitrate concentration ranged from 0.466 μM L⁻¹ to 8.822 μM L⁻¹ (Figure 3). The higher and lower nitrate concentrations were registered in the same year but during different seasons, i.e. pre-monsoon (2015) and post-monsoon (2015), respectively.

Ammonia concentration ranged from 0.159 to 66.500 μM L⁻¹ (Figure 3). The higher value was observed during POM-16, while the lower was recorded in SUM-15. The total nitrogen concentrations ranged from 9.349 to 132.106 μM L⁻¹ (Figure 3). The maximum and the minimum concentrations of TN were recorded during POM-16 and MON-15 respectively. The concentrations of dissolved inorganic phosphate (DIP) were found to range from 0.309 to 1.731 μM L⁻¹ (Figure 3). The maximum concentration was noticed in both monsoon (2015–2016) and it fell to a minimum in summer (2016). The total phosphate concentrations ranged from 0.547 μM L⁻¹ to 3.713 μM L⁻¹, the maximum being observed during POM 2016 and the minimum in SUM 2016 (Figure 3). The highest silicate value (32.829 μM L⁻¹) was observed during the PRM 2015, while the lowest silicate value (1.082 μM L⁻¹) was observed during the MON 2015 (Figure 3). Nitrogen to phosphorus ratio (N:P) also showed wide variations (from 5.87 to 76.64) (p<0.05) (Table 4S). Higher N:P ratios noticed during the POM season (2016) may be reasoned to nitrogen

fixation by *T. erythraeum* bloom. In contrast, a lower ratio was observed during the POM 2015 period. Statistical significance of the above-observed seasonality in N:P distribution was confirmed from ANOVA (Table 2S).

3.3. Chlorophyll-*a*

During the study period, the TCWs showed wide variations of chlorophyll-*a* ranging from 0.225 mg m⁻³ to 23.679 mg m⁻³ (Figure 4). The highest concentration of chl-*a* coincided with the occurrence of *T. erythraeum* bloom in POM 2016, during which the chl-*a* concentration (avg. 11.92±8.29 mg m⁻³) peaked because of higher algal (*T. erythraeum*) biomass (Table 1S). The lowest concentration of chl-*a* was recorded in monsoon 2016.

3.4. Trophic (TRIX) and eutrophication index

The distribution of the TRIX and EI values for TCWs were given in Figure 5. The coastal water has been categorized based on a trophic scale (TRIX) considering <2 as ultra-oligotrophic, 2–4 oligotrophic, 4–5 mesotrophic, 5–6 mesotrophic to eutrophic, and 6 to 8 considered as eutrophic (Penna et al., 2004) (Table 2). TRIX values in 2015

Table 3 Correlation matrix of hydro-biological variables during the study period (variables: SPM, suspended particulate matter; pH, hydrogen ion concentration; SAL, salinity; DO, dissolved oxygen; NO₂, nitrite; NO₃, nitrate; NH₄, ammonium; IP, inorganic phosphate; TN, total nitrogen; TP, total phosphorus; SiO₄, silicate; Chl, chlorophyll; Phyto-Dens, phytoplankton density; Phyto-count, phytoplankton species count; Zoo-Dens, zooplankton density; Zoo-count, zooplankton species count).

Correlation matrix (Pearson):																
Variables	WT	SPM	pH	SAL	DO	NO ₂	NO ₃	NH ₄	IP	TN	TP	SiO ₄	Chl- <i>a</i>	Phyto-Dens	Phyto-count	Zoo-Dens
SPM	-0.006															
pH	0.449	-0.117														
SAL	0.788	-0.373	0.417													
DO	-0.138	0.277	0.149	-0.338												
NO ₂	-0.302	0.138	-0.026	-0.349	0.566											
NO ₃	0.150	-0.260	0.243	0.197	0.076	0.500										
NH ₄	-0.218	-0.159	-0.488	-0.060	-0.654	-0.363	-0.391									
IP	-0.592	0.076	-0.494	-0.583	0.362	0.614	0.155	0.046								
TN	-0.109	-0.139	-0.402	-0.001	-0.610	-0.215	-0.200	0.920	0.043							
TP	-0.424	0.231	-0.500	-0.515	-0.263	-0.001	-0.161	0.519	0.282	0.480						
SiO ₄	-0.121	0.103	-0.064	-0.129	-0.015	0.502	0.701	-0.075	0.222	0.172	0.188					
Chl- <i>a</i>	-0.087	-0.228	-0.437	0.079	-0.490	-0.340	-0.289	0.674	0.080	0.682	0.466	0.030				
Phyto-Dens	-0.095	-0.271	-0.420	0.084	-0.501	-0.315	-0.293	0.802	-0.048	0.792	0.181	-0.037	0.638			
Phyto-count	0.412	-0.458	0.676	0.348	0.174	0.154	0.557	-0.401	-0.197	-0.270	-0.409	0.120	-0.359	-0.366		
Zoo-Dens	0.487	-0.108	0.718	0.437	0.298	-0.014	0.188	-0.416	-0.400	-0.391	-0.493	-0.207	-0.471	-0.457	0.687	
Zoo-count	0.188	0.103	0.482	0.151	0.510	0.396	0.337	-0.545	0.104	-0.401	-0.548	0.112	-0.540	-0.503	0.478	0.545

Values in bold are significantly different from 0 with a significance level alpha=0.1.

Table 4 Shows the 'P' values of the correlation analysis.

Correlation matrix (Pearson):

Variables	WT	SPM	pH	SAL	DO	NO ₂	NO ₃	NH ₄	IP	TN	TP	SiO ₄	Chl- <i>a</i>	Phyto-Dens	Phyto-count	Zoo-Dens
SPM	0.970															
pH	0.001	0.429														
SAL	< 0.0001	0.009	0.003													
DO	0.350	0.057	0.312	0.019												
NO ₂	0.037	0.351	0.859	0.015	< 0.0001											
NO ₃	0.310	0.074	0.096	0.180	0.608	0.000										
NH ₄	0.136	0.281	0.000	0.685	< 0.0001	0.011	0.006									
IP	< 0.0001	0.606	0.000	< 0.0001	0.011	< 0.0001	0.292	0.755								
TN	0.463	0.347	0.005	0.993	< 0.0001	0.143	0.174	< 0.0001	0.772							
TP	0.003	0.114	0.000	0.000	0.071	0.993	0.276	0.000	0.052	0.001						
SiO ₄	0.411	0.486	0.667	0.382	0.918	0.000	< 0.0001	0.614	0.130	0.243	0.201					
Chl- <i>a</i>	0.558	0.120	0.002	0.591	0.000	0.018	0.046	< 0.0001	0.587	< 0.0001	0.001	0.838				
Phyto-Dens	0.521	0.062	0.003	0.570	0.000	0.029	0.043	< 0.0001	0.747	< 0.0001	0.219	0.804	< 0.0001			
Phyto-count	0.004	0.001	< 0.0001	0.015	0.238	0.296	< 0.0001	0.005	0.178	0.064	0.004	0.416	0.012	0.011		
Zoo-Dens	0.000	0.465	< 0.0001	0.002	0.040	0.925	0.200	0.003	0.005	0.006	0.000	0.157	0.001	0.001	< 0.0001	
Zoo-count	0.201	0.487	0.001	0.306	0.000	0.005	0.019	< 0.0001	0.483	0.005	< 0.0001	0.450	< 0.0001	0.000	0.001	< 0.0001

Values in bold are significantly different from 0 with a significance level $\alpha=0.1$.

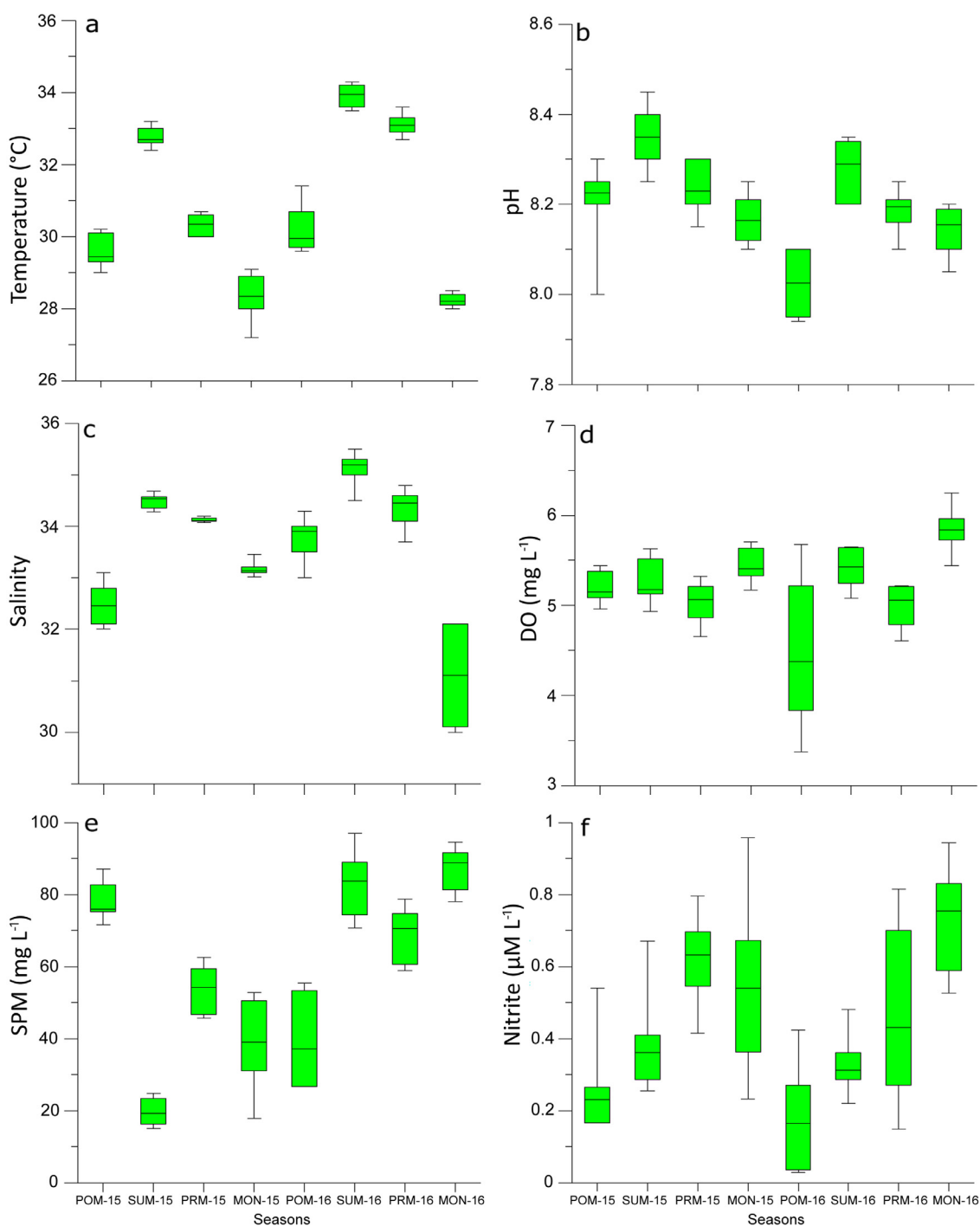


Figure 2 Seasonal variations of physico-chemical parameters in TCWs during 2015 and 2016. a) Surface water temperature; b) pH; c) salinity; d) dissolved oxygen; e) suspended particulate matter; f) nitrite.

showed significant seasonal variations ($p < 0.01$), it averaged 3.96 for POM, 3.78 for SUM, 4.01 for PRM, and 3.46 for MON (Table 1S). The lowest average was observed in MON and the highest average was in PRM. Overall spatial point of view in 2015 the TRIX unit was found at the maximum (4.27), about 0.5 km inshore from the Tuticorin new harbor mouth. Interestingly, this region is located near the Tuticorin thermal power station (TTPS) which is continuously influenced by coolant water discharge. The minimum value

(3.29) was observed along Tuticorin old harbor (TOH) region, about 2 km inshore from the coast. Similarly, TRIX values in 2016 varied significantly by season, with an average of 5.10 in POM, 3.51 in SUM, 3.58 in PRM, and 3.72 in MON (Table 1S). The TRIX values for 2016 were recorded at a minimum (3.18) in the inshore waters (about 5 km) of the TNH region whereas, the maximum value (5.96) was observed at 5 km inshore of TOH region (Table 4S). This maximum TRIX unit coincided with the period of Cyanophyta bloom which

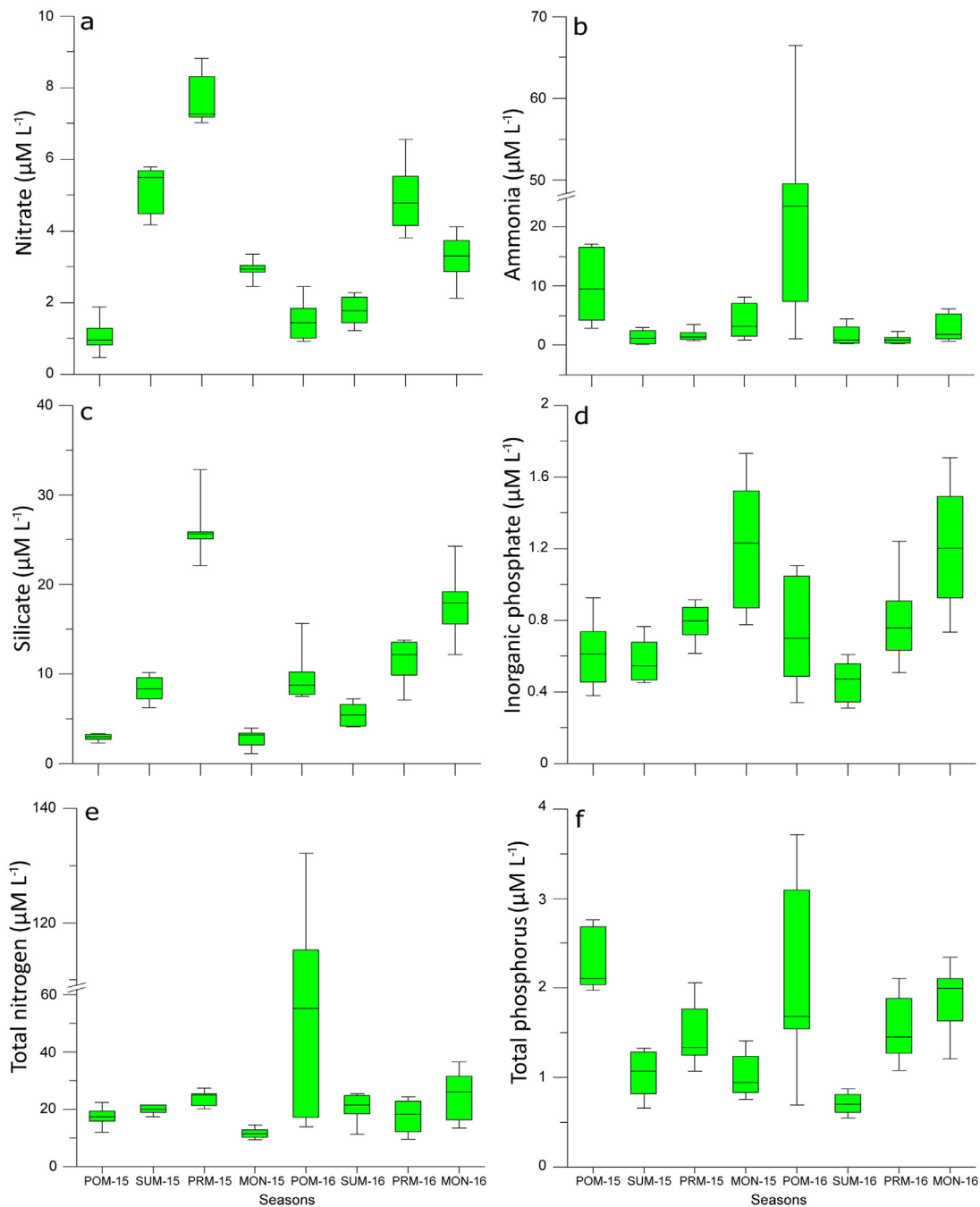


Figure 3 Seasonal variations of dissolved micro-nutrients in TCWs between 2015 and 2016. a) nitrate; b) ammonia; c) silicate; d) inorganic phosphate; e) total nitrogen; f) total phosphorus.

occurred during POM-2016. In ANOVA, the TRIX distribution revealed a significant overall variation in the study area (Table 2S). The seasonal and inter-annual variations were significant as observed from the ANOVA. However, the spatial TRIX variations were insignificant concerning seasons and years (Table 2S). According to the annual mean TRIX data, in 2015, 77% of the samples were oligotrophic (low productivity with TRIX units less than 4) and 23% were moderately productive (TRIX value between 4 and 5), indicating a mesotrophic state. The TRIX results for 2016 indicated that the water was moderate to highly productive. Specifically, during POM-16, the TRIX unit was greater than 5, in-

dicating a mesotrophic to eutrophic condition (23% of samples). Furthermore, 13% of the samples were moderately productive (TRIX 4–5, mesotrophic) and 64% were poorly productive (TRIX <4, oligotrophic).

The TCWs were subjected to the eutrophication index (EI) for two years (2015 and 2016), with values ranging from 0.72 to 21.61 (Table 4S). The seasonal mean of EI during 2015 was: POM, 3.44; SUM, 2.23; PRM, 3.11; MON, 2.51. During 2016, the mean of EI was: POM, 11.63; SUM, 1.28; PRM, 2.02; MON, 2.24. A significant variation was observed between the seasons of different years (Table 2S), the minimum average was recorded in SUM, and the max-

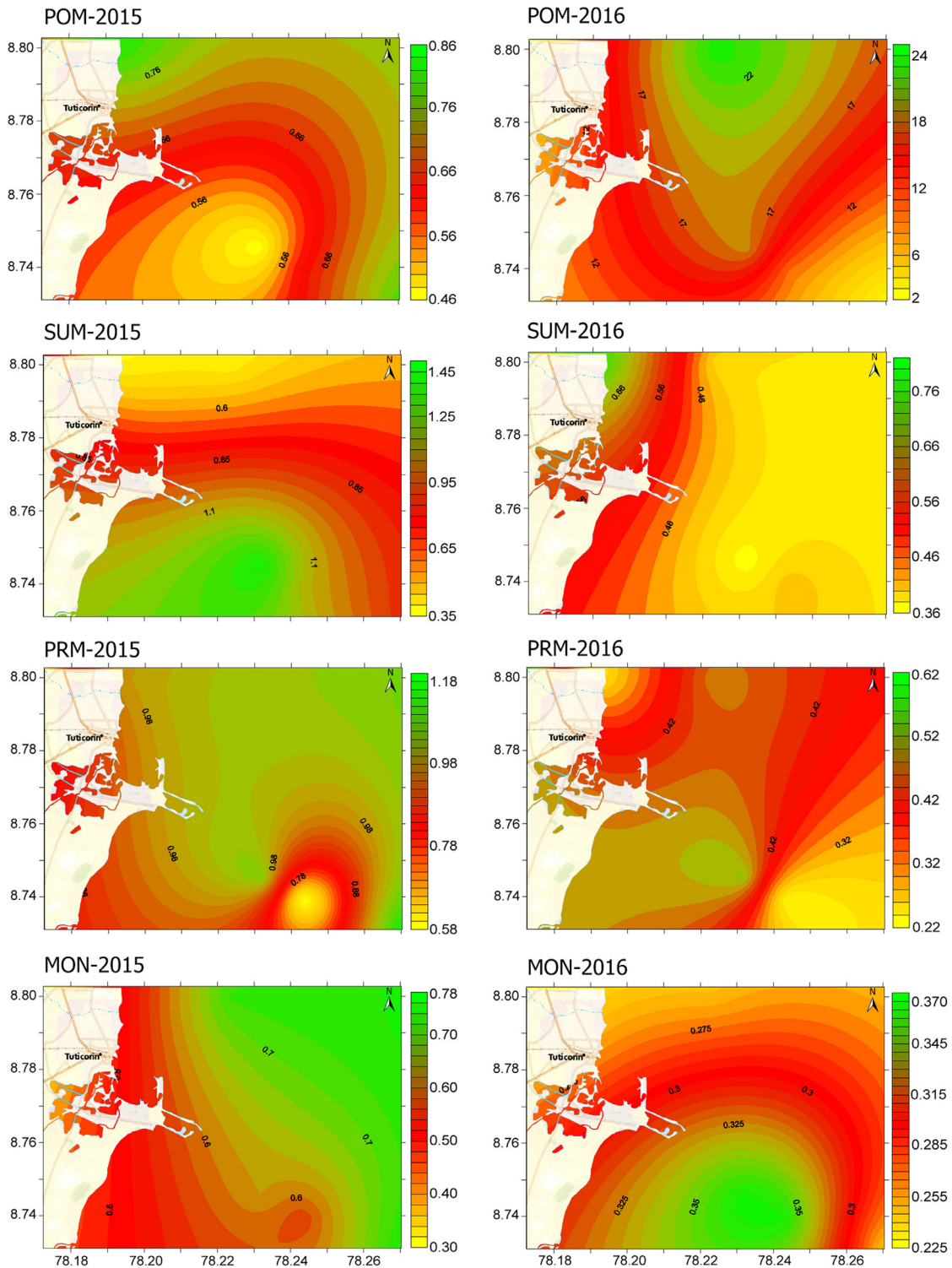


Figure 4 The contour plot showing the spatial-temporal distribution of chlorophyll-*a* concentrations (mg m^{-3}) in TCWs during 2015 and 2016 (axes *y* and *x* indicate Latitude ($^{\circ}\text{N}$) and Longitude ($^{\circ}\text{E}$), respectively).

imum average was recorded in POM. The annual mean of EI value during 2016 (4.29) was higher than in 2015 (2.82). Notably, the EI values were reported as greater than 2 in all the sampled stations during 2015. The maximum (5.43) and minimum (1.35) EI values in 2015 were recorded in the

POM season at 0.5 km and 5 km inshore from the TNH and TOH regions, respectively. In the year 2016, EI was abnormally high and it was above 20 during POM season. The maximum value (21.61) was observed 2 km away from the TNH inshore region during POM 2016. The minimum EI value

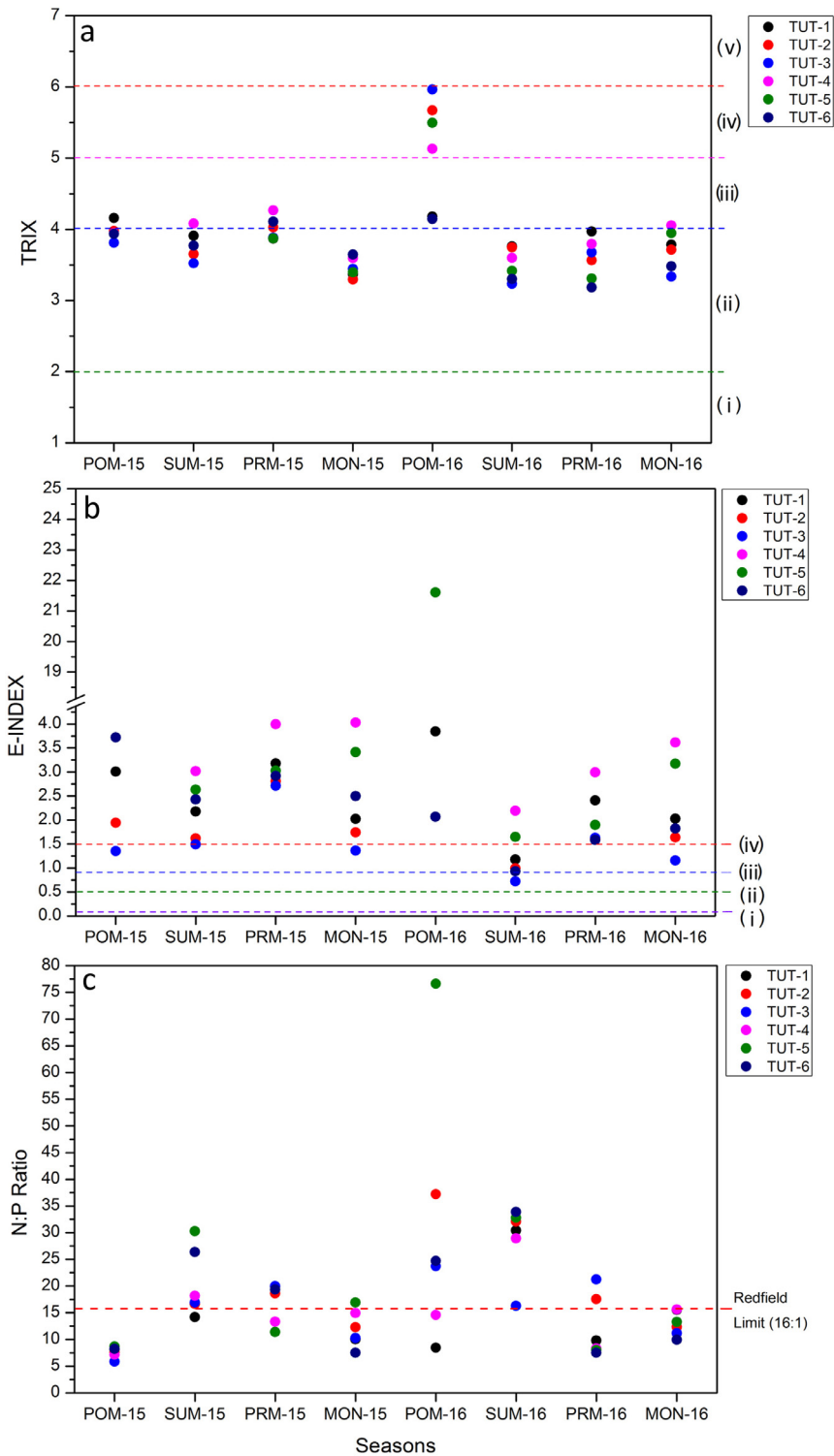


Figure 5 a) Spatial-temporal variation of TRIX level: (i) very poorly productive, (ii) poorly productive, (iii) moderately productive, (iv) moderate to highly productive, (v) highly productive. b) The spatial-temporal scale of water quality or eutrophication status: (i) high, (ii) good, (iii) moderate, (iv) poor. c) The spatial-temporal scale of N:P ratios in TCWs during 2015 and 2016.

(0.72) was recorded during SUM 2016 at 5 km distance from TOH region (Table 4S). Similar to that of TRIX, the distribution of EI values was also insignificant for the spatial scale.

3.5. Phytoplankton community structure

The phytoplankton community was represented by 86 species in the neritic waters of Tuticorin in the present

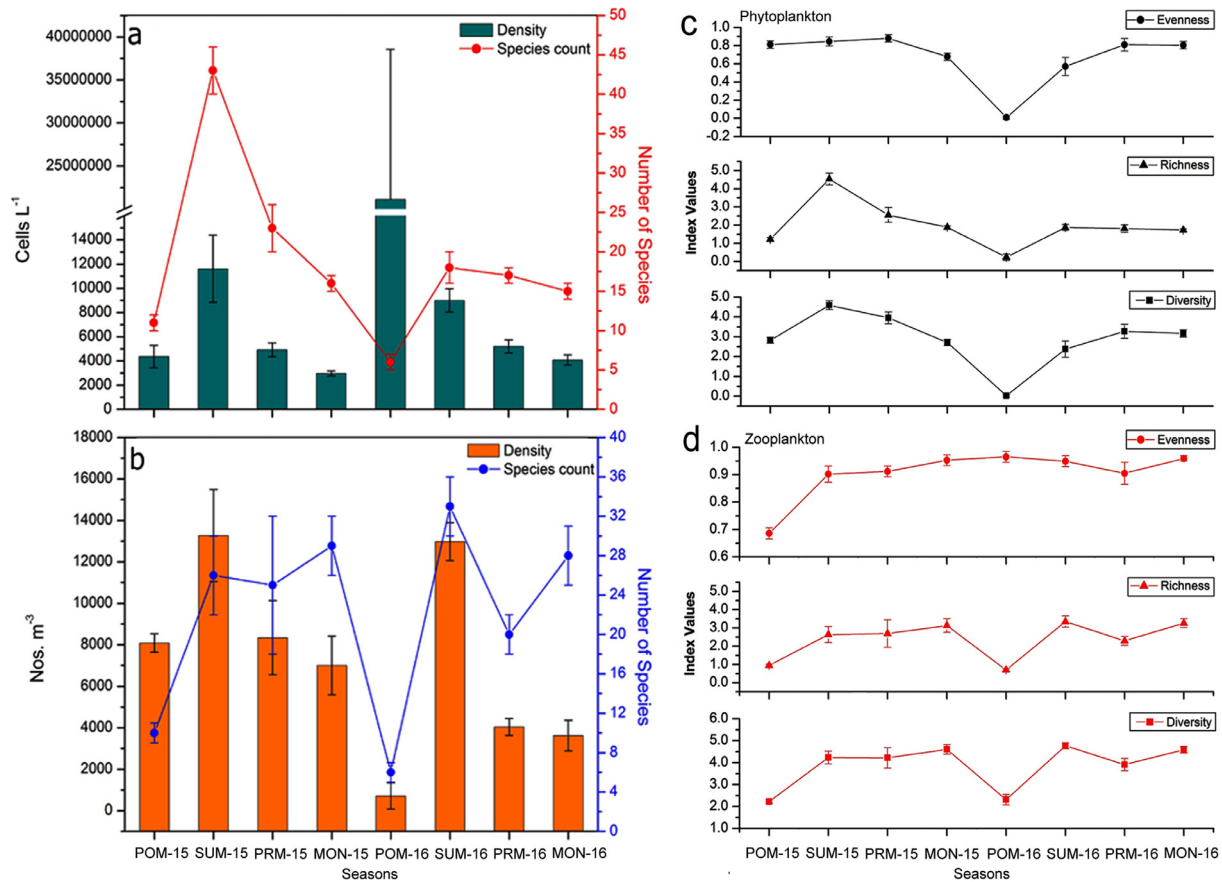


Figure 6 The image on the left depicts the seasonal abundance of plankton (a, phytoplankton and b, zooplankton) as well as the numerical distribution of species. The right side image depicts the seasonal pattern of various indices (diversity, richness, and evenness) for phytoplankton (c) and zooplankton (d).

work. Twenty-four phytoplankton species were dominant (contributing >1% of the total density) throughout the study, contributing to 86% of the total phytoplankton abundance. Three groups, namely Bacillariophyceae, Dinophyceae, and Cyanophyceae mainly represented the coastal water phytoplankton community. The phytoplankton species distribution showed significant variations on a temporal scale. Variations between years, seasons, and seasons of different years were significant (Table 3S). Insignificant spatial distribution of phytoplankton species indicated an almost homogeneous distribution pattern in these coastal waters. The most common members among the phytoplankton, based on percentage contribution were *Asterionella glacialis* (6.9%), *Chaetoceros coarctatus* (3.8%), *Chaetoceros curvisetus* (5.6%), *Coscinodiscus centralis* (4.2%), *Coscinodiscus radiates* (3.7%), *Nitzschia seriata* (3.0%), *Rhizosolenia alata* (5.4%), *Skeletonema costatum* (4.5%), *Thalassionema nitzschioides* (3.5%), *Thalassiosira rotula* (3.0%), *Thalassiosira subtilis* (5.2%), *Thalassiothrix frauenfeldii* (4.4%) and *Trichodesmium erythraeum* (13.8%). The average phytoplankton population density ranged from 2967 ± 204 to 21124771 ± 17439734 cells L⁻¹, with noticeable seasonal variations. The highest density was observed during POM-16, while the lowest was observed during MON-15 (Figure 6a). Phytoplankton species distribution followed a similar trend as phytoplankton population density,

which also showed significant seasonal variations. The inter-annual variation noted from the ANOVA could be due to the intense bloom of *T. erythraeum* during 2016 (Table 3S). Phytoplankton species diversity, richness, and evenness indices are illustrated in Figure 6c. The indices values ranged between 0.23–4.53, 0.02–4.59, and 0.01–0.88 for diversity, richness, and evenness respectively. The higher diversity and richness values recorded in SUM-15 indicated more species in good numbers during that period. The regression analysis plot of phytoplankton density against TRIX and EI indices is represented in Figure 15. The results indicated a positive correlation of phytoplankton with these two indices ($R^2=0.656$ and $R^2=0.594$ for TRIX and EI respectively).

3.6. Zooplankton community structure

The zooplankton population assemblages showed a more prominent seasonal variation than spatial variation. The population density and species distribution showed statistically significant variations overall. Moreover, the seasonal differences between 2015 and 2016 are significant, but there were no significant changes in spatial distribution (Table 3S). The population diversity consisted of 82 zooplankton species and certain larval stages of different groups. Among them, 34 species were dominant, contributing >1% individually and almost 87% cumulatively

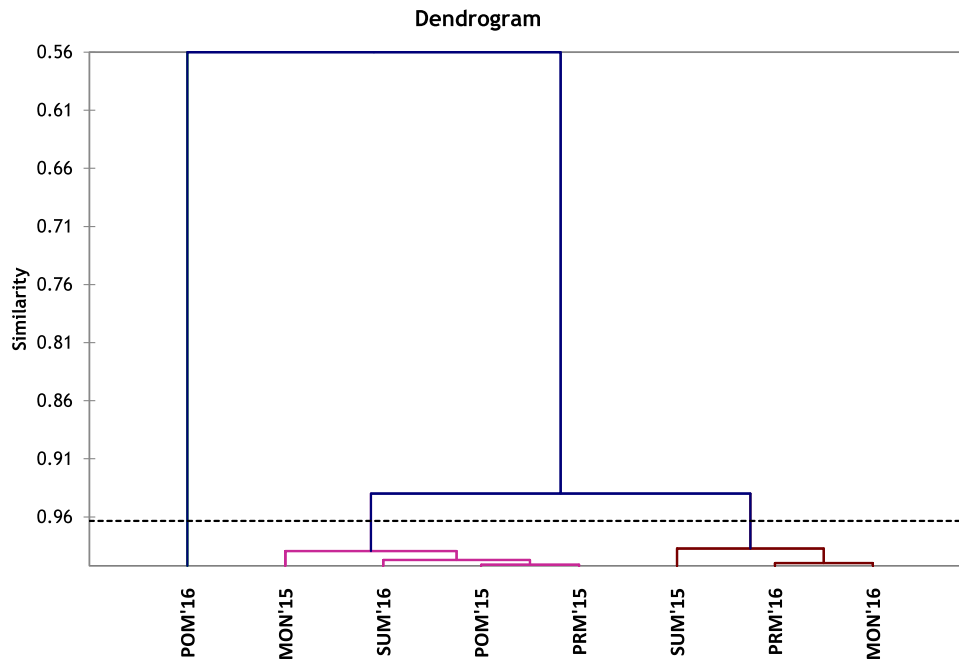


Figure 7 Dendrogram shows the similarities among seasons with respect to hydro-biological factors during the study period (2015 and 2016).

in the total zooplankton abundance of all seasons. Various groups, namely, Rotifers, Chaetognatha, Copepods, Euphausiids, and bivalve (larvae), represented the zooplankton community during the study. The most common zooplankton taxa, in terms of percentage density contribution, encountered were *Acartia danae* (4.8%), *Acartia spinicauda* (3.9%), *Acrocalanus gibber* (4.3%), *Acrocalanus gracilis* (4.6%), *Corycaeus danae* (3.7%), *Euterpina acutifrons* (5.1%), *Nannocalanus minor* (3.1%), *Oikopleura dioica* (2.5%), *Oithona brevicornis* (10.8%), *Oithona similis* (3.2%), *Paracalanus parvus* (5.3%), *Penilia avirostris* (1.0%) and *Sagitta enflata* (1.7%). Zooplankton average population density ranged from 711 ± 624 to 13270 ± 2222 nos. m^{-3} , where the highest density was recorded during SUM 2015 and the lowest density was recorded during POM 2016, respectively (Figure 6b). Zooplankton plays a major role in controlling phytoplankton proliferation through grazing. The abundance of zooplankton species slumped during the POM 2016 coinciding with *Trichodesmium* bloom. However, in the summer season, the species abundance was found to be higher in 2015 and 2016, respectively. A similar pattern was observed in preceding studies in this study region (Bharathi et al., 2018). ANOVA supported the above observation of seasonality in zooplankton population distribution (Table 3S). The variations in zooplankton species diversity, richness, and evenness indices have been depicted in Figure 6d. The indices ranged between 2.23–4.77, 0.70–3.35 and 0.69–0.97 for the species diversity, richness, and evenness, respectively. Relatively higher diversity and richness values were recorded in SUM-16. The regression analysis plot of zooplankton density against TRIX and EI indices is represented in Figure 2S. The relationship between zooplankton density and these two indices was negative and the coefficients of determination were $R^2=0.603$ and $R^2=0.583$ for TRIX and EI respectively. The results indicated that zoo-

plankton population density showed a decreasing trend with increasing trophic status.

3.7. Statistical analyses

Agglomerative hierarchical clustering (AHC) was conducted to determine the similarities among the seasons of the two years of sampling. The AHC, concerning all the environmental variables, developed 3 clusters (Figure 7). The POM season of 2016 alone formed a cluster because of the monospecific bloom of marine cyanobacterium. The alteration in hydro-biological properties of these waters during the bloom was significant enough to mark this period as a distinct one compared to other seasons. The second cluster is formed by the majority of the 2015 seasons, as well as the summer of 2016. The third cluster is composed of two subgroups in which the first subgroup comprises two seasons of 2016 and the second subgroup branches out from the first and associates with the summer of 2015. Interestingly, the two years seem to have formed two separate clusters except for the interchange of the summer season in between them. It perhaps indicated and confirmed the earlier observations of the distinctness of the coastal water environment during the two years, as shown by the TRIX and EI. However, the interchange of the summer season in the cluster formation could be due to too many factors such as rainfall, surface runoff, upwelling, water mass movement, etc. that take place at this location during this season, leading to such an observation.

The principal component analysis of hydro-biological parameters yielded 4 PCs (Figure 8). Altogether, the 4 PCs contributed to 76.65% of the total variability. PC 1 contributed 35.17% of the variability and parameters such as temperature, pH, DO, nitrate, ammonia, TN, TP, chl-*a*, phyto-

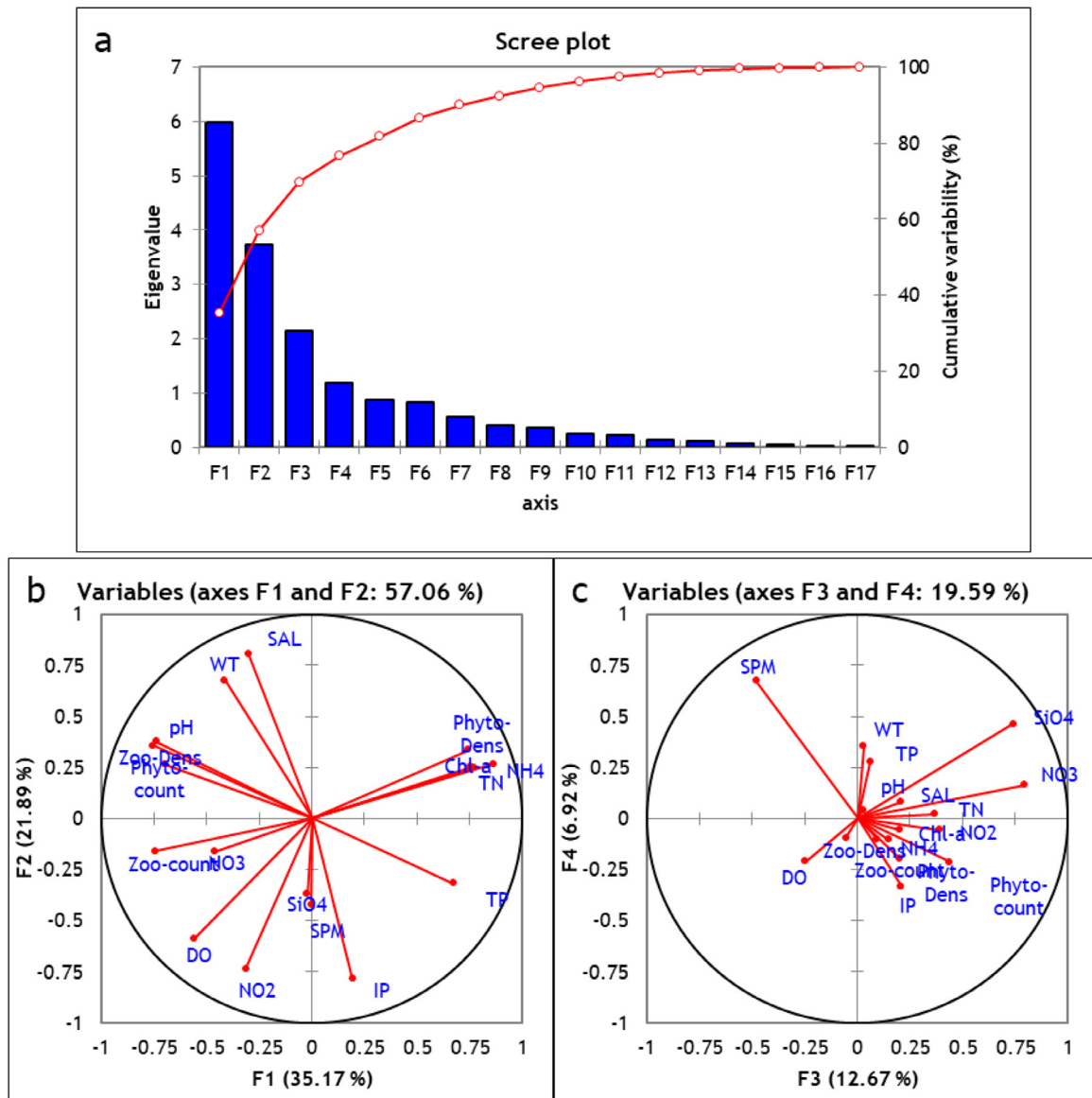


Figure 8 PCA plots. a) Scree plot of cumulative percentage and eigenvalues; b) biplot of F1 and F2; c) biplot of F3 and F4.

plankton density, phytoplankton species number, zooplankton density, and zooplankton species number showed significant loading on this PC (Figure 8). Of the above significant parameters, ammonia, TN, TP, chl-a, and phytoplankton density were positively loaded and the rest of the parameters were negatively loaded. This PC represented the *Trichodesmium* bloom event during which the population density of phytoplankton, chl-a concentration and nutrient contents were significantly high in the coastal waters as compared to other non-blooming periods. The above observation can further be confirmed from the AHC analysis, where the blooming season alone formed a distinct cluster. Similarly, the negative loadings were also corroborated with low diversity of plankton, low zooplankton count and relatively low DO concentration due to high *Trichodesmium* biomass. PC 2 contributed 21.89% of variability and parameters like temperature, SPM, salinity, DO, nitrite, and

phosphate were significantly loaded. This PC perhaps represented the relatively high salinity and temperature condition occurring with low SPM, nitrite, phosphate, and DO content that prevails during summer/pre-monsoon seasons in this coastal water. The third PC, which contributed 12.67% of the variance, indicated the process of nitrate and silicate enrichment in the coastal waters along with improvement in phytoplankton species diversity. This PC can be assigned to the winter (POM) environment during which this coastal water is enriched with the nutrients from the preceding monsoon season, and the biological activity in the coastal milieu gathers pace in relatively stable conditions before its climax in summer. The fourth PC contributed 6.9% of the variance and only two parameters viz. SPM and silicate were positively loaded. Since the number of significant loadings was very less, any particular process or phenomenon could not be assigned to this PC logically.

4. Discussion

4.1. Environmental variables

This present study shows a clear seasonal variability than spatial variability for all the variables. The lower water temperature was observed during the monsoon period due to continuous precipitation and cloud coverage, which has also been reported earlier by others (Kathiravan et al., 2017; Satpathy et al., 2009; Vajravel et al., 2017) along the southeastern coastal waters of India. The pH values in TCWs have previously been reported to range from 7.5 to 8.5, and the current study agrees with this range (Balakrishnan et al., 2017; Bharathi et al., 2018; Rajendran et al., 2018). Fluctuating pH values throughout the year could be ascribed to various natural phenomena such as CO₂ elimination by photosynthesis, fall of salinity and temperature, freshwater infiltration, and breakdown of organic debris (Rajasegar, 2003; Upadhyay, 1988). During summer, increased photosynthesis by phytoplankton could have removed dissolved carbon dioxide leading to increased pH (Das et al., 1997; Vajravelu et al., 2017). Salinity is a vital parameter for all organisms living in the marine environment (O’Conner and Lawler, 2004) which limits the diversity and distribution of planktonic and benthic communities (Balasubramanian and Kannan, 2005; Sridhar et al., 2006). Salinity fluctuations between summer and monsoon season were around 5 PSU, attributed to the dilution of coastal waters during monsoon rainfall. The observed salinity range was concurrent with earlier studies in the TCWs (Balakrishnan et al., 2017; Bharathi et al., 2018). Oxygen concentrations in the coastal environment might fluctuate by many physicochemical and biological processes. Relatively increased DO levels were found in the MON which occurs during freshwater input, reduced water temperature and salinity. Similar cases of elevated DO during MON have been presented along various Indian coasts (Balakrishnan et al., 2017; Bharathi et al., 2018; Madhav and Kondalarao, 2004; Satpathy et al., 2009). Accumulation of SPM in the summer season is very rare in the eastern coastal region of India (Satpathy et al., 2011) which has been found in our study during SUM 2016. The higher concentration of SPM in the summer season might be attributed to some physical (e.g., terrestrial water runoff, tidal mixing, and aerial deposition of dust) and biological processes (e.g., biological production and aggregation) (Bialogrodzka et al., 2018). The relatively high SPM content observed during the MON 2016 could be due to the fact that the freshwater influx considerably influences this study region during monsoon season, as has been reported by many researchers from the Bay of Bengal (Amir et al., 2019; Fernandes et al., 2009; Nisha and Achyuthan, 2014; Vajravelu et al., 2017), Arabian Sea (Chakraborty et al., 2019; Shynu et al., 2017) and GoM (Balakrishnan et al., 2017; Bharathi et al., 2018; Rajendran et al., 2018; Sathishkumar et al., 2021).

4.2. Water nutrients

Nitrite is the transient compound found as a resultant of ammonia oxidation or nitrate reduction (Satpathy et al., 2010). The present concentration of nitrite is relatively low

as compared to previous studies from the Tuticorin coast ($1.28 \mu\text{M L}^{-1}$) and various processes such as plankton excretion, ammonia oxidation, nitrate reduction, nitrogen recycling and bacterial putrefaction of planktonic detritus have been attributed to such observation (Alikunhi and Kathiresan, 2012; Asha and Diwakar, 2007; Govindasamy et al., 2000; Satheesh and Wesley, 2009). Nitrate, the utmost oxidized form of nitrogen, is an important indicator of aquatic pollution. In general, nitrate levels in seawater are influenced by freshwater inflow and terrestrial run-off comprising rock leaching, fertilizers, chemical from industries, decomposition of organic matter, and domestic and municipal sewage (Govindasamy et al., 2000; Rajaram et al., 2005; Santhanam and Perumal, 2003). The present observation of nitrate enrichment during PRM season could occur due to nutrient-rich bottom water mixing into the surface water through the upwelling process at this location (Nisha and Achyuthan, 2014). The lower nitrate concentrations observed during the POM season could be attributed to increased nitrate consumption by photosynthetic organisms and neritic water infiltration (Das et al., 1997; Gouda and Panigrahy, 1995; Govindasamy et al., 2000). *T. erythraeum* bloom observed during the POM sampling of 2016 could be credited for the peak ammonia concentration. A similar increase in ammonia concentration during *Trichodesmuim* bloom has been reported along the Indian coasts by numerous researchers (Mohanty et al., 2010; Padmakumar et al., 2010; Satpathy et al., 2007). The swift consumption of ammonia by marine photosynthetic plants led to its reduced concentration, while the preference for ammonia over nitrate by certain phytoplankton groups contributed to further reduction (Dugdale et al., 2007; Lipschultz, 1995). The maximum concentration coincided with the *T. erythraeum* bloom that fixes nitrogen in the water body. Similar findings of nitrogen enhancement in coastal waters have been reported during blooms of *T. erythraeum* by several researchers (Mohanty et al., 2010; Satpathy et al., 2007). Total nitrogen (TN) is an important parameter representing the ecosystem’s health. Similar to nitrate, TN concentration was minimum during monsoon, which contradicts the earlier reports of the Tamil Nadu coast (Kathiravan et al., 2017; Sahu et al., 2012). The growth of organisms and phytoplankton production in any aquatic ecosystem is dependent on phosphate to a large extent as it plays a major role in primary productivity (Jones, 1998). DIP concentration also serves as an index of eutrophication. The phosphate concentration is usually very high in untreated sewage and discharged from agriculture fields and industries. Phosphorus gets converted to organic phosphorus and polyphosphate upon interaction with other organic and inorganic substances in aquatic environments (Gouda and Panigrahy, 1993). TCWs had higher TP concentrations during the post-monsoon season of 2016, which might be attributed to the *T. erythraeum* bloom that occurred during the study. The lower values observed during summer could be rationalized by phosphate utilization of photoautotrophs and buffering processes of sediment under varying environmental conditions (Perumal et al., 2009). Silicate is an important nutrient required for phytoplankton growth, particularly for the diatoms to synthesize their frustules. Silicate concentration in coastal waters mainly varies due to freshwater input, adsorption onto sediment parti-

cles, co-precipitation with humic substances, interactions with minerals and chemicals, and utilization by diatoms and silicoflagellates (Sahu et al., 2012; Satpathy et al., 2009). Similar to that nitrate, the presently observed silicate values indicated minimal terrestrial input during the monsoon season. It indicated that this coastal region is perhaps influenced by phenomena like regeneration of silicate from bottom sediments, upwelling, and coastal circulation (Govindasamy et al., 2000; Rajasegar, 2003). The present finding contrasts earlier reports from Indian coasts, where most reports have recorded a significant increase in coastal water silicate concentration during the monsoon season (Rajasegar, 2003; Satpathy et al., 2009; Vajravelu et al., 2017). N:P ratios result from the interspecific competition among primary producers at different levels as their consumption is largely species-specific (Kautsky, 1982). Most of the observations indicated that this coastal water is nitrogen limiting, which is also supported by phytoplankton density which revealed a negative correlation with nitrate and nitrite indicating relatively high consumption of nitrogenous nutrients as compared to phosphate. The minimal external input of nitrogen compared to phosphate into the coastal waters might be the cause behind the above observations. The above observation is comparable to that of Anderson et al. (2002), but it also contradicts many reports of phosphate limitation (Bharathi et al., 2018; Heneash et al., 2015; Satpathy et al., 2010; Vajravelu et al., 2017).

4.3. Photosynthetic pigment

Chlorophyll-*a* is the chief photosynthetic pigment that acts as the indicator of phytoplankton biomass in the aquatic environment. Low salinity and low-temperature conditions prevailed during the MON season hinder the marine phytoplankton growth, and the same is represented in this study in terms of low pigment concentration observed during the MON and POM seasons (2015). The highest concentrations of chlorophyll-*a* coincided with the occurrence of *T. erythraeum* bloom. The current study was in agreement with earlier reports from various Indian coastal waters (Mohanty et al., 2010; Sarangi et al., 2004), where ~20 times higher chlorophyll-*a* content was reported during bloom to non-blooming periods. In general, relatively high values were observed during SUM and PRM periods, indicating the favorable environment that supported plankton growth in the tropics (Sardessai et al., 2007). Similar observations on the impact of monsoon on coastal productivity were reported from this coast (Bharathi et al., 2018; Rajendran et al., 2018) as well as various Indian coasts (Rajaram et al., 2005; Sardessai et al., 2007; Srichandan et al., 2019; Vajravelu et al., 2017).

4.4. TRIX and Eutrophication indices

The annual average of TRIX during 2016 (3.98) was higher than in 2015 (3.80). The coastal water can be categorized as poorly productive based on the annual average values of TRIX. The only period with relatively high TRIX values coincided with *T. erythraeum* bloom when the coastal water was moderate to highly productive. Cyanophyta bloom is the

major reason for increasing TRIX value during the present study, and earlier studies from the Caspian Sea, Iran, have reported similar observations (Nasrollahzadeh et al., 2008; Soloviev, 2005). The TRIX value also showed that the system, especially the near-shore waters (0.5 km away from the shore) is in the transition phase between oligotrophic-mesotrophic to mesotrophic-eutrophic conditions. This region, mostly affected by numerous untreated discharges from municipal, aquaculture, agriculture, industrial effluents, coolant waters from the TTPS, and other domestic sewages (Balakrishnan et al., 2017; Bharathi et al., 2018), will be under tremendous pressure shortly unless a systematic management plan is devised to control the coastal eutrophication. The presently observed values are comparable to Mangalore port area and Cochin backwaters, where the values have been reported in the range of 3.4–5.5 and 5.15 respectively (Rajaneesh et al., 2015; Rath et al., 2018). Other coastal and estuarine regions from India have reported relatively high TRIX values (Kodunagallur and Azhikode estuary – 6–7; Thane Creek – 6.7–8.8; Gopalpur coast – 4–7) as compared to the present study (Hardikar et al., 2021; Jayachandran and Nandan, 2012; Srichandan et al., 2019). The above results indicated that TCW is mostly oligotrophic with a few instances of mesotrophic observations. Mesotrophic-eutrophic conditions were rarely observed, only during the bloom occurrence.

Eutrophication index (EI) is a unique method to determine the eutrophication level in coastal water which was previously used by Kucuksezgin et al. (2019), Pavlidou et al. (2015), and Tugrul et al. (2019), in various coastal waters. The dissolved nutrients (phosphate, nitrite, nitrate, ammonia) and chl-*a* concentrations were used to calculate the state of water quality into various categories based on the range of EI values. Those categories are: <0.04 (high), 0.04–0.38 (good), 0.38–0.85 (moderate), 0.85–1.51 (poor) and >1.51 (bad) (Pavlidou et al., 2015; Primpas et al., 2010). Like TRIX, POM 2016 values of EI were very high, during which the *Trichodesmium* bloom was encountered. In general, the EI values for the study area indicated high eutrophication throughout the study period, which could be due to the discharge of effluents from industrial and domestic sources. Both EI and TRIX values for TCW, GoM form the baseline data for this study region and can be useful for future reference studies to assess the environmental alterations.

4.5. Plankton community

The health status or biological integrity of an aquatic ecosystem is assessed in terms of phytoplankton species composition, the relative abundance of various species, standing stock, the spatial and temporal distributions, etc. (Khattak et al., 2005). Phytoplankton in tropical coastal regions exhibits lesser variations than in temperate regions concerning their seasonal and annual variations (Qasim et al., 1972). The maximum population density of phytoplankton during POM 2016 occurred due to an immense bloom formation by *Trichodesmium erythraeum*. This species is dominated by warm surface water conditions that prevail during POM and summer (February–May) periods along the southeastern coast of India (Mohanty et al.,

2010; Santhanam et al., 1994). The minimum abundance was observed in MON 2015 which was attributed to intense precipitation, reduced temperature, salinity, pH, and the presence of high turbidity causing low phytoplankton production (Bharathi et al., 2018; Vajravelu et al., 2017). During summer, the desirable environmental conditions promote phytoplankton productivity (growth) in this location (Bharathi et al., 2018). The lower values were observed during POM-2016, which might indirectly affect the *Trichodesmium* bloom that dominated the phytoplankton community (Santhanam et al., 1994). Light and nutrient availability in the pelagic zone enhanced the primary production enabling the zooplankton communities to thrive in this period (Bot et al., 1996). Moreover, the copepods have higher grazing activity under warmer conditions leading to higher population densities during those periods (Lewandowska et al., 2014).

Trophic indices, TRIX and EI, showed a significant correlation with plankton community abundance. The phytoplankton abundance increases with an increase in TRIX and EI values. It indicated the classical correlation between phytoplankton growth and nutrient availability (Cutrim et al., 2019). On the other hand, the zooplankton community developed an inverse relationship with TRIX and EI. Zooplankton as grazers generally thrives in the aftermath of phytoplankton growth. Moreover, zooplankton densities are always inversely related to phytoplankton abundance in the process of secondary production. Similar correlations of trophic indices with plankton abundance have been reported in Indian and international studies (Bosak et al., 2012; Nasrollahzadeh et al., 2008; Rath et al., 2018; Vidjak et al., 2012).

5. Summary and conclusions

A clear pattern in seasonal variation of environmental parameters was noticed due to the impact of the MON. Physical properties such as temperature, salinity, and pH were relatively low during the MON season whereas, DO and suspended particulate matter content were relatively high. Unlike many Indian coasts, where the monsoonal input of nitrate and silicate is significant, nitrate and silicate concentrations were relatively high during PRM in the TCWs. However, phosphate concentration at this location is regulated by its terrestrial input through land runoff and anthropogenic input, as indicated by the high values observed during the MON season. An intense *T. erythraeum* bloom was witnessed during the POM season of 2016 and the bloom had a substantial impact on both environmental and biological variables of the coastal waters. The principal component analysis further highlighted the bloom's influence by indicating the event as distinctly separate from all the other processes/ phenomena in the coastal waters. During the study period (2015–2016), the overall TRIX range (3.18–5.96) indicated that the TCW environment was oligotrophic to eutrophic, whereas the EI values (0.72–21.61) indicated that the state of coastal waters was moderate to poor (2015 and 2016). Moreover, classifying TCW quality using various indices is the first study of its kind, and the results can be used for future studies. Since the study area is a bioreserve, the findings of the present study can be used for its

management and mitigation of eutrophication in the future to conserve biodiversity.

Declaration of competing interest

The authors declare that they have no competing interest.

CRedit author statement

Rengasamy Subramaniyan Sathishkumar: conceptualization, methodology, data curation, writing – original draft preparation, visualization, investigation, formal analysis. **Arumugam Sundaramanickam:** resources, supervision, project administration, funding acquisition. **Ajit Kumar Mohanty:** writing – reviewing and editing, software. **Gouri Sahu:** visualization, reviewing and editing. **Thangavelu Ramesh:** validation, supervision. **Kumar Balachandar:** investigation, formal analysis. **Ajith Nithin:** investigation, formal analysis. **Parthasarathy Surya:** investigation, formal analysis. **Krishnan Silambarasan:** formal analysis.

Acknowledgments

The authors would like to acknowledge the authorities of Annamalai University for providing essential amenities and also like to give an individual thanks to Prof. T. Balasubramanian, former Dean and Director of CAS in Marine Biology, Annamalai University. The authors are grateful to the anonymous reviewers and editors for their valuable comments that have aided to improve the manuscript.

Funding

This study was funded by the Ministry of Earth Sciences (MoES), National Centre for Coastal Research, Government of India (Project File No. MoES/ICMAM-PD/ME/CAS-MB/53/2017).

Supplementary materials

Supplementary material associated with this article can be found, in the online version, at <https://doi.org/10.1016/j.oceano.2022.07.002>.

References

- Alikunhi, N.M., Kathiresan, K., 2012. Phytoplankton productivity in interlinked mangroves, seagrass and coral reefs and its ecotones in Gulf of Mannar Biosphere Reserve Southeast India. *Mar. Biol. Res.* 8 (1), 61–73. <https://doi.org/10.1080/17451000.2011.596544>
- Al-Kandari, M., Al-Yamani, F., Al-Rifaie, K., 2009. Marine phytoplankton atlas of Kuwait's waters. *Kuwait Inst. Sci. Res., Safar*, 351 pp.
- Amir, M., Paul, D., Samal, R.N., 2019. Sources of organic matter in Chilika Lagoon, India inferred from stable C and N isotopic

- compositions of particulates and sediments. *J. Mar. Syst.* 194, 81–90. <https://doi.org/10.1016/j.jmarsys.2019.03.001>
- Anderson, D.M., Glibert, P.M., Burkholder, J.M., 2002. Harmful algal blooms and eutrophication: nutrient sources, composition, and consequences. *Estuaries* 25 (4), 704–726. <https://doi.org/10.1007/BF02804901>
- Asha, P.S., Diwakar, K., 2007. Hydrobiology of the inshore waters off Tuticorin in the Gulf of Mannar. *J. Mar. Biol. Assoc.* 49 (1), 7–11. <http://eprints.cmfri.org.in/id/eprint/2107>
- Balakrishnan, S., Chelladurai, G., Mohanraj, J., Poongodi, J., 2017. Seasonal variations in physico-chemical characteristics of Tuticorin coastal waters, southeast coast of India. *Appl. Water Sci.* 7 (4), 1881–1886. <https://doi.org/10.1007/s13201-015-0363-2>
- Balasubramanian, R., Kannan, L., 2005. Physico-chemical characteristics of the coral reef environs of the Gulf of Mannar Biosphere Reserve, India. *Int. J. Ecol. Environ. Sci.* 31 (3), 273–278.
- Bharathi, M.D., Patra, S., Sundaramoorthy, S., Madeswaran, P., Chandrasekar, D., Sundaramanickam, A., 2018. Seasonal variability in plankton food web composition in Tuticorin coastal waters, south east coast of India. *Mar. Pollut. Bull.* 137, 408–417. <https://doi.org/10.1016/j.marpolbul.2018.10.042>
- Białogrodzka, J., Stramska, M., Ficek, D., Wereszka, M., 2018. Total suspended particulate matter in the Porsanger fjord (Norway) in the summers of 2014 and 2015. *Oceanologia* 60 (1), 1–15. <https://doi.org/10.1016/j.oceano.2017.06.002>
- Bosak, S., Šilović, T., Ljubešić, Z., Kušpilić, G., Pestorić, B., Kriokapić, S., Viličić, D., 2012. Phytoplankton size structure and species composition as an indicator of trophic status in transitional ecosystems: the case study of a Mediterranean fjord-like karstic bay. *Oceanologia* 54 (2), 255–286. <https://doi.org/10.5697/oc.54-2.255>
- Bot, P.V.M., Van Raaphorst, W., Batten, S., Laane, R.W.P.M., Philippart, K., Radach, G., Frohse, A., Schultz, H., Van den Eynde, D., Colijn, F., 1996. Comparison of changes in the annual variability of the seasonal cycles of chlorophyll, nutrients and zooplankton at eight locations on the northwest European continental shelf (1960–1994). *Deutsche Hydrografische Zeitschrift* 48 (3), 349–364. <https://doi.org/10.1007/BF02799378>
- Chakraborty, P., Jayachandran, S., Lekshmy, J., Padalkar, P., Sitlhou, L., Chennuri, K., Shetye, S., Sardar, A., Khandeparker, R., 2019. Seawater intrusion and resuspension of surface sediment control mercury (Hg) distribution and its bioavailability in water column of a monsoonal estuarine system. *Sci. Total Environ.* 660, 1441–1448. <https://doi.org/10.1016/j.scitotenv.2018.12.477>
- Coelho, S., Gamito, S., Pérez-Ruzafa, A., 2007. Trophic state of Foz de Almagem coastal lagoon (Algarve, South Portugal) based on the water quality and the phytoplankton community. *Estuar. Coast. Shelf Sci.* 71 (1–2), 218–231. <https://doi.org/10.1016/j.ecss.2006.07.017>
- Conway, D.V., White, R.G., Hugues-Dit-Ciles, J., Gallienne, C.P., Robins, D.B., 2003. *Guide to the coastal and surface zooplankton of the south-western Indian Ocean. Occasional Publication of the Marine Biological Association of the United Kingdom* 15, 354 pp.
- Cutrim, M.V.J., Ferreira, F.S., dos Santos, A.K.D., Cavalcanti, L.F., de Oliveira Araújo, B., de Azevedo-Cutrim, A.C.G., Furtado, J.A., Oliveira, A.L.L., 2019. Trophic state of an urban coastal lagoon (northern Brazil), seasonal variation of the phytoplankton community and environmental variables. *Est. Coast. Shelf Sci.* 216, 98–109. <https://doi.org/10.1016/j.ecss.2018.08.013>
- Dakin, W.J., Colefax, A., 1940. *The plankton of the Australian coastal waters off New South Wales. Publications of the University of Sydney Department of Zoology, Monograph* 1, NSW, Australia, 215 pp.
- Das, J., Das, S.N., Sahoo, R.K., 1997. Semidiurnal variation of some physicochemical parameters in the Mahanadi estuary, east coast of India. *Indian J. Mar. Sci.* 26, 323–326. <http://nopr.niscair.res.in/handle/123456789/0>
- Goswami, S.C., 2004. *Zooplankton methodology, collection & identification - A field manual. National Institute of Oceanography, India, Dona Paula, Goa*, 26 pp. <http://drs.nio.org/drs/handle/2264/95>
- Domingues, R.B., Anselmo, T.P., Barbosa, A.B., Sommer, U., Galvão, H.M., 2011. Nutrient limitation of phytoplankton growth in the freshwater tidal zone of a turbid, Mediterranean estuary. *Estuar. Coast. Shelf Sci.* 91 (2), 282–297. <https://doi.org/10.1016/j.ecss.2010.10.033>
- Dugdale, R.C., Wilkerson, F.P., Hogue, V.E., Marchi, A., 2007. The role of ammonium and nitrate in spring bloom development in San Francisco Bay. *Estuar. Coast. Shelf Sci.* 73 (1–2), 17–29. <https://doi.org/10.1016/j.ecss.2006.12.008>
- EEA (European Environmental Agency), 1999. *Nutrients in European ecosystems. Environmental assessment report. Environ. Assess. Rep. No. 4. Office for Official Publication of the European Communities, Luxembourg*, 155 pp.
- Fernandes, L., Bhosle, N.B., Matondkar, S.P., Bhushan, R., 2009. Seasonal and spatial distribution of particulate organic matter in the Bay of Bengal. *J. Mar. Syst.* 77 (1–2), 137–147. <https://doi.org/10.1016/j.jmarsys.2008.12.002>
- Fiori, E., Zavatarelli, M., Pinardi, N., Mazziotti, C., Ferrari, C.R., 2016. Observed and simulated trophic index (TRIX) values for the Adriatic Sea basin. *Nat. Hazards Earth Syst. Sci.* 16 (9), 2043–2054. <https://doi.org/10.5194/nhess-16-2043-2016>
- Giovanardi, F., Vollenweider, R.A., 2004. Trophic conditions of marine coastal waters: Experience in applying the trophic index TRIX to two areas of the Adriatic and Tyrrhenian seas. *J. Limnol.* 63 (2), 199–218. <https://doi.org/10.4081/jlimnol.2004.199>
- Gouda, R., Panigrahy, R.C., 1995. Seasonal distribution and behavior of nitrate and phosphorous in Rushikulya estuary, east coast of India. *Indian J. Mar. Sci.* 24, 233–235. <http://nopr.niscair.res.in/handle/123456789/37362>
- Gouda, R., Panigrahy, R.C., 1993. Monthly variations of some hydrographic parameters in the Rushikulya estuary, east coast of India. *Mahasagar* 26 (2), 73–85.
- Govindasamy, C., Kannan, L., Jayapaul, A., 2000. Seasonal variation in physico-chemical properties and primary production in the coastal water biotopes of Coramandal coast. *Indian J. Environ. Biol.* 21 (1), 1–7.
- Grasshoff, K., Kremling, K., Ehrhardt, M., 1999. *Methods of Seawater Analysis. 3rd edn., Wiley-VCH, Weinheim, New York*, 89–224.
- Hardikar, R., Haridevi, C.K., Ram, A., Parthipan, V., 2021. Distribution of size-fractionated phytoplankton biomass from the anthropogenically stressed tropical creek (Thane creek, India). *Reg. Stud. Mar. Sci.* 41, 101577. <https://doi.org/10.1016/j.rsma.2020.101577>
- Heneash, A.M., Tadrose, H.R., Hussein, M.M., Hamdona, S.K., Abdel-Aziz, N., Gharib, S.M., 2015. Potential effects of abiotic factors on the abundance and distribution of the plankton in the Western Harbour, south-eastern Mediterranean Sea. *Egypt. Oceanologia* 57 (1), 61–70. <https://doi.org/10.1016/j.oceano.2014.09.003>
- Jayachandran, P.R., Nandan, S.B., 2012. Assessment of trophic change and its probable impact on tropical estuarine environment (the Kodungallur-Azhikode estuary, India). *Mitig. Adapt. Strateg. Glob. Change.* 17 (7), 837–847. <https://doi.org/10.1007/s11027-011-9347-1>
- Jones, R.I., 1998. Phytoplankton, primary production and nutrient cycling. In: Hessen, D.O., Tranvik, L.J. (Eds.), *Aquatic humic substances*. Springer, Berlin, Heidelberg, 145–175.
- Jørgensen, S.E., Xu, F.-L., Marques, J.C., Salas, F., 2010. Application of Indicators for the Assessment of Ecosystem Health. In: Jørgensen, S.E., Xu, F., Costanza, R. (Eds.), *Handbook of Ecolog-*

- ical Indicators for Assessment of Ecosystem Health. CRC Press, Taylor & Francis Group, Boca Raton, New York, 9–75.
- Kasthurirangan, L.R., 1963. A key for the identification of the more common planktonic copepoda of Indian coastal waters. Council of Scientific and Industrial Research (CSIR), New Delhi, 1–92.
- Kathiravan, K., Natesan, U., Vishnunath, R., 2017. Spatio-temporal variability of hydro-chemical characteristics of coastal waters of Gulf of Mannar. Marine Biosphere Reserve (GoMMBR), South India. Appl. Water Sci. 7 (1), 361–373. <https://doi.org/10.1007/s13201-014-0251-1>
- Kautsky, L., 1982. Primary production and uptake kinetics of ammonium and phosphate by *Enteromorpha compressa* in an ammonium sulfate industry outlet area. Aquat. Bot. 12, 23–40. [https://doi.org/10.1016/0304-3770\(82\)90004-3](https://doi.org/10.1016/0304-3770(82)90004-3)
- Khattak, T.M., Bhatti, N.Z., Murtaza, G., 2005. Evaluation of algae from the effluent of Dandot Cement Company, Dandot, Pakistan. J. Appl. Sci. Environ. Manag. 9, 147–149. <http://hdl.handle.net/1807/6436>
- Kucuksezgin, F., Tolga Gonul, L., Pazi, Idil, Kacar, Asli, 2019. Assessment of seasonal and spatial variation of surface water quality: Recognition of environmental variables and fecal indicator bacteria of the coastal zones of Izmir Bay, Eastern Aegean. Reg. Stud. Mar. Sci. 28, 100554. <https://doi.org/10.1016/j.rsma.2019.100554>
- Lewandowska, A.M., Hillebrand, H., Lengfellner, K., Sommer, U., 2014. Temperature effects on phytoplankton diversity—The zooplankton link. J. Sea Res. 85, 359–364. <https://doi.org/10.1016/j.seares.2013.07.003>
- Lipschultz, F., 1995. Nitrogen-specific uptake rates of marine phytoplankton isolated from natural populations of particles by flow cytometry. Mar. Ecol. Prog. Ser. 245–258. <https://doi.org/10.1016/j.seares.2013.07.003>
- Madhav, V.G., Kondalarao, B., 2004. Distribution of phytoplankton in the coastal waters of east coast of India. Indian J. Mar. Sci. 33 (3), 262–268. <http://nopr.niscair.res.in/handle/123456789/1678>
- McLusky, D.S., Elliott, M., 2004. The Estuarine Ecosystem: Ecology, Threats and Management. Oxford University Press, United Kingdom (UK), 214 pp.
- Mohanty, A.K., Satpathy, K.K., Sahu, G., Hussain, K.J., Prasad, M.V.R., Sarkar, S.K., 2010. Bloom of *Trichodesmium erythraeum* (Ehr.) and its impact on water quality and plankton community structure in the coastal waters of southeast coast of India. Indian J. Geo-Mar. Sci. 39 (3), 323–333. <http://nopr.niscair.res.in/handle/123456789/10669>
- Moncheva, S., Gotsis-Skretas, O., Pagou, K., Krastev, A., 2001. Phytoplankton blooms in Black Sea and Mediterranean coastal ecosystems subjected to anthropogenic eutrophication: similarities and differences. Estuar. Coast. Shelf Sci. 53, 281–295. <https://doi.org/10.1006/ecss.2001.0767>
- Nasrollahzadeh, H.S., Din, Z.B., Foong, S.Y., Makhloogh, A., 2008. Trophic status of the Iranian Caspian Sea based on water quality parameters and phytoplankton diversity. Cont. Shelf Res. 28 (9), 1153–1165. <https://doi.org/10.1016/j.csr.2008.02.015>
- Newton, A., Icely, J.D., Falcão, M., Nobre, A., Nunes, J.P., Ferreira, J.G., Vale, C., 2003. Evaluation of eutrophication in the Ria Formosa coastal lagoon. Portugal. Cont. Shelf Res. 23 (17–19), 1945–1961. <https://doi.org/10.1016/j.csr.2003.06.008>
- Nisha, V., Achyuthan, H., 2014. Physico-chemical parameters of the SW and post NE monsoon (2009) seawater along the continental slope, Tamil Nadu, east coast of India. Bay of Bengal. Cont. Shelf Res. 72, 99–106. <https://doi.org/10.1016/j.csr.2013.08.003>
- O’Conner, W.A., Lawler, N.F., 2004. Salinity and temperature tolerance of embryos and juveniles of pearl oyster, *Pinctada imbricate* Roding. Aquaculture 229, 493–506. [https://doi.org/10.1016/S0044-8486\(03\)00400-9](https://doi.org/10.1016/S0044-8486(03)00400-9)
- OECD (Organization for Economic Cooperation and Development), 1982. Eutrophication of Waters, Monitoring, Assessment and Control. OECD Publication, Paris, 154 pp.
- Omori, M., Ikeda, T., 1984. Methods in marine zooplankton ecology. Wiley, New York, 280–311.
- Padmakumar, K.B., Smitha, B.R., Thomas, L.C., Fanimol, C.L., Sree Renjima, G., Menon, N.R., Sanjeevan, V.N., 2010. Blooms of *Trichodesmium erythraeum* in the South Eastern Arabian Sea during the onset of 2009 summer monsoon. Ocean. Sci. J. 45 (3), 151–157. <https://doi.org/10.1007/s12601-010-0013-4>
- Pavlidou, A., Simbour, N., Rousselaki, E., Tsapakis, M., Pagou, K., Drakopoulou, P., Assimakopoulou, G., Kontoyiannis, H., Panayotidis, P., 2015. Methods of eutrophication assessment in the context of the water framework directive: Examples from the Eastern Mediterranean coastal areas. Cont. Shelf Res. 108, 156–168. <https://doi.org/10.1016/j.csr.2015.05.013>
- Penna, N., Capellacci, S., Ricci, F., 2004. The influence of the Po River discharge on phytoplankton bloom dynamics along the coastline of Pesaro (Italy) in the Adriatic Sea. Mar. Pollut. Bull. 48, 321–326. <https://doi.org/10.1016/j.marpolbul.2003.08.007>
- Perumal, N.V., Rajkumar, M., Perumal, P., Rajasekar, K.T., 2009. Seasonal variations of plankton diversity in the Kaduviyar estuary, Nagapattinam, southeast coast of India. J. Environ. Biol. 30 (6), 1035–1046. http://www.jeb.co.in/journal_issues/200911_nov09/paper_19.pdf
- Perumal, P., Sampathkumar, P., Santhanam, P., 1998. In: Monograph on zooplankton of Parangipettai coastal waters, 1. Annamalai University, India, 31 pp.
- Primpas, I., Tsirtsis, G., Karydis, M., Kokkoris, G.D., 2010. Principal component analysis: development of a multivariate index for assessing eutrophication according to the European water framework directive. Ecol. Indic. 10, 178–183. <https://doi.org/10.1016/j.ecolind.2009.04.007>
- Primpas, I., Karydis, M., 2011. Scaling the trophic index (TRIX) in oligotrophic marine environments. Environ. Monit. Assess. 178 (1–4), 257–269. <https://doi.org/10.1007/s10661-010-1687-x>
- Qasim, S.Z., Bhattathiri, P.M.A., Devassy, V.P., 1972. The influence of salinity on the rate of photosynthesis and abundance of some tropical phytoplankton. Mar. Biol. 12 (3), 200–206. <https://doi.org/10.1007/BF00346767>
- Raj Chandar, P., Rejeesh Kumar, P., 2012. Mapping and analysis of marine pollution in Tuticorin coastal area using remote sensing and GIS. Int. J. Adv. Remote Sens. GIS 1, 34–48. <http://citeseerx.ist.psu.edu/viewdoc/download?doi=10.1.1.299.6495&rep=rep1&type=pdf>
- Rajaneesh, K.M., Mitbavkar, S., Anil, A.C., Sawant, S.S., 2015. *Synechococcus* as an indicator of trophic status in the Cochin backwaters, west coast of India. Ecol. Indic. 55, 118–130. <https://doi.org/10.1016/j.ecolind.2015.02.033>
- Rajaram, R., Srinivasan, M., Rajasegar, M., 2005. Seasonal distribution of physico-chemical parameters in effluent discharge area of Uppanar estuary, Cuddalore, south-east coast of India. J. Environ. Biol. 26 (2), 291–297. <https://europemc.org/article/med/16161988>
- Rajasegar, M., 2003. Physico-chemical characteristics of the Vellar estuary in relation to shrimp farming. J. Environ. Biol. 24, 95–101. <https://europemc.org/article/med/12974418>
- Rajendran, V., Srinivasan, B., Rengaraj, C., Mariyaselvam, S., 2018. Quality assessment of pollution indicators in marine water at critical locations of the Gulf of Mannar Biosphere Reserve, Tuticorin. Mar. Pollut. Bull. 126, 236–240. <https://doi.org/10.1016/j.marpolbul.2017.10.091>
- Rath, A.R., Mitbavkar, S., Anil, A.C., 2018. Phytoplankton community structure in relation to environmental factors from the New Mangalore Port waters along the southwest coast of India. Environ. Monit. Assess. 190 (8), 481. <https://doi.org/10.1007/s10661-018-6840-y>

- Sahu, G., Satpathy, K.K., Mohanty, A.K., Sarkar, S.K., 2012. Variations in community structure of phytoplankton in relation to physicochemical properties of coastal waters, southeast coast of India. *Indian J. Geo-Mar. Sci.* 41 (3), 223–241. <http://nopr.niscair.res.in/handle/123456789/14169>
- Santhanam, P., Perumal, P., 2003. Diversity of zooplankton in Parangipettai coastal waters, Southeast Coast of India. *J. Mar. Biol. Ass. India* 45 (2), 144–151.
- Santhanam, R., Ramanathan, N., Venkataramanuja, K.V., Jegathesan, G., 1987. *Phytoplankton of the Indian Seas: An Aspect of Marine Botany*. Daya Publishing House, Delhi, 1–134.
- Santhanam, R., Srinivasan, A., Ramadhas, V., Devaraj, M., 1994. Impact of *Trichodesmium* bloom on the plankton and productivity in the Tuticorin Bay, southeast coast of India. *Indian J. Mar. Sci.* 23, 27–30.
- Sarang, R.K., Chauhan, P., Nayak, S.R., 2004. Detection and monitoring of *Trichodesmium* blooms in coastal waters off Saurashtra coast, India using IRS-P4OCM data1G/Sar. *Curr. Sci.* 86 (12), 1636–1641.
- Sardesai, S., Ramaiah, N., Prasanna, K.S., De Souza, S.N., 2007. Influence of environmental forcings on the seasonality of dissolved oxygen and nutrients in the Bay of Bengal. *J. Mar. Res.* 65 (2), 301–316. <https://doi.org/10.1357/002224007780882578>
- Sarma, V.V.S.S., Krishna, M.S., Viswanadham, R., Rao, G.D., Rao, V.D., Sridevi, B., Bandopadhyay, D., 2013. Intensified oxygen minimum zone on the western shelf of Bay of Bengal during summer monsoon: influence of river discharge. *J. Oceanogr.* 69 (1), 45–55. <https://doi.org/10.1007/s10872-012-0156-2>
- Satheesh, S., Wesley, S.G., 2009. Impact of December 26, 2004 tsunami on the hydrobiology of Kudankulam coast, Gulf of Mannar, India. *Environ. Monit. Assess.* 156 (1–4), 131. <https://doi.org/10.1007/s10661-008-0469-1>
- Sathishkumar, R.S., Sundaramanickam, A., Sahu, G., Mohanty, A.K., Ramesh, T., Khan, S.A., 2021. Intense bloom of the diatom *Hemidiscus hardmanianus* (Greville) in relation to water quality and plankton communities in Tuticorin coast, Gulf of Mannar, India. *Mar. Pollut. Bull.* 163, 111757. <https://doi.org/10.1016/j.marpolbul.2020.111757>
- Satpathy, K.K., Mohanty, A.K., Natesan, U., Prasad, M.V.R., Sarkar, S.K., 2010. Seasonal variation in physicochemical properties of coastal waters of Kalpakkam, east coast of India with special emphasis on nutrients. *Environ. Monit. Assess.* 164 (1–4), 153–171. <https://doi.org/10.1016/j.marpolbul.2020.111757>
- Satpathy, K.K., Mohanty, A.K., Sahu, G., Prasad, M.V.R., Venkatesan, R., Natesan, U., Rajan, M., 2007. On the occurrence of *Trichodesmium erythraeum* (Ehr.) bloom in the coastal waters of Kalpakkam, east coast of India. *Indian J. Sci. Technol.* 1 (2), 1–9.
- Satpathy, K.K., Mohanty, A.K., Sahu, G., Sarguru, S., Sarkar, S.K., Natesan, U., 2011. Spatio-temporal variation in physicochemical properties of coastal waters off Kalpakkam, southeast coast of India, during summer, pre-monsoon and post-monsoon period. *Environ. Monit. Assess.* 180 (1–4), 41–62. <https://doi.org/10.1007/s10661-010-1771-2>
- Satpathy, K.K., Sahu, G., Mohanty, A.K., Prasad, M.V.R., Panigrahy, R.C., 2009. Phytoplankton community structure and its variability during southwest to northeast monsoon transition in the coastal waters of Kalpakkam, east coast of India. *Int. J. Oceanogr. Oceanogr.* 3 (1), 43–74.
- Shynu, R., Rao, V.P., Samiksha, S.V., Vethamony, P., Naqvi, S.W.A., Kessarkar, P.M., Dineshkumar, P.K., 2017. Suspended matter and fluid mud off Alleppey, southwest coast of India. *Estuar. Coast. Shelf Sci.* 185, 31–43. <https://doi.org/10.1016/j.ecss.2016.11.023>
- Smith, D.L., 1977. *A Guide to Marine Coastal Plankton and Marine Invertebrate Larvae*. Kendal/Hunt Publ. Co., Dubuque, 16 pp.
- Smith, V.H., Tilman, G.D., Nekola, J.C., 1999. Eutrophication: impacts of excess nutrient inputs on freshwater, marine, and terrestrial ecosystems. *Environ. Pollut.* 100 (1–3), 179–196. [https://doi.org/10.1016/S0269-7491\(99\)00091-3](https://doi.org/10.1016/S0269-7491(99)00091-3)
- Soloviev, D., 2005. Identification of the extent and causes of Cyanobacterial bloom in September–October 2005 and development of the capacity for observation and prediction of HAB in the Southern Caspian Sea using Remote Sensing Technique (19th of February 2007). <http://archive.iwlearn.net/caspianenvironment.org/newsite/Caspian-AAB.htm>
- Srichandan, S., Baliarsingh, S.K., Prakash, S., Lotliker, A.A., Parida, C., Sahu, K.C., 2019. Seasonal dynamics of phytoplankton in response to environmental variables in contrasting coastal ecosystems. *Environ. Sci. Pollut. Res.* 26 (12), 12025–12041. <https://doi.org/10.1007/s11356-019-04569-5>
- Sridhar, R., Thangaradjou, T., Kumar, S.S., Kannan, L., 2006. Water quality and phytoplankton characteristics in the Palk Bay, southeast coast of India. *J. Environ. Biol.* 27 (3), 561–566.
- Strickland, J.D.H., Parsons, T.R., 1972. *A Practical Hand-Book of Seawater Analysis*, 2nd edn., Fish. Res. Board Canada, Ottawa, 310 pp.
- Subramanyan, R., 1946. A systematic account of marine plankton diatoms of the Madras Coast. *Proceedings of the Indian Academy of Sciences* 24, 85–197.
- Sukhanova, Z.N., 1978. Settling without inverted microscope. In: Sournia, A (Ed.), *Phytoplankton Manual*. UNESCO, Page Brothers, Norwich UK, 97 pp.
- Tugrul, S., Ozhan, K., Akcay, I., 2019. Assessment of trophic status of the northeastern Mediterranean coastal waters: eutrophication classification tools revisited. *Environ. Sci. Pollut. Res.* 26 (15), 14742–14754. <https://doi.org/10.1007/s11356-018-2529-6>
- Upadhyay, S., 1988. Physico-chemical characteristics of the Mahanadi estuarine ecosystem, east coast of India. *Indian J. Mar. Sci.* 17, 19–23. <http://nopr.niscair.res.in/handle/123456789/38450>
- Vajravelu, M., Martin, Y., Ayyappan, S., Mayakrishnan, M., 2017. Seasonal influence of physico-chemical parameters on phytoplankton diversity, community structure and abundance at Parangipettai coastal waters, Bay of Bengal, South East Coast of India. *Oceanologia* 60 (2), 114–127. <https://doi.org/10.1016/j.ocean.2017.08.003>
- Venkataraman, G., 1939. A systematic account of some south Indian diatoms. *Proc. Section B* 10 (6), 293–368, Indian Academy of Sciences, Springer, India. <https://www.ias.ac.in/article/fulltext/secb/010/06/0293-0368>
- Vidjak, O., Bojanić, N., Matijević, S., Kušpilić, G., Ninčević Gladan, Ž, Skejić, S., Grbec, B., Brautović, I., 2012. Environmental drivers of zooplankton variability in the coastal eastern Adriatic (Mediterranean Sea). *Acta Adriatica: Internat. J. Mar. Sci.* 53 (2), 243–260. <https://hrcak.srce.hr/94431>
- Vollenweider, R.A., Giovanardi, F., Montanari, G., Rinaldi, A., 1998. Characterization of the trophic conditions of marine coastal waters with special reference to the NW Adriatic Sea: proposal for a trophic scale, turbidity and generalized water quality index. *Environmetrics* 9 (3), 329–357. [https://doi.org/10.1002/\(SICI\)1099-095X\(199805/06\)9:3\(329::AID-ENV308\)3.0.CO;2-9](https://doi.org/10.1002/(SICI)1099-095X(199805/06)9:3(329::AID-ENV308)3.0.CO;2-9)
- Wickstead, J.H., 1965. *An Introduction to the Study of Tropical Zooplankton*. Hutchinson, London, 160 pp.
- Yang, B., Gao, X., Zhao, J., Lu, Y., Gao, T., 2020. Biogeochemistry of dissolved inorganic nutrients in an oligotrophic coastal mariculture region of the northern Shandong Peninsula, North Yellow Sea. *Mar. Pollut. Bull.* 150, 110693. <https://doi.org/10.1016/j.marpolbul.2019.110693>

Available online at www.sciencedirect.com

ScienceDirect

journal homepage: www.journals.elsevier.com/oceanologia

ORIGINAL RESEARCH ARTICLE

Plastic contamination of sandy beaches along the southern Baltic – a one season field survey results

Mikołaj Mazurkiewicz*, Paula Sancho Martinez, Weronika Konwent, Kajetan Deja, Lech Kotwicki, Jan Marcin Węśławski

Institute of Oceanology Polish Academy of Sciences, Sopot, Poland

Received 3 February 2022; accepted 23 July 2022

Available online 5 August 2022

KEYWORDS

Microplastic;
Marine litter;
Sources;
Coastal zone;
Baltic Sea

Abstract The subject of this study was microplastics ($>32 \mu\text{m}$), large micro-/macroplastics ($>2 \text{ mm}$) and plastic litter (visible by naked eye) contamination on sandy beaches and in coastal waters along the Polish coast of the Baltic Sea. Microplastics were studied with particular attention, with simultaneous observations in the water and across the beach. Other data was intended to serve as a background and as possible sources of microplastics. Most of the microplastics found were fibers $<1 \text{ mm}$ long, with blue fibers dominating, followed by transparent, red and green ones, both in sand and water samples. The concentration of microplastics on the beach sand ranged from 118 to 1382 pieces kg^{-1} , while in coastal waters from 0.61 to 2.76 pieces dm^{-3} . As for large micro-/macroplastics and plastic litter, there was no dominant litter along the coast. The amount of large micro-/macroplastics ranged from 2 to 124 pieces m^{-2} (or from 0.13 to 44.30 g m^{-2}). Regarding plastic litter, on average between 0.03 and 6.15 litter debris m^{-2} were found (or from 0.007 to 4.600 g m^{-2}). The study confirms that plastic pollution of the Polish coastal zone is a significant problem comparable with both the rest of the Baltic Sea and other seas and oceans. Similar color-based composition of microplastics among all studied sites suggests that they may have a common source, while the contamination of large micro-/macroplastics and plastic litter (both amount of particles and their composition) along the Polish coast is highly site-specific and may be influenced by various local factors.

© 2022 Institute of Oceanology of the Polish Academy of Sciences. Production and hosting by Elsevier B.V. This is an open access article under the CC BY-NC-ND license (<http://creativecommons.org/licenses/by-nc-nd/4.0/>).

* Corresponding author at: Institute of Oceanology Polish Academy of Sciences, Powstańców Warszawy 55, Sopot, Poland.
E-mail address: mikolaj@iopan.gda.pl (M. Mazurkiewicz).

Peer review under the responsibility of the Institute of Oceanology of the Polish Academy of Sciences.



<https://doi.org/10.1016/j.oceano.2022.07.004>

0078-3234/© 2022 Institute of Oceanology of the Polish Academy of Sciences. Production and hosting by Elsevier B.V. This is an open access article under the CC BY-NC-ND license (<http://creativecommons.org/licenses/by-nc-nd/4.0/>).

1. Introduction

Plastic pollution of the marine environment is a rising problem, affecting almost all areas of the global ocean, from tropical coasts to Arctic deep ocean basins (Mohamed Nor and Obbard, 2014; Tekman et al., 2017; Woodall et al., 2014). Due to the longevity and disposable nature of plastics, their contamination is expected to increase (Thompson et al., 2004). The marine environment appears to be the end point for most plastic pollutants discharged in coastal areas (Chenillat et al., 2021) where they undergo constant accumulation and fragmentation processes between shorelines and coastal waters environments (Barnes et al., 2009).

Plastics enter the marine environment through a variety of routes. Most of the debris is land-based and comes from littering, solid waste disposal, or is left by tourists during recreational activities (Jambeck et al., 2015; Williams et al., 2013). Much less plastic originates from the ocean, and comes from materials used in the fishing industry, such as fishing gear, rope, or synthetic packaging (Li et al., 2016). Rivers also play a significant role in delivering plastic pollution into the marine environment, by catching variously sized pieces of mismanaged plastics from land-based sources in the catchment area, and transporting them to marine basins even over long distances (Schmidt et al., 2017). Here, wastewater treatment plants can play a particular role, as each day they process large quantities of microplastics, e.g., released from clothes during washing (a single piece of clothing can shed > 1900 microplastic fibers during a single wash) (Browne et al., 2011). Even though wastewater plants may be efficient in capturing and removing microplastics, the high volume of effluents they release makes them a relevant source of plastic pollution in aquatic systems (Prata, 2018).

Plastic pollution can be dangerous to marine biota, as well as to humans. Various large plastic debris such as ropes, ribbons, or six-pack rings endanger birds and marine mammals, which can become entangled or trapped, causing death through starvation or predation (Williams et al., 2013). Plastic particles may also be confused for natural prey and consumed by organisms, which may lead to a reduction in food consumption and a decrease in their overall fitness (Derraik, 2002) moreover the chemical compounds that plastics contain may be bioaccumulated in organisms' tissues (Tanaka et al., 2013). Moreover, industrial additives to the plastic polymer matrix can elicit developmental abnormalities in embryos exposed to plastic pellets (Rendell-Bhatti et al., 2021). Furthermore, the consumption of plastics may be dangerous not only due to the chemical compounds they contain, but also due to their ability to adsorb and concentrate particulate organic pollutants and then desorb them in the intestines of organisms (Bakir et al., 2014). Plastic pollution also threatens the biodiversity of entire ecosystems. Large particles drifting with sea currents may act as rafts able to transport attached organisms (i.e. barnacles, bryozoans, or mollusks) over large distances, fostering the dispersal of alien species (Barnes and Milner, 2005; Węstawski and Kotwicki, 2018; Williams et al., 2013). For instance, drifting flotsam from the north Atlantic has been supposed to cause the reappearance of the blue mussel (*Mytilus* spp. complex) on far more Arc-

tic coast (west Svalbard) in recent years (Kotwicki et al., 2021).

The study provides novel information to understand the pattern of plastic occurrence in coastal waters of the Baltic Sea and their deposition on sandy beaches. The Southern Baltic, with the prevailing soft, sandy shores, strait exposed coastline and westerly winds creates specific conditions compared to the rocky, indented shores of the northern Baltic or the numerous bays and inlets of the diverse German coastline. In our study, we have expected fast transport and limited accumulation of plastic compared to the other regions of the Baltic, making simultaneous observations in the water and on the shores highly important. Special attention was paid on microplastics and their fate which were: 1) studied in detail regarding their size distribution, 2) tested for the partitioning among different parts of the beach and 3) tested for the relationship among microplastic concentration in water and in the sand in different parts of the beach. The data regarding large micro-/macroplastics and plastic litter were gathered to provide background data for more detailed, monitoring studies. The locations chosen in the study were selected to represent beaches of various levels of tourist impact and accessibility (from pristine beaches in a national park to beaches in tourist resorts) to provide a general perspective of contamination in the whole Polish coast.

2. Material and methods

2.1. Study area

The Baltic Sea is regarded as the largest brackish sea in the world, with an area of 420,000 km². The catchment area is more than four times larger (around 1650000 km²), and is inhabited by around 85 million people (HELCOM, 2018). The annual total riverine inflow to the Baltic Sea is around 475 km³ year⁻¹, composing about 2% of the total sea water volume (Wulff et al., 2001). About a quarter of the riverine water is carried by the two largest rivers that discharge to the sea: the Neva (Estonia, 78 km³ year⁻¹) and the Vistula (Poland, 34 km³ year⁻¹). The Baltic circulation is characterized by weak cyclonic currents and a near-shore current parallel to the coastline (from west to east along the Polish coast, Figure 1) (Leppäranta and Myrberg, 2009). The coastline around the Baltic Sea is highly diversified: the southern and eastern coasts (including the Polish coast) are dominated by sandy beaches (sandy spits) and coastal cliffs of different compositions (silts, sands, clay rocks), while the northern coast consists mostly of rocky shores, although sandy and gravel beaches may also be found (Rosentau et al., 2017). The Baltic Sea is a semi-enclosed water body with very dense marine traffic, responsible for around 15% of the world's marine cargo transport, which may be what fosters the amount of litter in its basin (Rytkönen et al., 2002).

Samples were collected at eleven sites along the Polish coast of the Baltic Sea in November and December 2017 (Figure 1). A total of 110 water and sediment samples were collected.

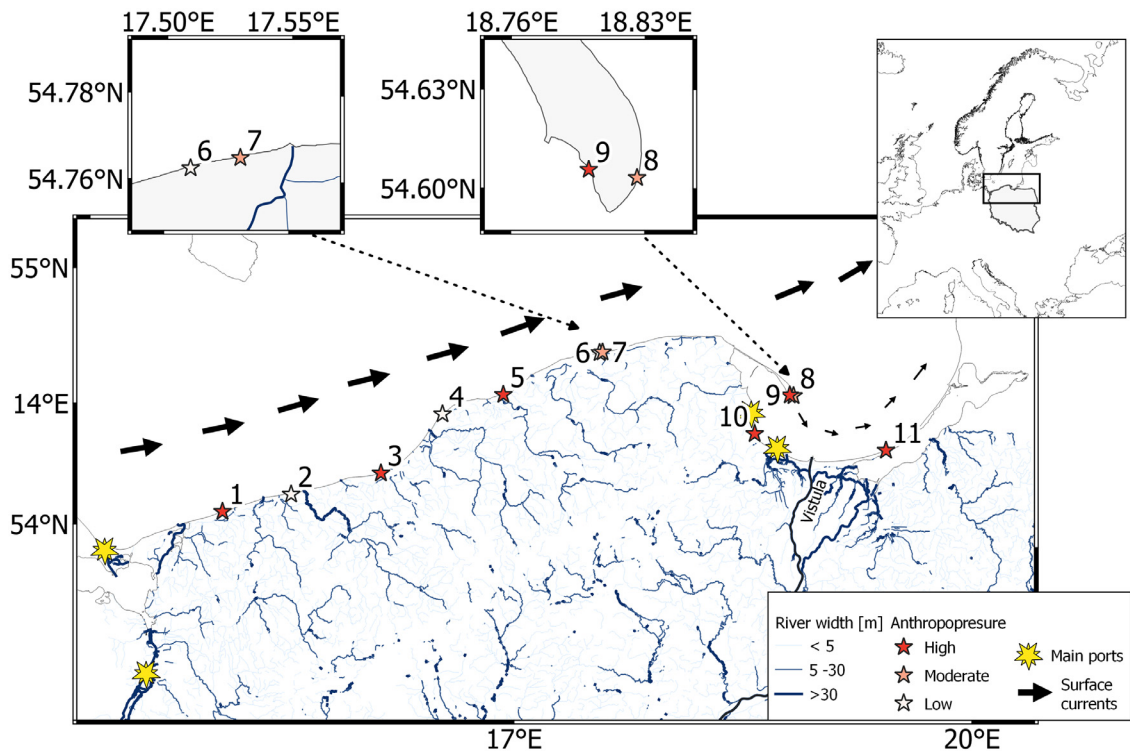


Figure 1 Map of sampling sites. Sea currents based on Babakov (2010) and European Environment Agency (2021).

2.2. Sampling design

2.2.1. Microplastics

Microplastics were defined as particles that were retained on the 32 μm mesh sieve (particles $>32 \mu\text{m}$). A similar lower size limit of microplastics was defined e.g., by Woodall et al. (2014), or Rowley et al. (2020). The upper size limit was not set, and all the particles retained on the sieve were analyzed.

At each site, two sediment samples for microplastics were collected, one in the driftline and one in the forehead of the dunes (below vegetation). Each sample consisted of sediments from an area of 0.15 m^2 . The surface layer of sand (about 2 cm thick) was collected with a metal spatula into a 1 dm^3 glass jar with a metal lid.

Also, at each site one water sample for microplastic analysis was collected in the coastal zone (approximate depth of 1 m). Using a 10 dm^3 metal bucket a volume of 100 dm^3 of water was filtered in situ on a 32 μm sieve. All the material retained on the sieve was rinsed using a wash bottle with distilled water and stored in a glass jar with a metal lid.

2.2.2. Large micro-/macroplastics

Large micro-/macroplastics were defined as particles >2 mm, but without an upper size limit. The lower size limit of 2 mm was used for example by Esiukova et al. (2021) to define large microplastics, while macroplastics are often defined as particles >5 mm (e.g., Schmidt et al. (2017)). At each site, three separate samples of large micro-/macroplastics were collected at three parts of the beach: driftline, the middle of the beach, and the forehead of the dunes (Figure 2). A surface layer (about 20 cm) of sand from

an area of 1 m^2 (1 \times 1 m rectangle) was sieved on a 2 mm mesh sieve. All the retained plastics were packed and stored for further analysis.

2.2.3. Plastic litter

Plastic litter was defined as all the particles detectable by the naked eye, similar to Oigman-Pszczol and Creed (2007) or Zalewska et al. (2021), and the size limit was not defined. At each site four transects were made across the whole beach, each 10 m apart from the others. Each transect was treated as a separate sample. All debris visible by the naked eye along the transect (around 1 m wide) was collected, packed, and stored for further analysis.

2.3. Laboratory procedures

2.3.1. Microplastics

Sediment samples were dried in an oven for 48 hours at 50°C. Subsequently, microplastics were extracted by a density separation technique (Stolte, 2014) from the 500 g of dried sediment. A ZnCl_2 solution (density around 1.6 g cm^{-3}) was used to separate all particles of lower density from the sediment grains. The floating material was then sieved on a 32 μm sieve and this step was repeated five times. Finally, the retained material was rinsed with distilled water and stored in a glass jar. Samples collected in the coastal zones that were rich in organic matter were treated with 30% H_2O_2 for 24 hours at 50°C in order to oxidize the organic debris. The remaining material was sieved through a 32 μm sieve, rinsed with distilled water, and stored in a glass jar.

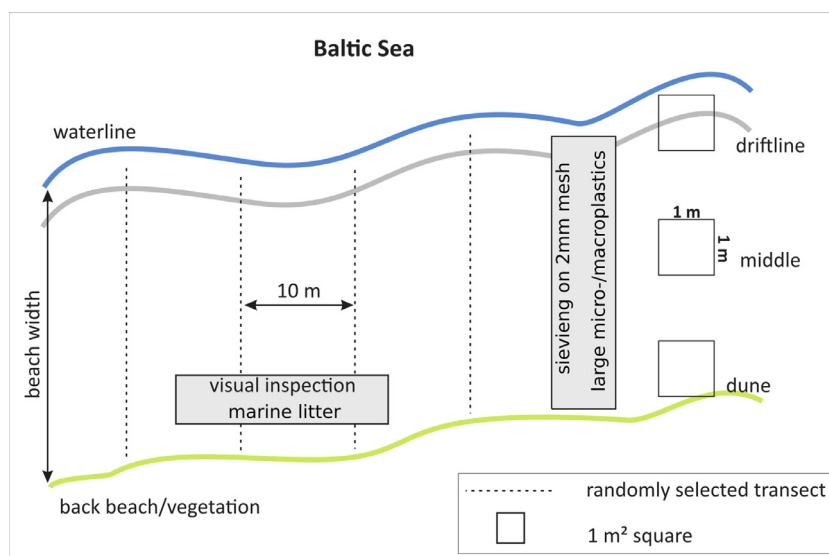


Figure 2 Large micro-/macroplastics and plastic litter sampling scheme at each site.

The final form of microplastic samples was a condensed solution of microplastic particles in water. Each sample was partially poured into a glass petri dish and visually inspected under the stereomicroscope (Leica M205C, equipped with 1.0x planochromatic objective). All the microplastics were enumerated, identified on the basis of color and shape and photographed at the highest possible magnification (between 10 × and 160 ×) using an attached camera (Leica DFC450, 5-megapixel resolution, number of pixels/pixel size: 2560 × 1920 / 3.4 μm × 3.4 μm). Next, their length was measured by the use of Leica Las Manual Measurements software.

To reduce the risk of contamination with microplastics from the air all the laboratory works were performed under the fume hood and also a benchtop fume hood was used during the microscopic analyses. Moreover, clean Petri dishes with distilled water were placed on the laboratory table for 24 h, close to the microscope where analyses were performed to estimate the possibility of contamination from the air. They collected from 8 to 11 white or transparent fibers, therefore a risk of contamination from air was estimated as <math><1 \text{ fiber h}^{-1}</math> and was considered negligible for the results.

2.3.2. Large micro-/macroplastic and plastic litter

Large micro-/macroplastics and plastic litter were sorted and enumerated on the basis of criteria from other publications (Esiukova, 2017; Hidalgo-Ruz and Thiel, 2013). They were grouped into the following categories: cigarette butts, hard plastic (e.g., lollipop sticks, pieces of toys, and fragments of larger hard plastics), soft plastic (e.g., plastic bags, sweets wrappers or similar and their fragments), pellets (nurdles), styrofoam, bottle caps, fibers/ropes and others (objects that did not fit any other category). They were then dried for 48 hours at 50°C, and weighed.

2.4. Calculations

At each site the amount of 0.1 m³ of water was collected, then the abundance of microplastics in each water sample was divided by 100 to obtain the concentration in 1 dm³ of the seawater, while the concentration of microplastics in each extracted sand sample was multiplied by 2 to obtain abundance in 1 kg of the sand (as 0.5 kg of dry sand from each sample was analyzed). To calculate the concentration of microplastics in 1 m² of the beach, the amount of microplastics found in the extracted sample (500 g of dry sand) was multiplied by the ratio of the mass of the whole sample collected at the site to 500 g of the analyzed sample and then multiplied by 6.66 (a ration between 0.15 m² sampled area and 1.00 m²).

The data regarding large micro-/macroplastics (abundance and mass separately) were averaged for each site providing average values per m² of the beach (average based on 3 samples collected at each site). Also, the plastic litter data were averaged for each site (average based on data from 4 transects), then they were divided by the beach width (distance from the driftline to the dunes forehead, Figure 2) providing an estimate of the plastic litter contamination per m² of the beach, comparable with the large micro-/macroplastics data. The width of the beach was estimated from satellite images provided by the wikimapia.org (www.wikimapia.org, accessed: December 2018).

The difference in microplastic fiber length was assessed using the Kruskal-Wallis rank test. For the *post-hoc* pairwise comparisons, the Dunn's test was used. Differences in microplastic abundance among sampling positions were checked using the Wilcoxon rank-sum test. The Spearman rank correlation test was used to investigate the relationship between the abundance of microplastic data among studied positions (water, driftline and dune).

All statistical operations were performed in R 4.1 (R Core Team, 2022).

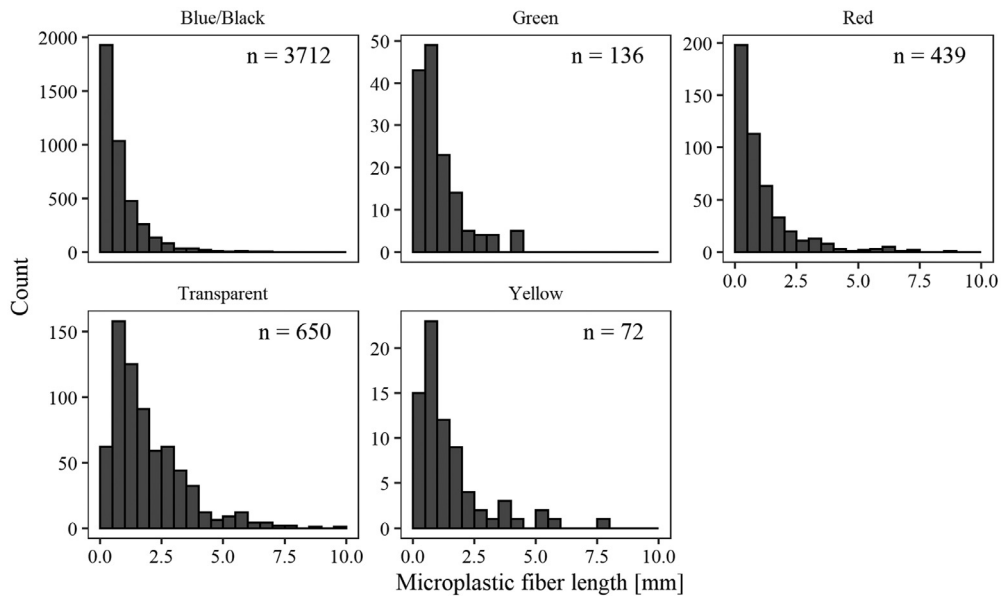


Figure 3 Distribution of microplastic fiber lengths for each fiber color (fibers from water and sand together). Only fibers <10 mm long are presented. Right closed bins, 0.5 mm wide; n – total number of measured fibers.

3. Results

3.1. Microplastics

In the whole study, 5286 particles were recorded, among them the majority were fibers (n=5129, 97.03% of all) and the rest were microplastic fragments (n=129, 2.44%) and other not-classified particles (n=28, 0.53%). 5019 fibers were measured, with a length between 0.03 and 19.61 mm. The length distribution of fibers was strongly right-skewed (Figure 3). Most of the fibers were shorter than 1 mm (36% were in a range 0.0–0.5mm and 27% were in a range 0.5–1.0 mm). When divided by colour, blue/black and red fibers were dominated by the shortest fibers (0.0–0.5 mm) while the rest was dominated by the fibers in a range between 0.5 and 1.0 mm.

The median length of microplastic fibers differed significantly among sampling positions ($\chi^2=12.97$, $df=2$, $p<0.01$) however, only fibers from coastal zone water were significantly shorter (619 μm) compared to driftline and dune (762 and 722 μm , respectively, Dunn’s test, $p<0.05$).

The concentration of microplastics in beach sand ranged from 118 to 536 pieces kg^{-1} dry sand (Figure 4); or from 1278 to 2412 pieces m^{-2} , except station 10, where a much higher number of microplastics was found (1382 pieces kg^{-1} dry sand; or 6498 pieces m^{-2}) with an overall median value of 293 pieces kg^{-1} dry sand (or 1932 pieces m^{-2}). The concentration of microplastics (number of pieces per kg dry sand) did not differ between driftline and dune positions (Wilcoxon test $W=40$, $p=0.19$), indicating a lack of partitioning of microplastics at different parts of the beach during the study period (autumn) i.e., during high hydrodynamic activity and strong winds.

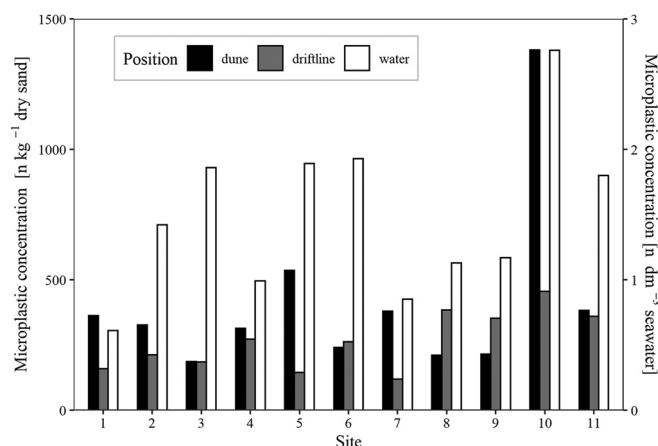


Figure 4 Concentration of microplastics in beach sediments and coastal zone water.

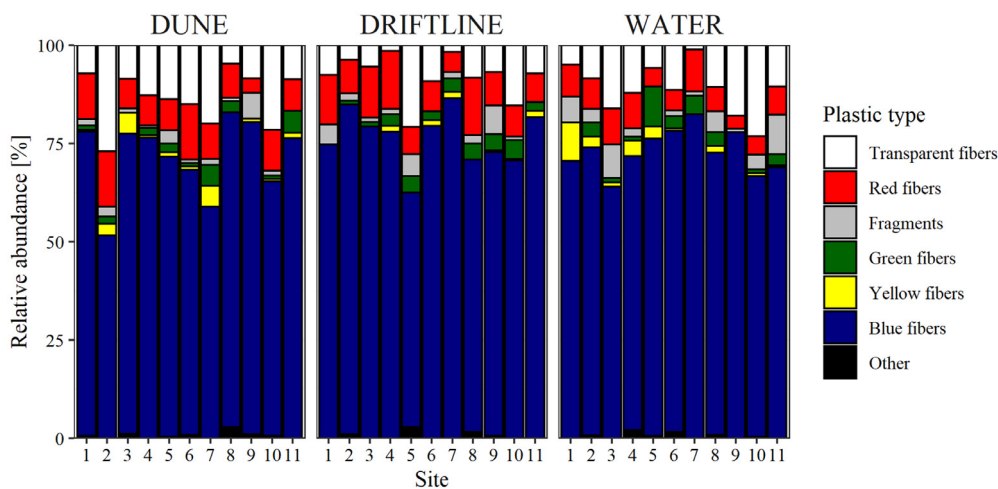


Figure 5 Composition of main groups of observed microplastics at each station and sampling position.

Microplastics abundance in water ranged from 0.61 to 2.76 pieces dm^{-3} with an overall median value of 1.42 pieces per dm^3 .

The Spearman's rank correlation analysis for the microplastic concentration among three investigated positions did not show any statistically significant correlation between any tested position pairs ($p > 0.05$).

All microplastic samples regardless of sampling position or station were dominated by blue fibers that constituted from 51.5% to 86.4% of abundance (Figure 5). Other minor contributions were transparent fibers (from 1.2 to 27.0%), red fibers (from 3.4 to 14.7%), green fibers (from 0.8, 10.1%) and microplastic fragments (from 0.6 to 10.0%).

3.2. Large micro-/macroplastics and plastic litter

The abundance and mass of large micro-/macroplastics and plastic litter varied widely and differed among sampling locations (Figure 6). The mean number of large micro-/macroplastics at the sampling site ranged from 2 to 124 pieces m^{-2} (Figure 6). Of the 11 sites surveyed, at only one site – site 6 in the national park – large micro-/macroplastics were not observed. Regarding plastic litter, on average, between 0.03 and 6.15 plastic debris m^{-2} were found at the site (Figure 6). The mean total mass of large micro-/macroplastics at the sampling sites ranged from 0.13 to 44.30 g m^{-2} . While the average mass of plastic litter at the sampling site ranged from 0.007 to 4.600 g m^{-2} . No patterns in large micro-/macroplastics and plastic litter abundance or mass were detected in relation to the location along the Polish coast.

The composition of large micro-/macroplastics varied widely and no one category of plastic was found to be dominant. The most common plastic categories were: hard plastic – at 9 sites, styrofoam – at 8 sites, and plastic fibers and pellets – at 7 sites. The most diverse site was site 8 – with eight plastic categories, the least diverse – site 2, with only one plastic category, while on average there were 5 plastic categories per station. The contributions of plastics at each site were very variable and could range from 4 to 100% abundance and 2 to 100% of mass for hard plastics,

and 3 to 50% abundance and 8 to 50% of mass for cigarette butts (Figure 7).

The plastic litter debris found during transect surveys was more diverse compared to large micro-/macroplastics samples. Hard and soft plastics were found at every location, while cigarette butts, ropes, and others were found at nine locations (Figure 7). The number of plastic categories at each station ranged from four to eight.

4. Discussion

4.1. Microplastic size distribution and concentration

The results presented in this study show that microplastic pollution of beaches of the southern Baltic Sea is a significant problem. Reported concentrations of microplastics in the sand and in water samples are comparable with other research, however only when values obtained with a similar sampling technique are taken into account (e.g., Bagaev et al., 2017; Hossain et al., 2021; Lots et al., 2017; Uurasjärvi et al., 2021). This is an important issue since factors like extraction technique, sample processing (the digesting solution used to remove organic matter), sieve mesh size used during the sampling or a sampling gear may significantly influence the results (Hidalgo-Ruz et al., 2012; Van Cauwenbergh et al., 2015).

Numerous studies report findings similar to ours regarding microplastic size distribution – domination of fibers smaller than 1 mm (e.g., Browne et al., 2010; Desforges et al., 2014; Fok et al., 2017) however, some studies report dominance of larger microplastics (1–5 mm) (Eriksen et al., 2013; Hossain et al., 2021). The prevalence of smaller particles may indicate a large distance from their source, resulting in high degradation and fragmentation en route to the sampling locations, e.g., due to the wave action (Barnes et al., 2009). The difference in size between the microplastic fibers of beach sediments and water could be a consequence of the wind action. Shorter fragments are lighter and may be more easily blown off from sedi-

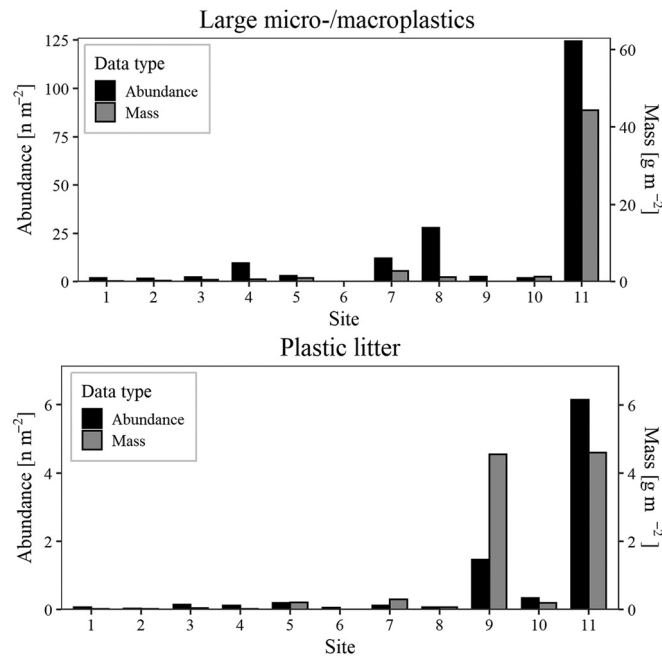


Figure 6 Mean abundance and mass of large micro-/macroplastics and plastic litter at each site.

ment grains, and have a higher potential to be transported by the wind into the water (Barnes et al., 2009). The reverse mechanism is also possible. Longer particles are heavier and may have a larger potential to remain stranded on the beach than shorter, lighter ones (Eriksen et al., 2014).

Regarding concentrations of microplastics in water samples the lower the mesh size used during sampling the higher the concentrations are found, for instance, the difference between values obtained with 80 μm and 450 μm mesh may be of several orders of magnitude (Hidalgo-Ruz et al., 2012). In various studies around the world, microplastic concentrations observed when a $\sim 300 \mu\text{m}$ mesh was used are low and around 0–10 particles m^{-3} , while when a $\sim 50 \mu\text{m}$ mesh was used they can reach values around 100–10000 (Aytan et al., 2016; Gewert et al., 2017), and the values reported in this study agree well with them. They also overlap quite well with results from the Baltic Sea, like this in the Gulf of Finland where concentrations between 200 and 1700 particles m^{-3} were obtained when a 50 μm filters were used (Uurasjärvi et al., 2021) or the study of Bagaev et al. (2017) in the central Baltic Sea where concentrations of microplastics between 70 and 2600 particles m^{-3} were noticed even though they used higher mesh filters (174 μm).

Concentrations of microplastics in sediments are not that easy to compare, due to various sampling and extraction techniques and units but our results appear to be consistent with observations worldwide, and are within the same order of magnitude (e.g., Hossain et al., 2021; Lots et al., 2017; Van Cauwenberghe et al., 2015). When compared with more local studies from the Baltic Sea coast, our results are slightly lower than those reported for the German coast (42–532 fibers kg^{-1} dry sand; Stolte et al., 2015) and slightly higher than those from the Russian coast (1–36 microplastics kg^{-1} dry sand; Esiukova, 2017). This could indicate a

west-to-east gradient of decreasing microplastic concentrations along the southern Baltic coast, which could be driven by the cyclonic water mass circulation in the Baltic Sea (Lehmann et al., 2002). However, the results of the study by Lots et al. (2017) deflate this argument, as they reported lower concentrations on the Danish coast (88–164 microplastics kg^{-1} dry sand) compared to much higher values at Klaipeda (700 microplastics kg^{-1} dry sand), which is on the eastern Baltic coast.

To date, two studies have been conducted on the Polish sandy beach coast and they reported lower results than ours. The study by Graca et al. (2017) observed microplastic contamination in sand ranging from 25 to 53 pieces m^{-3} . However, they used the NaCl solution for density separation, which has a lower density (around 1.2 g cm^{-3}) than the ZnCl_2 (1.5 g cm^{-3}) used in this study. Furthermore, they sieved the supernatant on a 45 μm sieve, while we used a 32 μm sieve, which could have led to results lower than ours. The study of Urban-Malinga et al. (2020) showed higher (between 76–295) microplastic contamination than Graca et al. (2017), but still lower than ours, but they also used a NaCl solution for the plastic separation, which may explain the difference.

Some authors have reported that microplastic pollution both in beach sediments and in the water column may be related to proximity to populated areas (Blumenröder et al., 2017; Pedrotti et al., 2016) or tourist activity (Retama et al., 2016), however, our results do not support such relationships. For instance, the concentration of microplastics in the national park (site 6) was comparable to other, urbanized localities characterized by high tourist activity like site 3 or site 9. Also, Esiukova (2017) found no spatial relationship in plastic contamination of Kaliningrad beaches, which was explained by rip currents and coastal eddies along the coast and strong storm activity which could lead to migration and dispersion of microplas-

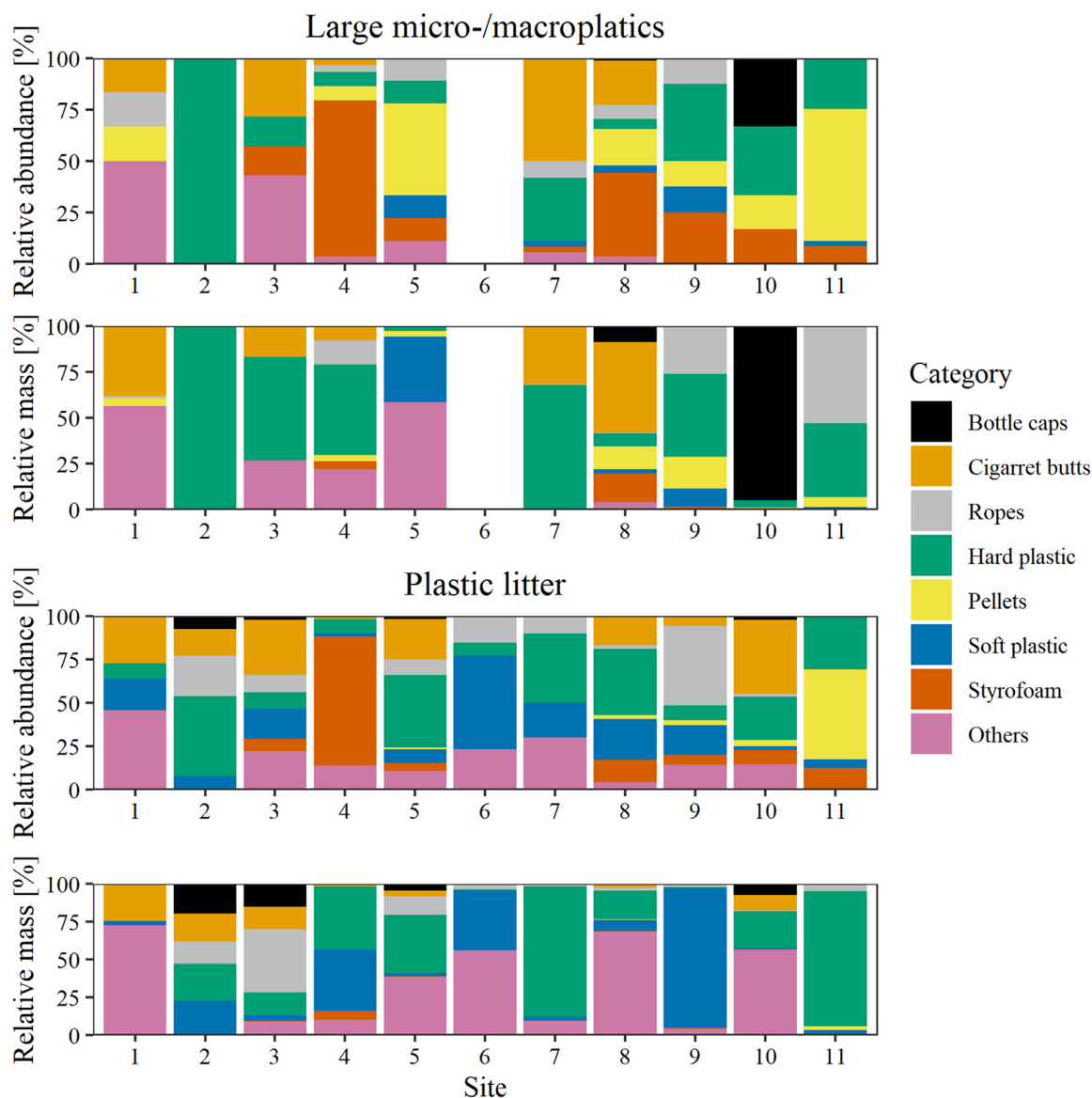


Figure 7 Composition of large micro-/macroplastics and plastic litter (based on mean values of abundance and mass of each plastic category) at each site.

tics over the coast. This also agrees with the study by [Urban-Malinga et al. \(2020\)](#), who also found significant concentrations of microplastics in the beach sediments of a Polish coastal national park, far from potential sources, and concluded that microplastics can be transported long distances along the coast by natural forces. These processes may be enhanced by wave action on beach sediments (especially in stormy seasons, as when the study was conducted), resulting in rapid removal of microplastics from the beach to coastal water ([Chubarenko and Stepanova, 2017](#)). Furthermore, another significant role may be played by processes of atmospheric transport and deposition, that may supply microplastics over long distances, to remote and nonurban locations ([Roblin et al., 2020](#)). As reported for the Gulf of Gdańsk, microplastic particles may be transported even from sources located 100km, and their deposition increases with the inflow of air masses from terrestrial areas and in wet periods ([Szewc et al., 2021](#)). Moreover, there is also

a possibility that microplastics may be emitted with sea sprays during stormy weather and further transported with air masses ([Ferrero et al., 2022](#)). Therefore, since our study was performed in the autumn season, which is characterized by high precipitation, strong winds, and frequent storms, it must be observed that the concentrations noted in our samples may be higher, compared with samples from other seasons.

Another potential source of microplastic particles could be the fragmentation of fishing gear, especially ropes and nets ([Wright et al., 2021](#)). In our study ropes were found at numerous sites, indicating high relevance of this source of contamination. To test if they may be responsible for microplastic contamination we checked if there is any correlation between the average concentration of microplastic particles per kg of sand and the mean mass of ropes found in large micro-/macroplastics samples or found in plastic litter samples, but both correlations were weak and not statis-

tically significant (Spearman's rank $\rho=0.08$, $p=0.82$ and $\rho=0.23$, $p=0.49$, respectively). This again suggests that microplastic contamination of beaches is a result of long transport of the particles, e.g., by sea currents or air masses and long deposition, rather than a result of local contamination with large litter and its on-site fragmentation.

4.2. Microplastics color-based composition

The color-based composition of microplastics recorded in our study (high dominance of blue/dark fibers) is similar to findings from other regions of the world (e.g., Blumenröder et al., 2017; Lots et al., 2017; Stolte et al., 2015). High similarity in microplastic color-based composition between beach sand and water samples may indicate a common primary source of contamination, but also a high level of microplastics exchange between the beach and coastal waters. This could also explain the lack of spatial patterns in microplastic density. Beaches and shores have the potential to accumulate microplastics. Particles washed ashore can easily return to the sea after a storm due to re-suspension, and can then subsequently accumulate on the coast as a consequence of wave action and coastal currents (Chubarenko and Stepanova, 2017; Fok et al., 2017; Schernewski et al., 2020).

Microplastics found in this study were identified only on the basis of visual inspection after the hydrogen peroxide oxidation, which was supposed to remove most of the organic matter. However no spectroscopic analysis was performed, therefore it must be noted that some of the particles, especially the transparent ones, that were assigned as microplastics could be confounded with natural particles like fragments of filamentous algae or cotton. The contribution of transparent fibers in samples was between 1.2 to 27.0% (on average 10.8%), so in the case when all the transparent fibers were not microplastics, our calculations regarding the total abundance of microplastics may be nearly 11% inflated. On the other hand, the presence of transparent microplastic fibers, sometimes in high proportions, was reported in the literature. For instance in the Hawai'ian beach sediments white and transparent debris constituted almost 72% of all the plastic particles (Young and Elliott, 2016). Almost identical results – transparent microplastics constituted 73% of all plastics – were obtained by Graca et al. (2017) in beach and marine sediment samples from the southern Baltic. Also, a review by Wang et al. (2021) showed that most microplastics in freshwater systems are white and transparent. Therefore, it is also possible that the number of transparent fibers was underestimated in our study. This could be the result of a “color selection bias” as light-coloured or transparent particles may evade visual detection and the error in their abundance estimation can reach even 60% (Stolte et al., 2015).

4.3. Large micro-/macroplastics and plastic litter

Based on the data obtained, there does not seem to be a dominant large micro-/macroplastics and plastic litter pollutant on the Polish coast. The litter that was found could originate from various sources such as tourist activities – cigarette butts and bottle caps, fishery – ropes, and local industrial activities – hard plastic elements, styrofoam,

plastic pellets. The results suggest that the amount and composition of large micro-/macroplastics and plastic litter is highly locally specific and could be influenced by various factors such as water currents, proximity to urban centers, recreational areas, shipping lines, or fishing grounds (Sheavly and Register, 2007). Plastics were found even in the national park, mostly soft plastics which could be carried by the wind, or ropes, which could be transferred by water currents, and stranded ashore (Jambeck et al., 2015). Among all the sites, site 11 seems to be an exception with a very high amount of litter, and an especially high contribution of plastic pellets, which were hardly found anywhere else. Site 11 was located in the Krynica Morska tourist resort, with no heavy industry. However, the abundance of pellets at this site could be explained by the presence of the Gdańsk container terminal (annual throughput capacity – 3 250 000 TEU; (“DCT Gdansk” (2021)) ~50 km west of the site and mouth of the Vistula River ~35 km west of the site. In this region, coastal currents flow in an easterly direction (Zajączkowski et al., 2010), so resin pellets that are discarded in the container terminal during unloading, or are carried by river water, could easily be transported to the site and stranded ashore (Ferreira et al., 2021).

To date, only a few studies on litter pollution have been conducted along the Baltic coasts. According to HELCOM (2018) report the Baltic coast is not free from litter pollution, and the litter that can be found on Baltic beaches is dominated by plastics, followed by paper and cardboard, metal, glass, and ceramics. Another large survey studies conducted on Swedish, Finnish, Estonian and Latvian beaches showed that plastic accounts for more than 50% of litter on beaches, with higher contributions on urban beaches, and is composed mostly of broken pieces of large plastic (MARLIN Baltic Marine Litter Project, 2013). The Polish coastline was evaluated as the most threatened among European countries by tourism and recreational activity along with natural processes of abrasion and erosion (Józwiak, 2010). Another study by Józwiak (1996) showed that the pollution of Polish beaches by litter is a serious problem along the whole coast and it was caused by high amounts of textiles, styrofoam, pieces of plastic packaging and their fragments, plastic bottles, cans, glass, paper, and wood. He also found that the amount of plastic packaging pieces grows exponentially which could be dangerous to the environment and wildlife. A more recent study concerning Polish coastline litter pollution was performed by Zalewska et al. (2021). Their 5-year time series showed that more than half of the top 10 litter types they collected were cigarette butts, followed by bottle caps, wood pieces and drink bottles. As a main source of litter, they pointed the tourism and recreational activities, while the fishing industry had a minor impact. They also found that two important factors can influence beach contamination by litter: seasonality (related to storm activity and tourism) and beach cleaning campaigns by municipalities, which can influence both the composition and amount of litter. Our study was carried out in one season (autumn) only, after the holiday season and during the storm period, which may explain the difference in the litter composition we observed compared to the above studies. However, the main sources of plastic litter remain similar.

5. Conclusions

Our study showed that plastic pollution of the Polish part of the Baltic coast is a significant problem, comparable to other parts of the European and world coastlines. Microplastics found in beach sediments and coastal water were similar in color-based composition, suggesting a common source of contamination. No spatial patterns were detected, plastic particles (microplastics, plastic litter) were noted even at pristine, nonurban locations like a national park. Our results indicate a complex and diverse combination of sources supplying plastic pollutants all over the coast like deposition from air, transport with coastal currents or tourist activity. What must be noted is the possibility that our results may be not fully representative from the annual perspective. The reason is the fact that samples were collected in the autumn season, after the peak of tourist activity, in a period characterized by strong winds and storminess. These factors may be responsible for the additional supply of both microplastics (e.g., by wet deposition) and larger plastics fragmentation as a result of wind action and wave transport onto the shore. Therefore, a seasonal or monthly study is needed, on both microplastics and larger plastics, to better understand the fate of plastic in a coastal zone.

Declaration of competing interest

The authors declare that they have no known competing financial interests or personal relationships that could have appeared to influence the work reported in this paper.

References

- Aytan, U., Valente, A., Senturk, Y., Usta, R., Esensoy Sahin, F.B., Mazlum, R.E., Agirbas, E., 2016. First evaluation of neustonic microplastics in Black Sea waters. *Mar. Environ. Res.* 119, 22–30. <https://doi.org/10.1016/j.marenvres.2016.05.009>
- Babakov, A., 2010. Wind-Driven Currents and their Impact on the Morpho-Lithology at the Eastern Shore of the Gulf of Gdańsk. *Arch. Hydroengineering Environ. Mech.* 57, 85–103.
- Bagaev, A., Mizyuk, A., Khatmullina, L., Isachenko, I., Chubarenko, I., 2017. Anthropogenic fibres in the Baltic Sea water column: Field data, laboratory and numerical testing of their motion. *Sci. Total Environ.* 599–600, 560–571. <https://doi.org/10.1016/j.scitotenv.2017.04.185>
- Bakir, A., Rowland, S.J., Thompson, R.C., 2014. Enhanced desorption of persistent organic pollutants from microplastics under simulated physiological conditions. *Environ. Pollut.* 185, 16–23. <https://doi.org/10.1016/j.envpol.2013.10.007>
- Barnes, D.K.A., Galgani, F., Thompson, R.C., Barlaz, M., 2009. Accumulation and fragmentation of plastic debris in global environments. *Philos. Trans. R. Soc. B Biol. Sci.* 364, 1985–1998. <https://doi.org/10.1098/rstb.2008.0205>
- Barnes, D.K.A., Milner, P., 2005. Drifting plastic and its consequences for sessile organism dispersal in the Atlantic Ocean. *Mar. Biol.* 146, 815–825. <https://doi.org/10.1007/s00227-004-1474-8>
- Blumenröder, J., Sechet, P., Kakkonen, J.E., Hartl, M.G.J., 2017. Microplastic contamination of intertidal sediments of Scapa Flow, Orkney: A first assessment. *Mar. Pollut. Bull.* 124, 112–120. <https://doi.org/10.1016/j.marpolbul.2017.07.009>
- Browne, M.A., Crump, P., Niven, S.J., Teuten, E.L., Tonkin, A., Galloway, T., Thompson, R.C., 2011. Accumulations of microplastic on shorelines worldwide: sources and sinks. *Environ. Sci. Technol.* 45, 9175–9179. <https://doi.org/10.1021/es201811s>
- Browne, M.A., Galloway, T.S., Thompson, R.C., 2010. Spatial patterns of plastic debris along estuarine shorelines. *Environ. Sci. Technol.* 44, 3404–3409. <https://doi.org/10.1021/es903784e>
- Chenillat, F., Huck, T., Maes, C., Grima, N., 2021. Fate of floating plastic debris released along the coasts in a global ocean model. *Mar. Pollut. Bull.* 165, 334565. <https://doi.org/10.1016/j.marpolbul.2021.112116>
- Chubarenko, I., Stepanova, N., 2017. Microplastics in sea coastal zone: Lessons learned from the Baltic amber. *Environ. Pollut.* 224, 243–254. <https://doi.org/10.1016/j.envpol.2017.01.085>
- DCT Gdansk [WWW Document], 2021. Balt. Hub – DCT Gdansk – Contain. Termin. DCT. <https://dctgdansk.pl/en/about-dct/terminal-specifications/> (accessed 03.02.2021).
- Derraik, J.G.B., 2002. The pollution of the marine environment by plastic debris: A review. *Mar. Pollut. Bull.* 44, 842–852. [https://doi.org/10.1016/S0025-326X\(02\)00220-5](https://doi.org/10.1016/S0025-326X(02)00220-5)
- Desforges, J.P.W., Galbraith, M., Dangerfield, N., Ross, P.S., 2014. Widespread distribution of microplastics in subsurface seawater in the NE Pacific Ocean. *Mar. Pollut. Bull.* 79, 94–99. <https://doi.org/10.1016/j.marpolbul.2013.12.035>
- Eriksen, M., Lebreton, L.C.M., Carson, H.S., Thiel, M., Moore, C.J., Bornerro, J.C., Galgani, F., Ryan, P.G., Reisser, J., 2014. Plastic Pollution in the World's Oceans: More than 5 Trillion Plastic Pieces Weighing over 250,000 Tons Afloat at Sea. *PLoS One* 9, 0–15. <https://doi.org/10.1371/journal.pone.0111913>
- Eriksen, M., Mason, S., Wilson, S., Box, C., Zellers, A., Edwards, W., Farley, H., Amato, S., 2013. Microplastic pollution in the surface waters of the Laurentian Great Lakes. *Mar. Pollut. Bull.* 77, 177–182. <https://doi.org/10.1016/j.marpolbul.2013.10.007>
- Esiukova, E., 2017. Plastic pollution on the Baltic beaches of Kaliningrad region, Russia. *Mar. Pollut. Bull.* 114, 1072–1080. <https://doi.org/10.1016/j.marpolbul.2016.10.001>
- Esiukova, E., Lobchuk, O., Haseler, M., Chubarenko, I., 2021. Microplastic contamination of sandy beaches of national parks, protected and recreational areas in southern parts of the Baltic Sea. *Mar. Pollut. Bull.* 173, 113002. <https://doi.org/10.1016/j.marpolbul.2021.113002>
- European Environment Agency, 2021. Baltic Sea physiography (depth distribution and main currents) [WWW Document]. URL <https://www.eea.europa.eu/data-and-maps/figures/baltic-sea-physiography-depth-distribution-and-main-currents>
- Ferreira, A.T., da, S., Siegle, E., Ribeiro, M.C.H., Santos, M.S.T., Grohmann, C.H., 2021. The dynamics of plastic pellets on sandy beaches: A new methodological approach. *Mar. Environ. Res.* <https://doi.org/10.1016/j.marenvres.2020.105219>
- Ferrero, L., Scibetta, L., Markuszewski, P., Mazurkiewicz, M., Drozdowska, V., Makuch, P., Jutrzenka-Trzebiatowska, P., Zaleska-Medynska, A., Andò, S., Saliu, F., Nilsson, D.E., Bolzacchini, E., Nilsson, E.D., Bolzacchini, E., 2022. Airborne and marine microplastics from an oceanographic survey at the Baltic Sea: An emerging role of air-sea interaction? *Sci. Total Environ.* 824, 153709. <https://doi.org/10.1016/j.scitotenv.2022.153709>
- Fok, L., Cheung, P.K., Tang, G., Li, W.C., 2017. Size distribution of stranded small plastic debris on the coast of Guangdong, South China. *Environ. Pollut.* 220, 407–412. <https://doi.org/10.1016/j.envpol.2016.09.079>
- Gewert, B., Ogonowski, M., Barth, A., MacLeod, M., 2017. Abundance and composition of near surface microplastics and plastic debris in the Stockholm Archipelago, Baltic Sea. *Mar. Pollut. Bull.* 120, 292–302. <https://doi.org/10.1016/j.marpolbul.2017.04.062>
- Graca, B., Szewc, K., Zakrzewska, D., Dołęga, A., Szczerbowska-Boruchowska, M., 2017. Sources and fate of microplastics in marine and beach sediments of the Southern Baltic Sea – a

- preliminary study. *Environ. Sci. Pollut. Res.* 24, 7650–7661. <https://doi.org/10.1007/s11356-017-8419-5>
- HELCOM, 2018. State of the Baltic Sea- Second HELCOM holistic assessment, 2011–2016. In: *Baltic Sea Environment Proceedings*, 155.
- Hidalgo-Ruz, V., Gutow, L., Thompson, R.C., Thiel, M., 2012. Microplastics in the marine environment: A review of the methods used for identification and quantification. *Environ. Sci. Technol.* 46, 3060–3075. <https://doi.org/10.1021/es2031505>
- Hidalgo-Ruz, V., Thiel, M., 2013. Distribution and abundance of small plastic debris on beaches in the SE Pacific (Chile): A study supported by a citizen science project. *Mar. Environ. Res.* 87–88, 12–18. <https://doi.org/10.1016/j.marenvres.2013.02.015>
- Hossain, M.B., Banik, P., Nur, A.A.U., Rahman, T., 2021. Abundance and characteristics of microplastics in sediments from the world’s longest natural beach, Cox’s Bazar, Bangladesh. *Mar. Pollut. Bull.* 163, 111956. <https://doi.org/10.1016/j.marpolbul.2020.111956>
- Jambeck, J.R., Geyer, R., Wilcox, C., Siegler, T.R., Perryman, M., Andrady, A., Narayan, R., Law, K.L., 2015. Plastic waste inputs from land into the ocean. *Science* (80) 347, 768–771. <https://doi.org/10.1126/science.1260352>
- Jóźwiak, T., 2010. Parametryzacja stanu zoologicznego wybrzeża południowego Bałtyku w świetle idei rozwoju zrównoważonego [Parameterization of the zoological status of southern Baltic coast in the light of the concept of the sustainable development]. Wydawnictwo Uniwersytetu Gdańskiego, 248 pp.
- Jóźwiak, T., 1996. Wpływ zmian zoologicznych na ekosystem polskiej strefy przybrzeżnej w latach 1992–1995 [An impact of the zoological changes on the ecosystem of the polish coastal zone in years 1992–1995] Ph.D. Thesis.
- Kotwicki, L., Weslawski, J.M., Włodarska-Kowalczyk, M., Mazurkiewicz, M., Wenne, R., Zbawicka, M., Minchin, D., Olenin, S., 2021. The re-appearance of the *Mytilus* spp. complex in Svalbard, Arctic, during the Holocene: The case for an arrival by anthropogenic flotsam. *Glob. Planet. Change* 202, 103502. <https://doi.org/10.1016/j.gloplacha.2021.103502>
- Lehmann, A., Krauss, W., Hinrichsen, H.-H., 2002. Effects of remote and local atmospheric forcing on circulation and upwelling in the Baltic Sea. *Tellus A Dyn. Meteorol. Oceanogr.* 54, 299–316. <https://doi.org/10.3402/tellusa.v54i3.12138>
- Leppäranta, M., Myrberg, K., 2009. *Physical oceanography of the Baltic Sea, Physical oceanography of the Baltic Sea*. Springer Praxis Publ., Chichester, 407 pp.
- Li, W.C., Tse, H.F., Fok, L., 2016. Plastic waste in the marine environment: A review of sources, occurrence and effects. *Sci. Total Environ.* 566–567, 333–349. <https://doi.org/10.1016/j.scitotenv.2016.05.084>
- Lots, F.A.E., Behrens, P., Vijver, M.G., Horton, A.A., Bosker, T., 2017. A large-scale investigation of microplastic contamination: Abundance and characteristics of microplastics in European beach sediment. *Mar. Pollut. Bull.* 123, 219–226. <https://doi.org/10.1016/j.marpolbul.2017.08.057>
- MARLIN Baltic Marine Litter Project, 2013. Final Report of Baltic Marine Litter Project Marlin – Litter Monitoring and Raising Awareness, 29 pp.
- Mohamed Nor, N.H., Obbard, J.P., 2014. Microplastics in Singapore’s coastal mangrove ecosystems. *Mar. Pollut. Bull.* 79, 278–283. <https://doi.org/10.1016/j.marpolbul.2013.11.025>
- Oigman-Pszczol, S.S., Creed, J.C., 2007. Quantification and classification of marine litter on beaches along Armação dos Búzios, Rio de Janeiro, Brazil. *J. Coast. Res.* 23, 421–428. [https://doi.org/10.2112/1551-5036\(2007\)23\[421:QACOML\]2.0.CO;2](https://doi.org/10.2112/1551-5036(2007)23[421:QACOML]2.0.CO;2)
- Pedrotti, M.L., Petit, S., Elineau, A., Bruzaud, S., Crebassa, J.C., Dumontet, B., Marti, E., Gorsky, G., Cózar, A., 2016. Changes in the floating plastic pollution of the mediterranean sea in relation to the distance to land. *PLoS One* 11. <https://doi.org/10.1371/journal.pone.0161581>
- Prata, J.C., 2018. Microplastics in wastewater: State of the knowledge on sources, fate and solutions. *Mar. Pollut. Bull.* 129, 262–265. <https://doi.org/10.1016/j.marpolbul.2018.02.046>
- R Core Team, 2022. R: A language and environment for statistical computing.
- Rendell-Bhatti, F., Paganos, P., Pouch, A., Mitchell, C., D’Aniello, S., Godley, B.J., Pazdro, K., Arnone, M.I., Jimenez-Guri, E., 2021. Developmental toxicity of plastic leachates on the sea urchin *Paracentrotus lividus*. *Environ. Pollut.* 269, 115744. <https://doi.org/10.1016/j.envpol.2020.115744>
- Retama, I., Jonathan, M.P., Shruti, V.C., Velumani, S., Sarkar, S.K., Roy, P.D., Rodríguez-Espinosa, P.F., 2016. Microplastics in tourist beaches of Huatulco Bay, Pacific coast of southern Mexico. *Mar. Pollut. Bull.* 113, 530–535. <https://doi.org/10.1016/j.marpolbul.2016.08.053>
- Roblin, B., Ryan, M., Vreugdenhil, A., Aherne, J., 2020. Ambient Atmospheric Deposition of Anthropogenic Microfibers and Microplastics on the Western Periphery of Europe (Ireland). *Environ. Sci. Technol.* 54, 11100–11108. <https://doi.org/10.1021/acs.est.0c04000>
- Rosentau, A., Bennike, O., Uscinowicz, S., Miotk-Szpiganowicz, G., 2017. The Baltic Sea Basin. In: Flemming, N.C., Harff, J., Moura, D., Burgess, A., Bailey, G.N. (Eds.), *Submerged Landscapes of the European Continental Shelf: Quaternary Paleoenvironments*. Wiley Blackwell, Chydon, 103–133. <https://doi.org/10.1002/9781118927823.ch5>
- Rowley, K.H., Cucknell, A.C., Smith, B.D., Clark, P.F., Morrill, D., 2020. London’s river of plastic: High levels of microplastics in the Thames water column. *Sci. Total Environ.* 740, 140018. <https://doi.org/10.1016/j.scitotenv.2020.140018>
- Rytönen, J., Siitonen, L., Riipi, T., Sassi, J., Sukselainen, J., 2002. Statistical Analyses of the Baltic Maritime Traffic, Res. Rep. no VAL34-012344, Finnish Environ. Inst., 152 pp. <https://publications.vtt.fi/julkaisut/muut/2002/VAL34-012344.pdf>
- Schernewski, G., Radtke, H., Hauk, R., Baresel, C., Olshammar, M., Osinski, R., Oberbeckmann, S., 2020. Transport and Behavior of Microplastics Emissions From Urban Sources in the Baltic Sea. *Front. Environ. Sci.* 8, 1–17. <https://doi.org/10.3389/fenvs.2020.579361>
- Schmidt, C., Krauth, T., Wagner, S., 2017. Export of Plastic Debris by Rivers into the Sea. *Environ. Sci. Technol.* 51, 12246–12253. <https://doi.org/10.1021/acs.est.7b02368>
- Sheavly, S.B., Register, K.M., 2007. Marine debris & plastics: Environmental concerns, sources, impacts and solutions. *J. Polym. Environ.* 15, 301–305. <https://doi.org/10.1007/s10924-007-0074-3>
- Stolte, A., 2014. The detection of microplastics in beach sediments, Ms. Thesis, Univ. Rostock, 144 pp.
- Stolte, A., Forster, S., Gerds, G., Schubert, H., 2015. Microplastic concentrations in beach sediments along the German Baltic coast. *Mar. Pollut. Bull.* 99, 216–229. <https://doi.org/10.1016/j.marpolbul.2015.07.022>
- Szewc, K., Graca, B., Dołęga, A., 2021. Atmospheric deposition of microplastics in the coastal zone: Characteristics and relationship with meteorological factors. *Sci. Total Environ.* 761, 143272. <https://doi.org/10.1016/j.scitotenv.2020.143272>
- Tanaka, K., Takada, H., Yamashita, R., Mizukawa, K., Fukuwaka, M., Watanuki, Y., 2013. Accumulation of plastic-derived chemicals in tissues of seabirds ingesting marine plastics. *Mar. Pollut. Bull.* 69, 219–222. <https://doi.org/10.1016/j.marpolbul.2012.12.010>
- Tekman, M.B., Krumpfen, T., Bergmann, M., 2017. Marine litter on deep Arctic seafloor continues to increase and spreads to the North at the HAUSGARTEN observatory. *Deep. Res. Pt. I Oceanogr. Res. Pap.* 120, 88–99. <https://doi.org/10.1016/j.dsr.2016.12.011>
- Thompson, R.C., Olsen, Y., Mitchell, R.P., Davis, A., Rowland, S.J.,

- John, A.W.G., McGonigle, D., Russell, A.E., 2004. Lost at sea: where is all the plastic? *Science* 304 (5672), 838. <https://doi.org/10.1126/science.1094559>
- Urban-Malinga, B., Zalewski, M., Jakubowska, A., Wodzinowski, T., Malinga, M., Pałys, B., Dąbrowska, A., 2020. Microplastics on sandy beaches of the southern Baltic Sea. *Mar. Pollut. Bull.* 155, 111170. <https://doi.org/10.1016/j.marpolbul.2020.111170>
- Uurasjärvi, E., Pääkkönen, M., Setälä, O., Koistinen, A., Lehtiniemi, M., 2021. Microplastics accumulate to thin layers in the stratified Baltic Sea. *Environ. Pollut.* 268. <https://doi.org/10.1016/j.envpol.2020.115700>
- Van Cauwenberghe, L., Devriese, L., Galgani, F., Robbins, J., Janssen, C.R., 2015. Microplastics in sediments: A review of techniques, occurrence and effects. *Mar. Environ. Res.* 111, 5–17. <https://doi.org/10.1016/j.marenvres.2015.06.007>
- Wang, Z., Zhang, Y., Kang, S., Yang, L., Shi, H., Tripathee, L., Gao, T., 2021. Research progresses of microplastic pollution in freshwater systems. *Sci. Total Environ.* 795, 148888. <https://doi.org/10.1016/j.scitotenv.2021.148888>
- Węśławski, J.M., Kotwicki, L., 2018. Macro-plastic litter, a new vector for boreal species dispersal on Svalbard. *Polish Polar Res.* 39, 165–174. <https://doi.org/10.24425/118743>
- Williams, A.T., Pond, K., Ergin, A., Cullis, M.J., 2013. The hazards of beach litter. In: Finkl, C.W. (Ed.), *Coastal Hazards*. Coastal Res. Library. Springer, Dordrecht, Heidelberg, New York, London, 753–780. https://doi.org/10.1007/978-94-007-5234-4_24
- Woodall, L.C., Sanchez-Vidal, A., Canals, M., Paterson, G.L.J., Coppock, R., Sleight, V., Calafat, A., Rogers, A.D., Narayanaswamy, B.E., Thompson, R.C., 2014. The deep sea is a major sink for microplastic debris. *R. Soc. Open Sci.* 1, 140317. <https://doi.org/10.1098/rsos.140317>
- Wright, L.S., Napper, I.E., Thompson, R.C., 2021. Potential microplastic release from beached fishing gear in Great Britain's region of highest fishing litter density. *Mar. Pollut. Bull.* 173, 113115. <https://doi.org/10.1016/j.marpolbul.2021.113115>
- Wulff, F.V., Rahm, L.A., Larsson, P., 2001. *A System analysis of the Baltic Sea*. Springer-Verlag, Berlin, Heidelberg, New York, 457 pp.
- Young, A.M., Elliott, J.A., 2016. Characterization of microplastic and mesoplastic debris in sediments from Kamilo Beach and Kahuku Beach, Hawai'i. *Mar. Pollut. Bull.* 113 (1–2), 477–482. <https://doi.org/10.1016/j.marpolbul.2016.11.009>
- Zajączkowski, M., Darecki, M., Szczuciński, W., 2010. Report on the development of the Vistula river plume in the coastal waters of the Gulf of Gdańsk during the May 2010 flood. *Oceanologia* 52 (2), 311–317. <https://doi.org/10.5697/oc.52-2.311>
- Zalewska, T., Maciak, J., Grajewska, A., 2021. Spatial and seasonal variability of beach litter along the southern coast of the Baltic Sea in 2015-2019 - recommendations for the environmental status assessment and measures. *Sci. Total Environ.* 774, 145716. <https://doi.org/10.1016/j.scitotenv.2021.145716>

Available online at www.sciencedirect.com

ScienceDirect

journal homepage: www.journals.elsevier.com/oceanologia

SHORT COMMUNICATION

Factors responsible for the sudden outburst of *Noctiluca scintillans* in the Chennai coastal waters, southeast coast of India – a case study

Pravakar Mishra, Mehmuna Begum*, Anitha Gera, B. Charan Kumar, Garlapati Deviram, Uma Kanta Pradhan, Athan Vashi, Debasmita Bandyopadhyay, Subrat Naik, Uma Sankar Panda, M.V. Ramana Murthy

National Centre for Coastal Research (NCCR), Ministry of Earth Sciences, NIOT Campus, Pallikaranai, Chennai, India

Received 27 September 2021; accepted 26 June 2022

Available online 13 July 2022

KEYWORDS

Noctiluca scintillans;
Diatoms;
Bloom;
Bioluminescence;
Chennai coast;
India

Abstract The paper discusses the factors associated with the sudden outbreak of the nocturnal heterotrophic bioluminescent dinoflagellate *Noctiluca scintillans* along the Chennai coast. The bloom occurred along a stretch of 16 km following a spell of heavy rain in August 2019. The density of *N. scintillans* varied from 1000 to 19000 cells/L, with a distinguished distribution pattern. High *N. scintillans* abundance was recorded at Panaiyurkuppam and Kovalam, with 19000 cells/L and 18000 cells/L, recorded respectively. Adequate nutrients brought by substantial rainfall and a high abundance of the diatom *Thalassiosira* sp. triggered the *N. scintillans* bloom. The low wind speed (5 m/sec), lowering of atmospheric temperature (from 24.00 to 31.00°C, $27.5 \pm 1.17^\circ\text{C}$), high rainfall (6 mm within one day), and low sea surface temperature (SST) (from 25.20 to 31.00°C, $29.37 \pm 1.17^\circ\text{C}$) are probable environmental cues. Local hydrodynamics and the diverging currents governed the presence and dispersion of the bloom in the region.

© 2022 Institute of Oceanology of the Polish Academy of Sciences. Production and hosting by Elsevier B.V. This is an open access article under the CC BY-NC-ND license (<http://creativecommons.org/licenses/by-nc-nd/4.0/>).

* Corresponding author at: National Centre for Coastal Research (NCCR), Ministry of Earth Sciences, NIOT Campus, Pallikaranai, Chennai-600100, India. Phone: +91 9791037418.

E-mail address: mehmuna@gmail.com (M. Begum).

Peer review under the responsibility of the Institute of Oceanology of the Polish Academy of Sciences.



<https://doi.org/10.1016/j.oceano.2022.06.005>

0078-3234/© 2022 Institute of Oceanology of the Polish Academy of Sciences. Production and hosting by Elsevier B.V. This is an open access article under the CC BY-NC-ND license (<http://creativecommons.org/licenses/by-nc-nd/4.0/>).

Noctiluca scintillans (Macartney) (Kofoid and Swezy, 1921), a heterotrophic dinoflagellate, is a cosmopolitan red tide-forming organism that produces bioluminescence sporadically (Liu and Hastings, 2007; Zhang et al., 2017). *Noctiluca scintillans* exists in two variants green and red. Green variants harbor symbiotic prasinophytes (green algae) providing characteristic green color, and red is strictly heterotrophic, forming a clutch of carotenoid pigments imparting characteristic red color (Zhang et al., 2017). The red carotenoid pigments accumulate in *N. scintillans* due to the grazing on diatoms that are essential for microplankton grazers (Shaju et al., 2018). The ecological characteristics of *Noctiluca* blooms are the formation of red tide, production of bioluminescence, and survival in low oxygenated waters (Gomes et al., 2014; Liu and Hastings, 2007; Turkoglu, 2013). The low oxygen caused by *N. scintillans* bloom impacts the ecosystem and biodiversity (Raj et al., 2020). The bloom of *N. scintillans* encountered in our study was non-toxic and harmless, unlike previously reported in the Gulf of Mannar, which had caused a devastating impact on flora and fauna caused by asphyxiation (Gopakumar et al., 2009).

Blooms of *Noctiluca* have been reported worldwide under various environmental conditions (Anderson et al., 2002). Along the southwest coast of India, occurrences of heterotrophic red *N. scintillans* during summer under the influence of upwelling have been reported (Gomes et al., 2014). They are also abundant in the productive zones of upwelling and enriched regions that support a high density of diatoms (Sahayak et al., 2005). The *N. scintillans* bloom is also related to the mixing process and depth of the mixed layer during seasonal changes. Upwelling along the coastal areas is often associated with the proliferation of smaller diatoms acting as a precursor for *N. scintillans* to proliferate (Sarma et al., 2019). Red *N. scintillans* blooms were encountered along Tamil Nadu coast (Aiyar, 1936), Rushikulya river, and off Rushikulya, south Odisha coast (Baliarsingh et al., 2016; Mohanty et al., 2007). Along the west coast of India, several episodes were reported predominantly in Kerala waters, off Quillon, Thiruvananthapuram coast, and also from offshore of Kochi (Joseph et al., 2008; Naqvi et al., 1998; Padmakumar et al., 2010; Sahayak et al., 2005; Venugopal et al., 1979).

N. scintillans bloom and bioluminescence were observed along the Chennai coast on 17, 18, and 19th August 2019. On 17th bioluminescence was observed at Akkrai beach, moving to Thiruvanniyur and Elliot beach on 18th and 19th, respectively. Field surveys were conducted four times at six locations viz., Marina, Elliot, Thiruvanniyur, Akkarai, Panaiyurkuppam, and Kovalam; at the shore, three days (19, 20, and 26th August 2019) and once on the offshore waters (21st August 2019) between 09:00 and 15:00, in duplicates to measure the physicochemical and microbiological parameters. The water temperature was measured by a mercury thermometer (Brannan, U.K) with an accuracy of $\pm 0.1^\circ\text{C}$. pH was measured with water quality multi-probe (Eureka 2, US); salinity was determined by Knudsen's titration method; dissolved oxygen (DO) was estimated using Winkler's method (Grasshoff et al., 1999). Biological oxygen demand (BOD) was measured after five days of incubation at 20°C in a BOD incubator. The samples were filtered using GF/C (0.45 μm) filter papers for the determination of nutrient concentrations, including dissolved inorganic nitrogen

(DIN) (nitrite+nitrate+ammonia), inorganic phosphate (IP), and silicate, following standard methods (Grasshoff et al., 1999). Total heterotrophic bacteria (THB) were analyzed by the standard plate count method using Zobell marine agar. Total coliform (TC) and Total *vibrio* (TV) were determined by group characterization as per Bergey's manual and American Public Health Association (APHA) (APHA, 1998); after identification, counts were expressed as Colony Forming Units per milliliter (CFU/mL). All the media used for culture were procured from Himedia, Mumbai, India.

Moderate Resolution Imaging Spectrometer (MODIS) derived Chlorophyll-*a* (Chl-*a*), and sea surface temperature (SST) datasets corresponding to the dates of the bloom were obtained from the database of MODIS-Aqua MODISA_L3. The sea surface temperature and surface Chl-*a*, on 19, 20, and 26th August 2019, day averaged 4 km resolution were obtained. The data were produced by the Ocean Biology Processing Group, Goddard Space Flight Centre, USA, to locate the spatial distribution. For phytoplankton identification and enumeration, 5-L seawater samples were collected with a plastic bucket and fixed with Lugol's iodine solution and 4% formaldehyde (Sournia, 1978). Phytoplankton abundance was estimated by Utermohl's sedimentation technique (Utermohl, 1931) followed by identification and enumeration with the aid of a phase-contrast microscope (Nikon Eclipse E600 Optiphot). Phytoplankton taxa were identified by standard taxonomic monographs of diatoms, dinoflagellates, and green and blue-green algae (Desikachary and Ranjithadevi, 1986; Subrahmanyam, 1946). Chl-*a* and pheophytin pigments were estimated using the spectrophotometric method (Parsons et al., 1992). Correlation analysis was carried out on physicochemical and biological data sets. Principal component analysis was employed by generating a correlation matrix for physicochemical and phytoplankton data set followed by factorization by extraction method (Kaiser, 1958).

The bloom formed brick red-colored patches on the sea surface over a large area of approximately 16 km along the coast (Figure 1a–b). This is due to the high abundance of red *N. scintillans* cells (Figure 1c). The MODIS images of 19 and 20th show high Chl-*a* pigment proximity to the coast; however, bioluminescence was not observed on 20th August at the same time. The image from the 26th shows the advection of Chl-*a* patch away from the coast. The averaged map of sea surface temperature and chlorophyll from 13 to 29th August 2019 shows the concentration of high pigment near the shore and slowly diminishing away into the offshore region in a thin layer (Figure 1d–e). The SST images of 19 and 20th August 2019 demonstrated an unseasonal temperature gradient, indicating a relatively low temperature close to the coast, gradually replaced by moderately warmer water on 26th August. Analysis of data from automatic weather station (AWS: IMD) at Ennore coastal stations from 8 to 28th August 2019 revealed that the wind direction was limited between 180 to 270° (southwest land breeze) during the bloom period, while it was 90 to 270° (varying from east to west in each typical day). This phenomenon might have pushed or confined the bloom close to the coast. The observed wind speed from 17 to 19th August was up to 5 m/sec and there was a drop of 3 to 7°C in atmospheric temperature during this period. The daily air temperature variation was less (24.0 to 31.0°C) and was relatively small during the

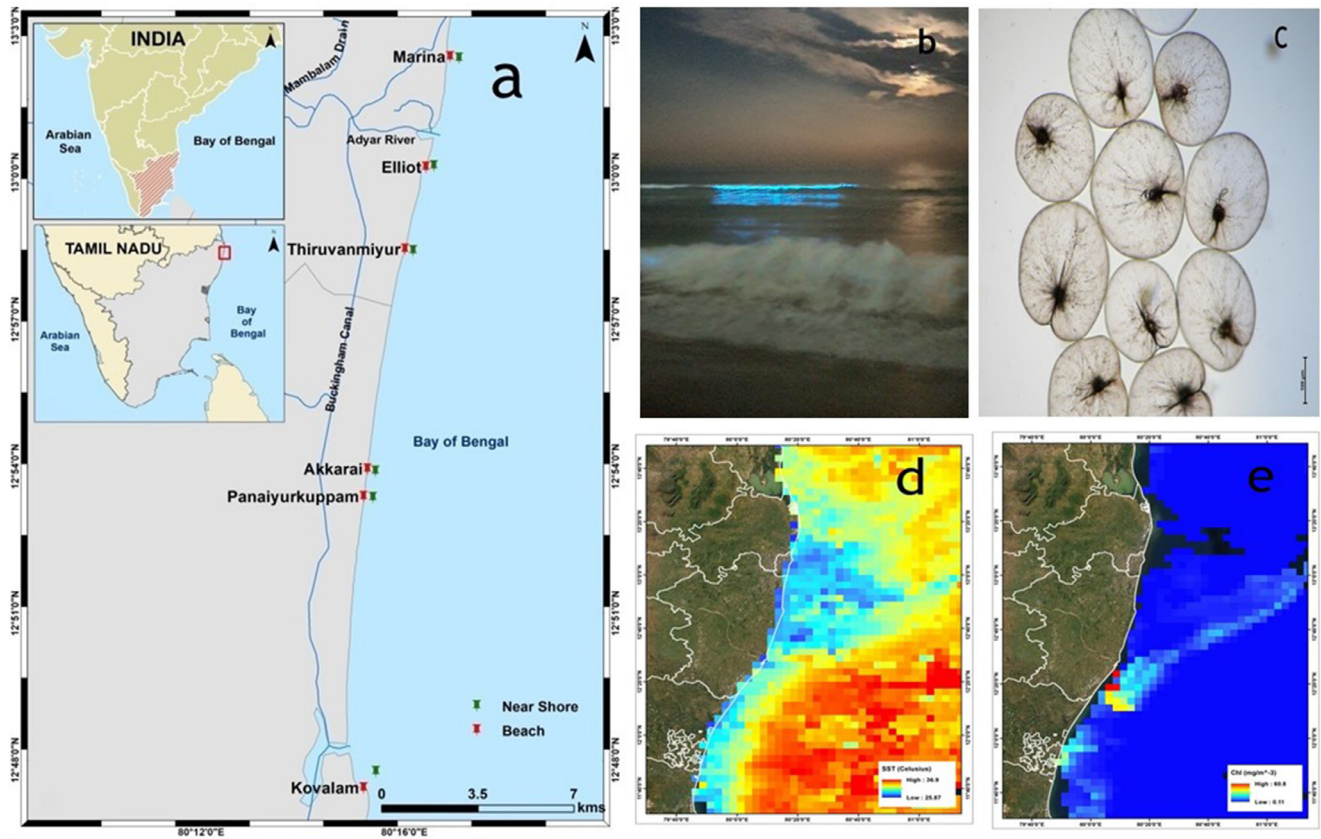


Figure 1 a) Study area map; b) bioluminescence; c) *Noctiluca scintillans*; d–e) averaged map of Sea Surface Temperature (SST) and chlorophyll: daily 4 km [MODIS-Aqua] SST – 2019-08-13 to 2019-08-29, Chl – 2019-08-13 to 2019-08-29.

bloom period, while on other days, the variations were significantly higher, from 24.0 to 37.0°C. The reduction in water temperature was likely due to the relatively high rainfall observed at Ennore (6 mm) on 14 and 15th August, resulting in subsequent runoff to the coastal water.

The surface current along the coastal waters off Chennai (north of 13.2°N) was equatorward, while it was poleward south of 12.8°N (Figure 2a–d). These two opposing currents converged into the offshore eastward current with a divergence occurring at 13°N. Station Elliot is at 13°N, while Akkarai and Thiruvanmiyur are located south of 13°N. Therefore, the departure of current was most apparent at Elliot. The total distance between Akkarai to Elliot is approximately 18 km. The current magnitude is around 0.3 m/s (1 km/h), taking about 18 h from Akkarai to Elliot, indicating the propagation of the bloom from Akkarai (South) to Elliot within a day. The maps with currents overlaid on chlorophyll confirmed that the Chl-*a* bloom pattern was oriented along the surface currents (Figure 2e). Furthermore, the surface currents were diverging and moving off the coast at Elliot, with the Chl-*a* pattern propagating along the progressive currents. The current pattern remained similar for three days from 17th to 20th August 2019.

The physicochemical and biological parameters collected at six different locations during four days of field sampling are provided in the supplementary table. The sea surface temperature varied between 25.20 to 31.00°C. The lowest was recorded from Akkarai during the bloom on the 19th and

appeared conducive for *N. scintillans* growth. Low temperature mediated *N. scintillans* blooms have been reported earlier (Dharani et al., 2004; Mohanty et al., 2007; Sahayak et al., 2005), and *N. scintillans* reproduce actively at low temperatures under experimental conditions (Cardosa, 2012). The swift disappearance of *N. scintillans* bloom can also be attributed to a change in water temperature, as *N. scintillans* is believed to thrive well within the temperature range of 16.0 to 27.0°C and diminish as the temperature rises beyond 27.0°C (Tsai et al., 2018). A low water temperature range (10.0 to 25.0°C) tends to support the growth and trigger the sudden appearance of red forms of *N. scintillans* along the coast (Elbrachter and Qi, 1998). Lower water temperature has been shown mediating phytoplankton blooms in the northern Tamil Nadu and southern Andhra coast (Mishra et al., 2006). Convincingly, an optimum amount of nutrients enhanced the diatom abundance (food), favouring *N. scintillans* growth. Further, the swift change in water temperature can also be considered a reasonable factor for *N. scintillans* blooming.

Salinity variation was insignificant to the bloom, varying from 34.30 to 34.80 PSU. However, on 19th August, a salinity drop was recorded from Elliot. The decline in salinity at Elliot was 0.50 units lower than in Marina and 0.10 units lower than in Thiruvanmiyur. The decrease in salinity occurs as a result of freshwater from the adjacent Adyar river during the low tide period. pH is comparatively higher on the 26th, maximum was at Elliot (8.15) and the lowest at

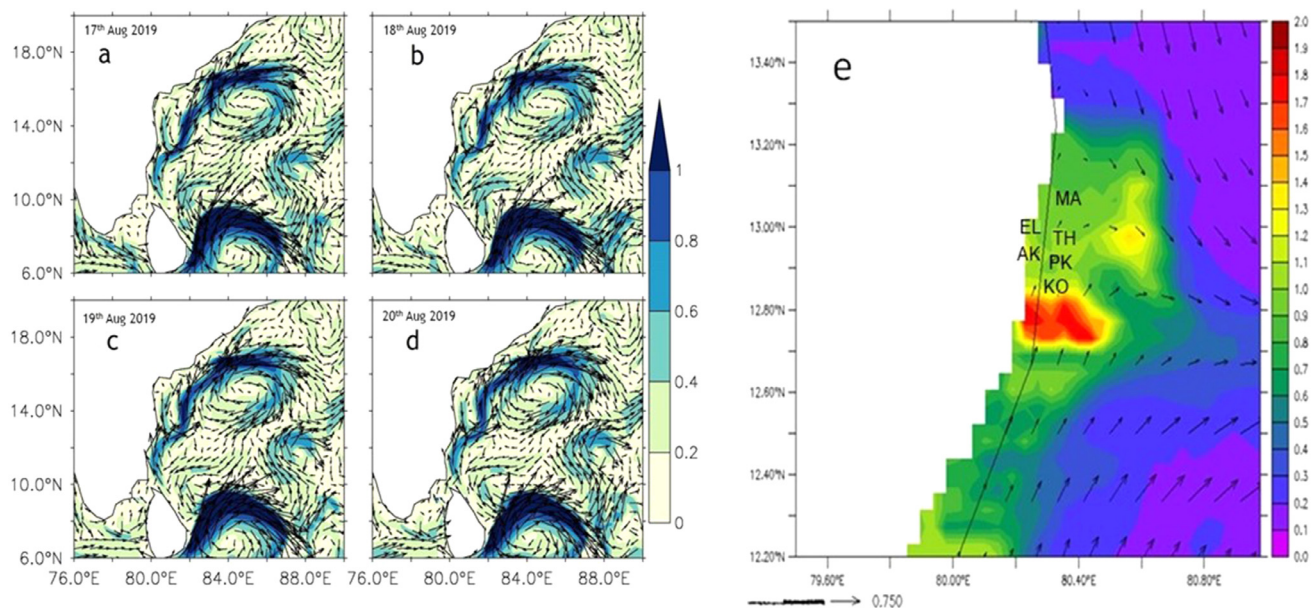


Figure 2 a–d) Current pattern showing convergence and divergence at 13°N (Latitude); e) Chl-*a* overlaid with current vectors [m/s] of 19th August 2019.

Akkarai (8.03). Initially (19 and 20th August), pH was comparatively lower at all the locations. Dissolved oxygen (DO) varied between 4.31 to 8.13 mg/L. A relatively low DO of 4.31 mg/L on 19th and 4.60 mg/L on 20th at Marina beach evidenced the rapid growth and subsequent degradation of *Noctiluca* cells. The correlation of DO with *N. scintillans* was significant and negative ($r=-0.82$; $p=0.04$) on the 26th at the shore. Substantial reduction of DO during the *N. scintillans* bloom has been commonly reported (Baliarsingh et al., 2016; Dharani et al., 2004; Mohanty et al., 2007; Sahayak et al., 2005). The average biological oxygen demand in these six locations was 3.35 mg/L and 3.27 mg/L on 19th and 20th August, respectively. The BOD values were 6.22 mg/L, at Elliot on the 19th, 4.78 mg/L at Kovalam on the 20th, and 4.48 mg/L at Thiruvannmiyur on the 26th of August 2019. A significant moderately negative correlation between BOD and *N. scintillans* ($r=-0.54$; $p=0.01$) was recorded on 26th and the highest BOD (7.38 mg/L) was noted at Elliot on 21st August 2019. This reflected the increased oxygen consumption followed by its demand by rapidly producing asexual, non-motile spores, homogenous algae, and the bacteria living in putrefying algal bloom (Dharani et al., 2004).

Although DIN (nitrite+nitrate+ammonia), phosphate, and silicate did not show any consistent pattern during bloom, their concentrations were relatively higher in Marina waters. This is attributed to the high nutrients from the adjacent Cooum river (Begum et al., 2021). DIN varied from 16.33 to 113.93 μM (highest at Kovalam) and relatively higher DIN on 26th in nearshore waters. Kovalam water is mainly influenced by the fishing community and related activities with inappropriate waste and sewage management. Phosphate fluctuated from 1.01 to 2.33 μM , and N:P ratios varied from 11.42 to 90.27, which is unlikely to limit diatom growth. The enhanced nitrogen concentration was due to the remineralization process by increased microbial activities after death and decay of pre-existing bloom (Paerl,

1987). *N. scintillans* can regenerate a significant amount of ammonia and phosphate supporting primary phytoplankton production (Tada et al., 2020). Silicate varied from 9.75 to 24.58 μM with Si:N ratio of 0.13 to 0.84 indicating limiting diatom growth. Theoretically, diatom growth will cease under silicate depletion; however, other phytoplankton can grow by utilizing available N and P (Anderson et al., 2002).

Chl-*a* concentrations increased gradually from 19th to 26th except on 21st August, values were low. It was high on 26th August in almost all the sites except for Akkarai and Kovalam. Chlorophyll-*b* (Chl-*b*) fluctuated remarkably with a defined peak of 64.78 mg/m³ on the 19th of August at Thiruvannmiyur and exceeded Chl-*a* values several times at some locations. Bloom of *N. scintillans* enhances the Chl-*b* content, as it is the prominent pigment present in dinophyceae (Dharani et al., 2004). The variation of DIN was high with relatively lower Chl-*a* except in Thiruvannmiyur on 19th August 2019. However, the scenario was reversed the next day at Elliot, Thiruvannmiyur, and Akkarai, where higher Chl-*a* content was observed. The concentration of DIN and Chl-*a* on 26th August reduced significantly supported by a strong negative correlation ($r=-0.90$; $p=0.01$), and maximum reduction in chl-*a* was recorded at Marina followed by Elliot and Panaiyurkuppam (Supplementary Table). N:P ratio versus Chl-*a* comparison indicated notable variation in terms of peaks and falls. The N:P ratio during this period represented effective nitrogen utilization, and P was not limiting the phytoplankton growth. However, on 26th August, a reduction of Chl-*a* content was recorded in Kovalam waters, possibly due to P limitation that crashed *N. scintillans* count. Earlier studies support that *Noctiluca* sp. is more vulnerable to P limitation than N (Zhang et al., 2017). The lowest Chl-*a* and *b* with corresponding low Si:N (0.13) were noted from Kovalam water on 26th August.

The highest *N. scintillans* count (19000 cells/L) was recorded at Panaiyurkuppam, the second highest at Kovalam

Table 1 Principal component analysis (PCA) loading of physicochemical parameters with phytoplankton.

Variables	PC1	PC2	PC3	PC4	PC5
WT [°C]	-0.08	-0.17	0.06	-0.53	0.15
Sal	-0.19	-0.26	0.08	0.19	0.10
pH	-0.04	0.44	-0.06	-0.32	0.28
DO [mg/L]	0.15	0.13	0.41	-0.26	0.27
BOD [mg/L]	0.23	0.10	0.13	-0.11	-0.29
NO ₂ [μM]	-0.32	-0.20	0.09	0.14	-0.14
NO ₃ [μM]	-0.38	0.15	-0.05	0.06	0.01
NH ₄ [μM]	-0.31	0.02	-0.20	-0.40	-0.01
PO ₄ [μM]	-0.10	-0.40	-0.27	-0.25	-0.17
SiO ₄ [μM]	-0.26	-0.33	0.03	-0.29	-0.18
DIN [μM]	-0.38	0.12	-0.08	-0.03	0.01
Chl- <i>a</i> [mg/m ³]	-0.15	-0.06	0.56	-0.10	0.12
Chl- <i>b</i> [mg/m ³]	-0.09	-0.19	0.55	0.01	0.00
N:P	-0.34	0.25	0.03	0.11	0.08
Si:N	0.28	-0.30	0.02	0.02	-0.08
<i>Noctiluca scintillans</i> [cells/L]	-0.03	-0.31	-0.04	0.24	0.45
<i>Thalassiosira</i> sp. [cells/L]	-0.30	0.06	0.06	0.31	0.05
Other diatoms [cells/L]	0.09	-0.20	-0.23	-0.02	0.65
Eigenvalues	6.03	3.36	2.37	1.38	1.14
%Variation	33.50	18.70	13.20	7.70	6.30
Cum. %Variation	33.50	52.20	65.30	73.00	79.30

[Variables presented with their measured units; PC values show their loadings]

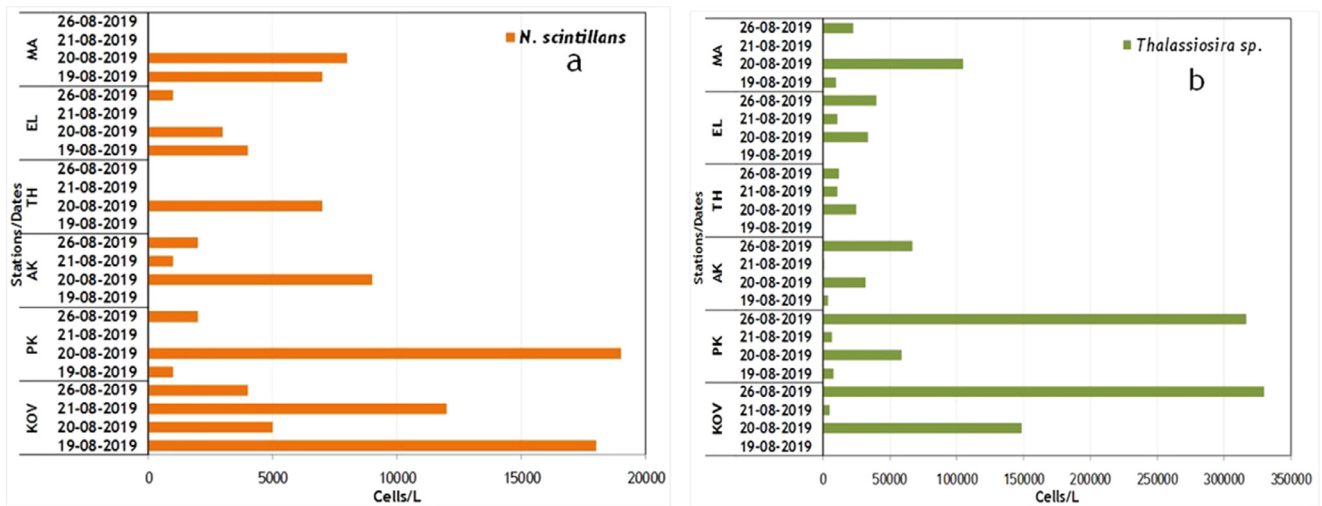


Figure 3 Density of a) *Noctiluca scintillans*; b) *Thalassiosira* sp. at Marina (MA), Elliot (EL), Thiruvanniyur (TH), Akkarai (AK), Panaiyurkuppam (PK) and Kovalam (KOV) on a) 19-08-2019; b) 20-08-2019; c) 21-08-2019; d) 26-08-2019.

on the 19th (18000 cells/L), followed by an abrupt decline (5000 cells/L) on the next day i.e., 20th August. However, the highest *N. scintillans* density (12000 cells/L) in the offshore water was encountered on 21st August, showing advection at Kovalam from shore to offshore within a day. The diatom *Thalassiosira* sp. was the successive dominant phytoplankton. The density of *N. scintillans* to *Thalassiosira* sp. was inversely related, denoting the latter being fed upon by the former. However, this condition was not similar at other locations such as Thiruvanniyur and Akkarai, where *N. scintillans* was not detected despite a fair abundance of *Thalassiosira* sp. in the respective sites. The density of *N. scin-*

tillans versus *Thalassiosira* sp. at Marina on 19th August was 7000 cells/L and 10000 cells/L, respectively, and at Elliot, it was 4000 cells/L with no *Thalassiosira* sp. Although *N. scintillans* was high at Kovalam (on 19th) bioluminescence was not observed, in contrast to Elliot water with a lesser number (4000 cells/L), where bioluminescence was observed. This can be attributed to prevailing conditions such as high wind, intense mixing, and turbulence. *N. scintillans* counts were relatively higher on 20th August at Panaiyurkuppam (19000 cells/L) compared to Akkarai (9000 cells/L) and Marina (8000 cells/L). On this day, high counts of *Thalassiosira* sp. ranging from 25000 to 149000 cells/L were noted. The

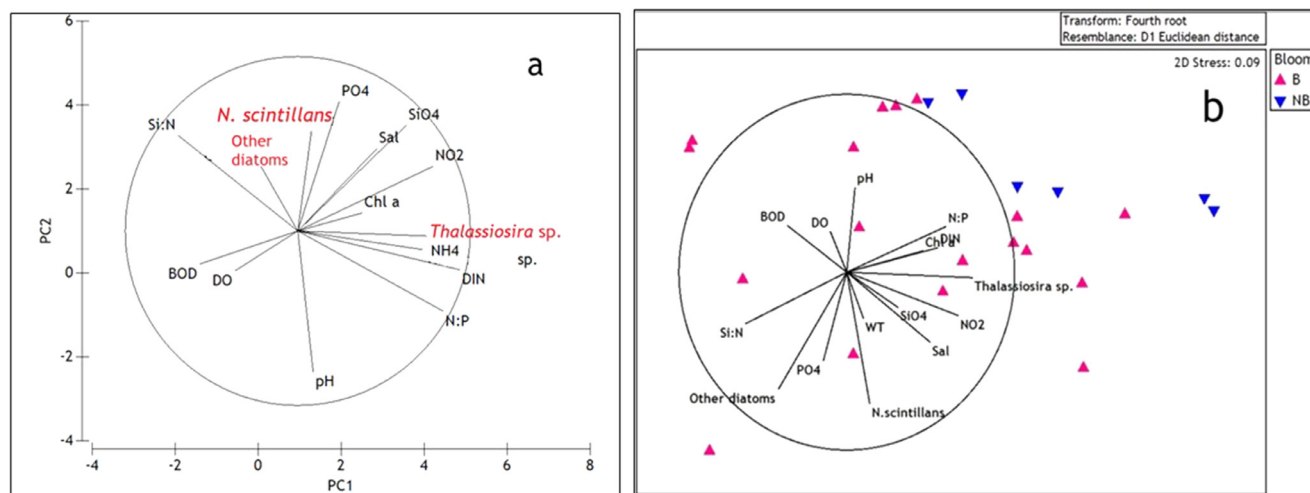


Figure 4 a) Principal component analysis (PCA) denoting the abundance and distribution of *Noctiluca scintillans*; b) non-metric Multi-Dimensional Scaling (nMDS) shows the expansion of bloom (B – bloom; NB – no bloom) inshore and offshore locations in accordance with physiochemical parameters loadings.

results confirmed that the high abundance of the diatom *Thalassiosira* sp. aided the proliferation of *N. scintillans*. This is also supported by the studies that diatom *Thalassiosira* sp. is the preferred food of *Noctiluca* (Buskey, 1995; Mcleod et al., 2012). *N. scintillans* recorded their maximum growth rate upon feeding *Thalassiosira* during the growth experiment (Buskey, 1995). Further, the study demonstrated that the high abundance of the diatom *Thalassiosira* sp. and lower water temperature (25.20, 29.00, and 29.14°C on 19, 20, and 26th, respectively) triggered *N. scintillans* to bloom along the coast. The intensified feeding activity of *N. scintillans* subsequently reduced the diatom growth; further, phosphate limited the growth of the diatoms led to the decline of *Noctiluca* in the water column (Zhang et al., 2017).

Principal Component Analysis (PCA) employed on physicochemical and biological parameters generated five components (Table 1). PC1 primarily shows the utilization of DIN (−0.38), particularly NO₃ (−0.38), and reduction in the *Thalassiosira* sp. (−0.30). A rise in BOD (0.23) was observed. PC2 revealed rising pH (0.44) in the system. PC3 indicated high Chl-*a* (0.56) and Chl-*b* (0.55) concurrently with elevated DO (0.41). PC4 represented the fall in WT (−0.53) in the system along with a growing population of *Thalassiosira* sp. (0.31) and *Noctiluca scintillans* (0.24). However, the reduction of NH₃ at this point, represented its utilization by *Thalassiosira* sp. PC5 exhibited the overall high population of *N. scintillans* in the water.

The distribution of *N. scintillans* and *Thalassiosira* sp. during the sampling period are illustrated in (Figure 3a–b). *N. scintillans* density was high on 19th at Kovalam and on 20th August at Panaiyurkuppam. The overall trend of *N. scintillans* density was following *Thalassiosira* sp. in the study locations. The PCA determined the role of physicochemical and biological parameters. The square-root transformed abundance data of *N. scintillans*, *Thalassiosira* sp., and other diatoms were subjected to Bray-Curtis similarity followed by the non-metric dimensional scaling (nMDS) method using Primer 7 and revealed various combinations of sampling locations. The distribution of *N. scintillans*, *Thalassiosira* sp., and other diatoms along with other influencing

physicochemical parameters are represented on the ordination plane (Figure 4a). The non-metric Multi-Dimensional Scaling (nMDS) plot showed moderate similarities between bloom (B) and no bloom (NB) locations (Figure 4b). The nMDS obtained a low-stress value (0.09) directed towards a lower stress level of 0.01, indicating a better representation of data. The results infer that bloom primarily occurred in the shore locations, with its extension recorded in the offshore region.

Increased bacterial population associated with phytoplankton bloom has been reported (Thomas et al., 2014). THB counts fluctuated and varied from 2.56×10^6 to 6.92×10^6 CFU/mL. The lowest count was recorded in Panaiyurkuppam and the maximum in Elliot on 26th and 19th August, respectively. Total coliform (TC) and total vibrio (TV) ranged from 2.90×10^2 to 3.60×10^4 , 1.20×10^4 to 3.16×10^5 CFU/mL, respectively. A peak in the bacterial population was due to the declining phase of the algal bloom. The correlation between increased microbial growth and the phytoplankton decline phase was noted by previous authors (Dharani et al., 2004; Yang et al., 2012). Phytoplankton bloom increases the particulate and dissolved organic matter in the water column resulting in an elevated bacterial population as dissolved organic matter is the primary energy source for bacteria in the ocean (Thomas et al., 2014). Our observations showed that after bioluminescence on 19th August, *N. scintillans* counts declined and microbial growth increased. Higher THB, TC, and TV counts were recorded during the early two days of bloom and decreased gradually on 26th August to varying extent. Bioluminescence was observed due to turbulence and intense wave breaking in the surf zone, stimulating bioluminescence in *N. scintillans* cells. However, the cells of *N. scintillans* and *Thalassiosira* sp. persisted till 26th August along the coastal waters. Within two days after the appearance of bioluminescence, the blooming cells slowly degenerated and moved away by the current, and finally declined.

Globally several studies have proposed various environmental factors responsible for the bloom and distribution of *Noctiluca scintillans*. This study reveals the prevailing eco-

logical conditions during the development of *N. scintillans* blooms and tracks bioluminescence along the coastal waters of Chennai for the first time. The variations in environmental factors such as atmospheric temperature associated with high rainfall resulted in changing the sea surface temperature, the availability of dissolved nutrients, and the high abundance of *Thalassiosira* sp. are responsible for the proliferation of *Noctiluca scintillans*. It is concluded that the study will help in understanding the importance of various physicochemical characteristics that are applicable to predict the formation of harmful planktonic blooms and their impact on other marine organisms and ecosystems.

Declaration of competing interests

The authors declare that they have no known competing financial interests or personal relationships that could have appeared to influence the work reported in this paper.

Acknowledgment

We are thankful to the Secretary, Ministry of Earth Sciences, Government of India, and Director, NCCR, for their support and encouragement. We are thankful to Mr. Dave Sivyer of Cefas, UK, for editing the draft. The study is funded by the Ministry of Earth Sciences, Government of India. The manuscript is NCCR publication contribution no MS-381.

Supplementary materials

Supplementary material associated with this article can be found, in the online version, at <https://doi.org/10.1016/j.oceano.2022.06.005>.

References

- Aiyar, R.G., 1936. Mortality of fish of the Madras coast in June 1935. *Curr. Sci.* 5, 488–489.
- Anderson, D.M., Glibert, P.M., Burkholder, J.M., 2002. Harmful algal blooms and eutrophication: Nutrient sources, composition, and consequences. *Estuaries* 25, 704–726. <https://doi.org/10.1007/BF02804901>
- APHA, 1998. Standards methods for the examination of water and wastewater, 20th edn. American Public Health Association, Washington DC.
- Baliarsingh, S.K., Lotliker, A.A., Trainer, V.L., Wells, M.L., Parida, C., Sahu, B.K., Srichandan, S., Sahoo, S., Sahu, K.C., Kumar, T.S., 2016. Environmental dynamics of red *Noctiluca scintillans* bloom in tropical coastal waters. *Mar. Pollut. Bull.* 111 (1–2), 277–286. <https://doi.org/10.1016/j.marpolbul.2016.06.103>
- Begum, M., Saravana Kumar, C., Naik, S., Pradhan, U.K., Panda, U.S., Mishra, P., 2021. Indian coastal waters: a concoction of sewage indicator bacteria! An assessment on recreational beaches. *Env. Mon. Ass.* 193 (455), 1–21.
- Buskey, E.J., 1995. Growth and bioluminescence of *Noctiluca scintillans* on varying algal diets. *J. Plankton Res.* 17 (1), 29–40.
- Cardosa, L.S., 2012. Bloom of *Noctiluca scintillans* (Macartney) Kofoid & Swezy (dinophyceae) in Southern Brazil. 2012. *Braz. J. Oceanogr.* 60 (2), 265–268.
- Desikachary, T.V., Ranjithadevi, K.A., 1986. Atlas of Diatoms. Madras Science Foundation, Madras 367 pp.
- Dharani, G., Nazar, A.K.A., Kanagu, L., Venkateswaran, P., Kumar, T.S., Ratnam, Krupa, Venkatesan, R., Ravindran, M., 2004. On the recurrence of *Noctiluca scintillans* bloom in Minnie Bay, Port Blair: Impact on water quality and bioactivity of extracts. *Cur. Sci.* 87 (7), 990–994.
- Elbrachter, M., Qi, Y.Z., 1998. Aspects of *Noctiluca* (Dinophyceae) population dynamics. In: Anderson, D.M., Cambella, A.D., Hallegraeff, G.M. (Eds.), *Physiological ecology of harmful algal blooms*. Springer, London, 315–336.
- Gomes, H.do.R., Goes, J.I., Matondkar, S.G.P., Buskey, E.J., Basu, S., Parab, S., Thoppil, P., 2014. Massive outbreaks of *Noctiluca scintillans* blooms in the Arabian Sea due to spread of hypoxia. *Nat. Commun.* 5, 4862. <https://doi.org/10.1038/ncomms5862>
- Gopakumar, G., Sulochanan, B., Venkatesan, V., 2009. Bloom of *Noctiluca scintillans* (Macartney) in Gulf of Mannar, southeast coast of India. *J. Mar. Biol. Ass. India* 51, 75–80.
- Grasshoff, K., Kremling, K., Ehrhardt, M., 1999. *Methods of seawater analysis*, 3rd edn. Verlag Chemie, Weinheim, Germany.
- Joseph, T., Shaiju, P., Laluraj, C.M., Balachandran, K.K., Nair, M., George, R., Nair, K.K.C., Sahayak, S., Prabhakaran, M.P., 2008. Nutrient environment of red tide-infested waters off south-west coast of India. *Environ. Monit. Assess.* 143 (1–3), 355–361. <https://doi.org/10.1007/s10661-007-9938-1>
- Kaiser, H.F., 1958. The varimax criteria for analytical rotation in factor analysis. *Psychometrika* 23 (3), 187–200.
- Kofoed, C.A., Swezy, O., 1921. The free-living unarmored Dinoflagellata. *Memoirs of the University of California.* 5 (i-viii) 1–562. <https://www.biodiversitylibrary.org/page/20306447>.
- Liu, L.Y., Hastings, J.W., 2007. Two different domains of the luciferase gene in the heterotrophic dinoflagellate *Noctiluca scintillans* occur as two separate genes in photosynthetic species. *Proc. Nat. Acad. Sci.* 104, 696–701. <https://doi.org/10.1073/pnas.0607816103>
- Mcleod, D.J., Hallergaeff, G.M., Hosie, G.W., Richardson, A.J., 2012. Climate-driven range expansion of the red-tide dinoflagellate *Noctiluca scintillans* into the Southern Ocean. *J. Plankton Res.* 34 (4), 332–337.
- Mishra, S., Sahu, G., Mohanty, A.K., Singh, S.K., Panigrahy, R.C., 2006. Impact of the diatom *Asterionella glacialis* (Castracane) bloom on the water quality and phytoplankton community structure in coastal waters of Gopalpur sea, Bay of Bengal. *Asian J. Water, Environ. Pollut.* 3, 71–77.
- Mohanty, A.K., Satpathy, K.K., Sahu, Gouri, Sasmal, S.K., Sahu, B.K., Panigrahy, R.C., 2007. Red tide of *Noctiluca scintillans* and its impact on the coastal water quality of the near-shore waters, off the Rushikulya River, Bay of Bengal. *Curr. Sci.* 93 (5), 616–618.
- Naqvi, S.W.A., George, M.D., Narvekar, P.V., Jayakumar, D.A., Shailaja, M.S., Sardesai, S., Sarma, V.V.S.S., Shenoy, D.M., Hema, N., Maheshwaran, P.A., Krishnakumari, K., Rajesh, G., Sudhir, A.K., Binu, M.S., 1998. Severe fish mortality associated with 'red tide' observed in the sea off Cochin. *Curr. Sci.* 75, 543–544.
- Padmakumar, K.B., Sree Renjima, G., Fanimol, C.L., Menon, N.R., Sanjeevan, V.N., 2010. Preponderance of heterotrophic *Noctiluca scintillans* during a multi-species diatom bloom along the southwest coast of India. *Int. J. Oceans Oceanogr.* 4 (1), 255–263.
- Paerl, 1987. Dynamics of blue-green algal (*Microcystis aeruginosa*) blooms in the lower Neuse River, NC.: Causative factors and potential controls. *Water Resources Research Institute of the University of North Carolina*, 229 pp.
- Parsons, T.R., Maita, Y., Lalli, C.M., 1992. *A Manual of chemical and biological methods for seawater analysis*. Pergamon Press, Oxford, New York.

- Raj, K.D., Mathews, G., Obura, D.O., Laju, R.L., Bharath, M.S., Kumar, P.D., Arasamuthu, A., Kumar, T.K.A., Edward, J.K.P., 2020. Low oxygen levels caused by *Noctiluca scintillans* bloom kills corals in the Gulf of Mannar, India. *Sci. Rep.* 10 (1), 22133. <https://doi.org/10.1038/s41598-020-79152-x>
- Sahayak, S., Jyothibabu, R., Jayalakshmi, K.J., Habeebrehman, H., Sabu, P., Prabhakaran, M.P., Jasmine, P., Shaiju, P., Rejomon, G., Threslamma, J., Nair, K.K.C., 2005. Red tide of *Noctiluca millaris* off south of Thiruvananthapuram subsequent to the “stench event” at the southern Kerala coast. *Curr. Sci.* 89 (9), 1472–1473. <http://drs.nio.org/drs/handle/2264/338>.
- Sarma, V.V.S.S., Patil, J.S., Shankar, D., Anil, A.C., 2019. Shallow convective mixing promotes massive *Noctiluca scintillans* bloom in the northeastern Arabian Sea. *Mar. Poll. Bull.* 138, 428–436. <https://doi.org/10.1016/j.marpolbul.2018.11.054>
- Shaju, S.S., Akula, R.R., Jabir, T., 2018. Characterization of light absorption coefficient of red *Noctiluca scintillans* bloom in the South Eastern Arabian Sea. *Oceanologia* 60 (3), 419–425. <https://doi.org/10.1016/j.oceano.2017.12.002>
- Sournia, A.Ed., 1978. *Phytoplankton Manual*. United Nations Educational, Scientific and Cultural Organization, Paris.
- Subrahmanyam, R., 1946. A systematic account of the marine plankton diatoms of Madras coast. *Proc. Ind. Acad. Sci.* 24, 85–197.
- Tada, K., Asahi, T., Kitatsuji, S., Nomura, M., Yamaguchi, H., Ichimi, K., 2020. Low-active high-density *Noctiluca scintillans* cells in surface seawater. *Oceanologia* 62 (3), 402–407. <https://doi.org/10.1016/j.oceano.2020.02.005>
- Thomas, A.M., Sanilkumar, M.G., Vijayalakshmi, K.C., Mohamed Hatha, A.A., Saramma, A.V., 2014. Dynamic Changes in Bacterial Population and Corresponding Exoenzyme Activity in Response to a Tropical Phytoplankton Bloom *Chattonella marina*. *J. Mar. Biol.* 2014, art. ID 918614, 6 pp. <https://doi.org/10.1155/2014/918614>
- Tsai, S.F., Wu, L.Y., Chou, W.C., Chiang, K.P., 2018. The dynamics of a dominant dinoflagellate, *Noctiluca scintillans* in the subtropical coastal waters of the Matsu archipelago. *Mar. Poll. Bull.* 127, 2553–2558. <https://doi.org/10.1016/j.marpolbul.2017.12.041>
- Turkoglu, M., 2013. Red tides of the dinoflagellate *Noctiluca scintillans* associated with eutrophication in the Sea of Marmara (the Dardanelles, Turkey). *Oceanologia* 55 (3), 709–732. <https://doi.org/10.5697/oc.55-3.709>
- Utermohl, V.H., 1931. Neue Wege in der quantitativen Erfassung des Planktons. (Mit besondere Beriicksichtigung des Ultraplanktons). *Verh. Int. Verein. Theor. Angew. Limnol.* 5, 567–595.
- Venugopal, P., Haridas, P., Madhupratap, M., Rao, T.S.S., 1979. Incidence of Red Water Along South Kerala Coast. *Ind. J. Mar. Sci.* 8, 94–97. <http://nopr.niscair.res.in/handle/123456789/39189>.
- Yang, C., Li, Y., Zhou, Y., Zheng, W., Tian, Y., Zheng, T., 2012. Bacterial community dynamics during a bloom caused by *Akashiwo sanguinea* in the Xiamen sea area, China. *Har. Algae.* 20, 132–141. <https://doi.org/10.1016/j.hal.2012.09.002>
- Zhang, S., Liu, H., Glibert, P.M., Guo, C., Ke, Y., 2017. Effects of prey of different nutrient quality on elemental nutrient budgets in *Noctiluca scintillans*. *Nat. Sci. Rep.* 7, 7622. <https://doi.org/10.1038/s41598-017-05991-w>

Available online at www.sciencedirect.com

ScienceDirect

journal homepage: www.journals.elsevier.com/oceanologia

SHORT COMMUNICATION

Sea spray volume flux estimation using joint statistics of wind and waves

Dag Myrhaug*, Bernt J. Leira, Gowtham Radhakrishnan, Håvard Holm

Department of Marine Technology, Norwegian University of Science and Technology (NTNU), Trondheim, Norway

Received 8 February 2022; accepted 23 July 2022

Available online 6 August 2022

KEYWORDS

Sea spray volume flux;
Joint wind and wave conditions;
Wind waves;
Stochastic method

Abstract This article provides estimates of the sea spray volume flux using joint statistics of wind and waves. This is achieved by combining the sea spray volume flux parameterization proposed by Xu et al. (2021) with the joint statistics of wind and waves provided by Bitner-Gregersen (2015). Both the sea spray volume flux formula and the joint statistics of wind and waves represent conditions for wind waves from the North-West Shelf of Western Australia. The expected value and the variance of the sea spray volume flux for a range of realistic wind and wave conditions are presented, as well as an illustrative example. Comparison is also made with data from Xu et al. (2021) showing a reasonable agreement for the relevant subset of the data.

© 2022 Institute of Oceanology of the Polish Academy of Sciences. Production and hosting by Elsevier B.V. This is an open access article under the CC BY-NC-ND license (<http://creativecommons.org/licenses/by-nc-nd/4.0/>).

1. Introduction

Knowledge of the sea spray is important in order to understand the interaction between the atmosphere and the ocean as the air-sea interface represents their coupling by

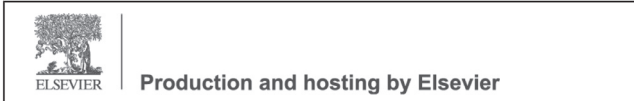
exchanging heat and momentum. This contributes to air-sea mixing processes which occur across the ocean surface, and knowledge about these processes is crucial in climate and ocean studies. The presence of the sea spray droplets may also affect the stability of the air-sea boundary layer. The physical processes in the air-sea mixed layer are commonly highly nonlinear depending on relevant air and sea parameters. Due to the lack of consistent theories on the sea spray, parameterizations in terms of bulk formulae are often used to represent this effect in atmospheric and weather forecasting models. Comprehensive reviews of the topic are given in, for instance, Massel (2007), Veron (2015) and most recently in Xu et al. (2021).

Xu et al. (2021) (hereafter referred to as X21) proposed a bulk formula for the wind-wave-dependent sea spray volume flux parameterized in terms of the mean wind speed

* Corresponding author at: Department of Marine Technology (NTNU), Otto Nielsens vei 10, NO-7491 Trondheim, Norway.

E-mail address: dag.myrhaug@ntnu.no

Peer review under the responsibility of the Institute of Oceanology of the Polish Academy of Sciences.



and the wave steepness representing conditions for wind waves (see Eq. (1)). This parameterization is based on a best fit to data collected during the period from January to October of 2015 from field observations situated at a 125 m water depth on the North-West Shelf of Western Australia (see X21 for more details of their work as well as a thorough review of the relevant literature).

The objective of this article is to demonstrate how the statistical properties of the sea spray volume flux can be estimated by using the X21 bulk formula together with joint statistics of wind and waves. The joint statistics of wind and waves are adopted from Bitner-Gregersen (2015) (hereafter referred to as BG15) given in terms of a parametric model for the joint probability density function of the mean wind speed, the significant wave height and the spectral peak period representing wind waves from the same region as the X21 formula is based upon. Results are provided in terms of the expected value and the variance of the sea spray volume flux for a range of sea state conditions.

In future applications of the X21 sea spray volume flux parameterization, it should be considered to implement the joint statistical properties of wind and waves as demonstrated here. It is believed that this will strengthen the application of the sea spray volume flux formula in meteorological and oceanographic models.

The article is organized as follows. This introduction is followed by the background of the sea spray parameterization used. Then the estimation of the sea spray volume flux using wind and waves statistics including an example is given. Comparison is also made with the X21 data. Finally, a summary and the main conclusions are provided.

2. Background

The bulk formula for the wind-wave-dependent sea spray volume flux V based on field measurements proposed by X21 is given as

$$\frac{V}{U_{10}} = 1.99\sqrt{s} \times 10^{-8} \quad (1)$$

Here U_{10} is the mean wind speed at 10 m above the sea surface, $s = H_s k_m / 2$ is the mean wave steepness, H_s is the significant wave height, $k_m = 2\pi / L_m$ is the mean wave number corresponding to the mean wave length for deep water waves $L_m = (g/2\pi)T_m^2$, T_m is the mean wave period, and g is the acceleration due to gravity. The present study uses joint statistics of U_{10} , H_s and the spectral peak period T_p . Thus, the relationship $T_m = 0.834T_p$ is used (Tucker and Pitt, 2001), which is valid for a mean JONSWAP wave amplitude spectrum with a spectral bandwidth parameter of 3.3. It should be noted that Eq. (1) is valid for $U_{10} \leq 22 \text{ m s}^{-1}$ and for H_s up to about 7 m (see Figure 3b in X21). Thus, based on this Eq. (1) is re-arranged to

$$v \equiv \frac{V}{CH_s^{\frac{1}{2}}} = uT_p^{-1}; 0 \leq u \leq u_1 = 22 \text{ m s}^{-1} \quad (2)$$

where $C = 3.38 \times 10^{-8} \text{ s m}^{-1/2}$ and $u \equiv U_{10}$. It should be noted that the grouping of the variables made in Eq. (2) is used since H_s is taken as the marginal variable in the subsequent analysis in Section 3.

One should also note that an alternative to Eq. (1) is to relate the sea spray volume flux to the wave slope variance. Bruch et al. (2021) studied the sea spray generation dependence on combined wind and waves by performing wind-wave tunnel experiments. The early work of Cox and Munk (1956) established a relationship between the wave slope variance and the wind speed. This relationship has been addressed by many researchers and more recently by Lenain et al. (2019) by performing airborne measurements of surface wind and slope statistics over the ocean. Thus, the recent knowledge of the relationship between the sea spray volume flux and the wave slope variance for combined wind and waves should be utilized in future studies by including the joint statistics of wind and waves.

3. Estimating sea spray volume flux using wind and wave statistics

3.1. Statistical expressions

Parametric models for the joint probability density functions (PDFs) of $u \equiv U_{10}$, H_s and T_p are provided in the literature, see for example a review by BG15. In the present study, the joint PDF of u , H_s and T_p provided in Appendix A is used by applying the relationship $T_m = 0.834T_p$ (see Section 2). This PDF is obtained as a fit to hindcast data, representing wind-sea from the North-West Shelf of Australia for the period 1994–2005 at a 250 m water depth. The data represents H_s up to about 7 m, i.e. similar, as for the X21 data. Although the BG15 PDF does not cover the same period as the X21 data (from January to October of 2015), this PDF is taken to illustrate the wind and wave conditions in the region, justifying the use of these data together with the X21 formula.

Here the conditional expected value of V given H_s , $E[V|H_s]$, and the conditional variance of V given H_s , $\text{Var}[V|H_s]$, are considered. Thus, from Eq. (2) it follows that the calculation of $E[V|H_s]$ and $\text{Var}[V|H_s]$ requires knowledge of $E[v^n|H_s]$ for $n = 1, 2$. Use of the results in Appendix A yields

$$E[v^n|H_s] = E[u^n|H_s]E[T_p^{-n}|H_s] \quad (3)$$

where (Bury, 1975, Ch. 2)

$$E[T_p^{-n}|H_s] = \int_0^\infty T_p^{-n} p(T_p|H_s) dT_p = \exp\left(-n\mu + \frac{1}{2}n^2\sigma^2\right) \quad (4)$$

and $p(T_p|H_s)$ is the conditional PDF of T_p given H_s (Eq. (A4)), and μ (Eqs. (A5), (A7)) and σ^2 (Eqs. (A6), (A8)) are the mean value and the variance, respectively, of $\ln T_p$. It should be noted that Eq. (3) is based on assuming that $u|H_s$ and $T_p|H_s$ are statistically independent (see Eq. (A1) in Appendix A).

Furthermore, based on Eq. (1), V is valid within a finite interval of u , and thus, the conditional PDF of u given H_s , $p(u|H_s)$ in Eq. (A9) in Appendix A follows the truncated Weibull PDF

$$p_t(u|H_s) = \frac{1}{N} p(u|H_s); 0 \leq u \leq u_1 = 22 \text{ m s}^{-1} \quad (5)$$

where

$$N = 1 - \exp\left[-\left(\frac{u_1}{\theta}\right)^\beta\right] \quad (6)$$

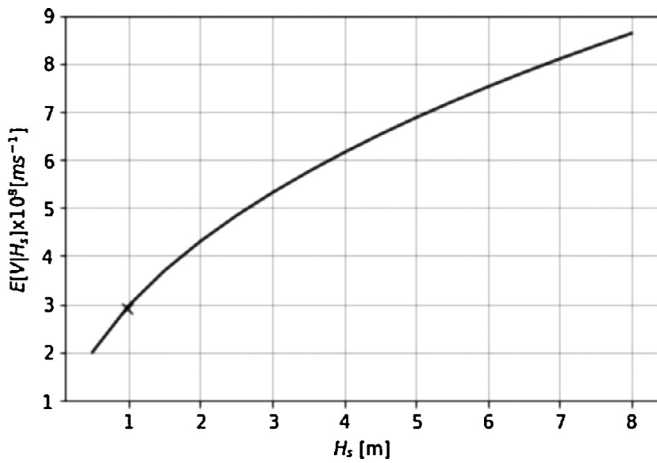


Figure 1 $E[V|H_s]$ versus H_s . The value corresponding to $E[H_s] = 0.97$ m is highlighted by a cross (x).

Thus, it follows that (Bury, 1975, Ch. 2)

$$E[u^n|H_s] = \int_0^{u_1} u^n p_t(u|H_s) dH_s = \frac{1}{N} \theta^n \left\{ \Gamma\left(1 + \frac{n}{\beta}\right) - \Gamma\left[1 + \frac{n}{\beta}, \left(\frac{u_1}{\theta}\right)^\beta\right] \right\} \quad (7)$$

where Γ is the gamma function, $\Gamma(x, y)$ is the incomplete gamma function, n is a real number (not necessarily an integer), $\Gamma(x, 0) = \Gamma(x)$ and $\Gamma(x, \infty) = 0$.

Now, Eqs. (2)–(4) and (7) yield

$$E[V|H_s] = \frac{1}{N} \theta \left\{ \Gamma\left(1 + \frac{1}{\beta}\right) - \Gamma\left[1 + \frac{1}{\beta}, \left(\frac{u_1}{\theta}\right)^\beta\right] \right\} \exp\left(-\mu + \frac{1}{2}\sigma^2\right) \quad (8)$$

$$E[v^2|H_s] = \frac{1}{N} \theta^2 \left\{ \Gamma\left(1 + \frac{2}{\beta}\right) - \Gamma\left[1 + \frac{2}{\beta}, \left(\frac{u_1}{\theta}\right)^\beta\right] \right\} \exp(-2\mu + 2\sigma^2) \quad (9)$$

Furthermore (Bury, 1975, Ch. 2)

$$\text{Var}[v|H_s] = E[v^2|H_s] - (E[v|H_s])^2 \quad (10)$$

by substituting Eqs. (8) and (9). Then

$$E[V|H_s] = CH_s^{\frac{1}{2}} E[v|H_s] \quad (11)$$

and the coefficient of variation is

$$R[V|H_s] = R[v|H_s] = \frac{(\text{Var}[v|H_s])^{1/2}}{E[v|H_s]} \quad (12)$$

Figures 1 and 2 depict $E[V|H_s]$ and $R[V|H_s]$, respectively, versus H_s in the range 0.5 m to 8 m. From Figure 1 it appears that $E[V|H_s]$ increases from $2 \times 10^{-8} \text{ m s}^{-1}$ to $8.62 \times 10^{-8} \text{ m s}^{-1}$ as H_s increases from 0.5 m to 8 m. From Figure 2 it appears that $R[V|H_s]$ decreases from 0.328 to 0.071 as H_s increases in the same interval. Thus, this behaviour indicates that the mean value of sea spray volume flux increases as the wave activity increases (Figure 1), while the ratio between the standard deviation of the sea spray volume flux and the mean value of the sea spray volume flux decreases as the wave activity increases (Figure 2).

3.2. Example and comparison with Xu et al. (2021)

Next, an example is given by estimating the results corresponding to the expected value of H_s , $E[H_s]$. Then, from Eqs. (A2) and (A3) it follows that (Bury, 1975, Ch. 2))

$$E[H_s] = \gamma + \alpha \Gamma\left(1 + \frac{1}{\rho}\right) = 0.322 + 0.605 \Gamma\left(1 + \frac{1}{0.867}\right) = 0.97 \text{ m} \quad (13)$$

Substitution in Eqs. (A5)–(A8) gives

$$\mu = 1.7903, \sigma = 0.1799 \quad (14)$$

while substitution in Eqs. (A10)–(A13) gives

$$\beta = 6.7385, \theta = 5.5172 \quad (15)$$

Then, it follows that $\left(\frac{u_1}{\theta}\right)^\beta = 1.12 \times 10^4$, which substituted in Eq. (6) gives N very close to 1, showing that truncation of the PDF in Eq. (5) is not required. It should be noted that this is the case for H_s exceeding about 0.5 m. Substitution of Eq. (15) in Eqs. (8)–(12) by neglecting the terms containing the incomplete gamma functions yields $E[v|E[H_s]] = 0.8734$, $E[v^2|E[H_s]] = 0.8118$, $\text{Var}[v|E[H_s]] = 0.04897$, $E[V|E[H_s]] = 2.91 \times 10^{-8} \text{ m s}^{-1}$, $R[V|E[H_s]] = 0.253$, respectively. The two latter values correspond to those depicted and highlighted in Figures 1 and 2, respectively.

Finally, the present results are compared with those shown in Figure 8 of X21 depicting the data of V versus U_{10} , which is reproduced in Figure 3. The comparison with the X21 data is made as follows using the results in Figures 1

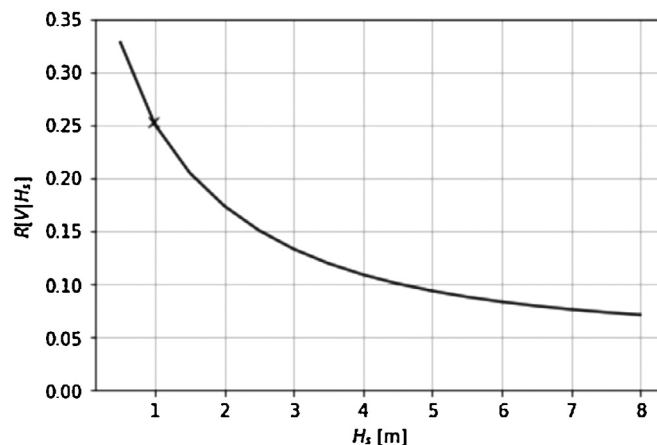


Figure 2 $R[V|H_s]$ versus H_s . The value corresponding to $E[H_s] = 0.97$ m is highlighted by a cross (x).

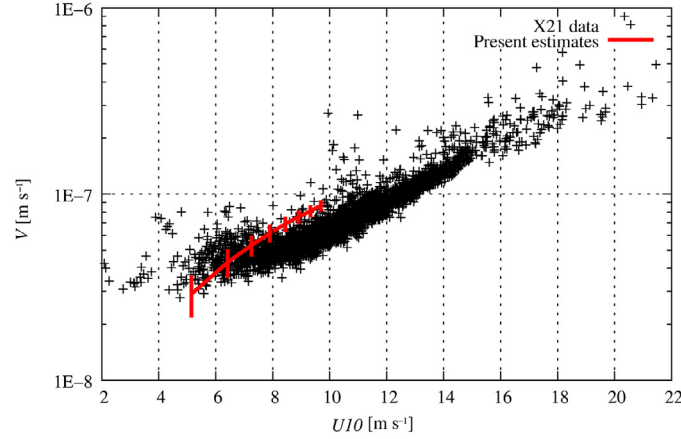


Figure 3 V versus U_{10} : +X21 data; the present estimates of $E[V|H_s] \pm SD$ for $H_s = 0.97, 2, 3, 4, 5, 6, 7, 8$ m corresponds to $U_{10} = 5.15, 6.42, 7.25, 7.90, 8.44, 8.91, 9.32, 9.69$ $m s^{-1}$.

and 2. First, the results in the example are used, where it follows from Eq. (7) that (neglecting the term containing the incomplete gamma function) $E[u^n|E[H_s]] = \theta^n \Gamma(1 + \frac{n}{\beta})$. Then, in this case, by using Eq. (15), $E[u|E[H_s]] = 5.15$ $m s^{-1}$. Furthermore, from the present example results it follows that the conditional standard deviation of V given $E[H_s] = 0.97$ m by using Eq. (12) is $SD = 0.736 \times 10^{-8}$ $m s^{-1}$, and accordingly $E[V|E[H_s]] \pm SD = (3.65 \times 10^{-8}, 2.17 \times 10^{-8})$ $m s^{-1}$. Next, for $H_s = 2, 3, 4, 5, 6, 7, 8$ m (i.e. covering the range of H_s for the X21 and the BG15 data), $E[u|H_s] = 6.42, 7.25, 7.90, 8.44, 8.91, 9.32, 9.69$ $m s^{-1}$, which combined with the results in Figures 1 and 2 yield $E[V|H_s] \pm SD$ as depicted in Figure 3. Thus, it appears that there is an overlap between these estimated values and some of the X21 data. However, the present comparison should be considered as preliminary since there is no consistency between the wind and wave conditions for the X21 data and the BG15 data. Thus, a further comparison is required in order to validate the present approach.

4. Summary and conclusions

The objective of this study has been to demonstrate how the statistical properties of the sea spray volume flux can be estimated by using the Xu et al. (2021) sea spray bulk formula together with joint statistics of wind and waves. This is achieved by combining the proposed sea spray formula with joint wind and wave statistics from Bitner-Gregersen (2015). Both the parametrized sea spray volume flux and the joint statistics of wind and waves represent conditions for wind and waves from the North-West Shelf of Western Australia. Results are provided in terms of the expected value and the variance of the sea spray volume flux for a range of sea state conditions representing wind waves. It appears that the conditional mean value of the sea spray volume flux for given H_s increases from 2×10^{-8} $m s^{-1}$ to 8.62×10^{-8} $m s^{-1}$ as H_s increases from 0.5 m to 8 m. The corresponding ratio between the conditional standard deviation and the conditional mean value decreases from 0.328 to 0.071 as H_s increases in the same interval.

Comparison is also made with the Xu et al. (2021) data showing reasonable agreement for the relevant subset of the data.

In future applications of the Xu et al. (2021) sea spray volume flux parameterization, it should be considered to implement the joint statistical properties of wind and waves as demonstrated here. This should enhance the utilization of the parameterization in atmospheric and weather forecasting models since a bulk formula is frequently used in these forecasting models as the sea spray droplets affect the stability of the air-sea boundary layer.

Acknowledgements

Dr. Xingkun Xu is acknowledged for providing the data shown in Figure 3.

Appendix A. Joint PDF of U_{10} , H_s and T_p

Here the joint PDF of $u \equiv U_{10}$, H_s and T_p provided by BG15 is used. This distribution is obtained as a fit to hindcast data representing wind-sea from the North-West Shelf of Australia sampled every hour for the period 1994 – 2005 at a 250 m water depth (see BG15 for more details). This joint PDF is given as (i.e. assuming that $u|H_s$ and $T_p|H_s$ are statistically independent)

$$p(H_s, T_p, u) = p(T_p|H_s)p(u|H_s)p(H_s) \quad (A1)$$

where $p(H_s)$ is the marginal PDF of H_s given by the 3-parameter Weibull distribution

$$p(H_s) = \frac{\rho}{\alpha} \left(\frac{H_s - \gamma}{\alpha} \right)^{\rho-1} \exp \left\{ - \left(\frac{H_s - \gamma}{\alpha} \right)^\rho \right\}; H_s \geq \gamma \quad (A2)$$

with the Weibull parameters α, ρ, γ given by

$$\alpha = 0.605 \text{ m}, \rho = 0.867, \gamma = 0.322 \text{ m} \quad (A3)$$

and H_s is in meters.

Furthermore, $p(T_p|H_s)$ is the conditional PDF of T_p given H_s represented by the lognormal PDF

$$p(T_p|H_s) = \frac{1}{\sqrt{2\pi}\sigma T_p} \exp \left[- \frac{(\ln T_p - \mu)^2}{2\sigma^2} \right] \quad (A4)$$

where μ and σ are the mean value and the standard deviation, respectively, of $\ln T_p$ given as

$$\mu = a_1 + a_2 H_s^{a_3} \tag{A5}$$

$$\sigma = b_1 + b_2 \exp(b_3 H_s) \tag{A6}$$

with

$$(a_1, a_2, a_3) = (0, 1.798, 0.134) \tag{A7}$$

$$(b_1, b_2, b_3) = (0.042, 0.224, -0.500) \tag{A8}$$

and H_s is in meters in Eqs. (A5) and (A6).

The conditional PDF of u given H_s is represented by the 2-parameter Weibull PDF

$$p(u|H_s) = \beta \frac{u^{\beta-1}}{\theta^\beta} \exp\left[-\left(\frac{u}{\theta}\right)^\beta\right]; u \geq 0 \tag{A9}$$

with the Weibull parameters β and θ given as

$$\beta = c_1 + c_2 H_s^{c_3} \tag{A10}$$

$$\theta = c_4 + c_5 H_s^{c_6} \tag{A11}$$

with

$$(c_1, c_2, c_3) = (1.250, 5.600, 0.660) \tag{A12}$$

$$(c_4, c_5, c_6) = (0.050, 5.514, 0.280) \tag{A13}$$

and H_s is in meters in Eqs. (A10) and (A11).

References

- Bitner-Gregersen, E.M., 2015. Joint met-ocean description for design and operations of marine structures. *Appl. Ocean Res.* 51, 279–292. <https://doi.org/10.1016/j.apor.2015.01.007>
- Bruch, W., Piazzola, J., Branger, H., van Eijk, A.M.J., Luneau, C., Bourras, D., Tedeschi, G., 2021. Sea-spray-generation dependence on wind and wave combinations: A laboratory study. *Boundary-Layer Meteorology* 180 (3), 477–505. <https://doi.org/10.1007/s10546-021-00636-y>
- Bury, K.V., 1975. *Statistical Models in Applied Science*. John Wiley & Sons, New York, 646 pp.
- Cox, C., Munk, W., 1956. Slopes of the sea surface deduced from photographs of sun glitter. *Bull. Scripps Inst. Oceanogr.* 6, 401–488.
- Lenain, L., Statom, N.M., Melville, W.K., 2019. Aiborne measurements of surface wind and slope statistics over the ocean. *J. Phys. Oceanogr.* 49 (11), 2799–2814. <https://doi.org/10.1175/JPO-D-19-0111.1>
- Massel, S.R., 2007. *Ocean Waves Breaking and Marine Aerosol Fluxes*. Springer, New York, 232 pp.
- Tucker, M.J., Pitt, E.G., 2001. *Waves in Ocean Engineering*. Elsevier, Amsterdam, 521 pp.
- Veron, F., 2015. Ocean spray. *Annual Rev. Fluid Mech.* 47, 507–538. <https://doi.org/10.1146/annurev-fluid-010814-014651>
- Xu, X., Voermans, J.J., Ma, H., Guan, C., Babanin, A.V., 2021. A wind-wave-dependent sea spray volume flux model based on field experiments. *J. Mar. Sci. Eng.* 9, 1168. <https://doi.org/10.3390/jmse9111168>